JAERI-Review
97-011

REACTOR ENGINEERING DEPARTMENT ANNUAL REPORT

(April 1, 1996 - March 31, 1997)

October 1997

Department of Reactor Engineering

日本原子力研究所
Japan Atomic Energy Research Institute

本レポートは，日本原子力研究所が不定期に公刊している研究報告書です。
入手の問合わせは，日本原子力研究所研究情報部研究情報課（〒319-11 茨城県那珂郡東海村）あて，お申し越しください。なお，このほかに財団法人原子力弘済会資料センター（〒319-11 茨城県那珂郡東海村日本原子力研究所内）で複写による実費領布をおこなっております。

This report is issued irregularly.
Inquiries about availability of the reports should be addressed to Research Information Division, Department of Intellectual Resources, Japan Atomic Energy Research Institute, Tokai-mura, Naka-gun, Ibarakiken 319-11, Japan.

編集兼発行　日本原子力研究所
印　　刷　ニッセイエブロ株式会社

JAERI-Review 97-011

Reactor Engineering Department Annual Report

(April 1, 1996 – March 31, 1997)

Department of Reactor Engineering

Tokai Research Establishment
Japan Atomic Energy Research Institute
Tokai-mura, Naka-gun, Ibaraki-ken

(Received August 26, 1997)

This report summarizes the research and development activities in the Department of Reactor Engineering during the fiscal year of 1996 (April 1, 1996 – March 31, 1997).

The major Department's programs promoted in the year are the design activities of advanced reactor system and the development of a high power proton linear accelerator to constract an intense neutron source for innovative neutron science. Other Major tasks of the Department are various basics researches on the nuclear data and group constants, the developments of theoretical methods and codes, the reactor physics experiments and their analyses, the fusion neutronics, the radiation shielding, the reactor instrumentation, the reactor control/diagnosis, the thermal hydraulics and the technology developments related to the reactor engineering facilities, the accelerator facilities and the thermal hydraulic facilities. The cooperative works to JAERI's major projects such as the high temperature gas cooled reactor, the fusion reactor and PNC's fast reactor project were also progressed.

The activities of the research committees to which the Department takes a role of secretariat are also summarized in this report.

Keywords: Reactor Engineering Department Annual Report, Advanced Reactor System, Nuclear Data, Reactor Physics, Thermal hydraulics, Fusion Neutronics, Radiation Shielding, Reactor Instrumentation, Reactor Control, Diagnosis, Transmutation System, Proton Linear Accelerator

---

平成８年度原子炉工学部年報

日本原子力研究所東海研究所
原子炉工学部

（１９９７年８月２６日受理）

本報告は、平成８年度における原子炉工学部の研究活動状況をとりまとめたものである。

当該年度に原子炉工学部において推進された主要な研究活動は、新型炉の概念設計及び強力な中性子源を建設し新たな中性子科学研究を展開するための大強度線形陽子加速器の開発である。また、原子炉工学部では、基礎基盤研究として核データと群定数、炉理論及びコード開発、炉物理実験及び解析、核融合中性子工学、放射線遮蔽、原子炉計測及び計装、原子炉制御及び診断、伝熱流動並びに炉工学施設、加速器施設及び伝熱流動施設の技術開発を行っている。さらに、高温ガス炉、核融合等の日本原子力研究所プロジェクト研究及び動力炉・核燃料開発事業団の高速炉研究への協力も推進している。

本報告では、原子炉工学部が運営を担当する研究委員会の活動報告もとりまとめられている。

東海研究所：〒319-11　茨城県那珂郡東海村白方白根２－４

原子炉工学部英文年報編集委員会：

前川　洋（委員長）、大久保　努（副委員長）、渡辺　博典、竹内　末広、片倉　純一、藤村　統一郎、大井川　宏之、八木　秀之、鍋島　邦彦、中根　佳弘、功刀　資彰、今野　力、辻本　和文、草野　譲一、永井　良治、加藤　義夫、田所　啓弘、丸山　慎（事務局）

Contents

Preface

The research activities of the Department of Reactor Engineering, Japan Atomic Energy Research Institute, during the fiscal year 1996 (April 1996 – March 1997) are presented in this report. The activities of the Department cover the broad field : physics of fission reactor, fusion reactor neutronics, shielding, reactor instrumentation diagnosis and control, thermal hydraulics, conceptual design of new type reactor, and accelerator technologies focussing on intense beam.

The total number of permanent staff working in the Department during the year was 138. The Department was funded from JAERI expenditure amounting to 1,833 million yen for FY 1996, excluding nuclear fuel cost and personnel expense. About 469 million yen was provided by the research contracts with external organizations ; Science and Technology Agency (STA) for non-destructive measurement technology of trans-uranic elements (TRU), for the large scale reflood test program and for the thermal hydraulic demonstration test for high conversion PWR, Power Reactor and Nuclear Fuel Development Corporation (PNC) for reactor physics constants of fast breeder reactor and covariances of major actinide data.

The Department has served as secretariat of Japanese Nuclear Data Committee, the Research Committee on Reactor Physics, Atomic and Molecular Data Research Committee, the Research Committee on Advanced Reactors and Committee on the International Conference on Physics of Reactors PHYSOR96.

The research activities have been conducted in the following fourteen laboratories with the support of two divisions.

Nuclear Data Center

This center has two research themes; nuclear data and atomic & molecular data. As to nuclear data, the research activities consist of nuclear data evaluation for JENDL (General purpose file and Special Purpose File) and nuclear data measurements. Much efforts has been placed to the covariance file evaluation and to the planning of the strategic development for the next version of JENDL, i.e., JENDL-3.3. As to atomic & molecular data, main efforts are devoted to compilation and evaluation of atomic and molecular collision data and of atomic spectrum data.

This center has a function of the National Center which disseminates the nuclear and atomic & molecular data to Japanese customers, contacts the foreign and international centers and

coordinates the international collaboration. This center also serves as a secretariat of Japanese Nuclear Data Committee and of Atomic and Molecular Data Committee.

Reactor Analysis Laboratory

Major research theme of this laboratory is development and improvement of software (data/code) in reactor physics to serve for reactor design and analysis. It aims development of high speed, high accuracy Monte Carlo codes and nodal codes. Efforts is now concentrated to develop a comprehensive code system used for reactor core design including thermal hydraulics, core management and kinetics. Another theme is production of multi-group nuclear data libraries to apply to feasibility study and preconceptual design of new type reactors.

Reactor Physics Laboratory

Analyses on the measured data have been made on the safety related reactor physics parameters for fast reactor. The international β_{eff} benchmark experiments have being conducted at FCA with the foreign participants from France, Russia, the United States and Korea. The mock-up experiments for a nitride fast reactor and the GEM reactivity effect were carried out to verify the improved safety margin in reactivity coefficients. As a part of the OMEGA program, the measurements of the nuclear data and thermo-physical data of minor actinides were continued under collaboration with ORNL of the United States.

Reactor physics experiments have been carried out at the Very High Temperature Reactor Critical Assembly (VHTRC) to verify the neutronics design of the start-up core of the High Temperature Engineering Test Reactor (HTTR) under construction at the Oarai site. The critical mass of the annular core of the HTTR was studied in the VHTRC-9 core.

Sensing Technology Laboratory

This laboratory carries out R&D work in the field of instrumentation and measurement under two themes. One covers general subjects of the nuclear and reactor instrumentation widely, where performed are R&Ds of a new type of neutron detectors, nondestructive measuring technologies to assess the material degradation of reactor components, synthetic-diamond radiation detectors for high energy neutron spectroscopy, a pop-top type Ge detector combined with a small Stirling refrigerator for in-situ gamma-ray spectroscopy in various fields, etc. The other is specified to the nondestructive measurement of TRU waste drums, where both the active and passive neutron assays are applied together with gamma-ray CTs.

Control and AI Laboratory

The research program of this laboratory aims to establish basic technologies for the operational safety and hazardless maintenance of nuclear power plants. Advanced diagnosis system technologies such as early fault diagnosis based on neural networks, an expert system and a reactor noise analysis are being developed to improve the operational safety. For the inspecting patrol of nuclear power plants, a human and autonomous mobile robot collaborative system with the high safety and reliability is also being developed.

Applied Radiation Laboratory

In the accelerator radiation shielding study field, 1) neutron energy spectra were measured behind polyethylene shields bombarded with 40- and 65-MeV quasi-monoenergetic neutrons, 2) compilation was completed for results of benchmark calculations on transmission of the same neutrons through iron and concrete shields, 3) effective dose equivalent of protons higher than 20 MeV was evaluated with HERMES calculation. In the spallation study field, spallation experiments were conducted on ,1) tungsten target bombarded with 0.9 and 1.2 GeV protons and, 2) lead assembly bombarded with 500 MeV protons. Code validation and improvement were continued.

Heat Transfer and Fluid Flow Laboratory

The transient thermal-hydraulic test program was continued to verify the core integrity during design basis events (DBEs) of LWRs. First series of abnormal transient simulation tests for a PWR core was started in 1996 and it was confirmed experimentally that the core cooling is attained during PWR DBEs. The code development work and fundamental thermal-hydraulic tests were also performed to establish reliable thermal-hydraulic analysis tools for advanced LWRs, fusion reactors and components exposed to very high heat flux.

Fusion Neutronics Laboratory

The shielding neutronics experiments under the ITER/EDA R&D task has ended up with the experiments on gap streaming, nuclear heating and induced radioactivity, providing a full set of experimental data for validation of calculation codes and data. There has been a great progress in the decay heat measurements on a large number of materials conducted under ITER/EDA R&D Task. Extensive data testing of the state of art nuclear data libraries has contributed to the completion of FENDL-2. Under the IEA collaboration, integral experiments on vanadium at FNS, the experiment on the low activation material characteristics at FZK, an inter-comparison of the TLD measurement have been in significant proress.

Passive Safety Reactor Systems Laboratory

The main task of this laboratory is to develop an innovative concept of the JAERI Passive Safety Reactor (JPSR). Experimental and analytical works including the construction cost estimation have been performed to improve the design concept. The design study of the JPSR has been completed. Another task is to demonstrate the thermal-hydraulic feasibility of a Pu active storage PWR concept by large scale experiments. Experiments on hydraulic characteristics for the lower and upper plena have been conducted.

Transmutation System Laboratory

The main research program of this laboratory is the studies on transmutation systems. The conceptual design studies of transmutation system driven by a proton accelerator and the associated calculational code systems including a spallation cascade code are developed.
The preliminary design studies of the research facilities for the accelerator-driven transmutation system are also carried out in the Neutron Science Research Project.

Proton Accelerator Laboratory

The high-intensity proton accelerator with a beam power of 8MW has been proposed for the Neutron Science Project (NSP) in JAERI. Primary configurations and accelerator parameters for RFQ, DTL and superconducting high β linac have been evaluated in order to meet the various requirements for the NSP accelerator. After a test stand of superconducting cavity development had been constructed, a fabrication and test of a single cell cavity of β=0.5 have been conducted. The peak field measurements were successfully performed with the observed peak field of 16MV/m and 18.6 MV/m at 4.2 and 2.1K respectively, which exceeded the specification for the proposed cavity. Preliminary study of a storage ring for a 5MW pulsed beam for neutron scattering experiments has been started.

Free Electron Laser Laboratory

The JAERI optical resonator distance measurement and alignment system was developed to realize their errors of <0.5mm and <8mrad, respectively. In order to realize a very long pulse operation, we continued to develop and to improve the electron gun and RF amplifier systems. Amplified spontaneous emission and intermittent oscillation in the wave length of around 29 mm have been observed by using the photoconductive Ge(Cu) detectors. The JAERI superconducting rf linac as an FEL driver was successfully operated to get an electron beam ranging from 14 to 23 MeV with an accelerating voltage of 4～8 MV/m, beam current of 7～14 A, and micropulse width of 40～16 ps.

Intense Neutron Source Laboratory

International Fusion Materials Irradiation Facility-Conceptual Design Activity (IFMIF-CDA) has been carried out under the IEA Co-operative Program. A final report and a cost report of the IFMIF-CDA have been completed and reported to the IEA Fusion Program Coordinative Committee (FPCC). The design studies of accelerator and target system will be continued for next phase.

Energy System Assessment Laboratory

In the research on energy system assessment, the development was promoted on the analytical model for estimating regional damages of air pollution, and on computer programs for using MARKAL and JALTES-II on personal computers. In the field of analytical studies, the potential of CO_2 emission reduction and its costs were analyzed for Japan in the common assessment of IEA/ETSAP (Energy Technology Systems Analysis Program) Annex-VI. In addition, the analysis was made on the role of high temperature nuclear heat in future energy systems of Japan. In the field of technology assessment, the new efficient system was designed for the UT-3 hydrogen production process by applying adiabatic reactors.

Reactor Engineering Facility Operation Division

This division operated four large-scale engineering facilities : FCA, VHTRC, FNS and Heat Transfer Fluid Flow Test Facilities in accordance with each experiment program and maintained in the monthly or the annual inspection. Consequently safety operations of these facilities were achieved and contributed sufficiently to the execution of each experimental study. Furthermore the experimental operation of VHTRC was closed by the achievement of final purpose of verification the calculation accuracy related to the nuclear design of HTTR.

Accelerators Division

The 20UR tandem accelerator and the super-conducting booster were operated as scheduled for various experiments. Almost all of the research programs have been successfully achieved. The development of a satellite control console of the tandem accelerator completed in March 1997 and began to assist the booster operation. An in terminal heavy ion injector using a compact ECR ion source was being developed, which will be useful to accelerate inert gas ions.

The Department is involved in the following project-oriented programs of JAERI;

(1) Design Studies of advanced reactors

(2) Technology development for OMEGA program

(3) Development of a high intensity proton accelerator

(4) Development of High Temperature Gas-cooled Reactor

(5) Engineering research for fusion reactor

The activities of the Department in FY 1996 have contributed to the essential progress in the field of reactor engineering.

Masayuki Nakagawa, Director

Department of Reactor Engineering

August 20, 1997

1. Nuclear Data, and Atomic and Molecular Data

Evaluation for JENDL Special Purpose Files has been progressed. As to the Covariance File development, estimation of uncertainties in resonance parameters of Fe-56, Pu-239, Pu-240 and U-238 was made for JENDL-3.2 data based on the measurement data. Covariance matrices of neutron cross sections for Cr-52, Fe-56, Ni-58 and Ni-60 were also evaluated. A completely new evaluation for neutron nuclear data of stable mercury isotopes(from Hg-196 to Hg-204) was made mainly based on the model calculations due to the lack of experimental data. As to the JENDL Intermediate Energy Files development, steady progress is continuing for JENDL High Energy File, JENDL PKA/KERMA File and JENDL Photonuclear data file. As to the JENDL Actinide File development, soft-rotator model analysis of collective band structures of even-even actinide nuclei was made. From this study, systematic trends of the parameters found could be guide to estimate the collective band structure of nuclei for which such data are poorly known.

Benchmark calculations were made in order to devise the data for the final FENDL/E-2.0 selection. Six materials were tested with Japanese fusion neutronics benchmark experiments using by MCNP-4A code.

Measurements of activation cross sections have been continued using JAERI facilities. An experimental program for measurements of neutron activation cross section at 17.5 to 30 MeV region has been progressed using JAERI TANDEM facility. Activation cross section measurements for (n,n α) reactions near 14 MeV were made using FNS facility. Activation cross sections for lanthanide isotopes at 14 MeV measured at FNS were also reported.

Mass chain evaluation has been continued within the international framework for ENSDF. The evaluation of mass chain A=129 were completed and published in Nuclear Data Sheets.

Decay and fission yield data library has been produced using JNDC library for ORIGEN 2 code to allow consistent calculation with AESJ recommended values in the decay heat calculations.

As to the atomic and molecular data, critically compiled spectroscopic data of highly ionized atoms for Ti, V, Cr, Mn, Fe, Co, Ni, Cu, Kr and Mo have been published. Analytic cross sections for collision of electrons with hydrocarbon molecules were obtained using modification of semi-empirical theory developed by Green and McNeal. These data are destined to be used in fusion energy devices development.

1.1 Estimation of Uncertainties in Resonance Parameters of ^{56}Fe, ^{239}Pu, ^{240}Pu and ^{238}U

T. Nakagawa and K. Shibata

(*E-mail:* nakagawa@cracker.tokai.jaeri.go.jp)

Uncertainties were estimated for the resonance parameters of ^{56}Fe, ^{239}Pu, ^{240}Pu and ^{238}U contained in JENDL-3.2. Errors of the parameters were determined from the measurements which the JENDL-3.2 evaluation was based on.

The resolved resonance parameters of ^{56}Fe were obtained from an analysis performed by Perey et al.[1] for most resonances except 27.7 keV s-wave and 1.15, 264, 357 keV p-wave ones. We adopted the standard deviations of neutron and radiative widths and the correlation coefficients obtained by them. The uncertainties in the four resonances mentioned above are given in Table 1.1.1.

Table 1.1.1 Resonance parameters and their standard deviations

Resonance	Γ_n (eV)	Γ_γ (eV)
1.15 keV p-wave	0.0617±0.0009	0.574±0.040
27.7 keV s-wave	1420±60	1.4±0.1
264 keV p-wave	0.7±0.3	0.64±0.3
357 keV p-wave	1000±100	1.0±0.1

The JENDL-3.2 evaluation of ^{239}Pu resolved resonance parameters were based on the work of Derrien[2] in the energy region below 2.5 keV. Derrien obtained covariances of the resonance parameters, and they were available in the energy range from 1 to 2.5 keV. The parameters and their standard deviations of the Reich-Moore type were converted to the ones of the Breit-Wigner type for estimating the uncertainty in self-shielding calculations. The uncertainties in unresolved resonance parameters were determined from calculations using the ASREP[3] code, and are given as follows: ΔD=5%, ΔS_0=10%, ΔS_1=15%, $\Delta\Gamma_f$(0+,1+)=15%, $\Delta\Gamma_f$(0-,1-,2-)=20% and $\Delta\Gamma_\gamma$=10%.

As for ^{240}Pu, the resolved resonance parameters are given in JENDL-3.2 below 4 keV. The width parameters for the 1.056 eV resonance were determined from those values given by Liou and Chrien[4] which are slightly different from the ones of Spencer et al.[5] Therefore, in the present work, the uncertainties were somewhat enlarged as compared with the original

ones given by Liou and Chrien, as shown in Table 1.1.2.

Table 1.1.2 1.056 eV resonance parameters

References	Γ_n (meV)	Γ_γ (meV)
Present work	2.32±0.12	32.4±2.0
ENDF/B-VI	2.45	30.6
Liu and Chrien[4]	2.32±0.06	32.4±0.6
Spencer et al.[5]	2.45±0.02	30.3±0.3

The uncertainties in the unresolved resonance parameters of ^{240}Pu are as follows: ΔD=5%, ΔS_0=10%, ΔS_1=30%, $\Delta \Gamma_f$=30% and $\Delta \Gamma_\gamma$=2 meV.

Concerning ^{238}U, the uncertainties in resonance energies were derived from the measurements of Olsen et al.[6,7] The errors of the neutron and radiative widths were based on the work of Olsen et al.[6,7] and Moxon et al.[8] An analysis of the ASREP calculation gave errors on the unresolved resonance parameters, i.e., ΔD=5%, ΔS_0=13%, ΔS_1=18%, ΔS_2=20% and $\Delta \Gamma_\gamma$=1.5%.

References

1) Perey F.G., et al.: Proc. Specialists' Meeting on Neutron Data of Structural Materials for Fast Reactors, Geel 1977, p.530 (1979), Pergamon Press.

2) Derrien H.: J. Nucl. Sci. Technol., 30, 845 (1993).

3) Kikuchi Y.: Unpublished.

4) Liou H. and Chrien R.E.: Proc. IAEA Consultants' Meeting on Uranium and Plutonium Isotope Resonance Parameters, Vienna 1981, INDC(NDS)-129/GJ, p.438 (1981).

5) Spencer R.R., et al.: Nucl. Sci. Eng., 96, 318 (1987).

6) Olsen D.K., et al.: Nucl. Sci. Eng., 69, 202 (1979).

7) Olsen D.K., et al.: Proc. Int. Conf. Nuclear Cross Sections for Technol., Knoxville 1979, p.677 (1980).

8) Moxon M.C., et al.: Proc. 1988 Int. Reactor Physics Conference, Jackson Hole 1988, I-282 (1988).

1.2 Evaluation of Covariance Data for Chromium Iron, and Nickel Contained in JENDL-3.2

S.Y. Oh* and K. Shibata

(*E-mail:* shibata@cracker.tokai.jaeri.go.jp)

An evaluation has been made for the covariances of neutron cross sections of ^{52}Cr, ^{56}Fe, ^{58}Ni and ^{60}Ni contained in JENDL-3.2. Reactions considered are threshold reactions such as (n,2n), (n,nα), (n,np), (n,p), (n,d), (n,t), and (n,α), a radiative capture reaction above the resonance region, and inelastic scattering to discrete and continuum levels. Evaluation guidelines and procedures were established during the work.

A generalized least-squares fitting code GMA[1] was used in estimating covariances for reactions of which JENDL-3.2 cross sections had been evaluated by taking account of many measured data. Figure 1.2.1 shows the ^{56}Fe(n,p) cross section and standard deviation obtained from the GMA analysis. For cross sections that had been evaluated by nuclear model calculations, a code KALMAN[2], which yields covariances of associated model parameters on the basis of the Bayesian statistics, was used in conjunction with nuclear model codes EGNASH[3] and CASTHY[4].

The evaluated uncertainties of a few % to 30 % in the cross sections look reasonable, and the correlation matrices show understandable trends. Even though there is no strict way to confirm the validity of the evaluated covariances, the tools and procedures adopted in the present work are appropriate for producing covariance files based on JENDL-3.2. The covariances obtained will be compiled into JENDL in the near future. Meanwhile, new sets of optical model and level density parameters are proposed by one of byproducts obtained from the KALMAN calculation.

References

1) Poenitz W.P.: Proc. Conf. Nuclear Data Evaluation Methods and Procedures, BNL-NCS-51363, p.249 (1981).

---

* An STA fellow from KAERI, Korea, during June 1996 – December 1996.

2) Kawano T.: To be published (1997).

3) Yamamuro N.: "A Nuclear Cross Section Calculation System with Simplified Input-Format, Version II (SINCROS-II)", JAERI-M 90-006 (1990).

4) Igarasi S. and Fukahori T.: "Program CASTHY – Statistical Model Calculation for Neutron Cross Sections and Gamma Ray Spectrum", JAERI 1321 (1991).

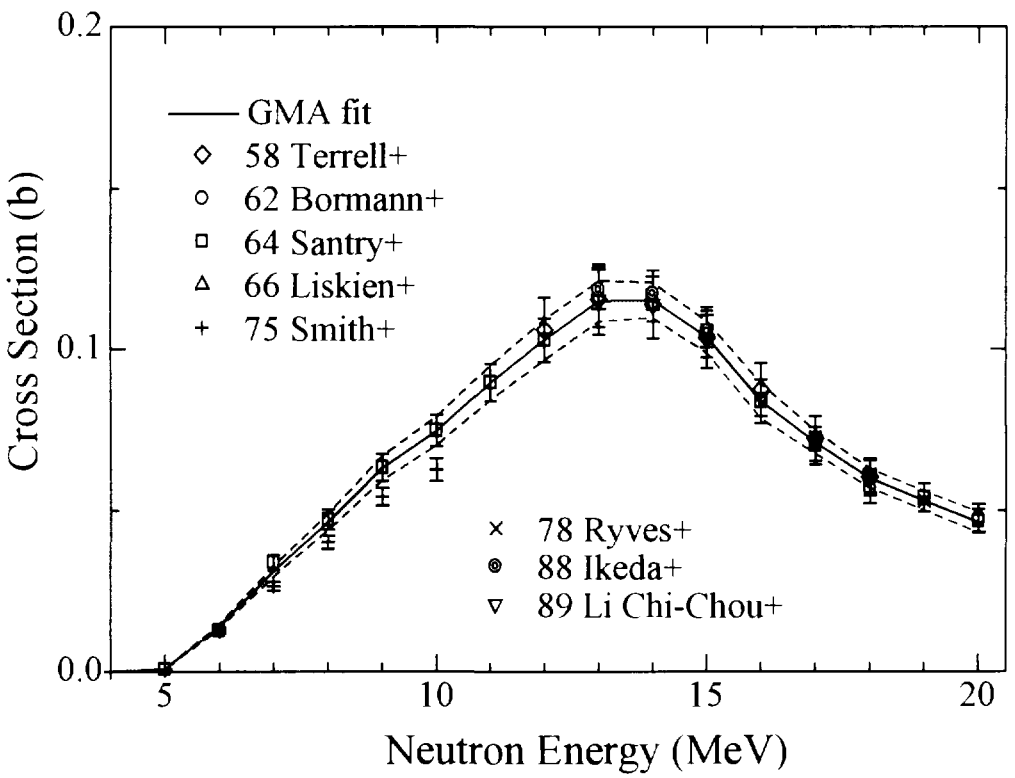

Fig. 1.2.1 ^{56}Fe(n,p) reaction cross section

1.3 Evaluation of Neutron Nuclear Data for Mercury

K. Shibata, T. Fukahori, S. Chiba and N. Yamamuro*
(*E-mail:* shibata@cracker.tokai.jaeri.go.jp)

Neutron nuclear data of stable mercury isotopes (^{196}Hg, ^{198}Hg, ^{199}Hg, ^{200}Hg, ^{201}Hg, ^{202}Hg, and ^{204}Hg) have been evaluated in the energy range of 10^{-5} eV to 20 MeV. The evaluation is mainly based on nuclear model calculations since experimental data are very scarce.

Resolved resonance parameters were given in the energy region below the following energy for each isotope except ^{204}Hg: 102.85 eV for ^{196}Hg, 459.14 eV for ^{198}Hg, 968 eV for ^{199}Hg, 8.58 keV for ^{200}Hg, 753.5 eV for ^{201}Hg, and 4.52 keV for ^{202}Hg. No background cross section was applied in the resonance region.

The resonance parameters were taken from the compilation of Mughabghab[1]. The multi-level Breit-Wigner was adopted to represent cross sections in the resonance region. No resonance parameters are given for ^{204}Hg. The scattering radius for each isotope was adjusted so as to reproduce measured total cross sections of natural mercury.

A computer code system SINCROS-Ⅱ[2], which is based on the multi-step Hauser-Feshbach code GNASH[3], was used to calculate the cross sections for the reactions (n,2n), (n,3n), (n,p), (n,d), (n,α), (n,np), and (n,nα). The calculation included the precompound process as well as the compound one. The cross section for the direct-interaction process of inelastic scattering was calculated by using the DWUCK[4] code, and it was fed into the SICROSS-Ⅱ code. Figure 1.3.1 shows the calculated (n,2n) cross section of ^{204}Hg together with measurements. In addition to cross sections, energy distributions of secondary neutrons and gamma-rays were obtained from the calculation, while their angular distributions were assumed to be isotropic in the laboratory system.

A statistical model code CASTHY[5] was applied to calculate the cross sections for the elastic and inelastic scattering, and the radiative capture together with the angular distributions of scattered neutrons. The cross sections for the competing process were provided by the SINCROSS-Ⅱ calculation. Then, the inelastic scattering cross section was given as a sum of the cross sections calculated by CASTHY and DWUCK.

---

* Data Engineering, Ltd.

The presently evaluated data have been compiled in the ENDF-6 format.

References

1) Mughabghab S.F.: "Neutron Cross Sections", Vol. 1, Part B, 1984, Academic Press.
2) Yamamuro N.: "A Nuclear Cross Section Calculation System with Simplified Input-Format, Version II (SINCROS-II)", JAERI-M 90-006 (1990).
3) Young P.G. and Arthur E.D.: LA-6947 (1977).
4) Kunz P.D.: Unpublished.
5) Igarasi S. and Fukahori T.: "Program CASTHY - Statistical Model Calculation for Neutron Cross Sections and Gamma Ray Spectrum", JAERI 1321 (1991).

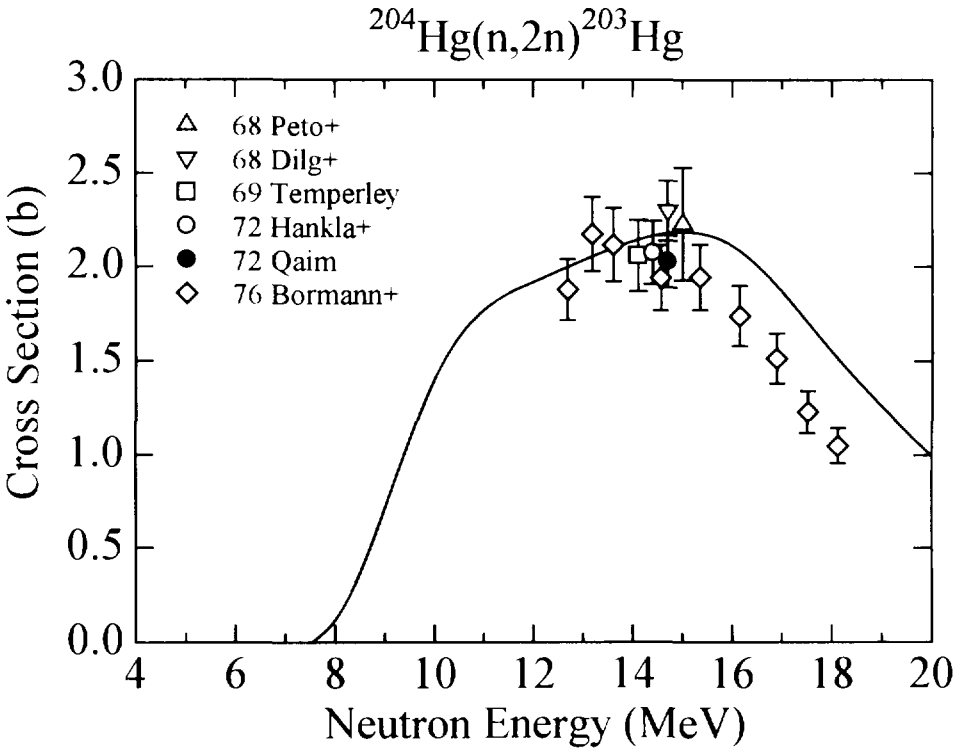

Figure 1.3.1 ^{204}Hg(n,2n) reaction cross section

1.4 Nuclear Data Evaluation and Compilation for JENDL Intermediate Energy Files

T. Fukahori and Japanese Nuclear Data Committee
(*E-mail*: fukahori@cracker.tokai.jaeri.go.jp)

The JAERI Nuclear Data Center started evaluation work in cooperation with Japanese Nuclear Data Committee (JNDC) to produce files related intermediate energy, which are JENDL High Energy File, JENDL PKA/KERMA File and JENDL Photonuclear Data File. In this paper, present status of these files are reported.

The JENDL High Energy File includes nuclear data for proton- and neutron-induced reactions. The evaluation work is separated into two phases. The energy range of the phase-I is up to 50 MeV, mainly for the International Fusion Material Irradiation Facility (IFMIF) [1]. The energy range for the phase-II is up to 2 GeV mainly for a project of JAERI Neutron Science Research Center. Below 20 MeV, the data of JENDL Fusion File[2] or JENDL-3.2[3] are adopted basically. The elements included in the JENDL High Energy File are summarized in Table 1.4.1. As an example of evaluated results, evaluated data of ^{209}Bi(n,xn) cross sections are compared with experimental data in Fig. 1.4.1. Though the experimental data by Tohoku University were measured after the evaluation, the evaluated results can reproduce the data satisfactory.

The JENDL Photonuclear Data File is being developed for gamma-ray induced reaction data up to 140 MeV. The photon absorption cross section is evaluated with the giant dipole resonance model and quasi-deuteron model, and the decaying processes are estimated with the statistical model with preequilibrium correction by using MCPHOTO and ALICE-F codes. The isotopes shown in Table 1.4.2 are included in the file. The evaluation work is now in a final stage.

The JENDL PKA/KERMA File is generated to supply primary knock-on atom (PKA) spectra, damage energy spectra, DPA (displacement per atom) cross sections and kerma factors by neutron-induced reactions in the energy region up to 50 MeV. The elements included in the file are listed in Table 1.4.3. A processing code system, ESPERANT[4] was developed to calculate above quantities from evaluated nuclear data file by using effective single particle emission approximation (ESPEA). As a trial task of ESPERANT, files of PKA spectra and

KERMA factors for 69 nuclides from F to Bi in the energy region up to 20 MeV have been generated for fusion application (FENDL-2 project) [5] from the JENDL Fusion File. For light mass nuclei, SCINFUL/DDX code which considers break-up reactions with PKA spectra is used as well as EXIFON code which can calculate with correction of preequilibrium process.

The present status of the JENDL Intermediate Energy Files was reported. In the first step of the JENDL High Energy File, evaluation work was concentrated to the neutron data below 50 MeV. The JENDL PKA/KERMA File will be produced just after the phase-I evaluation work for the JENDL High Energy File is finished.

References

1) Noda K.: Proc. of 1994 Symposium on Nuclear Data, Tokai, Japan, Nov. 17-18, 1994, JAERI-Conf 95-008, p.112 (1995).
2) Baosheng Y., et al.: J. Nucl. Sci. Technol., **29** 677 (1992).
3) Nakagawa T., et al.: ibid., **32** 1259 (1995).
4) Fukahori T., et al.: Proc. of the Third Specialists' Meeting on Nuclear Data for Fission Reactors, Tokai, Japan, Nov. 29-30, 1995, JAERI-Conf 96-005, p.130 (1996).
5) Ganesan S. and McLaughlin P.K.: "FENDL/E: Evaluated Nuclear Data Library of Neutron Nuclear Interaction Cross-Sections and Photon Production Cross-Sections and Photon-Atom Interaction Cross-Sections for Fusion Applications," IAEA-NDS-128 Rev.1 (1995).

Table 1.4.1 The elements to be included in the JENDL High Energy File

Phase-I (for neutron, < 50 MeV): 31 elements, 81 isotopes H, Li, Be, B, C, N, O, Na, Mg, Al, Si, Cl, K, Ca, Ti, V, Cr, Mn, Fe, Co, Ni, Cu, Ge, Y, Zr, Nb, Mo, W, Au, Pb, Bi
Phase-I (for proton, < 50 MeV): 14 elements, 42 isotopes Li, C, Al, Si, Cr, Fe, Ni, Cu, Nb, Mo, W, Ta, Pb, Bi
Phase-II (for neutron and proton, < 2 GeV): 39 elements, 101 isotopes H, Li, Be, B, C, N, O, F, Na, Mg, Al, Si, Cl, Ar, K, Ca, V, Cr, Mn, Fe, Co, Ni, Cu, Zn, Y, Zr, Nb, Mo, W, Au, Hg, Pb, Bi, Th, U, Np, Pu, Am, Cm

Underline: Evaluation has been finished.

Table 1.4.2 The nuclei to be included in the Photonuclear Data File

27 elements, 48 isotopes
^{2}H, ^{12}C, ^{14}N, ^{16}O, ^{23}Na, ^{24,25,26}Mg, ^{27}Al, ^{28,29,30}Si, ^{40,48}Ca, ^{46,48}Ti, ^{51}V, ^{52}Cr, ^{55}Mn, ^{54,56}Fe, ^{59}Co, ^{58,60,61,62,64}Ni, ^{63,65}Cu, ^{64}Zn ^{90}Zr, ^{93}Nb, ^{92,94,96,98,100}Mo, ^{181}Ta, ^{182,184,186}W, ^{197}Au, ^{206,207,208}Pb, ^{209}Bi, ^{235,238}U

Underline: Evaluation has been finished.

Table 1.4.3 The elements to be included in the PKA/KERMA File

29 elements, 78 isotopes
H, Li, Be, B, C, N, O, F, Na, Mg, Al, Si, Cl, K, Ca, Ti, V, Cr, Mn, Fe, Co, Ni, Cu, Zr, Ge, Nb, Mo, W, Pb, Bi

Underline: Processing from JENDL Fusion File blow 20 MeV has been finished.

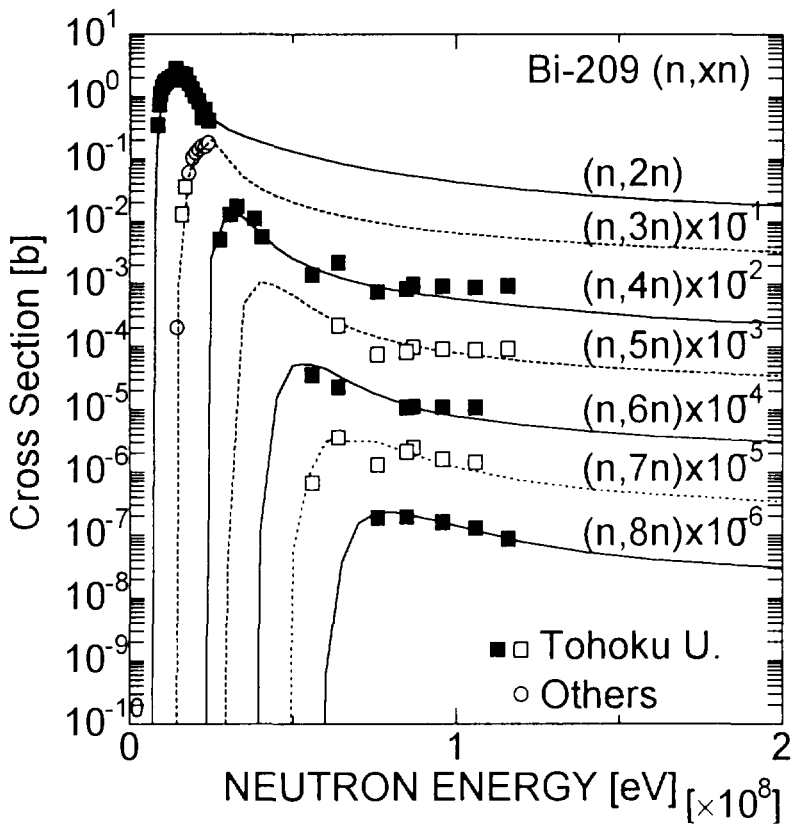

Fig. 1.4.1 Cross section for ^{209}Bi(n,xn)$^{210-x}$Bi reactions

1.5 Soft-rotator Model Analysis of Collective Band Structures of Even-even Actinide Nuclei

O. Iwamoto, S. Chiba and R. Kuwata*

(*E-mail:* iwamoto@cracker.tokai.jaeri.go.jp)

Positive-parity collective band structures of low-lying levels in even-even actinide nuclei were analyzed based on an extension[1] of the Davydov-Chaban soft rotator model,[2] which accounts for the rotation and β- and γ-vibrations of even-even nuclei with non-axial quadrupole deformation. The parameters to reproduce the 4-bands, i.e., the ground-state (G.S.) rotational band, the K $\approx$ 2 band, and the $n_\beta = 1$ and $n_\gamma = 1$ bands, were obtained, and their systematic trends were deduced.[3] The systematic trends of the parameters found in this work could be a guide to estimate the collective band structure of nuclei for which such data are poorly known.

The calculated band structure of ^{234}U is compared in Fig. 1.5.1 with the experimental data. The left part of this figure shows the experimentally-known band structure, and the right one was obtained by using the best-fit parameters for this nucleus. As demonstrated by this figure the soft-rotator model reproduces the structure of the ground-state rotational band, K $\approx$ 2 band, $n_\gamma = 1$ band, and $n_\beta = 1$ band very satisfactorily. Similar degree of agreement was obtained for ^{238}Pu and ^{246}Cm for which these 4 bands are known well.

The parameters have been obtained for ^{230,232}Th, ^{232,234,236,238}U, ^{238}Pu and ^{246}Cm nuclei. The systematic trends of parameters have been represented by quadratic or linear curves as a function of β_0, which were deduced by fitting with the least square method. As a way to assess the validity of the systematics of the parameters, the band structure of ^{244}Pu was calculated using $\beta_0 = 0.2931$. The result is compared with the experimental data in Fig. 1.5.2. Agreement of the present prediction with the experimental data is reasonably good. However, the energies of the high-spin states in the G.S. rotational band tend to be underpredicted. On the other hand, the 2^+ level around 1 MeV is

*Kyushu University

well explained as the band head of K $\approx$ 2 band. The soft-rotator model predicts the energies for n_β=1 and n_γ = 1 bands which are not known experimentally. Such ability of predicting the collective band structures will be a powerful aid in the coupled-channel and statistical model calculations of neutron cross sections for minor actinides because the inelastic-scattering (both by direct and statistical processes) to these low-lying discrete levels is one of the dominant reactions for minor actinides.

References

1) Porodzinskiĭ Y.V., Sukhovitskiĭ E.S.: Sov. J. Nucl. Phys. **53**, 41(1991).

2) Davydov A.S., Chaban A.A.: Nucl. Phys. **20**, 499(1960).

3) Iwamoto O., Chiba S., Kuwata R.: J. Nucl. Sci. Tech. **34**, 490(1997).

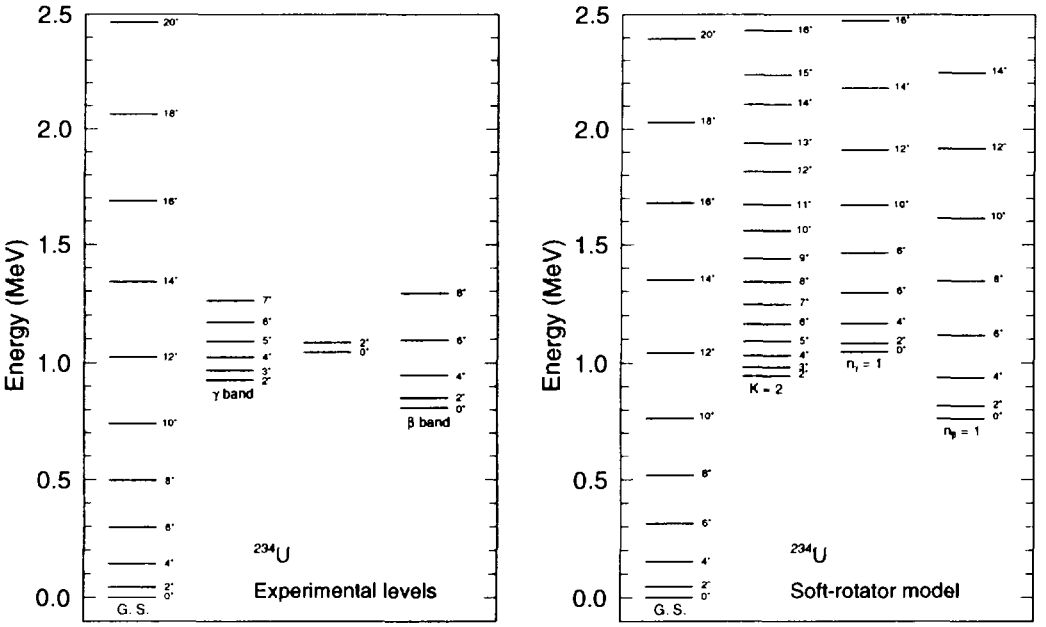

Fig. 1.5.1 Collective band structure of ^{234}U. Left: experimentally known levels, Right: levels calculated by the soft-rotator model.

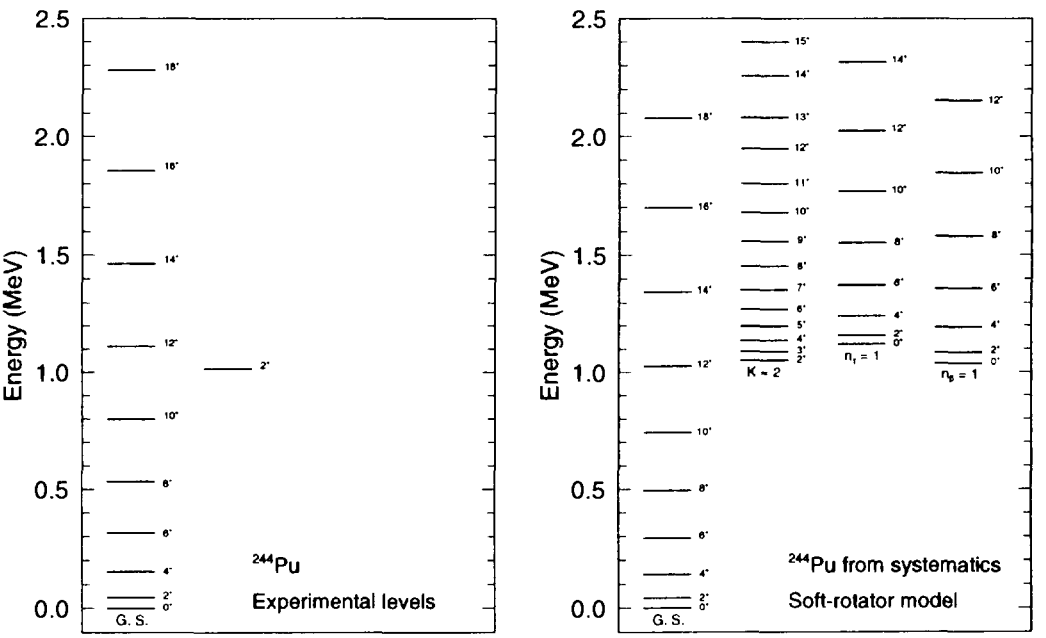

Fig. 1.5.2 Collective band structure of ^{244}Pu. Left: experimental data, Right: prediction of the soft-rotator model with the systematic trend of parameters.

1.6 Benchmark Calculation for the Final FENDL/E-2.0 Selection

F. Maekawa, M. Wada, C. Ichihara* and Y. Oyama
(*E-mail:* fujio@fnshp.tokai.jaeri.go.jp)

FENDL is the international reference nuclear data library for fusion applications, available from the IAEA. The first version of the general purpose FENDL library, FENDL/E-1.0, has been available since May, 1994. Cross section data for many isotopes in FENDL/E-1.0 have been updated by newly evaluated cross section data from national libraries, i.e., JENDL Fusion File [1] (Japan), ENDF/B-VI (USA), EFF-3 (European Union), BROND-2 (Russia) and CENDL (China), to produce FENDL/E-2.0. Benchmark testing of the candidate cross sections with fusion neutronics integral experiments was conducted for the update. In June, 1996, the IAEA Consultants' Meeting on Selection of Basic Evaluations for the FENDL-2 Library was held at Karlsruhe, Germany. [2] Results of the benchmark testing as well as microscopic cross section data were examined at the meeting, and the consultants selected the best evaluation for FENDL/E-2.0 for each isotope. These selected evaluations were approved finally at the IAEA Advisory Group Meeting on Extension and Improvement of the FENDL Library for Fusion Applications held at Vienna, Austria, March 1997. However, further actions were requested for some of the selected evaluations by the meeting. According to the request, we performed benchmark calculations as a part of the further actions.

The continuous energy Monte Carlo code MCNP-4A [3] was used for transport calculations. Six materials, i.e., carbon, nitrogen, silicon, iron, niobium and molybdenum, were tested with Japanese fusion neutronics benchmark experiments [4] conducted at D-T neutron source facilities, OKTAVIAN/Osaka University and FNS/JAERI.

Carbon: JENDL Fusion File was adopted as the base data. However, the elastic scattering cross section of carbon in the energy region approximately below the first excited level of ^{12}C at 4.4 MeV, was suggested to be replaced with ENDF/B-VI data by Nuclear Data Center (NDC) of JAERI. As a result of benchmark calculations with the FNS-TOF and FNS-Slab experiments, although no significant improvement due to the replacement is found as shown in Fig. 1.6.1, calculated results show good agreements with the experimental data.

Nitrogen: JENDL Fusion File was adopted basically. Both the (n,p) cross section above 6 MeV and the (n,γ) cross section in FENDL/E-1.0, which showed better agreement with microscopic experimental data compared to JENDL Fusion File, were implanted

---

* Research Reactor Institute, Kyoto University

in JENDL Fusion File by NDC. Although no significant improvement due to the implantation is found, the calculated results with the new cross section data agree well with the experimental data.

Silicon: New ENDF/B-VI evaluations for silicon isotopes, which were based on an accurate and high-resolution total cross section measurement, were submitted. The OKTAVIAN experiment was analyzed by the ENDF/B-VI data and the other candidate of JENDL Fusion File. As shown in Fig. 1.6.2, the calculated spectrum with ENDF/B-VI agrees with the measured spectrum as a whole while JENDL Fusion File gives larger spectrum fluxes below 1 MeV. The adoption of the ENDF/B-VI evaluations for FENDL/E-2.0 is reasonable.

Iron: The EFF-3 evaluation for ^{56}Fe was nominated because it was the unique evaluation based on an ultra-high resolution total cross section measurement in the unresolved resonance energy region up to ~ 7 MeV. The FNS experiments were analyzed with EFF-3 and FENDL/E-1.0. As a whole, both evaluations give similar results for neutron, and agree well with the experimental data. Figure 1.6.3 shows calculated to experimental (C/E) ratios of the ^{115}In(n,n')^{115m}In reaction rate which is mainly sensitive to 0.5-10 MeV neutrons, approximately corresponding to the unresolved energy region of iron. Both calculations give very good agreement with the measured data.

Niobium and Molybdenum: JENDL Fusion File was selected for both elements. According to the request, the total cross section between 0.5 and 4 MeV was modified and the (n,α) cross section was newly evaluated for niobium, and the (n,γ) cross section was re-evaluated for molybdenum, by NDC. As a result, prediction of the leakage neutron spectra of the OKTAVIAN experiment is improved for both elements. Figure 1.6.4 shows the molybdenum case.

In conclusion, these benchmark tests demonstrated validity of the modifications and newly submitted evaluations for the final FENDL/E-2.0 selection.

References

1) Chiba S., et al.: "Evaluation of the Double-Differential Cross Sections of Medium-Heavy Nuclei for JENDL Fusion File", JAERI-Conf 96-005, pp. 45-54 (1996).
2) Pashchenko A. B.: INDC(NDS)-356, IAEA (1996).
3) Briesmeister J. F. (Ed.): "MCNP - A General Monte Carlo N-Particle Transport Code, Version 4A", LA-12625-M, Los Alamos National Laboratory (1993).
4) Sub Working Group of Fusion Reactor Physics Subcommittee (Ed.): "Collection of Experimental Data for Fusion Neutronics Benchmark", JAERI-M 94-014 (1994).

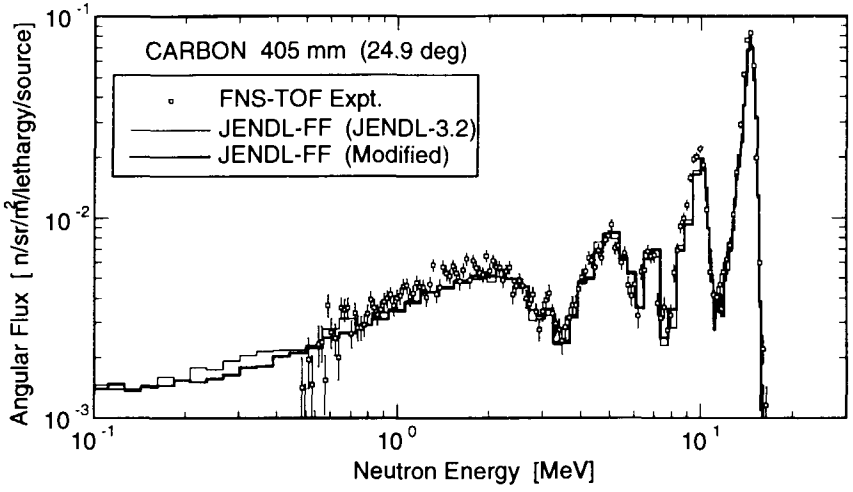

Fig. 1.6.1 Measured and calculated neutron spectra leaking from a carbon slab for the FNS-TOF experiment

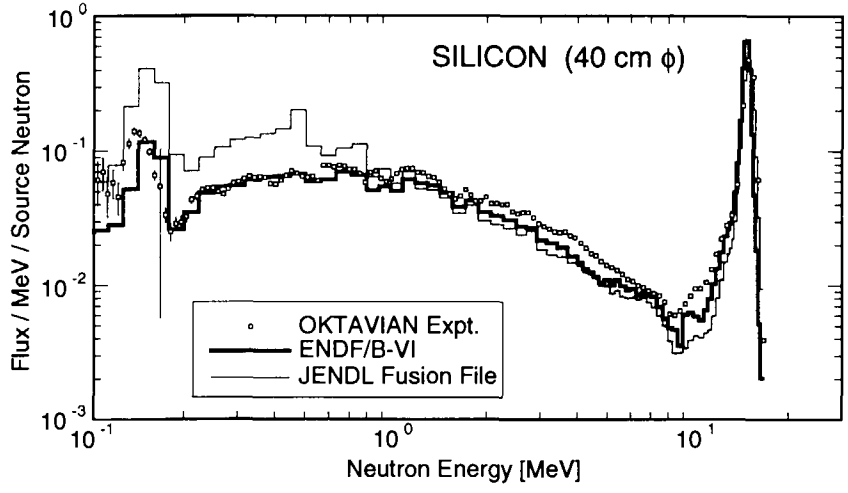

Fig. 1.6.2 Measured and calculated neutron spectra leaking from a silicon sphere for the OKTAVIAN experiment

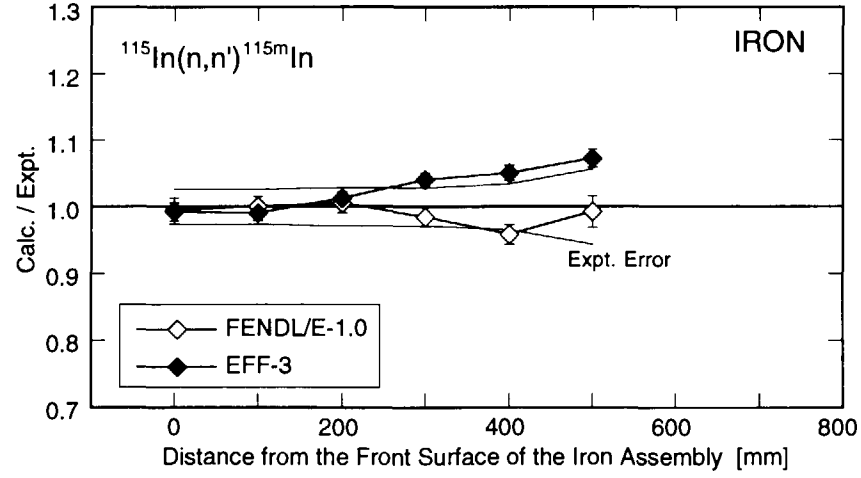

Fig. 1.6.3 C/E ratios of the $^{115}In(n,n')^{115m}In$ reaction rate for the FNS-Slab experiment on iron

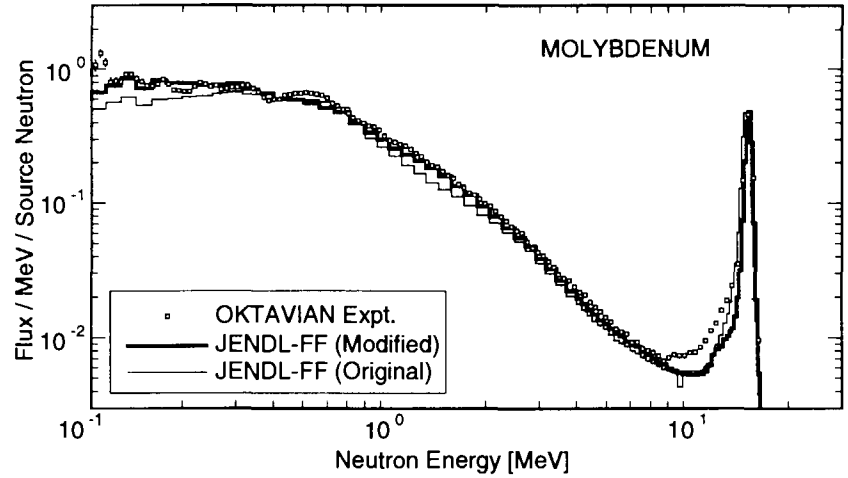

Fig. 1.6.4 Measured and calculated neutron spectra leaking from a molybdenum sphere for the OKTAVIAN experiment

1.7 Measurement of Activation Cross Sections for the Neutron Dosimetry at an Energy Range from 17.5 to 30 MeV by Using ^{7}Li(p,n) Quasi-monoenergetic Neutron Source (II)

Y. Uno, S. Meigo, S. Chiba, T. Fukahori, Y. Kasugai, O. Iwamoto and Y. Ikeda
(*E-mail:* uno@fnshp.tokai.jaeri.go.jp)

Since 1993, an experimental program for measurements of the neutron activation cross sections at 17.5-30.0 MeV region has been continued for high energy neutron dosimetry application. Cross sections of 24 reactions for Al, Co, Cu, Y, Nb, Tm , Au, ^{48}Ti and ^{58}Ni were measured in previous years. The second series of experiment for ^{45}Sc, nat-Cr, nat-Zn, nat-Rb, ^{103}Rh, nat-Ir, ^{52}Cr, ^{90}Zr and ^{65}Cu was performed in this fiscal year. The measured reactions are tabulated in Table 1.7.1.

Protons of 20.0, 22.5, 25.0, 27.5, 30.0 and 32.0 MeV were impinged on the thin ^{7}Li target (~ 2.0 mm thickness) and neutrons via the ^{7}Li(p,n) reaction were produced by using the JAERI TANDEM accelerator facility. The ^{7}Li target was cooled by water and protons passing through the target completely stopped in the cooling water layer behind the target. The neutron energy spectrum for each proton energy was measured by the time of flight (TOF) technique incorporating with an NE213 scintillation counter. The measured energy spectra are shown in Fig. 1.7.1. The energy spectrum of this neutron source has a quasi-monoenergetic peak corresponding to the combined reaction of ^{7}Li(p,n)^{7}Be[0.0 MeV] and ^{7}L(p,n)^{7*}Be[0.429 MeV]. The absolute flux of the peak neutrons was determined by a proton recoil telescope (PRT) counter.

The samples for the cross section measurement were irradiated in the forward direction. After each irradiation, γ-rays from the irradiated samples were measured with HP-Ge detectors. From the net count of full-energy peak of interest, the reaction rate was derived after necessary corrections. As shown in Fig. 1.7.1, there are a large amount of neutrons in a tail region below the peak corresponding to a breakup reaction of ^{7}Li(p,n) and reactions between protons and water. Therefore, the contribution of tail neutrons to the obtained reaction rate should be subtracted. The correction factor F was calculated by using the measured neutron spectrum $\phi(E)$ and estimated cross section $\sigma_{ref}(E)$ as follows:

$$F = \frac{\int_{peak} \phi(E) \cdot \sigma_{ref}(E)\ dE}{\int_{total} \phi(E) \cdot \sigma_{ref}(E)\ dE},$$

and the cross section σ was calculated by the following equation:

$$\sigma = \frac{R \cdot F}{\phi_{peak}} ,$$

where R was the obtained reaction rate and ϕ_{peak} was the absolute flux of the peak neutrons measured by the PRT counter. When there were no appropriate evaluated cross section data, the cross sections were calculated with SINCROS-II[1] or ALICE-F[2] code. The main sources of the experimental error were the statistical error of γ-ray count and the uncertainty of the absolute neutron flux determination. The total errors were in a range of 6-7 %.

References

1) Yamamuro N.: "A Nuclear Cross Section Calculation System with Simplified Input-Format Version-II (SINCROS-II)", JAERI-M 90-006 (1990).
2) Fukahori T.: "ALICE-F Calculation of Nuclear Data up to 1 GeV", Proc. Specialists' Meeting on High Energy Nuclear Data, Tokai, Ibaraki, Oct. 3-4, 1991, JAERI-M 92-039, 114 (1992).

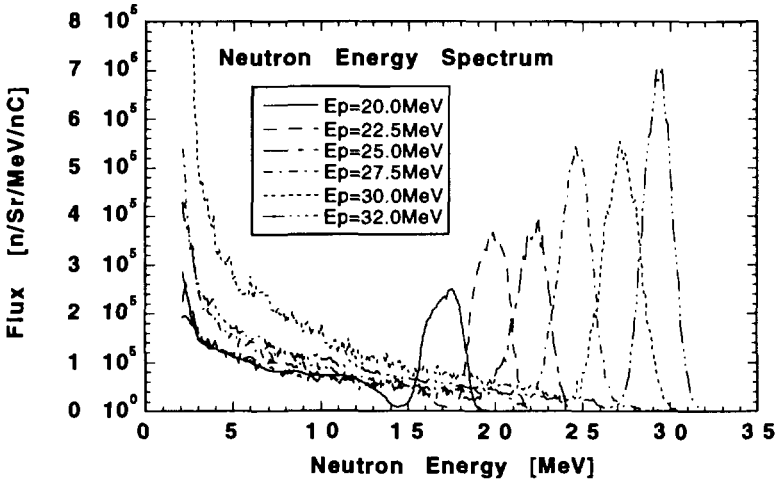

Fig. 1.7.1 Neutron energy spectra of the ^{7}Li(p,n) quasi-monoenergetic neutron source of the JAERI TANDEM accelerator facility

Table 1.7.1 List of reactions measured in the second series of experiment

Sample	Reaction			Half life
Sc	^{45}Sc	(n,2n)	^{44m}Sc	2.442d
			$^{44m+g}$Sc	3.927h
nat-Cr	^{50}Cr	(n,2n)	^{49}Cr	42.1m
		(n,2np)	^{48}V	15.976d
nat-Zn	^{64}Zn	(n,2n)	^{63}Zn	38.1m
		(n,3n)	^{62}Zn	9.26h
nat-Rb	^{85}Rb	(n,2n)	$^{84m+g}$Rb	32.9d
		(n,3n)	^{83}Rb	86.2d
Rh	^{103}Rh	(n,2n)	^{102m}Rh	207d
		(n,3n)	^{101m}Rh	4.34d
		(n,p)	^{103}Ru	39.254d
nat-Ir	^{191}Ir	(n,2n)	$^{190m1+m2+g}$Ir	11.78d
		(n,3n)	^{189}Ir	13.2d
^{52}Cr	^{52}Cr	(n,2n)	^{51}Cr	27.704d
^{90}Zr	^{90}Zr	(n,2n)	$^{89m+g}$Zr	3.27d
		(n,3n)	^{88}Zr	83.4d
		(n,p)	^{90m}Y	3.19h
^{65}Cu	^{65}Cu	(n,2n)	^{64}Cu	12.701h

1.8 Cross Section Measurement for (n,nα) Reactions by 14 MeV Neutrons

Y. Kasugai, Y. Ikeda, Y. Uno, H. Yamamoto* and K. Kawade*

(*E-mail:* kasugai@fnshp.tokai.jaeri.go.jp)

Activation cross sections of (n,nα) reactions by 14 MeV neutrons have been reported on several target nuclei. In most cases, however, only upper limits of cross sections were given because activities produced via (n,nα) reactions were weak[1]. We succeeded to measure very weak activities via (n,nα) reactions by using HPGe detectors with high efficiency and excellent energy resolution.

Cross sections of nine (n,nα) reactions listed in Table 1.8.1 were measured by means of the activation method. Sample sandwiched by Al or Nb foils were irradiated by D-T neutrons (FNS) at JAERI. Neutron flux at the sample position was determined from the reaction rate of $^{27}Al(n,p)^{27}Mg$ and $^{93}Nb(n,2n)^{92m}Nb$. The typical neutron flux at the irradiation position was 2.0×10^{8} n/cm^2/s. The pneumatic transport system was used for short-lived products. The sample and the arrangement of pneumatic tubes are shown in Fig. 1.8.1. After irradiation, gamma-rays emitted from the irradiated samples were measured with HPGe detectors. The main error sources were due to gamma-ray detection efficiency (2%), the standard reaction cross section of $^{27}Al(n,p)^{27}Mg$ or $^{93}Nb(n,2n)^{92m}Nb$ (3%), and statistical error of gamma-ray count (3-45%).

The cross sections measured in this work are shown in Figs. 1.8.2-1.8.10 with the data reported previously and the evaluation data of JENDL-3 and ENDF/B-VI. The cross sections of $^{91}Zr(n,n\alpha)^{87m}Sr$, $^{96}Zr(n,n\alpha)^{92}Sr$ and $^{109}Ag(n,n\alpha)^{105}Rh$ were measured for the first time. For the (n,nα) reactions on ^{71}Ga and ^{93}Nb, the partial excitation functions between 13.5 and 14.9 MeV were obtained for the first time by the measurement at multiple neutron energy points. Some of the evaluated values are much different from our data. The present data of $^{87}Rb(n,n\alpha)^{83}Br$ cross section is 30 times as large as both ENDF-B/VI and JENDL-3 evaluations. For the $^{51}V(n,n\alpha)^{47}Sc$ reaction, the upper limit of the cross section is given in this work because of the large contribution of the $^{50}V(n,\alpha)^{47}Sc$ reaction to the activity of ^{47}Sc. We subtracted the contribution by using the $^{50}V(n,\alpha)^{47}Sc$ cross section which was estimated from systematics at 30 ± 6 mb. The measured upper limit of the cross section is consistent with the JENDL-3 evaluation, while that is lower than the data reported previously[1].

The systematics of (n,nα) cross sections has not been established well because the available experimental data are not so many and because the accuracies are not enough. We

---

* Faculty of Engineering, Nagoya University

tried to find the systematics for (n,nα) cross sections on the basis of our data, but no distinct trend could be observed. More accurate data are needed for a detailed analysis of the systematics.

Reference

1) Qaim S. M.: Nucl. Phys. A, 458, 237 (1986).

Table 1.8.1 Measured reactions and decay parameters

Reaction	Half-life	Gamma-ray Energy (keV)	Intensity per decay(%)	Q-value (MeV)
$^{51}V(n,n\alpha)^{47}Sc$	3.34 d	159.4	68±2	-10.68
$^{65}Cu(n,n\alpha)^{61}Co$	1.65 h	67.6	84.7±0.4	-6.25
$^{71}Ga(n,n\alpha)^{67}Cu$	2.58 d	184.6	48.6±0.8	-5.47
$^{76}Ge(n,n\alpha)^{72}Zn$	1.98 d	144.7	83±2.0	-7.83
$^{87}Rb(n,n\alpha)^{83}Br$	2.38 h	529.7	1.30±0.03	-7.81
$^{91}Zr(n,n\alpha)^{87m}Sr$	2.80 h	388.4	82.3±0.8	-8.09
$^{96}Zr(n,n\alpha)^{92}Sr$	2.71 h	1384.1	90±10	-4.91
$^{93}Nb(n,n\alpha)^{89m}Y$	16.06 s	909.2	99.14	-5.55
$^{109}Ag(n,n\alpha)^{105}Rh$	1.47 d	319.2	19.0±0.4	-3.51

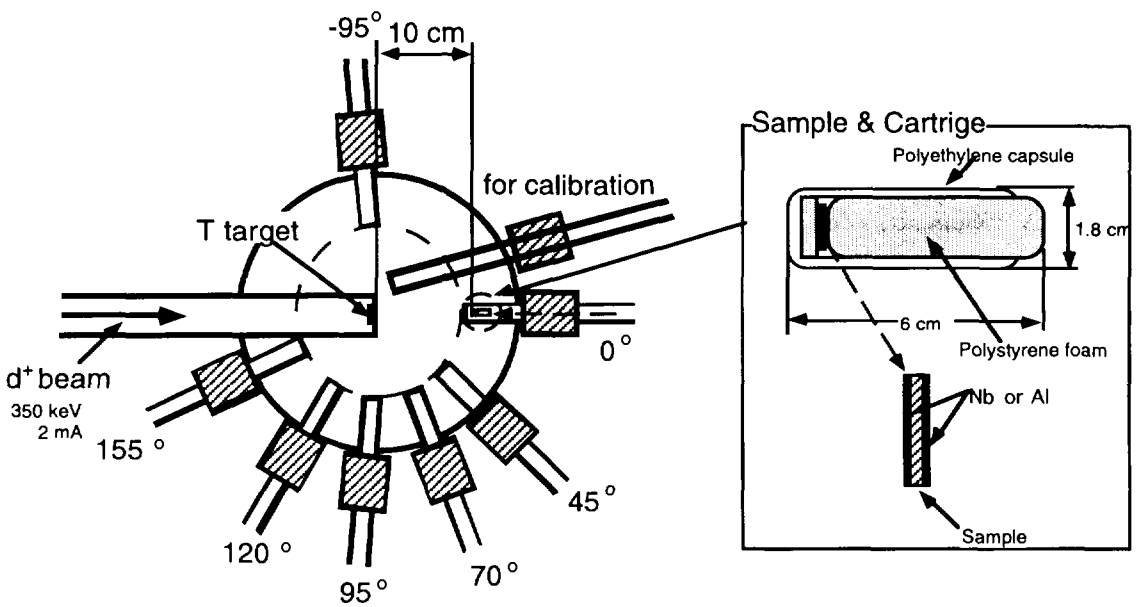

Fig. 1.8.1 Arrangement of pneumatic tubes around T-target, a sample cartridge and a sample

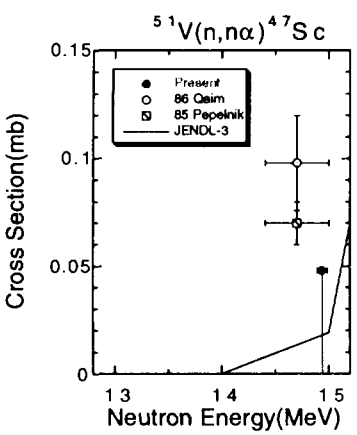

Fig. 1.8.2 $^{51}V(n,n\alpha)^{47}Sc$

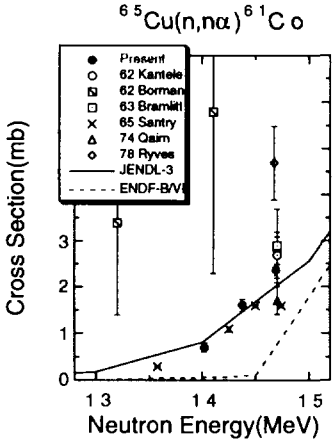

Fig. 1.8.3 $^{65}Cu(n,n\alpha)^{61}Co$

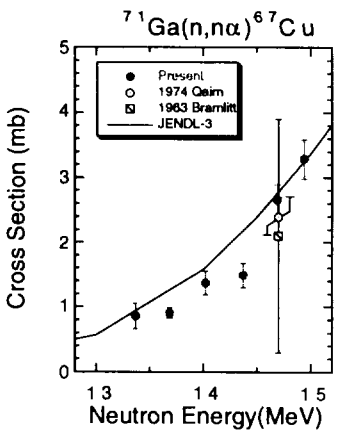

Fig. 1.8.4 $^{71}Ga(n,n\alpha)^{67}Cu$

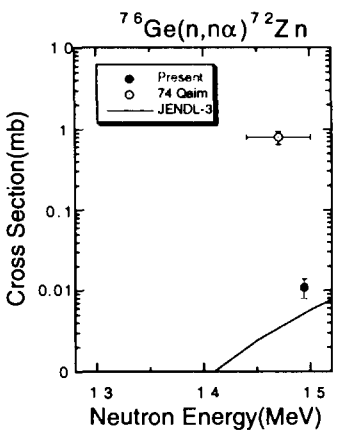

Fig. 1.8.5 $^{76}Ge(n,n\alpha)^{72}Zn$

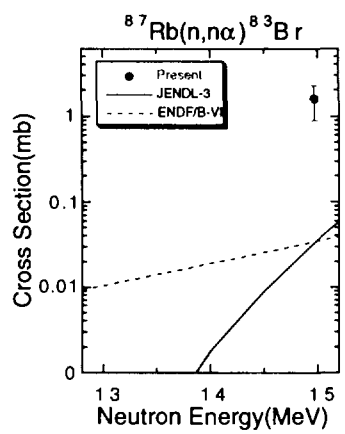

Fig. 1.8.6 $^{87}Rb(n,n\alpha)^{83}Br$

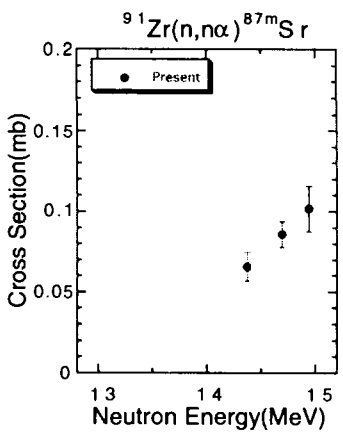

Fig. 1.8.7 $^{91}Zr(n,n\alpha)^{87m}Sr$

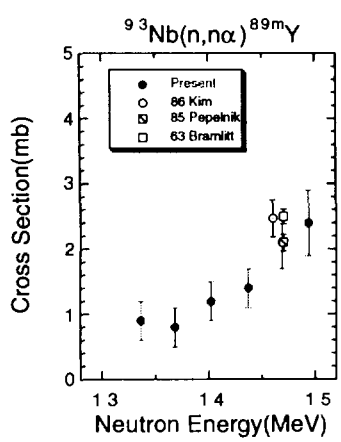

Fig. 1.8.8 $^{93}Nb(n,n\alpha)^{89m}Y$

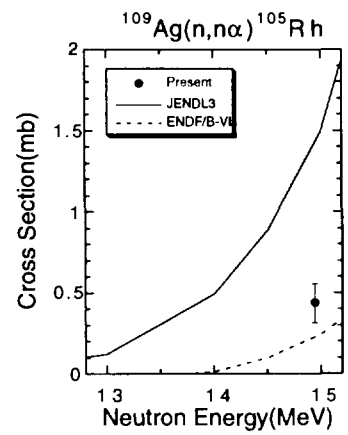

Fig. 1.8.9 $^{96}Zr(n,n\alpha)^{92}Sr$

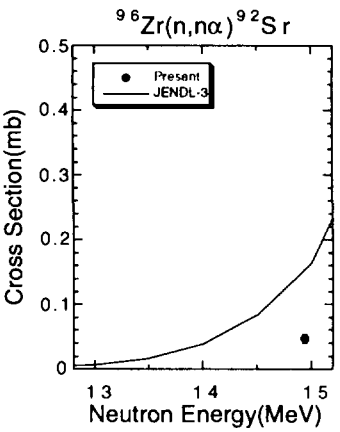

Fig. 1.8.10 $^{109}Ag(n,n\alpha)^{105}Rh$

1.9 Activation Cross Section Measurement for La, Ce, Pr, Nd, Gd, Dy and Er Isotopes by 14 MeV Neutrons

Y. Kasugai, Y. Ikeda and Y. Uno
(*E-mail:* kasugai@fnshp.tokai.jaeri.go.jp)

The cross sections by 14 MeV neutrons have been systematically measured by using D-T neutron source of the FNS (Fusion Neutronics Source) facility at JAERI since 1984. More than 250 reactions for 50 elements have been already reported[1,2]. In this study the cross section measurement for lanthanide isotopes is reported. The measured reactions are listed in Table 1.9.1 with associated decay data[3].

The cross section values were obtained by measuring the radioactivity induced with neutron irradiation. Neutrons were generated by bombarding a ^{3}T-target with d^{+} beam of 2 mA and 350 keV. A pneumatic sample transport system was used for measurement of the short-lived activities. The samples were irradiated at angles from 0 to 155 degree to the d^{+} beam in order to cover the neutron energies from 13.4 to 14.9 MeV. The distance between the neutron source and the irradiation positions was 10 cm. The samples were sandwiched with two aluminum or niobium foils. The neutron flux at the sample position was determined from the reaction rate and cross section of ^{93}Nb(n,2n)^{92m}Nb or ^{27}Al(n,p)^{27}Mg; the cross sections were calibrated by using ^{27}Al(n,α)^{24}Na cross section as a standard. The fluctuation of neutron flux was monitored every 10 seconds. The effective reaction energy of incident neutron at each irradiation position was measured by the ratio of reaction rate between ^{90}Zr(n,2n)^{89}Zr and ^{93}Nb(n,2n)^{92m}Nb. The experimental results of effective neutron energy corresponded well to the kinematics of E_{d+}=150 keV, where E_{d+} was the effective reaction energy of deuteron.

The samples except the ^{150}Nd-samples were natural abundance. The contributions of (n,γ) reactions to the (n,2n) reactions for ^{140}Ce, ^{142}Ce and ^{160}Gd were estimated to be negligibly small judging from the (n, γ) cross sections and the thermal neutron flux at the sample position. Gamma-rays emitted from the irradiated samples were measured with HPGe detectors of 115% and 25% in efficiency and a well-type HPGe detector.

Some of the results are shown in Figs.1.9.1-1.9.4 with the evaluated data of FENDL/A-2.0 and JENDL-ACT96 along with the data in literature. The cross section data of the ^{150}Nd(n,2n)^{149}Nd reaction are shown in Fig. 1.9.1. The present cross sections are almost constant in the energy range between 13.0 and 15.0 MeV, while the excitation function of FENDL-2 evaluation shows the decreasing trend. The JENDL evaluation agrees with the present data. The present experimental data for the ^{141}Pr(n,2n)^{140}Pr reaction are 50% lower than the FENDL-2 evaluation as shown in Fig. 1.9.2. For the ^{168}Er(n,p)^{168}Ho reaction, the

JENDL evaluation is higher than FENDL-2 evaluation by a factor of 2 as shown in Fig.1.9.3. The present result agrees with the FENDL-2 evaluation. For the $^{139}La(n,t)^{137m}Ba$ reaction, the present data show that the excitation function increases more rapidly than the FENDL-2 evaluation as shown in Fig.1.9.4. The measured data of $^{139}La(n,p)^{139}Ba$, $^{140}Ce(n,2n)^{139m+g}Ce$, $^{140}Ce(n,\alpha)^{137m}Ba$, $^{146}Nd(n,p)^{146}Pr$, $^{160}Gd(n,2n)^{159}Gd$ and $^{164}Dy(n,p)^{164}Tb$ show good agreement with the FENDL-2 evaluations, while those of $^{140}Ce(n,2n)^{139m+g}Ce$, $^{150}Nd(n,2n)^{149}Nd$, $^{164}Dy(n,p)^{164}Tb$ agree well with the JENDL evaluation.

References

1) Ikeda Y., et al.: JAERI-1312 (1987).
2) Konno C., et al.: JAERI-1329 (1993).
3) Browne E. B., et al.: Table of Radioactive Isotopes (1986).

Table 1.9.1 Measured reactions and associated decay data

Reaction	Half-life	Gamma-ray Energy(keV)	Intensity per decay(%)	Q-value (MeV)
$^{139}La(n,p)^{139}Ba$	1.410 h	165.9	24±4	+2.53
$^{139}La(n,t)^{137m}Ba$	2.552 m	661.7	90.11±0.06	-6.41
$^{140}Ce(n,\alpha)^{137m}Ba$	2.552 m	661.7	90.11±0.06	+5.30
$^{140}Ce(n,2n)^{139m}Ce$	56.4 s	754.2	92.45	-9.20
$^{140}Ce(n,2n)^{139m+g}Ce$	137.66 d	165.8	70.8986	-9.20
$^{140}Ce(n,p)^{140}La$	1.678 d	1596.5	95.40±0.08	-2.99
$^{142}Ce(n,2n)^{141}Ce$	32.50 d	145.4	48.2±0.03	-7.17
$^{141}Pr(n,p)^{141}Ce$	32.50 d	145.4	48.2±0.03	+0.20
$^{141}Pr(n,2n)^{140}Pr$	3.39 m	511(β^+)	98.7	-7.93
$^{142}Nd(n,2n)^{141m+g}Nd$	2.49 h	1126.9	8.0±0.3	-9.82
$^{146}Nd(n,p)^{146}Pr$	24.15 m	453.9	48±3	-3.37
$^{150}Nd(n,2n)^{149}Nd$	1.73 h	211.3	25.9	-7.38
$^{160}Gd(n,2n)^{159}Gd$	18.56 h	363.5	11±3	-7.45
$^{164}Dy(n,p)^{164}Tb$	3.0 m	215.1	21.2±0.7	-3.07
$^{168}Er(n,p)^{168}Ho$	3.0 m	741.3	36.6±1.0	-1.07

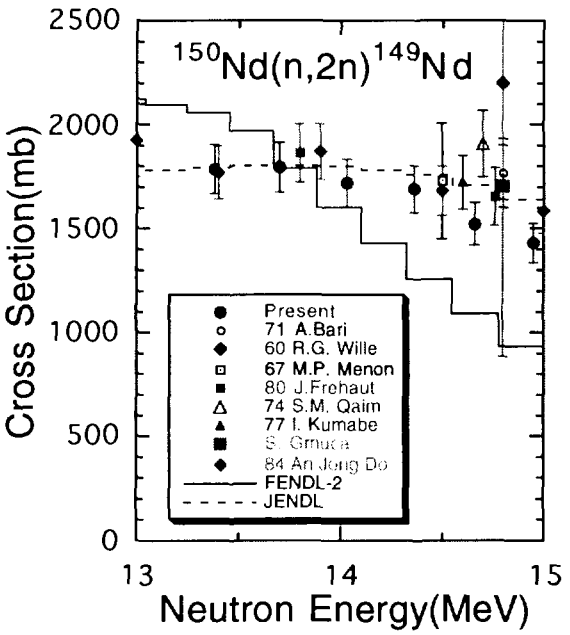

Fig. 1.9.1 $^{150}Nd(n,2n)^{149}Nd$

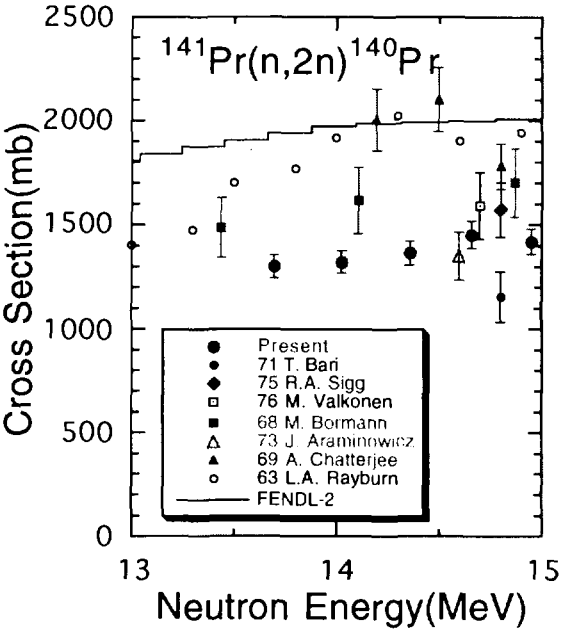

Fig. 1.9.2 $^{141}Pr(n,2n)^{140}Pr$

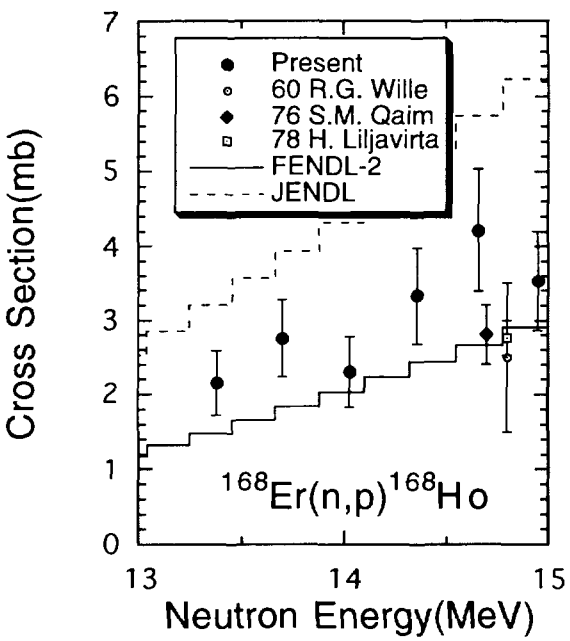

Fig. 1.9.3 $^{168}Er(n,p)^{168}Ho$

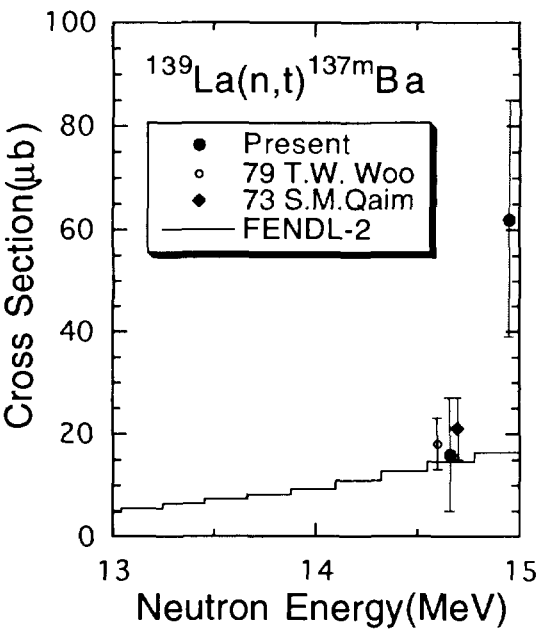

Fig. 1.9.4 $^{139}La(n,t)^{137m}Ba$

1.10 Evaluation and Compilation of Nuclear Structure and Decay Data in 1996

J. Katakura and ENSDF Group*
(*E-mail*: katakura@cracker.tokai.jaeri.go.jp)

The international nuclear structure and decay data evaluation network aims at complete and continuous nuclear structure data evaluation of all mass chains. As a member of the network, Japanese group, whose data evaluation center is Nuclear Data Center, Japan Atomic Energy Research Institute, has responsibility for evaluating 12 mass chains with A=118-129. In the fiscal year of 1996, the evaluation of A=129 mass chain were completed and published in Nuclear Data Sheets[1]. The evaluated data are also included in ENSDF (Evaluated Nuclear Structure Data File) file which is maintained by National Nuclear Data Center, Brookheaven National Laboratory as a computer readable data file.

In the evaluation of A=129 mass chain, all data available up to December 31, 1995 have been considered for inclusion. The updated data included in the evaluation are tabulated below.

Nuclide	Data Type	Nuclide	Data Type
^{129}Cd	Adopted Levels	^{129}Te	Adopted Levels, Gammas
^{129}In	Adopted Levels, Gammas		^{129}Sb β^- Decay (4.40 h)
	^{129}Cd β^- Decay (0.27 s)		^{129}Sb β^- Decay (17.7 min)
^{129}Sn	Adopted Levels, Gammas		^{129}Te IT Decay (33.6 d)
	^{129}In β^- Decay (0.61 s)		^{128}Te(n,γ) E=thermal
	^{129}In β^- Decay (1.23 s)		^{128}Te(d,p)
^{129}Sb	Adopted Levels, Gammas		^{128}Te(t,d)
	^{129}Sn β^- Decay (2.23 min)		^{130}Te(p,d)
	^{129}Sn β^- Decay (6.9 min)		^{130}Te(d,t)
	^{129}Sb IT Decay 17.7 min)		^{130}Te(^{3}He, α)
	^{130}Te(d,^{3}He)	^{129}I	Adopted Levels, Gammas
	^{130}Te(t, α)		^{129}Te β^- Decay (69.6 min)

* Members are H. Iimura, M. Oshima, S. Ohya, K. Ogawa, J. Katakura, M. Kambe, K. Kitao, T. Tamura, Y. Tendow, A. Hashizume and K. Miyano

Nuclide	Data Type	Nuclide	Data Type
^{129}I	^{129}Te β^- Decay (33.6 d)	^{129}Cs	(HI,xnγ)
	^{128}Te(p,p),(p,p') IAR	^{129}Ba	Adopted Levels, Gammas
	^{128}Te(^{3}He,d)		^{130}Ba(d,t)
	Coulomb Excitation		(HI,xnγ)
	^{130}Te(α,t)	^{129}La	Adopted Levels, Gammas
^{129}Xe	Adopted Levels, Gammas		^{129}La IT Decay
	^{129}I β^- Decay		(HI,xnγ)
	^{129}Xe IT Decay	^{129}Ce	Adopted Levels, Gammas
	^{129}Cs ε Decay		^{129}Pr ε Decay
	Coulomb Excitation		(HI,xnγ)
	(HI,xnγ)	^{129}Pr	Adopted Levels
^{129}Cs	Adopted Levels, Gammas		(HI,xnγ)
	^{129}Ba ε Decay (2.23 h)	^{129}Nd	Adopted Levels
	^{129}Ba ε Decay (2.16 h)		(HI,xnγ)

The new data of other mass chains Japan has the responsibility to are reviewd and being prepared for update of old mass chain evaluation.

References

1) Tendow Y.: Nucl. Data Sheets 77, 631 (1996)

1.11 Decay and Fission Yield Data Library for ORIGEN2 Code based on JNDC Nuclear Data Library of Fission Products

J. Katakura
(*E-mail*: katakura@cracker.tokai.jaeri.go.jp)

The Atomic Energy Society of Japan (hereafter referred as AESJ) released recommended decay heat values of major fissioning nuclides in 1990.[1] The recommended values have been accepted for LOCA analysis of ECCS performance evaluation by Atomic Energy Safety Committee in Japan. The recommended values, however, cover the time range of spent fuel storage and reprocessing. For the decay heat evaluation of spent fuel ORIGEN2 code[2] is often used, but the code has own library of decay and fission yield data which are different from those of JNDC Nuclear Data Library of Fission Products[3] (hereafter referred as JNDC library) that is the basis of the AESJ recommended values. The decay heat values calculated by the ORIGEN2 code are, therefore, inconsistent with the AESJ values. The situation has caused perplexity in the user-comunity of ORIGEN2 code in Japan. In order to remedy the situation, the decay and fission yield data library has been produced using the JNDC library for ORIGEN2 code.[4]

The library was produced by replacing the original ORIGEN2 data with those of the JNDC library. The number of nuclides contained in the ORIGEN2 library, however, is different from that in the JNDC library and the decay chain is also different from each other in the libraries. The number of the nuclides in the new library was kept to be the same as that in the original library, but for the decay chain that of the JNDC library was adopted. The fission yield data at the beginning of decay chain, therefore, were changed to the cumulative yield in order to satisfy total mass yield of 200 per fission.

The decay heat values calculated with the new library were compared with the AESJ recommendation. The difference between the calculation with the new library and the AESJ recommendation is shown in Fig. 1.11.1 for the case of ^{235}U burst fission. In the figure the calculation with the original library is also shown for comparison. The similar comparison for ^{239}Pu burst fission is shown in Fig. 1.11.2. As seen in these figures the original calculation shows 20 % to 25 % difference from the AESJ recommendation. The new calculation, however, shows much small difference, that is, 3 % at most, with the AESJ recommendation. In the case of 1-year-irradiation which is more realistic in an application than burst fission, the ORIGEN2 calculation with the new library gives agreement with the AESJ recommendation within less than 1 %, that agreement is enough for application.

References

1) "Recommended Values of Decay Heat and Method to Utilize the Data (Supplement to "Reactor Decay Heat and the recommended Values"): Atomic Energy Society of Japan, July 1990 [in Japanese]

2) Croff A.G.: ORNL-5621 (1980)

3) Tasaka T. et al.: JAERI 1320 (1990)

4) Katakura J.: J. Atom. Ener. Soc. Japan 38(7), 609 (1996) [in Japanese]

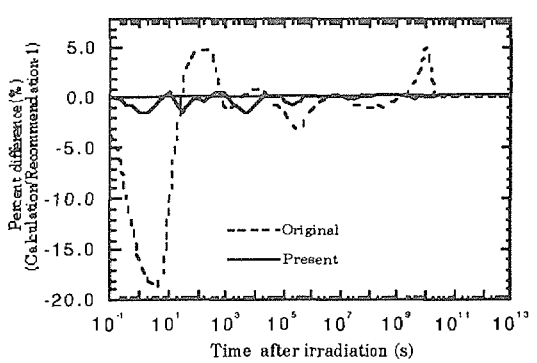

Fig. 1.11.1 Comparison of ^{235}U Burst Fission

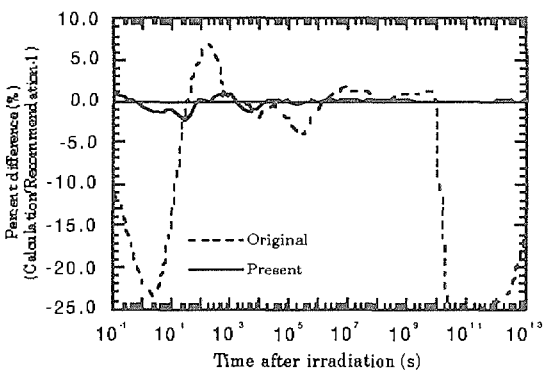

Fig. 1.11.2 Comparison of ^{239}Pu Burst Fission

1.12 Spectral Data for Highly Ionized Atoms: Ti, V, Cr, Mn, Fe, Co, Ni, Cu, Kr and Mo

T. Shirai, J. Sugar* and W.L. Wiese*
(*E-mail*: shirai@cracker.tokai.jaeri.jo.jp)

During the last 10 years we have published a series of spectroscopic data table for highly ionized heavy atoms that occur either as impurities in fusion energy devices or which have been injected into these hot plasmas for diagnostic purposes. These spectroscopic data are wavelengths, energy levels, ionization energies, and atomic transition probabilities, which are required both for modelling the energy balance and impurity cooling effects in such plasmas as well as for applying non-perturbing spectroscopic techniques to determine plasma parameters. In addition, spectroscopic data needs for highly ionized atoms exist in astrophysics, especially the physics of the solar corona, and in atomic physics research. A good bit of new spectral analysis work, both observations and calculations, had been done in recent years, and the results had not been tabulated conveniently before. We have thus critically compiled these spectroscopic data into single monographs for each element and have published, in order of nuclear charge, such tables for the spectra of Ti, V, Cr, Mn, Fe, Co, Ni, Cu, Kr, and Mo ions[1-10].

Since we have now compiled this series, we are presenting all these data in this single volume to provide users with the convenience of a single source. Our new tables include three significant improvements: First, in cases where new or improved data have been published, we included this updated material. This affects especially the early tables of Ti and Fe. Second, we have expanded some compilations by including additional lower ions, so that in each case all ions from the Ca-isoelectronic sequence to the H-isoelectronic are covered. Third, we have added a unified finding list, ordered in increasing wavelengths, which covers all transitions that we have compiled on these elements.

In the present tables we keep the data for each element together as separate subunits. This includes the respective introductory comments for the various spectra and the lists of references. We also include a few typical Grotrian diagrams as representative examples. However, we do not include the extensive Grotrian diagrams contained in our earlier publications because these would make this volume very large and unwidely. However we offer to provide such diagrams on request.

---

*National Institute of Standards and Technology

In all of our earlier compilations of Ti through Ni we began with the data compiled by Sugar and Corliss[11], using their selection of references as our source of wavelengths. This was supplemented by the extensive tabulation of wavelengths of Kelly[12], the review article by Fawcett[13], and for the more recent work, the bibliographic database of NIST. For wavelengths of forbidden lines we adopted the compilation by Kaufman and Sugar[14]. For transition probabilities, we adopted the data compiled by Martin *et al.*[15] and Fuhr *et al.*[16]. Again, we search the more recent literature for significant updates and additions. For the He and H sequences only theoretical results are give since they are considered to be more accurate than the experimental values.

In cases where no experimental wavelength data are available but for which *f*-values exist, the quoted wavelengths (λ) are calculated from the known energy levels using Ritz combination principle. The wavelengths are then used to calculate *A*-values from *f*-values.

References

1) Mori K., *et al.*: Atom. Data and Nucl. Data Tables **34**, 79 (1986).
2) Shirai T., *et al.*: J. Phys. Chem. Ref. Data **21**, 273 (1992).
3) Shirai T., *et al.*: J. Phys. Chem. Ref. Data **22**, 1279 (1993).
4) Shirai T., *et al.*: J. Phys. Chem. Ref. Data **23**, 179 (1994).
5) Shirai T., *et al.*: J. Phys. Chem. Ref. Data **19**, 127 (1990).
6) Shirai T., *et al.*: J. Phys. Chem. Ref. Data **21**, 23 (1992).
7) Shirai T., *et al.*: Atom. Data and Nucl. Data Tables **37**, 235 (1987).
8) Shirai T., *et al.*: J. Phys. Chem. Ref. Data **20**, 1 (1991).
9) Shirai T., *et al.*: J. Phys. Chem. Ref. Data **24**, 1577 (1995).
10) Shirai T., *et al.*: J. Phys. Chem. Ref. Data **16**, 327 (1987).
11) Sugar J. and Corliss C.: J. Phys. Chem. Ref. Data **14**, Suppl. 2 (1985).
12) Kelly R.L., *et al.*: J. Phys. Chem. Ref. Data **16**, Suppl. 1 (1987).
13) Kaufman V. and Sugar J., J. Phys. Chem. Ref. Data **15**, 321 (1986).
14) Fawcett B.C.: J. Opt. Soc. Am. B **1**, 195 (1984).
15) Martin G.A., *et al.*: J. Phys. Chem. Ref. Data **17**, Suppl. 3 (1988).
16) Fuhr J.R. *et al.*: J. Phys. Chem. Ref. Data **17**, Suppl. 4 (1988).

1.13 Analytic Cross Sections for Collisions of Electrons with Hydrocarbon Molecules

T. Tabata*, T. Shirai and H. Tawara**
(*E-mail*: shirai@cracker.tokai.jaeri.go.jp)

Data on cross sections of collision processes between electrons and hydrocarbon molecules are important in the study of thermonuclear fusion research, in which graphite or carbon-coated materials are commonly used as the inner walls of plasma devices. In such devices chemical sputtering due to interactions of carbon atoms with active atomic hydrogen produces a large quantity of hydrocarbon molecules. These molecules in turn collide with electrons and hydrogen atoms or molecules in plasma, and the collision products give serious effect on the behavior and characteristics of plasma.

Tawara *et al.*[1] (see also Tawara[2]) have reviewed the present status of experimental cross-section data for collisions of electrons with hydrogen molecules. The purpose of the present work is to give analytic expressions fitted to the data for a total of eighty-nine reactions compiled by these authors.

The fuctional forms used for the analytic expressions are those semiempirically developed by Green and McNeal[3] and modifications of these. A total of ten types of functions has been used. The use of such expressions allows one not only to interpolate but also extrapolate the data to some extent in contrast to polynomial fits, which frequently show physically unreasonable behavior just outside the energy range of available data.

The value of the threshold energy used for each reaction has been estimated from the behavior of the cross-section data at the lowest energies. The number of adjustable parameters in the analytic expressions is from two to twelve according to the type of the function. Values of the adjustable parameters have been determined by least-square fits to the data except some values that were assumed to guarantee reasonable behaviors outside the energy range of the available data.

The analytic expressions obtained are compared with the experimental data in Fig. 1.13.1, which shows that agreement is satisfying. The root-mean-square deviations of the expressions from the data are about several percent.

---

*Osaka Prefecture University

**National Institute for Fusion Science

References

1) Tawara H. *et al.* : *Atomic and Plasma-Material Interaction Data for Fusions* **2**, 41 (1992).

2) Tawara H.: in *Atomic and Molecular Processes in Fusion Edge Plasmas*, edited by R.K. Janev (Plenum, New York, 1995) p.461.

3) Green A. E. S. and McNeal R. J.: J. Geophys. Res. **76**, 133 (1971).

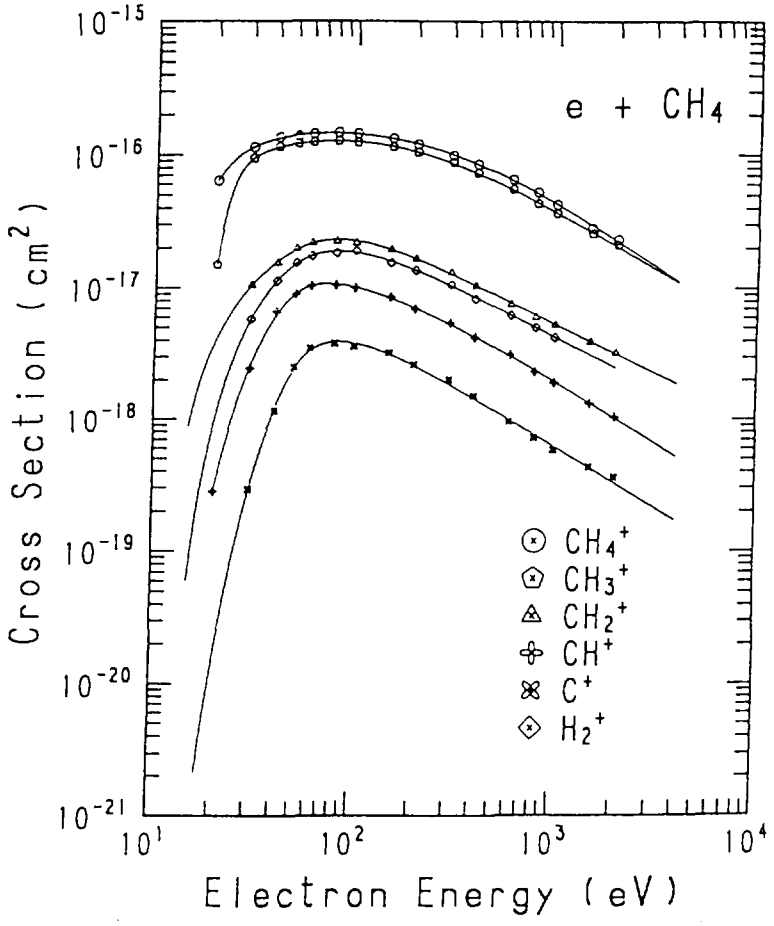

Fig. 1.13.1 Recommended cross sections for ion production in collisions of electrons with CH_4. Solid line: recommended data in the present work; symbols: experimental data.

2. Theoretical Method and Code Development

In the calculations by a continuous energy Monte Carlo code, users require cross section libraries at various temperatures. Some interpolation methods were investigated and a code ART was developed to generate easily a cross section library at an arbitrary temperature for a Monte Carlo code MVP. It was found that an interpolation based on Akima's method gives most accurate values to resonance region. The validation by criticality calculations of the TCA and VHTRC cores showed that the method can generate a library with good accuracy.

The continuous energy Monte Carlo method is the most reliable one in solving neutron transport problems. Since the MVP code based on this method employs a fast computational algorithm suitable for recent supercomputers, a burn-up analysis system MVP-BURN has been developed by coupling with an auxiliary modular code BURN. The NEACRP burn-up benchmark problem was solved to validate this system, and the results were compared with those by SRAC95 and other solutions submitted from various countries.

In order to help a designer in decision of design parameter values, a procedure was improved to search more efficiently a design window. The principle is to construct a multilayer neural network to simulate quickly the response of the analysis code. The procedure was applied to a fuel pin design of an LWR and it was found that the four-layered neural network is suitable from viewpoints of both of the accuracy and training time.

A new method was proposed to consider anisotropic effect by introducing a direction dependent correction factor into leakage operator in the transport equation of the homogenized system. The method was examined for a k_{eff} problem with simple plate geometry. All the transport calculations were performed by the Monte Carlo method. Solution by the present method agreed well with the one with heterogeneous configuration when the total cross section is not very small.

The ATRAS code system was revised to improve the accuracy of spallation neutronics and burnup analysis for accelerator-driven subcritical systems. By adding some lumped fission products cross sections, the neutron multiplication factor decreased by about 2.5 % in a burnup analysis. The NMTC/JAERI code predicted the number of emitted neutrons with a high accuracy by implementing new Random Neck Rupture HEF model. The nuclear code system SPACE was also upgraded for the IAEA accelerator-driven benchmark.

2.1 Library Generation Method at Arbitrary Temperature for a Continuous Energy Monte Carlo Code MVP

M. Nakagawa, T. Mori* and K. Kaneko**
(*E-mail:*nakagawa@mike.tokai.jaeri.go.jp)

The continuous energy Monte Carlo method has many advantages compared with the multi-group one. Use of accurate point-wise cross sections is one of them. It means that a cross section library is necessary at each temperature depending on a problem which a user solves. In an analysis of a power reactor, accordingly, many libraries will be necessary at different temperatures. However, It is not efficient to prepare libraries at many temperatures in advance because those require large size of storage in a computer system.

We have developed a method and a code ART to generate easily a cross section library at an arbitrary temperature for a Monte Carlo code MVP[1]. Energy region is usually divided into 1) high energy one with smooth cross section, 2) unresolved resonance region, 3) resolved resonance region and 4) thermal region. Region 1) is not temperature dependent and in 3) temperature dependent cross section can be calculated by Doppler broadening based on a reference library given at a fixed temperature. For regions 2) and 3), we have applied interpolation methods to an arbitrary temperature based on the tabulated values or assigned values at an evaluated nuclear data file. The interpolation methods have been developed and the results of verification calculations are described below.

Unresolved Resonance Region

The MVP code uses the probability table method in the unresolved resonance region. Unresolved resonance cross sections of averaged total, elastic scattering, capture, fission cross sections and their probabilities are prepared for each incident energy at 11 temperatures in advance. Those data were restructured into the probability table with equal probability bins. The interpolations were made for the cumulative probability distribution functions produced from the above tables. We have compared the accuracy of interpolation methods of Lagrange,

---

* Science and Technology Agency
** Integrated Technical Information Research Organization

Akima and Spline. Among them, the Akima method gives the most accurate interpolated values where a log-linear function is used. Figure 2.1.1 shows comparison in the first bin between the original and the interpolated fission cross sections of ^{235}U. The maximum deviation is about 0.6%.

Thermal Scattering Raw

Temperature dependence is very important in thermal scattering low, $S(\alpha, \beta)$. In the MVP library, $S(\alpha, \beta)$ is given for Be(metal & oxide), C(graphite & CH_2), H(benzene , H_2O, ZrH), D(D_2O), ^{238}U and Zr(ZrH). The secondary energy probability distribution is interpolated after modifying them into the cumulative probability distribution. Interpolation of elastic scattering cross section is made by using the interpolation formula assigned in the evaluated file. Inelastic scattering cross section is interpolated by a linear-linear function based on the Akima method. The interpolation errors are satisfactorily small.

Validation Calculations

In order to validate the library generation method and the ART code, we have analyzed criticality of the TCA and VHTRC assemblies which have water and graphite moderated UO_2 fueled cores, respectively. They are suitable for testing an adequacy of interpolated $S(\alpha, \beta)$ of H_2O and C(graphite). The old library[2] was generated at the temperatures given in the evaluated file and the new one is by the ART code.

The calculated k_{eff}s for TCA are compared in Table 2.1.1 where in case 1, the temperatures of all materials are 300K and in case 2, the fuel is at 1800K and the moderator at 600K. The values of k_{eff} agree within statistical uncertainties for both cases.

The criticality of VHTRC were calculated at 4 temperatures with the old library and 5 ones with the new library. The results are compared in Fig. 2.1.2. At 1500K, a small difference is observed. At this temperature, the old library is also generated by interpolating the data in the original evaluated file. This interpolation method is different from the one mentioned above and inferior in accuracy. From the above comparison, it can be said that the present method can generate a library at arbitrary temperature with good accuracy.

References

1) Mori T., Nakagawa M. and Sasaki M.: "MVP/GMVP: General Purpose Monte Carlo Codes," JAERI-Data/Code 94-007(1994).

2) Mori T., Nakagawa M. and Kaneko K.: "Neutron Cross Section Library Production Code System for MVP," JAERI-Data/Code 96-018(1996).

Table 2.1.1 Comparison of calculated k_{eff}s between two libraries

	Old library	New library
k_{eff}	1.00211	1.00274
FSD(%)	±0.0553	±0.0552
k_{eff}	0.99347	0.99346
FSD(%)	±0.0527	±0.0507

Total number of histories: 2.2×10^6

History/batch: 20,000

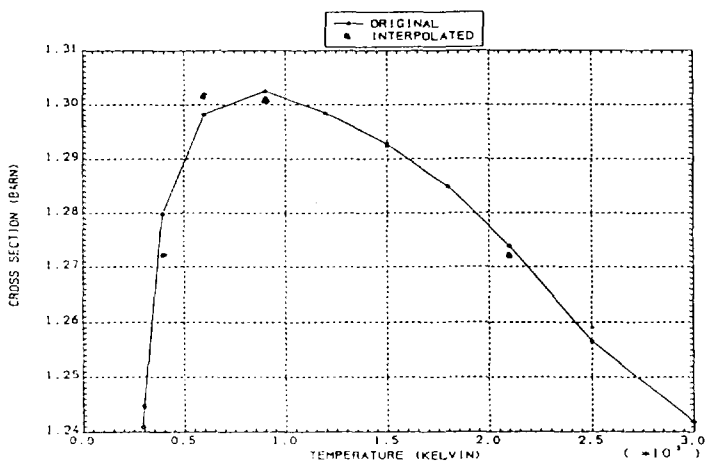

Fig.2.1.1 Comparison of fission cross sections of ^{235}U at 30keV

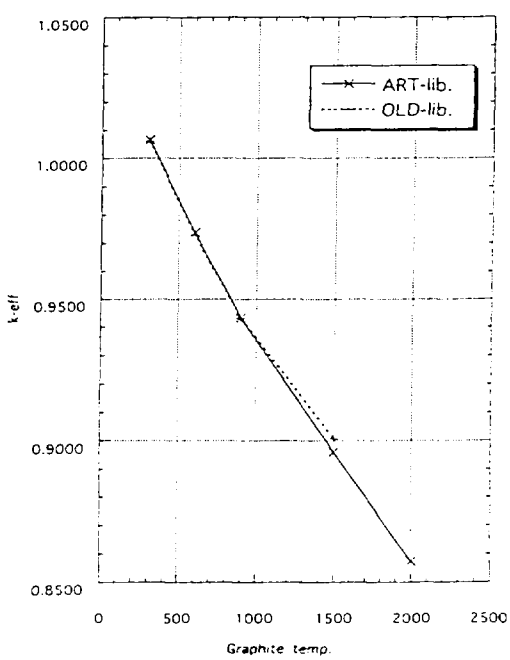

Fig.2.1.2 Temperature dependency of k_{eff}s of VHTRC

2.2 Cell Burn-up Calculation with a Continuous Energy Monte Carlo Code MVP

K. Okumura, K. Kaneko* and M. Nakagawa
(*E-mail:* okumura@mike.tokai.jaeri.go.jp)

The continuous energy Monte Carlo method is the most reliable method to solve neutron transport problems because of its precise geometrical modeling and continuous energy treatment. Recent progress of supercomputers makes it possible to apply this method to some burn-up problems. In spite of still expensive computation costs, the Monte Carlo method is very useful for the special burn-up problems in which we have few calculation experiences or the problems which are difficult to be treated by conventional deterministic neutron transport codes.

A continuous energy Monte Carlo code MVP[1] employs a fast computational algorithm suitable for recent vector and/or parallel computers. The speed-up factor of ten or more is realized on such supercomputers as compared with other scalar Monte Carlo codes. Therefore, MVP can reduce much computation time required for the repeated use of a Monte Carlo code at many burn-up time-steps. In order to apply it to cell burn-up calculation problems, we have developed the MVP-BURN system[2] by implementing an auxiliary modular code BURN which has a function to calculate buildup and decay of nuclides in irradiated materials (depletion calculation).

By using the continuous energy Monte Carlo code, microscopic reaction rates of all nuclides are obtained. Since the depletion calculation is possible if the microscopic reaction rates are given, the coupling of a Monte Carlo code and a depletion calculation code is realized only by implementing an interface program between them. The newly developed BURN code has the functions of the depletion calculation, file management, and interface with MVP. A whole burn-up calculation is performed by executing alternately these codes.

In order to investigate the accuracy of burn-up characteristics calculated by MVP-BURN, the system was applied to the numerical burn-up benchmark problem for a BWR fuel assembly with adjacent poisoned fuel rods[3]. Figure 2.2.1 shows the lattice geometry of the benchmark problem. The results of MVP-BURN were compared with those obtained by the collision probability method in SRAC95[4] and also with other ten solutions[3] submitted for international comparison. In both of the calculations by MVP-BURN and SRAC95, a poisoned fuel pellet was divided into eight annular depleting zones to consider the change of spacial

*Integrated Technical Information Research Organization (ITIRO), Tokyo

shielding effect of Gd_2O_3 during burn-up period, while other unpoisoned fuel pellets were not divided. As the changes of microscopic absorption rates of gadolinium nuclides through burn-up are so rapid, small intervals of burn-up step are required. The intervals 0.25GWd/t up to 8.0GWd/t and 0.5GWd/t thereafter were used for both codes. In the MVP-BURN calculation, a large number of neutron histories (670000) was taken to achieve a sufficiently accurate k_∞ ($1\sigma \approx 0.08\%$) in each burn-up step. It took about 27 minutes of computation time per burn-up step on FACOM VPP-500 computer (single CPU calculation).

Major calculated results are shown in Figs. 2.2.2 and 2.2.3. The maximum (and average) differences between the SRAC95 and MVP-BURN results are 0.85 (0.24)% on k_∞, 1.2 (0.56)% on power density of the unpoisoned fuel rod (No.4 pin), and 3.2 (2.4)% on that of the poisoned rod. As the maximum differences are almost comparable to those at the zero burn-up state (e.g. 0.81% on k_∞), they are mainly caused by inaccuracy of the SRAC95 calculation. However, general burn-up characteristics of both codes are similar in comparison with other solutions.

Applicability of MVP-BURN to a heterogeneous fuel assembly with burnable poison rods was validated by this benchmark calculation. However, it should be noted that the burn-up calculation even with the continuous energy Monte Carlo method can not always give us exact solutions, because depleting zones and burn-up time intervals are discretely treated.

References

1) Mori T. and Nakagawa M. : "MVP/GMVP : General Purpose Monte Carlo Codes for Neutron and Photon Transport Calculations based on Continuous Energy and Multigroup Methods", JAERI-Data/Code 94-007 (1994) [in Japanese].
2) Okumura K., Nakagawa M. and Kaneko K. : "Development of Burn-up Calculation Code System MVP-BURN Based on Continuous Energy Monte Carlo Method and Its Validation", to be published in Proc. of Joint Int. Conf. on Mathematical Methods and Supercomputing for Nuclear Applications (M&C and SNA'97), Saratoga Springs, NY (1997).
3) Maeder C. and Wydler P. : "International Comparison Calculations for a BWR Lattice with Adjacent Gadolinium Pins", NEACRP-L-271 (1984).
4) Okumura K., Kaneko K. and Tsuchihashi K. : "SRAC95 ; General Purpose Neutronics Code System", JAERI-Data/Code 96-015 (1996) [in Japanese].

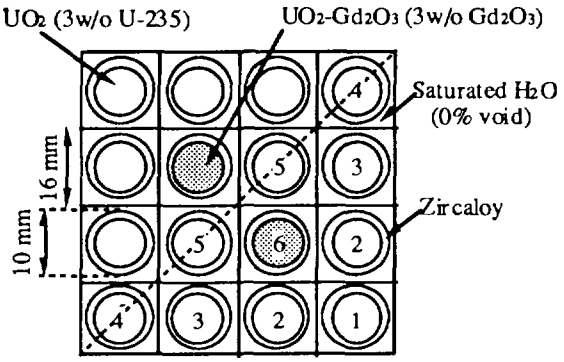

Fig. 2.2.1 Lattice geometry of the benchmark problem on BWR lattice with adjacent gadolinium pins[3)]

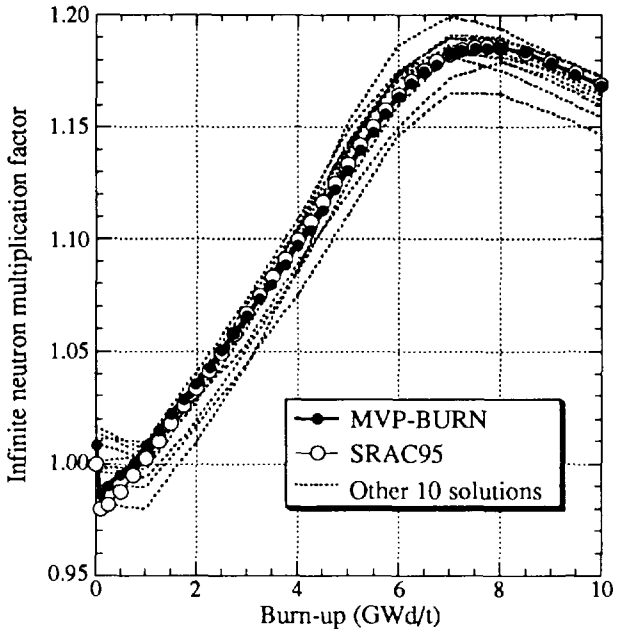

Fig. 2.2.2 Comparison of infinite neutron multiplication factors for various burn-up. The 10 solutions (Ref.3) are plotted only at 11 burn-up points (0, 1, 2,..., 10GWd/t).

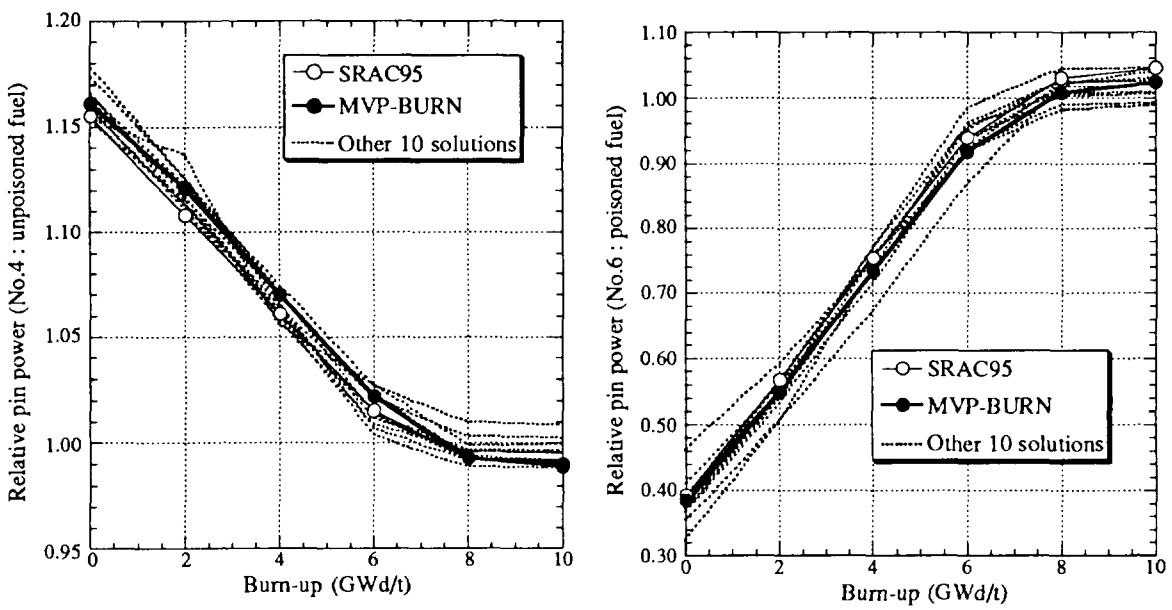

Fig. 2.2.3 Comparison of pin powers for various burn-up. (a) unpoisoned fuel rod and (b) poisoned fuel rod.

2.3 Improvement of Design Window Search Procedure using Neural Network

T. Kugo

(*E-mail:* kugo@mike.tokai.jaeri.go.jp)

To help a designer in decision of design parameter values, we have developed a procedure to search efficiently a design window using a neural network. A principle of the procedure is to construct a multilayer neural network to simulate quickly a response of an analysis code through a training with some teaching data. Then the computation time is reduced by using the trained neural network as a substitute of an analysis code. The success of this method relies on the ability of the estimation of the neural network. In this study, we investigate how a difference of the structure of neural network influences on the accuracy of the estimation by employing three- and four-layered neural networks.

The training of the neural network is performed using the error back propagation scheme[1] where connecting weights are modified on the basis of a steepest descent method to minimize the error

$$E_i \equiv \frac{1}{N}\sum_{k=1}^{N}\frac{1}{2}(T_{ik}-O_{ik})^2 \qquad (2.3.1)$$

where E_i is the mean error of estimation for the i-th output unit, T_{ik} the teaching data of the i-th output for the k-th learning patterns, O_{ik} the output from the i-th output unit for the k-th learning patterns and N the number of the learning patterns. The "overlearning" where the error of estimation for the learning patterns converges but the one for the unlearning patterns diverges, will sometimes occur in the above training scheme. It should be checked whether the overlearning occurs or not in the training process. The present method prepares not only learning patterns but also unlearning ones as illustrated in Fig.2.3.1 and we observe the error of the estimation for the unlearning patterns to check the overlearning.

We employed three- and four-layered neural networks with six neurons in hidden layers to solve a fuel pin design problem of a light water reactor. A searching space was defined by the following parameter ranges;

pin diameter: 9.0～12.0 mm, pin pitch: 10.0～15.0 mm and hot channel factor : 1.3～1.7.

Learning and unlearning patterns were prepared at 5x5x5 and 4x4x4 grid points in the above defined searching space, and 64 and 38 patterns satisfying the geometrical constraint were adopted for teaching data, respectively. Figure 2.3.2 shows training histories of learning and unlearning patterns on the coolant temperature. It is seen that the overlearning occured in the three-layered neural network. On the contrary, the error for four-layered one converged according to the training. To examine the correlation between the overlearning and the accuracy on the estimated design window, we compare design windows estimated by three- and four-layered neural network in Fig. 2.3.3. There is a notable discrepancy between two estimated design windows. It is important to avoid the overlearning to obtain reliable estimation. Two or more hidden layers will be needed to avoid it, but they will consume a lot of time for the training of the neural network. So the four-layered neural network is suitable to realize both of the high accuracy of the estimation and the saving of the training time.

Reference

1) Rumelhart D. E., Hilton G. E. and Williams R. J. : "Learning Internal Representations Error Propagation", in Parallel Distributed Processing, Vol.1, MIT Press, 318 (1986).

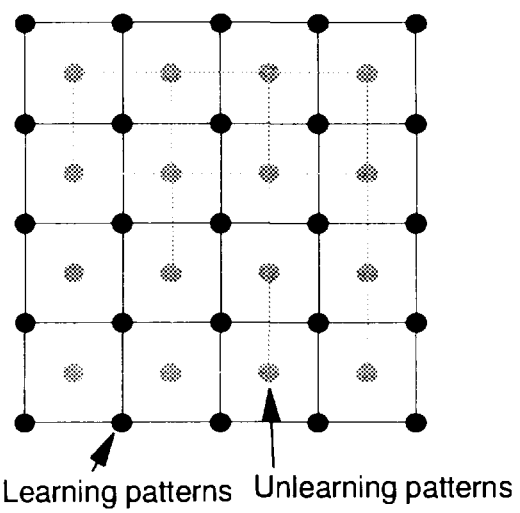

Fig. 2.3.1 An illustration of learning and unlearning patterns

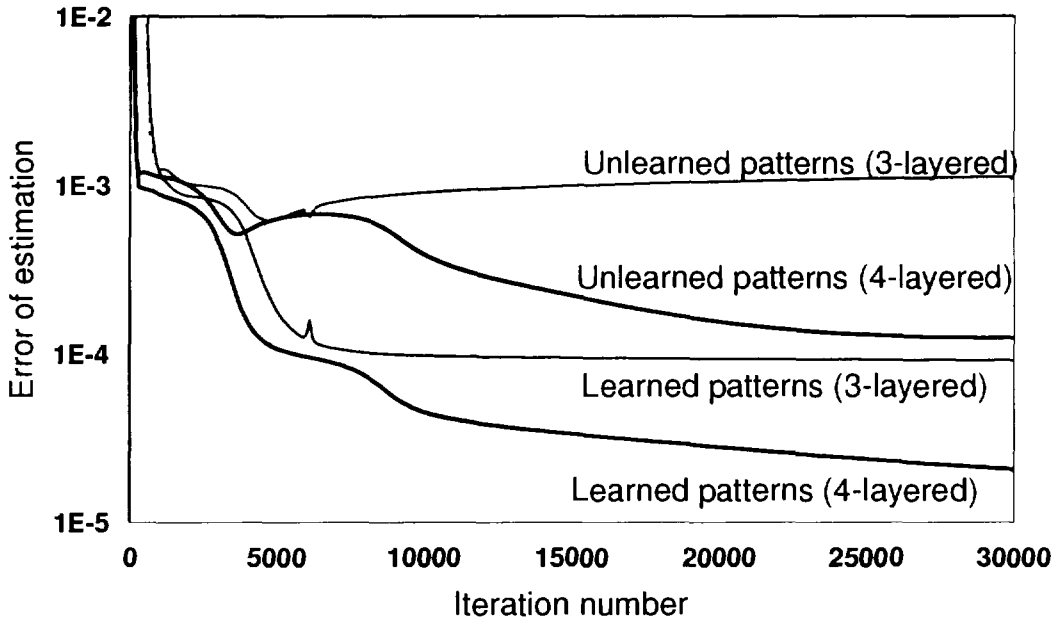

Fig.2.3.2 Training histories of learned and unlearned patterns

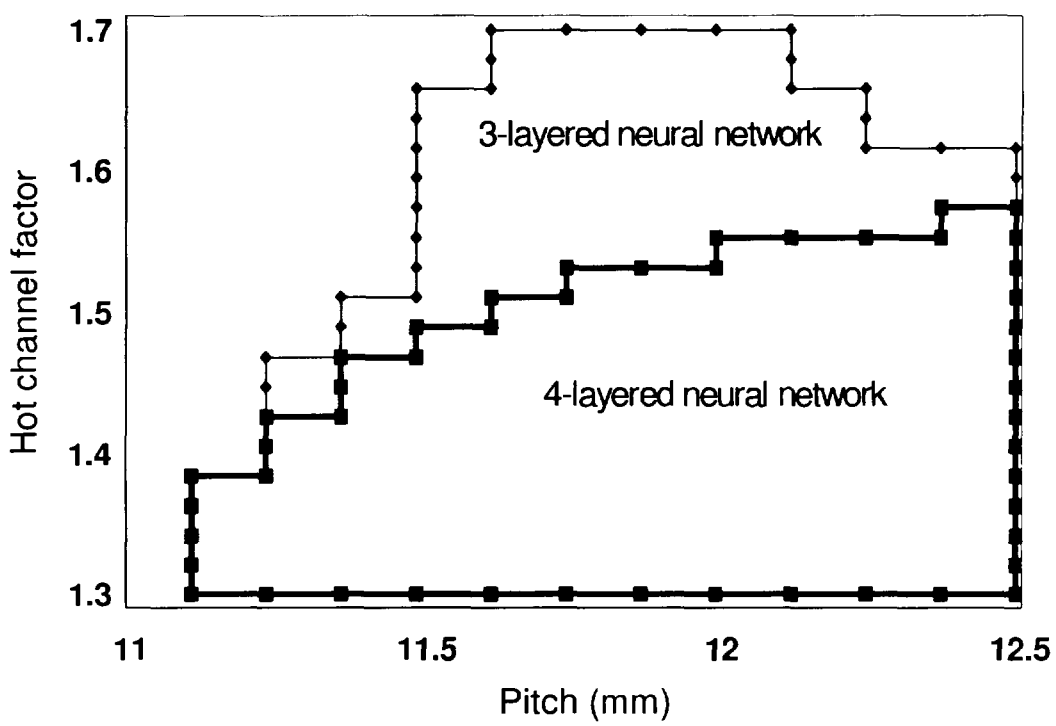

Fig.2.3.3 Comparison of design windows between 3- and 4-layered neural networks

2.4 Application of Anisotropic Neutron Streaming Effect to Transport Theory

H. Oigawa
(*E-mail:* oigawa@fca001.tokai.jaeri.go.jp)

In the cell homogenization procedure of the reactor physics calculation, the anisotropic neutron streaming effect caused by the cell heterogeneity has been taken into account by anisotropic diffusion coefficients based on Benoist's theory.[1] In the present study, a new method to apply this effect to the transport theory, instead of the diffusion theory, is proposed and examined for a simple plate cell geometry.

The basic idea, quoted from Lewis' work[2] , is to introduce a direction dependent correction factor, $\omega(\Omega)$, into the leakage operator in the transport equation of the homogenized system as Eq.(1).[2]

$$\omega(\Omega)\cdot\Omega\cdot\nabla\Psi^{H}(r,\Omega)+\Sigma_t^{H}\Psi^{H}(r,\Omega)=\langle\Sigma_0^{H}\Psi^{H}\rangle \quad , \tag{1}$$

where $\Psi^{H}(r,\Omega)$: the angular flux in the homogenized system,
Σ_t^{H} : the homogenized total cross section, and
$\langle\Sigma_0^{H}\Psi^{H}\rangle$: the source term.

The transport equation in the heterogeneous system is written as

$$\Omega\cdot\nabla\Psi(r,\Omega)+\Sigma_t\Psi(r,\Omega)=\langle\Sigma_0\Psi\rangle \quad , \tag{2}$$

where $\Psi(r,\Omega)$: the angular flux in the heterogeneous system, and
Σ_t : the total cross section.

In case of the plate cell geometry with one-directional neutron leakage as shown in Fig.2.4.1, the angular flux in the heterogeneous system can be separated into the cell fine structure and the global distribution.

$$\Psi(r,\Omega)=g(x,\Omega)\cdot cos(B_z\cdot z)+h(x,\Omega)\cdot sin(B_z\cdot z) \quad , \tag{3}$$

where $g(x,\Omega)$: the even component of the cell fine structure,
$h(x,\Omega)$: the odd component of the cell fine structure, and
B_z : the buckling of z-direction.

By substituting Eq.(3) into Eq.(2) and assuming that the scattering cross section is isotropic , equations which $g(x,\Omega)$ and $h(x,\Omega)$ obey are derived as Eqs.(4).

$$\Omega_x\cdot\frac{d}{dx}g(x,\Omega)+\Sigma_t g(x,\Omega)=\langle\Sigma_0 g\rangle - B_z\cdot\Omega_z h(x,\Omega) \quad \text{and} \quad \Omega_x\cdot\frac{d}{dx}h(x,\Omega)+\Sigma_t h(x,\Omega)=B_z\cdot\Omega_z g(x,\Omega) \quad . \tag{4}$$

On the other hand, in the homogeneous system, the second equation of Eqs.(4) is rewritten as

$$\Sigma_t^H h^H(\Omega) = B_z \cdot \Omega_z \omega(\Omega) g^H(\Omega) \approx B_z \cdot \Omega_z \omega(\Omega) \int_{cell} dx\ g(x,\Omega)/V_{cell} \quad , \tag{5}$$

where $g^H(\Omega)$ is approximated by the space average of $g(x,\Omega)$.

To conserve the neutron leakage between the heterogeneous system and the homogenized one, Eq.(6) should be satisfied.

$$\int_{cell} dx h(x,\Omega) = V_{cell} \omega(\Omega) h^H(\Omega) \quad . \tag{6}$$

By substituting Eq.(5) into Eq.(6), a definition of $\omega(\Omega)$ is obtained as

$$\omega^2(\Omega) = \left(\Sigma_t^H / B_z \cdot \Omega_z\right) \left\{ \int_{cell} dx h(x,\Omega) / \int_{cell} dx g(x,\Omega) \right\} \quad . \tag{7}$$

In this study, $g(x,\Omega)$ and $h(x,\Omega)$ were obtained for fine angular and spacial meshes by transforming Eqs.(4) into integral forms. Then, $\omega(\Omega)$ was calculated by Eq.(7).

Finally, a new unknown function, $\Phi(r,\Omega)$, is introduced to solve Eq.(1);

$$\Phi(r,\Omega) = \omega(\Omega) \Psi^H(r,\Omega) \quad , \quad \Sigma_t(\Omega) = \Sigma_t^H / \omega(\Omega) \quad . \tag{8}$$

By substituting Eqs.(8) into Eq.(1), a transport equation with direction dependent cross sections, $\Sigma_t(\Omega)$, is obtained:

$$\Omega \cdot \nabla \Phi(r,\Omega) + \Sigma_t(\Omega) \Phi(r,\Omega) = \left\langle \Sigma_0(\Omega') \Phi \right\rangle \quad . \tag{9}$$

This equation was solved by a Monte-Carlo method in the present work.

As an example, k_{eff} of the system indicated in Fig.2.4.1 was compared among four calculation methods : (1)Monte-Carlo calculation with heterogeneous configuration (reference), (2)Monte-Carlo calculation with the conventionally homogenized cross sections, (3)Monte-Carlo calculation with the direction dependent cross sections (present method) , and (4) Diffusion calculation with Benoist's diffusion coefficients. The total cross section in Region-2, Σ_{t2} ,was parametrically changed to investigate the influence of the cell heterogeneity.

The calculated results are shown in Fig.2.4.2. Conventional transport calculation with the homogenized cross section overestimates k_{eff} since it ignores the anisotropic neutron streaming effect. The present method shows very good agreement with the reference calculation, when Σ_{t2} is not very small (>0.07cm^{-1}). As Σ_{t2} decreases, however, the present method tends to underestimate k_{eff} . On the other hand, the diffusion calculation with Benoist's diffusion coefficients always underestimates k_{eff} because of the transport effect, i.e. the diffusion theory generally overestimates the neutron leakage. The difference between the present method and the diffusion calculation is not dependent on Σ_{t2}.

It can be concluded that the present method is valid to apply the anisotropic neutron streaming effect to the transport theory. In the case of strong heterogeneity, however, the present method underestimates k_{eff} as well as Benoist's theory does.

References

1)Benoist P. : "Theory of the Diffusion Coefficient of Neutrons in a Lattice Containing Cavities," CEA-R-2278 (1964).

2)Lewis E. E. : "A Generalization of the Benoist Formalism for Anisotropic Neutron Transport Computation," Proc. Int. Mtg. Advances in Mathematical Methods for Nuclear Engineering Problems, Munich, Germany, April 27-29,1981, pp.181-194, vol.1 (1981).

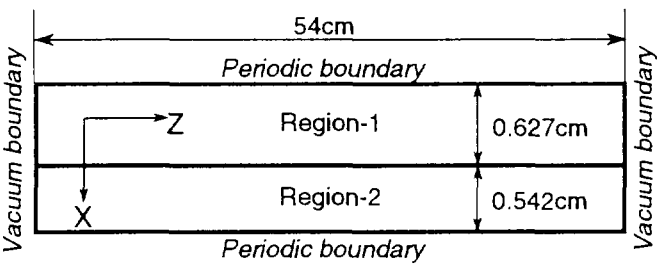

Cross section (1/cm)

	Σ_a	$\nu\Sigma_f$	Σ_t	Σ_s
Region1	0.01089	0.02009	0.28478	0.27389
Region2	0.00015	0.00000	0.13037	0.13022

Fig.2.4.1 Calculation model for simple plate cell geometry

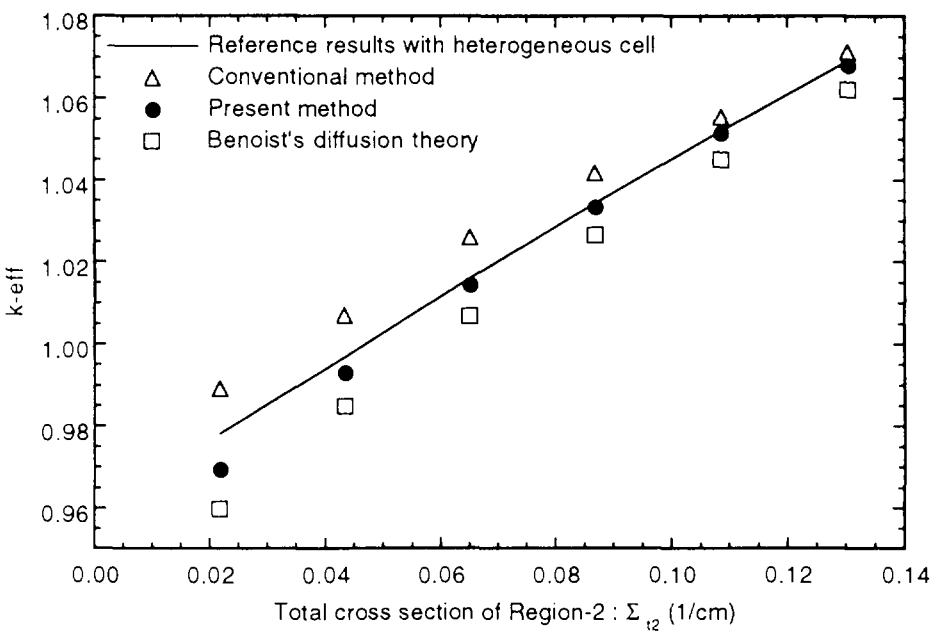

Fig.2.4.2 Comparison of k_{eff} by various methods

2.5 Development of the Design Code System for the Accelerator-driven Transmutation Research

T.Sasa, T.Nishida*, K. Tsujimoto and T.Takizuka
(*E-mail:* sasa@omega.tokai.jaeri.go.jp)

The ATRAS code system was revised to increase the accuracy of the spallation neutronics and burnup analysis of accelerator-driven subcritical systems.

For the core burnup analysis, estimation of the reactivity change caused by the accumulated fission products are important. We added some lumped fission products cross sections to the 73 group cross section library for the ATRAS code system. We selected the infinite diluted cross sections of lumped FP in JFS3-J2[1] cross section library for the fast reactor analysis. For the conversion process from JFS3-J2 library to ATRAS library, total cross sections in the energy range above 10 MeV, which were not prepared in the JFS3-J2 library, were assumed to zero and (n,2n) reaction of the lumped FP was not considered. Figure 2.5.1 shows one of the lumped FP cross section which was newly added to the ATRAS cross section library. We performed the burnup analysis of the accelerator-driven transmutation system with TRU-nitride fuel and tungsten disk spallation target with the revised library and the previous library. Comparison of the core averaged neutron energy spectrum are shown in Fig.2.5.2. Neutrons in intermediate energy region was decreased by the capture reaction of lumped FPs. The neutron multiprication factor after the 300 days operation including the lumped FP was determined about 2.5 % lower than the result with the previous library.

In the NMTC/JAERI code simulating the nuclear reaction and particle transport in the energy range higher than 20 MeV, the intranuclear reaction model consists of two step procedures, namely, the first step (cascade process) and the second step (equilibrium process). The high energy fission (HEF) reaction is assumed to compete with the particle evaporation process in the second step. The HEF reaction mechanism has a large influence on the total number of spallation neutrons emitted from a nucleus. In the present work we examined the Random Neck Rupture Model[2] as a new HEF model to predict the number of neutron emitted in the process with a higher accuracy. This model can deal approximately with the dynamical process of fast fission reaction through a scission point of a nucleus deformed like a dumbbell, while the former model installed in the current cascade code focuses only on the statistical property of fission reaction. It was recognized that the model can give more exact fission neutron yield for through its check run.

---

* Radiation Application Development Association

The nuclear code system SPACE, which had been developed in JAERI, has been upgraded for the IAEA Accelerator-driven system benchmark. We newly produced the microscopic cross section files of uranium 233, thorium 232 and natural lead with the 295 groups JSSTDL files for TWOTRAN-II to calculate the nucleonics of the Pb-cooled, ^{232}Th-^{233}U mixed oxide fuelled subcritical fast core proposed in the benchmark problem. The burnup code COMRAD in SPACE, which was based on the Bateman method, has also been improved to take into accounts the effect of the neutron absorption by fission products build up in the accelerator-driven system in the burning process of Th-U fuel. The thirteen nuclides as ^{133}Cs, ^{99}Tc, ^{147}Pm, ^{101}Rm, ^{95}Mo, ^{143}Nd, ^{103}Rh, ^{97}Mo, ^{145}Nd, ^{141}Pr, ^{149}Sm, ^{131}Xe and ^{129}I were selected as main fission products compiled in COMRAD after evaluating the build up effects of those nuclides with the ORIGEN-2 code. Figure 2.5.3 shows the comparison of the time evolution of reaction rates of fission products.

References

1) H. Takano, Y. Ishiguro:"Production and Benchmark Test of Group Constant Set, JFS3-J2," JAERI-M 82-135, (1982).

2) T. Fan, J. Hu and S. Bao:"Study of Multichannel Theory for the Neutron Induced Fissions of Actinide Nuclei," Nucl. Phys. A 591, pp.161-181, (1995).

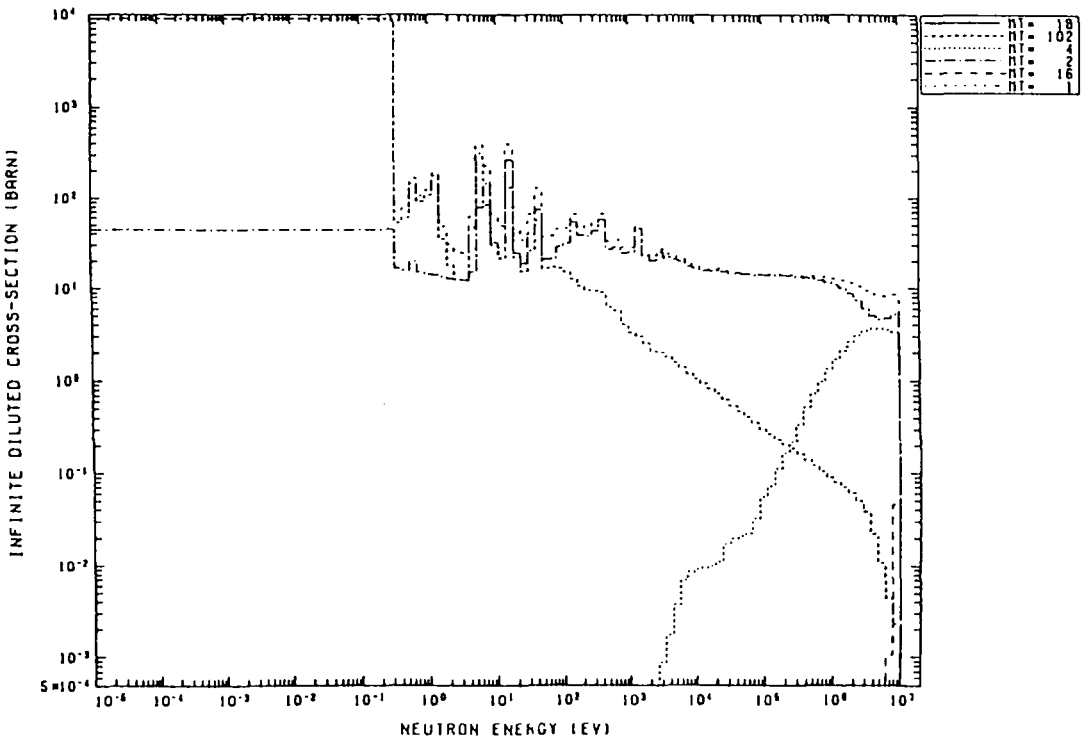

Fig.2.5.1 Infinite diluted cross section of the lumped FP from Pu-239

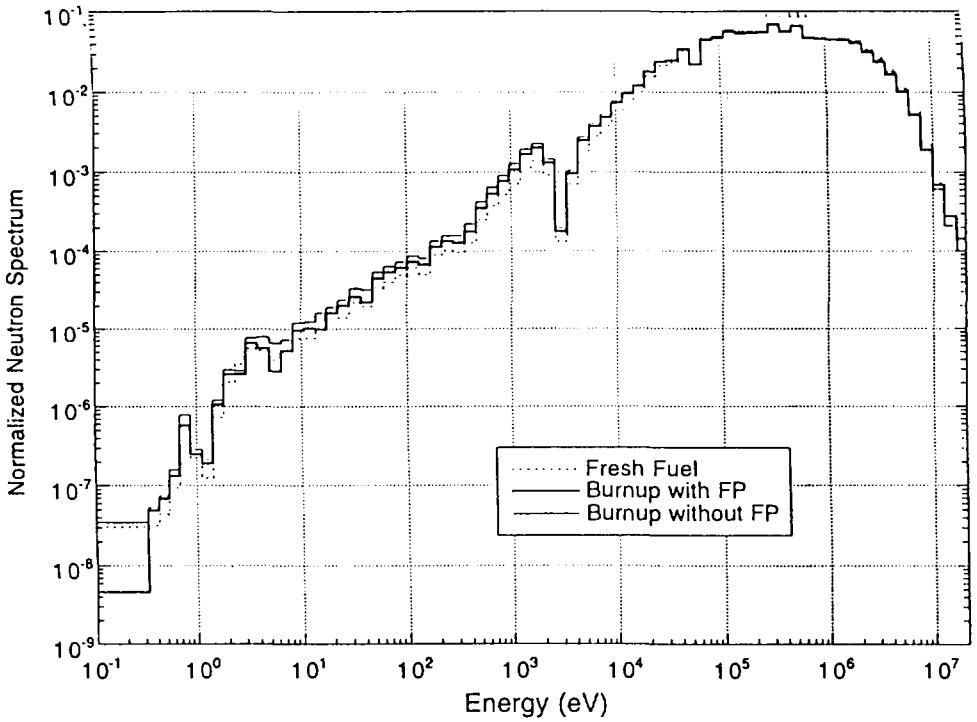

Fig.2.5.2 Core neutron spectrum of the TRU-nitride transmutation system

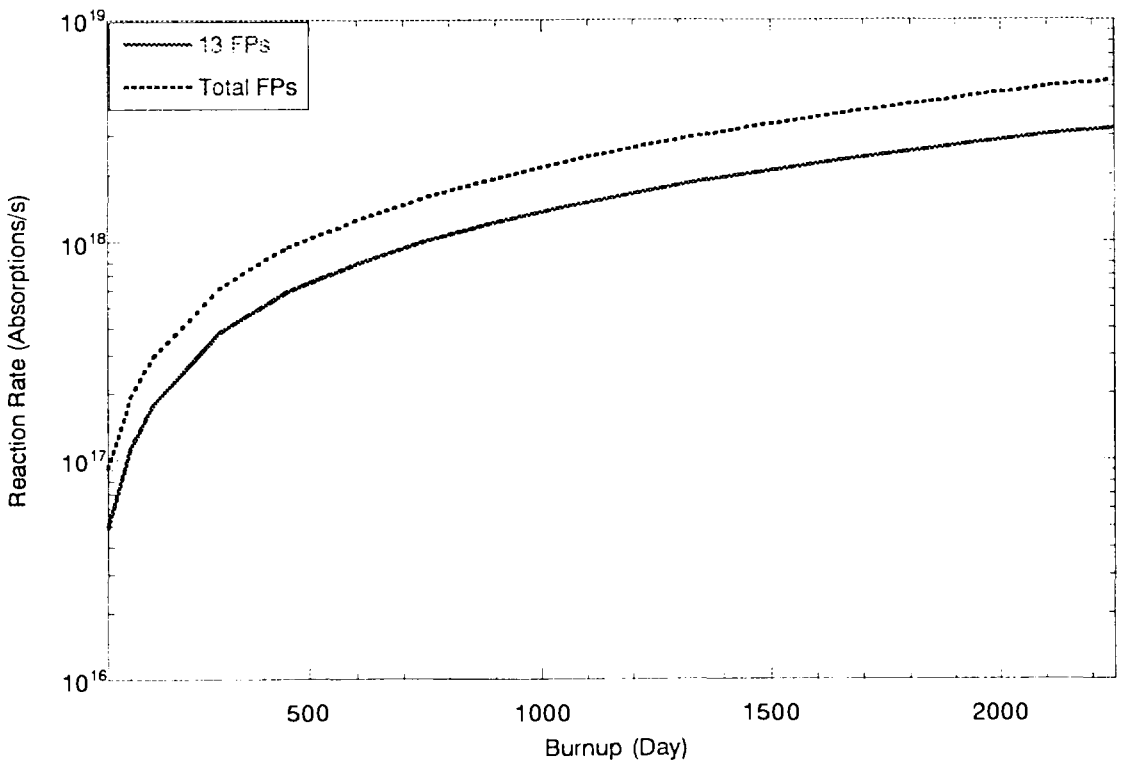

Fig.2.5.3 Time evolution of reaction rates of fission products

3. Reactor Physics Experiment and Analysis

The β_{eff} benchmark experiments have been carried out at FCA under the NEA/NSC /WPEC Subgroup on Delayed Neutron Data Validation. Six countries participate in these experiments : France (CEA), Italy (ENEA), Russia (IPPE), USA (LANL), Korea (KAERI) and Japan (JAERI and the Nagoya University). Each participant measures the β_{eff} by using their own measurement technique. Three different core configurations were selected at FCA so that these cores could be complementary to those of the MASURCA experiments. The first core, XIX-1 (U-core), went critical on Oct. 1995 ; followed by the second core XIX-2 (Pu/NU core) and the third core XIX-3 (Pu core).

The physics parameters measured on metallic-fueled and oxide fuel mock up core at FCA were analyzed as a benchmark-test of the present calculation tools; the JENDL-3.2 data file and the JAERI's standard calculation system for fast reactor neutronics.

The calculation accuracy of various methods were examined for In-Core-GEM reactivity worth measured at the FCA-XVII-1 core which simulated a prototype MOX fueled LMFBR. It was concluded that the diffusion theory should be used with great care to calculate the In-Core-GEM reactivity worth, and that it would be necessary to solve the dependence of the C/E values by the transport theory upon the sodium level.

Analyses on the reaction rate ratios in the moderator added fast reactor core showed that the Calculation/Experiment (C/E) values for C8/F9 and F8/F9 had the H/HM dependence ; the calculation underestimates the measured C8/F9, and overestimate the measured F8/F9, while there are good agreements in the F5/F9 between calculation and experiment.

To evaluate the calculation accuracy on reactor physics parameters of an HTTR core, the measured data in the VHTRC cores were analyzed with the SRAC code system and the nuclear data libraries based on the ENDF/B-IV and/or JENDL-3.2. It was concluded that the present calculation code satisfies the accuracy requirement of 10% for nuclear design of the reactivity worth of the HTTR Reserve Shutdown Absorber. Critical mass and Kinetic parameter at critical, $(\beta_{eff}/\Lambda)_c$, were measured at a room temperature 21℃ and an elevated temperature 200℃ in the VHTRC-4 core. In comparison with the experiments, the calculations underestimated the critical mass at 21℃ by 4% and 6% in each case of ENDF/B-IV and JENDL-3.2, respectively, while the agreement at 200℃ became better in both cases. The calculated $(\beta_{eff}/\Lambda)_c$ vales agreed fairly well with the measured one within 5%. An improvement in analysis method for $(\beta_{eff}/\Lambda)_c$ measurement at VHTRC was made by considering the delayed neutron contribution more precisely. By applying this method to analyses on the $(\beta_{eff}/\Lambda)_c$ values in the VHTRC-1 and VHTRC-4 cores, the discrepancies between calculation to experiment could be reduced from 10% to 5%.

3.1 Experimental Study for Nuclear Characteristics of Metal and Oxide Fuel LMFBR at FCA

S. Iijima, H. Oigawa, T. Sakurai, T. Nemoto and S. Okajima
(*E-mail:* iijima@fca001.tokai.jaeri.go.jp)

The benchmark experiment of a metallic-fueled LMFBR has been conducted on JAERI's Fast Critical Assembly (FCA) facility in order to examine nuclear characteristics of the advanced fuel core and to test calculated predictions of reactor physics parameters in a core design. A metallic-fueled core has hard neutron spectrum and its nuclear characteristics differ from those in a conventional oxide fuel core. Reactivity feedback parameters such as sodium void and Doppler reactivity and ^{238}U-capture to ^{239}Pu-fission ratio, which were sensitive to neutron spectrum and fuel composition, were measured in the mockup core of metallic-fueled LMFBR. In the test of calculated predictions of reactor physics parameters, the results of the metallic-fueled core were compared with those of the oxide fuel core. The physics parameters measured on metallic-fueled and oxide fuel mockup core have been analyzed using the same nuclear data, JENDL-3.2[1] and the same calculation method, JAERI's standard calculation system for fast reactor neutronics[2), 3)].

Criticality

The diffusion calculation in 25-group using anisotropic diffusion coefficients was made in the x-y-z model of the reference core. Transport and mesh-size corrections were applied to the diffusion calculation result. The transport correction is taken from transport and diffusion calculations in r-z geometry. In addition to the calculation based on the deterministic method, the continuous energy Monte Carlo calculation by the MVP code[4)] was made in the whole core model. The difference of C/E value between the deterministic method and the Monte Carlo calculation is small in the metal and the oxide core.

Table 3.1.1 Results of criticality

Assembly	Metal Core	Oxide Core
Experiment (k_{eff})	1.00244±0.00024	1.00733±0.00013
Calculation (C/E value)		
Deterministic	0.991	0.996
Monte Carlo[(a)]	0.996	0.994

(a) Monte Carlo calculation: 1,700,000 history

Sodium Void Reactivity Worth[5]

A central sodium void worth, which is dominated by non-leakage component, was used to test prediction accuracy in the cores with different composition and spectrum. The sodium void worth was measured at the central 3x3 drawers in the metallic-fueled and oxide fuel mockup core.

The sodium void worth was calculated by the exact perturbation method based on diffusion theory.

Table 3.1.2 Results of sodium void reactivity worth

Assembly	Metal Core	Oxide Core
Experiment		
Sodium Weight (g)	1018	814
Reactivity Worth (10^{-4} Δk/k)	1.922±1.2 % (3.5 ¢)	1.006±2.4 % (2.0 ¢)
Calculation (C/E value)	0.98	1.05

Doppler Reactivity Worth[6), 7), 8)]

Doppler reactivity was measured using a cylindrical metallic sample (natural uranium; 25 mm ϕ and 150 mm in length) inserted at the center of the core. Reactivity worth was measured for the Doppler sample heated from 300 K to 1100 K.

The diffusion calculation in 70-group was made in the r-z model which had the Doppler sample and its surrounding capsule region. A resonance interaction effect between the Doppler sample and the surrounding materials was examined by the PEACO-X code which was calculated the resonance shielding effect precisely in the heterogeneous geometry. The calculation by PEACO-X code gave ~ 10% larger Doppler reactivity worth than the conventional calculation in which the Doppler sample was treated as isolated.

Table 3.1.3 Results of Doppler reactivity worth

Assembly	Metal Core	Oxide Core
Experiment (10^{-6} Δk/k)	-7.47±2.8 %	-18.19±3.7 %
Calculation[(a)] (C/E value)	0.95	0.99

(a) by PEACO-X code

^{238}U Capture to ^{239}Pu Fission Ratio[9)]

The absolute values of ^{238}U capture rate and ^{239}Pu fission rate were measured at the center of the core by a foil activation technique with thin metallic depleted uranium foils and plutonium foils. The difference of ^{238}U capture to ^{239}Pu fission ratio between the metal core and the oxide core was about 20 %.

The reaction rates were obtained from the cell averaged 70-group microscopic cross section and the neutron flux by the diffusion calculation in r-z geometry.

Table 3.1.4 ^{238}U Capture to ^{239}Pu Fission Ratio

Assembly	Metal Core	Oxide Core
Experiment	0.1215±2.4%	0.1457±2.0%
Calculation (C/E)	1.00	0.99

Reference

1) Nakagawa T., et al. : J. Nucl. Sci. Technol., 32, 1259 (1995).
2) Nakagawa M. and Tuchihashi K. : "SLAROM", JAERI-1294 (1984).
3) Iijima S., et al. :"EXPARAM Code System", to be published in JAERI-Research.
4) Mori T., et al. : J. Nucl. Sci. Technol., 29, 1224 (1992).
5) Oigawa H. and Iijima S. : " Experimental Study on Sodium Void Reactivity Worth in Mockup Cores of Metallic-fueled and MOX-fueled Fast Reactors using FCA", JAERI-Research 95-007 (1995). (in Japanese)
6) Oigawa H. : J. Nucl. Sci. Technol., 28 , 1058 (1991).
7) Okajima S., et al. : J. Nucl. Sci. Technol., 33, 202 (1996).
8) Okajima S., et al. : J. Nucl. Sci. Technol., 31, 1097 (1994).
9) Sakurai T. and Nemoto T. : " Measurement and Analysis of Breeding Indices of ^{238}U Capture to ^{239}Pu Fission Rate Ratios at Fast Critical Assembly", JAERI-Research 95-054 (1995). (in Japanese)

3.2 Estimation of Prediction Accuracy of ^{238}U Doppler Effect up to 3,000 °C

S. Okajima
(*E-mail*: okajima@fca001.tokai.jaeri.go.jp)

The Doppler effect of ^{238}U plays an important role in the transient behavior of an FBR (Fast Breeder Reactor). For a better prediction of the transient behavior, the Doppler effect measurement at temperatures around the melting point of the fuel was preferable. For this reason, new experimental devices were developed and were used to measure the ^{238}U Doppler effect up to 2,000 °C in the Fast Critical Assembly (FCA) [1-2]. In order to estimate the Doppler effect beyond the experimental temperature range, the Doppler effect was extrapolated to the melting point of the oxide fuel by using curve fitting.

Experiment of High Temperature Doppler Effect in FCA [1-2]

Two measurement techniques were used to measure the Doppler effect of ^{238}U up to 2,000 °C: (a) a reactivity worth measurement up to 1,500 °C with a heated sample [1] and (b) a reaction rate measurement up to 2,000 °C with a heated foil [2]. The measurements were carried out in a mock-up core of an oxide-fueled fast reactor (FCA XVII-1 Assembly).

The experimental results are shown in Table 3.2.1 together with the C/E values. The C/E values of the Doppler reactivity worths are 0.94, 0.94 and 0.98 for the sample temperature of 800 °C, 1,100 °C and 1,500 °C, respectively. The calculation slightly underestimates the Doppler reactivity worth. The C/E values at the temperature of 1,500 °C and 2,000 °C are 1.05 and 1.02, respectively. The calculation of the activation Doppler effect agrees with the experiment within the experimental error.

Extrapolation of the Doppler Effect to 3,000 °C

In order to estimate the Doppler effect beyond the experimental temperature range, the measured Doppler reactivity worths were fitted as the following temperature function [3];

$$\frac{d\rho(T)}{dT} = C\,(T/T_0)^{-\gamma}, \qquad (1)$$

where T_0 is the reference temperature (293K), C and γ are fitting parameters, and $\rho(T)$ is the Doppler reactivity worth as a function of temperature. A non-linear least squares method was applied to fit the measured data and the inverse square of the experimental error was used as the weighting function. The standard deviation of the estimated value was determined by using the principle of propagation of error. Figure 3.2.1 shows the experimental data together with the fitted curve. From the curve the Doppler reactivity worths beyond the temperature of 1,500 °C are obtained within an estimation error of 10%. The estimated

Doppler reactivity worths at the temperature of 2,000 °C, 2,500 °C and 3,000 °C are -2.1 x 10^{-8}, -2.2 x 10^{-8} and -2.4 x 10^{-8} ($\Delta k/k$ / g of ^{238}U), respectively.

The ratio of the calculated Doppler reactivity worth to the estimated one at 2,000 °C was compared with the C/E value of the activation Doppler effect at the equivalent temperature (see Table 3.2.1). Both values coincide with each other within the error. By permitting a direct check on predictions of the change in reaction rate due to Doppler broadening of the resonances, the activation Doppler effect can be considered as complementary to the Doppler reactivity worth measurements. The calculation accuracy of the Doppler reactivity worth at 2,000 °C is confirmed by the C/E value of the activation Doppler effect.

From these results, it is concluded that the calculation predicts the Doppler effect in the temperature range from 20 °C to 3,000 °C with an estimation error less than 10%.

Conclusion

The Doppler effect was extrapolated to the melting point of the oxide fuel by using curve fitting. The calculated Doppler reactivity worths were in agreement with the extrapolated ones within the estimation error of 10%. The extrapolation using the experimental data of the high temperature Doppler effect contributes to the confirmation of calculation reliability of the Doppler effect at higher temperature.

References

1) Okajima S., Oigawa H., Mukaiyama T. and Andoh M. : J. Nucl. Sci. and Technol., 33, 202-210 (1996).
2) Okajima S., Oigawa H., Andoh M. and Mukaiyama T. : ibid., 34, 13-20 (1997).
3) Wirtz K. : Lectures on Fast Reactors, (Kernforschungszentrum Karlsruhe, 1978), p.160.

Table 3.2.1 Experimental and calculated results of high-temperature Doppler effect

Temperature	*Doppler reactivity worth*[1]		*Activation Doppler effect*[2]	
	Expt. ($\times 10^{-8}\Delta k/k$ / g of ^{238}U)	C/E	Expt.	C/E
800 °C	-1.36±3.7%	0.94	0.043±16%	0.92
1,100 °C	-1.63±3.1%	0.94	0.052±13%	0.91
1,500 °C	-1.84±3.8%	0.98	0.053±13%	1.05
2,000 °C	(-2.1±5%)*	(1.03)**	0.062±6.5%	1.02
2,500 °C	(-2.2±7%)*	(1.07)**		
3,000 °C	(-2.4±10%)*	(1.1)**		

* Estimated values by the extrapolation of the measured data up to 1500 °C (The data are fitted to temperature functions of Eq. (1)).

** Ratio between calculated and estimated values.

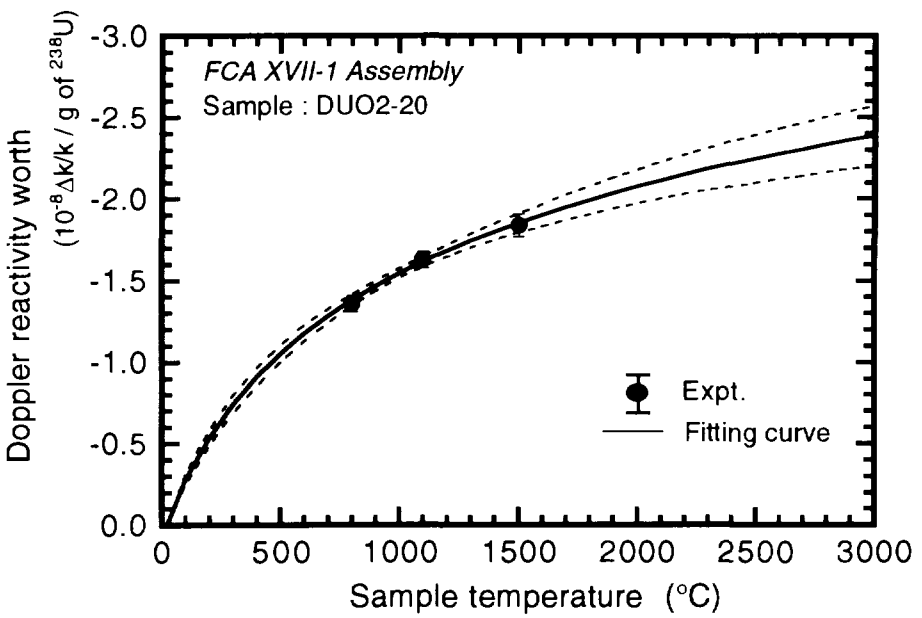

Fig. 3.2.1 Estimation of the Doppler effect in the higher temperature range by the extrapolation of the measured data up to 1500 °C[1] (The data are fitted to temperature functions of Eq. (1) (γ=1.13±0.18)).

3.3 Measurement of In-core GEM Reactivity Worth at FCA

H. Oigawa, S. Iijima and M. Andoh
(*E-mail:* oigawa@fca001.tokai.jaeri.go.jp)

Gas Expansion Module (GEM) is a device to enhance negative feedback reactivity in case of a loss-of-flow accident of sodium cooled fast reactors. The level of the sodium free surface in GEM is maintained above the top of the core in normal operation. When a loss of flow occurs, inert gas in GEM expands and reduces the sodium level, which results in the enhancement of the neutron leakage from the core.

The GEM installed in the central part of the core is called "In-Core GEM". In this case, the axial neutron streaming effect along the void is important to calculate reactivity worth caused by the reduction of the sodium level. It is, however, still difficult to calculate such an effect precisely, and therefore, the experimental validation of the calculation method is essential for the design of In-Core GEM.

In this study, In-Core GEM reactivity worth was measured at FCA XVII-1 core which simulated a prototype MOX fueled LMFBR and the calculation accuracy of various methods were examined.

Experiment

The central fuel drawers (5cmx5cmx76cm^L) were substituted by the drawers consisting of sodium plates as the In-Core GEM test region. The RZ model is shown in Fig.3.3.1. Although the effective radius of the test region was about one third of the actual GEM assembly, the same kind of difficulty is expected in calculation of GEM void reactivity worth governed by an axial neutron streaming effect along the void.

The sodium plates in the test region were canned by stainless steel. To simulate the void of the sodium in GEM, the sodium plates were replaced with void cans so as to conserve the amount of stainless steel.

The reactivity worth caused by the reduction of the sodium level from the top of the upper axial blanket to the center of the core were measured in four steps as shown in Fig. 3.3.2. The negative reactivity is observed with the decrease of the sodium level because of the enhancement of the neutron leakage. Near the core mid plane, however, the reactivity changes toward the positive side because of the neutron spectrum hardening. This phenomenon reduces the GEM effectiveness.

Calculation

Two sets of 70-group effective cross sections based on JENDL-2 and JENDL-3.2 were prepared using cell calculation code, SLAROM. For the test region, two kinds of cylindrical cell models were examined : one was a homogeneous super-cell model and the

other was a heterogeneous one. In the latter model, the array of stainless steel and sodium in the plate cell was approximated by a series of concentric cylinders. As for the diffusion coefficients, four formulas were examined ; (1)$D=1/(3\Sigma_{tr})$, (2)Rowlands'[1], (3)Benoist's[2], and (4) Takeda's[3]. The former two formulas were applied to the homogeneous super-cell and the latter two were to heterogeneous one.

The core calculations was performed in RZ model. In case of transport theory, S8 calculation with transport approximation was performed. The reactivity worths were calculated by the exact perturbation theory.

Results and Discussion

The measured and calculated GEM reactivity worths are compared in Table 3.3.1. As for the transport theory with JENDL-3.2, the calculated values are 4 - 24 % smaller than the experimental ones and the C/E values depend upon the sodium level. The calculation with JENDL-2 gives smaller values than that with JENDL-3.2. In Fig.3.3.2, the reactivity worths are divided into the non-leakage and the leakage term. The difference between JENDL-3.2 and -2 is caused by both terms.

As for the diffusion theory, good agreement with the transport theory was obtained by using Rowlands' coefficient in homogeneous super-cell, though $1/(3\Sigma_{tr})$ gives unacceptably large values.

In the heterogeneous cell model, Takeda's diffusion coefficient shows good agreement with the transport theory, while Benoist's does not. This result is not surprising since Benoist's diffusion coefficient was not formulized to be applied to the super-cell, but Takeda generalized the Benoist's theory to the super-cell.

It can be concluded that the diffusion theory should be used with great care to calculate the In-Core GEM reactivity worth. Moreover, it is necessary to solve the dependence of C/E values by the transport theory upon the sodium level.

References

1)Rowlands J. L. and Eaton C. R. : "Effective Diffusion Coefficients for Low Density Cylindrical Channels," Nucl. Sci. Eng., 76,263-281 (1980).

2)Benoist P. : "Theory of the Diffusion Coefficient of Neutrons in a Lattice Containing cavities," CEA-R-2278 (1964).

3)Takeda T, Arai K. and Yamaoka M. : "Unified Diffusion Coefficient for Analysis of Sodium-Void Worth in Fast Critical Assembly with Control-Rod Channels," J. Nucl. Sci. Technol., 18, 93-115 (1981).

Table 3.3.1 In-Core GEM reactivity worth in FCA XVII-1

Na level	Experiment	Transport theory		Diffusion theory (JENDL-3.2)			
		Homogeneous cell				Heterogeneous cell	
	($10^{-5}\Delta$ k/k)	JENDL-3.2	JENDL-2	$1/(3\Sigma_{tr})$	Rowlands	Benoist	Takeda
-30.5cm	-3.2±0.2[a]	-3.1(0.96)[b]	-3.0(0.93)	-13.2	-3.2	-14.5	-3.1
-45.7cm	-7.4±0.2	-6.6(0.89)	-6.4(0.87)	-31.3	-6.7	-33.6	-6.9
-66.0cm	-7.3±0.2	-6.2(0.85)	-5.8(0.80)	-40.3	-6.0	-43.3	-5.8
-76.2cm	-5.6±0.2	-4.3(0.76)	-3.8(0.67)	-38.9	-3.9	-42.1	-3.3

(a) Experimental error (b) Calculated to experimental value (C/E)

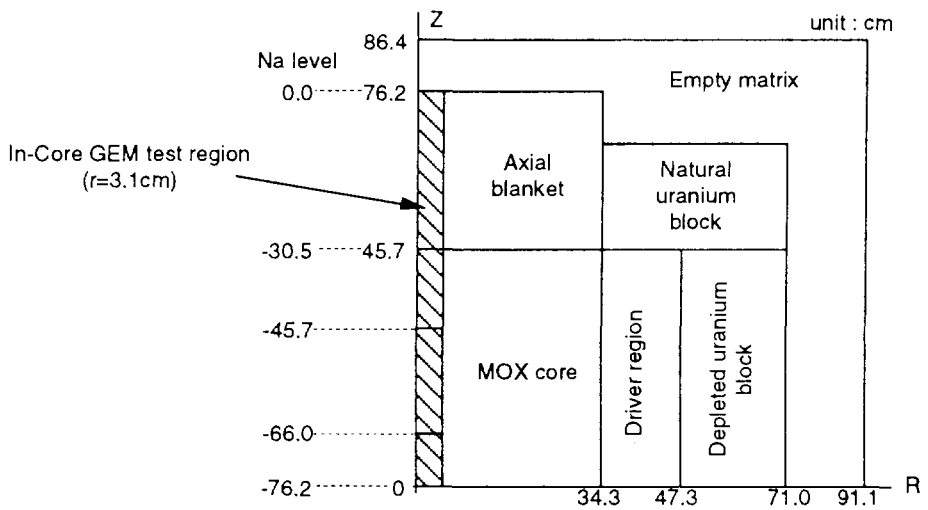

Fig.3.3.1 RZ-model of FCA XVII-1 with In-Core GEM test region

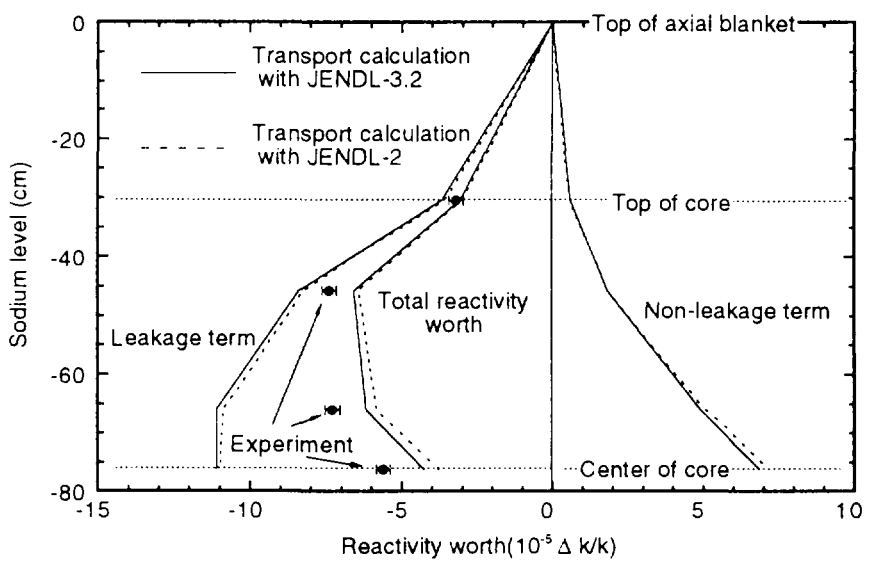

Fig.3.3.2 Comparison of In-Core GEM reactivity worth

3.4 Analysis of Reaction Rate Ratios Experiments for Moderator Added Fast Reactor Cores

M. Andoh, T. Nemoto, K. Tsujimoto, T. Osugi and Y. Kato
(*E-mail:* andoh@fca001.tokai.jaeri.go.jp)

New reactor concepts have been investigated to enhance safety margins for a metallic or nitride fuel fast reactor by adding small amount of moderator material into the core.[1)2)] A series of mockup experiments for moderator added metallic fuel fast reactor was carried out at FCA (Fast Critical Assembly) to obtain the experimental verification for improvement of reactivity coefficients.[3),4)] In this study, reaction rate ratios as spectrum indexes were measured to investigate calculation accuracy of neutron spectrum at the core center.

Mockup cores (FCA XVIII cores) consist of a test region (39cmx39cmx91cm), a buffer region and a driver region. The test region cell contains zirconium (Zr) and polystyrene (CH) plates to simulate moderator material, zirconium-hydride (ZrH). Atomic number density ratios of hydrogen to heavy nuclide (H/HM) of the test region cell were set to the values of 0.13, 0.05 and 0.02 by varying the void fraction of the CH plates from 45% to 95%.

The reaction rates were measured at the center of the core. The measured reaction rates were the fission reaction rates of ^{235}U (*F5*), ^{238}U (*F8*) and ^{239}Pu (*F9*) and the neutron capture reaction rate of ^{238}U (*C8*). A depleted uranium foil (^{238}U 99.96%) was used to obtain *C8* and *F8*. An enriched uranium (^{235}U 93.2%) foil and a plutonium (^{239}Pu 94%) foil were used to obtain *F5* and *F9*, respectively. These foils were irradiated simultaneously in the voided cell in the central drawer as shown in Fig. 3.4.1 so that the cell-averaged neutron spectrum could be achieved. The γ-rays from the foils were measured using HP Ge detector after the irradiation. The parallel fission chambers[5)] were used to correct *F5*, *F8* and *F9* that were obtained by the measurement of foils. Finally, reaction rate ratios *C8/F9*, *F8/F9* and *F5/F9* were obtained.

A collision probability code with ultra-fine group structure, PEACO-X[6)], was used to obtain the effective microscopic cross sections in the resonance energy region to consider the resonance interaction effect between nuclides in the foil and those in the adjacent core region. After the collision probability calculation, the ultra-fine group structure was collapsed to JFS-3[7)] type group structure (lethargy width=0.25). A super-cell calculation model in one-dimensional infinite slab geometry (an infinite slab foil in a voided region surrounded by homogenized fuel cell) was employed for the PEACO-X calculation. The effective microscopic cross sections of each nuclide except resonance energy region were calculated by the use of a conventional cell calculation code SLAROM[8)] with 70-group structure. The reaction rates of each nuclide were obtained by 70-group diffusion calculation in the R-Z geometry using

CITATION-FBR code[9]. The above calculations were performed with JENDL-3.2 library[10].

The results of the analysis are shown in Table 3.4.1. The calculation of *C8/F9* shows good agreement with the experiment except the case of H/HM=0.13 and C/E values slightly depend on the H/HM values. The calculation of *F8/F9* for each H/HM value overestimates the experiment. *F5/F9*, however, shows good agreement between the experiment and calculation. It can be considered that these tendencies come from the calculation accuracy of the neutron spectrum in the system that contains hydrogen, especially in the high energy region where the fission of ^{238}U occurs and in the low energy region where the neutron spectrum is softened by adding hydrogen.

References

1) Takano H., et al. : "A CONCEPT OF ADVANCED FAST BREEDER REACTOR WITH INSTANTANEOUS NEGATIVE TEMPERATURE COEFFICIENT," in Proc. of International Conference on Fast Reactor and Related Fuel Cycles, Oct. 28 - Nov. 1, 1991, Kyoto, Japan, p. 16.1(1991).
2) Tsujimoto K., et al. : "IMPROVEMENT OF REACTIVITY COEFFICIENT OF METALLIC FUEL LMFBR," in Proc. of International Conference on Reactor Physics and Reactor Computations, Jan. 23 - 26, 1994, Tel-Aviv, Israel, p. 397(1994).
3) Osugi T., et al. : "Mock-up Experiment for Moderator Added Fast Reactor (1) General Discussion and Na Void Effect," JAERI-Review 96-012, p. 58(1996).
4) Okajima S., et al. : "Mock-up Experiment for Moderator Added Fast Reactor (2) Doppler Effect," JAERI-Review 96-012, p. 61(1996).
5) Obu M. : "Preparation and Characteristics of Fission Chambers with Actinide Nuclides," JAERI-M 9757(1981).
6) Okajima S., et al. : "Measurement of Doppler Effect up to 2000 °C at FCA (3) -Development of a Cell Code, PEACO-X, with Ultra-fine Group Structure-," JAERI-M 92-185 (in Japanese), (1992).
7) Takano H. and Ishiguro Y. : "Production and Benchmark Tests of Fast Reactor Group Constant Set JFS-3-J2," JAERI-M 82-135 (1982).
8) Nakagawa M. and Tsuchihashi K. : "SLAROM: A Code for Cell Homogenization Calculation of Fast Reactor," JAERI 1294 (1984).
9) Iijima S. : "EXPARAM," private communication.
10) Nakagawa T., et al. : J. Nucl. Sci. and Tecnol., 32, 1259 (1995).

Table 3.4.1 Results of the analysis of the reaction rate ratios in FCA-XVIII

	C8/F9		F8/F9		F5/F9	
H/HM	Expt.	C/E	Expt.	C/E	Expt.	C/E
0.13	0.152 ±1.5%*	0.92	0.0186 ±1.2%	1.07	1.03 ±1.8%	1.02
0.05	0.143 ±1.3%	0.97	0.0224 ±1.8%	1.03	1.04 ±1.6%	0.99
0.02	0.133 ±1.2%	0.99	0.0233 ±1.8%	1.04	1.00 ±1.4%	1.00

*) Experimental error.

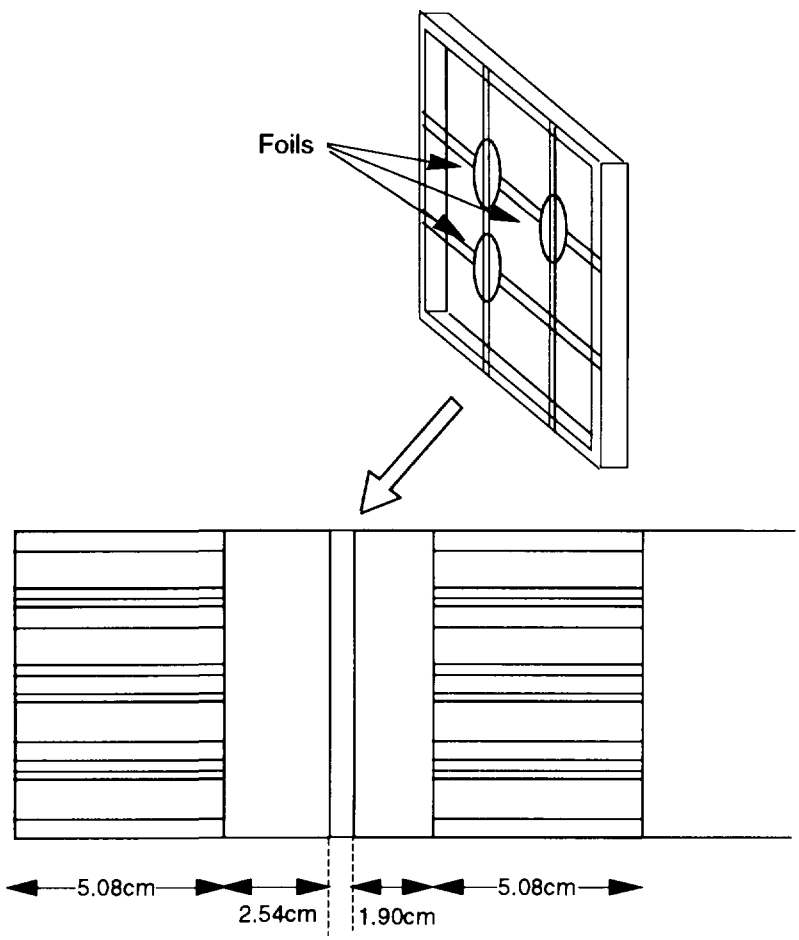

Fig. 3.4.1 View of the irradiation condition for the foils in the central drawer

3.5 Analysis of β_{eff} Benchmark Experiment in MASURCA

T. Sakurai and T. Nemoto
(*E-mail* : sakurai@fca001.tokai.jaeri.go.jp)

The effective delayed neutron fraction β_{eff} is an important parameter as a scale of reactivity worth of a nuclear reactor. International β_{eff} Benchmark Experiments were performed at fast critical facility MASURCA in France during April 1993 and March 1994 [1] under a framework of OECD/NEA/NSC . In the present study, analysis was performed for the β_{eff} experiments at two MASURCA cores : R2 which is a 30% enriched uranium core and Zona2 which is a 25% enriched MOX core. Main characteristics of these cores are given in Table 3.5.1. Each core consists of a simple cylindrical one-region core and a blanket which surrounds the active core both radially and axially. Experimental values and uncertainties of β_{eff} by each participant were already discussed in ref.1). We take the weighted average of these β_{eff} values ; 720pcm $\pm$2.6% for R2 and 346pcm $\pm$2.7% for Zona2.

The analysis was made by a transport theory code, TWOTRAN-II[2] using a two dimensional cylindrical model and homogeneous atom densities of MASURCA fuel cells. Seventy energy group constants set of JFS-3-J3.2 [3] which was processed from JENDL3.2 nuclear data file was used. The β_{eff} values were calculated by changing delayed neutron(D.N.) yields and spectrum as follows :

(a) D.N. yields evaluated by Tomlinson(fission spectrum) [4] and D.N. spectrum in JENDL3.2(2 MeV),
(b) D.N. yields and spectrum in JENDL3.2(2 MeV) and
(c) D.N. yields in JENDL3.2(2 MeV) and D.N. spectrum in ENDF/B-VI(2MeV).

Calculated values of β_{eff} are summarized in Table 3.5.2.

- The calculated β_{eff} of the cases (b) and (c) agree well within 0.6% at both cores of R2 and Zona2.
- The calculated β_{eff} of the cases (a) and (b) agree within 3% at R2 core.
- Significant difference of more than 5% between cases (a) and (b) is found in the calculated β_{eff} at Zona2 core.

This large difference is caused by :

- a large difference of D.N. yields of ^{238}U between Tomlinson(D.N. yield : 0.044) and JENDL3.2(D.N. yield : 0.048),

- a large contribution of ^{238}U to β_{eff} of Zona2 core(48%) as shown in Table 3.5.1.

Calculation/experiment ratios(C/E) of β_{eff} are summarized in Table 3.5.3. The calculation using Tomlinson D.N. yield underestimates the β_{eff}, while the calculation using JENDL3.2 D.N. yield overestimates the β_{eff} at Zona2 core as shown in Table 3.5.3.

From these results we conclude :

(1) There is no significant difference of calculated β_{eff} between D.N. spectra of JENDL3.2 and ENDF/B-VI at the present two cores and

(2) The recommended value of D.N. yield of ^{238}U is larger than 0.044 and less than 0.048 by taking account of the C/Es at Zona2 core.

Further β_{eff} experiments at FCA in JAERI are in progress on complementary core configurations to have D.N. yields to be recommended for calculating β_{eff}.

References

1) Bertrand P. et al.: Proc. of International Conference on the Physics of Reactors, Mito, Japan(1996).

2) Lathrop K.D. and Binkley F.W.: LA-4848-MS(1973).

3) Takano H., et al.: Proc. of International Conference on Nuclear Data for Science and Technology, Gatlinburg, USA(1994).

4) Tomlinson L.: AERE-R-6993(1972).

Table 3.5.1 Main characteristics of the β_{eff} cores in MASURCA [1)]

Core		R2	Zona2
- Dimension Radius x Height		48cm x60cm	50cm x 60cm
- Fuel		U metal	PuO_2-UO_2
- Fuel enrichment		30 %	25 %
- Moderator		Sodium	Sodium
- Contribution of main isotopes to β_{eff}*	^{235}U	77%	2%
	^{238}U	23%	48%
	^{239}Pu	------	43%

* Calculated results by JAERI

Table 3.5.2 Calculated β_{eff}

Case	D.N. data		β_{eff}	
	D.N. yield	D.N. spectrum	R2	Zona2
a	Tomlinson	JENDL3.2	730 (0.971)*	339 (0.949)
b	JENDL3.2	JENDL3.2	752 (1.000)	357 (1.000)
c	JENDL3.2	ENDF/B-VI	756 (1.005)	359 (1.005)

* Ratio of the calculated value to that of case b

Table 3.5.3 C/E of β_{eff}

Case	D.N. data		C/E	
	D.N. yield	D.N. spectrum	R2	Zona2
a	Tomlinson	JENDL3.2	1.013	0.980
b	JENDL3.2	JENDL3.2	1.044	1.031
c	JENDL3.2	ENDF/B-VI	1.050	1.037

3.6 International β_{eff} Benchmark Experiment in FCA
(1) Experimental Program

S. Okajima, T. Sakurai and T. Mukaiyama
(*E-mail*: okajima@fca001.tokai.jaeri.go.jp)

Purpose and Background

The effective delayed neutron fraction, β_{eff}, which allows the conversion between calculated and measured reactivity values, plays an important role in the theoretical interpretation of reactivity measurement. To improve the prediction accuracy of the β_{eff}, the program of the international benchmark experiment in FCA was planned. This program was the complementary nature to that in MASURCA facility of CEA-Cadarche which was carried out between 1993 and 1994[1]. In these programs five different core configurations were selected taking into consideration of the systematic change of the nuclide contribution from U-235, U-238 and Pu-239 to the β_{eff}. These experiments have been conducted under the NEA/NSC Working Party on International Evaluation Cooperation (WPEC), Subgroup 1.6 on Delayed Neutron Data Validation. The several countries participated in this experimental program. The β_{eff} measurement was carried out by each participant with their own measurement technique, and the measured results have been compared with each other. The primary intent of these benchmark experiments was to obtain an in-pile measurement of the β_{eff} with an accuracy better than 3% using a wide variety of experimental techniques. On the basis of these results, the reliability of delayed neutron data can be verified using current computational methods.

Benchmark Cores in FCA[2]

Three different core configurations were selected so that these cores could be complementary to those of MASURCA: XIX-1 (U-core), XIX-2 (Pu/U core) and XIX-3 (Pu core). Figure 3.6.1 shows the nuclide contribution to β_{eff} for each core. The systematic change of nuclide contribution was found. The nuclide contribution to β_{eff} in the XIX-2 core is similar to that in the MASURCA Zona2 core. The purpose of the XIX-1 core is to compare the experimental techniques among participating parties through the β_{eff} measurement for standard nuclide, U-235, since the contribution of U-235 in this core is about 95%. The purpose of the XIX-3 core is to evaluate the β_{eff} for Pu-239.

The main characteristics of these cores were shown in Table 3.6.1. The core is surrounded by an inner blanket of 30 cm thickness containing a significant amount of depleted uranium-oxide and sodium, and an outer blanket of 15 cm thickness containing only depleted uranium metal. The contribution of these blanket regions to β_{eff} was less than 10%.

The followings are participating groups; CEA/Cadarche (France), IPPE/Obninsk (Russia), KAERI (Korea), LANL (USA), Nagoya Univ. (Japan) and JAERI (Japan).

The experimental schedule was also shown in Table 3.6.1. The first core, XIX-1 core, construction started in October, 1995. The β_{eff} measurement in this core was carried out between January, and April, 1996. The measurement in the third core will finish in 1998.

References

1) Bertrand P. et al.: Proc. of Int. Conf. on the Physics of Reactors PHYSOR 96, Mito, Japan, E-190 - E-199, (1996).
2) Okajima S., Sakurai T. and Mukaiyama T. : Proc. of The 1996 Symposium on Nuclear Data, JAERI-Conf 97-005, 71-76, (1997).

Table 3.6.1 Majoir characteristics of the β_{eff} benchmark cores in FCA

Core name	Enrichment	Geometry R x H (cm)	β_{eff} (pcm)	Experimetal period
XIX-1	93% (U)	33 x 51	782 (96% : 4% : 0%)	Jan.'96 - Apr.'96
XIX-2	22% (Pu/U)	36 x 61	382 (12% : 46% : 41%)	Jul.'96 - Apr.'97
XIX-3	92% fiss. (Pu)	33 x 61	246 (8% : 9% : 80%)	Jul.'97 - Feb.'98
			Nuclide contribution to β_{eff} : (U-235 : U-238 : Pu-239)	

XIX-1 : Evaluation of β_{eff} for U-235
XIX-2 : Similar magnitude of β_{eff} to MASURCA ZONA2 core
XIX-3 : Evaluation of β_{eff} for Pu-239

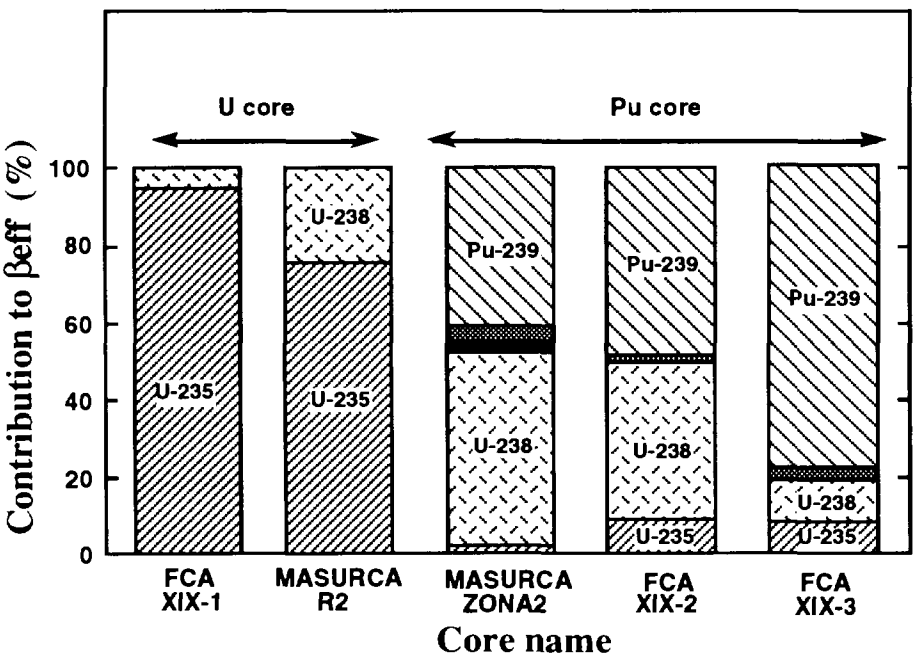

Fig. 3.6.1 Nuclide contribution to β_{eff} in the β_{eff} benchmark cores

3.7 International β_{eff} Benchmark Experiment in FCA
(2) Core Characteristics of the First Core(XIX-1 Core)

T. Sakurai and S. Okajima
(*E-mail* : sakurai@fca001.tokai.jaeri.go.jp)

The FCA XIX-1 core was built as the first core in a series of International β_{eff} Benchmark Experiment in FCA. Measurement and analysis were performed for reactor physics parameters such as (a) criticality, (b) central fission rate ratio and (c) fission rate and fission importance distributions. Main features of XIX-1 core are discussed in the former section. Fuel cells of this core consist of 93% enriched uranium plate and graphite plate as a moderator.

The fission rate ratio of $^{238}U/^{235}U$ at the core center and the fission rate distributions of ^{238}U and ^{235}U were measured by a foil activation technique [1] with thin metallic foils of depleted uranium and enriched uranium. The fission importance distributions were measured as distributions of pseudo-reactivity worth of a ^{252}Cf source by traversing the neutron source through radial and axial penetration holes. The reactivity worth was determined by positions of a control rod which keeps the reactor power at constant level.

Analysis of these experiments was made with 70 energy group constants set of JFS-3-J3.2 [2] which was processed from JENDL3.2 nuclear data file and a standard calculation system for fast reactor neutronics in JAERI [3]. The collision probability code SLAROM [4] was used to calculate effective cross section of each region in the XIX-1 core. The core calculation was made by the three dimensional diffusion calculation in x-y-z geometry with CITATION-FBR code [5].

Calculation/experiment ratios(C/E) are summarized in Table 3.7.1 and Figures 3.7.1 ~ 3.7.3.

(a) The diffusion calculation underestimates the k_{eff} by 1.4%. A correction for transport effect will be made in future to improve the C/E.

(b) The calculated central fission rate ratio agrees well with the measured one within 1%.

(c) Good agreements within 1% between the calculation and measurement were obtained for the ^{235}U fission rate and fission importance distributions. On the other hand, the calculation underestimates the ^{238}U fission rate distribution by more than 2% near boundary of active core and blanket.

References

1) Sakurai T. and Nemoto T.: JAERI Research 95-054(1995) (in Japanese).
2) Takano H., et al.: Proc. of International Conference on Nuclear Data for Science and Technology, Gatlinburg, USA(1994).
3) Nakagawa M., Abe J. and Sato W.: JAERI-M 83-066(1983) (in Japanese).
4) Nakagawa M. and Tsuchihashi K.: JAERI1294(1984).
5) Iijima S.: private communication.

Table 3.7.1 C/E* of k_{eff} and central fission rate ratio of $^{238}U/^{235}U$

- k_{eff}	0.986
- Fission rate ratio of $^{238}U/^{235}U$	1.01

* C/E based on diffusion calculation

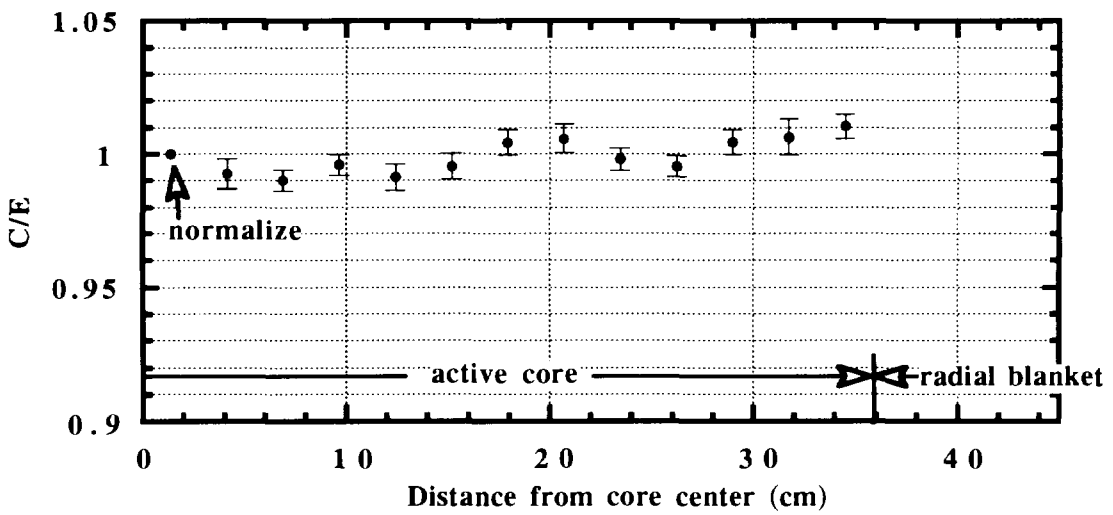

Fig. 3.7.1 C/E of radial distribution of ^{235}U fission rate

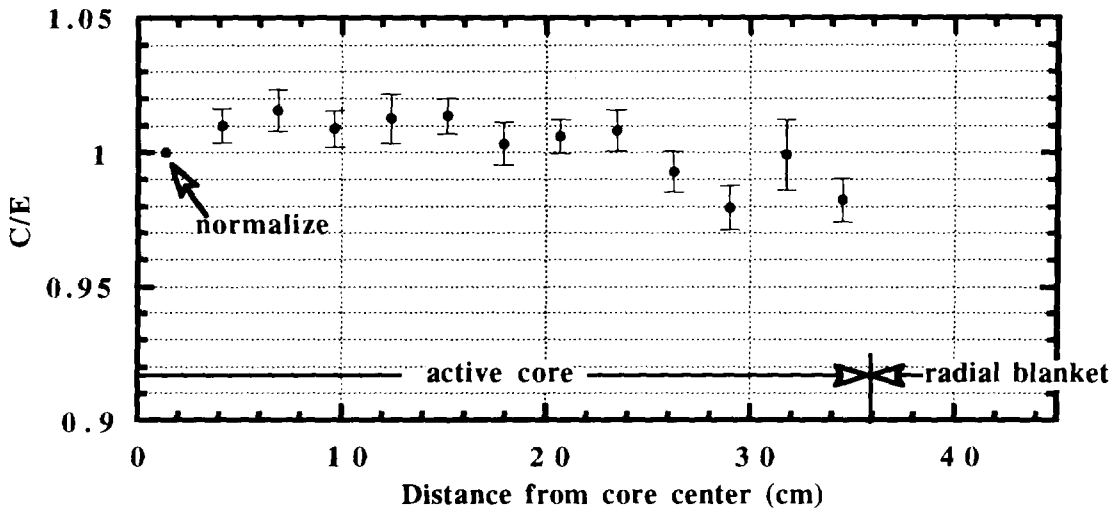

Fig. 3.7.2 C/E of radial distribution of ^{238}U fission rate

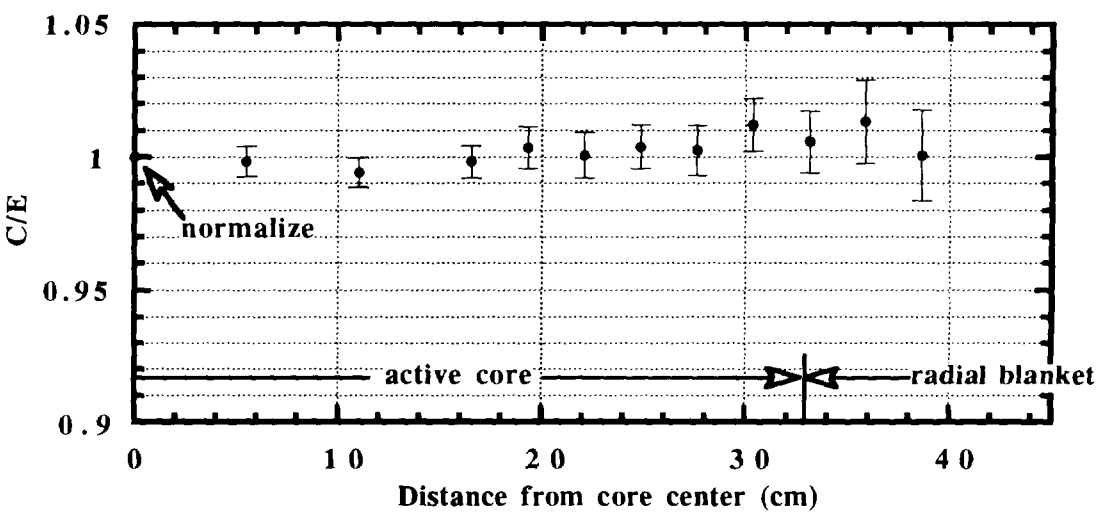

Fig. 3.7.3 C/E of radial distribution of ^{252}Cf fission importance

3.8 International β_{eff} Benchmark Experiment in FCA
(3) β_{eff} Measurements in the First Core(XIX-1 Core)

T. Sakurai, S. Okajima, H. Sodeyama, H. Song* and Y. Kim*
(*E-mail* : sakurai@fca001.tokai.jaeri.go.jp)

The effective delayed neutron fraction(β_{eff}) of FCA XIX-1 core was measured by (a)^{252}Cf source method [1] and (b)covariace-to-mean method. The covariace-to-mean method is a modification of a variance-to-mean method already presented in ref.2) etc.

^{252}Cf Source Method

The β_{eff} was obtained by the ^{252}Cf source method :

$$\beta_{eff} = \frac{S_{Cf}}{\rho_{Cf} \cdot R_f \cdot \bar{\nu} \cdot F_i} \cdot \left(\frac{\overline{\phi^+_{Cf}}}{\phi^+_{fuel}} \right) \quad (3.8.1) \qquad \text{and} \qquad F_i = \frac{\int dv \int dE\, \chi \phi^+ \int dE\, \nu \Sigma_f \phi}{\left(\int dE\, \chi \phi^+ \int dE\, \nu \Sigma_f \phi \right)_{center}} \quad (3.8.2),$$

where

ρ_{Cf} : an apparent reactivity due to emission of spontaneous fission neutrons from a ^{252}Cf source (in dollar unit) ,

S_{Cf} : the source strength (/s) ,

R_f : a fission rate of core material at the core center (/s cm^3) ,

$\bar{\nu}$: a neutron emission rate per fission averaged in the reactor ,

F_i : a normalization integral(cm^3) given as (3.8.2) and

$\left(\frac{\overline{\phi^+_{Cf}}}{\phi^+_{fuel}} \right)$: an importance ratio of source neutrons to reactor fission neutrons

The ρ_{Cf}, S_{Cf} and R_f were measured as described previously in ref.3) .The F_i, $\bar{\nu}$ and the importance ratio were calculated by the diffusion code in the three dimensional x-y-z geometry as described in the former section.

Covariace-to-mean Method

The β_{eff} is obtained by the covariance-to-mean method with an Eq.(3.8.3) for a ratio of covariance of counts of a couple of neutron detectors to mean of counts of the detector [4] when a prompt-neutron approximation is valid.

---

* Korea Atomic Energy Research Institute

$$\frac{\overline{m_1 m_2} - \overline{m_1} \cdot \overline{m_2}}{\overline{m_1}} = A_p \cdot \left[1 - \frac{1 - \exp(-\alpha_p \tau)}{\alpha_p \tau} \right] \quad (3.8.3),$$

$$A_p = \frac{\overline{c_2}}{R_f \cdot F_r} \cdot D_D \cdot D_S \cdot \left(\frac{1 - \beta_{eff}}{\beta_{eff} - \rho} \right)^2 \quad (3.8.4), \quad \text{and} \quad F_r = \frac{\int dv \int dE \Sigma_f \phi}{\left(\int dE \Sigma_f \phi \right)_{center}} \quad (3.8.5),$$

where

m_1 and m_2 : number of the counts of detectors #1 and #2 during time gate τ(s),

$\overline{c_2}$: a count rate of the detector #2(/s),

R_f : a fission rate of core material at the core center(/s cm^3),

F_r : a ratio of total fission rate in the reactor to a fission rate at the core center(cm^3) given as Eq.(3.8.5),

D_D : Diven factor, ρ : a reactivity(dk/k),

D_S : a spatial correction factor [5] and α_p : a prompt-decay constant(/s).

Measurement of covariance was made with a couple of BF3 detectros(#1 and #2) which were placed at the symmetrical position in the radial blanket. Neutron counts of the detectors #1 and #2 were processed with conventional electronics and multichannel scaler #1 and #2 which simultaneously start sweep for data accumulation. Each of the multichannel scalers had 8192 data channels and the preset time gate width(τ) of each channel was fixed at 0.1ms. The covariance-to-mean ratio was obtained as shown in Fig.3.8.1 where the ratios at time gates wider than 0.1ms were obtained by bunching [6] the data at the 0.1ms gate. To take account of the influence of delayed neutrons, a least-squares fit was made for the covariance-to-mean ratio in Fig.3.8.1 by using a modified equation :

$$\frac{\overline{m_1 m_2} - \overline{m_1} \cdot \overline{m_2}}{\overline{m_1}} = A_p \cdot \left[1 - \frac{1 - \exp(-\alpha_p \tau)}{\alpha_p \tau} \right] + A_d \cdot \left[1 - \frac{1 - \exp(-\alpha_d \tau)}{\alpha_d \tau} \right], \quad (3.8.6)$$

where the second term in the right side represents the contribution of delayed neutrons. The β_{eff} is determined from an amplitude A_p given as Eq.(3.8.4). The measurement of covariance was made at a slight subcriticality of 0.017%dk/k(0.022 dollar). The R_f was measured and the F_r, D_D and D_S were calculated.

Analysis of β_{eff} was made by the diffusion theory in the three dimensional x-y-z geometry as described in the former section. Delayed neutron yields and spectra evaluated in JENDL3.2 nuclear data file were used to calculate the β_{eff}.

The experimental values of β_{eff} are summarized in Fig.3.8.2. Good agreement of the two values of β_{eff} within 1% was obtained. Calculation/experiment ratio(C/E) of β_{eff} is 1.08 when the average of the two values of β_{eff} is used. Comparison of β_{eff} between each participants of the benchmark experiments will be made in future.

References

1) Fisher E. A.: Nucl. Sci. Eng., 62, 105(1977).

2) Moberg L. and Kockum J.: Nucl. Sci. Eng., 52, 343(1973).

3) Sakurai T. et al.: JAERI-M 93-181 p 51(1993).

4) Uhrig R. E.: "Randam Noise Techniques in Nuclear Reactor Systems" The Ronald Press Company, New York(1970).

5) Otsuka M. and Iijima T.: Nukleonik, 7, 488(1965).

6) Misawa T., Shiroya S. and Kanda K.: Nucl. Sci. Eng., 104, 53(1990).

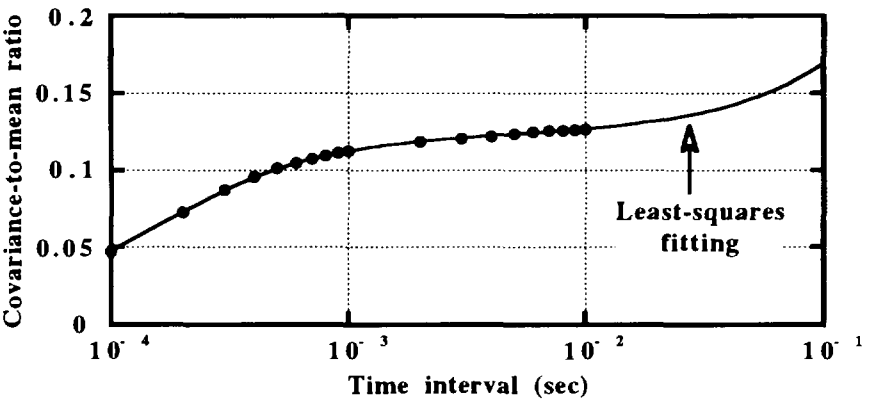

Fig. 3.8.1 Dependency of covariance-to-mean ratio on time interval

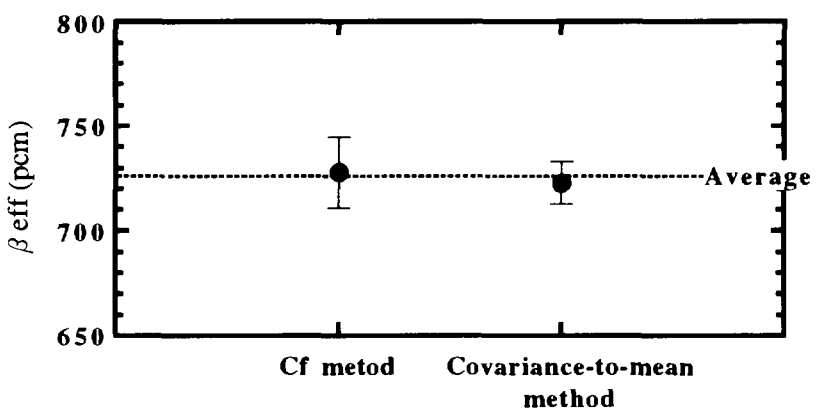

Fig. 3.8.2 Experimental values of β_{eff}

3.9 Measurement of Reactivity Worth of HTTR Mockup Reserve Shutdown Absorber at VHTRC -1 Core

F. Akino, M. Takeuchi, T. Ono and S. Fujisaki
(*E-mail* : akino@terzan.tokai.jaeri.go.jp)

In the design of HTTR[1], the Reserve Shutdown Absorber worth must be determined accurately. To examine the accuracy of neutronics calculation code, we measured the reactivity worth of an HTTR mockup Reserve Shutdown Absorber (RSS) rod in the VHTRC-1 core by the pulsed neutron source (PNS) method.

The VHTRC-1 core[2] is loaded with 4wt% enriched coated particle fuel. This core reaches a critical point by 280 fuel rods. The RSS rod consists of a stack of about 6100 neutron absorbing pellets (diameter : 9.9mm, length : 10.3mm, boron content :28.7wt%) inserted into a stainless steel tube (diameter : 97.5mm, length : 1135mm). These pellets are produced by sintering B_4C and graphite powders.

In the PNS experiment, the core loaded with 274 fuel rods was used and four BF_3 counters were installed in the core. The PNS target was located near the center of back surface of the fixed half assembly. The fuel rod loading pattern and arrangements of the BF_3 counters and the PNS target are shown in Fig.3.9.1 The decay constants of the pulsed neutrons with and without the RSS rod were measured. The outputs of the four BF_3 counters were collected using a multichannel time analyzer with four independent inputs in a multichannel scaling mode. To determine the prompt neutron decay constant, α, the raw data were fitted to an exponential function with a computer code ALPHA-D[3], taking account of the effect of delayed neutron modes. The final value of α was obtained by averaging the four α values for each detector position. The reactivity worth was determined by the revised King-Simmons' formula[4] with the correction for the change of the generation time and the effective delayed neutron fraction. We obtained the reactivity worth of the RSS rod as 19.6 $\pm$0.3 dollars. The neutron generation time and effective delayed neutron fraction were obtained by using 24 groups 3-dimensional diffusion calculation.

The effective cross sections were obtained with SRAC code system[5] using the nuclear data based on the ENDF/B-IV. The double heterogeneity of fuel compact and coated particle in the fuel block was taken into account in the cell calculation by collision probability method. The cross sections of central column with the RSS rod were prepared by the Sn method using the TWOTRAN code[6] (X-Y geometry, S_8 approximation). The calculational flow are shown in Fig.3.9.2. Thermal neutrons in the energy range from 10^{-5}eV to 1.125eV were divided into 39 groups and fast neutrons in the energy range from 1.125eV to 10MeV were divided into 22 groups. Using the neutron spectra obtained by the cell calculation, the cross section of 61 groups were condensed into 24 groups (thermal : 13 groups and fast : 11 groups) for the core calculation. The cross sections for reflector were condensed by means of

asymptotic spectrum consisting of fission, 1/E and Maxwellian spectra.

The core calculation was performed for the hexagonal and z geometry with using these cross sections by 3-dimensional diffusion code CITATION[7]. A cross section of the graphite block was subdivided into 24 triangular meshes, and in the axial direction, the half assembly of 120cm long was divided into 15 meshes. Effective multiplication factor was calculated for with and without the RSS rod in the central column. Then, the reactivity worth of the RSS rod in dollar unit are derived from the decrease of effective multiplication factor due to inserting the RSS rod, divided by the calculated effective delayed neutron fraction.

The calculated value obtained as 19.72 dollars. The agreement between calculation and experiment was fairly good. The result obtained satisfies the accuracy requirement 10% for nuclear design of the reactivity worth of the HTTR Reserve Shutdown Absorber.

References

1) Saito S., et al. : "Design of High Temperature Engineering Test Reactor (HTTR)", JAERI 1332(1994).
2) Akino F., et al. : J. At. Energy Soc. Jpn.(in Japanese), 31, 682 (1989).
3) Kaneko Y., et al. : Nucl. Sci. Eng., 50, 173 (1973).
4) Akino F., et al. : J. Nucl. Sci. Tech., 17, 593 (1980).
5) Tsuchihashi K., et al. : "Revised SRAC Code System", JAERI 1302 (1987).
6) Lathrop K.D. and Brinkley F.W. : " TWOTRAN- II : An Interfaced Exportable Version of the TWOTRAN Code for Two-Dimensional Transport ", LA-4848-MS (1973).
7) Fowler T.B., et al. : " Nuclear Reactor Code Analysis Code : CITATION ", ORNL-TM-2496, Rev.2 (1969).

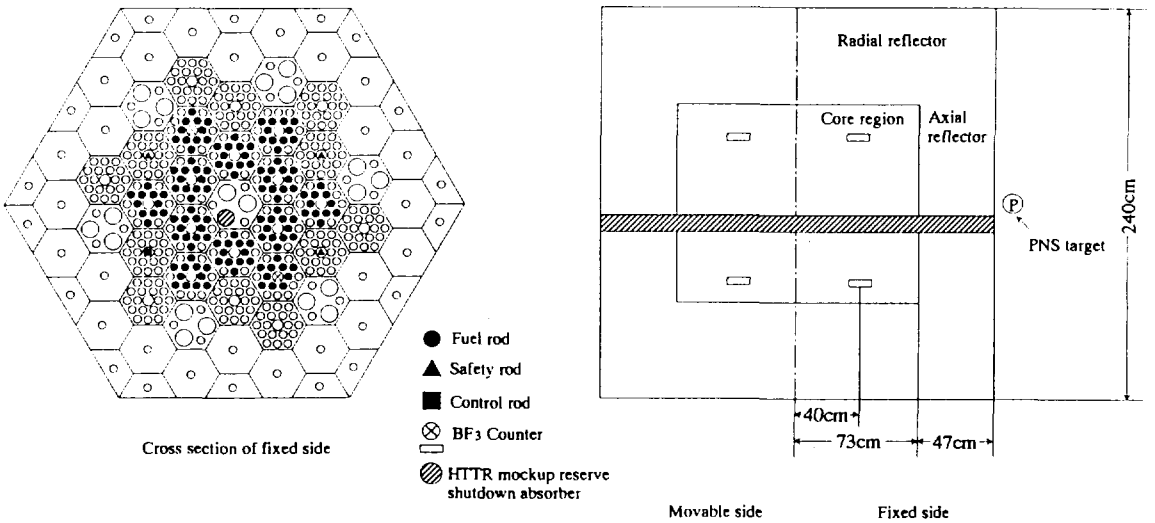

Fig.3.9.1 Arrangement of the HTTR mockup reserve shutdown absorber and fuel rods in VHTRC-1 core

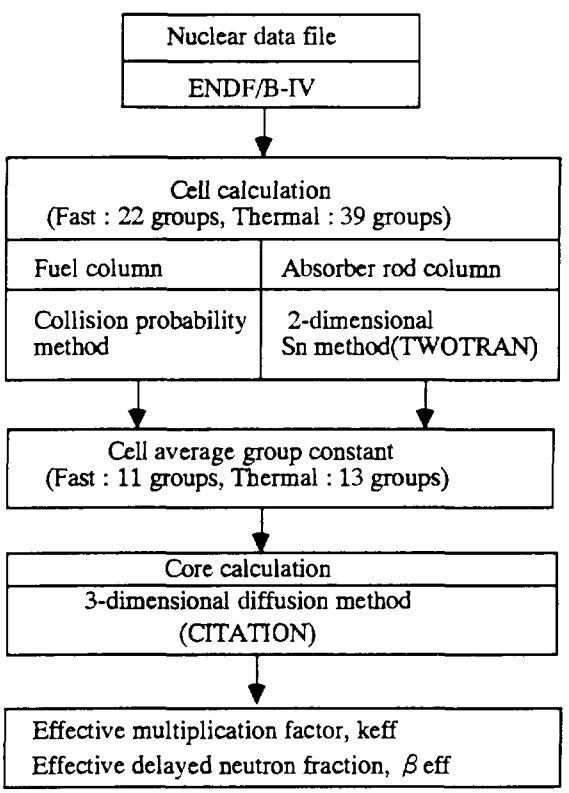

Fig.3.9.2 Calculation flow using the SRAC code system

3.10 An Improvement in Analysis Method for $(\beta_{eff}/\Lambda)_c$ Measurement by Pulsed Neutron Source Technique at VHTRC

T.Yamane
(*E-mail:* yamane@vhtrc01.tokai.jaeri.go.jp)

The pulsed neutron source (PNS) technique has been applied to a measurement of the kinetic parameter at critical, $(\beta_{eff}/\Lambda)_c$, at the VHTRC facility. In the analysis of experiments at VHTRC-1 core, we obtained the result that the discrepancy exceeded 10% in $(\beta_{eff}/\Lambda)_c$ value between calculation and experiment.[1] To investigate the cause of this large discrepancy, the analysis method had been reexamined from an experimental point of view, and an improved method was devised to reduce a systematic uncertainty. Improvements are made mainly in the following points.

1) The prompt neutron decay constant α at a subcritical state of reactivity ρ is determined by fitting the decay curves to an analytical expression using a data analysis code TDX that has been developed on the basis of the ALPHA-D code[2]. Main improvements from the ALPHA-D are made in the estimation of delayed neutron contribution, D(t), from multi-cycle accumulations more than three-cycle during periodic pulse injections.
2) The kinetic parameter $(\beta_{eff}/\Lambda)_c$ is determined directly as a fitting parameter by the least squares fitting to the in-hour equation using measured sets of α and ρ. The assumption of a linear relation between α and ρ in the previous analysis method is not introduced any more; it is still implicitly assumed that the parameters β_{eff} and Λ do not so largely change near critical state.

For validation of the present method, calculational simulations to PNS experiments with VHTRC-1 parameters were performed using analytical solutions based on the one-point reactor kinetics theory. The analysis results of these simulation experiments are shown in Table 3.10.1 where the quantity ND means the number of cycles accumulated for estimating D(t). The previous method, which corresponds to the case of a linear α-ρ relation with ND=3, underestimates the $(\beta_{eff}/\Lambda)_c$ value by 5.5% in comparison with the exact one. On the contrary, the present method can reproduce the $(\beta_{eff}/\Lambda)_c$ value with a good accuracy and reduce a systematic error within 0.3% when ND is larger than 30. The table also shows a large size of systematic error due to the assumption of linear α-ρ relation. A careful attention should be paid to this kind of systematic error, in particular, for the slow system characterized with a longer neutron generation time Λ and then a smaller α like a graphite system.

The PNS experiments for $(\beta_{eff}/\Lambda)_c$ measurements at VHTRC-1 and VHTRC-4 cores were re-analyzed by the present method and the results were compared with those by the

previous method, as shown in Table 3.10.2. From this table, it is inferred that the results obtained by the previous method would have possible systematic errors of 7% and 5% in the $(\beta_{eff}/\Lambda)_c$ values for VHTRC-1 and VHTRC-4 cores, respectively. In the same table, the ratios of calculated to experimental values (C/E) are also given, where calculations were performed with the SRAC code system[3] (SRAC93 version[4]) using the ENDF/B-IV based nuclear data library. By applying the present method, the accuracies of experimental values are improved and the discrepancies between calculations and experiments are lessened within 5%.

References

1) Akino F., et al.: J. Atomic Energy Soc. of Japan, 31(6), 682 (1989). (in Japanese)
2) Kaneko Y., Ohkubo S. and Akino F.: Nucl. Sci. Eng., 50, 173 (1973).
3) Tsuchihashi K., et al.: "Revised SRAC Code System," JAERI 1302 (1987).
4) Kugo T., et al.: "Improvement of SRAC Code," JAERI-Review 94-009, p.64 (1994).

Table 3.10.1 Analysis results of simulation experiments

α - ρ relation	Deviation from exact $(\beta_{eff}/\Lambda)_c$ value (%)		
	ND=3*	ND=30	ND=100
Linear	-5.5	-2.9	-2.3
In-hour eq.	-1.5	-0.26	-0.08

* ND: Number of cycles accumulated for estimating D(t).

Table 3.10.2 Results of $(\beta_{eff}/\Lambda)_c$ measurements at VHTRC-1 and -4 cores

Analysis method	VHTRC-1		VHTRC-4	
	(s^{-1})	C/E	(s^{-1})	C/E
Previous	4.89±0.02	1.09	5.03±0.03	1.08
Present (ND=30)	5.26±0.03	1.01	5.27±0.03	1.03

3.11 Temperature Effect on Critical Mass and Kinetic Parameter β_{eff}/Λ of VHTRC-4 Core

T.Yamane, F.Akino and H.Yasuda
(*E-mail:* yamane@vhtrc01.tokai.jaeri.go.jp)

A whole assembly heating experiment was carried out at an axially heterogeneous core VHTRC-4 to evaluate the calculation accuracy of temperature effect on reactor physics parameters of an HTGR core. Critical mass and kinetic parameter at critical, $(\beta_{eff}/\Lambda)_c$, were measured at a room temperature 21°C and an elevated temperature 200°C.

The VHTRC-4 core was loaded with 2, 4 and 6 %-enriched coated particle fuel in an axially zoning pattern. The core at a room temperature was initially loaded with 288 fuel rods and the critical point was measured using the calibrated control rods. When the assembly was heated up around 200°C, fifty-two fuel rods were added to the core so that the criticality was achieved again with an appropriate excess reactivity. Figure 3.11.1 shows the critical fuel-loading configurations. After the corrections for the reactivity worths of loading irregularities such as control-rod and safety-rod insertion holes, a gap between two half assemblies, electric heaters, etc., the minimum critical mass at each temperature was determined. The results are listed in Table 3.11.1. The critical mass increased by 15% as the assembly temperature rose from 21°C to 200°C.

Pulsed neutron source experiments were carried out at four slightly subcritical states of which reactivities were changed down to -40 cents in a step of approximately 10 cents by inserting the calibrated control rods. Figure 3.11.2 shows the relation of measured prompt neutron decay constants α_p's versus reactivities ρ_s's. The kinetic parameter $(\beta_{eff}/\Lambda)_c$ at each core temperature was determined by an improved analysis method described in Ref.1. As listed in Table 3.11.2, the measured $(\beta_{eff}/\Lambda)_c$ value was larger by 14% at 200°C than at 21°C.

Analysis was performed with the SRAC[2] code system, where the SRAC93[3] version was employed with two kinds of libraries based on the ENDF/B-IV and JENDL-3.2 nuclear data. Cell calculations were made by the collision probability method in sixty-one neutron energy groups. Three-dimensional whole core calculations were carried out with a diffusion code CITATION[4] in 16 neutron energy groups. In comparison with the experiments, the calculations underestimated the critical mass at 21°C by 4% and 6% in each case of ENDF/B-IV and JENDL-3.2 respectively, and the agreement at 200°C however became better in both cases. The calculated $(\beta_{eff}/\Lambda)_c$ values agreed fairly well within 5% with the measured one. It should be, however, noticed that the calculation accuracy of $(\beta_{eff}/\Lambda)_c$ depends upon that of critical mass since there exists a strong correlation between the neutron generation time Λ

and the critical size.

References

1) Yamane T.: Section 3.10 in this report.
2) Tsuchihashi K. et al.: "Revised SRAC Code System," JAERI 1302 (1987).
3) Kugo T. et al.: "Improvement of SRAC Code," JAERI-Review 94-009, p.64 (1994).
4) Fowler T. B., Vondy D.R. and Cunningham G.W.: "Nuclear reactor Core Analysis Code: CITATION," ORNL-TM-2496, Rev.2, (1971).

Table 3.11.1 Critical mass of VHTRC-4 core

Temperature (°C)	Measurement (kg-^{235}U)	Calculation (ENDF/B-IV) (kg-^{235}U)	C/E	Calculation (JENDL-3.2) (kg-^{235}U)	C/E
21.0	4.508±0.014	4.385	0.973	4.231	0.938
200.0	5.183±0.017	5.289	1.020	5.028	0.970

Table 3.11.2 Kinetic parameter $(\beta_{eff}/\Lambda)_c$ of VHTRC-4 core

Temperature (°C)	Measurement (s^{-1})	Calculation (ENDF/B-IV) (s^{-1})	C/E	Calculation (JENDL-3.2) (s^{-1})	C/E
21.0	5.27±0.03	5.477	1.039	5.126	0.973
200.0	6.01±0.03	6.186	1.029	5.711	0.950

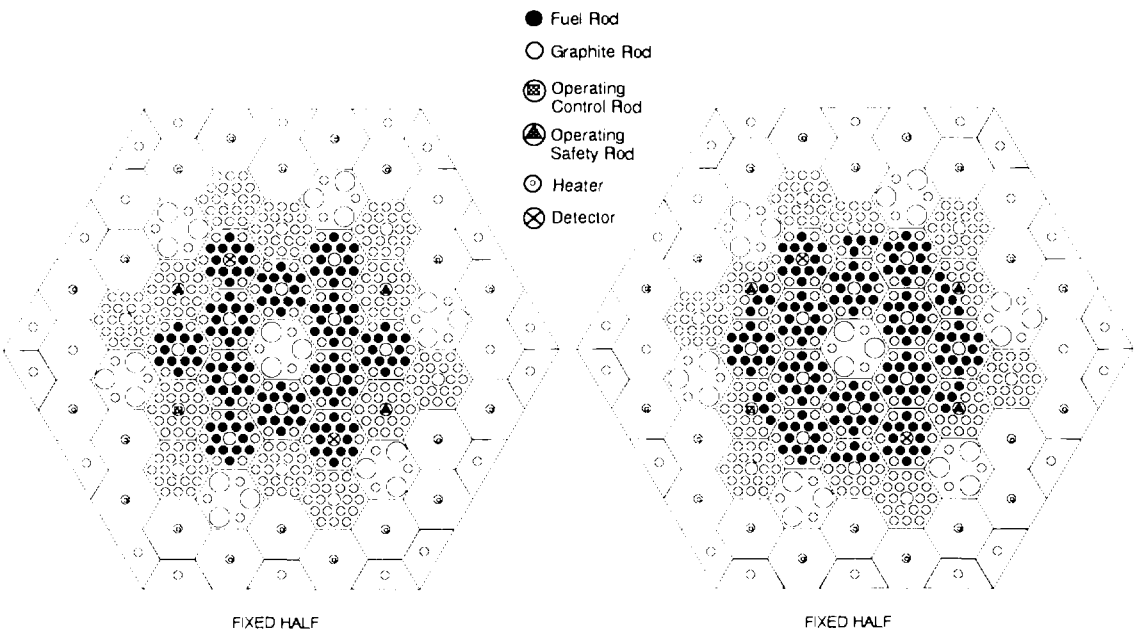

(a) 21°C core (b) 200°C core

Fig.3.11.1. Fuel loading configurations in critical cores at 21°C and 200°C.

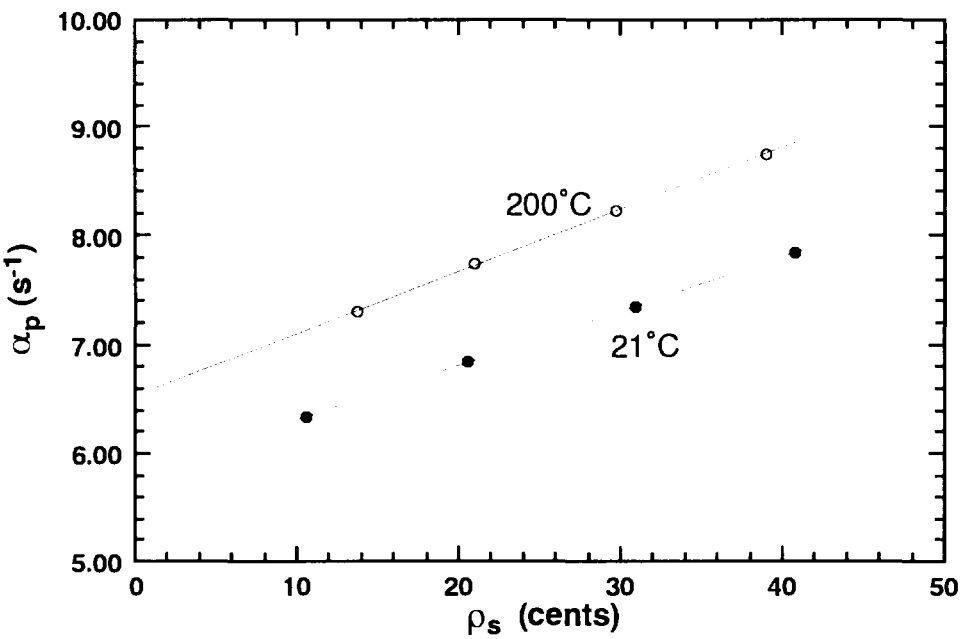

Fig.3.11.2. Measured α_p versus ρ_s at 21°C and 200°C.

4. Advanced Reactor System Design Studies

An innovative concept of the JAERI Passive Safety Reactor (JPSR) has been developed to meet needs for the nuclear energy in the future. In order to develop and improve the reactor design, experimental and analytical studies have been performed including the construction cost evaluation.

In this year, loss-of-coolant accident (LOCA) has been analyzed in detail with a best estimate code REFLA/TRAC. In the case of large break LOCA, the break was assumed to be double-ended break in a cold leg with break areas from 200 to 20% of the cold leg flow area. The results show the accident is terminated in safe only by the passive safety systems of the JPSR. In the case of small break LOCA (SBLOCA), the split break type was considered with break areas from 20 to 5% of the cold leg flow area. The results show the passive safety systems of the JPSR can keep the safety without activation of the automatic depressurization system (ADS), which was adopted to depressurize the reactor to induce coolant injection. The above results suggest the possibility of ADS elimination. This is favorable because the ADS itself might induce the LOCA. Very small break LOCA is being analyzed now to confirm the safety without the ADS.

A Containment vessel (CV) of the JPSR is passively cooled by natural air convection outside the CV in the case of accidents. The heat removal quantity was evaluated numerically with the 3-dimensional flow simulation code STREAM. The results show the CV could be safely cooled for a long time by the natural air convection.

A small-scale experiment has been performed to investigate the flow pattern in the JPSR lower plenum by applying the flow visualization technique. The results show installation of a perforated plate in the lower plenum makes the flow in the region relatively uniform.

The construction cost of the JPSR was estimated to be 20% higher than that of an existing PWR with the same output. The increase in size of the reactor vessel, steam generators etc. results in the higher cost in spite of the design simplification of the JPSR. After some possible improvements of design for reducing the cost, comparative cost performance can be expected for both reactors, since the system simplification of the JPSR may result in low operation and maintenance cost.

4.1 Large Break LOCA Analysis of JPSR with REFLA/TRAC Code

F. Araya, T. Teramae*, M. Ochiai, T. Iwamura and Y. Murao
(*E-mail:* araya@jpsrews1.tokai.jaeri.go.jp)

A design study of a passive safety light water reactor concept JPSR has been carried out with a primary objective to develop a safety-enhanced reactor concept at Japan Atomic Energy Research Institute (JAERI)1). One of major features of the concept is an adoption of passive safety systems. The safety of the concept under large break loss-of-coolant accident (LBLOCA) conditions has been confirmed by accident analyses with the transient thermal-hydraulic analysis code REFLA/TRAC, as shown in the following.

The passive safety systems adopted to JPSR is categorized into two groups, passive heat removal system and passive coolant injection system. The passive heat removal system consists of two kinds of residual heat removal systems (RHRs) named upper- and lower RHRs, and a pool water cooling system (PWCS). The RHRs are cooled by the water contained in a gravity-driven coolant injection (GDCI) pool placed inside the containment and the pool water is cooled by PWCS. These systems are designed so that the heat generated in the core is transferred to atmosphere by a series actuation of these systems without bulk boiling of the pool water. On the other hand, the coolant injection system is designed to consist of an accumulator system (ACC) and a gravity-driven coolant injection system (GDCIS). The concept of the passive safety systems is shown in Fig. 4.1.1.

Under LOCA conditions, the lower-RHR, PWCS, GDCI pool, ACC, GDCIS are designed to be used to keep the safety. The lower-RHR is designed to cool down the primary coolant system and lead to early actuation of ACC and GDCIS. The long-term cooling is also maintained by this system together with PWCS. ACC is an advanced type one which is originally designed for NP-212). GDCIS is designed to inject a coolant from the GDCI pool to the primary system when the primary pressure becomes lower than the GDCI pool head. As for the containment pressure, a pressure suppression system is adopted. This function is realized by introducing a steam discharged inside the isolation boundary to the GDCI pool through vent pipes.

The REFLA/TRAC input deck models major passive safety systems described above except PWCS. The break was assumed to be double-ended break in a cold leg with break areas from 200 to 20 % of the cold leg flow area. Only one train of each passive safety system connected to the intact loop was assumed to be actuated. At the beginning of the transient calculation, the reactor scram, the main coolant pump trip and the steam generator

---

*: Mitsubishi Heavy Industries, Ltd.

isolation were assumed to occur.

Figure 4.1.2 shows the JPSR behaviors under 200% LBLOCA conditions. As shown in this figure, the cladding temperature increases after the initiation of LOCA and reaches to the maximum value of 900 K. After reaching the maximum value, it continuously decreases due to large negative core flow and low power generation rate in the core. ACC and GDCIS is actuated properly and the core inlet flow is kept positive after about 80 s. This means that the long-term cooling is maintained. The similar behaviors to the 200% LBLOCA case are calculated in the LBLOCA calculations with the 200 to 20% break ares. The cladding temperature in each case is kept very low value than the safety evaluation limit as shown in Fig. 4.1.3. As shown in the figure, the maximum temperature is appeared in the 100 % LBLOCA case and is evaluated to be less than 1000 K.

Based on the results shown above, it can be said that the safety of JPSR under the 200 to 20% LBLOCA conditions is kept only by the passive safety systems.

References

1) Y. Murao, et al., J. Nucl. Sci. Technol., Vol. 32, No. 9, pp 855-867 (Sep. 1995).
2) M. Nishimoto, et al., Proc. ICONE-4, Vol. 3, pp. 269-275 (1996).

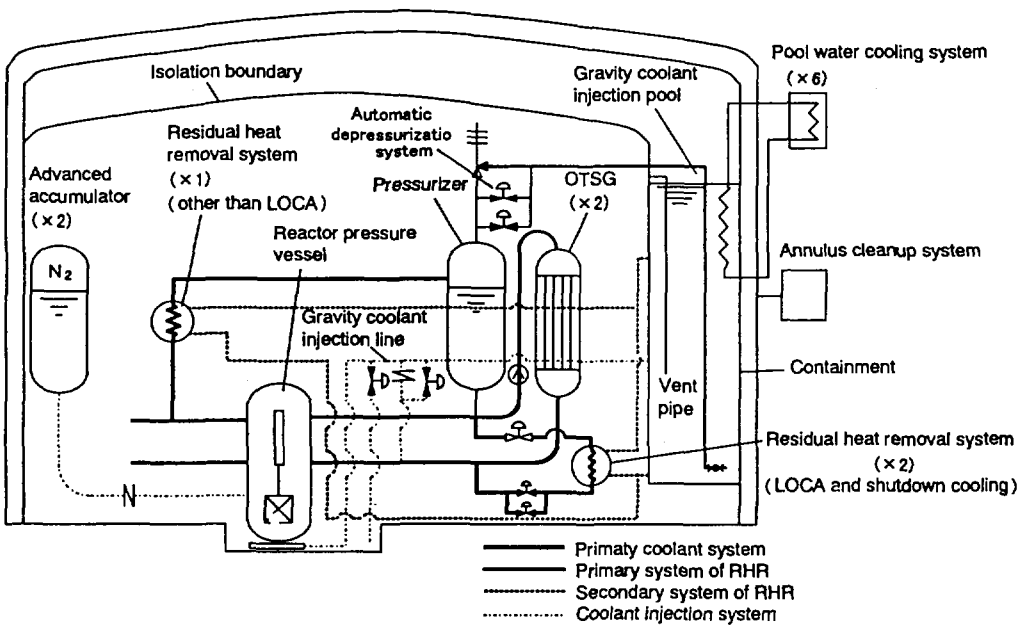

Fig. 4.1.1 Concept of passive safety systems

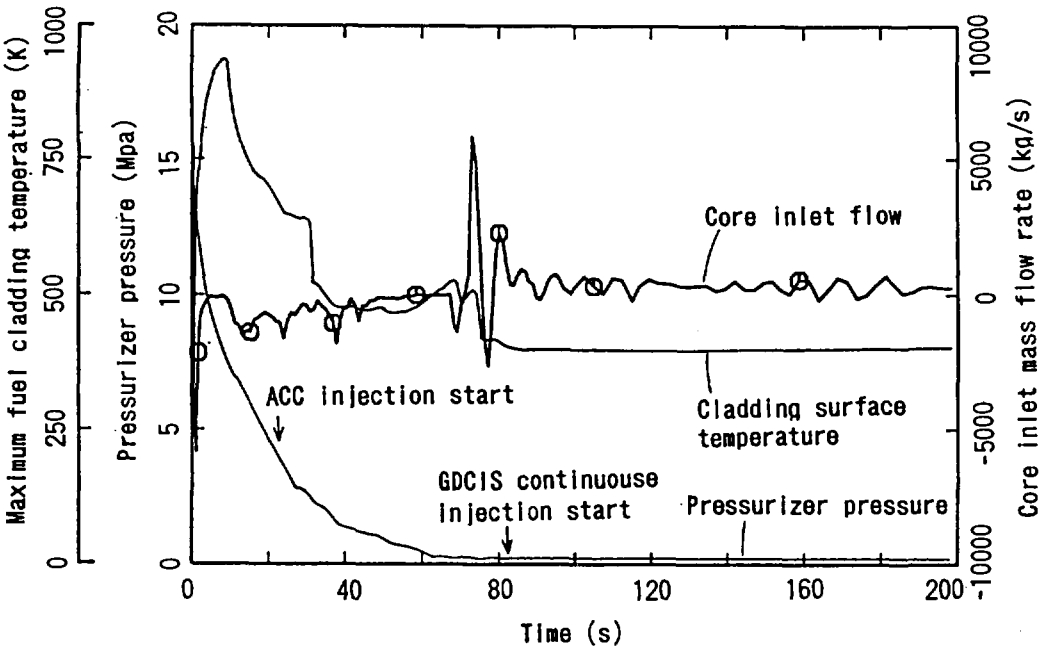

Fig. 4.1.2 JPSR behaviors in 200% LBLOCA

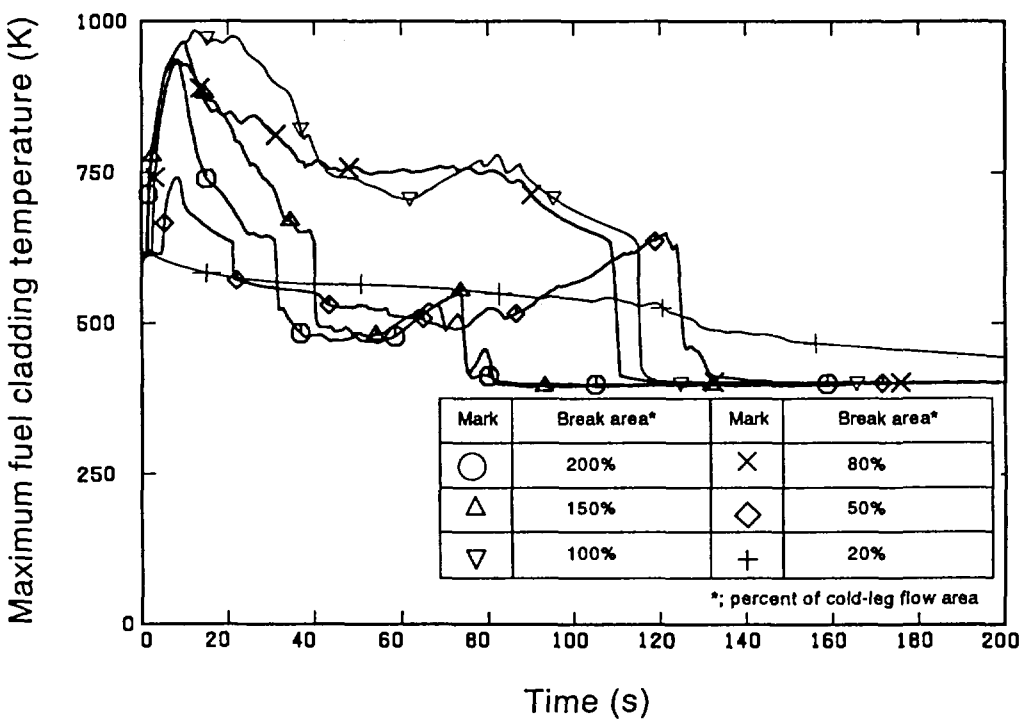

Fig. 4.1.3 Maximum fuel cladding temperatures

4.2 Small Break LOCA Analysis of JPSR with REFLA/TRAC Code

T. Teramae* , F. Araya, M. Ochiai and Y. Murao
(*E-mail* : teramae@jpsrews1.tokai.jaeri.go.jp)

The feasibility of the passive safety system concept adopted to a passive safety light water reactor JPSR has been confirmed by performing transient thermal-hydraulic analyses with the REFLA/TRAC code. Small break LOCA (SBLOCA) analysis was performed, in order to confirm the safety in SBLOCA conditions.

The noding diagram for the REFLA/TRAC calculations is shown in Fig.4.2.1. The model covers most of the important components other than pool water cooling system (PWCS). The core power is calculated by a point kinetics model. The whole system is modeled only by one-dimensional components.

In the calculations, the split break type was considered for SBLOCA. The calculation covers a range of break area from 20% to 5% of a cold leg flow area. An accumulator (ACC) and a gravity driven coolant injection system (GDCIS) were assumed to be actuated only in a intact loop. Heat removal systems (RHRs) were assumed to be actuated, too. But, lower RHR was assumed to be actuated only in intact loop. Although JPSR has an automatic depressurization system (ADS), it was not actuated in the calculations. The signals of the reactor scram and the main coolant pump trip were assumed to be caused by a low pressurizer pressure at 12.8 MPa.

As a representative of SBLOCA cases, the 5% SBLOCA case is presented here. The calculated results are shown in Fig.4.2.2 and Fig.4.2.3. As shown there, ACC is actuated at around 300 s. GDCIS actuation is delayed until 950 s. GDCIS injection flow is very oscillatory. However, the core is covered by the coolant and the core heat-up is not experienced. These results show that the passive safety systems can keep the safety without ADS in SBLOCA conditions.

The safety of JPSR was demonstrated by REFLA/TRAC calculations which cover a rage of the break area from 20% to 5% of the cold leg flow area. Namely it is confirmed by the analyses that the passive safety systems could keep the safety without ADS in the 5% to 20% SBLOCA conditions.

---

* MITSUBISHI HEAVY INDUSTRIES, LTD.

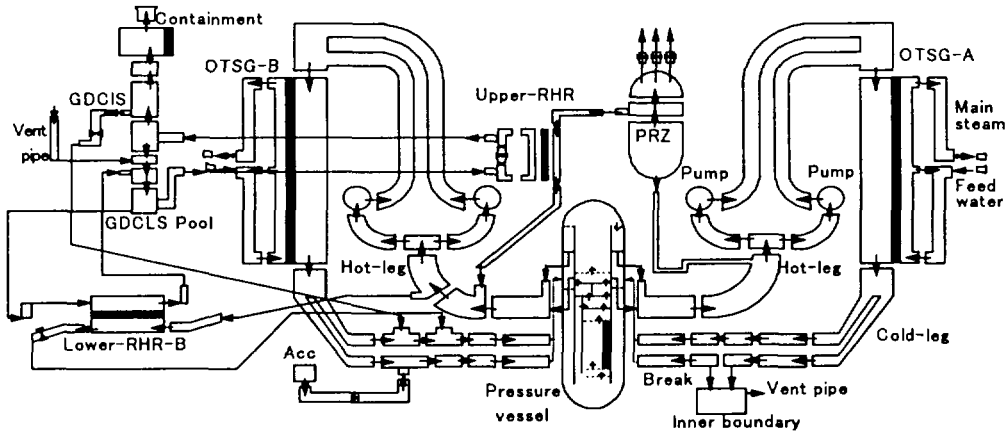

Fig. 4.2.1 Noding diagram for the REFLA/TRAC calculations

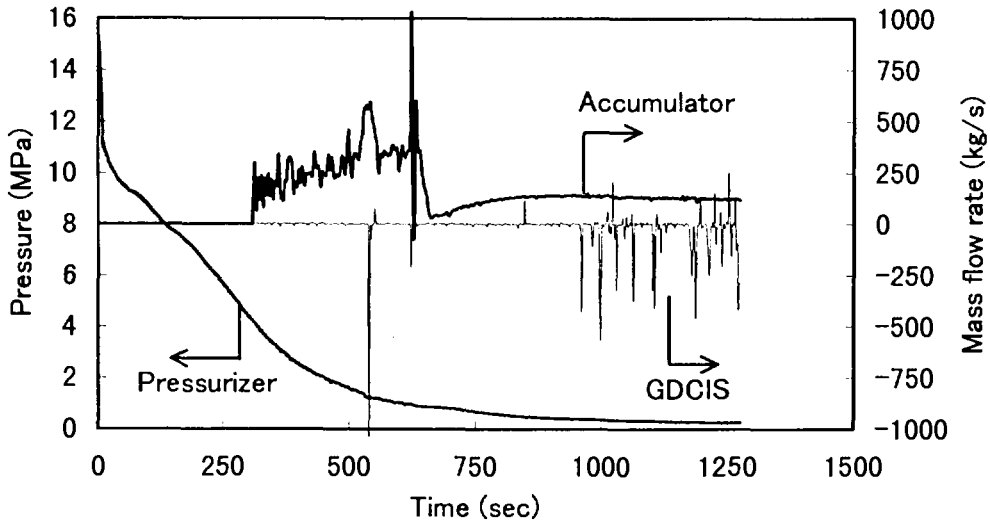

Fig. 4.2.2 Pressurizer pressure, ACC flow rate and GDCIS flow rate transients during 5% SBLOCA

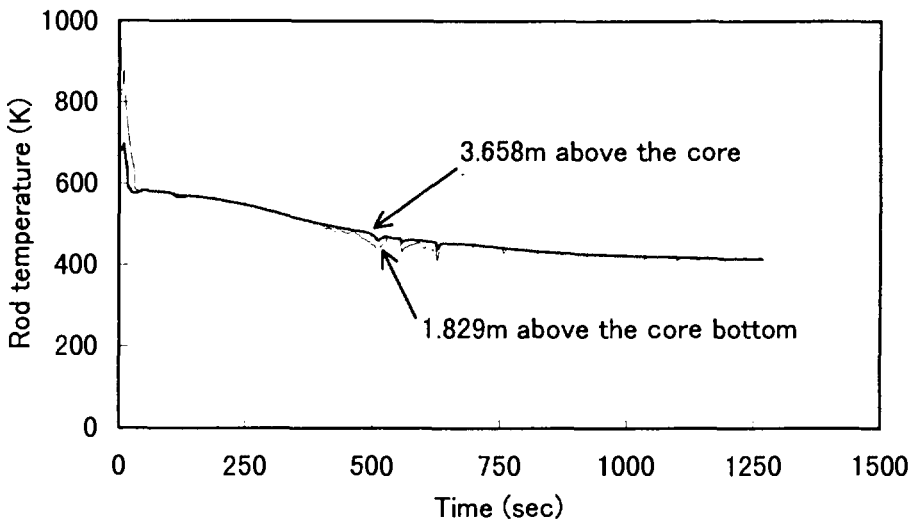

Fig. 4.2.3 Fuel clad temperatures transients during 5% SBLOCA

4.3 Natural Flow Simulation for Outside of JPSR Containment Vessel

H. Yoshida

(*E-mail:* yoshida@jpsrews1.tokai.jaeri.go.jp)

One of passive safety features of the JPSR (JAERI Passive Safety Reactor) system is heat removal from the containment by the natural air convection in a case of the accident. Air flow channel of the JPSR is more complicated comparing with the similar cooling system adopted in the several innovative reactor concepts [1),2),3)], since six air coolers are installed around the containment vessel (CV) which is covered with an external structure (we call this external structure "stack wall"). To adopt the cooling of the CV by natural air convection, the actual heat removal quantity must be estimated in the numerical analysis.

The 3-dimensional single phase numerical simulation code STREAM was used to analyze the single-phase flow pattern and temperature distribution around the CV. The analyzed region is half-cylindrical shape (the diameter and height are 200m). The number of the computation grids is 47,250 (=45(r)×10(θ)×50(z)). To simulate heat removal from the air cooler, constant volume heat generation condition is given. The CV outer wall (hemisphere part) temperature is assumed to be constant (=120°C, the saturation temperature of approximately 0.2MPa water). The atmospheric temperature is set at 50°C. We adopted conservative assumption in which thermal radiation has no effect on natural air-cooling of the CV.

Calculation parameters and results are shown in Table 4.3.1. Except the case 4, air coolers don't work. In the case 4, air coolers remove 0.5% of rated power (Qc=1.83×10^{9}W). Three types of stack wall shape are examined. In the case 2, Qt is larger than that of the cases 1 or 3. Especially, Qt is very small when type C stack wall is used, and the stack wall needs to enhance the heat

Table 4.3.1 Calculation parameters and results

Case No.	Stack shape (Fig. 4.3.1)	Qa / Qc (%)	Qt / Qc (%)	Qw / Qc (%)
1	A	0	1.02	1.02
2	B	0	1.84	1.84
3	C	0	0.12	0.12
4	A	0.5	0.95	0.45

Qa : Air cooler removal heat (input parameter, W)
Qt : Total removal heat from CV (W)
Qw : Net removal heat by natural air convection (=Qt-Qa)
Qc : Thermal reactor power (=1.83×10^{9}W)

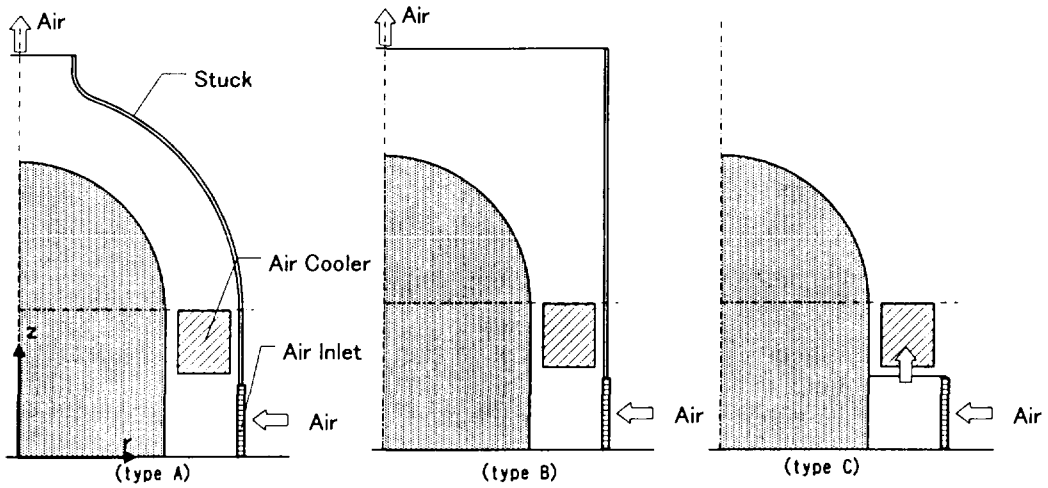

Fig. 4.3.1 Tested stack shapes

removal. Total heat removal is almost the same amount in the cases 1 and 4. Heat release from the air cooler doesn't enhance the total heat removal, and net heat removal by natural convection is decreased.

Velocity vectors of air flow near the CV in symmetric plane are shown in Fig. 4.3.2. If the type A stack wall is used, flow area near top of the CV is smaller than that of the air inlet. Then, air flow is accelerated around the CV top. Nevertheless, total flow rate of the air is not so large, since flow resistance becomes very large. In the case 2 stack wall, maximum velocity is smaller and total flow rate is larger than those in the case 1. Cool air flow was observed around the stack wall in the inverse direction in Fig. 4.3.2(B), due to the following two actions: (1) Air near the CV wall is heated, and accelerated by the buoyancy force. Then pressure near there is lower than that around the stack wall. (2) In the air coolers, flow area is small, and air flow is restrained. If the type C stack wall is adopted, air flow velocity becomes small. Then total heat removal rate is also small. In the opposite side of the air inlet, velocity in the case 4 is larger than that in the case 1. In the case 4, air is heated in the air cooler and accelerated. However, flow resistance near the CV top is very large, then air flows to the opposite side of the air inlet, and velocity in this region is larger compared with the case 1. Then, Qt is almost the same in the cases 1 and 4.

We have concluded that more than 1 % of the rated power can be released from the wall by natural air convection. Except for short period after accidents, heat that is released from the core is smaller than 1 % of the rated power. The CV can be cooled by the natural air convection, and pressure in the CV is kept lower than design pressure (0.3MPa) in the long term.

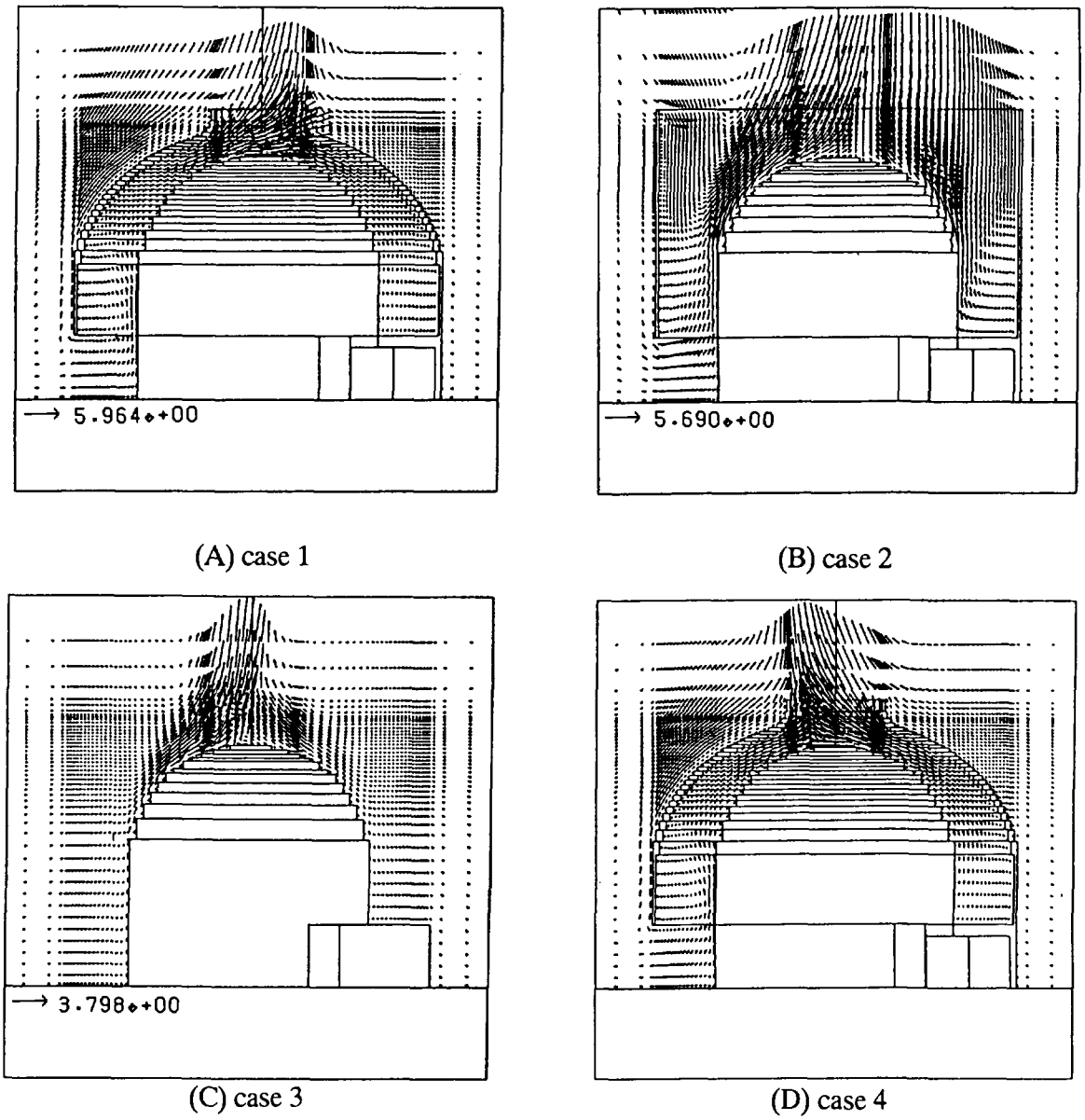

(A) case 1 (B) case 2

(C) case 3 (D) case 4

Fig. 4.3.2 Velocity distribution around the containment vessel

References

1) Penderson, D. R., et al.:"Experimental and analytical studies of passive shutdown heat removal from advanced LMRs," International Topical Meeting on Safety of Next Generation Power Reactors, Seattle (1992).

2) Kennedy, M. D., et al.: "Advanced PWR passive containment cooling system testing," International Topical Meeting on Safety of Next Generation Power Reactors, Pittsburgh (1994).

3) Cheng, X., et al.: "Passive containment cooling for next generation water cooled reactors," ICONE-4, New Orleans (1996).

4.4 Small-scale Experiment on JPSR Lower Plenum Flow

K. Kunii

(*E-mail:* kunii@jpsrews1.tokai.jaeri.go.jp)

It is necessary to investigate the flow pattern in the JPSR lower plenum ,especially that beneath the core which is very important for core- heat removal. For the purpose, a small-scale experimental study changing inner structures in the lower plenum has been performed by applying the flow visualization and image processing technique which is effective to simultaneously measure flow velocities at many points in the lower plenum.

Experimental Technique The small- scale (1:10 length- scale) transparent container was applied to simulate the JPSR's reactor pressure vessel. Flow fields in the container were obtained by using the particle tracking velocimetry (PTV[1,2]) method. A 3- D flow field was analyzed virtually by combining several vertical and horizontal 2-D flow fields. Table 4.4.1 shows the parameters of Euler similarity law and experimental condition. According to the similarity law, each inlet flow rate at cold-legs was set to 50 L/min.

Table 4.4.1 Parameters of similarity law and experimental conditions

	practical reactor	experiment
ρ [kg/m^3]	755.8	1000
U [m/s]	2.51	0.0367
ΔP[Pa]	113 000	30.4～40.6
D [m]	4.00	0.40
ν [m^2/s]	1.26×10^{-7}	1.0×10^{-6}
Eu [-]	2.11×10^{-2}	$2.22\sim1.66\times10^{-2}$
Re [-]	7.97×10^{7}	1.47×10^{4}
Ud [m/s]	7.12	0.0700

where, as reference, Ud : average velocity in downcomer

Flow Pattern in Lower Plenum without Inner Structure This case is important to obtain the basic flow pattern before installing any inner structure. Figures 4.4.1a～e show the flow patterns at an arbitrary time but mostly indicate a time - average flow pattern. Virtually making up a 3- D flow field by combining these 2- D flow fields, it was found that the flow distribution was very complicated with 3- D vortexes. The flow pattern beneath the core had a complicated distribution which had to be made uniform. In addition, it was noticed that the flow-symmetry was not achieved in both horizontal and vertical 0° cross- sections. It would be necessary to

obtain more data to clarify that since the reason has not been sure.

Effect of Perforated Plate on Flow Pattern The flow patterns are shown in Figs.4.4.2a~c. This case is the trial installing a simple perforated plate beneath the core. Geometry of the plate was 10 mm of thickness and 64 holes (diameter ; 14.8 mm) in staggered arranging (pitches; 20.0 mm). Comparing with Figs.4.4.1a~c, it was found that by installing the plate the flow was made uniform considerably beneath the core with little time-dependency.

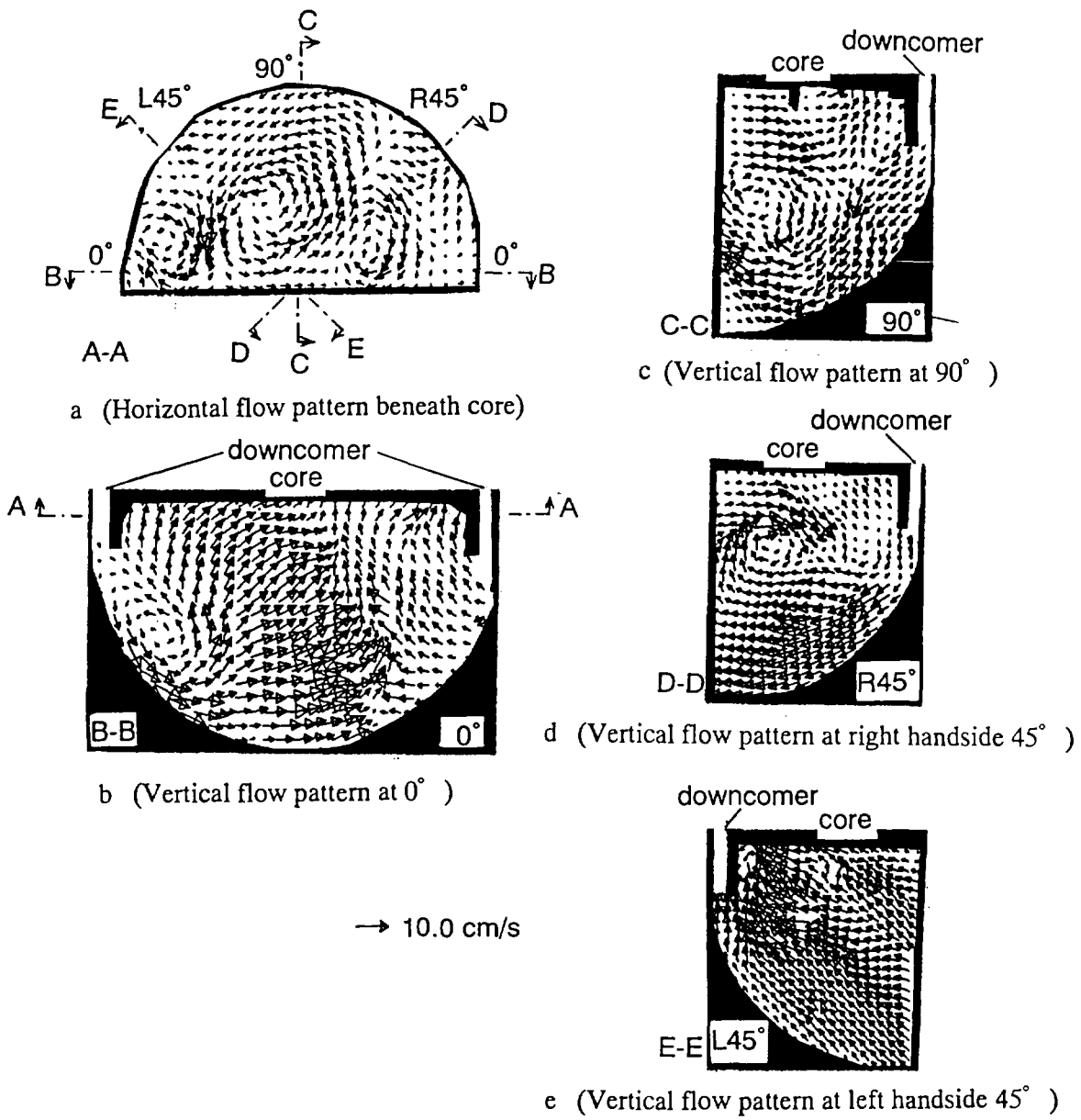

Fig.4.4.1 Flow pattern in lower plenum without inner structure

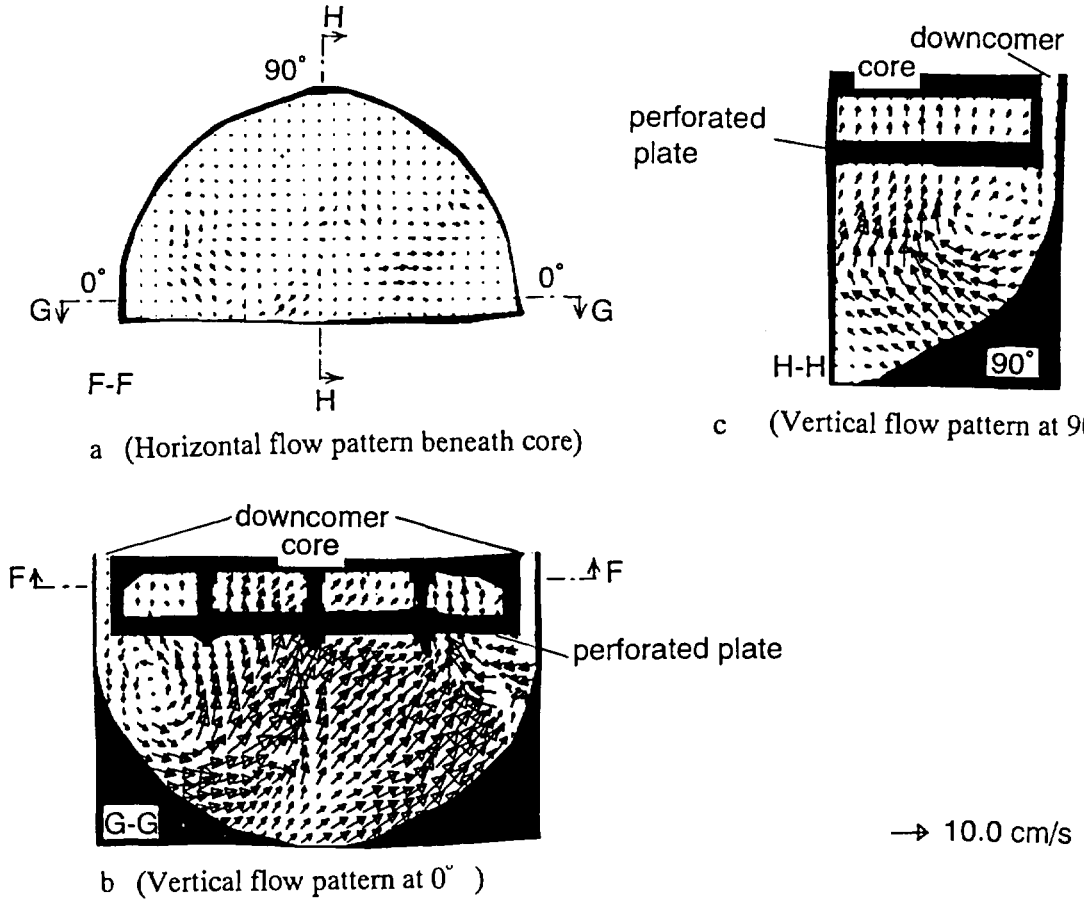

Fig.4.4.2 Flow pattern in lower plenum installing a perforated plate

Conclusions 3-D flow patterns in the JPSR lower plenum were investigated on a small-scale experiment (1:10 length- scale), so that an expectation to make the flow uniform by installing a perforated plate was obtained.

References

1) T. Kobayashi et al.:"Development of a Real- time Velocity Measurement System for High Reynolds Fluid Flow Using a Digital Image Processing Design", ASME FED, Vol.128, pp.9-14(1991).

2) I. Nezu et al.:"Coherent Structure in Compound Open-channel Flows by Making Use of Particle- tracking Visualization Technique", Hydraulic Measurement and Experimentation, ASCE, pp.406-415(1994).

4.5 Estimation of Construction Cost of JPSR

T.Okubo, F.Araya and M.Ochiai
(*E-mail:* okubo@jpsrews1.tokai.jaeri.go.jp)

In the design of the JAERI's Passive Safety Reactor (JPSR)[1], simplification of the system has been intended to be introduced as much as possible, in addition to the passive safety enhancement. Although the construction cost is expected to be desirably reduced in passive safety reactors due to the system simplification, they are, on the other hand, expected to have another undesirable factor to increase the construction cost due to their generally large passive safety components. Therefore, it is important to estimate the effect of the passive components on the construction cost, and to consider the most economical design to achieve the required function based on this information.

For this purpose, the construction cost for the JPSR was estimated. The technique adopted for the estimation was to break down the construction processes for a specified system component into basic ones and to determine the unit prices for materials, fabrication cost and so forth for each process, and to apply these unit prices to the material amount and fabrication processes based on the current design information, and then, to accumulate all these related cost values together for the concerned component. Proceeding the same estimation to all necessary components considered in the design, the total amount of the construction cost was obtained. The basic unit prices were obtained from the cost data base developed for the plant construction cost including nuclear energy plants.

In the present estimation, only the cost for the machine equipments and the building were covered, excluding costs for land, interest, fuel and so forth. The construction cost for a 600 MWe class Japanese PWR was also estimated as the reference with the same technique to investigate the differences between the JPSR and the PWR. Estimated results are shown in Fig. 4.5.1. In the figure, costs for the JPSR and the PWR are compared in eleven divided subsystems or items. Since the JPSR's nominal power (630 MWe) is about 10 % higher than for the reference 600 MWe class PWR, values for the JPSR are converted to those corresponding to the same nominal power as the reference PWR based on the exponential scaling of the power ratio. This figure shows the construction cost for the PWR is 120 Billion

yen (GY), which is considered to be in the range for the Japanese 600 MWe class PWR construction data[2], and the value for the JPSR is about 20 % higher than this.

From the figure, it is recognized that subsystems with the major increase in cost are the reactor internals (denoted as #2), the primary cooling system (#3) and the engineering safety system (#4). Especially, the last one gives the largest increase in cost of about 12 GY. The increase mainly results from the air cooler system introduced to remove heat from gravitational injection pool. At present, this system is designed as natural circulation water type in stainless steel tube heat exchangers operated under the ambient condition. Therefore, there considered to exist large possibility to change the design to make the system more compact and economical, resulting in a significant cost down. The cost increase reasons for the reactor internals are increase in the size of the reactor internals corresponding to the reactor vessel size increase and increase in numbers of control rods resulting from the soluble boron free core design. For the primary cooling system, increase in size of the reactor vessel, the steam generators and the pressurizer is the major contribution.

Since simplification of the system has been intended to be introduced, the cost for the auxiliary system (#5) was expected to be reduced. There is estimated reduction of about 3 GY due to simplification of the chemical volume control system. There is, however, a newly introduced passive RHR system, and this results in increase in cost canceling the above reduction. Since the capacity of this RHR system as well as another RHR system involved in the engineering safety system is very large and there is another possibility to reduce the cost by optimizing the capacities of these components.

References

1) Murao, Y., Araya, F., Iwamura, T. and Okumura, K.: "A Concept of Passive Safety Pressurized Water Reactor System with Inherent Matching Nature of Core Heat Removal", *J. Nucl. Sci. Technol.*, 32[9], 855 (1995).

2) *For instance*, Hokkaido Electric Power Company: "Tomari (No.1 and No.2) Safety Analysis Report" (1982)

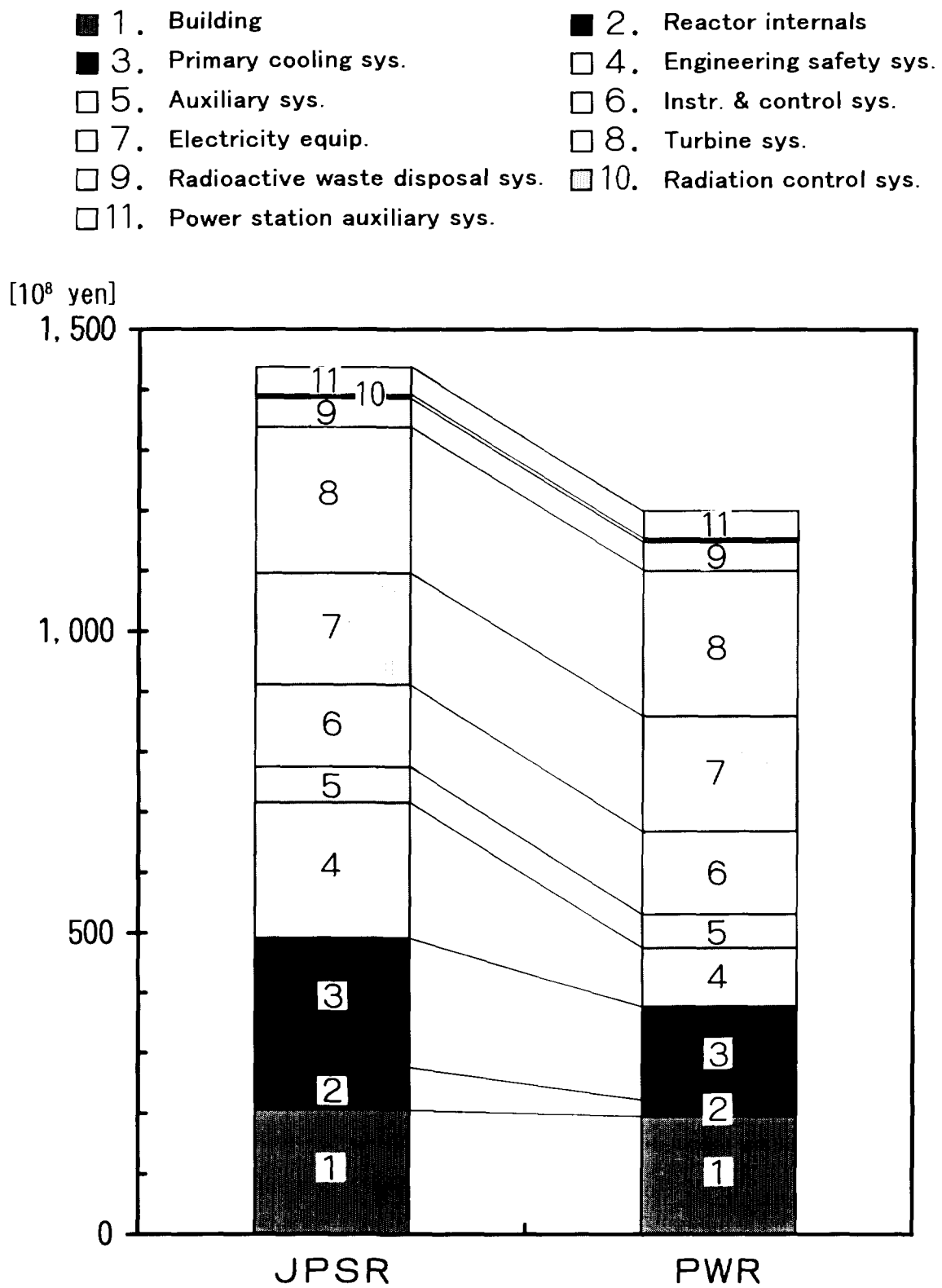

Fig. 4.5.1 Comparison of estimated construction costs between JPSR and PWR at the same power basis of 600 MWe class PWR

4.6 Applicability of Existing DNB Evaluation Methods to Fast Transient in Triangular Wide Pitch Lattice Core for Advanced Reactors

X.Jiang*, T.Okubo and F.Araya
(*E-mail:* okubo@jpsrews1.tokai.jaeri.go.jp)

A concept of an integral type reactor (ITR) has been developed at JAERI based on a passive safety reactor SPWR (System-integrated PWR)[1] and an advanced marine reactor MRX[2]. A triangular lattice fuel assembly, which is different from that of the high conversion pressurized water reactor (HCPWR), is proposed to be used in the core of this kind of reactor, and a small inertia canned-motor pump is adopted simultaneously in this system, which would cause a very fast reduction of the core flow rate if a pump trip accident occurs. Therefore, the evaluation of the core thermal margin, *i.e.* the departure from nucleate boiling ratio (DNBR), under the pump trip accident conditions becomes very important in the safety analyses for the design of the ITR. And hence, a series of fast transient DNB experiments for the triangular wide pitch lattice core were conducted and an investigation on an applicability of the existing quasi-steady-state evaluation method[3] to these fast transients has been performed.

To simulate the pump trip accident transients of the ITR in those experiments, core flow rates were reduced by the rate of 13～25%/s around the DNB onset time, which is considered to be much faster transient than expected in the current PWR (which is considered to be about 6%/s around the DNB onset time). The core heating power change rate was another experimental parameter with the changing rate of -20～+3%/s, including 0%/s (constant power).

In the DNBR analyses, the COBRA-IV-I subchannel analysis code[4] was used to obtain local and instantaneous thermal-hydraulic conditions during the transient, and the existing DNB correlations, *i.e.* EPRI-Columbia correlation, B&W-2 correlation and modified W-3 correlation, which are considered to be general correlations in the DNBR predictions for steady-state conditions, were used to obtain DNBR. The predicted DNBR values with these correlations at the DNB onset points for the experimental conditions are summarized in

* A visiting engineer from NPIC based on the STA Scientist Exchange Program

Fig.4.6.1. It shows that the EPRI-Columbia correlation is applicable to the transient DNB onset in the core of ITR. The average DNBR value with the EPRI-Columbia correlation is 1.08 and its standard deviation is ± 0.07. For the modified W-3 and B&W-2 correlations, the average DNBR values are 1.14 and 1.29, respectively. These values are larger than that of the EPRI-Columbia correlation.

As a conclusion from these comparisons, the existing quasi-steady-state DNB evaluation method has been revealed to be applicable to the prediction analyses of the transient DNB for the ITR. The evaluation method with the COBRA-IV-I subchannel analysis code and the EPRI-Columbia correlation has been confirmed to be applicable within the error of 15% to the fast transient expected for a pump trip accident in the ITR triangular wide pitch lattice core.

References

1) Oikawa, T., *et al.*: "Review of updated design of SPWR with PSA Methodology", the third JSME/ASME Joint International Conference on Nuclear Engineering, Vol.3, PP.1341~1348, April 23-27,1995.

2) Hoshi, T., *et al.*: "R&D status of an integral type small reactor MRX in JAERI", the third JSME/ASME Joint International Conference on Nuclear Engineering, Vol.2, PP.739~743, April 23-27,1995.

3) Celata,G.P. *et al.*: "CHF behaviour during pressure, power and/or flow rate simultaneous variations", Int. J. Heat Mass Transfer, Vol.34, No.3, pp.723~738 (1991).

4) Wheeler, C.L., *et al.*: "COBRA-IV-I: An Interim Version of COBRA for Thermal-hydraulic Analysis of Rod Bundle Nuclear Fuel Elements and Cores", BNWL-1962 (1976).

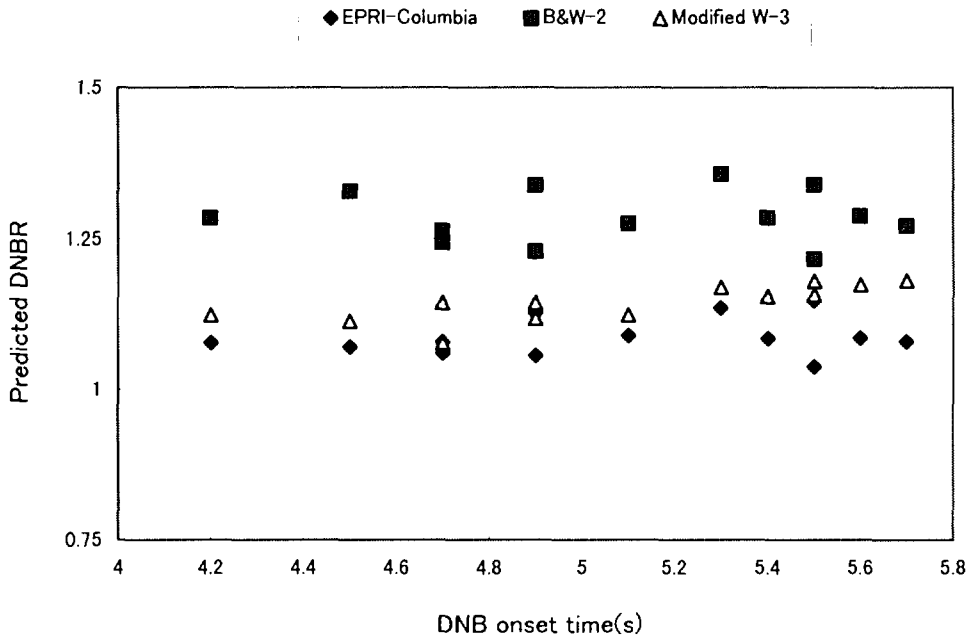

Fig. 4.6.1 Predicted DNBR with COBRA-IV-I code and DNB correlations

5. Fusion Neutronics

Accomplishment of the ITER shielding neutronics experiments under the ITER/EDA R&D task (T-218) should be highlighted in the fusion neutronics research area. The task ended up with the second experiment on gap streaming providing a full set of experimental data for validation of calculation codes and data. Extensive experimental analyses have been conducted by using MCNP-4A along with FENDL-1 and JENDL-FF. In parallel, nuclear heating and induced radioactivity experiments have been carried out in collaboration with US-Home team. The objective of these experiments was to validate nuclear data bases of KERMA and activation cross section libraries to be applied in the ITER nuclear design. Summarizing the outcomes through those experimental analyses, followings were addressed; (1) nuclear responses in SCM region, e.g, nuclear heating, fast neutron flux, can be predicted within ± 30 % with the use of the state of art nuclear data, FENDL-1, JENDL-FF, (2) adequacy of the calculation code and nuclear data for the local gap streaming between two shield blanket modules are assured with uncertainties range of ± 30 %, (3) nuclear heating relevant nuclear data, i.e., KERMA for most of major structural materials were validated to be in an accuracy within ± 20 %, (4) accuracy of activation cross sections of FENDL-A2 has been proved to be within ± 30 % for almost all elements of major structural materials. There has been a great progress also in the decay heat measurements conducted under ITER/EDA R&D Task for safety and environment area (T-339). Decay heat measurements for a large number of materials have been carried out systematically by using a newly developed whole energy absorption spectrometer and analyzed by using FENDL-A1, A2 and JENDL-ACT96 activation libraries.

Extensive data testing of nuclear data libraries of candidates for FENDL-2 has been conducted as the selection procedure. As a result, a number of data in JENDL-FF have been selected for the FENDL-2 as the most adequate data. The fusion blanket nuclear characterization extended the scope to the advanced breeder and structural materials as a long term research project. Integral experiments on vanadium was carried out for validation of nuclear data in JENDL-FF and FENDL-1. This experimental effort is recognized as a part of activities under IEA collaboration. The preliminary analysis resulted in the strong suggestion for the revision of JENDL-FF data. The other activity for IEA was the joint experiment on the low activation material characteristics done at FZK by using a d-Be white neutron source up to 20 MeV. In this fiscal year, a detailed analysis was carried out. The inter-comparison of the TLD measurement technique between FNS/JAERI and FNG/ENEA has been also organized under the IEA as the forth research item of technical development for fusion.

As applications of 14 MeV neutrons, several research projects were conducted on neutron sputtering yield measurements, precise measurements of decay gamma-ray branching for short-lived radio-nuclides, investigation of irradiation effects on several functional materials, e.g., optical fiber, insulator, GsAs, CCC, etc. In order to enhance the availability of the FNS facility, a collimator system for extracting fine 14 MeV neutron beam has been installed.

5.1 Analysis of Bulk Shielding Experiment with Simulated Superconducting Magnet by Using DOT-3.5 with FENDL/E-1 and JENDL Fusion File

C. Konno, F. Maekawa, Y. Oyama, M. Wada, Y. Kasugai, H. Maekawa and Y. Ikeda
(*E-mail:* konno@fnshp.tokai.jaeri.go.jp)

The experiment on a bulk shielding assembly simulating the superconducting magnet (SCM)[1] was reported with the analysis by the MCNP-4A[2] code and the nuclear data libraries of JENDL Fusion File (JENDL-FF)[3] and FENDL/E-1.1[4] in the last annual report. Recently the analysis of this experiment was conducted by the two-dimensional S_N transport code DOT3.5[5] with JENDL-FF and FENDL/E-1.1. Two different versions of multigroup libraries [175-n & 42-γ groups, P_5 Legendre expansion] with the self-shielding correction were generated by using the TRANSX2.15[6] code from the old and revised FENDL/MG-1.1[7] matxs files. The σ_0(background cross section) values of ^{56}Fe, ^{55}Mn, ^{Nat}Mo, ^{181}Ta and ^{209}Bi are insufficient in the old FENDL/MG-1.1 matxs file, while they are sufficient in the revised FENDL/MG-1.1 matxs file. The multigroup library of JENDL-FF was also obtained with the TRANSX 2.15 code from the matxs files of JENDL-FF newly processed by the NJOY91.128[8] code with the same process conditions as those in the revised FENDL/MG-1.1 matxs file. The angular quadrature of S_{16} was adopted. The experimental assemblies were modeled in the R-Z cylindrical shape as shown in Fig. 5.1.1. Figure 5.1.2 shows the details of the SCM region.

Figure 5.1.3 shows the ratios of the calculated to measured data (C/E) for reaction-rates, neutron fluxes and gamma-ray heating rate along with the previous C/E results by MCNP-4A. MCNP-JFF, MCNP-F1, DOT-JFF, DOT-F1[old] and DOT-F1[rev.] mean the calculations by MCNP-4A with JENDL-FF and FENDL/E-1.1, and by DOT3.5 with JENDL-FF and the old and revised FENDL/MG-1.1 matxs files, respectively. DOT-JFF and DOT-F1[rev.] agree within 40 % with the measurements and show almost the same results as the MCNP calculations. On the contrary, DOT-F1[old] largely underestimates the neutrons in the eV region because of the insufficient self shielding correction in ^{181}Ta, σ_0 of which is 10^{10} [infinite dilution].

The DOT calculations were additionally done with the library processed from the revised FENDL/MG-1.1 matxs file which omitted the gamma-ray production data in the matxs file of the specified nucleus (e.g. tantalum) included in the conductor region of Fig. 5.1.2. The contribution of the nuclei involved in the conductor region to the gamma-ray heating rate was estimated from difference between the gamma-ray heating rates of the additionally calculated DOT and DOT-F1[rev.]. Figure 5.1.4 shows the estimated contribution at the depth of 711 mm with the volume fraction in the conductor region. It is remarkable that the contribution of gamma-rays emitted from tantalum to the gamma-ray heating rate in

the conductor region was more than 30 %, although the volume fraction of tantalum in the conductor region was only 1.2 %. The analysis suggested that it was quite important to deal with heavy nuclei of small quantity such as tantalum precisely in the shielding design.

References

1) Konno C., et al.: "Bulk Shielding Experiment with Simulated Superconducting Magnet", JAERI-Review 96-012, pp. 114 - 116 (1995).
2) Briesmeister J.F. (edited): "MCNP - A General Monte Carlo N-Particle Transport Code Version 4A", LA-12625-M, Los Alamos National Laboratory, (1993).
3) Chiba S., Yu B. and Fukahori T.: "Evaluation of JENDL Fusion File", JAERI-M 92-027, pp. 35-44 (1992).
4) Ganesan S. and McLaughlin P.K.: "FENDL/E, Evaluated Nuclear Data Library of Neutron Interaction Cross Sections, Photon Production Cross Sections and Photon-Atom Interaction Cross Sections for Fusion Applications, Version 1.1 of November 1994", IAEA(NDS)-128, Rev. 3 (1996).
5) Rhodes W.A. and Mynatt F.R.: "The DOT-III Two Dimensional Discrete Ordinates Transport Codes", ORNL-TM-4280 (1973).
6) MacFarlane R.E.: "TRANSX 2: A Code for Interfacing MATXS Cross-Section Libraries to Nuclear Transport Codes", LA-12312-MS (1992).
7) MacFarlane R.E.: "FENDL/MG-1.1, Library of multigroup cross sections in GENDF and MATXS format for neutron-photon transport calculations". Summary documentation Pashchenko A.B. , Wienke H. and Ganesan S.: IAEA(NDS)-169, Rev. 3 (1996).
8) MacFarlane R.E. and Muir D.W.: "The NJOY Nuclear Data Processing System,

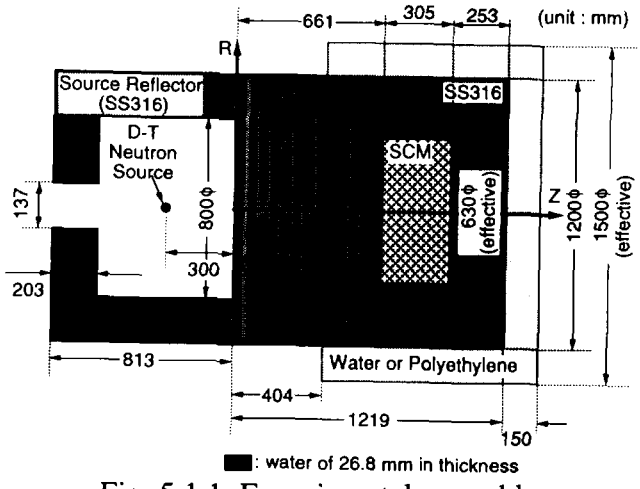

Fig. 5.1.1 Experimental assembly

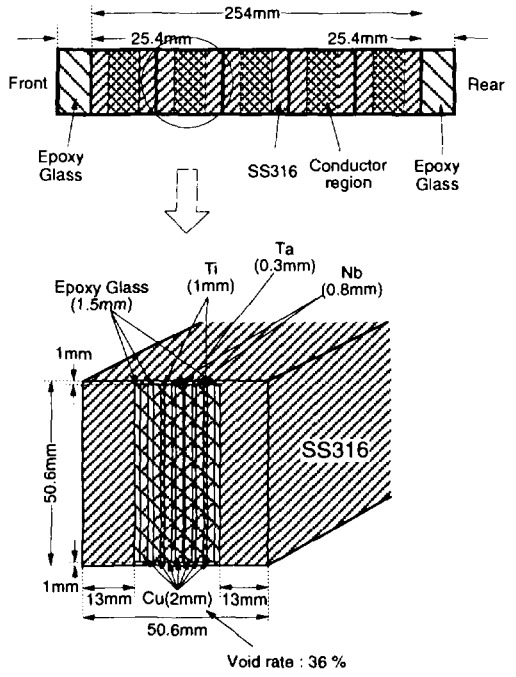

Fig. 5.1.2 Details of the SCM region

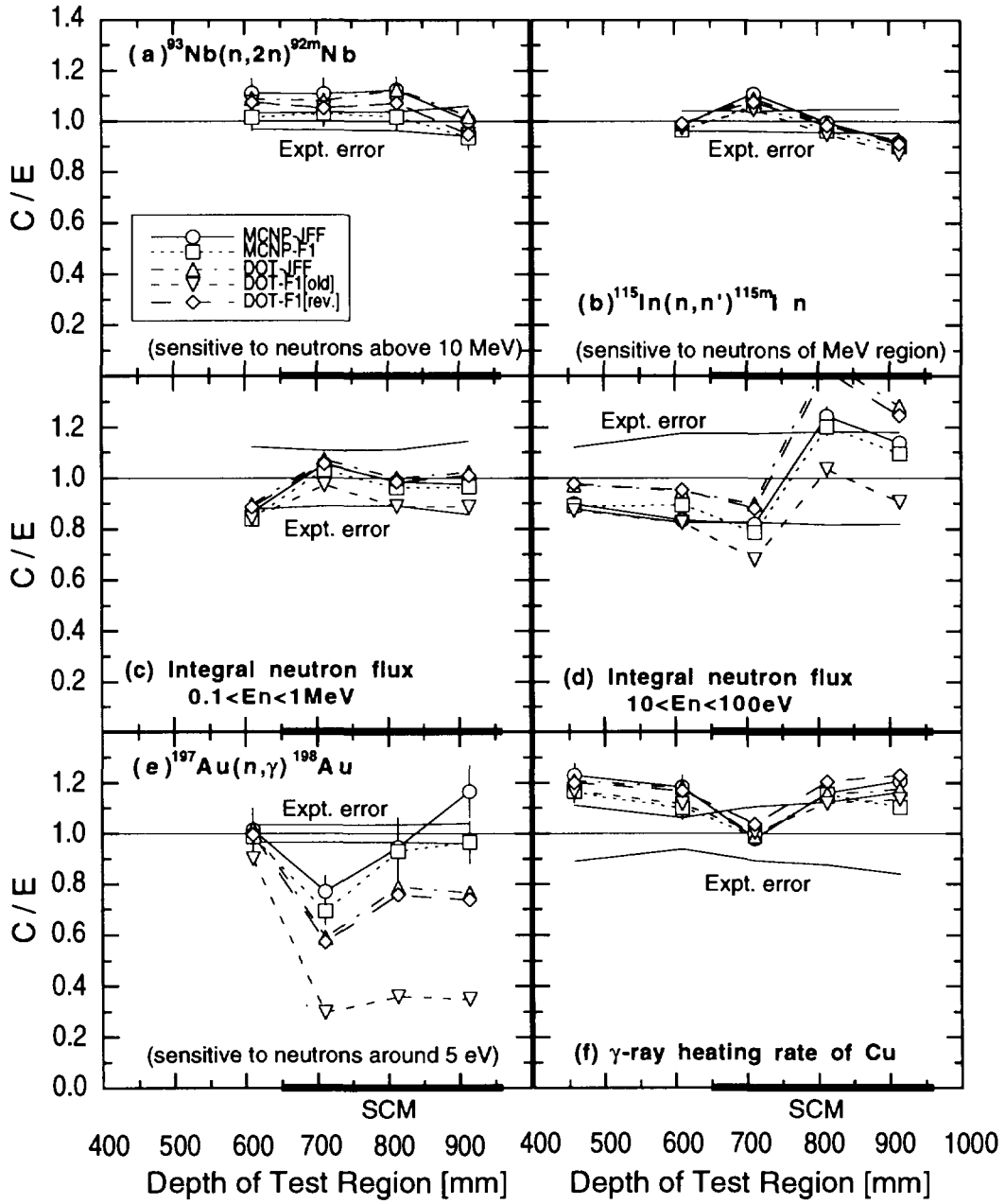

Fig. 5.1.3 Ratios of the calculated to measured data

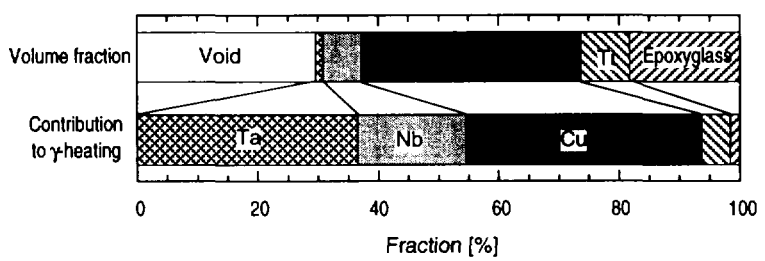

Fig. 5.1.4 Volume fraction in the conductor region and contribution to γ-ray heating rate

5.2 Gap Streaming Experiment for ITER - Source Characterization -

F. Maekawa, C. Konno, Y. Kasugai, Y. Oyama, Y. Uno, M. Wada,
H. Maekawa and Y. Ikeda
(*E-mail:* fujio@fnshp.tokai.jaeri.go.jp)

In the current design of International Thermonuclear Experimental Reactor (ITER), shielding/breeding blanket modules are attached on the back plate. This assembling method results in presence of a number of gaps of ~ 20 mm between the adjacent blanket modules. It is concerned that the gaps significantly degrade shielding performance of the blanket modules due to the streaming effect of neutrons and photons through the gaps. To investigate the gap streaming effect, a benchmark experiment focussing on the gap streaming effect was conducted at FNS/JAERI as an R&D task (T-218) of ITER/EDA.

An experimental assembly made of iron was installed in a large opening prepared in a room wall of the second target room of FNS. In this experimental configuration, neutrons and gamma-rays scattered by the other room walls come into the experimental assembly. Structural materials of the rotating neutron target (RNT) for D-T neutron generation also scatter source D-T neutrons producing lower energy neutrons and gamma-rays. These scattered neutrons and gamma-rays as well as the source D-T neutrons should be considered as the source for the experiment, and should be known precisely for the successive experimental analysis. Therefore, the source characterization experiment was performed as the first stage of the gap streaming experiment.

On a vertical plane at 1.7 m from the RNT, where the front surface of the experimental assembly was to be located, spatial distributions of the following quantities were measured: (i) neutron spectrum between 10 keV and 1 MeV by proton recoil gas proportional counters, (ii) dosimetry reaction rate by the foil activation method, (iii) fission rate of ^{235}U and ^{238}U by micro fission chambers and (iv) gamma-ray heating rate by TLD. As shown in Fig. 5.2.1, detector positions were selected mainly on the two horizontal lines at Y=0 and -200 mm where the gap entrances were to be located when the experimental assembly was moved to the nominal position.

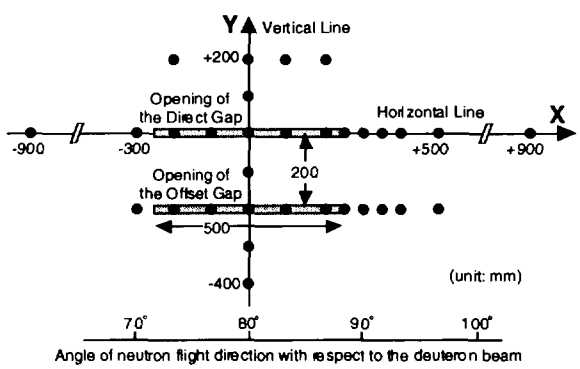

Fig. 5.2.1 Detector positions scattered on the plane at 1.7 m from the target for the source characterization experiment

As the three dimensional model was needed, the continuous energy Monte Carlo transport code MCNP-4A [1] was used for the analysis of the source characterization experiment. Cross section data in JENDL Fusion File [2] were used. A calculation routine for D-T neutron generation was implanted in the "source" subroutine of MCNP-4A. The following effects were considered in the routine: (i) the probability function of D-T reaction as a function of the deuteron energy in the $TiT_{1.7}$ target calculated with stopping power data and the D-T reaction cross section, (ii) the angular distribution of generated neutrons, (iii) the kinematics of the D-T reaction to determine the generated neutron energy, and (iv) the collimated deuteron beam diameter of 15 mm. And then, the RNT assembly, experimental room walls, the accelerator and the experimental assembly were modeled in detail.

According to a preliminary calculation for the source characterization experiment, calculated threshold reaction rates agreed fairly well with the measured data. Quantities related to low energy neutrons, however, were not predicted accurately by the calculation because of improper chemical composition of the concrete wall and modeling of the experimental setups in the experimental room. To predict low energy neutrons adequately, therefore, the room wall thickness, the hydrogen content in the room wall and densities of materials for the experimental setups were adjusted.

The measured fission rates of ^{235}U and ^{238}U, and gamma-ray heating rates are compared with the calculated results shown in Fig. 5.2.2. At the +300 mm position of the measured ^{238}U fission rate distribution, a large dip of ~ 30 % due to attenuation of the source D-T neutrons by the structural materials of the RNT is clearly observed. The distribution is reproduced very well by the calculation. The measured horizontal distributions of the ^{235}U fission rate and the gamma-ray heating rate are almost flat, and predicted adequately by the calculation. Figure 5.2.3 shows calculated neutron spectra with and without modeling of the room walls, comparing with the measured data. The figure indicates that the presence of the room walls considerably increases low energy neutron flux. Thus, the room walls should be modeled precisely. The calculated spectrum with modeling the room walls agrees with the measured data.

In summary, the calculation predicts high energy neutrons within ± 10 % and low energy neutrons and gamma-rays within ± 20 %. These good agreements between the measurement and calculation show validity of the calculation model determined through the source characterization experiment. The calculation model is to be used for the analyses of the successive gap streaming experiment.

References

1) Briesmeister J. F. (Ed.): "MCNP - A General Monte Carlo N-Particle Transport Code, Version 4A", LA-12625-M, Los Alamos National Laboratory (1993).

2) Chiba S., et al.: "Evaluation of the Double-Differential Cross Sections of Medium-Heavy Nuclei for JENDL Fusion File", JAERI-Conf 96-005, 45 (1996).

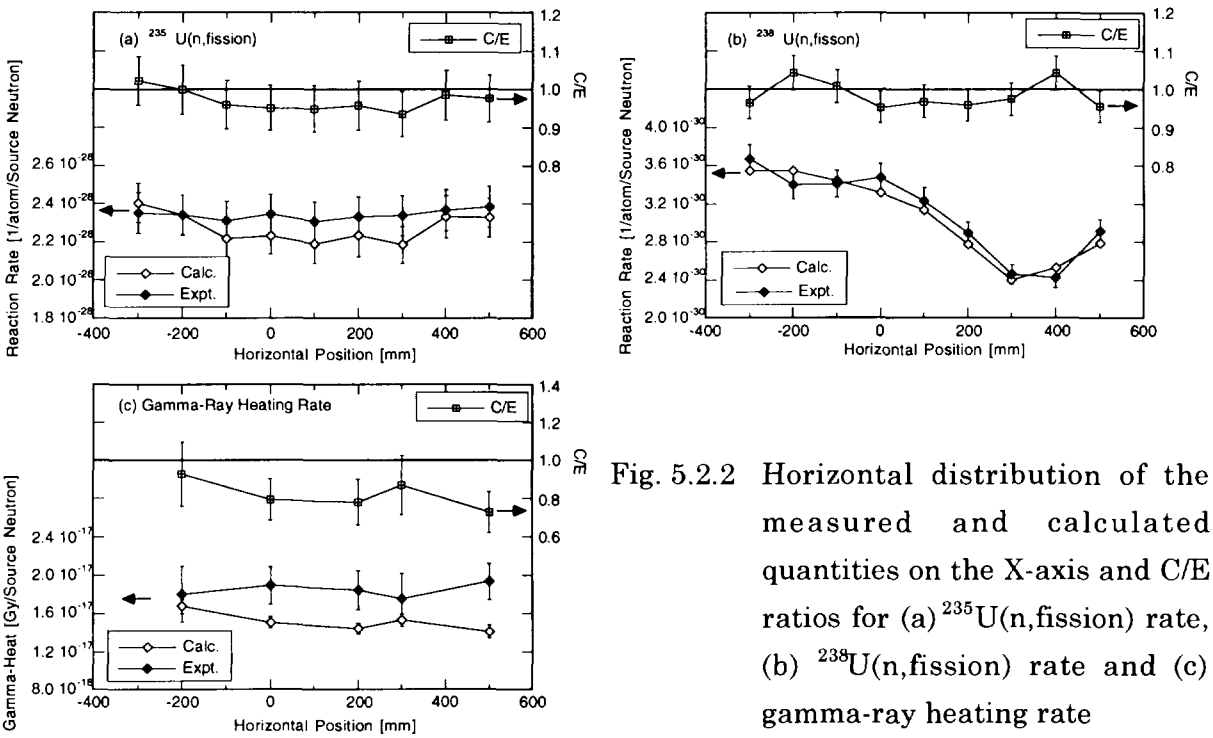

Fig. 5.2.2 Horizontal distribution of the measured and calculated quantities on the X-axis and C/E ratios for (a) ^{235}U(n,fission) rate, (b) ^{238}U(n,fission) rate and (c) gamma-ray heating rate

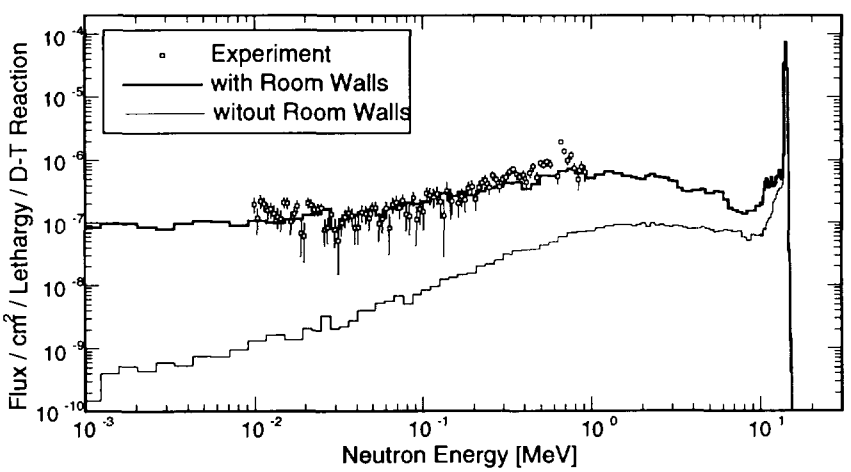

Fig. 5.2.3 Calculated neutron spectra at 1.7 m from the RNT with and without modeling of the room walls compared with the measured spectrum

5.3 Gap Streaming Experiment for ITER - Experiment -

C. Konno, F. Maekawa, Y. Oyama, Y. Uno, Y. Kasugai, M. Wada, H. Maekawa and Y. Ikeda
(*E-mail:* konno@fnshp.tokai.jaeri.go.jp)

In the global shield of ITER it is necessary to properly estimate the influence of neutron streaming due to gap of about 20 mm which appears between the blanket modules since the blanket in ITER has a module structure[1]. A gap streaming experiment was performed by using the FNS D-T neutron source at Japan Atomic Energy Research Institute as the ITER/EDA R&D Task T-218, in order to examine the effects due to gap between shield blanket modules in ITER. The experiment had three phases. The first one is defined as neutron source characterization (Source Characterization Experiment) as described in Sec. 5.2. The second (Experiment-1) aimed at the gap effect for welding part between shield blanket and back plate, where the helium production rate is a key design parameter for rewelding. The third (Experiment-2) focused on the influence of the gap on troidal field coil, where the gamma-ray heating rate and radiation damage are key design parameters. The analysis of this experiment is presented in Sec. 5.4.

Experiment-1

The experimental assembly was an iron slab of 1.6 m in height, 1.4 m in width, and 500 mm in thickness, in which a gap (22 mm in height, 500 mm in width and 300 mm in depth) and a cavity (140 mm in height, 500 mm in width and 100 mm in depth) were made in the height of 1.8 m (the same height as the beam line of FNS) [Direct gap] or 1.6 m [Offset gap]. Figure 5.3.1 shows the experimental assembly. This assembly was installed in the auxiliary shield (3.1 m in height, 2.5 m in width, layered structure of iron and polyethylene). The overall experimental assembly was embedded in a large hole opened in a wall, which separated two target rooms, in order to reduce background neutrons. The distance from D-T neutrons to the front surface of the experimental assembly was 1.7 m. A B_4C plate of 13 mm in thickness was attached to the front surface of the experimental assembly in order to reduce low energy neutrons which were difficult to estimate by the calculation.

Neutron spectrum of keV region, various reaction-rates, gamma-ray spectrum and gamma-ray heating rate were measured inside the gap, on the surface of cavity and the rear surface of the experimental assembly . Some measurements were also performed without the gap. The influence of the gap is given as the ratio of the fission rates of ^{235}U and ^{238}U to those without the gap. The results are shown in Fig. 5.3.2. The direct gap increases the fission rate of ^{238}U along the gap line by 20 times and on the upper surface of the cavity by 50 %, while

the offset gap increases along the gap line by 3 - 4 times. On the contrary, the increase of the fission rate of ^{235}U due to the gap is much smaller; it is 20 % along the direct gap line and only a few % on the upper and lower surface of the cavity. The influence of the gap between the shield blanket modules should be considered accurately in the shield design of ITER from the view of the helium production which is sensitive to neutrons above a few MeV.

Experiment-2

The front part of experimental assembly was the same as that in Experiment-1. The bulk iron region of 300 mm in thickness was attached to the rear side. Measurements were performed on the rear surface of the experimental assembly with and without gap and/or cavity. Figure 5.3.3 shows the influence of the gap on the fission rates of ^{235}U and ^{238}U, i.e. the ratio of the fission rates of ^{235}U and ^{238}U to those without the gap. The direct gap and offset gap increase the fission rate of ^{238}U by 10 times and 2.8 times, respectively. On the other hand, the influence of the gap is small and at most 10 % as for the fission rate of ^{235}U. From the comparison between Figs. 5.3.2 and 5.3.3, it is founded that the influence of the direct gap on the rear surface in Experiment-2 is smaller by about 50 % than that in Experiment-1 because of attached 300 mm thick bulk iron layer, while the influence of the offset gap is almost the same on the rear surface in Experiment-1 and -2.

Reference

1) Ioki K., et al. : "ITER Shield Blanket and Vacuum Vessel," Proc. 16th IEEE/NPSS Symposium on Fusion Engineering, Champaig, 1995, to be published.

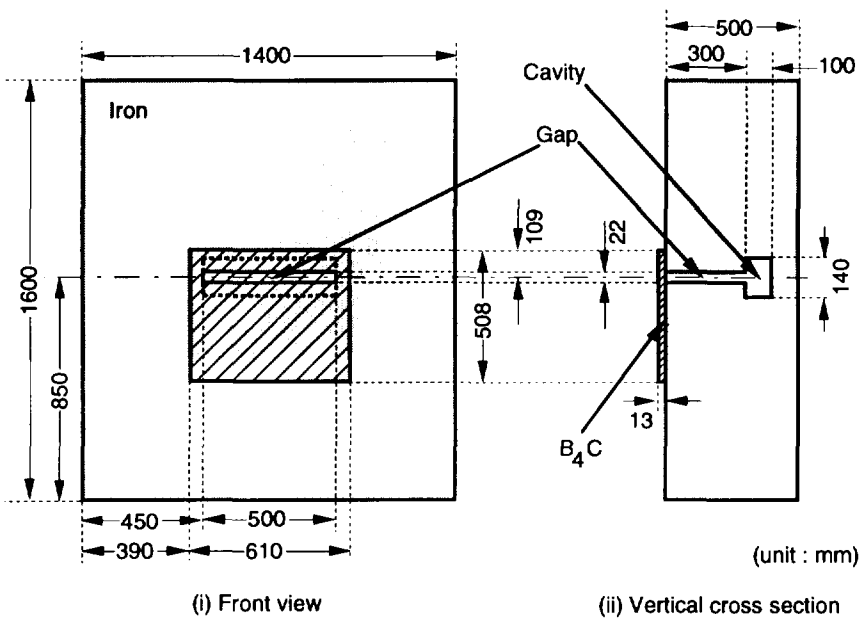

Fig. 5.3 1 Detailed structure of the direct gap assembly in Experiment-1

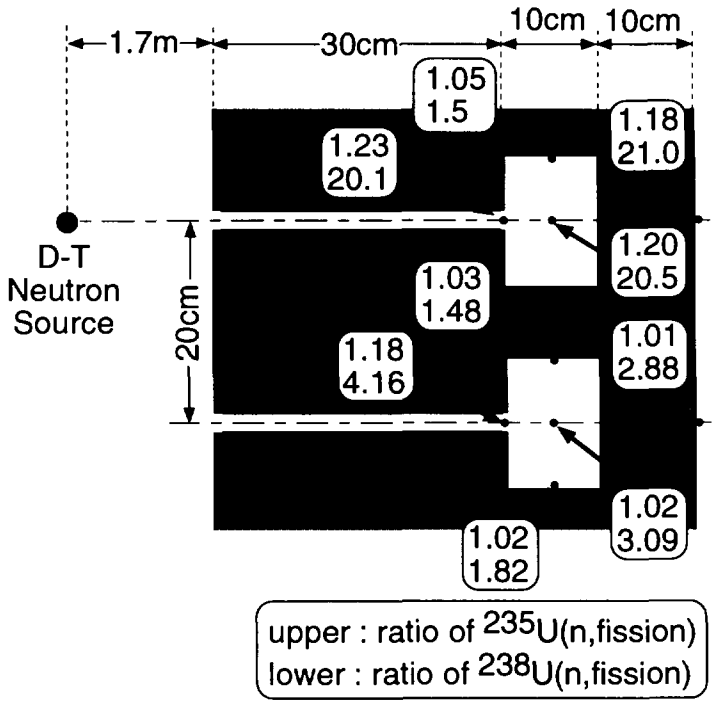

Fig. 5.3.2 Ratios of the measured fission rates of ^{235}U and ^{238}U with gap to those without gap in Experiment-1

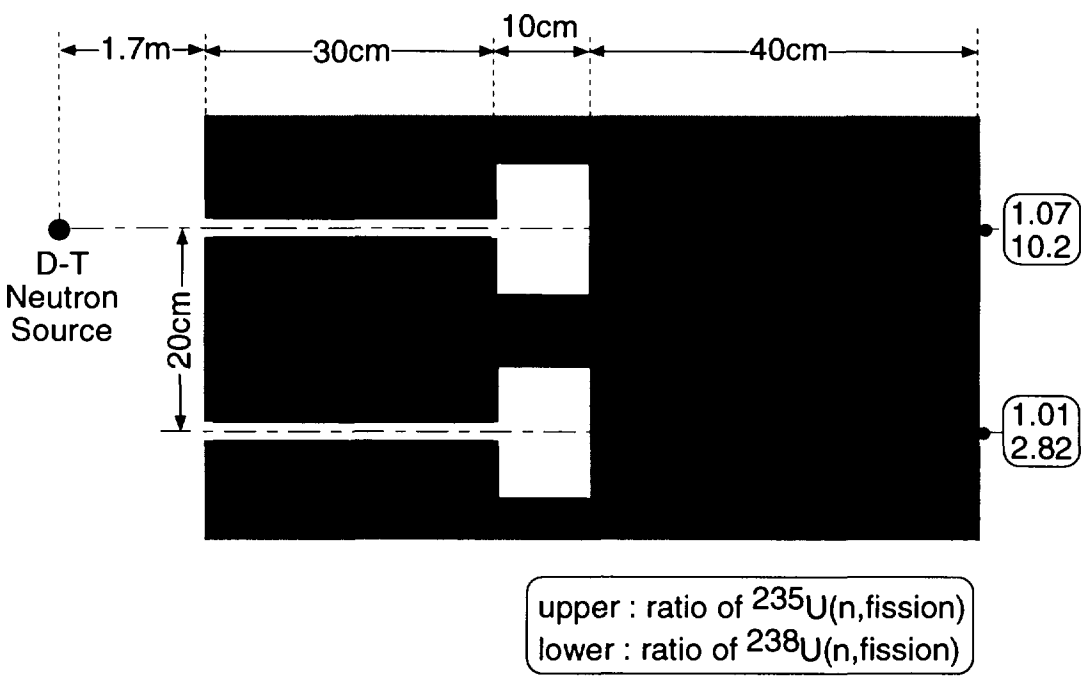

Fig. 5.3.3 Ratios of the measured fission rates of ^{235}U and ^{238}U with gap to those without gap in Experiment-2

5.4 Gap Streaming Experiment for ITER - Analysis -

F. Maekawa, C. Konno, M. Wada, Y. Kasugai, Y. Oyama, Y. Uno,
H. Maekawa and Y. Ikeda
(*E-mail:* fujio@fnshp.tokai.jaeri.go.jp)

The gap streaming experiment [1] conducted at FNS/JAERI was analyzed as an R&D task (T-218) of ITER/EDA. The objective of the analysis is to demonstrate capability of the Monte Carlo transport calculations for prediction of the two major shielding design parameters: (1) helium production rate (HPR) at the connection legs between the blanket modules and the back plate, and (2) nuclear responses in the troidal field coil (TFC) behind the vacuum vessel.

Analysis

The continuous energy Monte Carlo transport calculation code MCNP-4A [2], which had been used for many designs of ITER/EDA, was used with two nuclear data libraries, FENDL/E-1.0 [3] and JENDL Fusion File [4]. Calculated results with the two nuclear data libraries were not so different from each other. In most of cases, the differences were less than 10 %. Therefore, we discuss about the results obtained with FENDL/E-1.0.

The experimental assemblies were modeled precisely. The experimental circumstances determined through the source characterization experiment [5] were appended to the calculation model. Track length detectors were located at the corresponding experimental detector positions. The source biasing method, and the particle splitting and Russian roulette method with cell importance parameters were used as variance reduction techniques. Although the variance reduction techniques were adopted, it took a great amount of computation time, typically 1 ~ 2 weeks for one case of calculation with an engineering work station, because of large attenuation of particle fluxes in the experimental assembly and small solid angles of the track length detectors viewing from the D-T neutron source.

Some aspects in use of Monte Carlo codes for streaming and shielding calculations are found through the analyses: considerable experience and time are needed for optimization of the variance reduction parameters, and Monte Carlo calculations require much computation time to obtain statistically reliable results even now when very fast computers are available.

Experiment-1 for HPR at the Connection Legs

The measured and calculated results in the gap (Z= 0~300 mm), inside the cavity (Z= 300~400 mm) and on the rear surface of the experimental assembly (Z= 500 mm) are compared. (See Fig. 5.4.1 for the geometrical configuration.) As a whole, agreements

between the experiment and the calculations are very good. The measured nuclear responses for high energy (> 0.5 MeV) neutrons are predicted within 20 % by the calculations, while those for low energy neutrons and gamma-rays are predicted within 30 %, for all the detector positions.

The rewelding points on the connection legs of the blanket modules and the back plate are located apart from the gap center line to reduce HPR. Figure 5.4.1 shows reduction of nuclear responses obtained by the experiment and calculation. It is defined as ratios of response at the cavity side to the cavity center. The experimental reduction factors for the $^{27}Al(n,\alpha)^{24}Na$ reaction rate, which cross section is similar to the helium production cross section of SS-316, are ~ 1/30 and ~ 1/3 for the direct and the offset gap configurations, respectively. The reduction factors for the nuclear responses of interest are adequately predicted by the calculations.

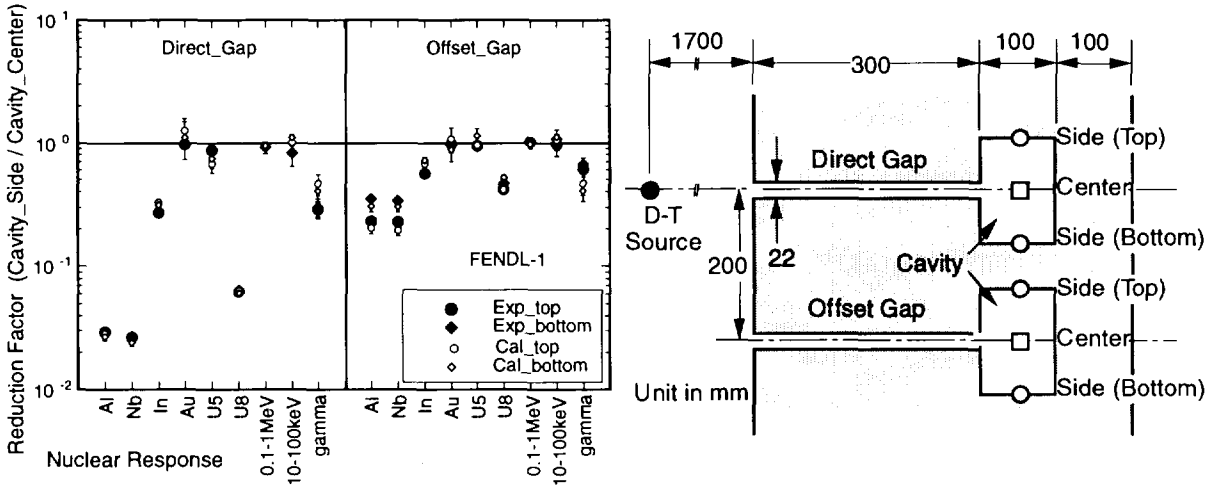

Fig. 5.4.1 Reduction factors of various nuclear responses ($^{27}Al(n,\alpha)^{24}Na$, $^{93}Nb(n,2n)^{92m}Nb$, $^{115}In(n,n')^{115m}In$, $^{235}U(n,f)$, $^{238}U(n,f)$, integral fluxes of 0.1-1 MeV and 10-100 keV and gamma-ray heating rate) obtained by the experiment and calculations, and a sketch of the geometry for the gaps, cavities and detector positions

Experiment-2 for Nuclear Responses of TFC

Here, we define a peaking factor as a ratio of a nuclear response for the gap configuration to the bulk assembly without the gap and cavity. Results of two nuclear responses along the rear surface of the assembly (Z= 800 mm) are shown in Fig. 5.4.2. When the experimental and calculated peaking factors are compared, a large difference is found in the integral fluxes of > 10 MeV as shown in Fig. 5.4.2 (a). The calculated peaking factors are larger than the experimental ones. The difference is consistent to the results [6] of the 14-MeV neutron transmission experiment on bulk iron that the

calculated 14-MeV neutron fluxes become smaller compared to the experimental data as the transmission length increases. The peaking factors of the gamma-ray heating rate, shown in Fig. 5.4.2 (b), are not so large, at most ~ 1.2, and the experimental and calculated peaking factors agree within the uncertainty ranges of the experiment and calculations.

As a whole, all the calculated results including both high and low energy neutrons and gamma-rays agree within ~ 30 % with the measured data. Therefore, any nuclear parameters on TFC can be estimated within uncertainty of 30 % by MCNP-4A if the complicated geometry of the ITER blanket is treated precisely.

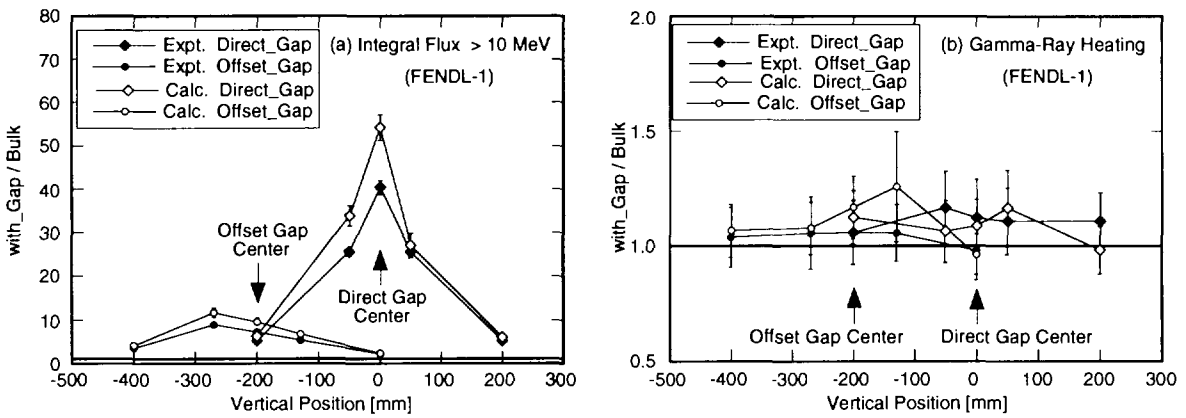

Fig. 5.4.2 Comparisons of the measured and calculated peaking factors for (a) the integral flux > 10 MeV and (b) the gamma-ray heating rate

References

1) Konno C., et al.: "Gap Streaming Experiment for ITER - Experiment -", Section 5.3 in this Annual Report (1997).
2) Briesmeister J. F. (Ed.): "MCNP - A General Monte Carlo N-Particle Transport Code, Version 4A", LA-12625-M, Los Alamos National Laboratory (1993).
3) Ganesan S. and McLaughlin P. K.: IAEA-NDS-128 (1995).
4) Chiba S., Fukahori T., Yu B. and Kosako K.: "Evaluation of Double-Differential Cross Sections of Medium-Heavy Nuclei for JENDL Fusion File", JAERI-Conf 96-005, 45 (1996).
5) Maekawa F., et al.: "Gap Streaming Experiment for ITER -Source Characterization-", Section 5.2 in this Annual Report (1997).
6) Maekawa F. and Oyama Y.: Nucl. Sci. Eng., 125, 205 (1997).

5.5 Experiment and Analysis of Nuclear Heating on Structural Materials in a Graphite Assembly Driven by D-T Neutrons

Y. Ikeda, A. Kumar*, F. Maekawa, Y. Kasugai and M. Wada
(*E-mail:* ikeda@fnshp.tokai.jaeri.go.jp)

The experiments on nuclear heating were carried out at the FNS facility under the ITER/EDA R&D sub-task of T-218 in order to provide experimental data for validating the nuclear data relevant to nuclear heat deposition in fusion reactor structural components. The measurements were conducted on potential candidates for fusion reactor structural materials, i.e., Be, graphite, Al, Si, SiC, Ti, V, Cr, Fe, Ni, Cu, Zr, Nb, Mo, W. The central zone of the assembly consisted of graphite blocks with a central channel hole of 50 mm in diameter. The outer zone was filled with SS-304 and polyethylene. As the reference arrangement, six graphite probes were placed throughout the hole to obtain the heat deposition distribution in the assembly. The second arrangement held each probe other than graphite at the first probe location of the graphite arrangement. The experimental assembly was placed at very close position to the D-T neutron target. For the total heating rate measurement with the calorimetric method[1,2], the probe of each material in a cylindrical shape, on which thermal sensors of 6 kW thermistor (TM: Techno Seven Co. Ltd.) were attached, was inserted in the central hole. D-T neutrons were generated by bombarding a tritiated target with a 20 mA deuteron beam of 350 keV. The assembly was irradiated with D-T neutrons of 3 to 5 minutes duration pulses separated by 3 to 5 minutes. The temperature rise in the probe material due to nuclear heating was measured by detecting resistance change in TM with a constant current of 5 to 20 mA. It was observed that there were clear temperature rises corresponding to the neutron pulses. The nuclear heating rates were derived from the temperature rises with use of available specific heats. The g-ray heating components at locations between two adjacent probes were also measured with TLD. In order to validate neutron transport calculation, dosimetry activation foil measurements were carried out.

The calculations have been performed using the MCNP-4A Monte Carlo transport code with JENDL-3.2 and FENDL-1 nuclear data libraries. The foil activation rates were calculated using IRDF-90 version 2 dosimetry file. In Fig. 5.5.1, C/E values for heating rates at graphite probes along the central axis are plotted. Figure 5.5.2 shows ratios of calculated to measured for the volume averaged heating rates in the probes. The followings are the status of the results based on the experimental analysis:

Total Heating

C: Both JENDL and FENDL gave excellent agreements with measurements. JENDL tends to be slightly larger than FENDL at the first location. This is due to 10 % higher

---

* University of California, Los Angeles

KERMA factor at 14 MeV region as suggested in the previous experiments.

Cr: Both JENDL and FENDL agreed with the experiment within 10%. The result is consistent with the result in the copper assembly.

Cu: Both calculations excellently agreed with the measurement.

Fe: JENDL overestimated the experiment by 15 % and FENDL underestimated it by 8 %. Considering experimental error of 8 %, FENDL seems adequate.

Ni: Both JENDL and FENDL agreed with the experiment.

SS: Both calculations agree with the experiment. However, JENDL is higher by 10 % than FENDL. It may be due to the difference in the KERMA data. The results are consistent with those in the copper assembly.

Al: JENDL seemed adequate. FENDL, however, overestimated the experiment by 25 %.

Mo: Both JENDL and FENDL slightly overestimated by 8 %. However, it can be concluded that both are reasonable.

Nb: Both are adequate.

V: JENDL underestimated by 18 % and FENDL overestimated by 28 %. Both KERMA data should be checked carefully.

W: Both JENDL and FENDL gave overestimations by around 10 %. The overestimation is consistent with the previous results.

Zr: Both JENDL and FENDL underestimated by 20 %. The KERMA data should be checked.

Si: Though JENDL slightly underestimated by 8 %, it seemed adequate. While, FENDL largely overestimated by 50 %. Apparently, the FENDL KERMA data should be revised after a careful investigation.

Ti: JENDL underestimated by 20 %. However, FENDL agreed with the measurement. FENDL seems adequate.

Gamma-Heating

Experimental data were obtained with errors less than 30%. The measured heating rates at the front side were systematically lower than those at the back side. If the contribution from the D-T source was underestimated, it could be explained.

All calculations are in agreement within 30 % with experiments. It is concluded that there is no serious problem in the gamma-heating data. The result provided an uncertainty range in the design calculations relevant to the nuclear heating.

References

1) Ikeda Y., Kumar A., et al.: Fusion Technology, 21, 2190 (1992).

2) Ikeda Y., Kumar A., et al.: Fusion Engineering and Design, 28, 769 (1995).

3) Ikeda Y., Kumar A., et al.: Fusion Technology, 28, 1, 156 (1995).

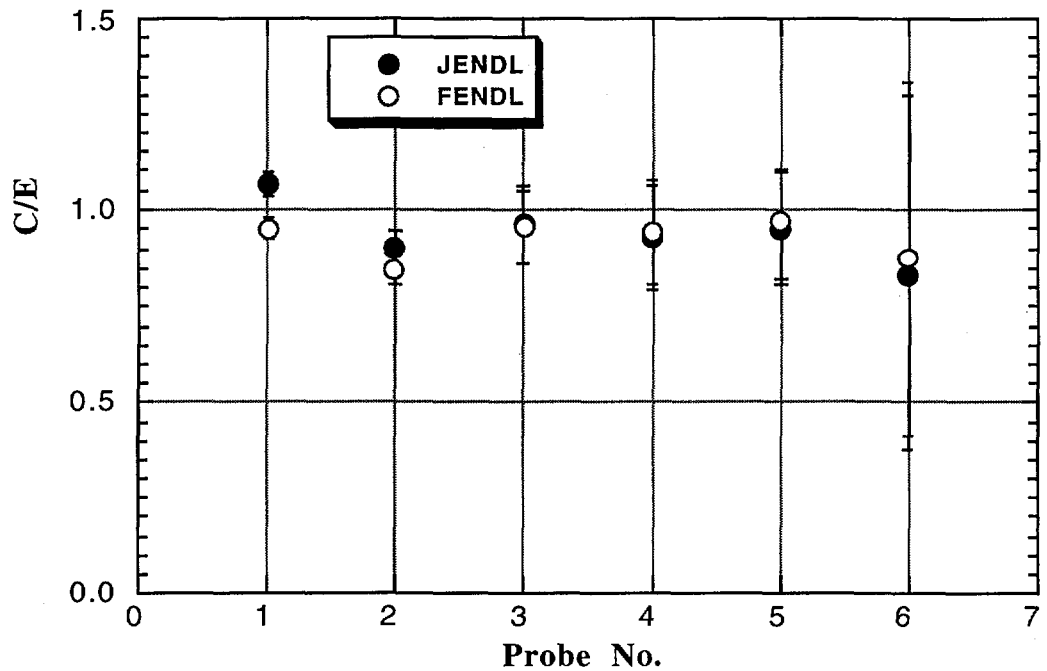

Fig. 5.5.1 C/E values of volume averaged nuclear heating rates of graphite probes along the central axis

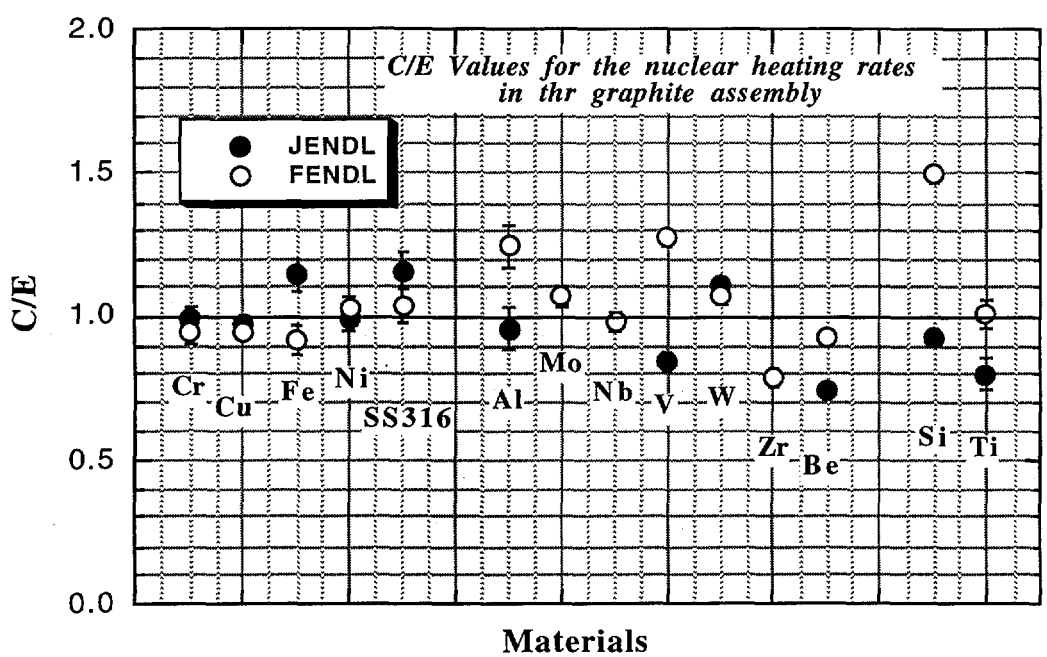

Fig. 5.5.2 C/E values of nuclear heating rates of different material probes at the first probe location in the graphite assembly

5.6 Measurements of D-T Neutron Induced Radioactivities in Elements and Analysis with JENDL and FENDL Activation Files

Y. Kasugai, A. Kumar*, F. Maekawa, M. Wada and Y. Ikeda,
(*E-mail*: kasugai@fnshp.tokai.jaeri.go.jp)

The importance of the induced radioactivity in D-T fusion environment is recognized as one of the most critical issues from the safety point of view. The ITER development has addressed important tasks undertaken as R&D for an experimental validation of all process requested for the activation relevant design calculation. Integral experiments on the induced radioactivity in the graphite assembly were conducted. Two irradiation positions with different neutron spectra in the assembly were selected. Induced radioactivities in materials of Al, Mg, Ti, V, Mn, Fe, Ni, SS-316LN, Cu, Zn, Nb, Mo, Ag, In, Sn, Dy, Hf, Ta, W and Pb were investigated. The parameters were cooling time, neutron spectrum, cross section libraries, which should be considered in the experimental analysis. As the neutron transport code, a continuous energy Monte Carlo code MCNP-4A was employed coupled with FSXLIB-J3.2 and FENDL/MC based on JENDL-3.2 nuclear data file and FENDL/E1, respectively. For the activation calculations, ACT4 of the THIDA code system with the JENDL activation library[1] (JENDL-ACT96), FENDL-A1[2] and FENDL-A2 (updated version of FENDL-A1) activation libraries was used.

The neutron source and experimental assemblies were the same as those in the nuclear heating experiment. (See the previous section) Two positions for foil irradiation were selected to be at positions between the first and second probes, and third and fourth probes for the nuclear heating measurements described in the previous section. These positions were named, hereafter, as A and B. The samples of Al, Mg, Ti, V, Mn, Fe, Ni, SS-316LN, Cu, Zn, Nb, Mo, Ag, In, Sn, Dy, Hf, Ta, W and Pb were irradiated with D-T neutrons at two positions in the graphite assembly, namely, position A at 50.2 mm from the bottom of the experimental channel and position B at 151.2 mm. The size of sample was 10 x 10 x 0.01~0.5 mm^3. The weight of the sample ranged from 10 ~300 mg. After irradiation, induced radioactivities were measured by gamma-ray spectroscopy with Ge detectors at cooling time from several minutes to about one year. Experimental data were derived as the radioactivity intensity per unit volume (Bq/cm^3). The radioactivities were identified by gamma-ray energies and their intensity relationship. The decay rate
was derived from gamma-ray counts, detector efficiency, gamma-ray emission probability and other corrections needed, e. g., gamma-ray collection time, half-lives, etc.

Three dimensional code MCNP-4A was used for modeling the rotating target geometry and the probe-vacuum chamber system. The library, FSXLIB-J3.2, was used for

---

* University of California, Los Angeles

neutron interactions and photon production in MCNP calculation in the whole system. The FENDL-1 library was also applied for the MCNP calculation. The neutron spectra obtained by two libraries were almost identical. ACT4 of the THIDA code system was used as the radioactivity inventory code. The activation cross section libraries based on the JENDL-ACT96 activation file with 125 neutron energy groups and FENDL-A1 and A2 with 175 neutron energy groups were used for the induced radioactivity calculations. Induced radioactivities corresponding to the experimental conditions were calculated by those codes to be compared with the measured value. Figure 5.6.1 shows C/E values of radioactivities induced in the SS-316 at Position A after D-T neutron irradiation fo 6 hrs. There is no significant difference among the calculations. C/E values of some radioactivities for molybdenum at Position B after 30 min. irradiation are plotted in Fig. 5.6.2. Almost all the cases give C/E values in a range from 0.7 to 1.3. In particular, for the major structural materials, the calculations agreed within 20 % with the measurements. It can be stressed that FENDL-A2 always shows better results than FENDL-A1.

References

1) Nakajima Y. : "JENDL Activation Cross Section File," JAERI-M 91-032, 43 (1991).
2) Pashchenko A. B.: "Status of FENDL activation file and plans for the future developments," Proc. Int. Workshop on Nuclear Data for Fusion Reactor Technology, Del Mar, California, USA, 3 - 6, May 1993.

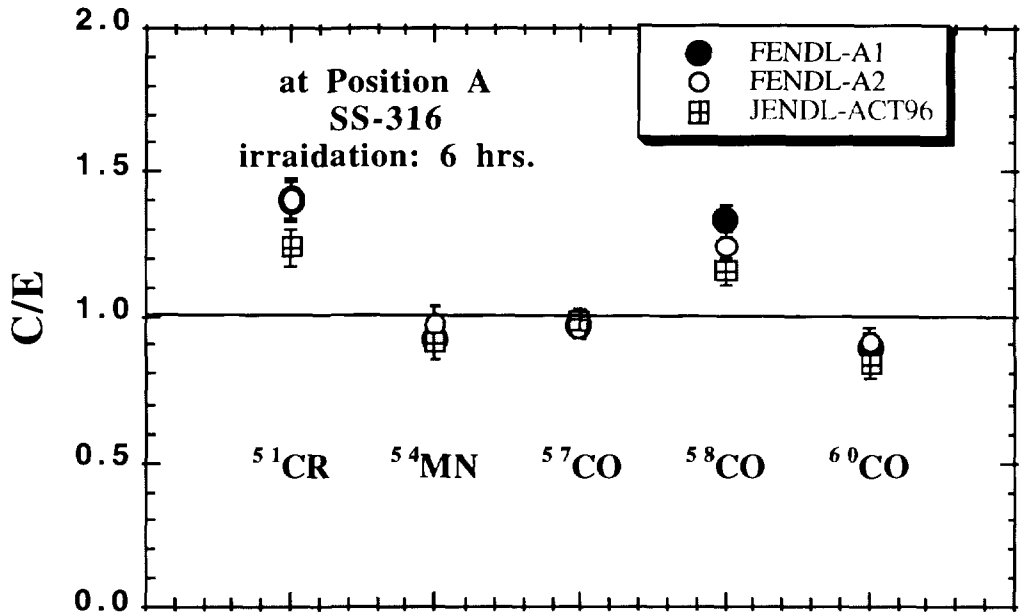

Fig. 5.6.1 C/E values of several long-lived radioactivities in the SS-316 sample irradiated by D-T neutrons for 6 hr.

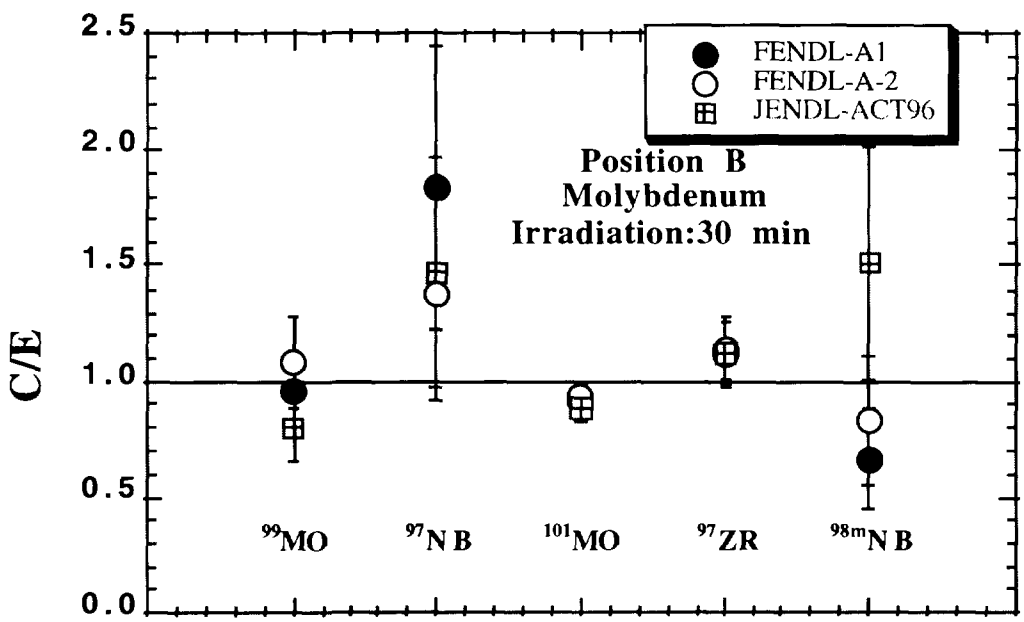

Fig. 5.6.2 C/E values of several long-lived radioactivities in the molybdenum sample irradiated by D-T neutrons for 30 min.

5.7 Development of Fusion Dosimetry Technique with a Microcalorimeter

Y. Ikeda and A. Kumar*
(*E-mail:* ikeda@fnshp.tokai.jaeri.go.jp)

One of recent technical developments addressed to improve the nuclear data for a fusion reactor was achieved in the direct nuclear heating measurement with a calorimetric method.[1-2] It was generally understood that a low Z material is sensitive to neutrons rather than γ-rays because of low interaction coefficient of γ-rays with a low Z material. On the other hand, high Z materials such as tungsten and lead tend to have dominating contribution from γ-rays because of large γ-ray absorption coefficient. On the basis of these nuclear properties, a technique incorporating with the micro-calorimetric method is proposed for the neutron and γ-ray dosimetry in D-T neutron driven fields.

The experimental system consisted of a host medium at the center region followed by a polyethylene zone. As the host media, SS-316, copper and graphite were chosen to provide different neutron and γ-ray environments. A cross sectional view of the assembly is shown in Fig. 5.7.1. Along the central axis, probe materials to be tested for the nuclear heating measurement were deployed in a hole with 50 mm in diameter. The experimental assembly was irradiated with D-T neutrons produced via the $^{3}T(d, n)^{4}He$ reaction by using FNS. The net heating to the D-T neutron irradiation was obtained by subtracting values of resistance change rate from those before and after neutron pulses. Heating rate in units of erg/g/10^{12} n/s, were derived from the measured net resistance change in the attached thermistor using data for a coefficient of temperature vs. resistance, specific heat, cycle time, and neutron yield. The experimental procedure is described in detaile in Ref-1,2).

The experimental analysis was carried out by MCNP-4A[3] calculations with nuclear data based on JENDL-3.2[4] and FENDL-1[5]. For the data of tungsten at the first location in the graphite assembly, the C/E values were 1.02 ± 0.05. These agreements suggest that calculations are valid for the nuclear heating in the tungsten probe. It is shown that most of the nuclear heating in tungsten probe is attributable to γ-rays throughout the assembly. The neutron fractions are less than 5 %. On the other hand, heating in graphite probes are dominated by neutrons. More than 90 % of the total at front region is due to the neutron heating. However, the γ-ray contribution increases up to 20 % with the depth in the assembly. By assuming that those calculated ratios are valid as far as the medium of interest is concerned, these doses could be extracted from the total heating measurements of two probes with extreme profiles for neutron and gamma.

The method proposed here is in principle based on the linear combination of the two different responses, i.e., two extreme sensitivities to neutron and γ-ray for the low and high Z

---

* University of California at Los Angeles (UCLA)

materials, respectively. Here, we use graphite as the low Z probe for neutrons and tungsten as the high Z probe for γ-rays. Let the total heating of graphite and tungsten be denoted by T(C) and T (W). T (C) and T (W) possess both neutron and gamma contributions, given as

$$T(C) = ND(C) + GD(C),$$
$$T(W) = ND(W) + GD(W).$$

Here, ND and GD denote neutron and gamma doses, respectively. Solving for ND and GD, one finds,

$$ND \sim= a \quad x\ (1 - CF(C)\gamma)\ x\ T(C),$$

and

$$GD \sim= b \quad x\ (1 - CF(W)\ ex\text{-}\gamma)\ x\ T(W),$$

where a and b are conversion factors for the absorbed dose from heating rate, and CF(C)γ and CF(W)ex-γ, ratios of the total heating rates of tungsten and graphite, and calculated ratios of internal and external γ-ray contributions in the tungsten probe as a function of the probe position in the assembly. From Fig. 5.7.2, we can assume that CF(C)γ is identical to CF(W)ex-γ. Then, we know all parameters for extracting ND and GD. Consequently, dose rates for neutrons and γ-rays can be derived from measured heating rates of graphite and tungsten. It is noted that as a high Z gamma detector, lead or bismuth could be more preferable than tungsten because of the smaller cross sections for neutrons in those materials than that in tungsten, resulting in less internal gamma contribution.

References

1) Ikeda Y., Kumar A., et al.: Fusion Engineering and Design, 28, 769 (1995).
2) Ikeda Y., Kumar A., et al.: Fusion Technology, 28, 1, 156 (1995).
3) Breismeister J. F., editor: "MCNP- A General Monte Carlo Code for Neutron and Photon Transport: Version 3A," report no. LA-7396-M, Rev. 2 (Sept. 1988).
4) Shibata K., et al.: "Japanese Evaluated Nuclear Data Library, Version-3," JAERI 1319 (1990).
5) Ganesan S. and Wienke H., "FENDL/MC-1.0 Library of Continuous Energy Cross Sections in ACE Format for Neutron-Photon Transport Calculations with the Monte Carlo N-Particle Transport Code System MCNP 4A," IAEA-NDS-169 (1995).

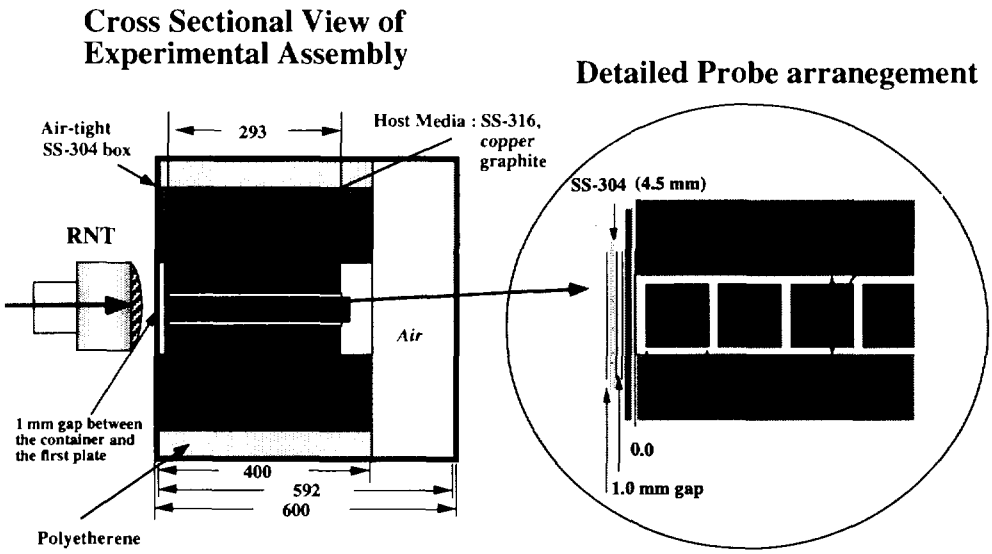

Fig. 5.7.1 Cross sectional view of the calorimetric experimental system for nuclear heating measurement

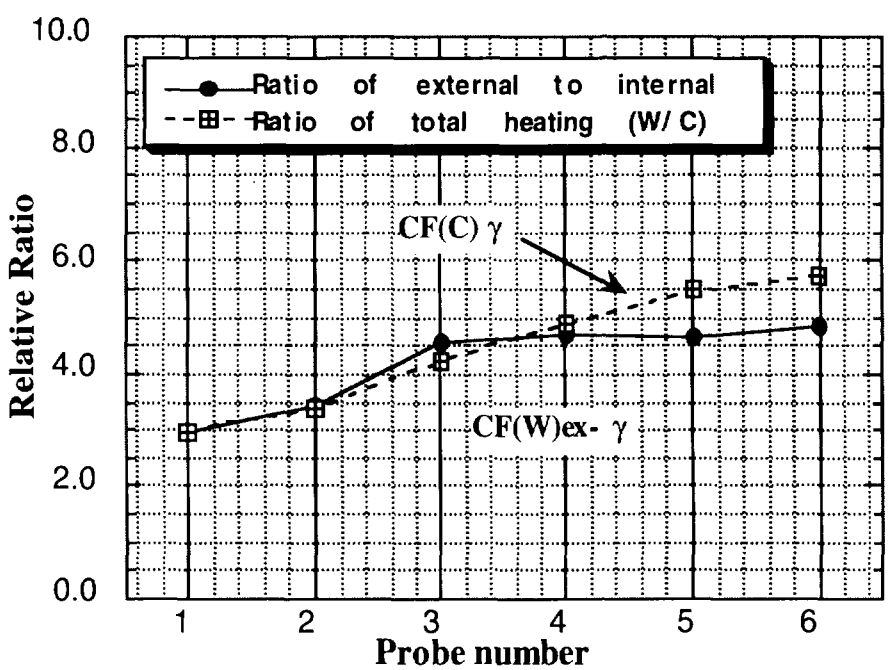

Fig. 5.7.2 Relation between ratios of total heating rate of graphite probe and tungsten probe, and external to internal γ-ray fractions in tungsten probe

5.8 Decay Heat Measurement on Fusion Reactor Materials

F. Maekawa, Y. Ikeda, M. Wada and E. T. Cheng*
(*E-mail:* fujio@fnshp.tokai.jaeri.go.jp)

As an R&D task of decay heat measurement (T-339) for safety and environment under ITER/EDA, the Whole Energy Absorption Spectrometer (WEAS) [1] has been developed to obtain experimental decay heat data on fusion reactor materials irradiated by D-T neutrons. In this fiscal year, decay heat data on 32 fusion related materials were measured with WEAS. Preliminary validation of decay heat calculation codes and data bases used for safety analysis of fusion reactors was also performed.

Sample materials used in the measurements are listed in Table 5.8.1. About a half of them are metallic thin foils with an area of 25 x 25 mm^2 while the rest are powder sandwiched by two thin plastic tapes of 24 x 24 mm^2. The powder samples are used because of their availability due to chemical and physical stability. Carbon and oxygen atoms contained in parts of the powder samples do not cause significant decay heat except for ^{16}N nuclei with very short half-life of 7.13 s produced by the $^{16}O(n,p)$ reactions. The metallic foil samples were sandwiched by the same ones to compensate escape of recoil-atoms from the samples. The plastic tapes for the powder samples functioned as a recoil-atom stopper. An aluminum foil of 50 μm in thickness with the same size as the sample was attached to the sample for determination of D-T neutron fluence with utilizing the $^{27}Al(n,\alpha)^{24}Na$ reaction rate.

The samples were irradiated with D-T neutrons at the Fusion Neutronics Source (FNS) facility in JAERI. Pulse height spectra were measured with WEAS at various

Table 5.8.1 Sample materials used for the decay heat measurement

Metallic Foil Sample		Powder Sample	
Al	Mo	B_4C	Y_2O_3
Ti	Ta	Na_2CO_3	SnO
V	W	SiO_2	$BaCO_3$
Fe	Pb	S	Re
Co	SS304	K_2CO_3	Bi
Ni	SS316	CaO	
Cu	Inconel-600	Cr	
Zr	NiChrom	Mn	
Nb	CF_2	$SrCO_3$	

* TSI Research, Inc., 225 Stevens Ave., Solana Beach, CA 92075, USA

cooling time. To obtain decay heat data for a wide range of half-lives, three combinations of irradiation and cooling time were adopted: 5 min irradiation for 1 ~ 60 min cooling time, 1 hour irradiation for 1 ~ 12 hour cooling time and 7 hours irradiation for > 0.5 days cooling time. Accordingly, decay heat data for a wide cooling time from 1 min to 200 days were measured. The high sensitivity feature of WEAS enabled to measure decay heat for such a long cooling time. For example, the ^{60}Co ($T_{1/2}$ = 5.27 years) activity produced by the $^{63}Cu(n,\alpha)$ reaction in a 31 mg copper sample irradiated for 7 hours was ~ 18 Bq after 200 days cooling. This decay heat corresponded to 8 pW, and was clearly measured by WEAS in 10 minutes.

The decay heat calculation was performed with two calculation codes, REAC*3[2] and ACT4 in the THIDA code system[3]. The activation cross section library FENDL/A-2.0[4] was commonly used for both calculations. In addition, the USACT93[5] and JENDL Activation File[6] were used for REAC*3 and ACT4, respectively. Decay data libraries developed individually for the REAC*3 and ACT4 codes were used. The source neutron spectrum at the sample position used in the calculations was calculated with the Monte Carlo transport calculation code MCNP-4A[7] with simulating the kinematics of a D-T reaction, the structure of neutron target and the pneumatic tube used in the experiment. Therefore, the peak energy of D-T neutrons and low-energy neutrons scattered by surrounding materials were taken into account precisely in the source spectrum.

As an example of the measured and calculated decay heat, decay curves for a copper sample irradiated for 1 hour are shown in Fig. 5.8.1. The curves consist of fast and slow decay components corresponding to ^{62}Cu ($T_{1/2}$ = 9.73 min) from the $^{63}Cu(n,2n)$

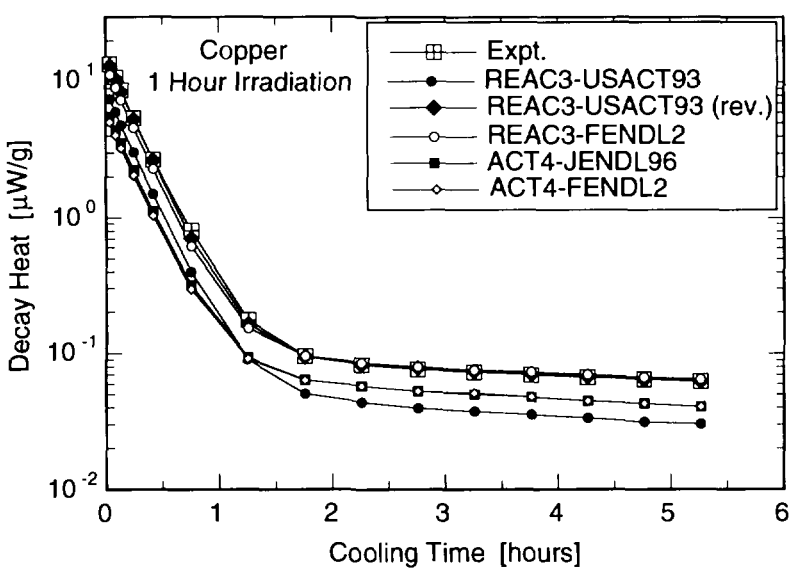

Fig. 5.8.1 Measured and calculated decay heat for a copper sample

reaction and ^{64}Cu ($T_{1/2}$ = 12.7 hr) from the $^{65}Cu(n,2n)$ reaction, respectively.

The REAC calculation with FENDL shows good agreement with the experiment. The REAC calculation with USACT93, however, gives smaller decay heat values as a whole by 50 % compared with the experiment. The reason was found that decay energies due to annihilation gamma-rays for the positron emitting isotopes, ^{62}Cu and ^{64}Cu, were disregarded in the decay data library used, although cross section data in USACT93 were reasonable. Thus, the decay data library was revised to include the annihilation gamma-ray energies, and decay heat was calculated again. The result was, as shown by black diamonds in Fig. 5.8.1, improved to give a good agreement with the measured data. Note that the revised decay data library was used for the REAC calculation with FENDL2.

The ACT4 calculations with both FENDL and JENDL also predict the decay heat values considerably lower than the measured ones. The calculated values for ^{62}Cu and ^{64}Cu are ~ 40 % and ~ 67 % of the measured ones, respectively. It was found that decay energies of ^{62}Cu and ^{64}Cu were not treated correctly in the ACT4 code. After the correction of the decay energies, ACT4 predicted the decay heat of copper adequately.

References

1) Maekawa F., Ikeda Y. and Cheng E. T.: "Decay Heat Measurement on Aluminum, Copper and Type 304 Stainless Steel Irradiated by D-T Neutrons", to be published in Fusion Eng. Des. (1997).
2) Mann F. M.: "REAC*2: Users Manual and Code Description", WHC-EP-0282, Westinghous Hanford Company (1989).
3) Seki Y., et al.: "THIDA-2: An Advanced Code System fro Calculation of Transmutation, Activation, Decay Heat and Dose Rate", RSICC computer code collection, CCC-410, Oak Ridge National Laboratory (1987).
4) Pashchenko A. B.: "Summary Report for IAEA Consultants' Meeting on Selection of Evaluations for the FENDL/A-2 Activation Cross Section Library", INDC(NDS)-341, International Atomic Energy Agency (1996).
5) Mann F. M.: "REAC*3 Nuclear Data Libraries", Proc. Int. Conf. Nucl. Data Sci. Technol., Jülich, Germany, May 12-17, 1991 (1992) pp. 936-938.
6) Nakajima Y.: "Status of the JENDL Activation File", JAERI-Conf 96-008, 50 (1996).
7) Briesmeister J. F. (Ed.): "MCNP - A General Monte Carlo N-Particle Transport Code, Version 4A", LA-12625-M, Los Alamos National Laboratory (1993).

5.9 Benchmark Experiment on Vanadium with D-T Neutrons

F. Maekawa, Y. Kasugai, C. Konno, I. Murata*, Kokooo*, M. Wada,
Y. Oyama, Y. Ikeda and A. Takahashi*
(*E-mail:* fujio@fnshp.tokai.jaeri.go.jp)

Vanadium-alloy is one of advanced structural materials for fusion reactors which can be accepted by the public because of its low-activation property. As vanadium is the major constituent of the vanadium-alloy, benchmark experiments on vanadium are strongly required to validate evaluated nuclear data libraries used for designs of the fusion reactors. The leakage neutron spectrum measurement from spherical vanadium shells of 35 and 105 mm in thickness in the energy range above 0.07 MeV done by Möllendorff et al. was the unique existing benchmark experiment. [1] For validation of low energy neutron cross sections and secondary gamma-ray data for vanadium, there are, however, no benchmark experimental data. To provide supplementary experimental data on vanadium, a benchmark experiment was conducted at the Fusion Neutronics Source (FNS) facility at JAERI.

A cubic experimental assembly of $(254\ mm)^3$ made of pure vanadium was placed at a 200 mm distance from the D-T neutron source. Four side surfaces and a rear surface of the assembly were covered with a graphite reflector of 51 mm in thickness to reduce leakage neutrons out of the assembly and incoming background neutrons from the outside. Two experimental channels to insert detectors into the assembly were located at 76 and 178 mm depths measured from the front surface. The following nuclear parameters were measured at the front surface of the assembly and in the two experimental channels; (i) neutron spectrum (> 1.5 MeV) by a 14 mm ϕ NE213 liquid organic scintillation spectrometer, (ii) neutron spectrum (20 keV ~ 1 MeV) by proton recoil gas proportional counters, (iii) neutron spectrum (1 eV - 300 eV) by the slowing down time method, (iv) dosimetry reaction rates of the $^{27}Al(n,\alpha)^{24}Na$, $^{93}Nb(n,2n)^{92m}Nb$, $^{115}In(n,n')^{115m}In$ and $^{197}Au(n,\gamma)^{198}Au$ reactions by the foil activation method, (v) gamma-ray spectrum by a 40 mm ϕ BC537 liquid organic scintillation spectrometer and (vi) gamma-ray heating rate by TLD.

Transport calculations were performed by the continuous energy Monte Carlo code MCNP-4A[2] with evaluated nuclear data files, i.e., JENDL Fusion File (JENDL-FF)[3], FENDL/E-1.0 (FENDL-1)[4] and European Fusion File version-3 (EFF-3). The cross section data of vanadium in JENDL Fusion File are to be selected for FENDL/E-2.0.

---

* Department of Nuclear Engineering, Osaka University

Those in FENDL/E-1.0 are taken from ENDF/B-VI.

In the energy region above 20 keV, in general, calculated neutron spectra with the three cross section files agree well with the measured spectrum as shown in Fig. 5.9.1. The three threshold reaction rates of Al, Nb and In are predicted within 10 % by the three files. Integral neutron fluxes in the energy ranges of 20 - 100 keV and 0.1 - 1 MeV by the three calculations agree within ~ 20 % with the experimental data.

In the energy range below 300 eV, as shown in Fig. 5.9.1, the calculated spectra with EFF-3 and FENDL-1 follow the measured spectrum, while the calculated spectrum flux with JENDL-FF is about a half of the measured data. This trend is also found in the gold reaction rate which is sensitive to low energy neutrons. A reason of the large underestimation by JENDL-FF is attributable to low elastic scattering cross section at ~ 1 keV, as shown in Fig. 5.9.2. The smaller elastic scattering cross section reduces slowing down of neutrons at ~ 1 keV, and also, enhances leakage of neutrons outside the experimental assembly due to the longer mean free path. Accordingly, neutron spectrum fluxes below ~ 1 keV are predicted smaller by the smaller elastic scattering cross section. The experimental results support EFF-3 and FENDL-1.

Figure 5.9.3 shows the measured and calculated gamma-ray spectra. The spectrum by JENDL-FF agrees very well with the measured spectrum. EFF-3 gives a larger flux spectrum over the whole energies. The spectrum by FENDL-1 is smaller than the measured one. Especially, the prominent peak at ~ 1.6 MeV by FENDL-1 is not so clear as the experimental spectrum. Figure 5.9.4 shows measured[5] and evaluated gamma-ray production cross sections at En= 14.5 MeV. The present experimental results for secondary gamma-rays are consistent with the results for the differential gamma-ray production cross sections.

References

1) Möllendorff U., et al.: "A 14-MeV Neutron Transmission Experiment on Vanadium", presented at 19th Symposium on Fusion Technology, Lisbon, September 1996.
2) Briesmeister J. F. (Ed.): "MCNP - A General Monte Carlo N-Particle Transport Code, Version 4A", LA-12625-M, Los Alamos National Laboratory (1993).
3) Chiba S., et al.: "Evaluation of the Double-Differential Cross Sections of Medium-Heavy Nuclei for JENDL Fusion File", JAERI-Conf 96-005, 45 (1996).
4) Ganesan S. and McLaughin P. K., IAEA-NDS-128 (1995).
5) Takayama T., et al.: "Gamma-ray Production Cross Sections with 14 MeV Neutrons for 8 Elements fro Z=22 to 29", JAERI-M 91-032, 255 (1991).

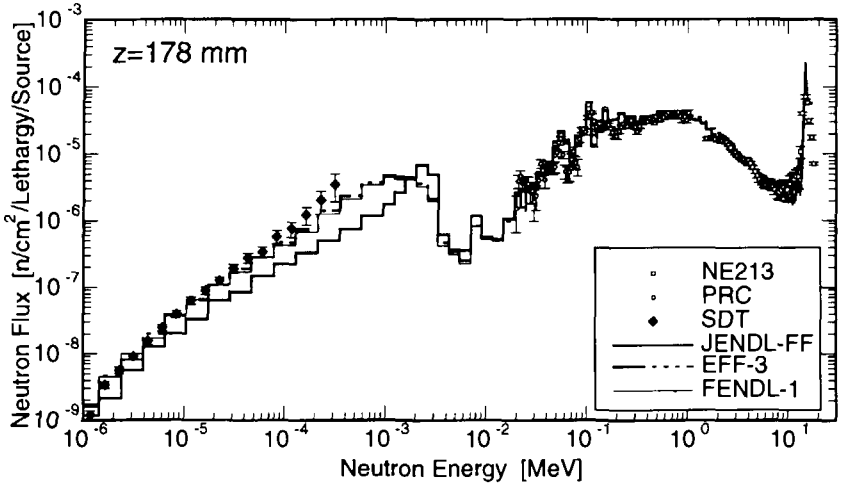

Fig. 5.9.1 Measured and calculated neutron spectra at z=178 mm

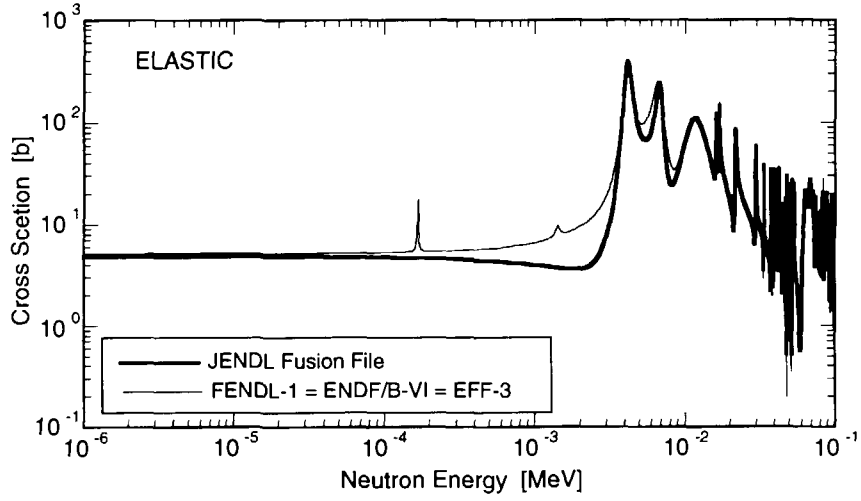

Fig. 5.9.2 Elastic scattering cross sections in the evaluated nuclear data libraries

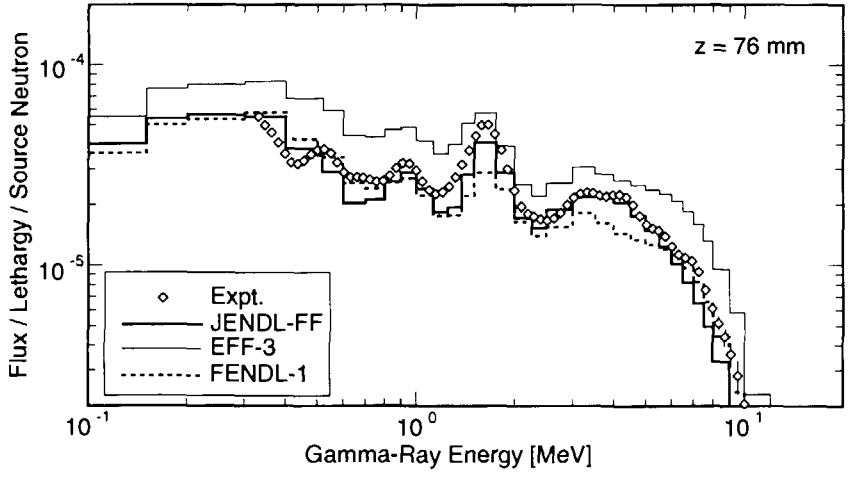

Fig. 5.9.3 Measured and calculated gamma-ray spectra at z=76 mm

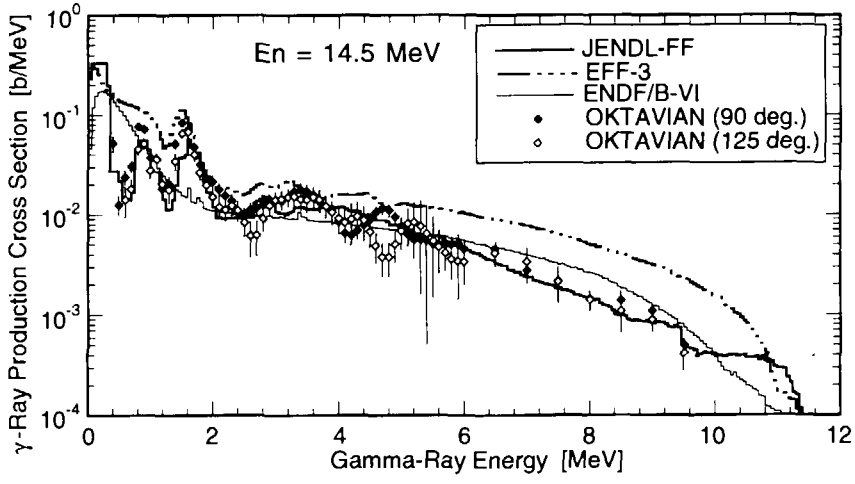

Fig. 5.9.4 Measured [5] and evaluated gamma-ray production cross sections at En = 14.5 MeV

5.10 Further Investigation on Multigroup Library of Copper

C. Konno, F. Maekawa and M. Wada
(*E-mail:* konno@fnshp.tokai.jaeri.go.jp)

An analysis by DOT3.5[1] with JENDL-3.2[2] was newly performed for the benchmark experiment[3),4)] on a copper slab assembly (630 mm in effective diameter and 608 mm in thickness) bombarded by D-T neutrons. Some remarks on the multigroup library were deduced from the comparison of the DOT calculations with the calculation by the continuous energy Monte Carlo code MCNP-4A[5] and the FSXLIB-J3R2[6] library processed from JENDL-3.2.

Two multigroup libraries (neutron 125 groups, γ 40 groups and P_5 Legendre expansion with self-shielding correction) were made from JSSTDL-295n-104γ[7] of JENDL-3.2 and newly processed matxs files from JENDL-3.2 by the NJOY91.128[8] code. The DOT calculations with these two libraries are denoted as DOT(JSSTDL) and DOT(NJOY), respectively. The angular quadrature of S_{16} was adopted.

Insufficient self-shielding correction in JSSTDL system

Figure 5.10.1 shows the measured and calculated neutron spectra at the depth of 228 mm. We focus our attentions on the difference among the calculations. All the calculations agree each other in the neutron energy above 40 keV. On the contrary, the discrepancy among the calculations appears in the neutron energy below 40 keV. Particularly the neutron flux of DOT(JSSTDL) below 7 keV is smaller by one order of magnitude than the measurement and other calculations. We found that the reason of the discrepancy was due to the incomplete self-shielding correction for the scattering matrix, i.e., the f-table (self shielding correction coefficient) for elastic scattering cross section was used for the scattering matrix in the JSSTDL system. On the contrary, the f-table for the scattering matrix in the NJOY system is appropriately prepared. Since this insufficient self-shielding correction method is adopted not only for copper but also for all nuclei in the JSSTDL system, it should be noted that Sn calculations with the JSSTDL library sometimes give incorrect results.

Overcorrection of self-shielding for the resonance around 500 eV in copper

From Fig. 5.10.1 it is also noted that the neutron spectra of MCNP and DOT(NJOY) are different below 500 eV. This is probably due to the overcorrection of the self-shielding of the large sharp resonance around 500 eV in copper. It was confirmed that the DOT calculation with the multigroup library of the finer group structure around 500 eV agreed with the MCNP calculation better. It is considered that the self-shielding correction in the

multigroup library is not so perfect for a large sharp resonance even in the NJOY system.

Self-shielding correction for multigroup dosimetry cross section

The agreement of the DOT calculation with measurement for the reaction rate of $Cu(n,x)^{64}Cu$, which is sum of $^{63}Cu(n,\gamma)^{64}Cu$ and $^{65}Cu(n,2n)^{64}Cu$, was very poor (the ratio of the calculation to the experiment was 2.5 at the depth of 510 mm) compared with the MCNP calculation in the previous paper[3] on this benchmark experiment. The reaction rate of $Cu(n,x)^{64}Cu$ was derived in general by using the multigroup dosimetry cross section of $Cu(n,x)^{64}Cu$ without self-shielding correction in the DOT calculation, while it was obtained by using the continuous energy dosimetry cross section of $Cu(n,x)^{64}Cu$ in the MCNP calculation. We thought that the multigroup dosimetry cross section of $Cu(n,x)^{64}Cu$ without self-shielding correctionwas not adequate. In order to test this idea, we made the 125-group dosimetry cross section of $Cu(n,x)^{64}Cu$ with self-shielding correction by the TRANSX2.5[9] code from the ^{63}Cu and ^{65}Cu data in ENDF/B-VI[10]. The cross section is shown with that without self-shielding correction in Fig. 5.10.2. Figure 5.10.3 shows the ratio of the calculation to the experiment (C/E) for the reaction rate of $Cu(n,x)^{64}Cu$. The DOT calculation id slmodt the same as the MCNP calculation if the self-shielding corrected multigroup dosimetry cross section is adopted. It is concluded that the self-shielding correction for multigroup dosimetry cross section is essential for the precise activation calculations including (n,γ) reactions for principal material with DOT

References

1) Rhodes W.A. and Mynatt F.R. : ORNL-TM-4280 (1973).
2) Nakagawa T. et al. : J. Nucl. Sci. Technol., 32, pp. 1259 - 1271 (1995).
3) Konno C., et al. : Fusion Engineering and Design, 28, pp. 745 - 752 (1995).
4) Maekawa F. and Oyama Y. : JAERI-Conf 96-008, pp. 187 - 192 (1996).
5) Briesmeister J.F. (edited): LA-12625-M, Los Alamos National Laboratory, (1993).
6) Kosako K., et al. : JAERI-Data/Code 94-20 (1994).
7) Nakagawa T. : private communication (1995).
8) MacFarlane R.E. and Muir D.W.: LA-12740-M (1994).
9) MacFarlane R.E. : LA-12312-MS (1992).
10) Rose P.F. (edited) : BNL-NCS-17541 (1991).

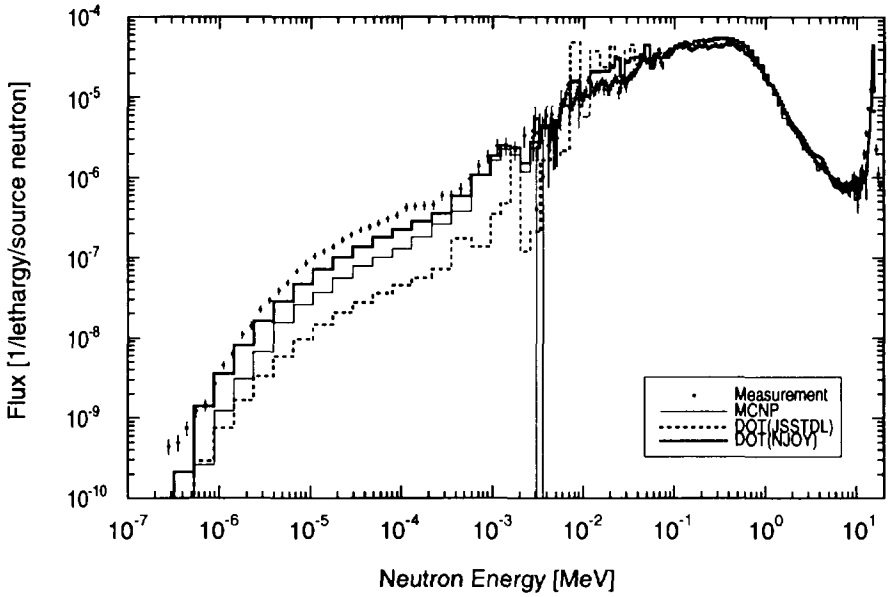

Fig. 5.10.1 Measured and calculated neutron spectra at the depth of 228 mm

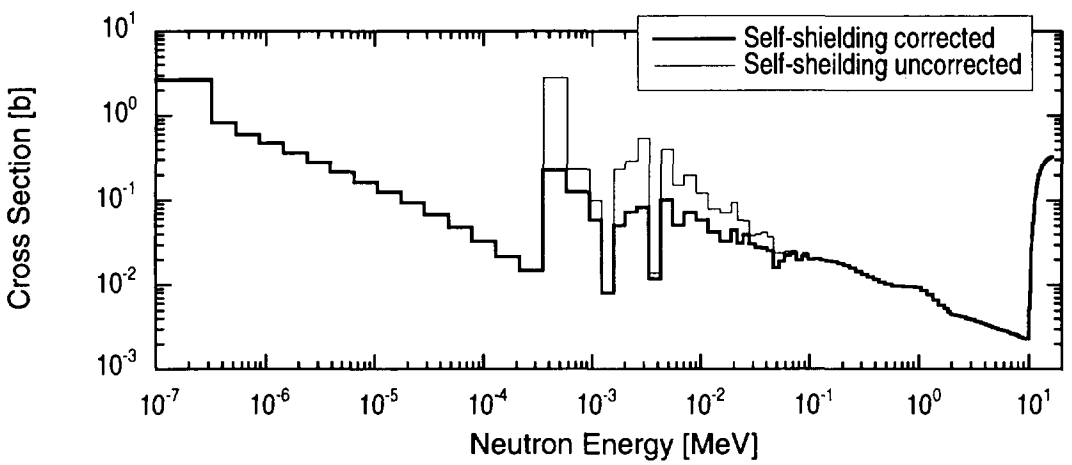

Fig. 5.10.2 Multigroup dosimetry Cross sections of $Cu(n,x)^{64}Cu$ with and without self-shielding correction

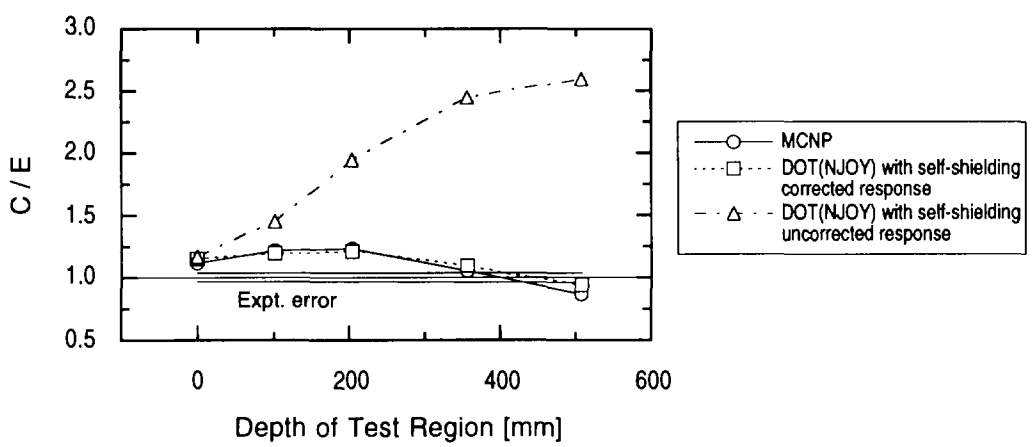

Fig. 5.10.3 C/E of the reaction rate of $Cu(n,x)^{64}Cu$

5.11 Activation Experiment on Fusion Reactor Materials Bombarded by d-Be Neutron Source

F. Maekawa, Y. Ikeda, U. Möllendorff* and P. Wilson*
(*E-mail:* fujio@fnshp.tokai.jaeri.go.jp)

In February 1996, an integral activation experiment was conducted at Forschungszentrum Karlsruhe (FZK), Karlsruhe, Germany, with utilizing a d-Be neutron source available at the Karlsruhe Isochronous Cyclotron (KIZ). This endeavor corresponded to the item #3, "Integral Experiments for Development of Low Activation Materials," of the sub-task "Fusion Neutronics" under the IEA Collaboration. The d-Be neutron source provides a white energy spectrum, unlike those based on D-T neutron sources. The d-Be neutron field is an advantage for integral activation experiments because of a broader neutron energy for validating evaluated activation cross section data up to 20 MeV. On the other hand, the d-Be neutron spectrum was not known so well as the D-T neutron spectrum. Therefore, the first stage of the experiment was devoted to a determination of the neutron spectrum at the sample position by the multi-foil activation technique. And then, two structural materials for fusion reactors were irradiated.

Activation foil samples of 5 x 5 mm^2 for the dosimetry purpose were stacked in sample packets. Typical dosimetry reactions used for D-T neutron field characterization were employed. Four (n,3n) reactions of yttrium, silver, thulium and gold, threshold energies of which were higher than 15 MeV, were selected for detecting neutrons of > 15 MeV. A sample packet was attached on a beryllium target of 12.2 mm in thickness. The target was positioned inside the KIZ cyclotron as shown in Fig. 5.11.1, and bombarded by a deuteron beam of 10 ~ 15 μA at 19 MeV. Three irradiations were conducted changing the irradiation time, 10 minutes, 1 hour and 5 hours. Most of produced neutron energies were below 19 MeV suitable for validation of activation cross section libraries up to 20 MeV. Two structural materials of fusion reactors, SS316LN (ITER-grade, 10 mm ϕ x 0.5 mm) and F82H (low-activation ferrite steel, 10 mm ϕ x 1.0 mm), were also irradiated. After the irradiations, radioactivities of the samples were measured with a HP-Ge detector.

A source routine to simulate neutron generation by the d-Li reaction, McDeLi [1], has been developed at FZK for the IFMIF project. McDeLi was modified at FZK for the d-Be reaction, and provided to JAERI. The source neutron spectrum at the d-Be neutron field was calculated with the MCNP-4A Monte Carlo transport code [2] and the modified

---

* Forschungszentrum Karlsruhe, Karlsruhe, Germany

McDeLi routine with simulating precisely the irradiation field. The dosimetry reaction rates were calculated with the cross sections in FENDL/A-1.0[3].

According to the preliminary comparison of the measured and calculated reaction rates, the calculated high threshold (n,3n) reaction rates were much smaller than the experimental data. Moreover, gamma-rays from ^{87g}Y produced by the ^{89}Y(n,3n) reaction, threshold energy of which was 21 MeV, were observed in the measured gamma-ray spectrum. These results suggested that a certain amount of neutrons of which energies were higher than the incident deuteron energy of 19 MeV were produced by the d-Be reaction due to the positive Q-value (+4.4 MeV) of the reaction. Hence, the source routine was modified to generate such high energy neutrons. As a result, the large discrepancies between the calculated and measured high threshold reaction rates were considerably reduced.

Next, the calculated neutron spectrum was adjusted to be consistent with the measured dosimetry reaction rates by the unfolding technique with the SAND-II code[4]. Figure 5.11.2 shows the source neutron spectra before and after the adjustment. Higher energy part of the spectrum is enhanced by the adjustment. The adjusted spectrum is to be utilized for analyses of integral activation experiments using the d-Be neutron field in the KIZ cyclotron.

Measured gamma-ray spectra from the SS316LN and F82H samples normalized by the sample weight and the counting time are shown in Fig. 5.11.3. Although the analysis of the activation experiment has not been completed for longer cooling time, it is clearly exhibited that induced radioactivities in the low-activation F82H steel sample are ~ 1 order smaller than those in the SS316LN sample. This is mainly due to the reduction of nickel content in F82H.

References

1) Wilson P. and Fischer U.: "Analysis and Implementation of a Monte Carlo High Energy Neutron Source for IFMIF", presented at 19th Symposium on Fusion Technology, Lisbon, Portugal, September 1996, to be published in Fusion Eng. Des. (1997).
2) Briesmeister J. F. (Ed.): "MCNP - A General Monte Carlo N-Particle Transport Code, Version 4A", LA-12625-M, Los Alamos National Laboratory (1993).
3) Pashchenko A. B.: "Status of FENDL Activation File and Plans for the Future Developments", to be published in Fusion Eng. Des. (1997).
4) McElroy W. N., et al.: Nucl. Sci. Eng., 27, 533 (1967).

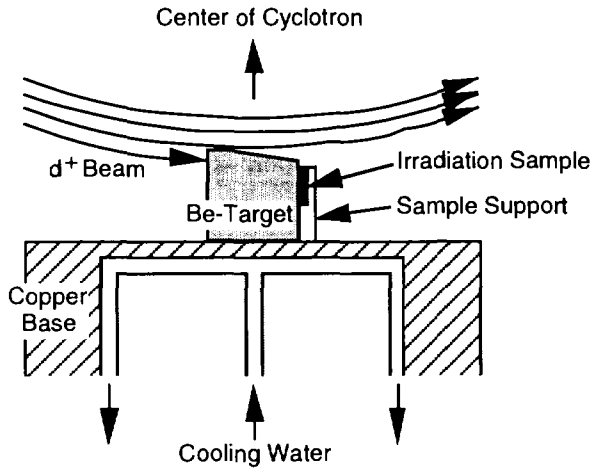

Fig. 5.11.1 Sketch of the beryllium target and the irradiation samples introduced in the KIZ cyclotron

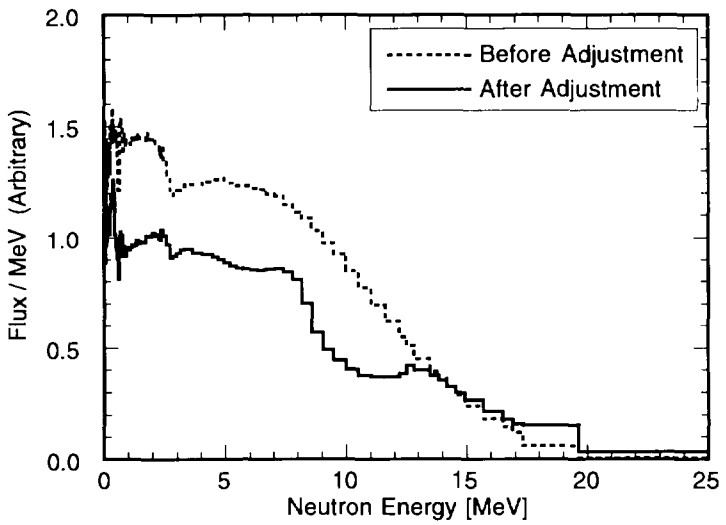

Fig. 5.11.2 Neutron spectra at the sample position produced by the d-Be reaction before and after the adjustment procedure

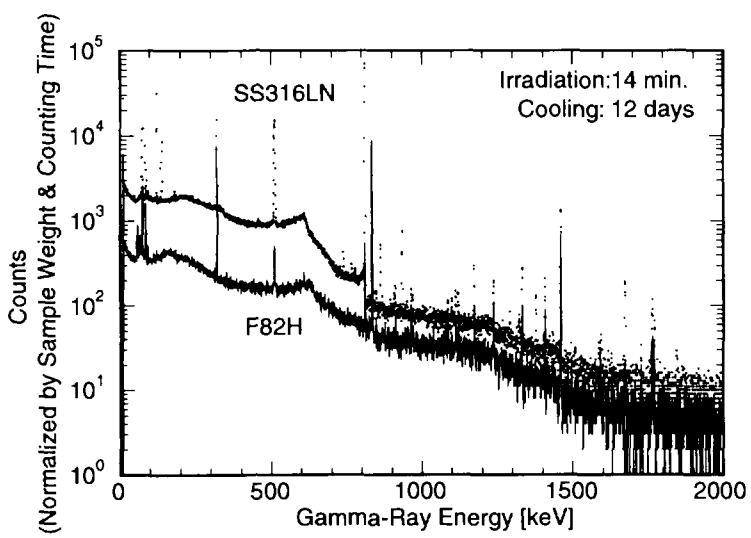

Fig. 5.11.3 Measured gamma-ray spectra from the SS316LN and F82H samples normalized by the sample weight and the counting time

5.12 Use of Gamma Rays from the Decay of 13.8-sec ^{11}Be to Calibrate a Ge Detector for Measurements up to 8 MeV

Y. Ikeda, D. L. Smith[a)], F. Maekawa, Y. Kasugai, K. Kawade[b)] and Y. Uno
(*E-mail:* ikeda@fnshp.tokai.jaeri.go.jp)

Calibration procedures for Ge detectors are described in an ANSI standard[1)] and various other literatures[2,3)]. Efficiencies are then deduced from the recorded full-energy-peak yields of standard radioactive sources. For convenience these data can be fitted with smooth empirical or semi-empirical fomulas[4)]. However, using this approach it is difficult to obtain a calibration > 3 MeV due to the scarcity of gamma-ray sources covering this energy range. Higher-energy gamma-ray can be generated by (n,γ) or (p,γ) reactions[5,6)] using an accelerator, reactor neutron or proton radiation source. ^{11}Be is an attractive auxiliary calibration source if a neutron generator and rapid sample transport apparatus are available. It can be produced by the ^{11}B(n,p)^{11}Be reaction. The reaction Q value is -10.724 MeV and the cross section is 5.5 mb at 14 MeV[7)]. ^{11}Be decays by β- emission (100 %) with 13.8 sec half-life, and the decay gamma branching is adequately known (see Table 5.12.1). Although some of these gamma-rays are relatively weak, it is still possible to obtain adequate yield in the full-energy-peak lines of a recorded spectrum by resorting to cyclic activation, i.e., by repeatedly alternating irradiation and γ-ray counting of a sample containing a boron compound.

Table 5.12.1 Gamma-rays from β- decay of 13.8 sec ^{11}Be[8)]

Eγ(keV)	Iγ(%)	Eγ(keV)	Iγ(%)	Eγ(keV)	Iγ(%)
478	0.39	2895	0.081	5852	2.13
692	0.0344	4444	0.054	6790	4.48
1771	0.263	4666	1.82	7975	1.90
2124	35.5	5019	0.467		

Eγ: Gamma-ray energy in keV

Iγ: Gamma-ray branching ratio in %, taken from Ref-8).

A several-gram boron carbide (B_4C) sample was placed in a plastic capsule and carried by a pneumatic transport device to a position near the target of the FNS D-T 14 MeV neutron generator for irradiation[9)]. After ~30 sec the sample was retrieved to a remote, shielded location

a) Argonne National Laboratory
b) Faculty of Engineering, Nagoya University

and counted with a Ge detector for ~30 sec. This procedure was repeated many times until adequate statistics precision was achieved. The measured gamma-ray spectrum is shown in Fig. 5.12.1. Almost all gamma-ray peaks corresponding to the ^{11}Be decay were observed. A Ge detector calibration < 2 MeV was carried out first using several conventional radioactive sources. Full-energy-peak counts for the ^{11}Be gamma-rays were then divided by the relative intensities given in Table 5.12.1 and sum-coincidence corrections were applied. This yielded relative efficiencies from 0.5 - 8 MeV thus extending the original calibration curve to higher energies.

A Ge detector efficiency curve generated by this approach is shown in Fig. 5.12.2. This result demonstrates that ^{11}Be is a worthy calibration source when it can be produced and used easily.

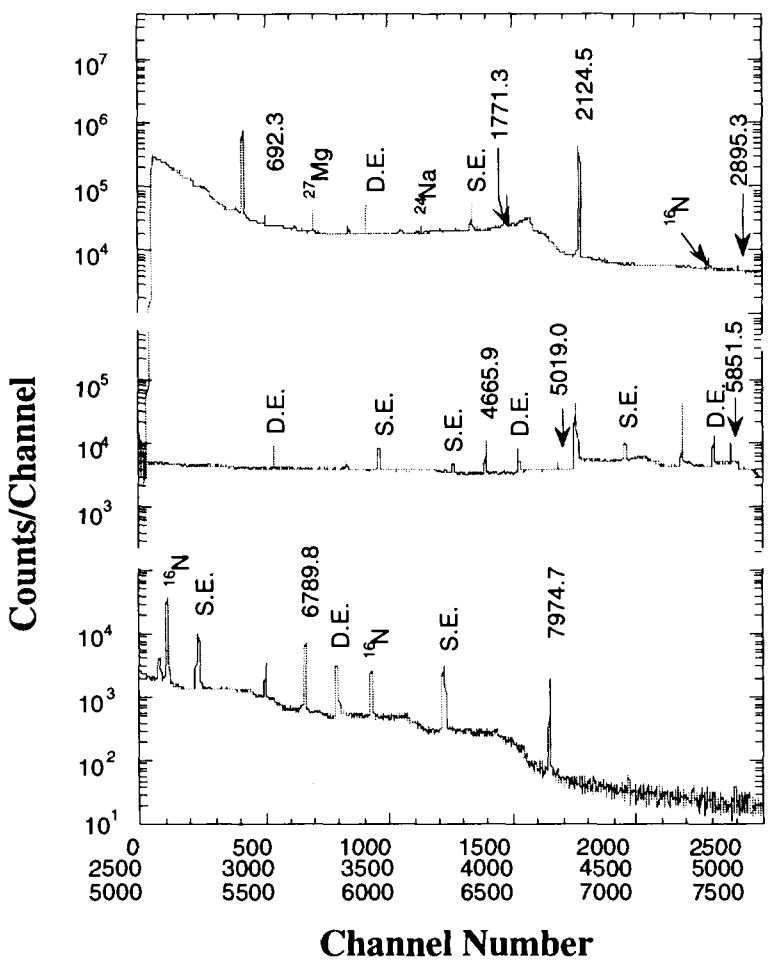

Fig. 5.12.1 The gamma-ray energy spectrum measure with the Ge detector

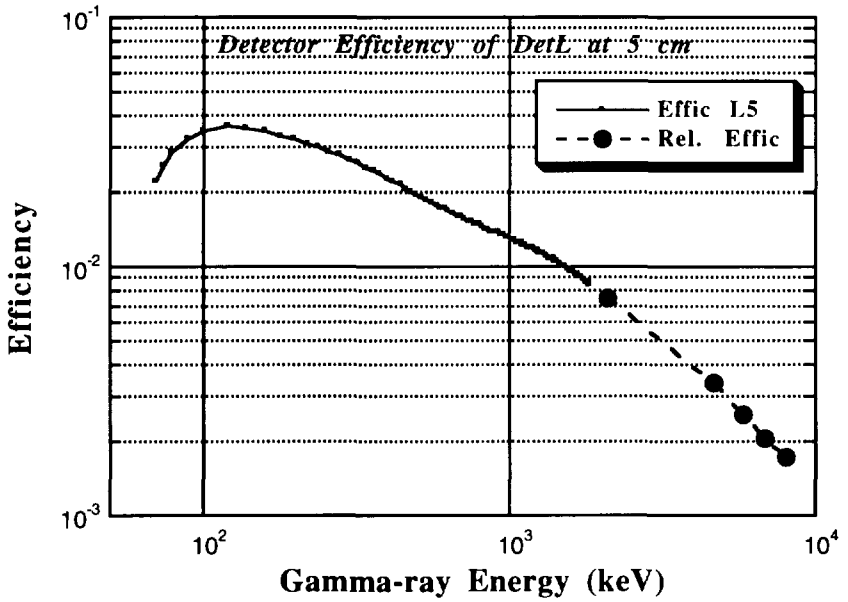

Fig. 5.12.2 The gamma-ray detector efficiency curve up to 8 MeV used for the measurement

References

1) ANSI Standard N42. 14-1978 (Reaffirmed 1985), American National Standards Institute, Institute of Electrical and Electronics Engineering, 345 E, 47th St., New York, NY, USA.
2) Singh B. P. and Evans H. C.: Nuclear Instruments and Methods 97, 475 (1971).
3) McNelles, L. A. and Campbell, J. L.: Nuclear Instruments and Methods 109, 241 (1973).
4) Gray P. W. and Ahmad A.: Nucl. Instr. and Meth. in Phys. Research A237, 577 (1985).
5) Stelts M. L. and Chrien R. E.: Nuclear Instruments and Methods, 155, 253 (1978).
6) Smith D. L., Meadows J. W. and Whalen J. F.: Nucl. Sci. and Engineering, 77, 256 (1981).
7) Evaluated Nuclear Data File, ENDF/B-VI, Brookhaven National Laboratory (1991).
8) Brown E. and Firestone R. B.: Table of Radioactive Isotopes, J. Wiley, New York (1985).
9) Nakamura T., et al.: Proc. 4th Symp. on Accel. Sci. and Technol., Riken, Japan (1982).

5.13 Measurement of Sputtering Yields by 14.9 MeV Neutrons

B.J. Ye*, Y. Kasugai and Y. Ikeda
(*E-mail:* bjye@fnshp.tokai.jaeri.go.jp)

With the application of intense neutron fluxes in science, technology and power generation, the effects of high energy neutron bombardment become important, not only in the bulk material, but also at the surface. One of these surface effects is neutron sputtering, i.e., the removal of atoms (or clusters and microsize particles) from the bombarded surfaces. Unfortunately, neutron sputtering yields are still poorly investigated, mainly because the neutron fluences available are a factor of 10-100 lower. Experimental data for the neutron sputtering yield are very scarce and contradictory. Different measurements on Nb, for example, had resulted in widely scattered sputtering yields[1-3] and had large difference with the results predicted by theory[4]. Usually, the experimental data were much higher than theoretical predictions[5]. The highest reported sputtering ratios have been associated with the observation of micron sized "chunks" of target material. If the higher sputtering ratios were correct, neutron sputtering would be a critical issue for fusion reactors.

An experimental study on the systematics of sputtering yields by 14.9 MeV neutrons has been carried out at the FNS facility. Sputtering yields (S_n) have been measured by subjecting a target material with collectors on each side to a given neutron fluence. The present measurement was performed in the air, which was the same as the method used by Y. Ikeda in 1992[6]. This method needed to measure the change of the activity at the collector with the distance between the target and the collector foils. In present measurement, the distances of 0.2, 0.5, 1.0, 2.0, 3.0 and 5.0 mm from the target to the collector were used to deduce the function of S_n varing with the distance. The thickness of the sample foils was from 0.02 mm to 0.25 mm. The size of sample was 25×25 mm^2. The plastic film of 0.013 mm in thickness and 20 mm in diameter was used as the collector foil. The samples were irradiated by D-T 14.9 MeV neutrons. The activities of all the samples and collectors were measured by using four Ge detectors. Because the activity of the collector was very weak, especially for high Z target, the activities of the collectors for some samples were only measured in two or three distances. From data obtained for different distances we deduced the S_n value at 0 mm distance. Figure 5.13.1 shows a typical example for deducing the S_n from data for aluminium. The sputtering yields for sixteen kinds of materials (aluminium, magnesium, scandium, titanium,

*A visiting scientist from the University of Science and Technology of China by STA exchange scientists program.

vanadium, iron, cobalt, nickel, zirconium, niobium, palladium, silver, cadmium, indium, rhenium and gold) have been measured in this method.

In order to deduce the systematics of the sputtering yields, S_ns were reduced by corresponding cross section values. We denoted the reduced sputtering yield as RS_n. We have

$$RS_n = \frac{S_n}{\sigma(barn)} . \quad (1)$$

All data have been classified according to the type of (n, 2n), (n, α) and (n, p) reactions and are plotted in Fig. 5.13.2 with respect to the atomic number (Z) of target materials. It was found that RS_ns present a strong correlation with Z. RS_ns decrease with increase of Z. A power function

$$RS_n = aZ^b , \quad (2)$$

can describe this process very well, where a and b are fitting parameters. The data of eleven, six and seven reactions for (n, 2n), (n, α) and (n, p), respectively, have been measured to fit the parameters. The ratios of the experimental RS_n to the systematic one are plotted in Fig. 5.13.3. It shows for most of reactions the deviation of RS_n between experimental values and systematic results is within the range of 20 %. Only for the $^{59}Co(n,\alpha)^{56}Mn$ reaction the experimental RS_n is 40 % larger than the systematic one.

In the present work, the neutron sputtering yields for eighteen reactions were given in the first time. We have also measured the backward sputtering yields which are a factor of 5 to 180 lower than the forward sputtering yields depending on materials and reactions.

References

1) Behrisch R., et. al.: J. Nucl. Mater., 53, 183(1974).
2) Jenkins L., et. al.: J. Nucl. Mater., 63, 438(1976).
3) Kaminsky M. and Das S.: J. Nucl. Mater., 53, 162(1974).
4) Behrisch R.: Nucl. Fusion, 12, 695(1972).
5) Behrisch R.: Nucl. Instr. Meth., 132, 293(1976).
6) Ikeda Y. and Konno C.: JAERI-M, 93-046, 316(1993).

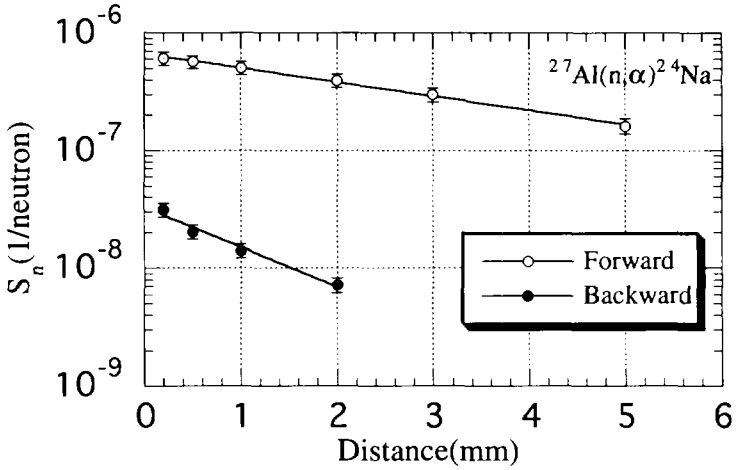

Fig. 5.13.1 Dependency of the sputtering yield on distances between target and collectors for aluminium

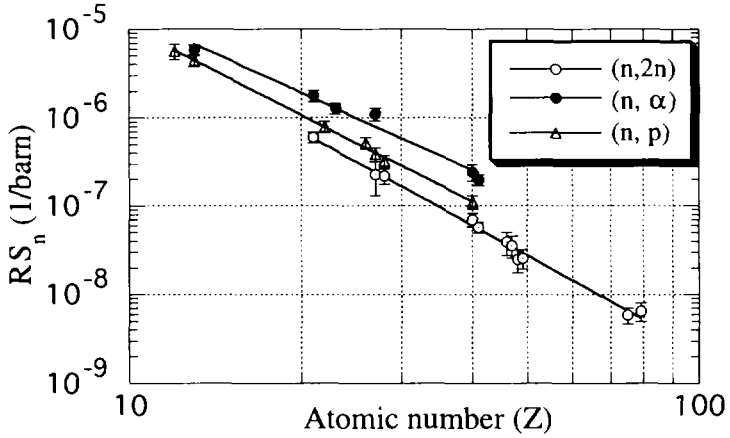

Fig. 5.13.2 The systematic trends of reduced sputtering yields as a function of atomic numbers (Z) of target materials for (n,2n), (n,α) and (n,p) reactions

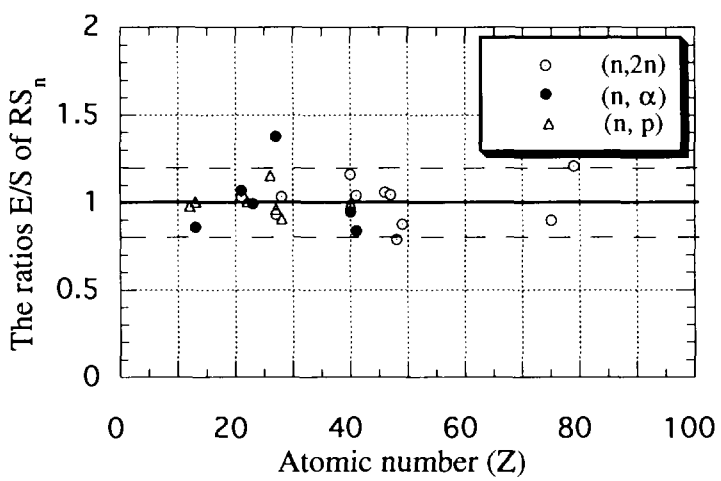

Fig. 5.13.3 The ratios of the experimental RS_n to the systematic one are plotted with respect to Z

6. Radiation Shielding

A series of shielding experiments have been continued for polyethylene slabs by using 40- and 65-MeV quasi-monoenergetic neutron sources equipped at the 90-MeV AVF cyclotron TIARA facility as a Universities-JAERI cooperative project research programme. Measured neutron energy spectra were compared with results of Monte Carlo calculation using MORSE-CG code and DLC multigroup cross section library. The agreement was generally satisfactory, although, calculated spectrum was about twice as high as measured one in the most thick case. Dose equivalents were also evaluated at various thickness.

Benchmark calculations based on the accelerator shielding experiments on concrete and iron slabs using the same quasi-monoenergetic neutron sources were compiled. Comparisons were shown between the calculations with MORSE-CG, MCNP4A and a modified version of HETC-KFA2 codes. Disagreements were mostly within several tens percents except the 100 cm thick concrete(C/E:3) and 70 cm thick iron(C/E:2 to 10) cases by the modified HETC .

The 'proton fluence'-to-'effective dose equivalent' conversion factors for proton energies from 20 MeV to 10 GeV were calculated with the HERMES code system for anterior-posterior and posterior-anterior geometries of an adult hermaphroditic anthropomorphic phantom. The results were compared with the effective dose and the effective absorbed dose. Dose equivalents of testes and ovaries behind 10 and 30 cm thick iron slabs irradiated with protons are evaluated on the way of the above calculation. The contributions of neutrons and secondary protons were investigated.

6.1 Measurements and Calculations of Neutron Energy Spectra behind Polyethylene Shields Bombarded by 40- and 65-MeV Quasi-monoenergetic Neutrons

H. Nakashima, N. Nakao[1], M. Nakao[2], Su. Tanaka, Y. Sakamoto, Y. Nakane, Sh. Tanaka and T. Nakamura[2]
(*E-mail :* nakasima@shield2.tokai.jaeri.go.jp)

A series of shielding experiments has been carried out for concrete and iron by using 40- and 65-MeV quasi-monoenergetic neutron sources constructed at the 90-MeV AVF cyclotron TIARA facility of JAERI as a Universities-JAERI co-operative project research programme. In the present work following the shielding experiments, we measured the energy spectra of neutrons behind polyethylene shields up to 183 cm thickness using the same quasi-monoenergetic neutron sources, because polyethylene shield, of which large content of hydrogen attenuate neutrons of 10-keV- to 1-MeV effectively, is often used by combined with the iron shield.

The cross sectional view of the experimental setup is shown in Fig. 6.1.1. The 118.5-cm x 118.0-cm-wide and 30.5-cm-thick polyethylene slabs were assembled to the thickness from 30.5- to 183.0-cm. Neutron energy spectra above a few MeV were measured with a 12.7-cm-diam. by 12.7-cm-long cylindrical organic liquid scintillator, BC501A, and neutron spectra down to thermal energy with a multi-moderator spectrometer (Bonner ball) which was a 5.08-cm-diam. spherical ^{3}He proportional counter (10 atm) surrounded by four spherical polyethylene moderators of various thickness, 1.5-, 3.0-, 5.0- and 9.0-cm. The neutron energy spectra were obtained from the measured pulse-height distributions using the FERDOU unfolding code and the measured response matrix, and using the SAND-2 unfolding code and the cited response functions, respectively. The initial guess spectra for this unfolding were obtained from the Monte Carlo calculations described later. The Bonner ball detector gives the spectra over the entire energy range from thermal to the source peak energy, and the BC501A detector gives the spectra above a few MeV.

For the analysis of the measurement, Monte Carlo calculations were performed with the MORSE-CG code and the DLC119 multi-group cross section library. The DLC119 has an

---

[1] Tanashi Branch, Radiation Safety office, Radiation Science Center, High Energy Accelerator Research Organization, Midori-cho 3-2-1, Tanashi, Tokyo 188, Japan
[2] Cyclotron and Radioisotope Center, Tohoku University, Aoba, Aramaki, Aoba-ku, Sendai 980, Japan

neutron energy structure of 66 groups between thermal and 400-MeV with a P_5 Legendre expansion.

The measured and calculated neutron energy spectra on the beam axis behind polyethylene shields of various thicknesses are compared in Figs. 6.1.2 and 6.1.3 for 43- and 68-MeV p-Li neutron sources, respectively. These show a general tendency that the MORSE calculation gives results rather in good agreement with the measured results. By looking in detail, the calculated spectra are in good agreement with the BC501A spectra above a few MeV for thinner polyethylene shield but become higher with the shield thickness. Comparison of the fluxes integrated in the peak and continuum energy regions between the calculations and measurements shows that the discrepancy increases with the shield thickness and the value reaches to about a factor of 2.

As for the neutron spectra off the beam axis, the calculations tend to underestimate the measured peak fluxes behind 30.5 cm thick polyethylene shield for 43-MeV, while they slightly overestimate on the beam axis. As already pointed out in the iron experiment, angular distributions of elastic scattering cross section given by the Legendre expansion coefficients in the calculation have some problems.

Dose equivalents were also estimated by folding the measured and calculated neutron energy spectra with the neutron-flux-to-dose-equivalent conversion factor cited from ICRP21 publication. Neutrons above 10 MeV which occupy around 90 % of total flux have dominant contribution to dose equivalents. The ratios of calculated to experimental values are therefore similar to those of peak neutron fluxes, and are between 1.07 and 2.06.

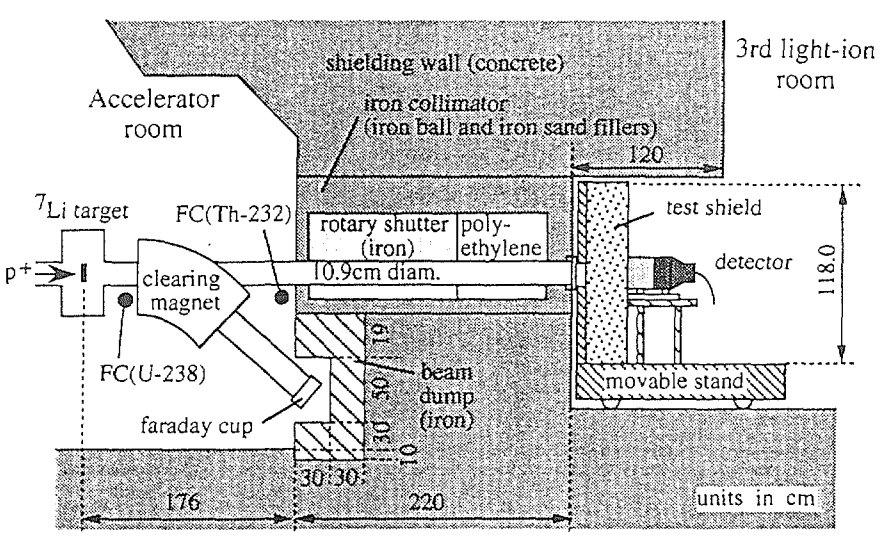

Fig. 6.1.1 Cross sectional view of the experimental arrangement at TIARA facility.

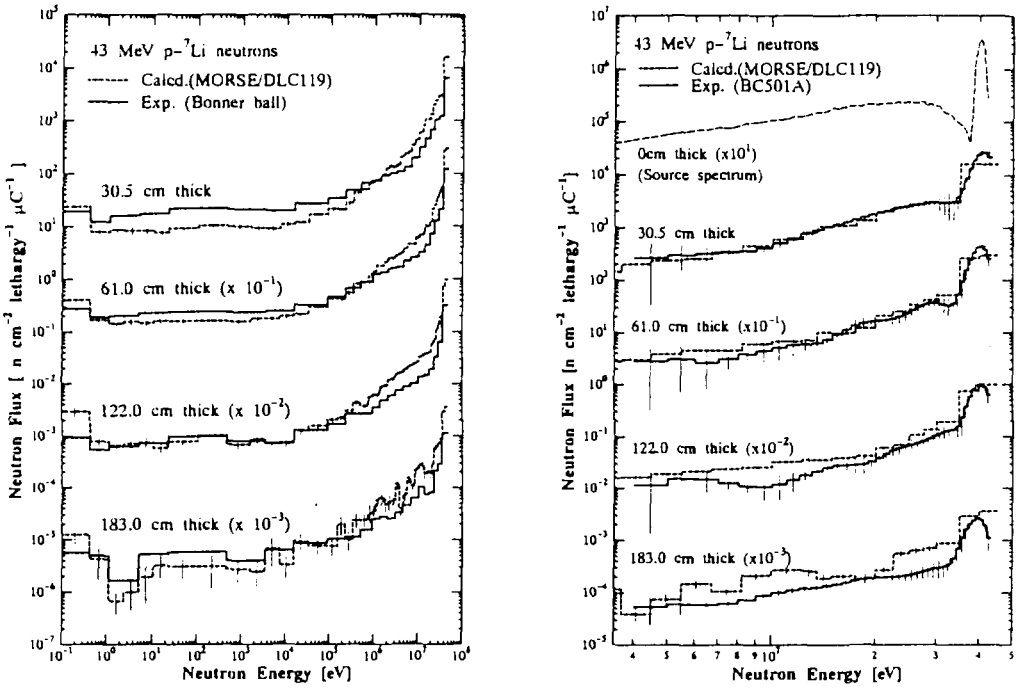

Fig. 6.1.2 Comparison of measured and calculated neutron energy spectra behind shields of various thickness bombarded with 43 MeV p-Li neutrons. (a) The energy spectra measured with Bonner ball detector. (b) The energy spectra measured with BC501A detector.

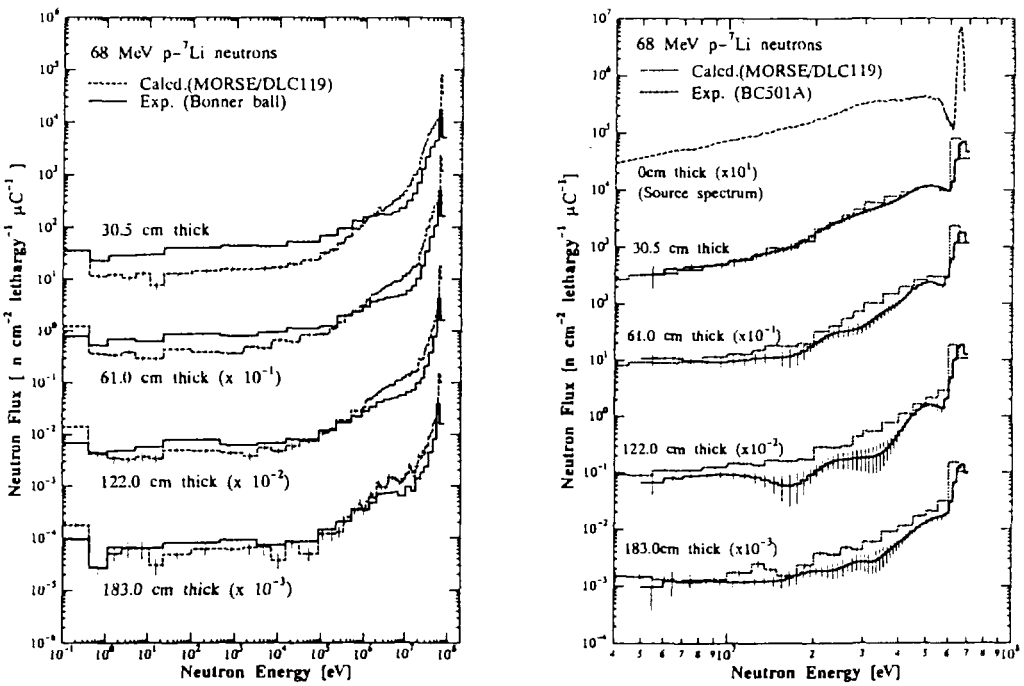

Fig. 6.1.3 Comparison of measured and calculated neutron energy spectra behind shields of various thickness bombarded with 68 MeV p-Li neutrons. (a) The energy spectra measured with Bonner ball detector. (b) The energy spectra measured with BC501A detector.

6.2 Intercomparisons of Benchmark Calculations for the Transmission of 40- and 65-MeV Quasi-monoenergetic Neutrons through Iron and Concrete Shields

Y. Nakane, H. Nakashima, N. Nakao* and K. Ueki**
(*E-mail:* nakane@shield2.tokai.jaeri.go.jp)

To evaluate calculation codes and the nuclear data for neutrons around several tens MeV, intercomparisons of benchmark calculations with MORSE-CG (MORSE), MCNP4A (MCNP) and modified version of HETC-KFA2 (modified HETC) codes were carried out for the transmission of 40- and 65-MeV quasi-monoenergetic neutrons through iron and concrete shields.

Figure 6.2.1 shows the cross sectional view of the facility with the experimental arrangement[1,2]. Quasi-monoenergetic source neutrons of 40 and 65 MeV which were generated in ^{7}Li-targets bombarded with 43- and 68-MeV protons reached the experimental room through an iron collimator embedded in the concrete wall. An iron test shield of 10 to 130 cm thickness was assembled on a movable stand with 10 cm thick iron slabs of 120 cm × 120 cm rectangular surface. A concrete test shield of 25 to 200 cm thickness was also assembled on the movable stand with 120 × 120 × 25 cm slabs. To measure the neutron energy spectra, a 12.7 cm diameter × 12.7 cm long BC501A liquid scintillation detector was placed behind the test shields.

The neutron spectra behind the concrete and iron shields were calculated with the MORSE using the DLC-119/HILO86[3] and HILO86R[4] multigroup cross-section data sets, respectively. The neutron spectra behind the shields were also calculated for the 65-MeV source neutron with the MCNP using the DLC-119/HILO86 multigroup cross-section data set. The calculations in the energy region above 20 MeV with the modified HETC were made[2] using the total and elastic scattering cross sections obtained from the data due to Pearlstein's systematics[5]. In all calculations, measured spectra of source neutrons were used as the source spectra, and source neutrons were assumed to be emitted uniformly in a sharp cone of 5.94 × 10^{-4} steradian considering the geometry of the collimator. In the MORSE calculation, the next event track length estimators having the same size as that of the detector were placed

* High Energy Accelerator Research Organization (KEK), Tanashi, Tokyo
** Ship Research Institute, Mitaka, Tokyo

at the detector positions to estimate the flux in the detector. For the cases of concrete shields thicker than 150 cm and iron shields thicker than 100 cm, the exponential transform method was used to reduce the fractional standard deviation. In the MCNP calculation, the track length estimators were used to consider the detector shape. Both the concrete and iron shields were divided in thin slab cells of 2.5 cm thickness, and the energy dependent weight window bounds were assigned in each cell. In the modified HETC calculation, the track length estimators were used.

Calculated results were compared with the measured ones. For the concrete shield, the neutron fluxes of the peak region for the 40-MeV source neutron calculated with the MORSE agreed with the measured ones within 26% for all the cases of shield thickness, while those of the continuum region were more than twice higher than the measured ones for the 150 cm thickness. For the 65-MeV source neutron, the fluxes of both the peak and continuum regions calculated with the MORSE agreed with those measured within 24% for all shield thickness. The fluxes of both the peak and continuum regions calculated with the MCNP for the 65-MeV source neutron agreed with those measured within 22% for all shield thickness. The flux calculated with the modified HETC for both the 40- and 65-MeV source neutrons agreed with measured ones within 30% for the 25 cm thickness, though the spectra for the 100 cm thickness were more than three times higher than measured ones as shown in Figure 6.2.2.

For the iron shield, the fluxes of both the peak and continuum regions for the 40-MeV source neutron by the MORSE calculation agreed with the measured ones within 33% for all shield thickness except for the 70 cm thickness and the continuum region. The fluxes of both the peak and continuum regions for the 65-MeV source neutron by the MORSE calculation agreed with the measured ones within 50% for all shield thickness except for the 130 cm thickness. The large disagreement for the 130 cm thickness was caused by the poor statistics of the calculations, in spite of using the exponential transform method. The fluxes calculated with the MCNP for the 65-MeV source neutron agreed with those measured within 30% for the 20 and 40 cm thickness, though the calculated flux of the continuum region for 100 cm thickness was about twice higher than the measured ones as shown in Figure 6.2.3. The results of the modified HETC for both the 40- and 65-MeV source neutrons agreed with measured ones within 35% for the 20 cm thickness, although the flux for the 70 cm thickness and the 65-MeV source neutron was about twice higher than the measured one, and that for the 40-MeV source neutron was about ten times higher than the measured one.

References

1) Nakao N. et al.: Nucl. Sci. Eng., 124, 228 (1996).

2) Nakashima H. et al.: Nucl. Sci. Eng., 124, 243 (1996).

3) Alsmiller R. G. et al.: ORNL/TM-9801 (1986).

4) Kotegawa H. et al.: JAERI-M 93-020 (1993).

5) Pearlstein S.: J. Astrophys., 346, 1049 (1989).

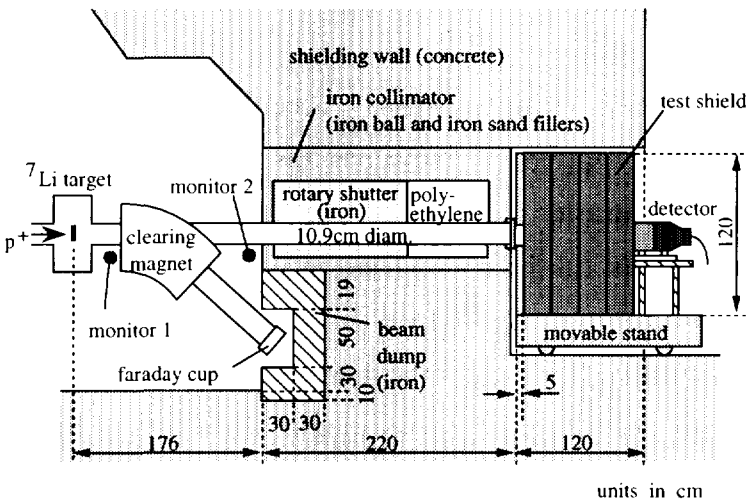

Fig. 6.2.1 Cross sectional view of the facility with the experimental arrangement

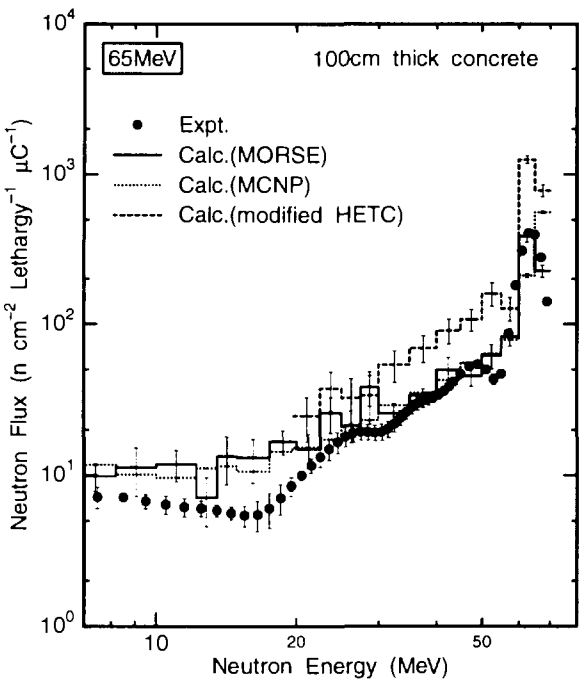

Fig. 6.2.2 Transmitted spectra through 100-cm-thick concrete shield for the 65-MeV source neutron

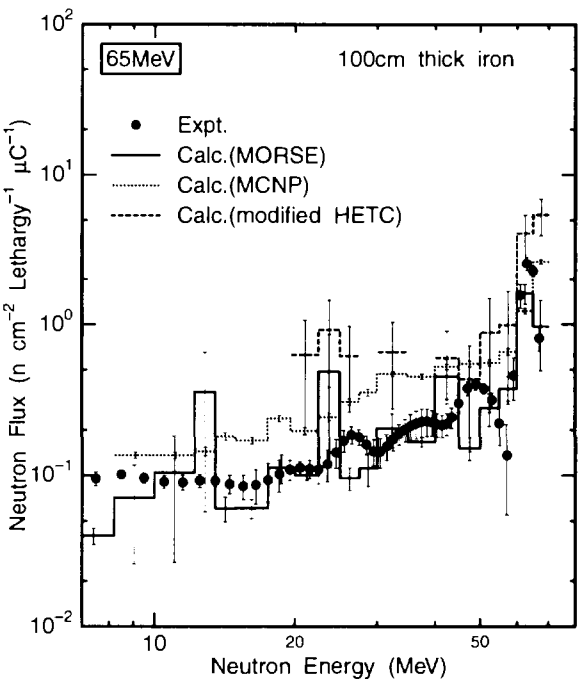

Fig. 6.2.3 Transmitted spectra through 100-cm-thick iron shield for the 65-MeV source neutron

6.3 Evaluation of Fluence to Dose Equivalent Conversion Factors of High Energy Radiations (V) – Effective Dose Equivalent of Protons Higher than 20 MeV and Dose Equivalent of Their Secondary Radiation behind Iron Shield –

Y. Sakamoto, S. Iwai [*1], T. Uehara [*1], O. Sato [*2], N. Yoshizawa [*2], S. Furihata [*2] and S. Takagi [*2]

(E-mail: sakamoto@shield2.tokai.jaeri.go.jp*)*

Along with the increase of high intensity accelerator facilities, the evaluation of effective dose equivalent of high energy radiations has come up to an important problem from the view point of radiation protection. The "proton fluence"-to-"effective dose equivalent" conversion factors has been evaluated in succession to those of neutrons and photons. The effective dose equivalent (H_E) and the effective absorbed dose (D_E) are defined respectively as the weighted sum of the dose equivalent and the absorbed dose (D_T) of twelve specified organs and a remainder consisting of ten organs as follows,

$$H_E = \sum_T W_{T,60} \sum_j Q_j D_{jT}, \quad (1)$$

$$D_E = \sum_T W_{T,60} D_T, \quad (2)$$

$$D_T = \sum_j D_{jT}, \quad (3)$$

where $W_{T,60}$ is the appropriate tissue weighting factor defined in the ICRP60 [1], Q_j is the mean quality factor of the j-th charged particle or recoiled nuclei in water medium and D_{jT} is the average absorbed dose in the T-th organ by the j-th charged particle or recoiled nuclei. On the other hand, the effective dose (E) is defined in the ICRP60 as the weighted sum of the equivalent dose of organs (H_T) as follows,

$$E = \sum_T W_{T,60} H_T = \sum_T W_{T,60} W_R D_T, \quad (4)$$

where H_T is defined as the average organ-absorbed-dose (D_T) multiplied by a radiation weighting factor (W_R).

The "proton fluence"-to-"effective dose equivalent" conversion factors at 14 proton energies from 20 MeV to 10 GeV have been calculated with the HERMES code system [2] for AP (anterior-posterior: uniform parallel beam from the front side of the body to the rear

[*1] Mitsubishi Heavy Industries, Ltd.

[*2] Mitsubishi Research Institute, Inc.

side) and PA (posterior-anterior: uniform parallel beam from the rear side to the front side) geometries using an adult hermaphroditic anthropomorphic phantom [3, 4]. Figure 6.3.1 shows D_E, H_E and E for the unit fluence of protons from 20 MeV to 10 GeV. There is no maximum point of the absorbed dose of proton having the energy above 200 MeV within the phantom because of long proton range. The difference of each doses for the AP and PA geometries is small. The magnitude of E obtained by using the value W_R=5 adopted in the ICRP60 is two and a half times as large as that of H_E. The average quality factor (H_E/D_E) of protons is less than 2 for both AP and PA geometries.

Figure 6.3.2 shows the energy spectra of radiations behind 30 cm thick iron slab irradiated by 0.1, 1 and 10 GeV protons. Above 1 GeV, incident protons can penetrate 30 cm thick iron, and pions and muons are produced. As the intensity of pions is below a half of that of neutrons, the contribution of pions and muons whose dose conversion factors are same order of those of neutrons and protons [5], is smaller than the contribution of neutrons and protons to total dose equivalent. Dominant radiations behind iron slab are neutrons and secondary protons. The dose equivalents of the testes and ovaries behind 10 and 30 cm thick iron slabs irradiated by protons with 3 different energies are shown in Fig.6.3.3. The difference of dose equivalents between tetes and ovaries is small in the case of neutrons, but is very large in the case of protons because the ovaries are located in the center of body and lower energy protons cannot reach them. The increase of iron thickness brings the increase of contribution of dose equivalent by neutrons to total dose equivalent.

References

1) ICRP Publication 60. 1990 Recommendations of the International Commission on Radiological Protection. Annals of the ICRP21 (1-3) (1991).
2) Cloth P. et al.: "HERMES: A Monte Carlo Program for Beam-Materials Interaction Studies", KFA-IRE-E AN12/88 (1988).
3) Yamaguchi Y.: "DEEP Code to Calculate Dose Equivalents in Human Phantom for External Photon Exposure by Monte Carlo", JAERI-M 90-235 (1990).
4) Cristy M. and Eckerman K.F.: "Specific Absorbed Fractions of Energy at Various Ages from Internal Photon Sources", ORNL/TM-8381/V1-V7(1987).
5) ICRP Publication 51. Data for Use in Protection Against External Radiation, Annals of the ICRP, 17, No.2/3 (1987).

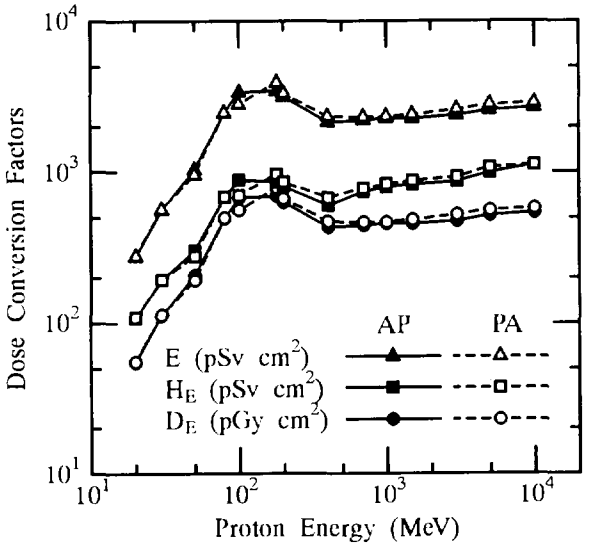

Figure 6.3.1 Comparison of the effective absorbed dose (D_E), the effective dose equivalents (H_E) and the effective dose (E) for parallel beam of high energetic protons.

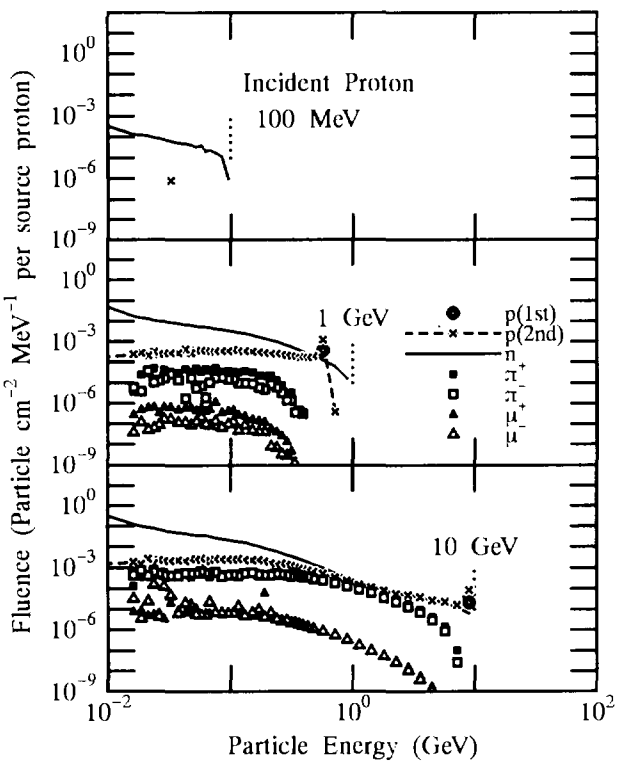

Figure 6.3.2 Radiation spectra behind 30 cm thick iron slab irradiated by proton.

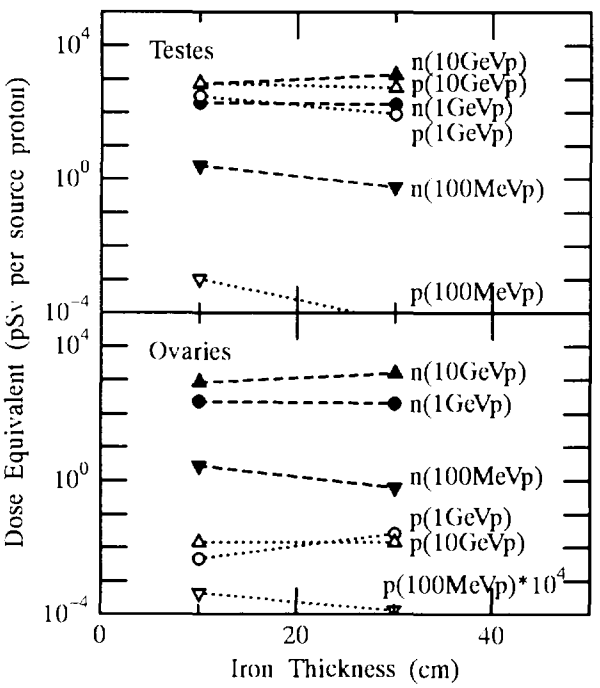

Figure 6.3.3 Dose equivalent of testes and ovaries behind 10 and 30 cm thick iron slabs irradiated by proton.

7. Reactor and Nuclear Instrumentation

In R&D works of reactor and reactor-relevant instrumentation, efforts were made to develop an advanced neutron detector for future reactors and methods for nondestructive detection of defects in aged reactor components. The advanced neutron detector is of a position sensitive fission counter by which fast neutrons are aimed to be detected for the accurate measurement of reactor core power distributions. Thence the adoption of ^{232}Th as a fast-neutron sensitive fissionable material and Ar-N_2 mixed gas as ionization gas was studied. Computer simulation calculation presented pulse height distributions of neutron signals to be produced in the detector. Since nondestructive detection of defects and flaws in reactor components is very important and still advanced techniques are needed in this field, a method of detecting positions of magnetic dipoles was explored and a new device was proposed. The device is a magnetic flux sensor that is surrounded by superconducting and ferromagnetic cylinders. This constitution brings about the directional sensitivity to detect magnetic dipoles of only one direction and thus better spatial resolution in detection of neighboring two dipoles. Also a new eddy-current-testing (ECT) probe was invented, and experiments were carried out to detect flaws and defects in a metal plate by it. Because the probe has exciting coils of parallerogrammic shape, it has no blind spot in detection of both vertical and horizontal flaws. Another topic is R & D of nondestructive measurement to assess α-radioactivity in TRU wastes. During the period under review, main efforts were concentrated on optimization of a neutron detection system for active assay. Here the neutron detection efficiency was investigated as a function of the number of neutron detectors in a "detector bank" and its position and also of the number of detector bank. This study showed that our present system built in the NUCEF (the Nuclear Fuel Cycle Engineering Research Facility) is of approximately optimal design. As concerns advanced radiation detectors, a dedicate electronic system was developed to amplify signals from a pop-top type Ge detector and control a threefold Stirling refrigerator for cooling the detector. Development of synthetic-diamond radiation detectors progressed also. Wave forms of output signals from a charge sensitive pre-amplifier connected with the detector were investigated to study the electron trapping-detrapping effect and the Hall mobility.

7.1 Analysis on Signals from Synthetic Diamond Radiation Detectors

J. Kaneko, M. Katagiri and Y. Ikeda
(*E-mail :* kin@fnshp.tokai.jaeri.go.jp)

A diamond radiation detector has excellent features of high radiation resistance, high temperature operation, high chemical resistance, tissue-equivalent, etc. Recently it has been available to get high purity synthetic type IIa diamond single crystals made by a high pressure and a high temperature process. The authors reported the first stage of development for a diamond radiation detector using such a synthetic type IIa diamond single crystal in the reference[1]. Although the detector showed a high energy resolution of 0.81% for 5.486 MeV alpha particles, a problem of a polarization effect resulting in limitation on a counting rate remained to be solved. Therefore, it is strongly required to understand behavior of charge carriers in the diamond crystal for improving the performance of diamond radiation detectors. Then signals from diamond detectors can be analyzed in detail.

Data of diamond radiation detectors used in this research were summarized in a Table 7.1.1. All these detectors are made of high purity type IIa diamond single crystals, and have a simple metal - diamond - metal structure. The properties of these detectors were measured mainly by means of 5.486 MeV alpha particles from an ^{241}Am radioactive source. A charge sensitive preamplifier was connected to an entrance window of a diamond detector. As shown in the Table 7.1.1, these detectors showed roughly 1% energy resolution constantly. However, these detectors have a severe problem on a low level limit of counting rates due to polarization effect. In general, this problem can be improved by a special contact made by an ion implantation technique. However, sometimes a contact made by an ion implantation technique has a property of rectification. On this research, behavior of charge carriers, i.e., electrons and holes, should be measured in the same electrical condition except bias polarities, so both ohmic

Table 7. 1. 1 Diamond Radiation Detectors used in this research

Detector Number	Crystal Thickness	Contact Type	Energy Resolution (5.486MeV alpha)
Type IIa #1 super	0.3mm	Pt - Pt	0.9 %
Type IIa #7	0.1mm	Pt - Pt	1.2 %
Type IIa #8	0.3mm	Al - Ti/Pt	0.9 %

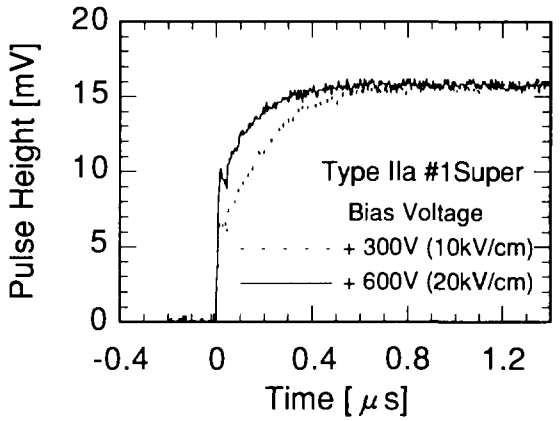

Fig. 7. 1. 1 Leading edges of signals from a charge sensitive preamplifier and the detector #1 listed in the Table 7.1.1

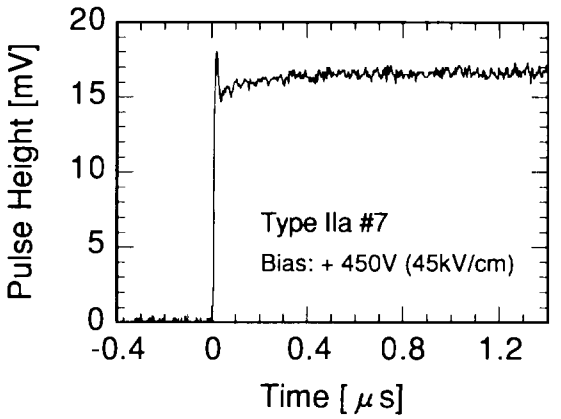

Fig. 7.1.2 Leading edge of a signal from the charge sensitive preamplifier and a thin detector, i. e., the detector #7

contacts were suitable. At low counting rates, it is possible to neglect the influence of polarization effect.

Fig. 7.1.1 shows typical leading edges of signals from a charge sensitive preamplifier and a type IIa diamond radiation detector. In this measurement, the entrance window was biased in positive. The 5.486 MeV alpha particles stopped near the entrance window; a range of a 5.486 MeV alpha particl in a diamond crystal is 13 to 17 micro meters. So the rises of these signals were mainly due to the motion of holes. As reported in the reference[1], there are fast and slow components caused by trapping and detrapping effect in the signal from the diamond detector of 0.3mm thickness. When bias voltage was increased, the pulse height of the fast components increased. It means that velocity of holes increased, and then holes traversed long distance than a measurement condition that lower bias voltage was supplied until getting trapping.

Fig. 7.1.2 shows a leading edge of a signal from a thin detector, i.e., the detector #7. In this measurement, charge carriers needed to traverse only 0.1mm. Moreover, high bias voltage, 45kV/cm, was supplied. Therefore, the large part of charge carriers arrived to the contacts without getting any trapping. Although there is a spike at the leading edge caused by

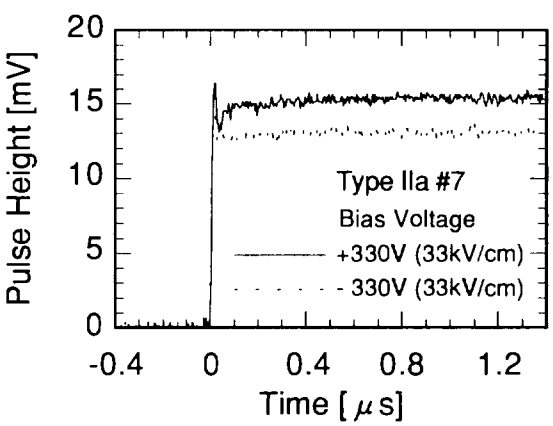

Fig. 7. 1. 3 Comparison between leading edges of signals from the charge sensitive preamplifier and the detector #7 biased in positive or negative

insufficiency of electrical circuit regulation, it has very fast rise time less than 20 ns.

Fig. 7.1.3 is a comparison between signals biased in positive and negative. There are completely same conditions except bias polarity on these measurements. There are only fast components in the leading edge of both signals; Although signals which had maximum pulse heights were chosen, there are big differences in the pulse heights. From this results, it is obvious that trappings occurred on electrons, and these charge carriers could not be set free in this time scale again.

Fig. 7.1.4 a) and b) show 5.486 MeV alpha spectra obtained by the same circuit condition and bias voltage except bias polarities and measurement times. It was expected easily from Fig. 7.1.3 that there is big difference in the peak channels in Fig. 7.1.4 a) and b). From these result, it can be said that trapping on electrons occurred even a detector which is very thin and biased in high electrical field, 33 kV/cm. Because, if there is a no capture, the peaks of 5.486 MeV alpha particles should be the same channels.

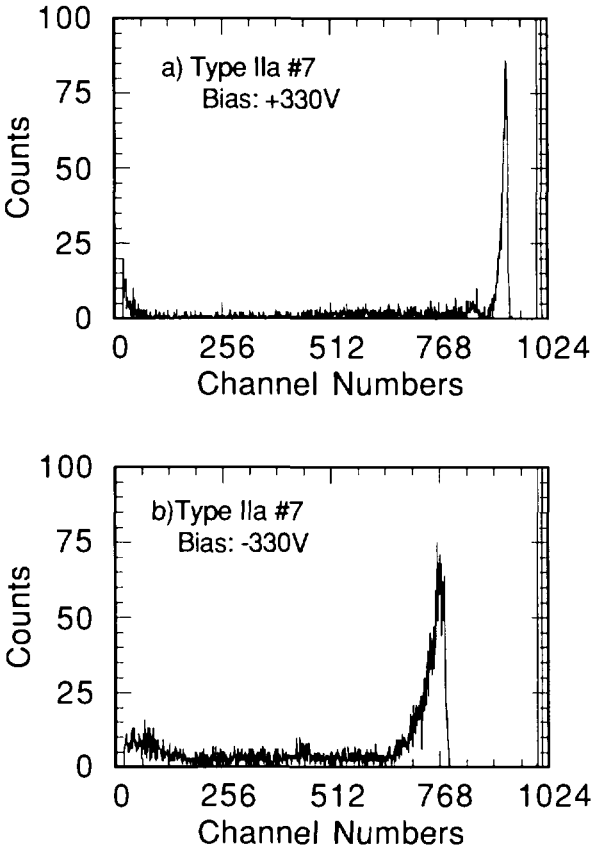

Fig. 7. 1. 4 5.486 MeV alpha spectra obtained by the detector #7 with positive and negative bias conditions

The most important problem on this development is captures of electrons in diamond crystals. Though diamond crystals used were very high purity crystals, the captures of electrons occur extremely. Maybe, these captures caused by nitrogen impurities which is assumed to be about 1ppm. If it is possible to reduce the impurities in diamond during a crystal growth, it is expected to solve this problem.

References

1) Kaneko J. and Katagiri M.: Nucl. Instr. and Meth. A383, p.p. 547-548 (1996).

7.2 Calculational Study of Output Signal Pulses from Fission Counters for Detecting Fast Neutrons

H. Yamagishi and K. Ara

Pulse height distributions (PHDs) of output signals fom fission counters were studied for development of a fast-neutron-fission-counter (FNFC) that can be used for reactor power distribution monitoring. Figure 7.2.1 shows a schematic diagram to explain a fundamental operation configuration of the FNFC. In this study, electrodes (Anode and Cathode) of the FNFC are constructed with a shape of parallel plates. As a sensitive material to fast neutrons, thorium (^{232}Th) is coated with a thin thickness on the surface of electrodes. The fission cross section of ^{232}Th depending on neutron energy is shown in Figure 7.2.2. Generally, the electrode gap is of a few millimeters (mm). As ionizing gas, mixture gas of ($Ar+N_2$) is filled with a pressure of several atmospheres (atm) in the counter vessel. In this study, electric charges of the FNFC outputs that were generated by detecting fast neutrons were calculated to investigate the PHDs.

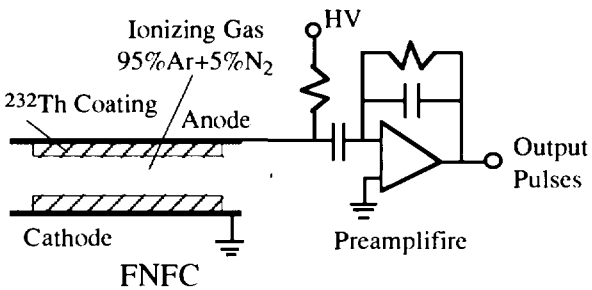

Fig. 7.2.1 Principle of Fission Counter for Fast Neutrons

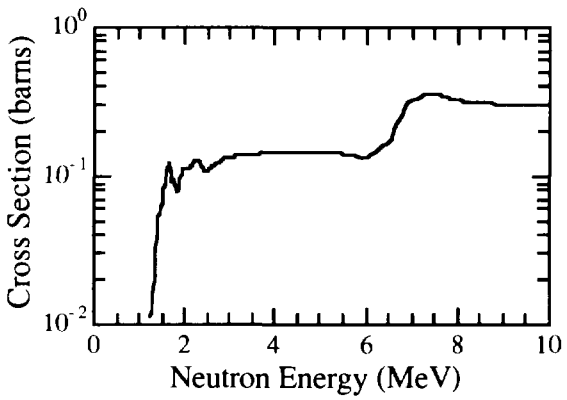

Fig. 7.2.2 Fission Cross Section of ^{232}Th

Figure 7.2.3 shows the schematic diagram of calculation model for the case that a fission occurs in the cathode. Two fission fragments (FFs) produced in ^{232}Th of the electrode fly to opposite direction, respectively: the probability of FF flight is uniform in all directions. The FF flies into the electrode gap and ionizes the gas. The FNFC provides a signal pulse with a small electric charge by one fission. The stopping power (dE/dx)

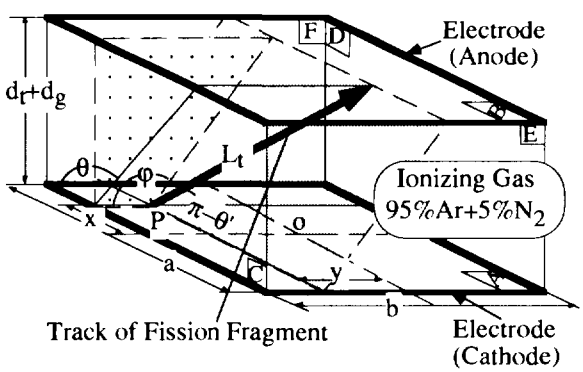

Fig. 7.2.3 Dimensions of Fission Counter for Calculation of Output Signal

of materials to a heavy ion such as a FF is given by Eq. (7.2.1) which is an experimental equation proposed by Bridwell and Moak[1), 2)].

$$\left(\frac{dE}{dx}\right)\left[MeV/\left(kg/m^2\right)\right]=\frac{2064.5}{A_2}\sqrt{\frac{TA_1Z_2}{Z_1}} \quad \text{---------- (7.2.1)}$$

Here T is an energy (MeV) of a heavy ion; A_1 and Z_1, mass and atomic number of the heavy ion, and, A_2 and Z_2, mass and atomic number of a material (Thorium, Argon or Nitrogen). Hence the stopping power $(dE/dx)_{mix}$ of a mixture of material elements is given by Eq. (7.2.2);

$$\left(\frac{dE}{dx}\right)_{mix}\left[MeV/\left(kg/m^2\right)\right]=\sum_i \omega_i\left(\frac{dE}{dx}\right)_i \quad \text{---------- (7.2.2)}$$

where ω_i is the weight percentage of i element; $(dE/dx)_i$, the stopping power of i element.

In case the fission occurs in the Th-coating of cathode and either FF finally reaches the anode (B-area) as shown in Figure 7.2.3, track lengths of the FF in the Th-coating and in the gas are given by Eq. (7.2.3) and (7.2.4), respectively;

$$L_t=\left|\frac{d_t}{\sin\varphi\cdot\sin\left[\tan^{-1}\left(\frac{\tan\theta}{\sin\varphi}\right)\right]}\right| \text{---(7.2.3)} \qquad L_g=\left|\frac{d_g}{\sin\varphi\cdot\sin\left[\tan^{-1}\left(\frac{\tan\theta}{\sin\varphi}\right)\right]}\right| \text{---(7.2.4)}$$

$$\tan^{-1}\left[\frac{d_t+d_g}{a/2-x}\right]\le\theta\le\pi-\tan^{-1}\left[\frac{d_t+d_g}{a/2+x}\right] \qquad \tan^{-1}\left[\frac{d_t+d_g}{b/2-y}\right]\le\varphi\le\pi-\tan^{-1}\left[\frac{d_t+d_g}{b/2+x}\right]$$

where L_t, the track length in Th-coating; L_g, the track length in gas; d_t, the depth from the surface of electrode where fission occurs; d_g, the electrode gap; and, φ and θ, angles of the flight direction in the electrode gap.

In case that the FF flies from A-area to C, D, E or F-area, each track length can be deduced by the same way as that in the above case of B-area. The energy of FF decreases with flying through the Th-coating and the ionizing gas. The FF ionizes the gas and produces an electric pulse in the FNFC. The value of electric charge (P_h) that quantfies the pulse height of signal output from the FNFC is calculated by Eq. (7.2.5);

$$P_h(\ell,\varphi,\theta)=\frac{1}{w_g}\int_0^{\ell_g}\left(\frac{dE}{dx}\right)_g dx \quad \text{---------- (7.2.5)}$$

where ℓ_g is the flight distance ($\rho_g L_g$ kg/m^2) of FF in ionizing gas; $(dE/dx)_g$, the stopping power of mixture ionizing gas; and, w_g, w-value. The ρ_g is the density of ionizing gas. A PHD is constituted with pulses that are generated by the FFs produced at every position: x=0 ~ a, y=0 ~ b, d_t=0 ~ maximum thickness of ^{232}Th, in the cathode and the anode.

The PHDs were calculated with following conditions: a=10mm, b=10mm, electrode

gap=1mm, thickness of Th coating=1, 2, 3, 4 and 5mg/cm^2, ionizing gas=95%Ar+N_2, gas pressure=5 atm, w-value of mixture gas=26.4 MeV. Adopted physical constants of the FFs are as follows: the light FF (energy T_L=97 MeV, A_{L1}=95, Z_{L1}=38), the heavy FF (T_H=65 MeV, A_{H1}=139, Z_{H1}=54).

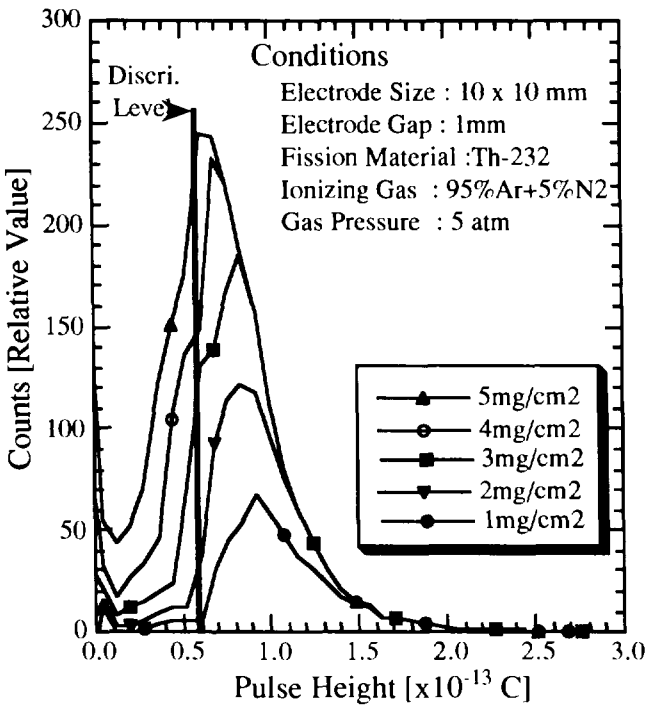

Fig. 7.2.4 Calcurated Result of Charge Pulse Height Distributions of Fast Neutron Fission Counter

Figure 7.2.4 shows the calculated results for various thicknesses of the Th-coating. The calculated results are of signal pulses due to fast neutrons; they do not contain the contribution of pulses due to alpha-rays. The calculated results show that the pulse heights (P_p) of the most frequent pulses in the PHDs decrease with the increase of Th-coating thickness. In the case of a Th-thickness of 1mg/cm^2, the P_p is of 0.92x10^{-13}C. Each P_p of FNFCs with Th-thickness of 2, 3, 4 and 5mg/cm^2 is of 0.84x10^{-13}C, 0.84x10^{-13}C, 0.68x10^{-13}C and 0.60x10^{-13}C, respectively.

Though this study, we found that the FNFC having Th-coating and ionizing gas of (95%Ar+5%N_2) of pressure 5atm, is able to detect fast neutrons of the energy above 1MeV. In case that the Th-coating thickness is less than 3mg/cm^2, the FNFC can provide a performance of high of signal-to-noise ratio.

References

1) Bridwell, L., and Bucy, S., *Nucl. Sci. Eng.* 37:224 (1969)
2) Bridwell, L., and Moak, C. D., *Phys. Rev.* 156:242 (1967)
3) H.Yamagishi, JAERI-Review 95-014, pp176 (Sep. 1995)
4) H.Yamagishi, K.Ara, et al., JAERI-Review 96-012, pp136 (Sep. 1996)

7.3 Experiments for Selective Detection of Magnetic Dipoles Using Superconducting and Ferromagnetic Cylinders

K. Sakasai and K. Ara

(*E-mail*: sakasai@stsp2a0.tokai.jaeri.go.jp)

Noninvasive techniques are essentially important in measuring magnetic fields produced by ionic currents accompanied with electrical activities of various human tissues. The same situation occurs in non-destructive testing of metallic substance. The authors have introduced a selective detection system for magnetic dipoles using superconducting and ferromagnetic cylinders for non-destructive testing of metallic substance[1),2)]. After the effectiveness of the system was confirmed by the magnetic field analysis[3),4)], experiments were conducted.

Figure 7.3.1 shows a experimental setup, where a high-T_c Bi-Sr-Ca-Cu-O based superconducting cylinder and a iron one are adopted. The superconducting cylinder is made by depositing a superconducting layer on the surface of a silver cylinder. The thickness of the layer is about 0.2 mm. The critical temperature and critical current density of the cylinder are around 90 K and 800 A/cm^2, respectively. The magnetometer used in the experiments was developed for low temperature use and has a sensitivity of 4.26 V/G at 77K. It has a good linearity in a magnetic field range between -2 G and +2 G. The outside diameter and the sensitive length of the magnetometer are about 1mm and 20 mm, respectively. In the experiments, the system was directly immersed in liquid

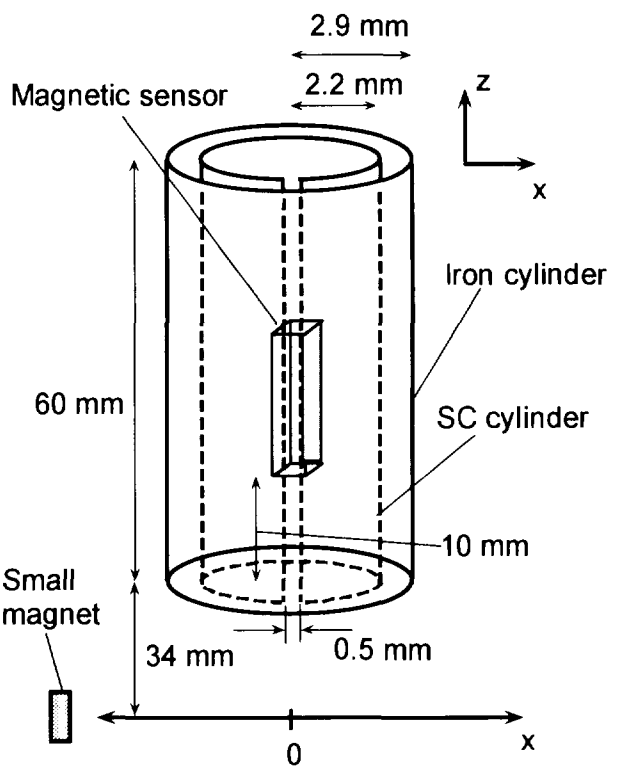

Fig. 7.3.1 Experimental setup

nitrogen and the z-component of the magnetic fields was measured as a function of positions of a small magnet that equivalently works as a magnetic dipole.

The experimental results are shown in Fig.7.3.2, where the measured magnetic fields are normalized to the respective peak values. The curve of the case with superconducting and iron cylinders has a more sharp peak than that of the case without cylinders. When we define the spatial resolution of the sensor as the full width of the curve at a half value of the measured peak, the spatial resolution with superconducting and iron cylinders and without cylinders are 3.84 cm and 5.82 cm, respectively. This means that the spatial resolution of the system is improved by using superconducting and iron cylinders.

The improved spatial resolution suggests that better positioning of dipoles will be possible with the system. This is very clear when magnetic fields

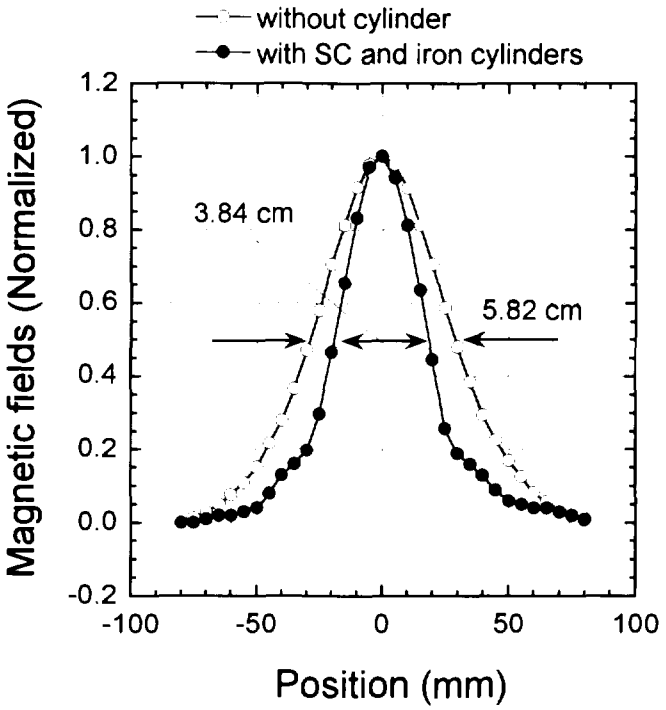

Fig. 7.3.2 Experimental results

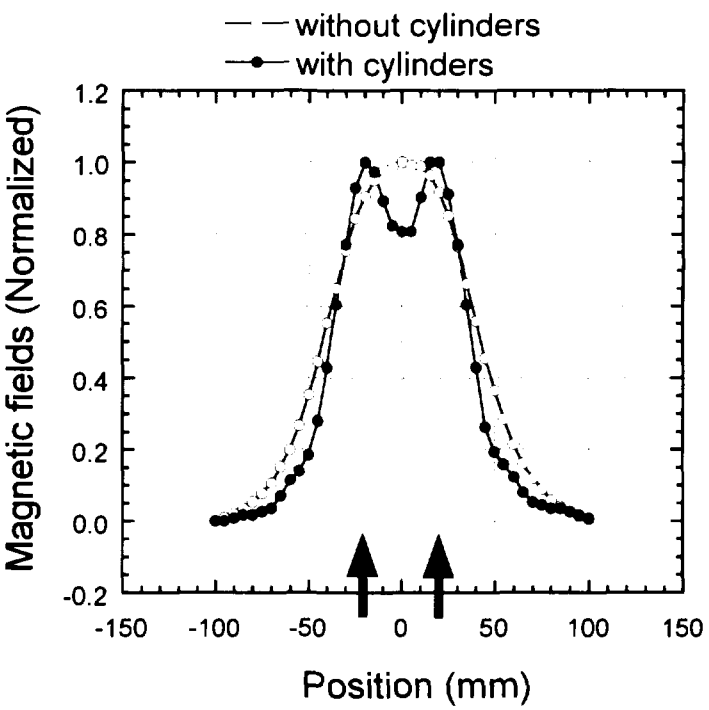

Fig. 7.3.3 Magnetic fields by two parallel dipoles

caused by two parallel dipoles are tried to be detected. Figure 7.3.3 shows the results of magnetic field detection by the system in case that 40 mm-distant two parallel dipoles are exist. In the figure, two arrows show the positions and directions of the dipoles. As seen in the figure, two clear peaks can be detected in case with cylinders but only one peak without cylinders. Here, the positions of peaks are clearly corresponding to those of two dipoles, showing better positioning of the dipoles by the system.

In conclusion, the system proposed by authors for selective detection of magnetic dipoles was proved to be very effective, and it could be useful for nondestructive detection of flaws in metallic components and structures.

References

1) Sakasai K., Kishimoto M. and Ara K.: "Detection of Magnetic-flux Sources by a System of Perfect Diamagnetic Substance and Magnetic Sensor (in Japanese)", *J. Mag. Soc. Jpn.*, **16,** 337-342(1992).

2) Sakasai K., Kishimoto M. and Ara K.: "Experiments for Selective Detection of Magnetic Flux Sources Using a System of High-T_c Superconductors and a Magnetic Sensor (in Japanese)", *J. Mag. Soc. Jpn.*,18, 709-714(1994).

3) Sakasai K., Kishimoto M. and Ara K.: "Method for Selective Detection of Magnetic Flux Sources, Using a System of Superconductors, a Ferromagnetic Substance, and a Magnetic Sensor (in japanese)", *J. Mag. Soc. Jpn.*, 19, 593-596(1995).

4) Sakasai K. and Ara K.: "A possible device for selective detection of magnetic field sources using superconducting and ferromagnetic cylinders", *Rev. Sci. Instrum.*, 68(4), 1739-1742(1997).

7.4 Development of an ECT Probe Having Exciting Coils of Parallerogrammic Shape

N. Ebine*, S. Takeuchi** and K. Ara

(*E-mail:* ebine@popsvr.tokai.jaeri.go.jp)

Steam generator (SG) tubes in PWR power plants have been inspected with the eddy current test (ECT) method during in-service inspection periods, and ECT probes of bobbin coil type have been widely used. This type of probe has, however, a poor detection sensitivity to circumferential flaws since flows of eddy currents is limited only to the circumferential direction in the SG tube. Hence the authors proposed an ECT method to detect efficiently the magnetic flux component only distorted by flaws, and its effectiveness was proved by basic experiments[1]. Based on the experimental results, a new type of ECT probe was invented. The probe consists of exciting coils having a parallerogrammic shape and an array of differential coils for detection of magnetic flux distorted by flaws. This probe structure aims to eliminate inherent blind spots where the probe misses the detection of flaws. A fundamental structure of the probe was then fabricated in trial, and flaw detection tests by it were conducted. The results are presented in this paper.

Figure 7.4.1 shows a fundamental structure of the proposed new ECT probe. The elemental unit of detection coil is a single differential coil that is wound on a pair of Permalloy wires of 0.2 mm in diameter. The number of turns of each coil in the unit is 75. The coil wire is of enameled Cu of 0.05 mm in diameter. Four units are set in the two positions of 3 mm inside from the front and end (right and left

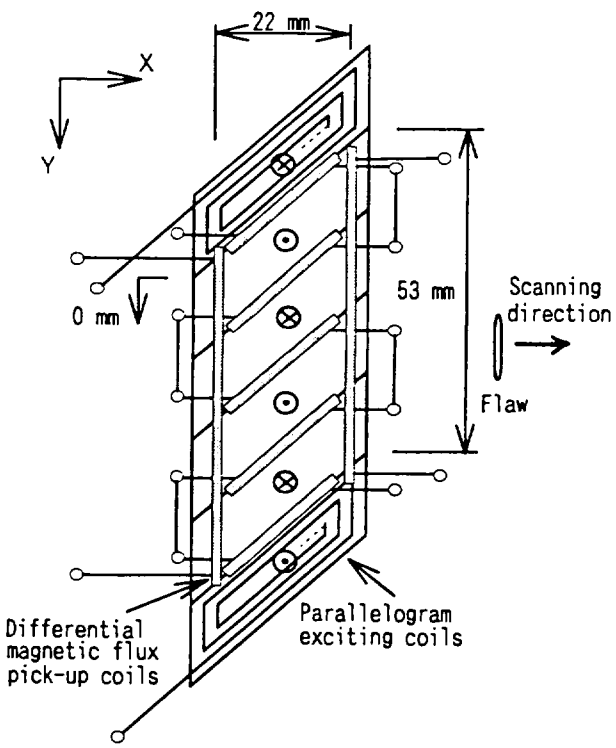

Fig. 7.4.1 A parallerogrammic ECT

* Department of Reactor Safety Research, JAERI. ** MTI Co., Ltd.

in the figure) edges of the exciting coil (parallelogrammic) to the scanning direction. Three units are in the oblique area between the two parallelogrammic coils. All units are connected in a series to compose the detection coil as a whole.

The probe is assembled so that blind spots of the differential coil group on the left side can be covered by active areas of the right side one during a course of scanning. Even if a flaw passes through a blind spot of one group, it could be detected by other group. In the area between the two parallelogrammic coils, an oblique distribution of magnetic flux and thus an oblique flow of eddy currents are induced. These are very effective for detection of both the vertical and horizontal slit flaws.

Examples of the experimental results of flaw detection by the probe are shown in Fig. 7.4.2, where the results for both vertical and horizontal flaws of 5 mm long, 0.4 mm wide and 0.15 mm deep are shown. The induced voltage clearly increases at the points where detection coils are located.

These results clearly show that the probe can detect both the vertical and horizontal flaws without missing at any position of the area covered by the probe coils. Any of blind spots cannot be found in obtained results: namely the flaw can be detected at least once by one of three detection coils located in the vicinity of three different coil edges.

When signal forms shown in Figs. 7.4.2(a) and (b) are compared, mountain and valley

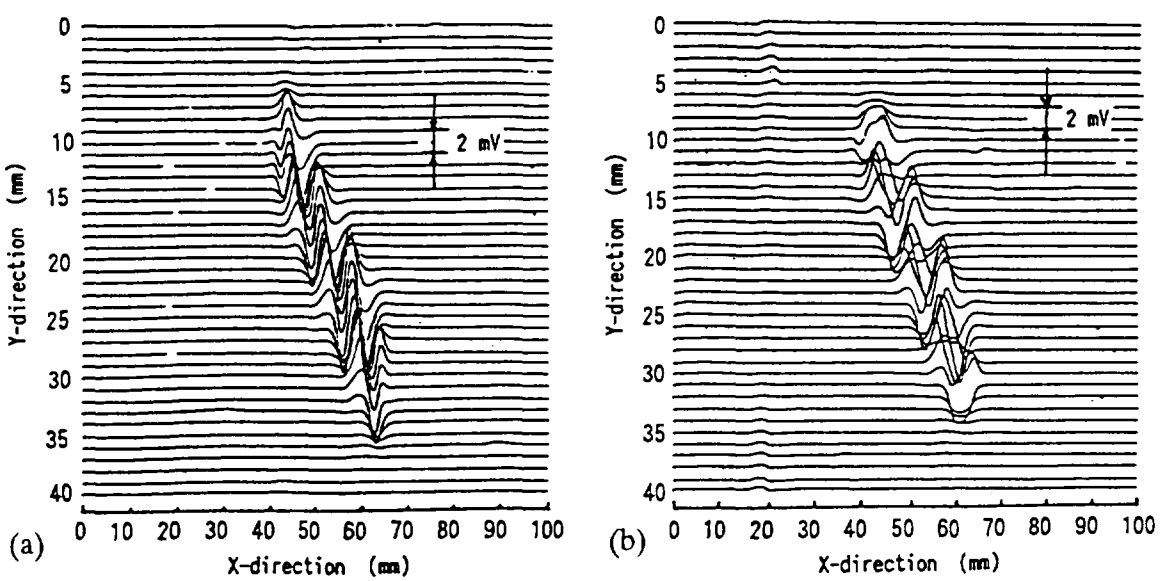

Fig. 7.4.2 Detection results; (a) a holizontal flaw and (b) a vertical flaw.
(a slit of 5mm long, 0.4mm wide and 0.15mm deep)

peaks in terms of output signal amplitude are sharp in case of the horizontal flaw and smooth in case of the vertical flaw. These differences in signal form could give important information about the flaw direction and shape identification.

The results of the output voltage for the inner and outer hole with various depths are shown in Fig. 7.4.3. These plots are of the peak values of the output voltage when the flaw passes at the position of Y=15 mm. The reason why the detection voltage of the inner hole at a excitation frequency of 200 kHz becomes saturated at the depth of about 0.2 mm is due to the magnetic-field penetration-depth of about 0.22 mm for aluminum at this frequency. In case of the outer surface flaw, the output voltage becomes small, but detection of an outer hole of 1.0 mm in diameter and of 15% (0.15 mm) in hole depth is possible.

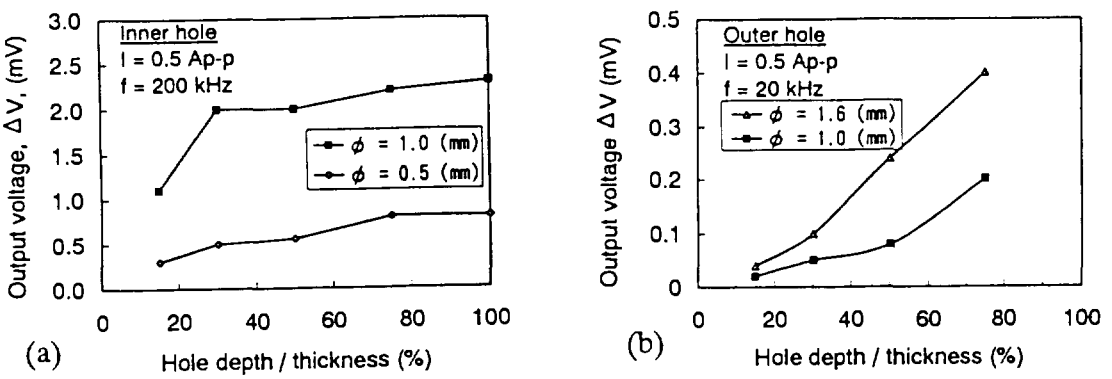

Fig. 7.4.3 Relation between detected voltages and flaw depths; (a) inner surface hole and (b) outer surface hole

In conclusion, it is confirmed that the components of magnet flux distorted by flaws can be detected thoroughly by the probe of parallelogrammic exciting coils and the array of differential detection coils. There is no blind spot in the probe. Both the vertical and horizontal flaws and even the small hole of 0.5 mm in diameter can be detected successfully.

References

1) Ebine N., Takeuchi S. and Ara K.: "Experimental Studies on a Structure of Eddy Current Probe for Detection of Magnetic Flux Disturbed by a Flaw (in Japanese)", Trans. I.E.E. of Japan, 115-A, 999-1006(1995).

7.5 Optimization of the Active Neutron Detection System for High Sensitivity Measurement

M. Haruyama, K. Ara and Y. Sugimoto
(*E-mail* haru@stsp2a0.tokai.jaeri.go.jp)

Objectives

As a part of developing the technology of screening shallow land disposable TRU wastes, we performed a feasibility study of increasing the detection sensitivity of TRU nuclides assayed with the active neutron detection system already installed in NUCEF.

The study consists of two parts: verification of the reliability of the calculation method for the evaluation of detection sensitivity by comparing with experiments, and extended simulation calculations of the detection sensitivities for future candidate modifications to the present detection system.

Verification of the Reliability of the Calculation Method

Figure 7.5.1 shows a plan of the present active neutron detection system installed in NUCEF. The measurement cavity is of a rectangular parallel-pipe with 90 cm width, 90 cm depth and 110 cm height and accommodates a 200*l* waste drum. The cavity is surrounded with a graphite wall of 30 cm thickness, a polyethylene wall of 10 cm thickness and then a boron loaded polyethylene wall of 10 cm thickness toward the outer direction. Two pulsed neutron generator heads are set vertically at two corners of the cavity. A neutron detector bank containing fourteen ^{3}He proportional counters surrounded by a polyethylene moderator and wrapped with a cadmium shield is located along a vertical surface of the graphite wall.

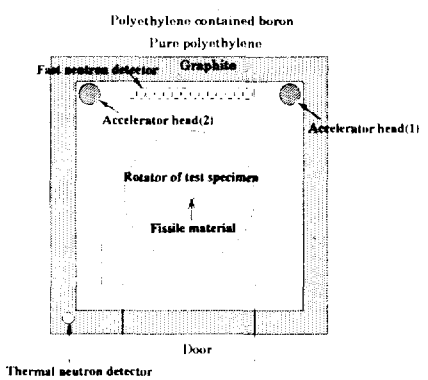

Fig7.5.1 Measurement geometry for detection efficiency on active methods (plan cross section)

Figure 7.5.2 shows the counts of ^{3}He counters in the detector bank by detecting fast neutrons emitted from a fissile sample located at the center of the cavity as a function of fissile weight of the sample. The fast neutrons detected come from the fissions induced by the thermal neutron field formed with moderating the generator neutron pulses in the graphite moderator wall. The detection sensitivity of the system was about 1.5×10^{2} counts/mg Pu as the slope of the linear relationship. The measurement time was 200 s at the generator pulse repetition rate of 50 pulses per second. The total number of neutrons generated was about 1.49×10^{10}. It is attributed to the self-shielding of samples for thermal neutrons that the

response is depressed than the linear relationship above 100 mg of fissile material. The figure also shows MVP[1] calculation results corresponding to the experimental results. The detection sensitivity was calculated by a continuous energy Monte Carlo program MVP with an MVP neutron cross-section file mainly based on the JNDL file. The agreement between calculations and experiments was satisfying.

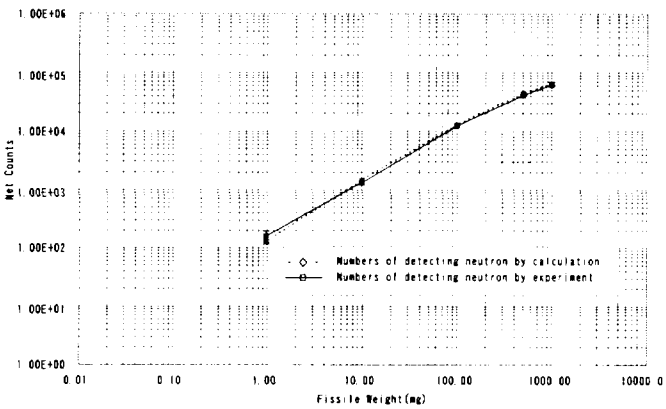

Fig7.5.2 Numbers of detection neutron versus 97%Pu weight (Ratio of calculation and measurement)

The reliability of calculation was ascertained through the comparisons between calculated and experimental results described in this and next paragraphs.

Effect of the Increase of the Number of Detector Banks

The system was designed to increase the number of detector banks up to four each placing in front of four vertical faces of the cavity. Although the increase of detector banks increases the neutron detection efficiency, it increases the absorption of thermal neutrons according as the increase of detector banks in the cavity and lessens the number of fissions arisen in the fissile sample. The overall detection sensitivity, which is determined as the product of the fast neutron detection efficiency of the bank(s) and the conversion factor of generator neutrons to thermal neutron fissions in the sample, does not increase so much as the neutron detection efficiency. The experimental detection sensitivity of four banks is about 2.7 times larger than that of one bank, whereas the maximum sensitivity point is at one bank. The effect of the decrease of the thermal neutron field is larger than that of the increase of the detection efficiency. The MVP calculation reproduced well these effects.

Effect of the Increase of the Number of ^{3}He Counters

Fourteen ^{3}He counters are used in the present detector bank. There is a possibility to change the number of ^{3}He counters without changing the size of cadmium sheath. The detection efficiency of the detector bank for fission neutrons are calculated for changing the number of counters between 6 and 24. The maximum point was at 20 and the efficiency was about 5% larger than the present value.

Effect of the Increase of ^{3}He Gas Pressure

The gas pressure of the present ^{3}He counters is 4 atm. The increase of the pressure is expected to increase the detection efficiency of the neutron detectors and then the detection sensitivity of the system. The MVP calculation showed that the increase to 12 atm will improve the detection sensitivity by about 25%.

Effect of Graphite Addition around Detector Banks

The thickness of graphite wall of the present system is 30 cm and sufficiently thick compared to ordinary active neutron systems. Nevertheless we can expect a larger sensitivity with adding graphite around the detector bank. We examined this effect of adding graphite up to 8 cm thickness around a detector bank with MVP calculations. The optimum thickness was between 4 and 5 cm and the effect was about 16%.

Result

Table 7.5.1 summarizes the results of the extended simulation calculations. The effects of calculation models ①, ③ and ④ are not independent with each other and we can not expect an multiplicative effect between them. The effect ② is expected to be multiplicative with other effects. We can expect an overall effect of about 31% between ① and ② and that of 45% between ② and ③.

Table7.5.1 Result of extended simulation calculations for improvement of sensitivities of the active experiment apparatus

Model of simulation	Calculation condition And Range and parameters	Range of effect (Ratio to original values)	Best value	notes
① Improvement by the increase of the number of detectors	Straight array 6～24 detectors	0.75～1.05	20 detectors 1.05	·Change of accelerator heads position ·Detector bank is change for insertion numbers
② Improvement by the increase ^{3}He filling gas pressure of the detector	2.5cmϕ × 100cm L 4 atm～12 atm	1.00～1.25	12 atm 1.25	Region 2.5cmϕ × 100cm L No change
③ Improvement by adding graphite at around covered of the detector bank	Graphite thickness 0～8 cm	1.00～1.16	about 4.5 cm 1.16	Addition of Graphaite up to 8cm by geometric condition
④ Improvement by the increase number of detector banks	14 detectors／bank 1～ 4 banks	1.00～0.35	I bank 1.00	
Total improve rate against original occasion of 14 detectors			1.31	① and ② satisfied
Total improve rate against original occasion of 14 detectors			1.45	② and ③ satisfied

References

1) Mori T. and Nakagawa M. : JAERI-Data / Code 94-007(1994)

7.6 Development of Electronic Circuits for Electrically-cooled Ge Gamma-ray Detector

M. Katagiri, T. Senzaki, K. Kaneko, A. Birumachi, T. Kozawa and Y. Kobayashi
(*E-mail : kata@stsp2a0.tokai.jaeri.go.jp*)

A small maintenance-free Ge detector, which can be used without a dewar for keeping liquid nitrogen, has been required for various gamma-ray spectroscopy applications. We have developed small electrically-cooled Ge gamma-ray detectors using the Stirling refrigerator for cooling the detector element[1][2][3]. It is necessary to develop an exclusive electronics circuit for efficient use of this Ge detector with portability. We, therefore, developed a small low-power-consumption amplifier circuit and an AC power supply with a control circuit for cooling the detector element.

A schematic diagram of the electronics circuits developed is illustrated in Fig.7.6.1. The electronics circuit consists of a preamplifier, a main amplifier, a high voltage supply with a filter, a temperature monitor circuit, a CPU for control, a DC-DC converter and a DC-AC power supply. The circuit is designed to cooled down a Ge detector of 20% relative detection efficiency with two Stirling refrigerators. The PWM(Pulse Width Modulation) method is employed to convert DC 12V to AC 17V(50Hz) because the method has a high conversion efficiency of 75%. The circuit can be operated by a DC12V battery. The cooling down of the Ge detector and the control of detector temperature are made by the CPU with monitoring the detector temperature. The operation of refrigerators will be stopped when the temperature of their displacer becomes

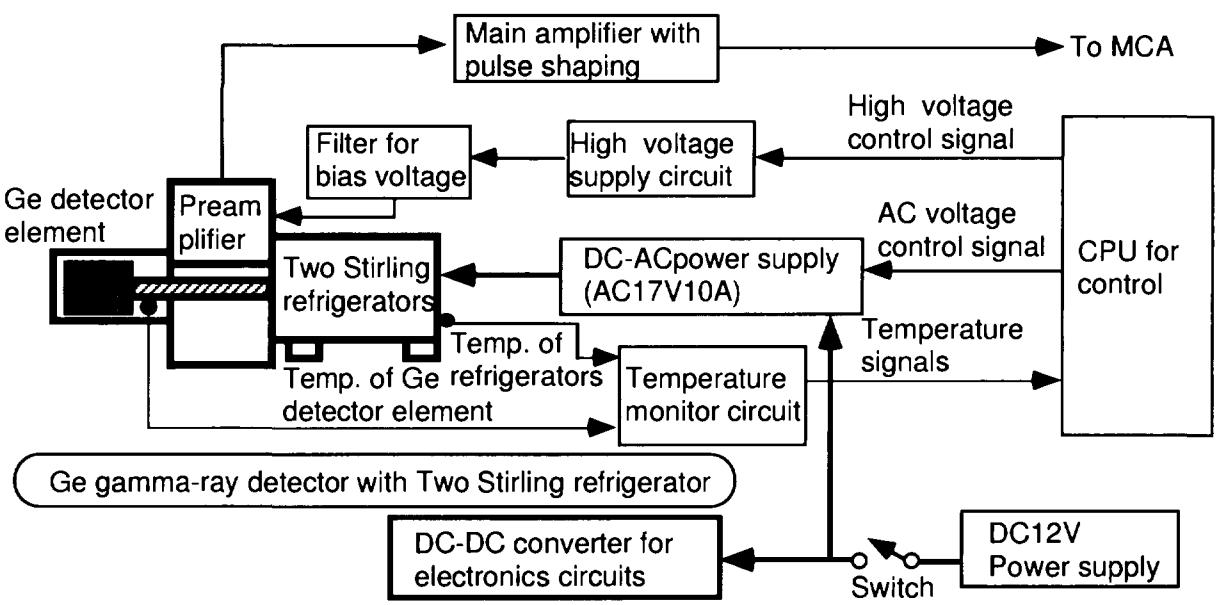

Fig. 7.6.1 Schematic diagram of the electronics circuits for Electrically-cooled Ge detector

over 60°C. The preamplifier and the main amplifier are composed of an AMPTEK A250 and some low-noise operational amplifiers, respectively. A schematic diagram of the small and low-power-consumption amplifiers developed is shown in Fig.7.6.2.

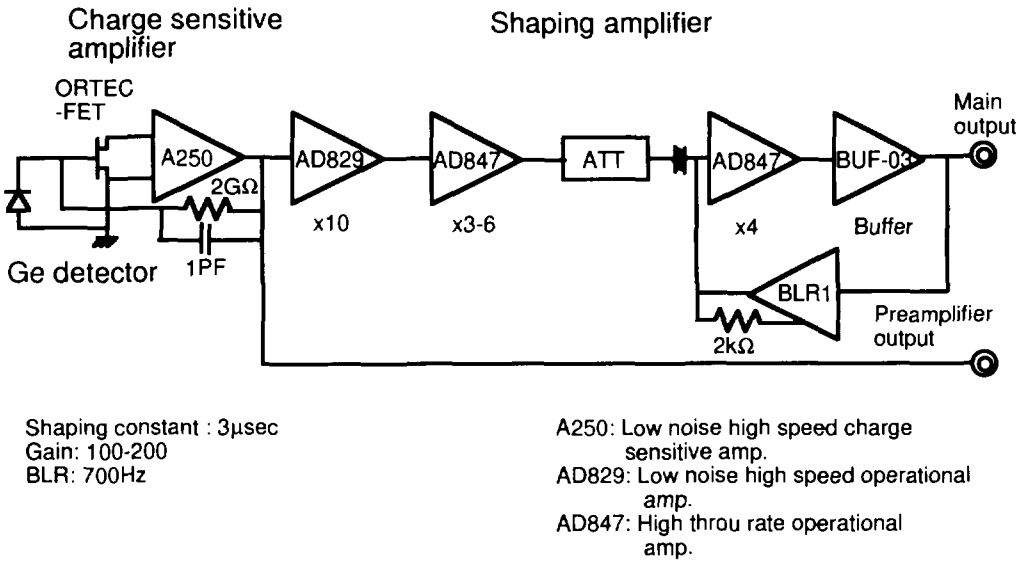

Fig. 7.6.2 Schematic diagram of the preamplifier and the main amplifier

The experiments were carried out to evaluate various characteristics of this electronics circuit. The characteristics of cooling-down and temperature keeping with Ge detector is shown in Fig. 7.6.3. At 10,000s after AC 16.3V was supplied on the Stirling refrigerators, the Ge detector had been cooled down to 103K ≈. Thereafter, the detector temperature was kept constant within a variation of 0.5K by the PID control with CPU. This control performance is sufficient to prevent the peak shift and to obtain the good energy resolution of the Ge detector. The supply of bias voltage to the Ge detector was started automatically supplied when the temperature had reached 105K. The rate of 1V/150ms up to a bias voltage of 255V and then the rate of 1V/60ms up to 2000V were used during the supply of bias voltage.

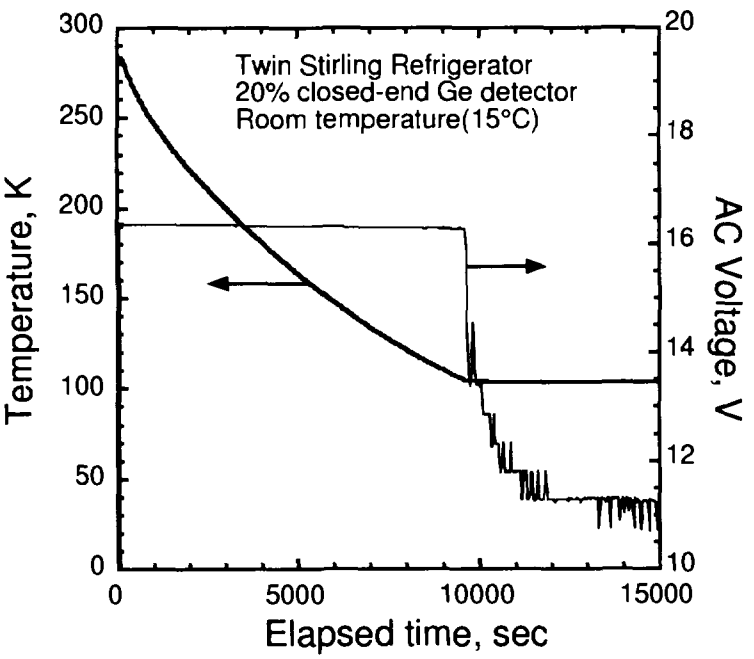

Fig.7.6.3 Characteristic for cooling down and keeping temperature of Ge detector

These operations were done perfectly according to the design.

A gamma-ray spectrum for the ^{60}Co source were measured at three operation conditions of the Stirling refrigerator: namely, a normal operation condition, a condition of AC 0V and a condition of non-operating DC-AC power supply. A gamma-ray spectrum obtained at normal operation condition is shown in Fig. 7.6.4. The FWHM energy resolution for 1.33MeV at three operation conditions are 3.3keV, 2.8keV and 2.4keV, respectively. The best energy resolution is obtained when the operation of DC-AC power supply is stopped. It is revealed that the worse energy resolution is due to the high frequency noise(150kHz) produced in the DC-AC power supply. For resolving this problem, the practical way of assembling the Ge detector and the electronics circuits must be improved.

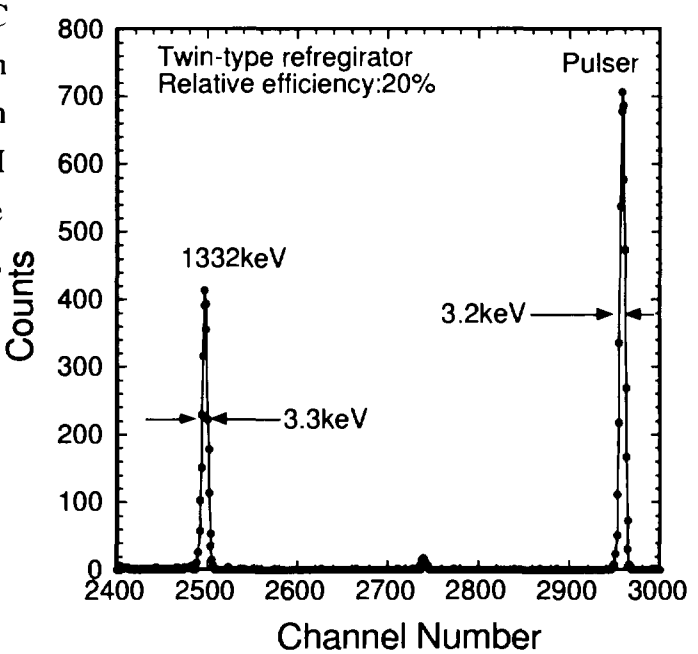

Fig. 7.6.4 Gamma-ray spectrum of ^{60}Co measured at the condition of normal operation

A Ge gamma-ray detection system with two Stirling refrigerators was completed by developing the inclusive electronics circuits. This system can be in service at about three hours after DC voltage was switched on. Hence, it will be applied to various gamma-ray spectroscopy applications.

References

1) Katagiri M. et al.:" Small Electric-cooled Germanium Gamma-ray Detector", KEK Proceeding 94-7, Radiation Detector and Their Uses, 174 (1994).

2) Katagiri M. et al.: " General-Purpose Germanium Gamma-ray Detector Cooled by Two Stirling Refrigerators", KEK Proceeding 95-1, Radiation Detector and Their Uses, 219 (1995).

3) Katagiri M. et al.: " PopTop-Type Germanium Detector Cooled by Stirling Refrigerators", KEK Proceeding 96-4, Radiation Detector and Their Uses, 209 (1995).

8. Reactor Control, Diagnosis and Robotics

In large PWRs with high the coolant flow rate, more fluctuation of neutron flux is observed. This fluctuation occasionally brings forth safety protection actions to reduce the power. The study reveals that large fluctuations of reactor power are not random but coherent and the strength of thermohydraulic fluctuation in the core does not always determine the neutron-flux fluctuation. The two way effect, or the coupling between the thermohydraulic and neutronics plays an important role to cause large neutron-flux fluctuation.

A nuclear power plant monitoring with artificial neural network was tested by using an on-line PWR simulator. The new technique called "adaptive learning" enables the neural network model to follow the changes of reactor dynamics. The results show that this monitoring system can detect the early symptoms of small anomaly during transient operation as well as steady state operation, and sooner than the conventional alarm system.

Auto-associative neural network has been applied successfully to the monitoring of nuclear power plant operation. However, physical interpretation of the network structure and its parameters is not obtained sufficiently, because of the nonlinearity of the network. The contribution ratio function is introduced in order to express the contributions ratio of sigmoidal function in the neural network. The contribution ratio of hidden layered neuron to output layered neuron and the contribution of input variables to output of hidden layered neuron are calculated. The results indicate that the autoassociative neural network can express a regression relation among multi-variables.

For the inspecting patrol of nuclear power plants, a human and robot collaborative system is proposed. Basic idea of this system is that while in the normal situation the robot takes an autonomous action, in abnormal situation when unexpected problem occurred human operators act to help the robot solve the problem. Thereby the system incorporates the ability to cope with the abnormal event quickly. One of the key technologies for a human and robot collaborative system is to correct the error of position estimation from internal sensors by using the difference of the actual and estimated TV images. In the error compensation process, human action plays a role of corresponding of feature points between actual and estimated images. This method has a great advantage of avoiding the computational burden caused by usual image processing.

8.1 Experimental Analysis of Coherent Neutron-flux Fluctuation Observed in a PWR

T. Suzudo, E. Türkcan* and J.-P. Verhoef*
(*E-mail:* suzudo@clsu3a0.tokai.jaeri.go.jp)

Unlike BWRs, PWRs have been considered stable, because there are no voids in the coolant during normal operation and, as a result, the neutronics are not strongly coupled to the thermohydraulics. Therefore few people have examined their fluctuation during normal operation condition from the viewpoint of dynamical stability. The neutron-flux fluctuation in the PWR is smaller than that of the BWR; for instance, the root-mean-square value of a PWR with nominal power of ~500 MW is always less than 0.5 % of full power [1].

Recently however, large PWRs with nominal power of 1300 MW or more have been and will be built. In general, the more power generated from the reactor, the more strongly the thermohydraulics is coupled to the neutronics because the coolant has to remove more heat generated in the fuel. In these large PWRs, therefore, the coolant flow rate through the core is much higher, and is more likely to result in a greater neutron-flux fluctuation caused by thermohydraulics. Some local neutron-flux fluctuation in the large PWR was, in fact, occasionally so large that the peak-to-peak amplitude went up to ~10 % of full power in the end of fuel cycle, and, as a result, power was often reduced by the automatic control system. We know the fluctuation is mainly caused by the combination of neutronics and thermohydraulics, which makes it complicated as a result of the nonlinearity; the concept called "complexity" is often used to represent such a phenomenon. It is said that, in the term of complexity, a random phenomenon becomes ordered when the system deviates far from its equilibrium state, i.e., when the power of reactors becomes larger. Therefore, it is likely that large fluctuations of reactor power are not random but coherent or ordered, as experienced in BWRs. From the reason mentioned above, we have experimentally analyzed the operation signals measured at the PWR plant in the Netherlands.

Figure 8.1.1 shows a typical power spectral density (PSD) of the ex-core neutron-flux signal. The PSD for the DC signal has a peak at ~0.1 Hz and a trough at ~0.18 Hz (see Fig. 8.1.1a), and the graph smoothly connects to that of the AC signal at ~0.3 Hz (see Fig. 8.1.1b), above which no meaningful peaks or troughs are seen.

Next, we will look into coherent motions of the neutron-flux using the coherence and phase difference between each pair of ex-core neutron-flux at different positions. First, detector pairs vertically deviated were investigated and their coherences and phase

---

* The Netherlands Energy Research Foundation

differences were found to almost be unity and nil, respectively, indicating that the ex-core neutron-flux does not vary with the vertical position, that is, the neutron-flux fluctuation is almost coherent in the longitudinal direction. Second, detectors pairs azimuthally deviated were investigated, and, we found, there are several frequency ranges in which the neutron-flux seems to form coherent motion; they are for instance the second azimuthal mode at ~0.03 Hz, and core-wide modes at ~0.1 and 0.2–0.5 Hz. The mode distribution with respect to the frequency including higher frequency range is shown in Fig. 8.1.2.

Finally, the coherence and the phase difference between an ex-core neutron-flux signal and the thermohydraulic signals were examined. The coherences between the neutron-flux signal and the primary loop temperature and pressure indicate peaks at ~0.1 Hz, suggesting that the neutron-flux oscillation at ~0.1 Hz is related to the thermohydraulics. The phase between the neutron-flux signal and the parameters at this frequency is completely reversed. This implies the oscillation is caused not by one-way thermohydraulic effect but by a two-way effect; the neutronics is effected by itself through the thermohydraulics, i.e., by a negative coolant temperature feedback. The fact that the frequency range of this mode is narrow (see Fig. 8.1.2), supports this hypothesis, because the fluctuations which survive in feedback loops must have a specific frequency determined by system parameters. Note that further investigation indicated that the result shown in the figure hardly depended on the position of ex-core neutron detector and on whether Loop 1 or Loop 2 was considered. At the same time, we have investigated the coherence between an ex-core neutron-flux signal and the core-exit temperature[2]. The result indicated that the coherence was strong at less than 0.03 Hz. The linear phase between the two signals indicated that this coherence was built by a one-way effect from thermohydraulics to neutronics.

In conclusion, the strength of thermohydraulic fluctuation in the core does not always determine the neutron-flux fluctuation. The two-way effect, or the coupling between the thermohydraulic and the neutronics plays an important role to cause large neutron-flux fluctuation.

References

1) Türkcan E.: Prog. Nucl. Energy, Vol. 9, 437(1982).
2) Suzudo T., Türkcan E. and Verhoef J. P. : In-Core Instrumentation and Reactor Core Assessment, 14–17 October, Mito, Japan, 3.2, 1996.

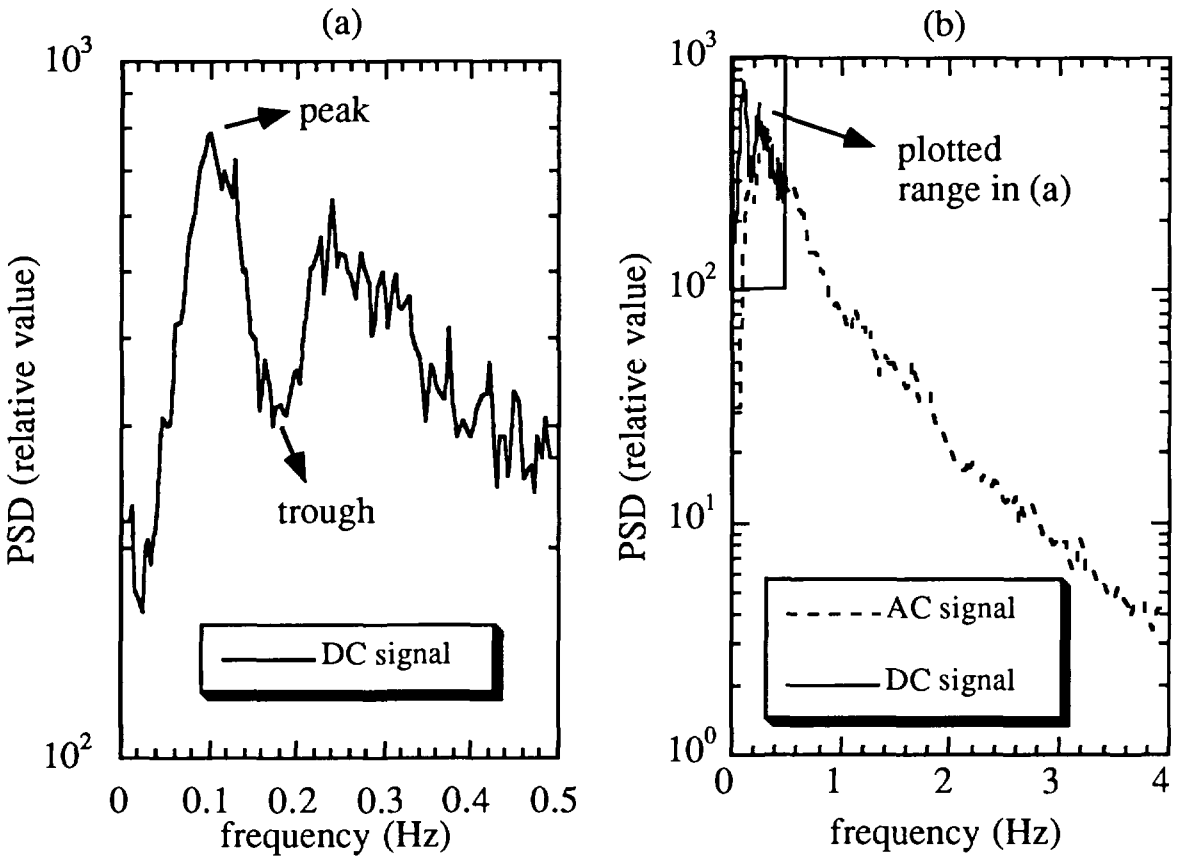

Fig. 8.1.1 PSDs of ex-core neutron-flux signal

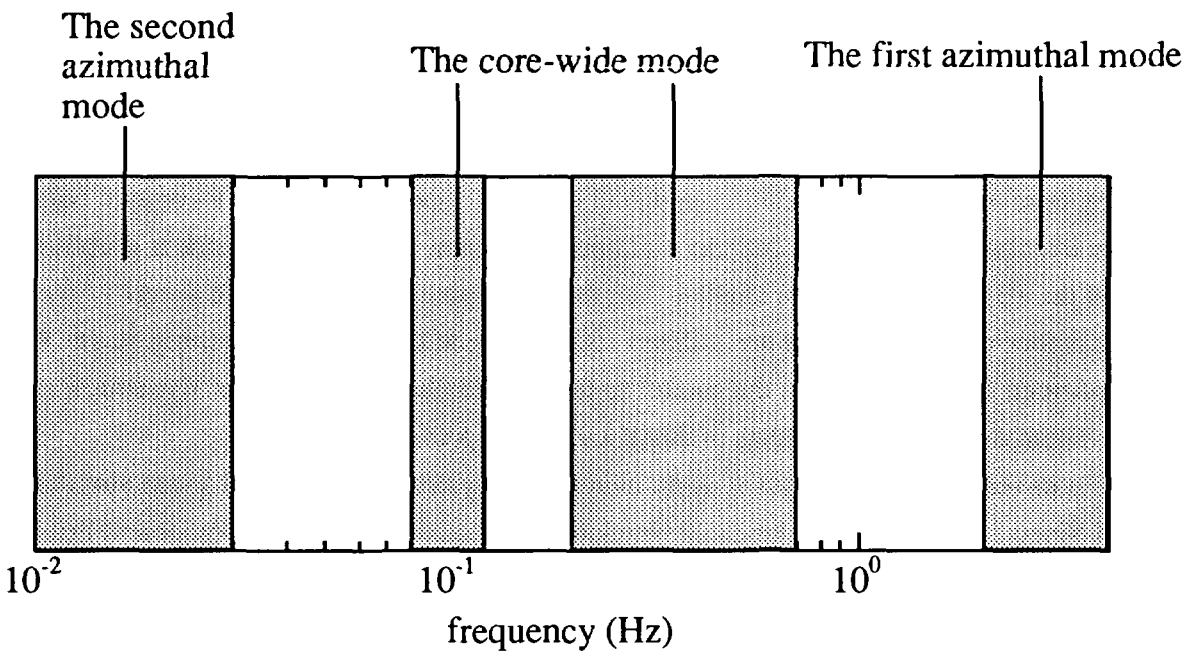

Fig. 8.1.2 Coherent oscillation mode varying with the frequency

8.2 Anomaly Detection in Nuclear Power Plant with Adaptively Learned Neural Network

K. Nabeshima, S. Nose*, K. Kudo* and K. Suzuki
(*E-mail:* nabe@clsu3a0.tokai.jaeri.go.jp)

The condition monitoring of a nuclear power plant (NPP) is of major concern during operation. The conventional monitoring method is to set the fault threshold level for each plant parameter and to alert when the monitored signal exceeds its threshold level. However, when anomalies are detected, they are possibly too developed to cope with. Therefore, it is necessary to develop model-based monitoring methods to detect symptoms of anomaly.

The major advantage of artificial neural network (ANN) is an ability to model multi-output process system from the measurement information without using physical expressions. This is a benefit in the area of the power plant monitoring, apart from other numerous application areas. To construct the dynamic model of the NPP, three-layered auto-associative neural network, trained by backpropagation learning algorithm, was used. For neural network utilization 12 plant signals are picked out: they are ex-core neutron flux, generated electric power, hot-leg temperature in primary loop-B and loop-C, primary water flow, feedwater pressure and steam pressures, steam flows and feedwater flows of secondary loop-B and loop-C. These signals are most significant for the plant surveillance. The basic idea of anomaly detection method is to monitor the deviation between process signals measured from actual plant and corresponding output signals from the ANN plant model.

We have realized that the initial plant model can not be used during whole fuel cycle, and that the model must be changed to follow the slow change of reactor dynamics, which is caused by operational condition shifts and fuel burn-up. Therefore, a new technique called "adaptive learning" is proposed here[1]. In monitoring process, the neural network is adaptively trained, if the all testing errors are smaller than the corresponding testing fault severity levels. Certain number of previous data are utilized for training at the adaptive learning stage. We have confirmed that this enables the model to follow the changes of reactor dynamics, and that the system detects the symptoms of small anomalies precisely.

We developed an ANN plant wide monitoring system for the PWR plant simulator designed Surry-1, USA. Several kinds of simulated malfunction caused by equipment failure during steady state operation were used to evaluate the capability of the neural network monitoring system[2]. All results show that this monitoring system can detect the early symptoms of small anomaly sooner than the conventional alarm system. The present work is an attempt

* Kyushu University, Fukuoka

to evaluate the usefulness of the adaptive learning algorithm and the monitoring system during transient operation.

The results in case of "Volume Control Tank Level Control Fails Low" are shown in Fig. 8.2.1. The solid line indicates the measured signals from the simulator. The dotted line represents the estimated values by neural network. The diamonds indicate the deviation between measured signals and estimated values. Two horizontal broken lines show the fault severity levels, defined by the largest deviation during initial learning. If the deviation is in the range between two horizontal lines during monitoring, the plant condition should be considered normal. In this case, the malfunction was added at 600 s.

This power decrease operation is faster than the learning data, the neural network without adaptive learning cannot follow this new transient operation, so that the monitoring system alerts the anomaly before the malfunction is added, as shown in Fig. 8.2.1a.
On the other hand, the monitoring system with adaptively learned neural network detects anomalies when the deviations exceed the limit at 638 s (see Fig. 8.2.1b). The conventional alarm system could detect this anomaly 3594 s after the malfunction start. The results show that this monitoring system can detect the early symptoms of small anomaly during the transient operation as well as steady state operation.

References

1) Nabeshima K., et al:"Proc. of Third International Conference on Nuclear Engineering", Vol.3, 1551 (1995).

2) Nabeshima K., et al:"Specialists' Meeting on Monitoring and Diagnosis Systems to Improve Nuclear Power Plant Reliability and Safety", Barnwood, UK, May 14-17 (1996).

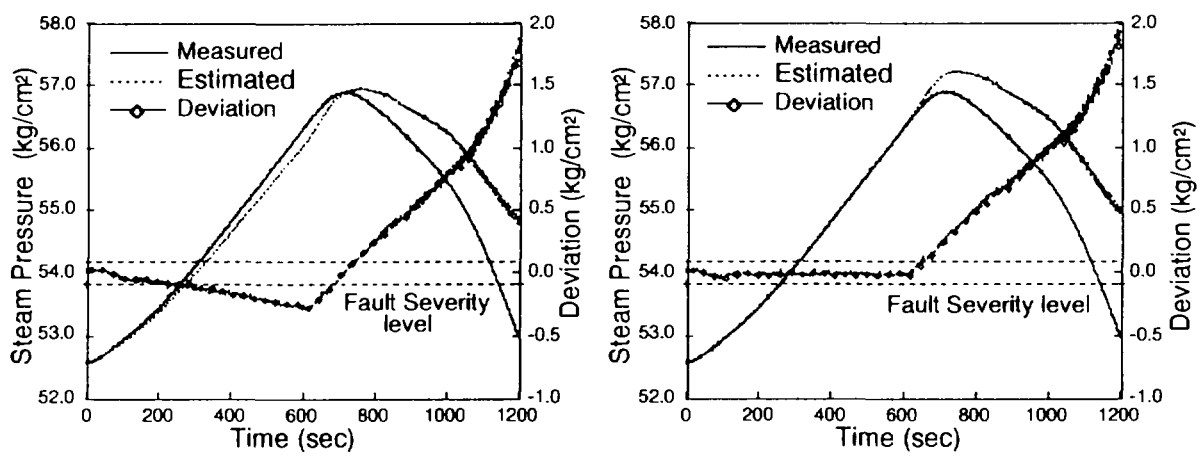

(a) Without adaptive learning (b) With adaptive learning

Fig. 8.2.1 Results in case of "Volume Control Tank Level Control Fails Low"

8.3 Statistical Approach to Understand Auto-associative Neural Network

K. Hayashi
(*E-mail:* hayashi@clsu3a0.tokai.jaeri.go.jp)

Auto-associative neural network has been applied successfully to the monitoring of nuclear power plant operation. It is well known that neural networks have a high model fitting capability, which is caused by the flexible structure made from parallel and layered connections of simple nonlinear functions. This feature makes another advantage that the modeling can be done without any prior mathematical assumption on target system. However, physical interpretation of the network structure and parameters obtained numerically becomes much difficult because of existence of the nonlinear elements inside the network. Therefore, any criterion or limitation on usage of neural network for obtaining a suitable result is not yet established.

Objective of this study is to clarify the meanings of network structure and the model parameters of neural network, and to establish criterion or limitation of the usage. This study focuses to the auto-associative type neural network in which the output variables are the same as the input variables. Therefore, the autoregressive model is very similar to regression model in statistics, excepting with existence of nonlinear elements; usually sigmoidal function. It is easy to understand that the auto-associative neural network without nonlinear elements is equivalent to regression model completely.

The contribution of nonlinear elements in the neural network could not be evaluated exactly by analytical way. Therefore, a contribution ratio function calculated numerically was introduced in order to express the contributions of sigmoidal function in linear approximations of the neural network. When it is assumed that the structure of auto-associative neural network is a feed forward type with three layers and that the nonlinear element uses a logistic function, the contribution ratio of j-th hidden layered neuron to k-th output layered neuron at a certain system state "s" is defined as

$$\Delta\gamma_{kj}(s) = \frac{\Delta Fu_{kj}(s)}{\sum_{m=1}^{M} \Delta Fu_{km}(s)} \qquad (8.3.1)$$

where $\Delta Fu_{kj}(s)$ expresses a change of hidden layered neuron output between two different system states "s" and "s-1" and it is calculated from

$$\Delta Fu_{kj}(s) = Fu_{kj}(s) - Fu_{kj}(s-1) \qquad (8.3.2)$$

$\Delta\gamma_{kj}(s)$ is named as "signal power contribution ratio" here.

In the same manner, the contribution ratio $\Delta\gamma_{ki}(s)$ of each network input variable $x_i(s)$ to the output layered neuron is also defined as ;

$$\Delta\gamma_{ki}(s) = \sum_{j=1}^{M} \Delta Fu_{kj}(s)\Delta Pu_{ji}(s) \qquad (8.3.3)$$

where $\Delta Pu_{ji}(s)$ expresses the contribution of each input variable to the output of hidden layered neuron and calculated from the following equation.

$$\Delta Pu_{ji}(s) = \frac{\left(c_{ji}\Delta x_i(s)\right)^2}{\sum_{n=1}^{K}\left(c_{jn}\Delta x_n(s)\right)^2} \qquad (8.3.4)$$

where c_{ji} is a weigh of hidden layered neuron and $\Delta x_i(s)$ means a difference of input variable between "s" and "s-1" system states, as

$$\Delta x_i(s) = x_i(s) - x_i(s-1). \qquad (8.3.5)$$

Examples of each new contribution function are shown in **Fig. 8.3.1** and **Fig. 8.3.2**. It is easy to find from the former graph that the contribution of each hidden neuron changes by the amplitude of input variable x1. Furthermore, the contributions of input variables x2, ..., x12 to the output variable y1 change due to the amplitude of the input variable x1, as shown in the latter graph. This means that the auto-associative neural network can express a regression relation among multi-variables, depending on each system state. Therefore, it could be concluded that the auto-associative neural network is equivalent to a state-varying regression model.

References

1) Hayashi K. : "Modeling of nuclear power plant using auto associative neural network," Coordination research reports No.94 - Inverse problem and its around (3), pp.61-76, 1997, Institute of Statistical Mathematics. (In Japanese).

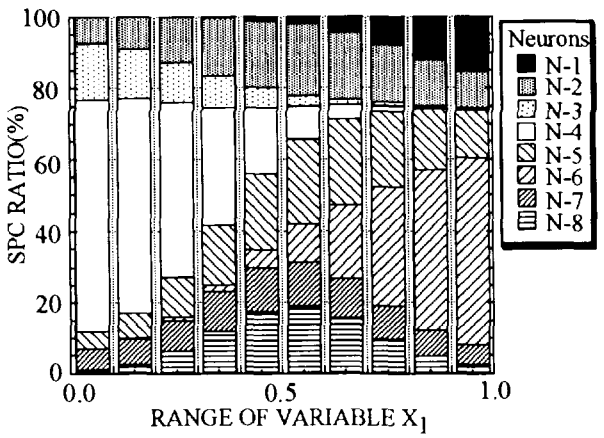

Fig.8.3.1 Signal power contribution ratios of eight hidden layered neurons to the network output variable (Ex-core Neutron signal).

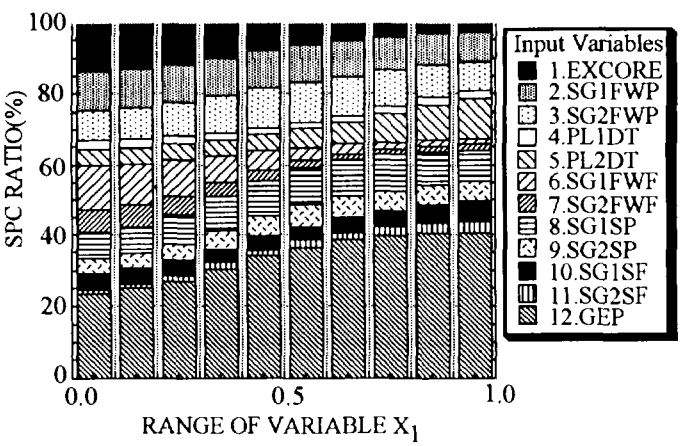

Fig.8.3.2 Signal power contribution ratios of twelve network input variables to the network output variable (Ex-core Neutron signal).

8.4 Development of a Human and Robot Collaborative System for the Inspecting Patrol of Nuclear Power Plants

N. Ishikawa and K. Suzuki
(*E-mail:* ishikawa@clsu3a0.tokai.jaeri.go.jp)

Autonomous mobile robot is widely studied in the robotics research field to realize the self-consistent system for performing the given task in the unstructured environment. Although self-consistent autonomous system has an advantage of reducing the labor of human, it is not always suitable to use this system for the tasks in nuclear power plants. For the inspecting patrol of nuclear power plants, we propose a human and robot collaborative system with the high safety and reliability. Conceptual idea of this system is that while in the normal situation the robot takes an autonomous action, in abnormal situation when unexpected problem occurred human operators act to help the robot solve the problem. Thereby the system incorporates the ability to cope with the abnormal event quickly. The system is constructed by adding the interfacing function between human and robot to ordinary autonomous system. Schematic diagram of the system is depicted in Fig. 8.4.1 The interfacing function can be categorized into 3 parts: hardware, software and algorithms. As a hardware constructing the interfacing function the wireless modem is utilized to transmit the sensor data obtained by inspection activities and command issued by operator in problem-solving phase. Software means the graphical user interface (GUI) on host computer through which the human monitors the sensor data and operates the robot manually in the case of abnormal situation. Algorithms are required for performing the collaborative procedure, being explained in next paragraph of introducing the positioning tool.

The function of the positioning tool is to estimate the robot position with high accuracy for navigation. The position is estimated from the rotational speed of wheels measured by encoders and the angular velocity of the robot measured by a gyroscope. To improve the estimation accuracy, the data from gyroscope is used when sudden odometric error (e.g. slip of the wheel) occurred.[1] Since the gyroscope used here is piezoelectric vibration type and has comparatively large drift, the compensation of the drift based on lowpass filtering is incorporated. However, the error of the position estimation from internal

sensors (encoder and gyroscope) increases with the distance of navigation. To reduce this error, landmarks are usually utilized. Considering the difficulty of installing new landmarks in nuclear power plants, we adopt the compensating method utilizing the image from TV camera. The error of position estimation from internal sensors is corrected by using the difference of the actual and the estimated TV images. The estimated image is generated based on the position obtained from internal sensors. Corresponding of feature points(e.g. the apex of object) between actual and estimated images required for compensation is performed by human. This method has a great advantage of avoiding the computational burden caused by image processing. This compensation algorithm adopts human collaborative procedure. Figure 8.4.2 shows the illustrative sketch of positioning tool which will be implemented on the host computer.

Reference

1) Ishikawa N., et al.: "Experimental Evaluation on Position Estimation of Mobile Robot by the Combined Use of Odometry and Gyro", JAERI-Research 97-033 (1997) (in Japanese).

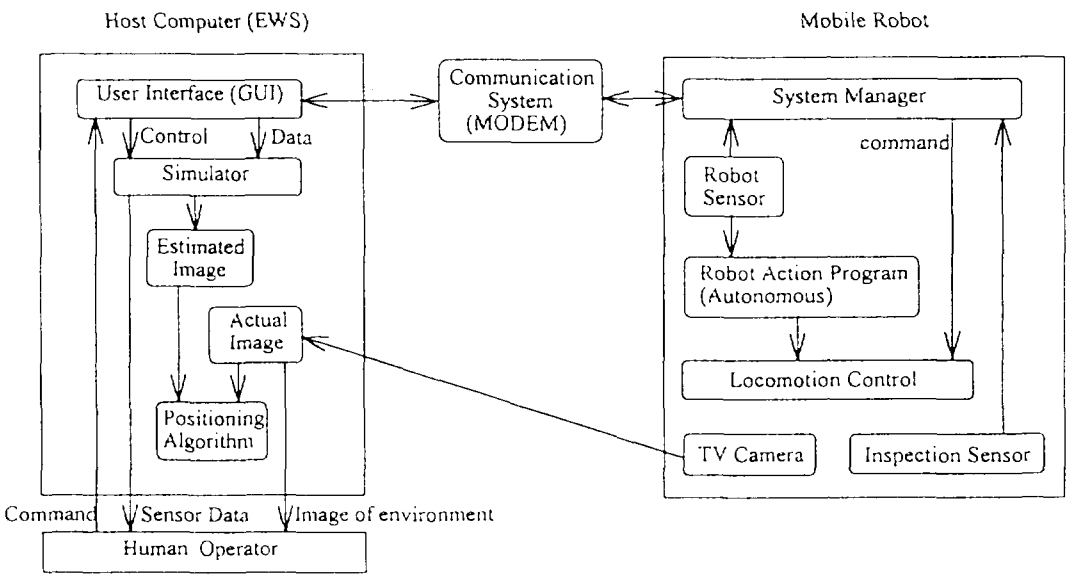

Fig. 8.4.1 Configuration of human and robot collaborative system

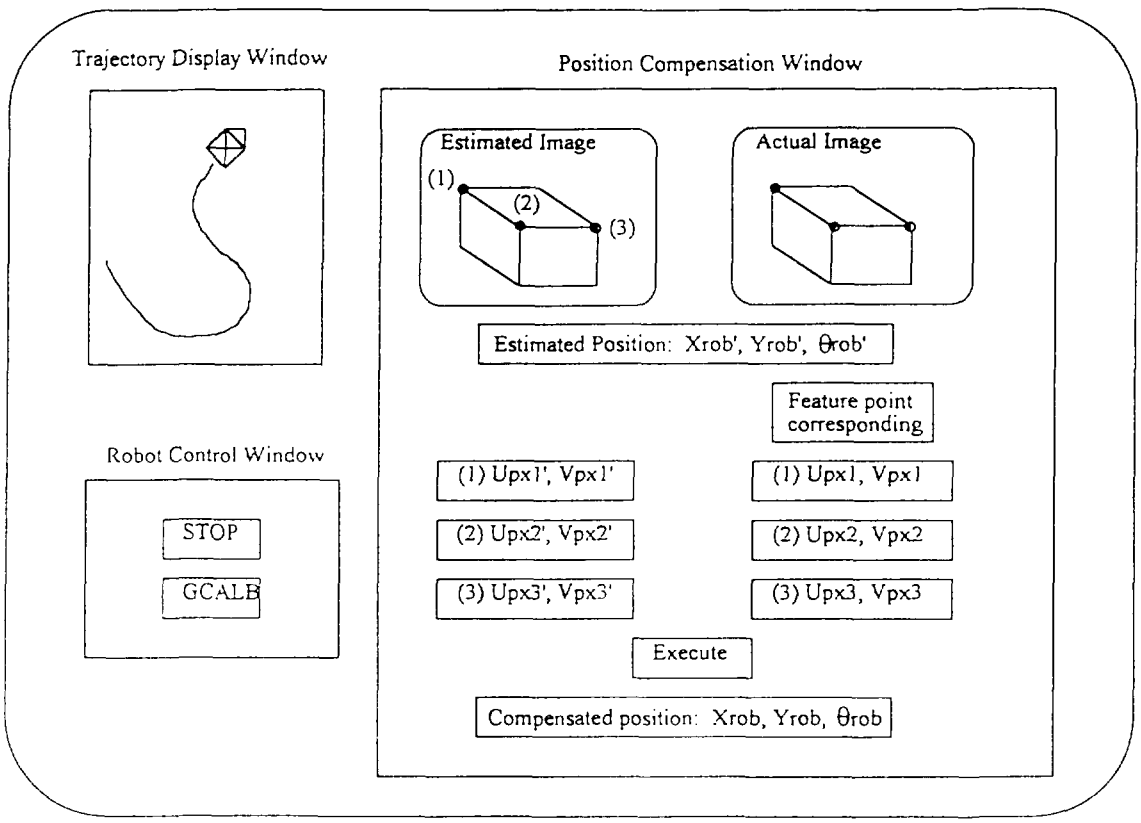

Fig. 8.4.2 Illustrative sketch of positioning tool

9. Heat Transfer and Fluid Flow

There are two major subjects of research associated with heat transfer and fluid flow.

The first subject is the transient thermal-hydraulic demonstration test program, which is the second phase of the large-scale reflood test program. The test program aims at demonstrating the core integrity during the design basis events (DBEs) of light water reactors (LWRs). In FY 1995, the construction of the test section with a PWR configuration was completed. The facility has a full height core with a 5x5 bundle of a PWR configuration and a flow control system supplying coolant at specified conditions which simulate transients during DBEs of PWR, BWR and their improved ones. In FY 1996, first series of abnormal transient simulation tests for PWR was performed and it was confirmed that the core cooling is attained during PWR DBEs. Post-CHF tests were also performed using a single rod test section to quantify the safety margin during DBEs. The analyses of major DBE transients in PWR and BWR were also performed to specify the test conditions using the J-TRAC code and the TRAC-BF1 code.

The second subject is the development and verification of the best-estimate codes for thermal-hydraulic analyses of next-generation nuclear systems such as advanced LWRs with passive safety system, fusion reactor, a target of an intense neutron source, etc. To establish an analytical tool based on multidimensional two-phase flow model for design of passive safety reactors, a multidimensional two-phase flow analysis code has been developed and applicability of existing constitutive equations (lift force model and turbulent dispersion model) for a developing bubbly flow was investigated systematically. A series of experiments on natural circulation two-phase flow instability, thermal-hydraulic safety simulation tests for a fusion reactor, and a model experiment for the mechanism of critical heat flux were also performed to get validation data checking the applicability of system analysis codes for design of passive safety reactor design and fusion reactor safety assessment codes, respectively.

Major results obtained in FY 1996 are described in the following sections

9.1 Abnormal Transient Simulation Tests at Core Thermal-hydraulic Transient Test for LWRs

T. Iguchi, A. Ohnuki, C. Iwaki, M. Kureta, K. Nakajima, H. Watanabe
Y. Watanabe, T. Sato, M. Kimura and H. Akimoto
(*E-mail*: iguchi@hfl1.tokai.jaeri.go.jp)

"Abnormal Transient Simulation Tests" are in progress as a part of "Large scale reflood test program II" sponsored by Science and Technology Agency of Japan. The purpose of the tests is to confirm the core integrity during unexpected transients and accidents, i.e. design basis events (DBEs), of light water reactors (LWRs).

The PWR DBEs chosen for "Abnormal Transient Simulation Tests" are listed below. These DBEs were chosen, since they were considered severe based on previous licensing calculations.

①Power increase events
- Uncontrolled rod assembly (fast) withdrawal
- Uncontrolled rod assembly (slow) withdrawal

②Flow reduction events
- Pump seizure accident of 4-loop PWR
- Loss-of-flow accident of 4-loop PWR
- Pump seizure accident of 2-loop PWR
- Loss-of-flow accident of 2-loop PWR

③Depressurization event
- Abnormal depressurization due to unexpected opening of valve

Test conditions (Pressure, fluid temperature and flow rate at inlet of test section) were determined to simulate conservatively the core boundary conditions during PWR DBEs, by referring to the results of licensing calculation and our own calculation with 1D J-TRAC code (J-TRAC code with one dimension model). Power distribution in horizontal plane of the test section were determined to simulate the power distribution in PWR core. Power level

supplied to the test section were determined by taking into account the difference of thermal characteristics between the heated rod in the test section and the nuclear fuel. Major differences taken into account are in initial stored energy and thermal time constant. According to the measured data, the transient test conditions were well simulated at all "Abnormal Transient Simulation Tests" .

Figure 9.1.1 shows an example of measured clad temperature. This result was obtained in a test simulating 4-loop PWR pump seizure accident. Clad temperature increases after transient initiation because of flow reduction. Then clad temperature decreases because of power reduction. Maximum discrepancy between the clad temperature and the saturation temperature is less than 10 K. Thus, significant heat-up of the heated rod is not observed at any elevation at this test.

Figure 9.1.2 shows measured clad temperatures at "Abnormal Transient Simulation Tests" other than 4-loop PWR pump seizure accident simulation test. Maximum discrepancy between the clad temperature and the saturation temperature is less than 30 K. Thus, it is confirmed that the core cooling is attained during PWR DBEs.

Test conditions at "Abnormal Transient Simulation Tests" were determined referring to one dimensional calculation (1D J-TRAC code), as described above. Therefore, further "Abnormal Transient Simulation Tests" are necessary in order to take into account the effect of multi-dimensional in-core thermal hydraulics for confirming core cooling during PWR DBEs. This is because the real in-core thermal-hydraulics in PWRs are considered to be multi-dimensional due to the wide core and the corewise horizontal power distribution. These tests are scheduled in 1997.

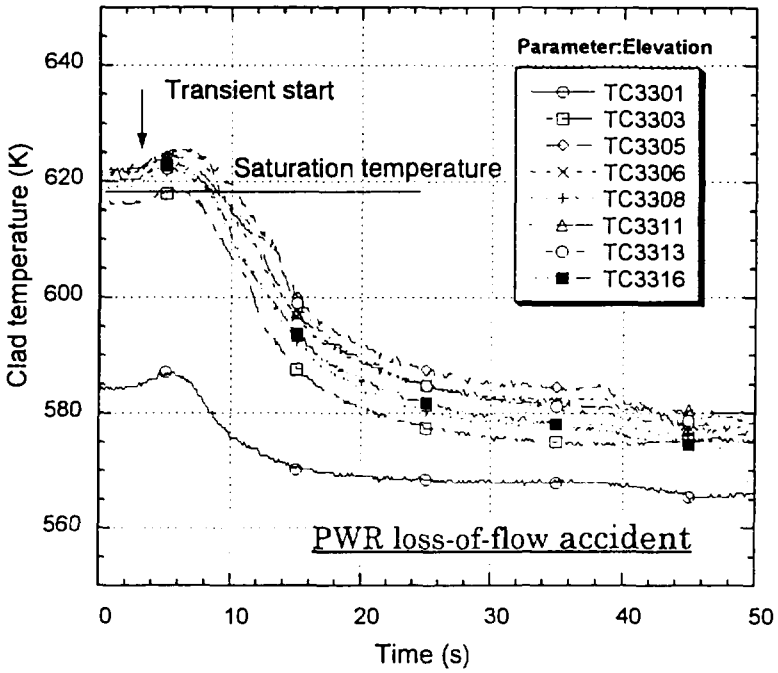

Fig.9.1.1 Clad temperature at PWR loss-of-flow accident simulation test

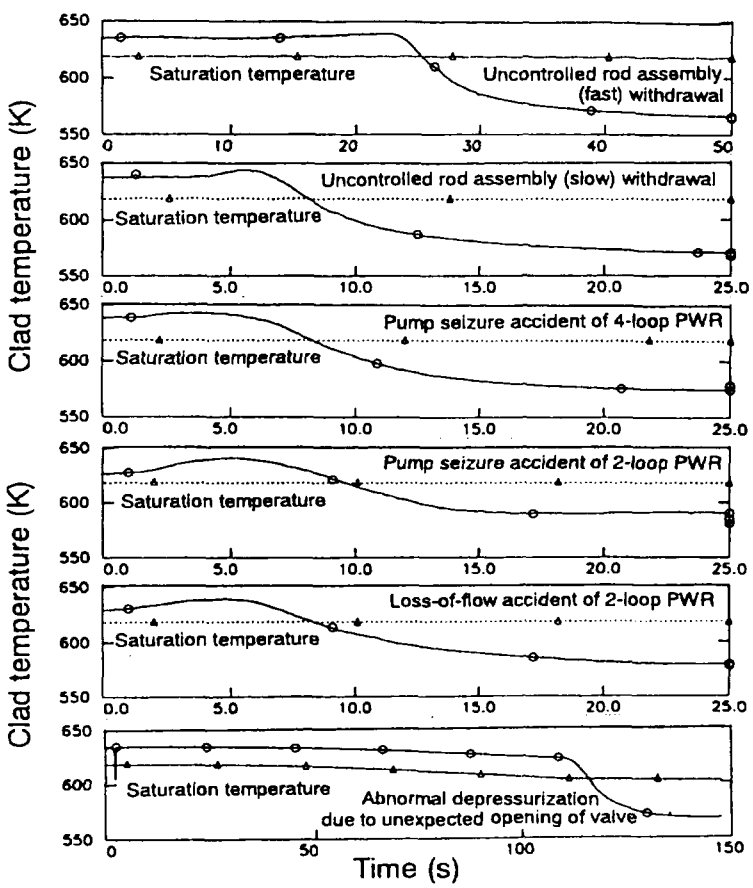

Fig.9.1.2 Clad temperature at PWR Abnormal Transient Simulation Tests

9.2 Post CHF Heat Transfer Tests with Thermal Hydraulic Demonstration Test Facility

C. Iwaki, T. Iguchi, A. Ohnuki, M. Kureta and H. Akimoto
(*E-mail*: iwaki@sag.nel.rdc.toshiba.co.jp)

Post-CHF tests were performed to study the post-CHF heat transfer and rewetting behavior under DBEs and beyond-DBE conditions. The test were performed with a single rod test section of Thermal Hydraulic Demonstration Test Facility. The single rod test section consists of a rod-type electrical heater and a surrounding round flow channel. Rod diameter, heated length of the rod and channel diameter are 9.5mm, 3.66m, and 14.2mm, respectively. Axial power shape of the heated rod is chopped cosine with a peaking factor of 1.55. Test procedure is a traditional way. Power supplied to the heated rod was increased step by step. The power increase was continued until the superheat of cladding became almost 300 K. Then, power was decreased until rewetting took place.

Major experimental conditions of the present tests are as follows.:

- Pressure : 2MPa to 15.5MPa
- Mass velocity : approximately 200 kg/m^{2}s to 3000 kg/m^{2}s
- Maximum clad temperature: 920 K

The clad temperature of the heated rod was measured with ungrounded sheathed thermo-couple of 0.5 mm outer diameter, which was buried on the clad of the heated rod.

Figure 9.2.1 shows the measured clad temperature at 7MPa and 15.5MPa. Several clad temperatures at several elevations indicate sudden increase from nearly saturation temperature accompanying with small temperature oscillation. (Analog data indicate temperature oscillation clearly, although this figure does not indicate it clearly.) When power increases further, clad temperature becomes stable. Thus, it is oscillatory at lower superheat and stable at higher superheat. It is stable even at lower superheat under higher pressure, as noticed from these figures. Therefore, scattering of data is small for higher pressure, and then the

clear boiling curve can be obtained as shown in Fig. 9.2.2. Boiling curve obtained in the present test indicates the transition from nucleate boiling to stable film boiling clearly under forced convective and high pressure conditions.

Heat transfer coefficient at stable clad temperature was calculated by assuming fluid temperature was saturation. The calculated heat transfer coefficient is shown in Fig. 9.2.3. X axis is superheat. Parameter is mass velocity, in upper figure, and parameter is pressure in lower figure. Figures indicate that the higher superheat gives the lower heat transfer coefficient. When superheat is low (less than 100 K - 250 K depending on pressure), superheat effect on heat transfer coefficient is significant. On the other hand, when superheat is large, the effect is little. And, heat transfer coefficient is higher at higher mass velocity and lower pressure.

Figure 9.2.4 shows the relation between Re number and Nu number. Data in this figure were chosen when superheat was larger than 200 K. This figure indicates that Nu number is almost proportional to 0.8 power of Re number. This suggests that the forced convection is dominant at higher superheat.

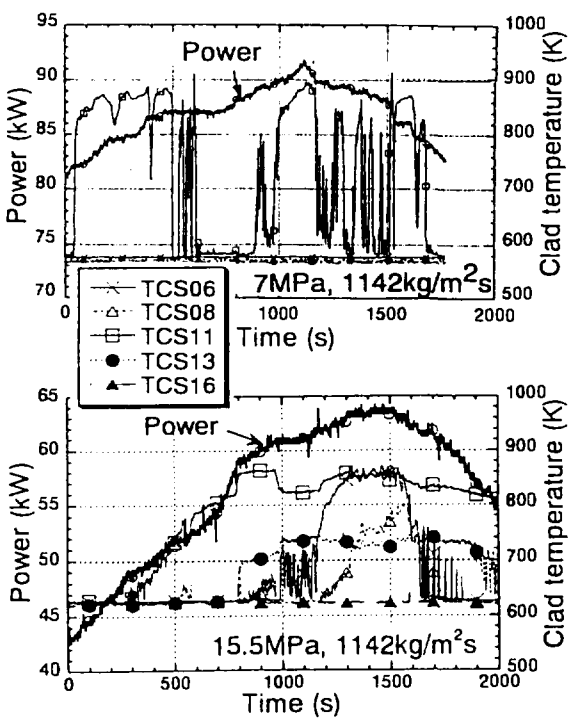

Fig. 9.2.1 Measured clad temperature

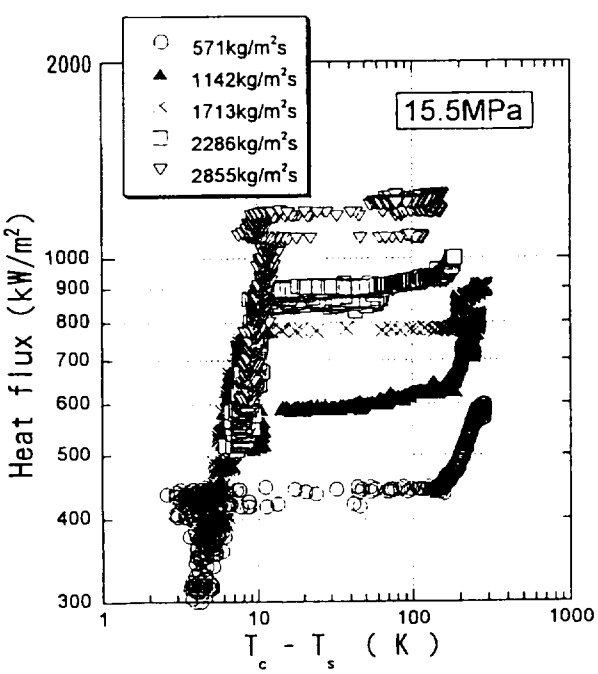

Fig. 9.2.2 Boiling curve

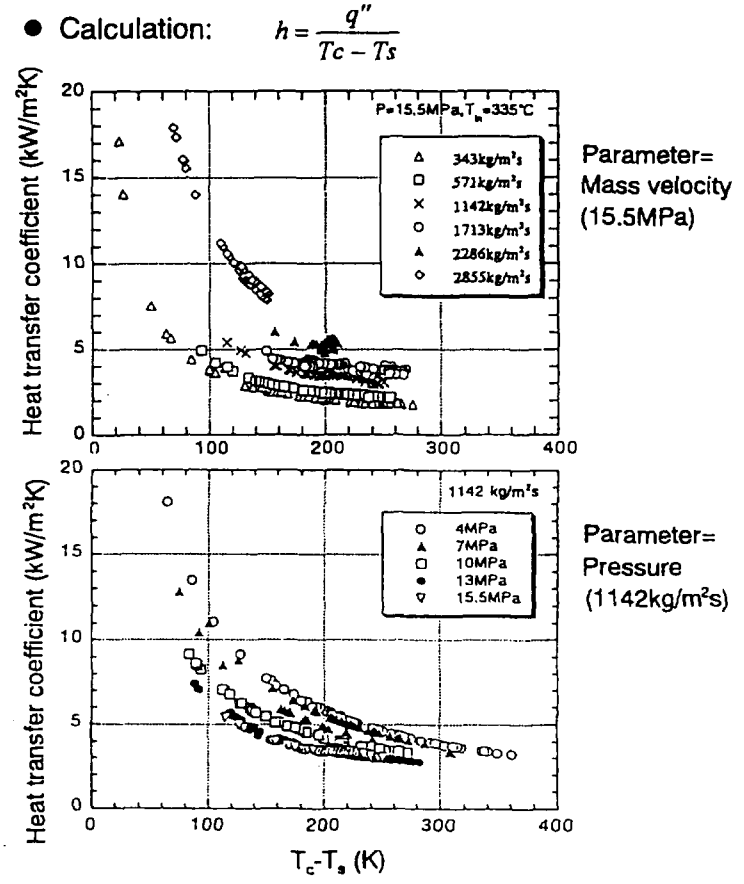

Fig. 9.2.3 Heat transfer coefficient

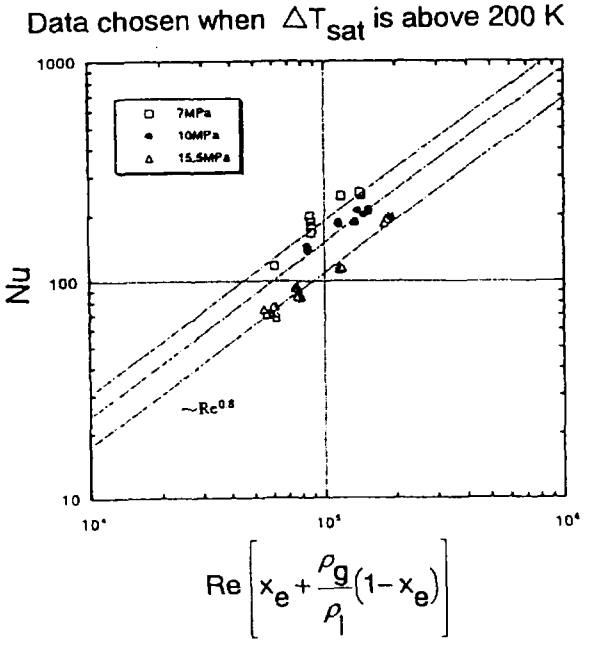

Fig. 9.2.4 Relation between Nu and Re numbers

9.3 Assessment of Boundary Conditions in Core Thermal-hydraulic Test for LWRs by J-TRAC Three Dimensional Calculations

A. Ohnuki, T. Iguchi, M. Kureta and H. Akimoto
(*E-mail*: ohnuki@hfl1.tokai.jaeri.go.jp)

In the core thermal-hydraulic transient test for LWRs[1], we are performing simulation tests to evaluate the core integrity of LWRs against abnormal operational events or accidents. In order to perform the simulation tests, it is necessary to know the core boundary conditions (Pressure, core power, flow rate and coolant temperature) because the test facility properly simulates only the core part. The core boundary conditions are estimated through predictions with reliable analysis codes, i.e. J-TRAC, TRAC-BF1 codes. In analyzing transient phenomena in PWR, J-TRAC code[2] is used but most of the system calculations are performed with one-dimensional nodarization. To check the validity of the one-dimensional (1D) calculations, we performed system calculations with three-dimensional (3D) nodarization for reactor vessel.

Four-loop PWR (1100MWe) was modeled in the analysis. The reactor vessel was divided by 23 (12 in core) in the axial direction, 5 (3 in core) in the radial direction and 8 in the azimuthal direction. The fuel assembly is 17x17 type one and the radial peaking factor for high power rod and the axial peaking factor are 1.552 and 1.495, respectively. The radial power distribution for average power rod was derived from the estimated results for initial period of equilibrium core[3]. The 3D calculations were performed for the following severe events chosen based on previous licensing calculations: Flow reduction events (Pump seizure and loss-of-flow accidents), power increase events and depressurization events. The DNB heat flux was evaluated by EPRI correlation[4].

The calculated results in the 3D case were almost the same as those in the 1D case against over-all behavior such as pressure at pressurizer, total core inlet flow rate, thermal-hydraulic behavior in each loop and so on. However, the radial distribution of flow rate and fluid temperature in the core were calculated in the 3D calculations. Figures 9.3.1 and 9.3.2 show the calculated results in the 3D case for the pump seizure (one loop) accident. At the bottom of core, the axial mass velocity at core center region is about 3 % higher than that at core periphery region but on the contrary the axial mass velocity at core center is about 5 % lower than that at core periphery at the top of core. The fluid temperature becomes higher in the core center region than that in the periphery region due to the distribution of the mass

velocity and the core power. The DNBR derived from the EPRI correlation became lower in the core center region due to the above distribution. These results indicate that the effect of the reduction of axial mass velocity in the core center region should be evaluated in the core thermal-hydraulic transient test. To evaluate the reduction of DNBR due to the radial distribution, it was found to be enough to perform tests under about 3 % lower core inlet flow rate than average one through calculations for the severe events mentioned above.

References

1) Iguchi T. et al.: JAERI-Review 96-012 (1966) 172.
2) Akimoto H. et al.: Proc. 5th Int. Topical Mtg. On Reactor Thermal Hydraulics (NURETH-5), Vol. 4 (1992) 1797.
3) Mitsubishi Atomic Power Industry: MAPI-1066 (1986) in Japanese.
4) Reddy D.G. and Fighetti C.F.: EPRI NP-2609, Vol. 2 (1982).

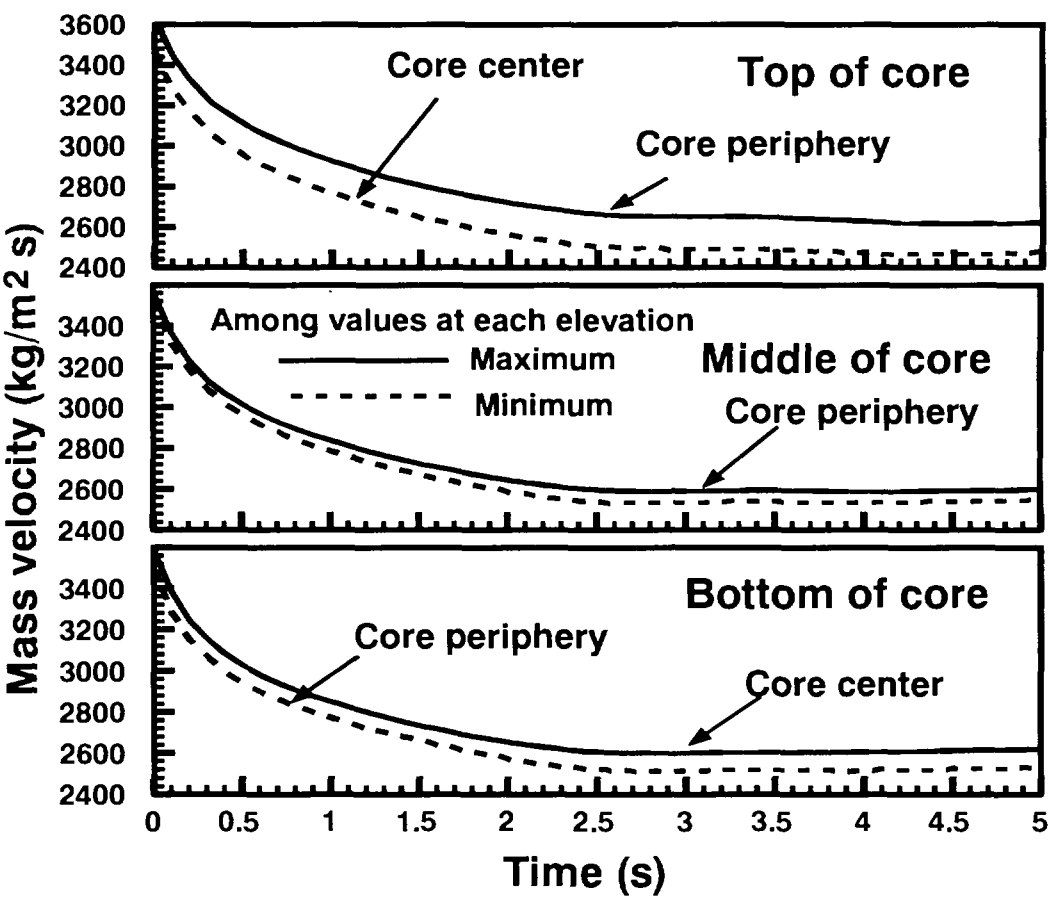

Fig. 9.3.1 Comparison of radial distribution of axial mass velocity at each elevation

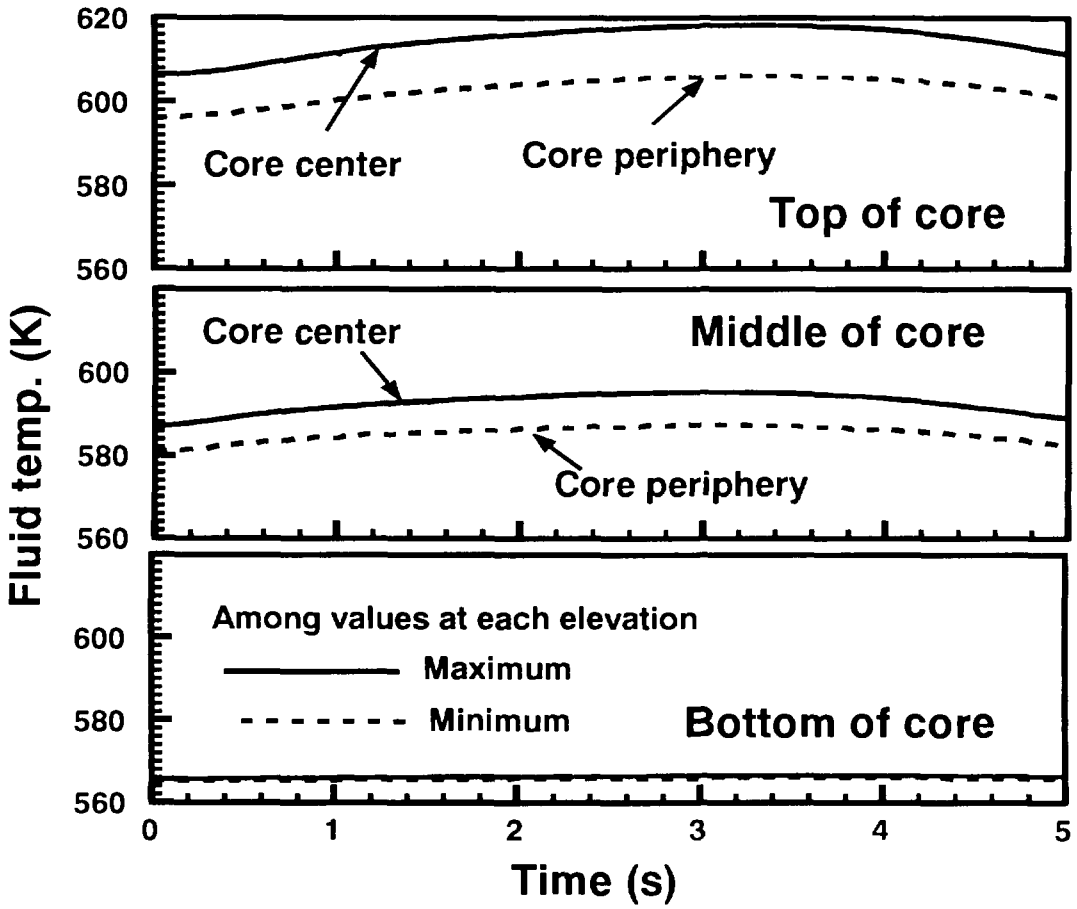

Fig. 9.3.2 Comparison of radial distribution of fluid temperature at each elevation

9.4 Prediction of Developing Bubbly Flow along a Large Vertical Pipe by Multidimensional Two-fluid Model

A. Ohnuki and H. Akimoto
(*E-mail*: ohnuki@hfl1.tokai.jaeri.go.jp)

Development of reliable constitutive equations is necessary to establish an analytical tool based on multidimensional two-fluid model for design calculations of passive safety reactors. To construct the constitutive equations, we developed a multidimensional two-fluid model code with a two-phase k-ε turbulent model as a driver code[1] and investigate the applicability of existing constitutive equations to an air-water two-phase flow along a large vertical pipe (inner diameter D of 0.48 m and 0.2 m). In this section, the predictability of existing constitutive equations (lift force model and turbulent dispersion model)[2)3)] is discussed for a developing bubbly flow along the large vertical pipe (D of 0.48 m)[4].

The effect of lift force on the distribution of phase and liquid velocity is investigated by the change of coefficient C_L of lift force model. Figure 9.4.1 compares the distribution of void fraction and liquid velocity along the large vertical pipe. The air and water flow rate (superficial air velocity: 0.14 m/s and superficial water velocity: 0.18 m/s) are relatively low in this calculation and the flow pattern in the experiment was an agitated bubbly flow. The locations of L/D = 3.8, 1.7 and 0.2 (L: length of flow path) are the top, middle and bottom regions in the test section, respectively. It is found that a negative value of C_L is needed to predict the measured data qualitatively and quantitatively.

The negative value of C_L produces the lift force acting toward the pipe center under an upward flow with a convex liquid velocity distribution. Tomiyama et al. [5] reported through experiments and numerical analyses that the lift force acting on a large and distorted bubble directs toward the center of a flow path in an upward flow. Since the flow rate condition in this calculation is near the bubbly-slug flow transition condition by Mishima and Ishii[6], large and distorted bubbles might be dominant although no slug bubbles occupying the flow path were not observed in the experiment.

The effect of turbulent dispersion force on the distribution of phase and liquid velocity is investigated by the change of coefficient C_{td} of turbulent dispersion model. Figure 9.4.2 compares the distribution along the large vertical pipe. The values of C_L was -0.2 in this comparison. The following remarks can be stated from this comparison:

(1) The distribution of liquid velocity is insensitive to C_{td}.

(2) The phase distribution is better predicted with a larger value of C_{td} above about middle of test section, while it is better predicted with C_{td} less than 0.2 at the bottom of test section.

The results of (2) indicate that the whole behavior along the large vertical pipe is difficult to be predicted with a constant C_{td}, although the phase distribution at a elevation is predicted reasonably with a proper value of C_{td}.

From the above results, it is concluded that the developing bubbly flow is predicted reasonably using a lift force model to produce a lift force acting from wall to the pipe center although the change of phase distribution along the developing region is difficult to be predicted accurately using a turbulent dispersion model with a constant empirical coefficient. Since these remarks are obtained under a low flow rate condition, the study under several flow rate conditions should be performed to investigate the applicability of the existing constitutive equations in the future.

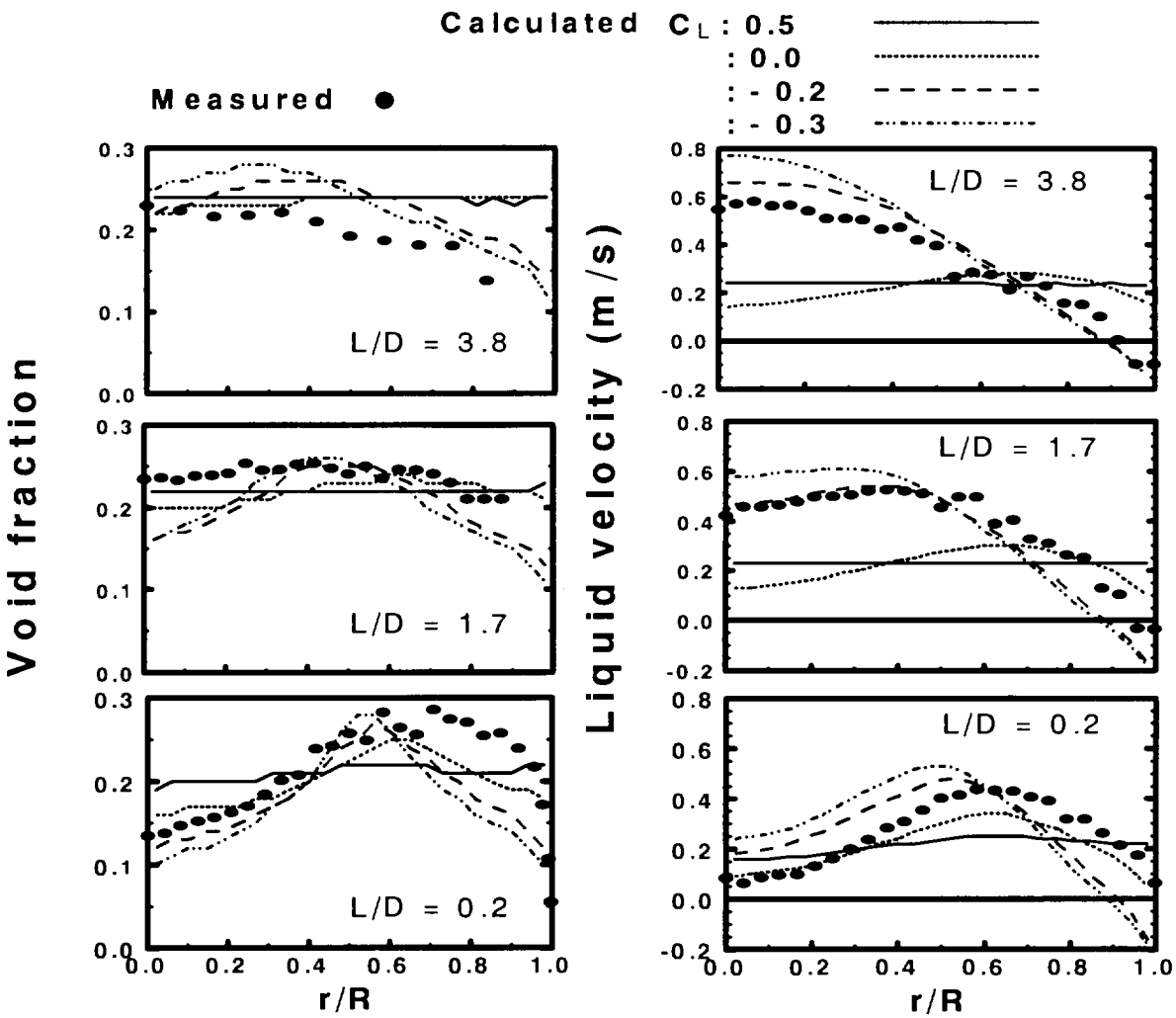

Fig. 9.4.1 Sensitivity analyses for lift force along large vertical pipe

References

1) Ohnuki A. et al.: JAERI-Data/Code 96-033 (1996) in Japanese.
2) Drew D. A. and Lahey Jr. R. T.: Int. J. Multiphase Flow, 13[1] (1987) 113.
3) Lahey Jr. R. T. and de Bertodano M. L.: ASME/JSME Thermal Eng. Proc., Vol. 2 (1991) 193.
4) Ohnuki A. et al., Proc. of The 2nd Int. Conf. on Multiphase Flow '95-Kyoto, Vol. 3 (1995) FT1-17.
5) Tomiyama A. et al.: Proc. of The 2nd Int. Conf. on Multiphase Flow '95-Kyoto, Vol. 1 (1995) PD1-11.
6) Mishima K. and Ishii M., Int. J. Heat Mass Transfer, 27[5] (1984) 723.

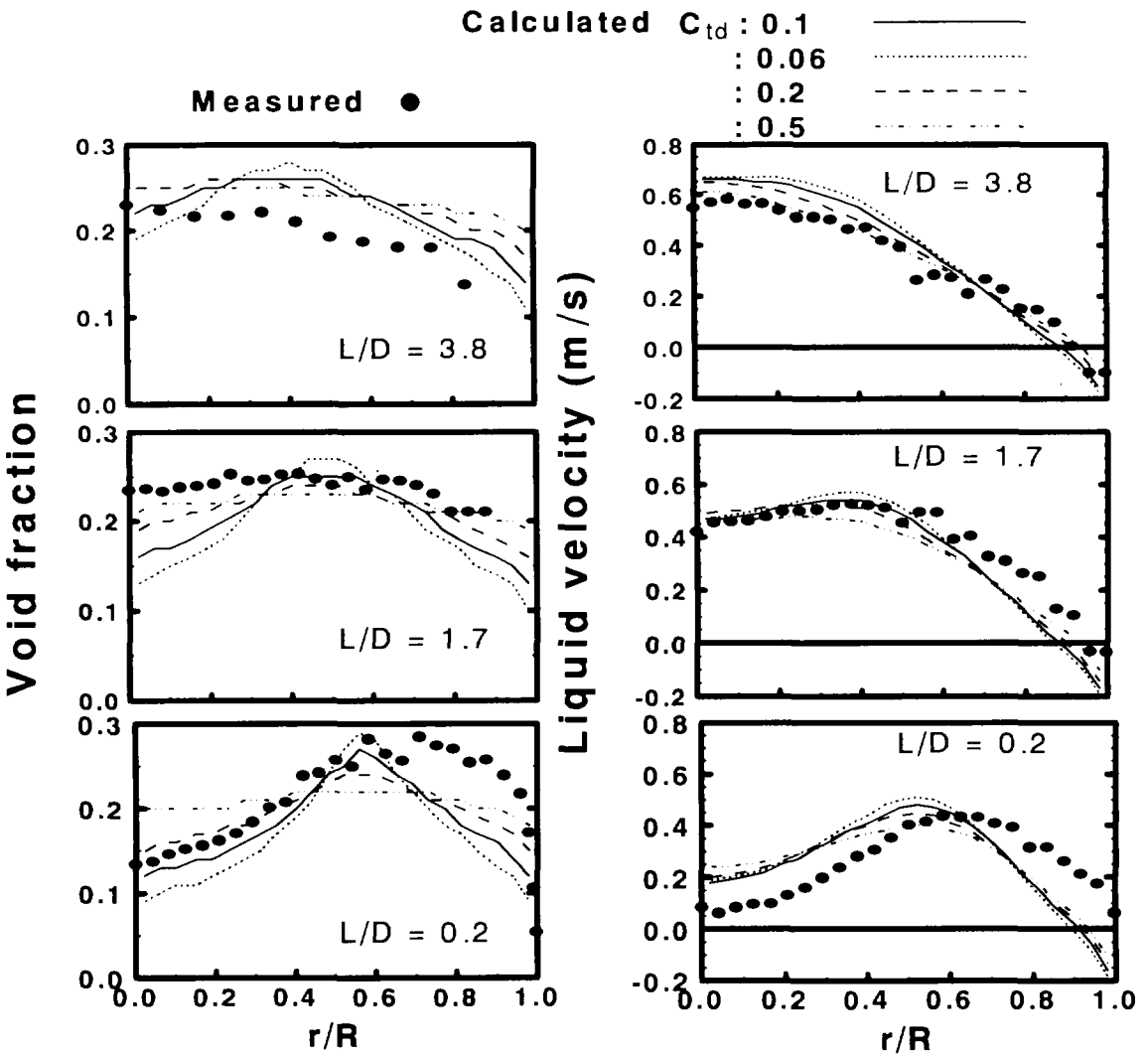

Fig. 9.4.2 Sensitivity analyses for turbulent dispersion force along large vertical pipe

9.5 Burnout in the Rectangular Flow Channel

M. Kureta and H. Akimoto
(*E-mail*: kureta@hfl1.tokai.jaeri.go.jp)

Systematic understanding of burnout for subcooled forced-convection boiling water in a rectangular flow channel is necessary to establish a cooling methods for the heat removal under very high heat flux conditions. It may be applicable to such wide fields as heat removal from a target of an intense neutron source and high-energy light beam, a fusion reactor component, etc. These components receive a high heat flux of 10 to 100 MW/m^2 from one side.

Experiments are performed to measure critical heat flux (CHF) for the system cooled by highly subcooled water at a high velocity. The water flows vertically up-flow thorough a rectangular flow channel by forced convection as shown in Fig. 9.5.1. Channel gap is 3 mm, channel width from 7 to 22 mm, heated width from 5 to 20 mm and heated length from 50 to 200 mm. The exit of the channel is opened to the atmosphere. Test data were taken over inlet velocity range from 1 to 15 m/s and inlet water temperature range from 30 to 90 ℃. The one side of the flow channel is heated by the copper film of 5 μ m thick on the printed wiring board electrically. In order to make parameter effects on CHF clear, experiments were carried out parametrically. The heat flux on the copper film was calculated from the measured voltage at every 12mm section and measured electric current. CHF was determined by the burnout of the copper film. Some representative experimental runs involved the use of photographic techniques to trace the development of the boiling process prior to CHF observed thorough the transparent flow channel made of the polycarbonate resin.

Most of the CHF data were taken in the minus exit quality region. In order to investigate the relation between the subcooled boiling-flow characteristics and the trigger mechanism of the burnout, the maximum vapor length were measured from photos which were taken just before burnout. Fig. 9.5.2 shows the relation between maximum vapor length, CHF and inlet velocity. Fig. 9.5.2 indicates that the maximum vapor length decrease almost lineally if the vapor becomes larger than 0.1 mm. The experimental program investigated the effect of width, length, velocity and inlet water temperature. Fig. 9.5.3 shows that the effect of the heated width W_h on CHF for inlet water temperature T_{in}=30℃ and heated length L_h=50mm. The figure shows that the effect of W_h on CHF was comparatively small. Fig. 9.5.4 shows that the effect of L_h on CHF for T_{in}=30℃ and W_h=10mm. The figure indicates that the

CHF increases with decreasing L_h. The same tendency has been reported in the case of small-diameter tubes[1]. The effect of heated length appears to be remarkable, particularly when T_{in} is small. Generally burnout occurs at the exit of the heated channel. It was found that the vapor length at the exit decreased with decreasing L_h from the observation. The channel with short heated length makes the vapor small at the same heat flux condition and increases CHF. Fig. 9.5.5 shows that the effect of T_{in} on CHF for L_h=50mm and W_h=10mm. The figure indicates that the CHF increases with increasing inlet velocity u_{in} and with decreasing T_{in}. The effect of inlet water temperature appears to be remarkable, particularly when L_h is small. The highest CHF attained in this experiment was 15MW/m^2 in a channel with W_h=10mm, L_h=50mm, u_{in}=15m/s and T_{in}=30℃.

CHF data were compared with several existing CHF mechanistic models to find and develop models to be used in the design calculation. Katto[2], Celata[3] et al. have developed the CHF models based on the liquid sublayer dryout mechanism. These models assumed that the burnout occurs when a thin liquid sublayer beneath an elongated vapor blanket characterized by bubbly detachment diameter and Helmholtz instability at the liquid sublayer/vapor interface is completely depleted during the passage time of vapor blanket. The predictability of the models to rectangular flow channels heated from one side has been investigated by comparing with present data as shown in Fig. 9.5.6. From the comparison for Celata model, it was found that his model gives over-prediction when inlet water temperature and heated length are smaller. Katto model gives void fraction higher than 0.7 in applying his model. Modified Katto model which was changed to k = k1 or k2 and quality was assumed zero gives relatively good agreement with most of the present data.

References

1) Kureta M. et al. : Trans. JSME, 61-591, B, (1996) 4109-4116, in Japanese.
2) Katto Y. : Int. J. Heat Mass Transfer, 35-5 (1992) 1115-1123.
3) Celata G. P. et al. : Int. J. Heat Mass Transfer, 37-1 (1994) 347-360.

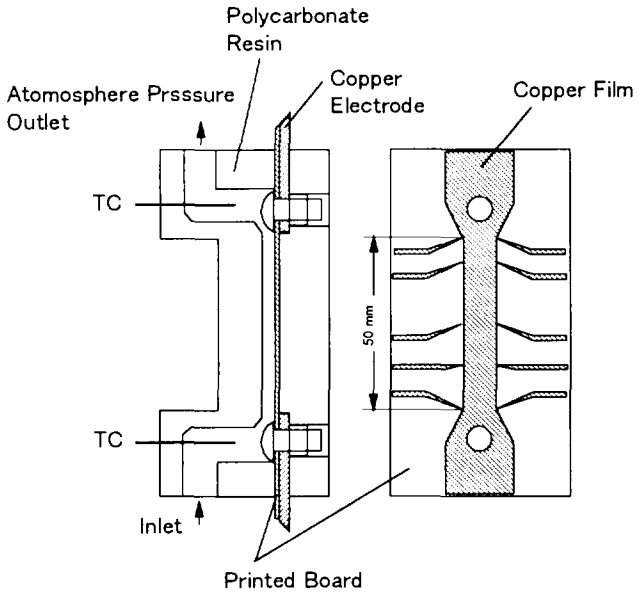

Fig. 9.5.1 Schematic of test section

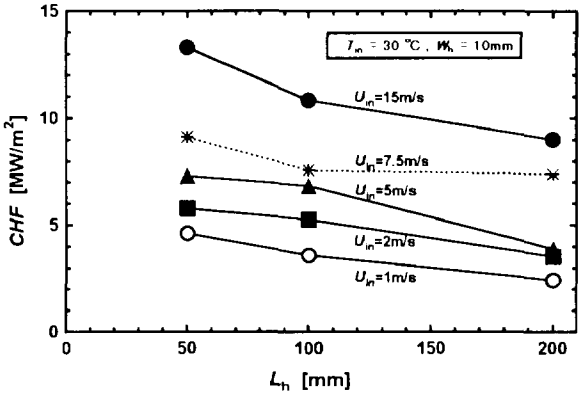

Fig. 9.5.4 Effect of heated length on CHF for T_{in}=30℃, W_h=10 mm

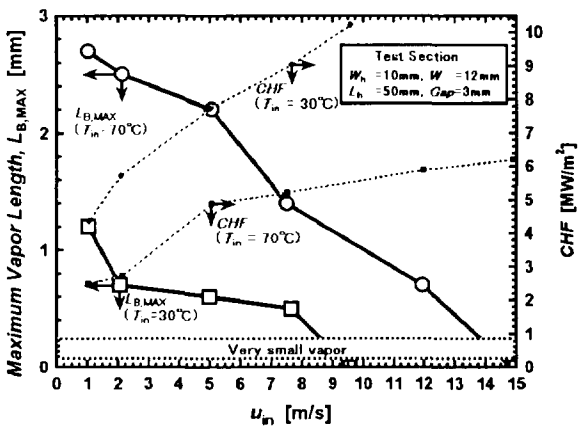

Fig. 9.5.2 Relation between maximum vapor length, CHF and inlet velocity

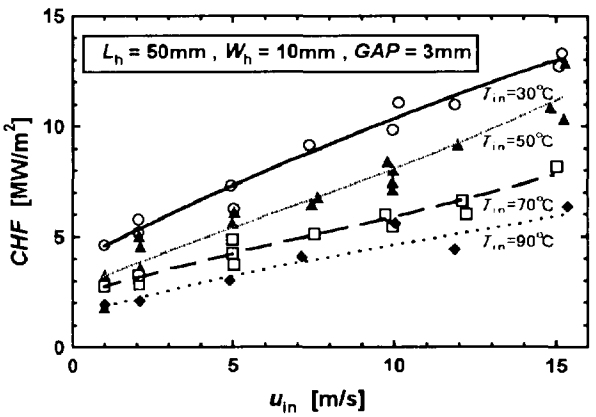

Fig. 9.5.5 Effect of inlet water temperature on CHF for W_h=10 mm, L_h=50mm

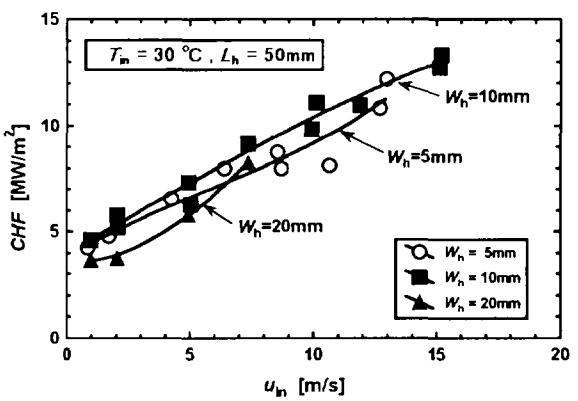

Fig. 9.5.3 Effect of heated width on CHF for T_{in}=30℃, L_h=50 mm

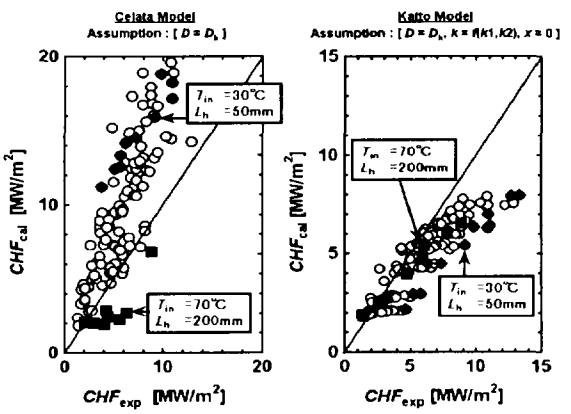

Fig. 9.5.6 Comparison between the present CHF data and Celata and Katto models

9.6 Phenomenological Analysis of Experiments for Natural Circulation Two-phase Flow Instability

J. U. Knebel* and F. Araya
(*E-mail:* araya@jpsrews1.tokai.jaeri.go.jp)

In concepts of next generation light water reactors natural circulation is used to passively remove the heat generated in the core to heat exchangers. With natural circulation flow the driving forces are very low and flow instabilities can possibly occur. Flow instabilities are not desirable in boiling two-phase flow process, as sustained flow oscillations may induce mechanical vibrations of components and cause problems in system control and/or degradation of heat removal capabilities. In order to avoid such conditions during the design phase, thermo-hydraulic computer codes are used to predict the boundary of flow instability and to allow the designer to improve the system. However, these codes are not well verified for natural circulation flow, especially not for unstable flow conditions. In order to give a data-base to verify the applicability of the codes to unstable flow conditions, a series of experiments on the natural circulation two-phase flow instability was performed at JAERI.

The experiments are performed in the high-pressure water loop HPWL shown in Fig. 9.6.1. The main parts of the loop are a heated section, a slide valve, a riser, a cooler, an orifice flow meter and a pressurizer. The main flow pipe is made with a 2-B pipe (inner diameter of 43.1 mm). The heated section consists of a seven hexagonal arranged heater rods with a equivalent hydraulic diameter of 10.75 mm and 1400 mm heated length. The heat is supplied by Joule heating of AC electric power. The power distribution is a cosine shape. The valve is used to vary the friction at the outlet of the heated section. The orifice flowmeter is a quarter circle type orifice with a 10.53 mm diameter. The system pressure can be varied from 0.4 MPa to 16MPa. The height difference between centers of the heated section and the cooler is 4.9m. HPWL is well instrumented with 13 differential pressure gauges, one pressure gauge and 13 thermocouples in the natural circulation loop.

The independent parameters in the experiments are the system pressure, the heater power and the flow resistance at the outlet of the heated section. The system pressure is controlled by the pressurizer heater and spray system. The flow resistance is changed by changing the resistance valve area (stem position). In the present state of the test facility, the cooler secondary side is at atmospheric pressure only. Thus, the inlet temperature at the heater section is not actively controlled and therefore determined by the system characteristics of the natural circulation loop. The stable/unstable boundary is found experimentally by reducing

---

* Invited foreign researcher from Forschungszentrum Karlsruhe FZK, Germany.

the heater power at the same pressure and resistance condition, starting from an unstable condition. The range of the system parameters in the experiments performed up to now are listed in Table 9.6.1.

The results obtained by the experiments can be summarized as follows: (1) The coupling between buoyancy effects and phase change is considered by the non-dimensional combination $N_{PCh} \cdot N_{Fr}^{-1/2}$ for the abscissa and subcooling N_{Sub} for the ordinate in the stability diagram. Here, N_{PCh}, N_{Fr} and N_{Sub} are the phase change number, Froude number and subcooling number, respectively. The distinction between the stable and unstable region over a wide range of the system pressures is possible on this newly proposed stability diagram as shown in Fig. 9.6.2. (2) Increasing the Froude number N_{Fr} makes the natural circulation system less stable. (3) Increasing the resistance coefficient at the exit of the heated section makes the system less stable. (4) When increasing the heating power, the inlet velocity at the heated section is increasing linearly. (5) Increasing the pressure always stabilizes the system. The mean time period of an oscillation is about 2 to 3 times of the mean traveling time. The experimental results shows that the observed flow oscillations are of the density wave oscillation.

Table 9.6.1 System parameter ranges

Parameter	Range
Pressure (MPa)	0.3 to 15.4
Heating power (kW)	4.4 to 160
Resistance valve stem position (%)	25, 30, 35, 40, 100

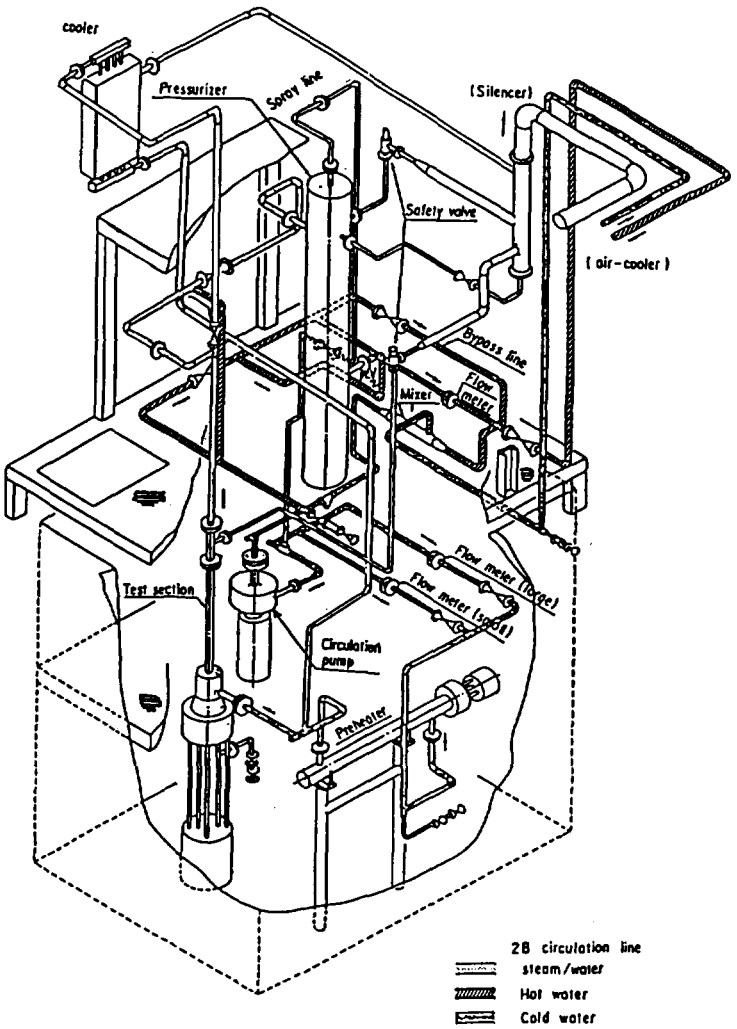

Fig. 9.6.1 Bird's eye view of the high-pressure water loop.

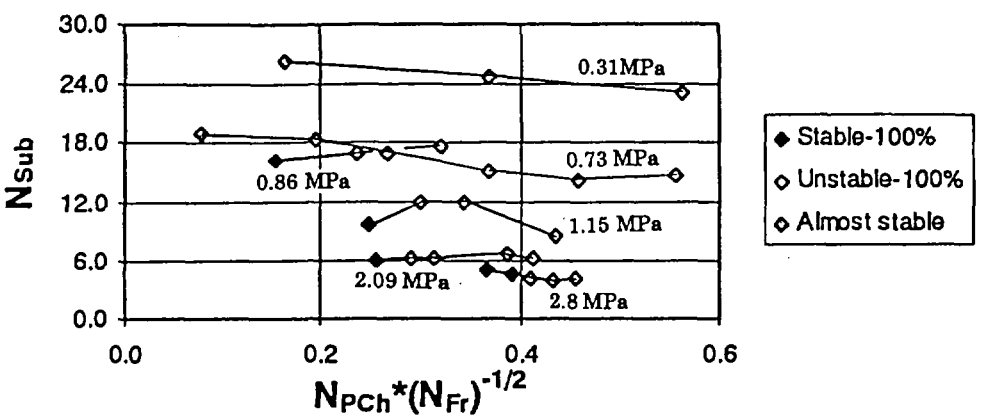

Fig. 9.6.2 Stability diagram for natural circulation as N_{Sub} vs. $N_{PCh} \cdot N_{Fr}^{-1/2}$ (cases of 100% of resistance valve stem position).

9.7 Fusion Safety Experiments

T. Kunugi and K. Takase
(*E-mail*: kunugi@popsvr.tokai.jaeri.go.jp)

Two experimental studies on the thermal-hydraulic safety for a fusion reactor, ingress of coolant events (ICE) and loss of vacuum events (LOVA), have been carried out as ITER[1] safety R&D subtasks since 1995 to obtain validation data for fusion safety analysis codes under ICE and LOVA conditions.

The severest scenario of ICE and LOVA in the fusion reactor can be considered as follows[2]: When the plasma-facing components (PFCs) in the vacuum vessel (VV) are broken by some damage, such as the plasma disruption, the cooling water is discharged into the VV and evaporates on the PFCs (This is the ICE). The rapid evaporation of the water will make a shock wave and lead to a pressurization in the VV. As a result of this, the high pressure may cause the destruction of the VV and then a lot of activated materials and tritium may be released from breaches to the outside of the VV (This is the LOVA).

The ICE experimental apparatus[3] is shown in Fig. 9.7.1. It consists of the VV, a boiler, a water injector, a water nozzle, a suppression tank and a vacuum pump. The VV can be heated up to 400°C by heater plates installed in the VV. The water nozzle is set on the inside wall of the VV and connected to the water injector. In the ICE experiments, the water with high pressure and temperature produced by the boiler was discharged into the VV from the water nozzle through the water injector, and the pressure rise and temperatures in the VV were measured quantitatively.

Figure 9.7.2 shows the transient behavior of pressure rise in the VV. Here, experimental conditions are as follows: the injection time is 10 s; the water nozzle diameter is 2 mm; the wall temperature in the VV is 250°C; and the water temperature is 200°C. The inside pressure of the VV increased rapidly while the water was injected into the VV and reached 0.45 MPa at 10 s. After the water injection it became 0.71 MPa at 70 s and then saturated.

On the other hand, the LOVA experimental apparatus[4] is shown in Fig. 9.7.3. It mainly consists of the VV, the weight measuring system and the preliminary flow visualization system. The VV is an annular enclosure with six simulated breaches and set on the weight measuring system. Two simulated breaches can be opened instantly and simultaneously by using pneumatic gate valves. The weight measuring system is composed of an electronic balance and data acquisition instruments. The exchange mass in the VV under the LOVA conditions can be measured by this electronic balance. The preliminary flow visualization system consists of a CCD camera, a slit light, a monitor TV, and a smoke generator. A

buoyancy-driven exchange flow through the breach can be visualized qualitatively by smoke.

Figure 9.7.4 shows the variation of exchange mass for different breach combinations[5]. Here, T1-B shows the case that T1 and B breaches were opened simultaneously; S1-B and T1-T2 are similar to above; and T1 shows the case that the T1 breach was only opened. For the T1-B case, the exchange mass increased rapidly to around 50 s from the beginning of the experiment and reached a saturation value of 0.43 kg in the time range of more than 100 s. The S1-B case showed almost the same feature as the T1-B case. On the other hand, the exchange mass at the T1-T2 case showed lower values than those of the T1-B and S1-B cases. Furthermore, the exchange mass at the T1 case increased monotonously, and it at 300 s was a half of that of the T1-B case. It was clarified from the LOVA experiments that the exchange mass depended upon the breach positions and numbers.

References

1) ITER Conceptual Design, IAEA ITER DS No. 18, IAEA (1991).
2) Kunugi T., et al.: Symposium on Fusion Engineering, Vol.16, 313(1995).
3) Takase K., st al.: Fusion Technology, Vol.30, No.3, 1453(1996).
4) Takase K., st al.: Symposium on Fusion Engineering, Vol.16, 317(1995).
5) Takase K., st al.: Fusion Technology, Vol.30, No.3, 1459(1996).

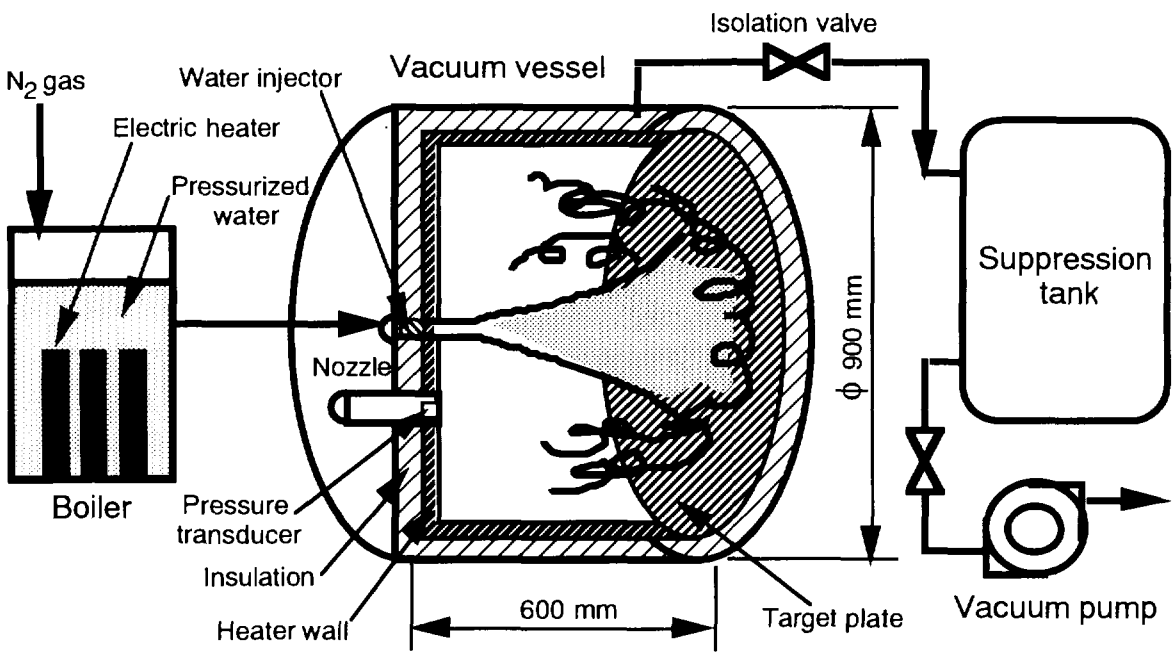

Fig. 9.7.1 Schematic drawing of the ICE experimental apparatus

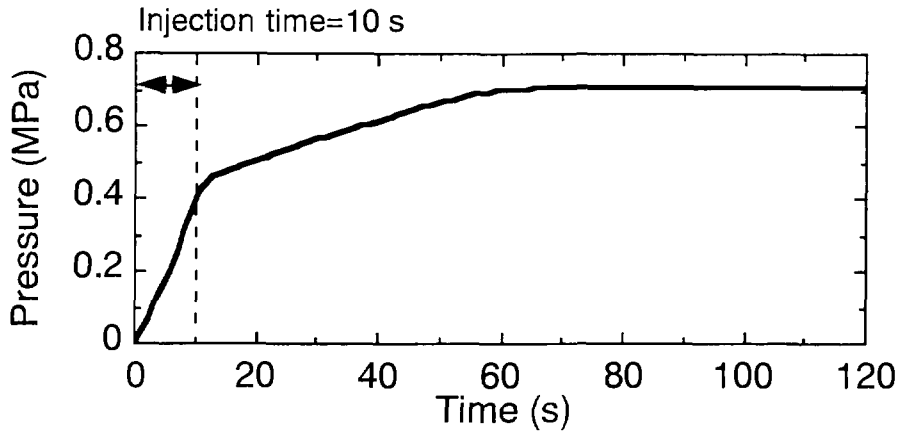

Fig. 9.7.2 Pressure rise in the VV vs. time under the ICE condition

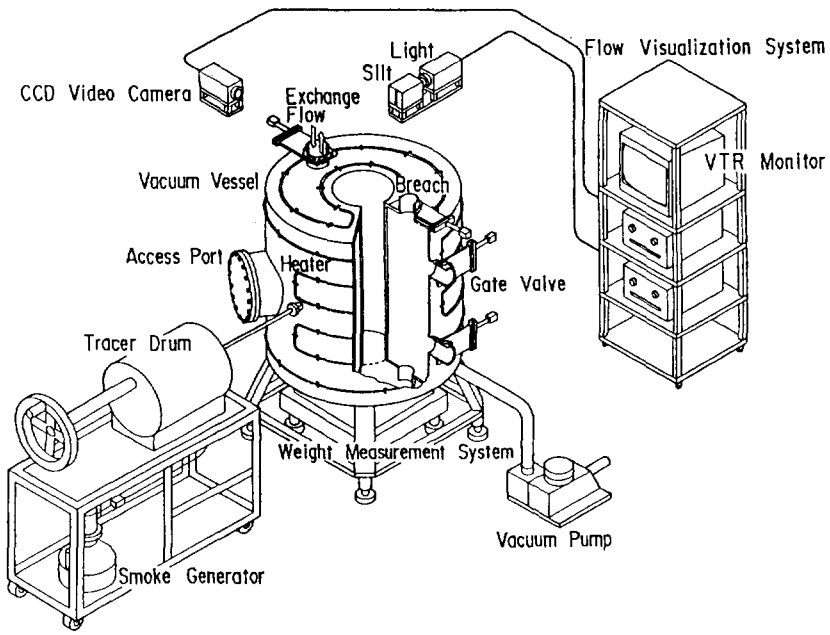

Fig. 9.7.3 Schematic drawing of the LOVA experimental apparatus

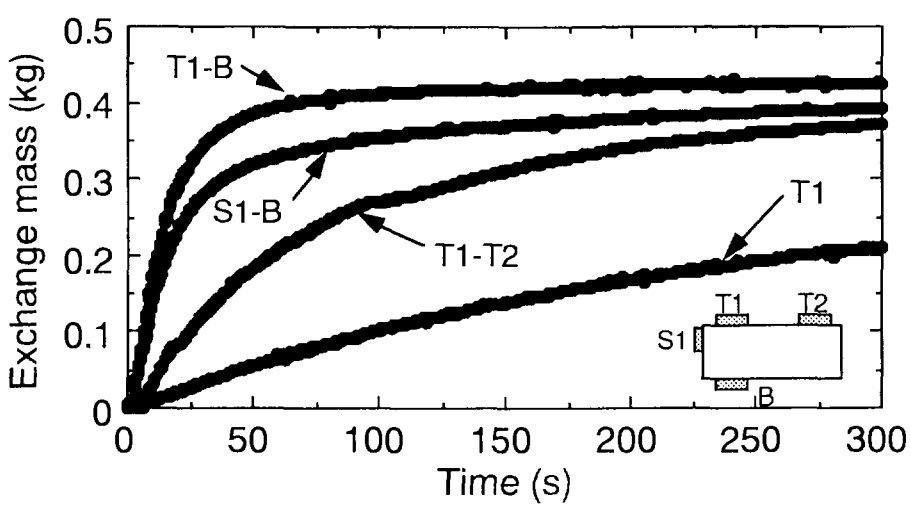

Fig. 9.7.4 Exchange mass vs. time under the LOVA conditions

10. Transmutation System

The construction of the research facilities for the accelerator-driven transmutation system are planned in the Neutron Science Research Project. Target thermal-hydraulic experiment facility, high-power target experiment facility, transmutation reactor physics experiment facility and transmutation experimental reactor are included in this project. The preliminary design studies for these facilities has been carried out.

The conceptual design for accelerator-driven transmutation system with TRU-metallic fuel has been proposed. However, nitride fuel has many advantages over metallic fuel. The neutronics and burnup analyses are performed for the system with TRU-nitride fuel. In this system, the fuel with composition of (72MA-28Pu)-^{15}N are arranged as pin-bundle type assemblies around tungsten target and cooled by sodium flow. The tungsten target is injected by the proton beam with energy of 1.5 GeV. The calculation was performed by ATRAS code system with JENDL-3.2 library. The calculational results showed that the burnup swing in the system with nitride fuel was much smaller than that of metallic fueled system.

The calculation code systems for accelerator-driven system (ADS) are adapted to two different benchmark problems proposed by OECD/NEA and IAEA for the verification of the performances of these code systems. The benchmark problem proposed by OECD/NEA is a part of the NSC benchmark project on Physics Aspects of Different Transmutation Concepts. The purpose of another benchmark proposed by IAEA is to assess performances of ADS to achieve consensus on calculation methods and associated nuclear data. The calculations were performed by the ATRAS code system and a part of SPACE code system with the JENDL-3.2 library.

In order to study the transport of neutrons in a spallation target, reaction rate distribution on the surface of a cylindric tungsten target were measured with activation detectors of ^{27}Al, ^{31}P, ^{32}S, ^{209}Bi and so on. This study was a cooperative work between JAERI and Institute of Theoretical and Experimental Physics, Russia. The experiment was carried out at the booster beam line of Institute of High Energy Physics in Russia. The experimental analysis were calculated with the Monte Carlo simulation code systems of NMTC/JAERI-MCNP4A, LAHET and HERMES.

10.1 Research Facilities for the Accelerator-driven Transmutation Study at the Center for Neutron Science

T. Sasa, K. Tsujimoto, T. Nishida and T. Takizuka
(*E-mail:* sasa@omega.tokai.jaeri.go.jp)

In the neutron science research project, construction of the research facilities for the accelerator-driven transmutation are planed as shown in Fig. 10.1.1. This report summarizes the preliminary design study for the four facilities indicated in Fig. 10.1.1.

Target thermal-hydraulics experiment facility

Basic thermal-hydraulics experiments for the spallation target and beam window are planned to be performed at this facility using the 2 MW pulse proton beam. Tungsten disk target assembliy similar to the transmutation plant are used for the target. No fuel assemblies are placed and reflector assemblies surround the target assemblies as a shield. Whole assemblies and beam window are cooled by liquid sodium.

We performed the thermal-hydraulic analysis at the steady state and at the transients caused by the beam on and off. Transient response under the pulse beam operation must be analyzed more in detail. Figure 10.1.2 shows the bird's-eye view of the facility.

High-power target experiment facility

Reflecting the results got at the target thermal-hydraulics experiment facility, we will perform various tests for the target subassemblies under the similar exposure condition of the transmutation plant by the 7 MW continuous proton beam. The system configration of the experimental facility are almost same to that of the target thermal-hydraulics experiment facility.

We carried out the thermal-hydraulics analysis and got the satisfactory results.

Transmutation reactor physics experiment facility

We examined the feasibility of the multipurpose subcritical assembly for the development of various accelerator-driven nuclear system concepts such as transmutation

systems and fuel breeding systems operated with very low-power pulse proton beam.

Transmutation experimental reactor

A transmutation subcritical experimental reactor is planned to verify the technical feasibility of the accelerator-driven system and the performance of minor actinide transmutation. We divided the plan into two stages. In the first stage, transmutation performance will be tested using minor actinide fuel pellet and uranium oxide fuel at 30 MW of thermal power. Then fuel is changed to uranium nitride in the second stage, and verify the transmutation performance by minor actinide fuel pin or fuel assembly at a thermal output of 60 MW.

We carried out preliminary nuclear analysis and design of the whole system. Table 10.1.1 shows the transmutation performance of this reactor in the first and second stages. From this results, transmutation rate in the first stage seemed too low and some revision of the core design or reexaminations of the incident beam strength must be necessary.

For the transmutation research facilities, existing fast reactor technology can widely applicable. However, there still remain some difficulties such as the material property data under the proton-neutron irradiation.

Table 10.1.1 Transmutation performance of the transmutation experimental reactor

fuel	Flux point	Reaction rate (/sec./1-target atom) and ratio to Pu-MA-Nitride core								average energy (MeV)	frac. of flux >1MeV
		Np-237	Am-241	Am-243	Cm-243	Cm-244	Cm-245	Tc-99	I-129		
Pu-MA Nitride (800MWth)	Core Average	7.97E+15	7.24E+15	5.50E+15	3.19E+16	9.54E+15	2.86E+16	3.68E+15	2.19E+15	0.831	27.4%
Nitride: U(U-235 20%)N Core average (30MWth)	Core Average	2.54E+14	2.13E+14	1.57E+14	1.50E+15	3.12E+14	1.32E+15	1.89E+14	1.08E+14	0.602	18.7%
		0.032	0.029	0.029	0.047	0.033	0.046	0.051	0.049		
	Peak point at R=10cm, Z=32cm from top	3.95E+14	3.29E+14	2.44E+14	2.20E+15	4.83E+14	1.97E+15	2.92E+14	1.70E+14	0.613	18.2%
		0.050	0.045	0.044	0.069	0.051	0.069	0.079	0.078		
Oxide: U(U-235 20%)O, Core average (30MWth)	Core Average	2.05E+14	1.73E+14	1.28E+14	1.49E+15	2.54E+14	1.30E+15	1.97E+14	1.10E+14	0.547	16.7%
		0.026	0.024	0.023	0.047	0.027	0.045	0.054	0.050		
	Peak point at R=10cm, Z=32cm from top	3.42E+14	2.88E+14	2.13E+14	2.32E+15	4.22E+14	2.06E+15	3.25E+14	1.84E+14	0.564	16.3%
		0.043	0.040	0.039	0.073	0.044	0.072	0.088	0.084		

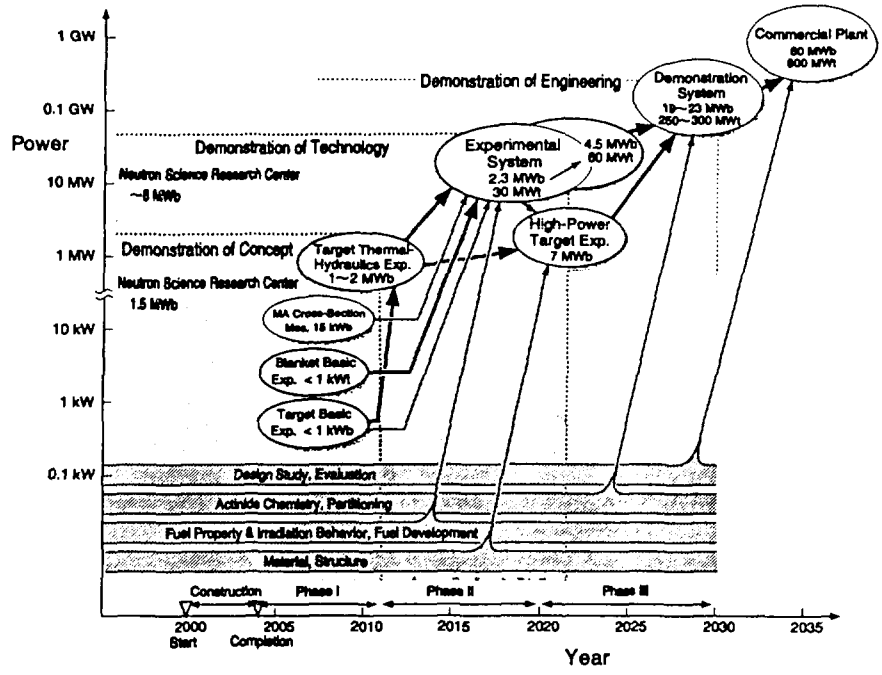

Fig. 10.1.1 Scenario for development of accelerator-driven transmutation system

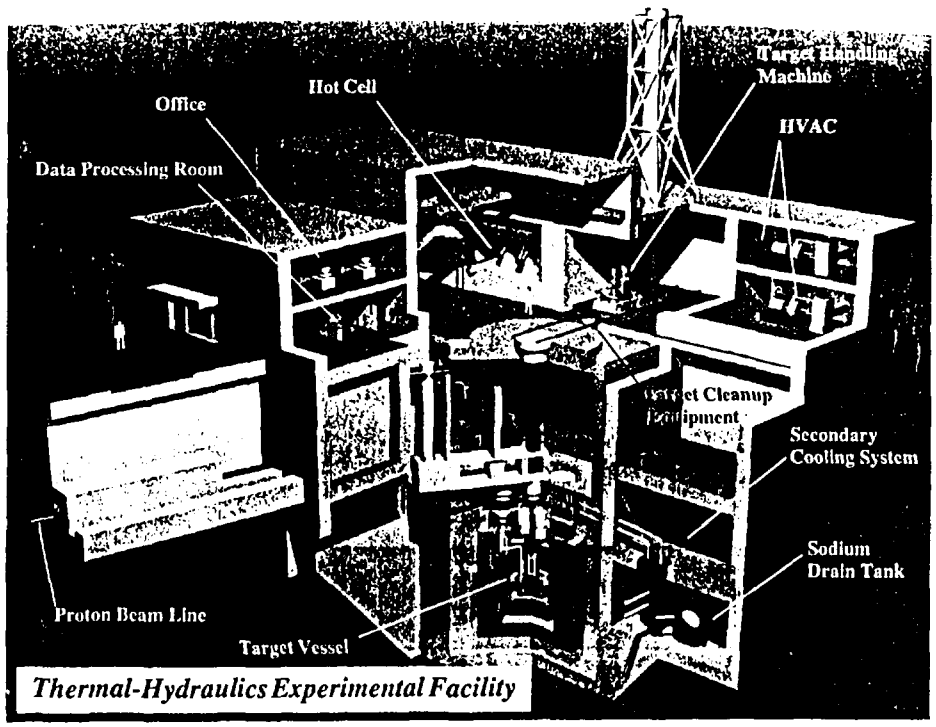

Fig. 10.1.2 Bird's-eye view of the target thermal-hydraulics experiment facility

10.2 Design Study of the Accelerator-driven Transmutation System with TRU-nitride Fuel

T. Sasa, K. Tsujimoto, T. Nishida* and T. Takizuka
(*E-mail:* sasa@omega.tokai.jaeri.go.jp)

TRU-nitride fuel has many advantages over TRU-metallic fuel such as high thermal conductivity, high TRU density, capability of dry reprocessing and so on. Therefore, we tried to change the TRU metallic fuel to the nitride one and reexamined the neutronics and burnup analyses of the accelerator-driven transmutation system with solid tungsten disk target.

Since nitride fuel has higher thermal conductivity than metallic one, we revised the design of the target sub-assembly to shorten the overall length of the target from 1.4 m to 1.0 m. We used target disks with three different thicknesses of 1.5 mm, 70 mm and 130 mm. Figure 10.2.1 shows the cross sectional view of the revised target sub-assembly. According to this revision, engineering design flexibility of the subcritical core was improved without significant changes in neutronic characteristics.

The fuel is TRU-mononitride with a composition of (Np, Am, Cm - Pu)N. In order to prevent the generation of ^{14}C, ^{15}N enriched nitrogen was used to nitration of TRU. About 28% of Pu was added only to the virgin core to reduce the reactivity increase caused by the generation of Pu from Np. The fuel is fabricated to a form of particles without coating. The ZrN particles were added as inert matrix to suppress the excessive power density during the whole fuel lifetime. Both particles are mixed and filled into the clad made from 316SS by the vibropack method. The fuel pin is assembled as a pin-bundle ductless type fuel subassembly to improve the decay heat removal. Irradiation period was estimated about 1500 days according to the limitation of maximum neutron fluence on the stainless steel clad. Incident proton energy to the target was set to 1.5 GeV. System specification was listed in the Table 10.2.1.

The neutronics and burnup calculation was performed with the ATRAS code system with the 73 group cross section file from JENDL-3.2 library.

Results of neutronics calculation are summarized in Table 10.2.2. Figure 10.2.2 shows the power density distribution in the subcritical core. Obtained characteristics for the virgin core were almost similar to those for the metallic fueled one except for the initial neutron multiprication factor and the burnup characteristics. Initial neutron multiprication factor was higher and reactivity change during burnup were much smaller than that of metallic fueled system.

---

* Radiation Application Development Association

Table 10.2.1 System specifications

Proton beam energy	1.5 GeV
Proton beam radius	25 cm
Proton beam profile	uniform
Target/Core	concentric cylinders with a height of 1 m
Radii	25 cm / 90 cm
Target	tungsten (disk layer type)
Upper target	disk thickness 1.5 cm
Middle target	disk thickness 7.0 cm, gap 7.0 cm
Lower target	disk thickness 13 cm
Fuel	
Material	(72MA-28Pu)^{15}N (MA:Np, Am, Cm)
Fuel pin outside diam.	5.43 mm
Pin pitch	6.47 mm
Effective fuel height	100 cm
Inert matrix	ZrN particle
Mixing ratio of ZrN	30 %
Filling factor	55 %
Bond	He gas
Clad thickness	0.4 mm (316SS)
Reflector	stainless steel
Primary Coolant	liquid sodium
Inlet temperature	340 ℃
Outlet temperature	440 ℃
TRU initial inventory	3650 kg

Table 10.2.2 Neutronics calculation results

Initial k-effective	0.942
Thermal output	24.2 MW/mA
TRU disappearance	
Np	-303.1 kg/year
Am	-183.6 kg/year
Cm	+70.0 kg/year
Average neutron energy	670 keV
Neutron fraction	
above 1 MeV	19 %
Average neutron flux	4.1 x 10^{14} (n/cm^2/mA)
Maximum reactivity swing	+ 1.8 % $\triangle$k/k at 600 days

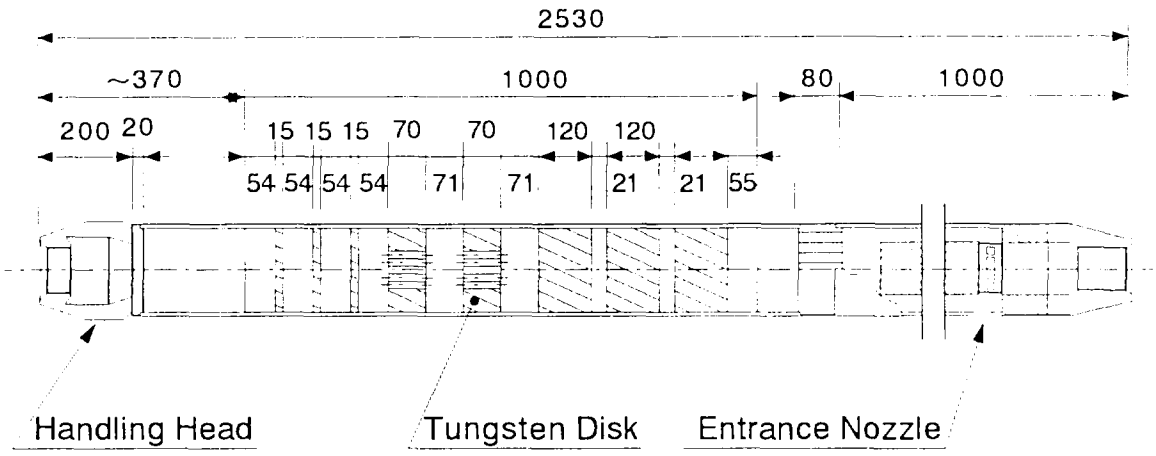

Fig. 10.2.1 Tungsten disk layer type spallation target subassembly

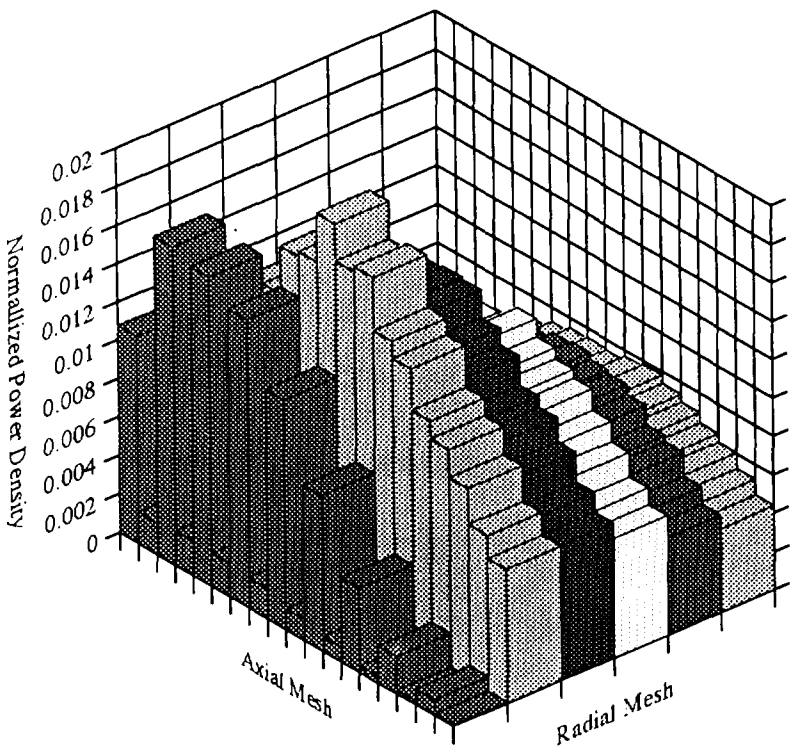

Fig. 10.2.2 Power density distribution

10.3 Benchmark Calculations with ATRAS and Other Code System for the Accelerator Driven System

K. Tsujimoto, T. Nishida, T. Sasa and T. Takizuka
(*E-mail*:ktsuji@omega.tokai.jaeri.go.jp)

The calculation code systems for Accelerator Driven System(ADS) has been developed. For the verification of the performances of these code systems, they are adapted to two different benchmark problems proposed by OECD/NEA and IAEA.

The benchmark problem for ADS proposed by OECD/NEA is a part of the NSC benchmark project on Physics Aspects of Different Transmutation Concepts. The benchmark consists of three stages. The first stage considers the UO_2 fueled PWR reactor. In the recycling stage, the MOX fuel defined in the first stage is fed either into a PWR or fast reactor. In the partitioning and transmutation stage, three possibilities are considered: another MOX fueled PWR, another fast reactor and an accelerator driven subcritical core.

The two dimensional model for this ADS benchmark probelm is shown in Fig. 10.3.1. This system consists of two-region tungsten target injected by proton beam with an energy of 1.0 GeV, minor actinide (MA) and plutonium nitride fueled core and reflectors, each of which is cooled by sodium flow. The Pu and MA composition is corresponds to that obtained through partitioning after 7 years cooling of products from reprocessing the fuel burned up to 33 GWd/t. While three more fuel compositions are proposed, only results for this composition are presented in this paper. The requested results are the spallation neutrons, nuclear characteristics of transmutation system and burnup characteristics.

The calculation was performed by the ATRAS code system with the JENDL-3.2 library. The spallation neutrons in the energy above 20 Mev is calculated by the NMTC/JAERI code. The neutron transport calculation below 20 MeV were carried out by the TWODANT code with 73 group cross section. The BURNER code was used for the burnup calculation. The initial nuclei densities for MA and pultonium in fuel region and the transmutation ratio during the burnup of 200 GWd/t are shown in Table 10.3.1.

The purpose of another benchmark proposed by IAEA is to assess performances of ADS to achieve consensus on calculation methods and associated nuclear data. The benchmark problem is divided into several phases. The goal of the phase one can be defined as a verification of burnup reactivity swing as well as some important reactivity

effects for fast spectrum ADS with an external neutron source at different subcritical levels.

The calculation model for this benchmark problem is lead cooled fast spectrum ADS using Th-^{233}U fuel cycle with an external neutron source by spallation reaction. The spallation neutrons are generated in the lead target bombarded by the proton beam with an energy of 1.0 GeV. The thermal power generated in this system is assumed to be as constant at 1500 MW during the burnup period of of 2250 days. The proton beam intensity should be adjusted to yield this thermal power, while the external neutron source position and 25 group spectrum is provided. The geometrical position and material arrangements are shown in Fig. 10.3.2. The nuclei densities are presented, however the initial enrichment of ^{233}U has to be adjusted to get given initial subcriticalities, 0.94, 0.96 and 0.98.

The calculation was performed with a part of SPACE code system. The multiplication factors were calculated with the transport calculation code TWOTRAN-II using 25 group cross sections. The 25 group cross sections are generated by the weighting flux calculated by the ANISN code and 295 group JSSTDL cross section library based on JENDL-3.2. The fuel composition at each time step were calculated by the burnup calculation code COMRAD with the one group cross section based on the JSSTDL library. The change of k-eff for three different initial subcriticalities are shown in Fig. 10.3.3.

Table 10.3.1 Initial number densties of MA and Pu in fuel region and transmutation rate during burnup of 200 GWd/t

Nuclide	Initial number density ($\times 10^{24}$/cm^3)	Transmutation rate (%)
Np-237	3.353E-03	36.99
Pu-238	1.251E-05	0.37
Pu-239	4.947E-04	15.99
Pu-240	1.977E-04	2.23
Pu-241	7.257E-05	2.79
Pu-242	4.588E-05	0.37
Am-241	3.289E-03	33.46
Am-243	7.293E-04	5.76
Cm-244	1.579E-04	2.23

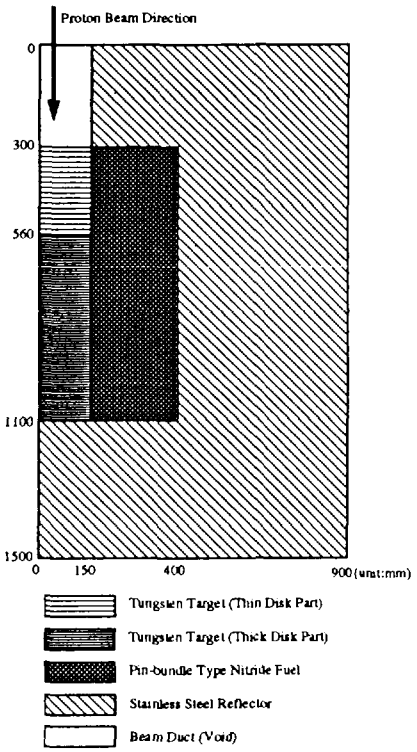

Fig. 10.3.1 Calculation model of benchmark problem propsed by OECD/NEA

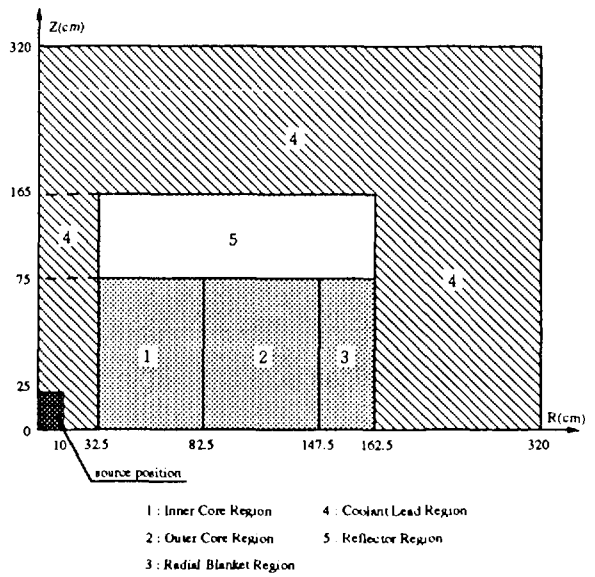

Fig. 10.3.2 Calculation model of benchmark problem propsed by IAEA

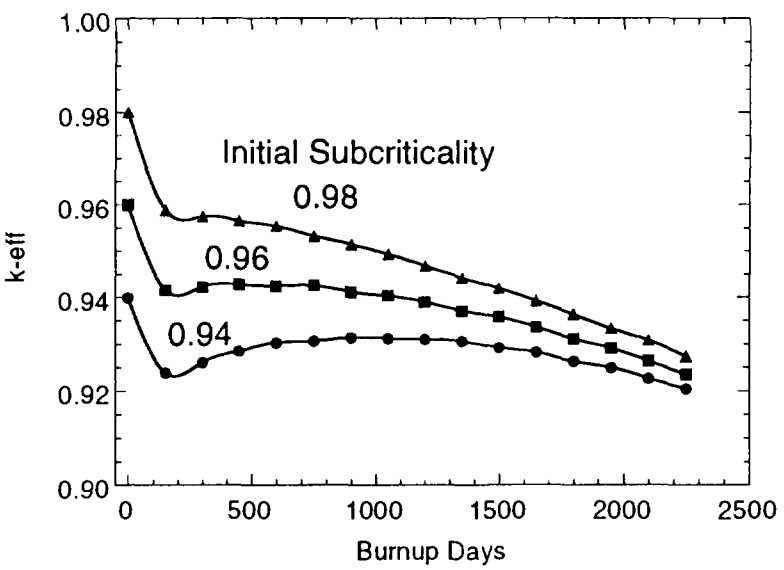

Fig. 10.3.3 Change of multiplication factor with burnup in calculation of IAEA propsed benchmark problem

10.4 Measurement and Analysis of Reaction Rate Distribution on Thick Tungsten Target Surface for 0.895 and 1.21 GeV Proton Bombardment

H. Takada, S. Meigo, T. Sasa, T. Fukahori, N. Yoshizawa*, S. Furihata*,
V. I. Belyakov-Bodin** and G. I. Krupny**
(*E-mail* : takada@omega.tokai.jaeri.go.jp)

In order to study the transport of neutrons in a spallation target, reaction rate distributions on the surface of a thick tungsten target were measured with various activation detectors for the 0.895 and 1.21 GeV proton incidence as a cooperative work between JAERI and Institute of Theoretical and Experimental Physics under the contract of International Science and Technology Center project #157.

The experiment was carried out at the booster beam line of Institute of High Energy Physics in Russia. The proton beam having a profile of Gaussian distribution with a FWHM of 2.4 cm was injected into a cylindrical tungsten target of 20 cm in diameter and 60 cm in length whose density and the purity were 19.25 g/cc and 99.95%, respectively. Activation detectors of ^{27}Al, ^{31}P, ^{32}S, ^{209}Bi and so on were put on the cylindrical surface of the target. Reaction rates of the detectors were obtained by the γ and ß ray measurements using a Ge-detector and a polystyrene scintillation counter, respectively. The errors of the reaction rates were about 6.6% for the γ-ray measurement, while about 22% for the ß-ray one.

The reaction rates were calculated with the Monte Carlo simulation code systems of NMTC/JAERI-MCNP4A[1,2], LAHET[3] and HERMES[4] using the nuclide production cross sections of JENDL-Dosimetry file and those calculated by the ALICE-F code[5]. The following models and data were employed in the code systems: The preequilibrium process was taken into account with an exciton model and a multistage multistep preequilibrium exciton model in NMTC/JAERI and LAHET, respectively. The level density parameter derived by a formula of Ignatyuk was selected for the evaporation calculation in those codes, while that proposed by Baba was employed in HERMES. As for the nucleon-nucleus cross sections, NMTC/JAERI calculation employed the systematics derived by Pearlstein in the energy region below 1 GeV and the geometric cross sections above 1 GeV. LAHET calculation utilized the elastic cross sections obtained by a global phenomenological optical model and those compiled in the NASA

* : Mitsubishi Research Inc., Tokyo
**: Institute of Theoretical and Experimental Physics, Moscow, Russia

library[6] in the energy regions below and above 400 MeV, respectively. In HERMES calculation, the elastic cross sections compiled in HILO library[7] and those from NASA library were employed in the energy regions below and above 150 MeV, respectively.

The calculated reaction rates are compared with the experimental ones in Figs. 10.4.1 to 10.4.4. The reaction rate increases with the distance from the front surface up to about 8 cm and then decreases rapidly irrespective of the incident proton energy. It is observed that HERMES tends to give lower reaction rates than the other code systems. NMTC/JAERI-MCNP4A and LAHET reproduce the experimental results better than HERMES. It was also found from a detailed comparison that the calculated results of LAHET were in satisfactory agreement with the experimental ones with the C/E ratio of 0.8 to 1.2 at the positions up to 30 cm from the front surface because LAHET gave higher neutron yield in the energy region below 60 MeV than the other code systems. At the position of 55 cm, however, all the code systems estimate the reaction rates extremely higher. It is necessary to investigate the accuracy of total, elastic and non-elastic neutron cross sections employed in the code systems.

References

1) Nakahara, Y., Tsutsui, T. : "NMTC/JAERI A Code System for High Energy Nuclear Reactions and Nucleon-Meson Transport Code", JAERI-M 82-198, (1982), [in Japanese].
2) Briesmeister, J.F. (Ed.) : MCNP A General Monte Carlo N-Particle Transport Code, Version 4A, LA-12625, (1993).
3) Prael, R.E., Lichtenstein, H. : LA-UR-89-3014, "Users Guide to LCS: The LAHET Code System", (1989).
4) Cloth, P., et al.: "HERMES A Monte Carlo Program System for Beam Materials Interaction Studies", Jül-2203, (1988).
5) Fukahori, T. :"ALICE-F Calculation of Nuclear Data up to 1 GeV", Proc. of the Specialists' Mtg. on High Energy Nucl. Data, Oct. 3-4, 1991, JAERI, Tokai, JAERI-M 92-039, pp. 114-122 (1992).
6) Alsmiller, R. G. Jr., Barish, J. : "Neutron-Photon Multigroup Cross Sections for Neutron Energies ≤ 400 MeV", ORNL/TM-6486, (1981).
7) Wilson, J. W., Costner, C. M. : "Nucleon and Heavy-Ion Total and Absorption Cross Section for Selected Nuclei", NASA TN D-8107, (1975).

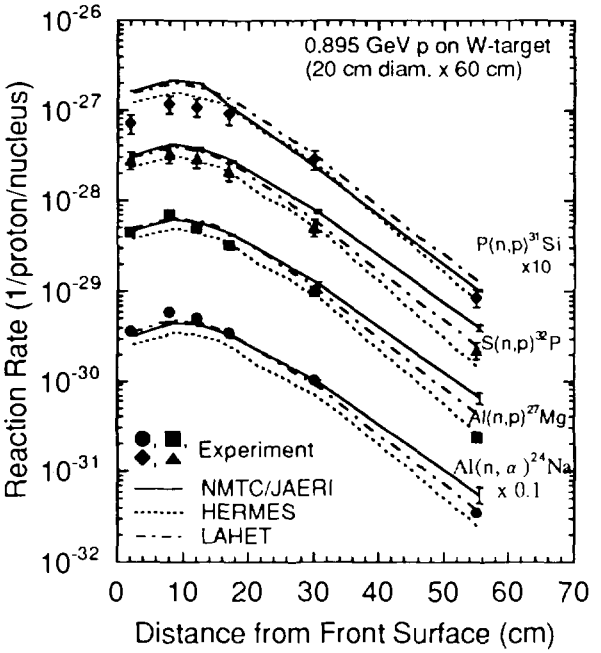

Fig. 10.4.1 Reaction rates of $S(n,p)^{32}P$, $P(n,p)^{31}Si$, $Al(n,p)^{27}Mg$ and $Al(n,\alpha)^{24}Na$ for the 0.895 GeV proton incidence on thick tungsten target. The solid marks indicate the experimental results. The solid, dotted and dot-dashed lines stand for the calculated results of NMTC/JAERI-MCNP4A, HERMES and LAHET, respectively.

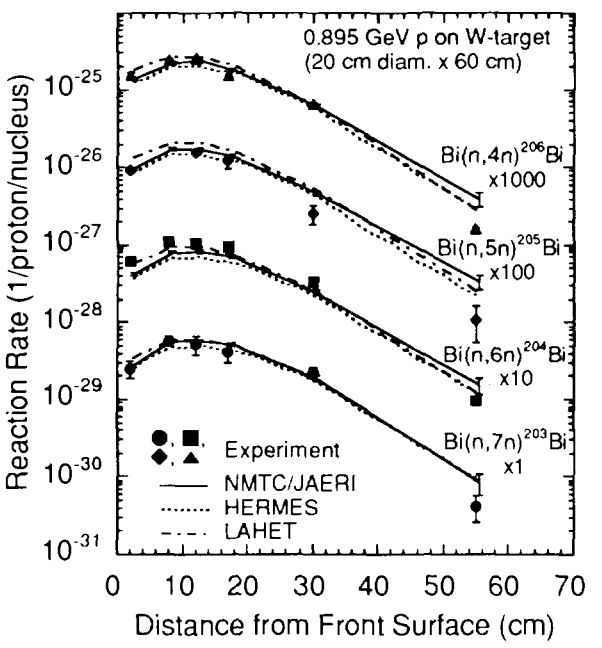

Fig. 10.4.2 Reaction rates of $Bi(n,4n)^{206}Bi$, $Bi(n,5n)^{205}Bi$, $Bi(n,6n)^{204}Bi$ and $Bi(n,7n)^{203}Bi$ for the 0.895 GeV proton incidence on thick tungsten target. The notes to the marks and lines are the same as for Fig. 10.4.1.

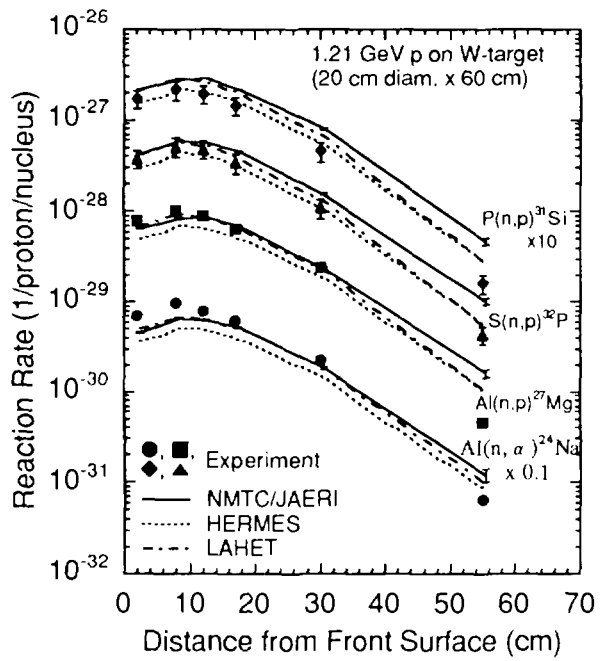

Fig. 10.4.3 Reaction rates of $S(n,p)^{32}P$, $P(n,p)^{31}Si$, $Al(n,p)^{27}Mg$ and $Al(n,\alpha)^{24}Na$ for the 1.21 GeV proton incidence on thick tungsten target. The notes to the marks and lines are the same as for Fig. 10.4.1.

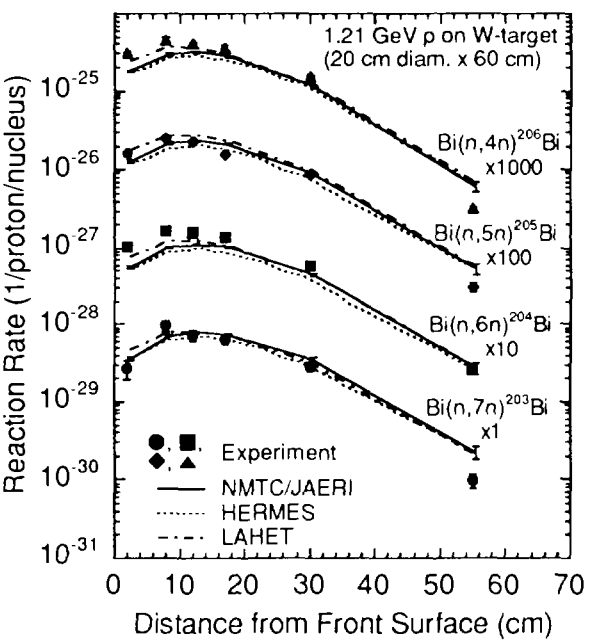

Fig. 10.4.4 Reaction rates of $Bi(n,4n)^{206}Bi$, $Bi(n,5n)^{205}Bi$, $Bi(n,6n)^{204}Bi$ and $Bi(n,7n)^{203}Bi$ for the 1.21 GeV proton incidence on thick tungsten target. The notes to the marks and lines are the same as for Fig. 10.4.1.

11. Accelerator Development

The final report of the conceptual design activity of International Fusion Materials Irradiation Facility (IFMIF- CDA) is completed at the end of 1996. The basic design parameters of cw deuteron linac are examined from the view points of the system integration and the availability, and the basic design and cost estimation for the total lithium target system have been improved. The stability of the target flow has been studied by simulating the target flow with water for non- heating condition. The impact of source term uncertainty to the calculated irradiation parameters such as neutron flux and dpa has been analyzed on the neutronics calculation.

Several developments for the superconducting rf- linac based FEL facility have been made: a beam loss current monitoring system based on a Si photo diode and CsI or BGO scintillators, a measurement of a long FEL resonator length using Ti- sapphire laser and detecting light pulse enhancement due to the interference between a newly coming light and stored light pulses in the resonator. Grid pulser circuits in the electron gun have been also improve to eliminate the fluctuation in micro pulse. Various measurements have been carried out to improve the beam quality for electron beam bunching, spontaneous emission and effects of the undulator filed roll-off.

R&D activities and conceptual design studies for high intensity proton accelerator have been in progress for the Neutron Science Project (NSP). The characteristics of a 2MeV proton beam has been systematically studied with and multi- cusp type H^+ ion source and an high intensity RFQ, and a basic performance of a H^- with multi- apertures has been measured for the operation with and without cesium. Primary configurations and accelerator parameters for CW- DTL and superconducting high β linac have been evaluated in order to meet the various requirements for the NSP accelerator which has been discussed for the proposed research facilities. An associated RF control system has been also considered to estimate various uncertainties for frequency shift, phase error and voltage variation. Electromagnetic properties and beam dynamics calculation have been made to evaluate behavior and quality of accelerated particles. Structural analysis of superconducting cavities has been carried out to ensure the strength under vacuum load and cooled condition. After a test stand of superconducting cavity development had been constructed, a fabrication and test of a single cell cavity of β=0.5 have been conducted. The peak field measurements were successfully performed with the observed peak field of 16MV/m and 18.6 MV/m at 4.2 and 2.1K respectively, which exceeded the specification for the proposed cavity. Preliminary study of a storage ring for a 5MW pulsed beam for neutron scattering experiments has been started. Many technical problems expected for such an high intensity ring have been checked such as latticed properties, beam injection, radio- frequency cavity and beam extraction in order to clarify the necessary R&D items.

11.1 Conceptual Design Study of IFMIF Accelerator System

M. Sugimoto, M. Kinsho, M. Chernogubovsky and Y. Houjyo*
(*E-mail*: sugimoto@ifmif.tokai.jaeri.go.jp)

The final report of the conceptual design activity of International Fusion Materials Irradiation Facility (IFMIF) is completed at the end of 1996[1]. The basic design parameters of the high intensity cw deuteron linac for the IFMIF described in the interim report[2] are examined from the view points of the system integration and the availability. Two design integration meetings[3,4] were held and the following design issues were discussed:

(1) Practical development path to obtain the 140 mA dc deuteron ion source with long lifetime,

(2) Recent development of high power rf tube in 175 MHz frequency region,

(3) Radiation and activation source models of RFQ and DTL,

(4) Superconducting linac (SCL) option as a high energy section alternative, and 100 kW solid state rf amplifier module used for each SCL cavity,

(5) Refinement of HEBT system to satisfy the users requirement of the beam profile on the target, and

(6) Cost estimation of the accelerator system.

The major changes from the baseline design parameters are summarized in Table 11.1.1[5]. The number of ion sources per 125 mA linac module was two to achieve the higher availability of the injector section, however, it reveals that the on-line replacement of the failed ion source is impossible in the high radiation environment. The single ion source arrangement is preferable to design the short LEBT with a good matching property to RFQ. The maximum output power from one rf module was assumed to be 1.3 MW before, and it is reduced to 1.0 MW to increase the availability margin by operating at the reduced rating. This affects the energy gain per DTL tank and it is reduced from 5 MeV to 4 MeV, roughly. So, in the final design, the extra two DTL tanks and the associated rf stations are necessary, and the output energy step becomes 4 MeV. This also increases the cost of the accelerator by about 20 %. The cost of the SCL option mainly depends on the cost of the solid state rf amplifier module

---

* Hitachi Corporation

and it becomes comparable now. The refined schematic view of power distribution over the IFMIF accelerator system and the major parameters for each linac structure (RFQ and DTLs) are shown in Fig. 11.1.1.

Table 11.1.1 Baseline design parameter changes of the IFMIF accelerator system

Parameter	Interim design	Final design
Number of ion sources per beamline	2	1
Output energy	30, 35, 40 MeV	32, 36, 40 MeV
Number of DTL Tanks	6	8
Number of RF stations	10	12
Max. Output Power per RF Station	1.3 MW	1.0 MW

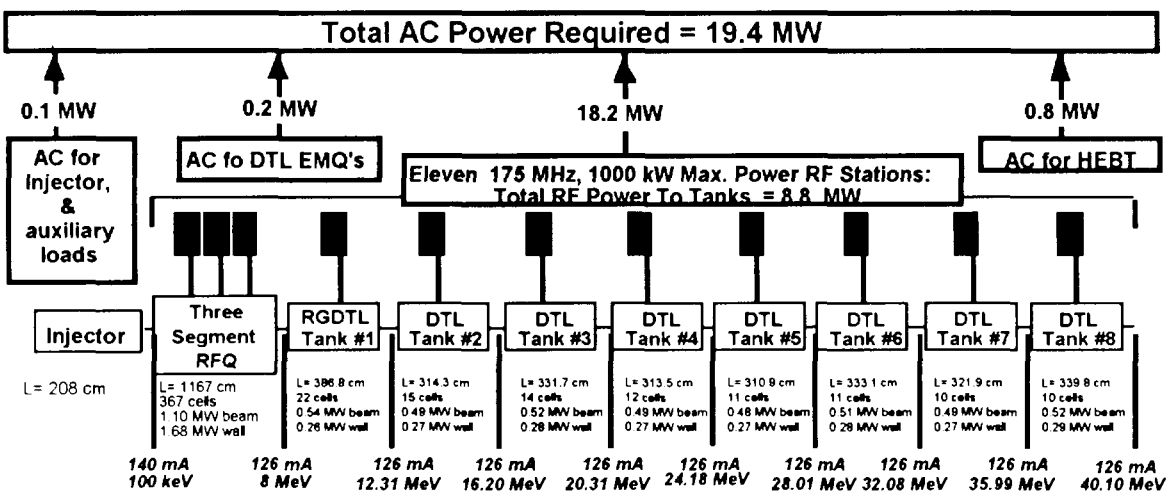

Fig. 11.1.1. Power distribution for IFMIF accelerator system and major features of RFQ and DTL.

Since the ion source performance is critical for the overall availability of the accelerator system, we are interested in all developmental works related to the high current, high brightness, and stable positive light ion sources. The recent ECR source can produce ~100 mA proton beam with enough quality for IFMIF and it will be reduced to ~70 mA for deuteron case. So, twice of the source intensity should be demonstrated. On the other hand, the cathode-driven volume source can produce ~70 mA deuteron beam at 35 kV extraction voltage. It is an enough intensity if it can be scaled up to 100 kV extraction for IFMIF. The key issue for this source is a long-lived cathode to obtain the high availability. The H_2^+ beam is also required for tuning process, but we expect ~50 mA is possible. The search of the

source condition is required to obtain both D^+ and H_2^+ beams with the optimal characteristics using a single source. The beam neutralization is occurred in the LEBT (> 90 %) and is disappeared at the entrance region of RFQ. The effect of the ion source fluctuation to the RFQ matching is important to reduce the beam loss inside of the RFQ. If a pulsed mode operation is necessary for the tuning process, the above problem becomes a critical issue.

The segmented RFQ developed at LANL[6] is a reference design of IFMIF RFQ, which is the best choice from the beam dynamics view point but some additional considerations[7] are required to achieve the stable high power operation. The high power test of the segmented RFQ can answer for the inter-gap field problem presented in Ref. 7. The RF power feed for RFQ is another problem: it is desirable to keep the balance and symmetry of the RF field in each quadrant of the RFQ. The beam excitation called as the beam load is also balanced among the RFQ segments.

The beam dynamics simulation code is indispensable to design the IFMIF accelerator system. The particle tracking codes used for the relatively low current linacs so far have some difficulties when the results are compared with the experiments. The suppression of the beam halo is one of the main issues of the IFMIF system, and it requires a extremely precise calculation of the small portion ($1/10^8$) of the accelerated and transported beam. The seek for the best combination of the fast-and-approximate method and the slow-and-precise method is started from the beginning of 1997.

Reference

1) IFMIF-CDA Team: "IFMIF International Fusion Materials Irradiation Facility Conceptual Design Activity Final Report", ENEA Frascati Report, RT/ERG/FUS/96/11 (1996).
2) "IFMIF International Fusion Materials Irradiation Facility Conceptual Design Activity Interim Report", ORNL/M-4908 (1995).
3) IFMIF-CDA Team: "Minutes of the Second IFMIF-CDA Design Integration Workshop", May 20-25, 1996, JAERI, Tokai, Japan, JAERI-Conf 96-012 (1996).
4) "3rd Design Integration Meeting of the IFMIF", October 14-25, 1996, Frascati, Italy.
5) IFMIF-CDA Team: "Addendum to IFMIF-CDA Interim Report", JAERI-Tech 96-036 (1996).
6) Young L.: "An 8-meter-long Coupled Cavity RFQ Linac", Proc. 1994 Linear Accelerator Conf. Aug. 21-26, 1994, Tsukuba, Japan, 178 (1994).
7) Chernogubovsky M. and Sugimoto M.: "Conceptual Design of IFMIF Accelerator RF Systems", JAERI-Research 96-064 (1996).

11.2 Conceptual Design Study of IFMIF Target System

Y. Kato, H. Nakamura, M. Ida, K. Itoh*, Y. Kukita* and H. Maekawa
(*E-mail*: kato@ifmif.tokai.jaeri.go.jp)

The conceptual design activity of international fusion materials irradiation facility (IFMIF - CDA) which started in January 1995 has been performed in cooperation with E.U. and USA. The results were summarized in the final report of IFMIF-CDA[1]. As the target group activity, some improvements for the basic design and the cost estimation for total target system have been made. The stability of target flow has been studied by simulating the target flow with water for non-heating condition[2]. In this experiment a stable target flow has been demonstrated and a data base for investigation of Li jet conditions has been produced.

(1) Conceptual design of a primary lithium system and target assembly

According to the improvements for the lithium system design, the total inventory of lithium was revised to about 21 m^3. Also the parameters of target lithium flow were revised as in Table 11.2.1. A schematic illustration of target configuration is shown in Fig. 11.2.1.

Table 11.2.1 Lithium jet parameters

Jet thickness, m :	0.025 (for 40MeVD$^+$)	Inlet temperature, C :	250
	0.022 (for 36MeVD$^+$)	Outlet temperature, C :	300 (for 15 m/s)
	0.019 (for 32MeVD$^+$)	(Surface temperature, C :	290 (for 15 m/s)
Jet width, m :	0.26	Peak temperature, C :	450 (for 15 m/s)
Jet velocity, m/s :	15 (range 10-20)	Beam footprint, cm:	5 x 20

In the target assembly, the backwall will get the neutron damage of more than 50 dpa/y and the replaceable backwall was adopted as a reference design. A target assembly that has a bolt fixed and lip-weld type replaceable backwall was designed.

In the primary lithium loop, the main electromagnetic pump was designed to have max. flow rate of 120 L/s and provide a flow up to 110 L/s to the operating target, as well as 10 % of this total flow to the second target for removal of decay heat from the target structure.

(2) Components design of lithium purification system

The lithium purification sub-loop consists of a system of cold trap and hot trap to remove various impurities and auxiliary supporting equipment. The impurity elements expected are the Deuteron (D), Tritium (T), Beryllium (Be-7), Carbon (C), Nitrogen (N) and Oxygen (O). The cold trap will remove D, T, Be-7 C and O. Total tritium production rate is estimated at 10 g/y.

---

* Nagoya University

It is important to minimize the tritium inventory in the system, since this could be the dominant source term in the event of a radiological release. Then the tritium is planned to remove by the cold trap with protium sparging method and as an option , by hot trap with yttrium getter. Nitrogen will be removed by hot trap with titanium getter. The most highly radioactive impurity is expected to be Be-7 which has a 53 day half life. If the cold trap does not functioned, the Be-7 will build up to a saturated activity of 4.5×10^{15} Bq. The remote handling system is required to exchange the cold trap contained Be-7.

(3) Water Simulation Experiment for IFMIF TargetSimulation of Li jet by water[2])

Non-dimensional numbers such as Reynolds, Froude and Weber numbers were preserved to simulate the Li target flow condition by water flow. Since the kinematic viscosity of water at room temperature is close to that of Li at the IFMIF operating temperature (~250 °C), the size of the test section and velocity enable to preserve Re and Fr. The jet free surface condition being represented by We was simulated by changing the jet average velocity. The experiments were performed in a water loop (Fig. 11. 2. 2), mostly under atmospheric pressure. A two-dimensional double-reducer nozzle being newly proposed for the IFMIF provided a high-speed (≤ 17 m/s) stable water jet (240 mm-wide and 24 mm-thick) with uniform velocity distribution at the nozzle exit. There was no flow separation in the nozzle and no liquid entrainment from the jet free surface.

Test results and discussions

The jet free surface was covered by two-dimensional and/or three- dimensional waves, the size of which did not change much over the tested jet length of ~130 mm (Fig. 11. 2. 3). The wave amplitude attenuation effect due to the centrifugal force was estimated assuming that the local wave energy is preserved on the jet surface. The obtained amplitude attenuation factor indicates that the longer waves are attenuated more than shorter waves, and that the Li jet surface would be covered by longer waves than on the water jet (Fig. 11. 2. 4).

The jet velocity profile changed around the nozzle exit from uniform to that of free-vortex flow where the product of the radius of stream line and local velocity is constant in the jet thickness (Fig. 11. 2. 5). The depth-wise distribution of static pressure due to centrifugal force caused such a change in the velocity profile. The jet thickness increased immediately at the nozzle downstream because of the above change in the velocity profile. One-dimensional momentum equation predicted well the jet thickness along the length of the jet (Fig. 11. 2. 6) when the initial change in the jet thickness was taken into account.

References

[1] IFMIF CDA Team, "IFMIF International Fusion Materials Irradiation Facility, Conceptual Design Activity, Final Report," RT/ERG/FUS/96/11, ISSN/1120-5563 (1997).

[2] H. Nakamura et al., "Water Experiment of High-Speed, Free-Surface, Plane Jet along Concave Wall," Proc. of NURETH-8 (1997) in press.

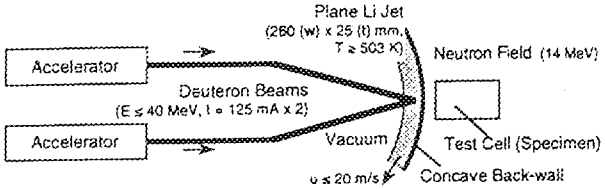

Fig. 11. 2. 1 Schmatic Illustration of Target Configuration for Neutron Generation

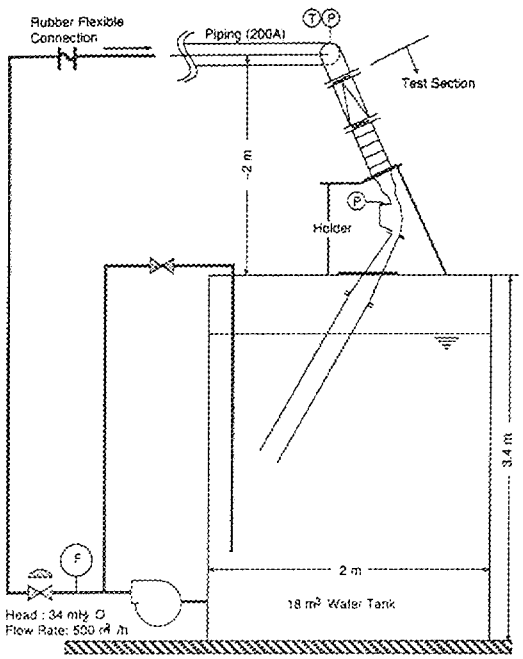

Fig. 11. 2. 2 Schematic of Test Facility

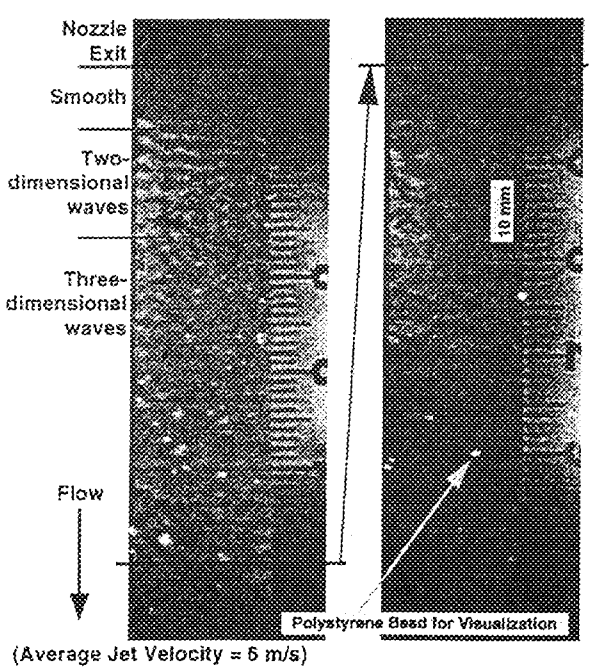

Fig. 11. 2. 3 Typical Interfacial Condition (High-Speed Video 1000 fps)

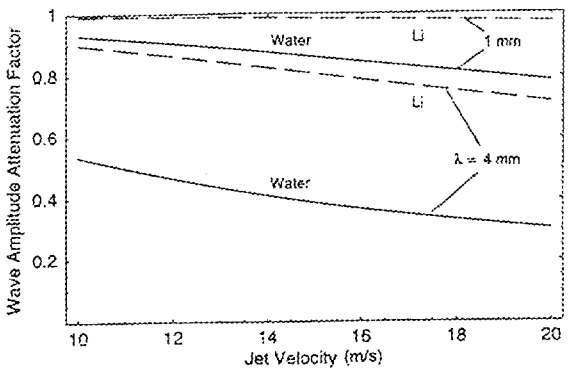

Fig. 11. 2. 4 Wave Amplitude Attenuation Factor

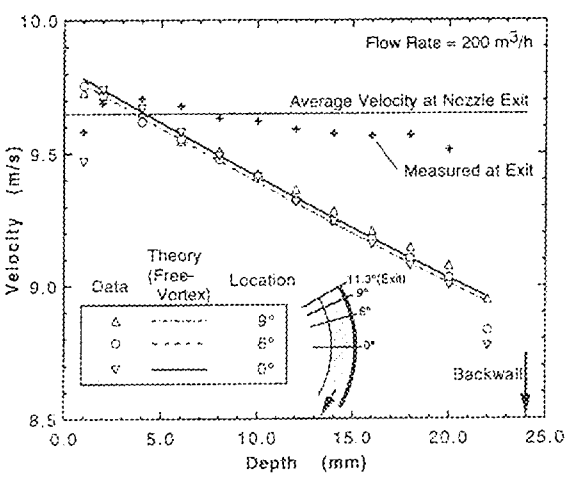

Fig. 11. 2. 5 Velocity Profile in Jet Flow

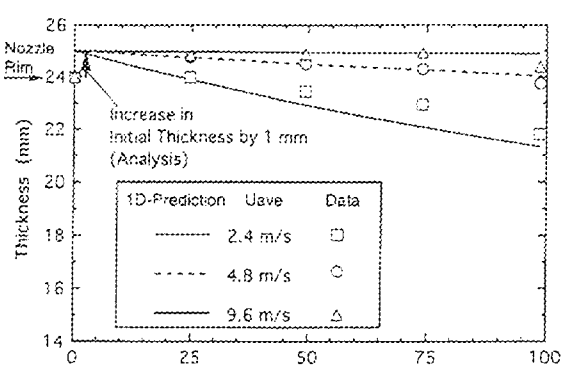

Fig. 11. 2. 6 Jet Thickness along Back-wall (Comparison with modified prediction)

11.3 Preliminary Analyses of Li Jet Flows for the IFMIF Target

M. Ida, Y. Kato, H. Nakamura and H. Maekawa
(*E-mail* : ida@ifmif.tokai.jaeri.go.jp)

The conceptual design activity (CDA) of the International Fusion Materials Irradiation Facility (IFMIF) to provide a neutron irradiation field has started in February 1995 under the auspices of the International Energy Agency (IEA). The IFMIF target assembly is shown in Fig. 11.3.1. Two deuteron (d^+) beams at 32 to 40 MeV with the total current of 250 mA are irradiated onto a rectangular region (50 mm-high x 200 mm-wide) of the Li target. Neutrons are generated by d-Li stripping reaction in the target.

About 95% of the kinetic energy of the d^+ beam power is deposited and turns into heat in the target. The liquid Li target should remove the generated heat to keep the stability and the integrity of the target flow. Furthermore, the target Li flows in the beam target region of about 10^{-3} Pa. To meet these conditions, the target Li flows at high-speed of 10 to 20 m/s, along a concave wall. In the Li flow, static pressure distribution due to the centrifugal force results in a significant increase of the saturation temperature with the depth from the free surface.

The two-dimensional numerical analyses of the target jet flow were performed to clarify the thermal and hydraulic characteristics of the Li target flow. A commercial computer code FLOW-3D was employed for the analyses because the code can deal with turbulent flows with a free-surface using the VOF (volume of fluid) model. The following 5 items were performed to study the target flow behavior and to test the predictive capability of the FLOW-3D code as a tool for the analysis of flow dynamics. They were reported in JAERI-Research 97-030.

Temperature Distribution in Target Flow

The effect of back-wall radius and average velocity on the temperature distribution in the target jet flow was evaluated.(See Figs. 11.3.2 through 11.3.4) The adequacy of the CDA requirements and a range of these parameters were evaluated. The conclusions are as follows.

1) There is enough temperature margin of Li boiling at the free surface and at the peak temperature location in the jet flow in all the cases, to avoid respectively significant vaporization and voiding. The minimum temperature margin is 20 K at the free surface.

2) The effect of the back-wall radius on temperature distribution is negligible. There is no remarkable migration of hot portion of fluid towards the jet free surface. The heat conduction in the deeper side of the peak temperature location takes place, but is not influential to the temperature distribution.

Calculation of Boundary Layer

The applicability of the FLOW-3D code was examined to evaluate the boundary layer development along the wall. The conclusions are as follows.

1) The calculation using the RNG model, out of three turbulence models in the code, with fine meshing gives the results very close to the theoretical prediction, though all the models over-predicts the boundary layer thickness. The k-e model predicts the thickness largely, especially in case of small mesh size. The velocity profile in the boundary layer calculated using the LES model is qualitatively different from that of the theoretical prediction.

2) The thickness of the calculated boundary layer increases steeply when the boundary layer starts to develop, and is followed by a gradual development. The amount of the initial steep increase in the boundary layer thickness decreases with the size of the cell attached with the wall.

Jet Thickness

The effects of boundary layer development on the jet thickness were evaluated by changing the back-wall radius assuming an extremely long jet to enhance the flow behavior. The conclusions are as follows.

1) The jet thickening rate is roughly equal to that of the displacement thickness of the boundary layer.

2) The effect of centrifugal force on jet thickness is negligible.

Interfacial Wave

The interfacial wave generation on the jet free surface was attempted to simulate by using the FLOW-3D code. The conclusions are as follows.

1) No wave is calculated to appear in the two dimensional calculations performed by changing such parameters as the turbulence model, mesh size, surface tension, physical viscosity and the existence of a "projection".

2) The jet becomes thinned as the low velocity portion near the free surface, due to the boundary layer on the front wall of upstream nozzle, is accelerated by the viscosity effect. This acceleration near the free surface may be one of the causes for the wave generation.

Target Flow Response in Case of Backwall Rupture

The jet behavior was evaluated for the case that the pressure outside the target assembly is higher than the static pressure at the back-wall due to the centrifugal force. The jet flow is found to be separated at the downstream of an assumed opening within few milliseconds or less, causing large deformation of the jet shape when the outside pressure is higher than 30 kPa. A large gas bubble is formed when the outside pressure is equal to 100 kPa.

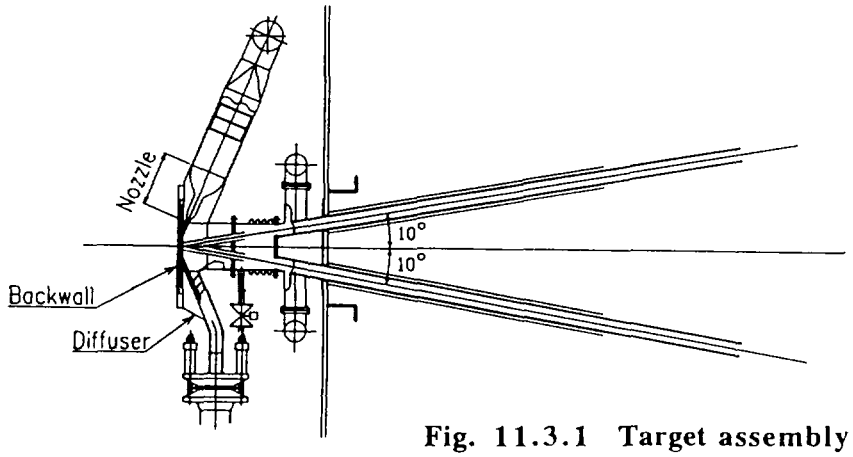

Fig. 11.3.1 Target assembly

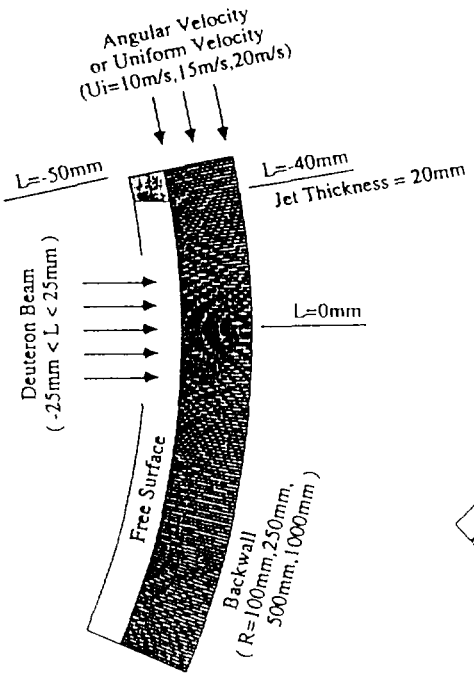

Fig. 11.3.2 Calculation model

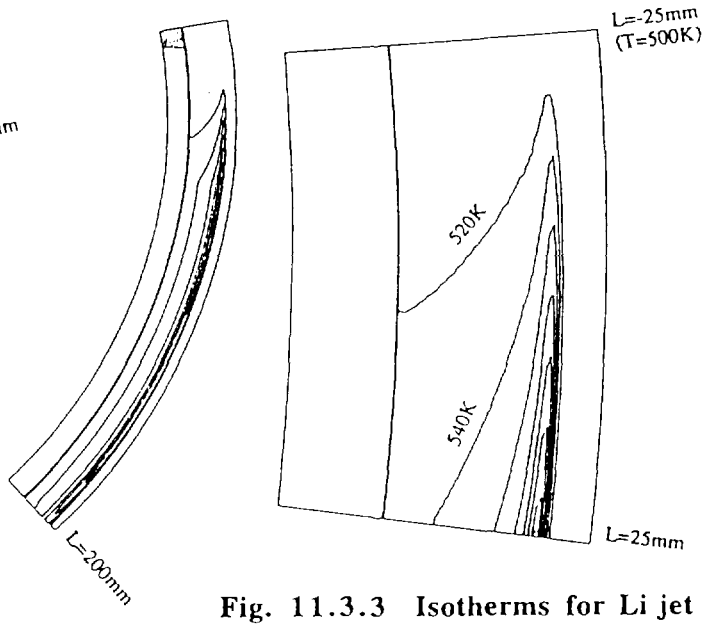

Fig. 11.3.3 Isotherms for Li jet

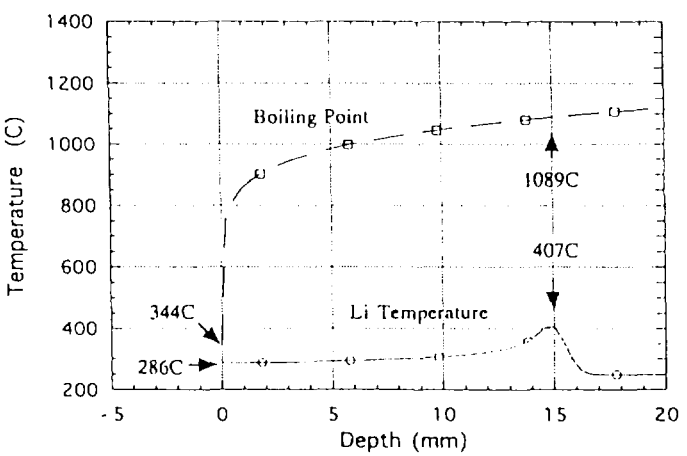

Fig. 11.3.4 Distribution of Li temperature and boiling point

11.4 Impact of Source Term Uncertainty on Neutronics Analysis of D-Li Neutron Irradiation Facility (IFMIF)

Y. Oyama, K. Kosako* and K. Noda
(*E-mail:* oyama@fnshp.tokai.jaeri.go.jp)

A 14 MeV neutron irradiation facility, International Fusion Material Irradiation Facility (IFMIF), has been planned and designed in the conceptual design activity (CDA) under the collaborative program of International Energy Agency (IEA) Implementing Agreement for a Program of Research and Development on Fusion Materials[1]. The IFMIF facility produces neutrons with peak energy of around 14 MeV by d-Li reactions by a high current deuteron linear accelerator and a high speed Li flow target. The irradiation parameters such as neutron flux and dpa were estimated to optimize the accelerator and target design parameters by neutron transport codes using the previously developed source model.[2] However, since the present source model was obtained from a rather simple nuclear reaction model, it brought the uncertainty to the calculated flux and spectrum of emission neutrons. Therefore, it is very important to know the uncertainty level of the calculated irradiation parameters originating from the source term uncertainty.

The comparison of the calculated forward emission spectrum of neutrons with the FMIT model[3] and Sugimoto's experiment[4] measured at 32 MeV is summarized in Table 11.4.1. A good agreement can be found for the JAERI calculation, except for the high energy region. Both the results for thick target spectra are very similar to the experiment in a gross structure, but the absolute intensity is different. More than 99 % of neutrons are generated with the energy below 30 MeV. This approves to neglect a high energy part of emission spectrum. For neutrons below 15 MeV, its fraction is 69% and the C/Es are 0.96 and 0.79 for JAERI and FMIT, respectively. Generally the FMIT spectrum gives lower C/E value except a high energy part.

Neutron transport calculations to obtain neutron irradiation parameters were performed inside the test module loaded with the test material samples[5]. A test module was placed in front of the target with the shape of 50x 200 mm square and the depth of 200 mm. As standard loading modules, the following four cases were considered: for iron sample, 1) Fe 50%, He 50%, and 2) Fe 50%, NaK 30%, Void 20%, and for SiC sample, 3) SiC 50%, He50%, and 4) SiC 50%, NaK 30%, Void 20%. The test matrices with the standard loading were averaged by the volume fraction and homogenized. A neutron transport calculation was performed using the

---

* Sumitomo Atomic Energy Industries Ltd.

Monte Carlo code, GMVP, which was a vectorized version modified from MORSE-CG. The nuclear data library used was HILO86/J3 that was modified from HILO86 by replacing the data below 20 MeV by JENDL-3.1 incorporating a self-shielding factor.

Contributions of source neutrons with three energy groups as shown in Table 11.4.2 were calculated on the parameters such as Fe dpa, heating and He production for the Fe/He cooled module. It is concluded that He production is most sensitive to higher energy, i.e., 30 % for neutrons above 20 MeV, and dpa has lower sensitivity. On the other hand, nuclear heating is less sensitive to such high energy range. The table summarizes the uncertainties of source function for corresponding energies based on the comparison with Sugimoto experiment. Sensitivity of source term to nuclear responses should be exactly determined from the uncertainty of source function, i.e., uncertainties of energy spectra for every emission angle. However, here, to simplify and to roughly estimate an impact of the source term, the uncertainty of source term is assumed to be represented by that of the forward emission spectrum. From the table, impacts of the source function uncertainty of nuclear responses such as dpa, heating, and gas production are as follows: 1) A 75-85 % fraction of dpa for Fe is determined by neutrons below 20 MeV. 2) A 10% uncertainty of neutron emission above 20 MeV contributes to those of the total dpa only by 2- 3 % , of the total heating by 1 % and of the He production by 2-3 %. 3) A 10% uncertainty of 10-20 MeV neutrons contributes to those of the total dpa by 4-5 %, of the total heating by 6% and of the He production by 6 %. 4) Multiplying the sensitivities by the source term uncertainty, the uncertainties of nuclear responses by the ESNIT and the FMIT models ranged in ~ 8% and ~ 17%, respectively.

References

1) IFMIF-CDA Team, edited by Martone M.: "IFMIF-International Fusion Materials Irradiation Facility Conceptual Design Activity, Final Report", ENEA Frascati Report, RT/ERG/FUS/96/11 (December, 1996).
2) Oyama Y., Yamaguchi Y., Kosako K. and Maekawa H.:"Calculation of Neutron Field Generated at Thick Li Target Bombarded with 10-40 MeV Deuterons for Energy Selective Neutron Irradiation Test Facility," JAERI-M 92-191 (1992)
3) Mann F. M., Watson J.W., Ullmann J. and Wyckoff W. G. : J. Nucl. Materials, 85 & 86, 467 (1979).
4) Sugimoto M.: private communication, Japan Atomic Energy Research Institute (1994).
5) Oyama Y., Noda K., kosako K., Yamano N. : J. Nucl. Materials., 233-237, 1577 (1996) .

Table 11.4.1 Comparison of Integrated Forward Flux in C/E (Calculated to Experimental one) [Ed=32 MeV, Angle=0 degree]

Energy range [MeV]	Sugimoto Experiment [n/sr/s/mA]	Fraction to total flux of 1-50 MeV	JAERI Model	C/E	FMIT Model	C/E
1-2	1.28e+10	0.051	1.21e+10	0.945	7.95e+9	0.623
2-10	7.66e+10	0.304	8.46e+10	1.104	6.70e+10	0.874
10-15	8.40e+10	0.333	7.12e+10	0.848	6.13e+10	0.730
15-30	7.76e+10	0.308	7.06e+10	0.911	5.46e+10	0.703
30-40	1.10e+9	0.004	1.31e+8	0.119	2.28e+8	0.208
40-50	1.63e+8	0.00065	not given	------	1.68e+8	1.029
Total	2.52e+11	1.00	2.39e+11	0.946	1.91e+11	0.758

Table 11.4.2 Uncertainties of Calculated Nuclear Responses

Energy range	Uncertainty of Source Function		Uncertainty of calculated responses					
MeV			dpa of Fe		Total heating		^{4}He production	
	JAERI	FMIT	JAERI	FMIT	JAERI	FMIT	JAERI	FMIT
1-10	+8%	-16%	+1.6-3.2%	-(3.2-6.4)%	+3%	-6%	+1-1.5%	-(1.9-3)%
10-20	-14%	-27%	-(6.3-7.7)%	-(12-15)%	-7.7%	-15%	-(8.3-8.5)%	-(16-16.5%)
> 20	-7%	-36%	-(1.1-1.8)%	-(5.4-9)%	-0.56%	-2.9%	-(1.4-2)%	-(7.2-10)%
total	-5%	-24%	-(4-6)%	-(21-30)%	-5%	-30%	-9%	-(27-30)%

11.5 Loss Monitor System for the JAERI Superconducting rf Linac-based FEL

E.J.Minehara and E.Tanaka
(*E-mail:* minehara@felwu0.tokai.jaeri.go.jp)

In order to decrease substantially the hard X- and gamma-rays radiation level at the JAERI FEL facility, we have developed a beam current loss monitoring system being distributed along the beam line of the JAERI superconducting rf linac. Usually, we first try to maximize a transmission of an electron beam through the rf linac by adjusting beam optical elements, and by monitoring the beam current. Once we succeed to transport the electron beam with about a full transmission, and we can not use a current monitor system to reduce a smaller amount of the beam loss than a few %. In order to reduce the beam loss smaller than 0.01% or less, we have to use a more sensitive monitor for the current loss than the current monitor.

Preliminary and experimental results showed the reduction of about one and half orders of magnitudes in the JAERI FEL experimental hall. Plastic, NaI(Tl) crystal and Glass scintillators have been used to reduce the radiation level. In order to monitor the radiation level induced by an electron beam loss, we have developed a new semiconductor radiation monitor using a Si-photo diode[1], CsI or BGO scintillators and a charge-sensitive hybrid amplifier[2]. In a heavy radiation circumference, we used to remove the scintillation crystal or glass to reduce the monitor sensitivity, and reduce the bias voltage. Design options of the photon detectors and monitoring ways will be discussed.

In the Fig.11.5.1, a typical pulse shape from the loss monitor prototype of Si-photo diode is shown to have a rise time of 30μs and a fall time of about a few hundreds μs. The rise time is the same with a beam pulse duration, and the fall time an amplifier time constant. The pulse is taken about 2 meters after the JAERI superconducting rf-linac based FEL driver. The monitor was fixed about one and half meter from the stainless-steel beam duct, and one the floor, and heavily-shielded with several 50mm-thick Pb blocks.

References

1) Hamamatsu Photonics Co. "Si PIN Photo diode S3590-05".
2) Hamamatsu Photonics Co. "a charge-sensitive hybrid amplifier H4083".

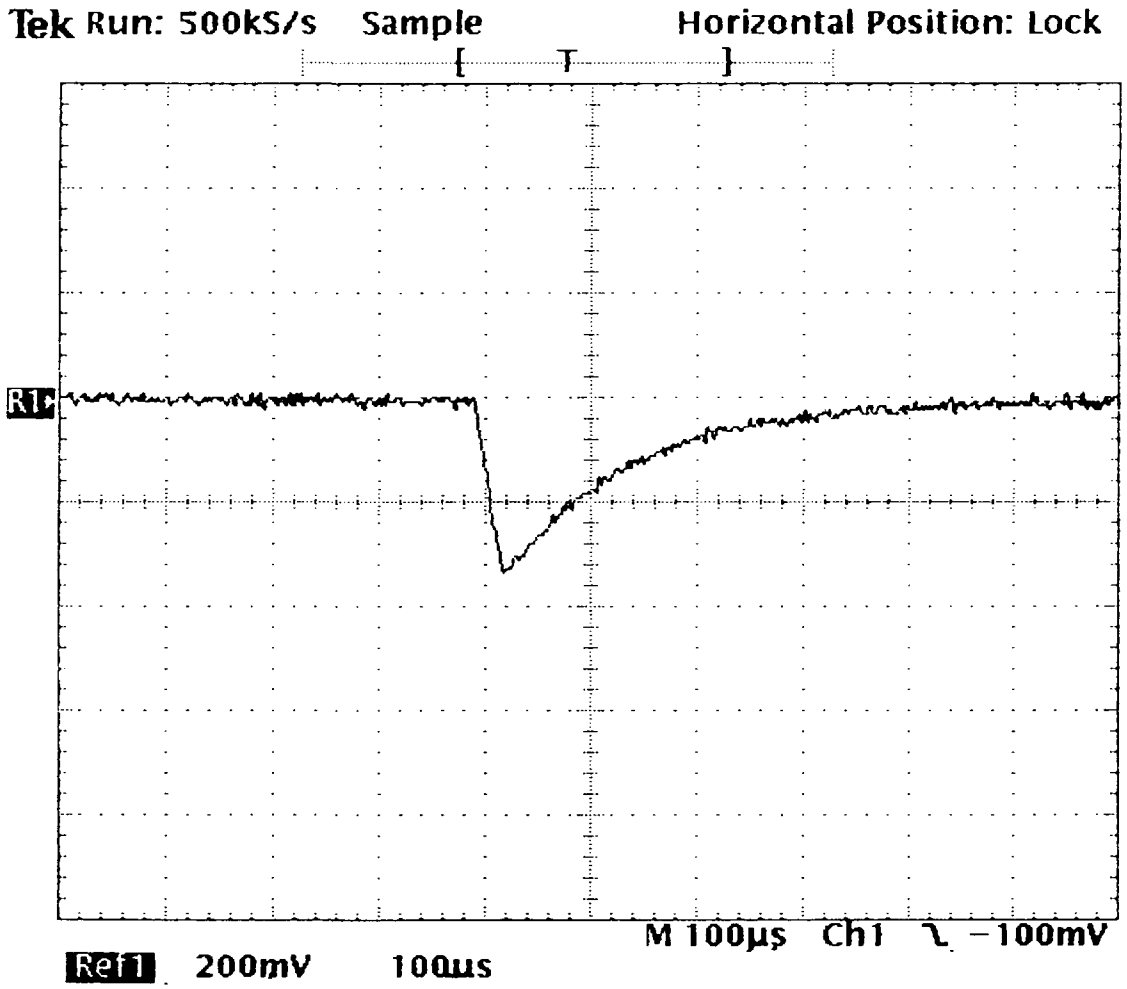

Fig.11.5.1 A typical pulse shape from a loss monitor prototype of Si-photo diode is shown, and has a rise time of 30µs and a fall time of about a few hundreds µs.

11.6 Precise Measurement of Resonator Length at JAERI FEL

N. Nishimori, E. Minehara, M. Sugimoto, M. Sawamura, R. Nagai and N. Kikuzawa
(*E-mail:* nisi@milford.tokai.jaeri.go.jp)

At the JAERI FEL, the repetition rate of the electron beam is absolutely set to 10.4125 MHz restricted by performance of the grid pulser electron gun. Then the resonator length must be 14.4 m to get the overlap between the radiated light and newly coming electron beam. For such a long FEL resonator, the miss adjustment of the resonator length cause a serious difficulty to achieve lasing, because the mirror movement over several millimeters is usually requested to adjust the resonator length. The sophisticated method using an external laser developed by Stanford University[1] was improved and adopted to make a direct measurement of the resonator length.

The experimental setup is shown in Fig. 11.6.1. A commercially available mode-locked Ti:sapphire laser (TSUNAMI) with 80 fs pulse duration and wave length of 790 nm was used for the experiment. The repetition rate was set to 83.3 MHz equivalent to the eighth harmonic of the repetition rate of the JAERI FEL. The laser beam was injected into the resonator through a 2 mm hole on the upstream mirror and the beam axis was adjusted to reach the center of the downstream mirror. The laser power at exit of TSUNAMI was 210 mW and it in the resonator was 3.7 mW. Adjustment of an inclination of the downstream resonator mirror was made by observing the reflected laser beam on a paper screen with a slit at the entrance of the undulator. Then the downstream mirror was

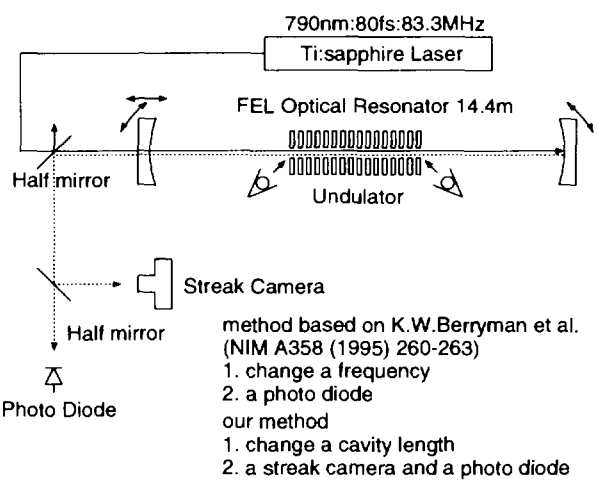

Fig. 11.6.1 The experimental setup to measure the resonator length at the JAERI FEL. An external Ti:sapphire laser was injected into the resonator through a 2 mm hole on the upstream mirror. The stored laser beam was outcoupled through the hole, and separated from the incident laser beam by a beam splitter cube. It was transported to the detector system, and measured by a streak camera and a photo diode simultaneously.

adjusted for both incident and reflected beams to overlap each other. The upstream resonator mirror was adjusted with similar procedure at the exit of undulator.

The stored light was outcoupled through the 2 mm hole and transported to the detector system composed of a streak camera (Hamamatsu Synchroscan Streakunit M1955) and an Avalanche photo diode (APD, Hamamatsu C5331-01). A time structure of the stored light was measured by those detectors.

At first we studied the time structure of outcoupled lights from the optical resonator by the streak camera. Since the frequency of the trigger signal for the streak camera was set to 83.3 MHz, time differences between the trigger and stored laser light signals were proportional to the resonator length difference from the resonance and the number of round-trips.

Scanning by the streak camera was made by 100 μm step. At longer resonator length than the resonance, the peak area was broad in up side as shown in the Fig. 11.6.2. But it was gradually narrower with decrease of ΔL and a line shaped structure was obtained around ΔL = 0 mm. At shorter resonator length than the resonance, the peak area became broad in down side. The time structure at the shorter resonator length is almost symmetric with that at the longer. During the scanning, the holed mirror was moved to change the resonator length. From the change of time structures, the resonance point could be roughly determined with the accuracy of 100 μm or less.

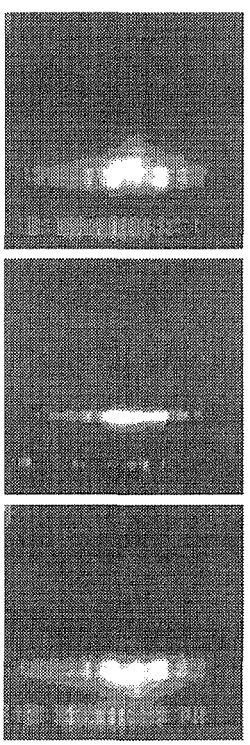

Fig. 11.6.2 The two dimensional time structures observed by a streak camera when the mirror distance was slightly changed. Figures are assigned from the upper ΔL = +0.55 mm、 0.00 mm and -0.45 mm, respectively.

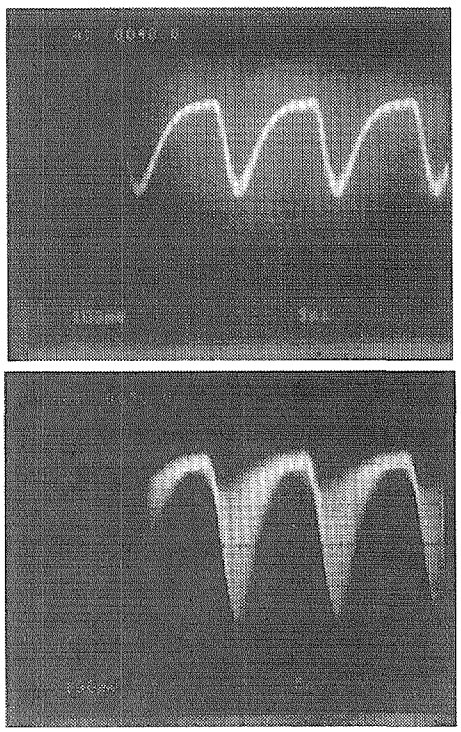

Fig. 11.6.3 Wave forms of photo diode signals on the oscilloscope. The upper shows a wave form at 34 μm longer resonator length. The lower shows it at the resonance.

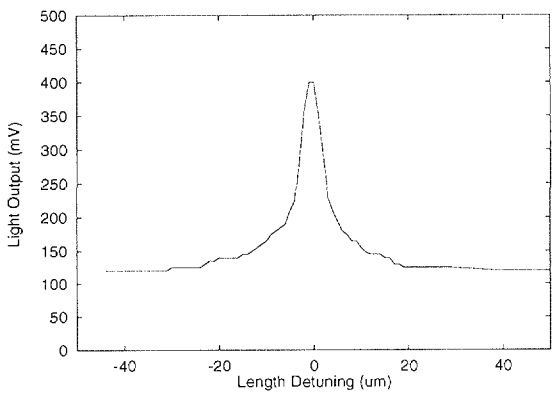

Fig. 11.6.4 The resonator length dependence of light output observed by a photo diode. The factor 3.3 enhancement was observed at the resonance. The measurement was made with the evacuated resonator.

After the rough determination of the resonator length, scanning by the APD was made by 1 μm step. The almost same wave form as shown in the upper of Fig. 11.6.3 was only seen on the oscilloscope outside the resonance region. But in the range of ± 10 μm from the resonance point, the peak height gradually began to become large, and the wave form shown in the bottom of Fig. 11.6.3 was observed on the resonance. The resonator length dependence of the peak height is shown in Fig. 11.6.4. The enhancement had been expected to reach to 10 times the background at the peak[1], but the factor of 4 enhancement was obtained in the measurement. From the Fig. 11.6.4, the resonance was determined within the accuracy of 1 μm.

References

1) K.W. Berryman P. Haar and B.A. Richman, Nucl. Instr. and Meth. **A358**, 260, (1995).

11.7 Improvement of Grid Pulser in the Electron Gun

N. Nishimori, R. Nagai, E. Minehara, M. Sugimoto, M. Sawamura and N. Kikuzawa
(*E-mail:* nisi@milford.tokai.jaeri.go.jp)

At the JAERI FEL, the electron gun is operated with a bunched mode to reduce the drop of the high voltage which is used to extract the electron beam. The electron beam is accelerated to the anode when the cathode voltage is lower than the grid. Therefore the repetition rate of the electron beam is controlled by changing the cathode voltage periodically. Such a circuit to control the cathode voltage is called a grid pulser. A stability of the grid pulser makes a direct effect to the electron beam, and is important to realize the stable operation of the accelerator and FEL.

Recently, following serious problems were observed in the electron beam pulses. 1) A micro-pulse had double or triple peaks, not a single peak. 2) A rapid droop was observed within a range of a macro pulse width. 3) A fluctuation of the height of each micro-pulse is large. Then we checked the output signal of the grid pulser as shown in Fig. 11.7.1. From the figure, some indications to solve the problems were obtained. 1) A shoulder was observed at the peak of the micro-pulse around -50 V. 2) A base line shift of the grid pulser signal was observed only with beam load. 3) The pulse height was not stable. To solve these problems we investigated the grid pulser circuit.

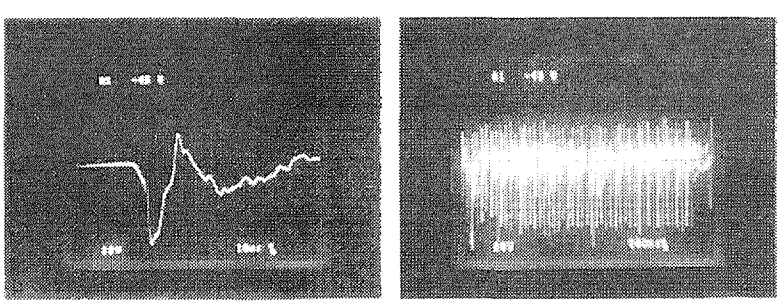

Fig. 11.7.1 The figures show the grid pulser signals obtained before the improvement. The time scale was 10 ns/div for the left and 500 ns/div for the right. The voltage scale was 20V/div for both sides.

Here we explain the signal flow of the grid pulser circuit briefly. Fig. 11.7.2 shows the circuit diagram of the grid pulser. As shown in the figure, the input signal is a TTL signal made by a commercially-available high precision pulser with a repetition rate of 10.4125 MHz. The input signal is amplified by FET consisting of three stages. An output signal of K298 in a final amplification stage should be ranged from -100 V

to +10 V and drive the tube named 7211. Then an output signal of 7211 should be ranged from -200 V to 0 V and drive the electron gun.

After the careful investigation of the grid pulser circuit, following improvements were made as solutions to above three problems. 1) As shown in the figure, the capacitor labeled "A" was opened because of the lack of resistance against the high voltage. Then we changed it into new one having high resistance. 2) It was expected that the base line shift was caused by the bias voltage change of the grid pulser and the current originated from the electron beam made the voltage drop on the resistor labeled "B". Then we shifted it between the ground and the bias. 3) To eliminate the fluctuation in micro-pulse due to instability in the pulsing circuit, the signal line was shielded by the ground line. After improvements itemized above, the grid pulser signals were obtained and shown in Fig. 11.7.3. They have no shoulder around peak, are stable throughout the macro-pulse range, and little base line shift was observed.

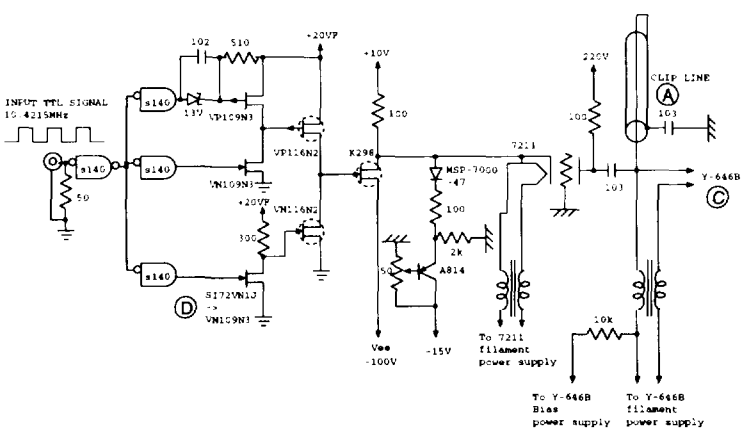

Fig. 11.7.2 The circuit diagram of the grid pulser.

The electron beam pulse after the improvement is shown in the right of Fig. 11.7.4. The beam is composed of series of micro-pulses having single peak and almost the same pulse height. The rapid droop shown in the left of Fig. 11.7.4 was not observed after the improvements, but the slight increase was observed over a 0.8 ms macro pulse duration.

In spite of above improvements, some problems have been left as a open question. The output signal of 7211 should be -200V, but it is -80V, the reason is that the input signal of K297 is -70 V, although it should be -100V. Therefore using a snap off-diode and a clip-line is not worth and they have been removed.

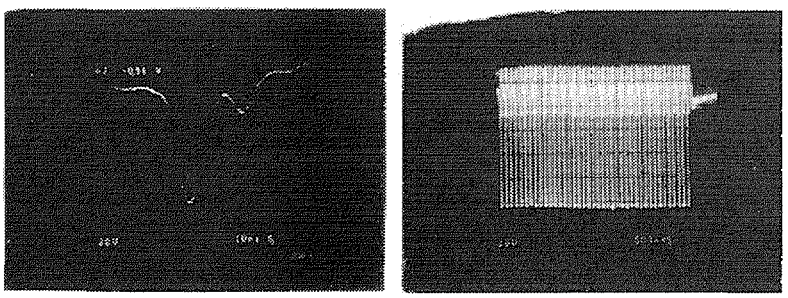

Fig. 11.7.3 The figures show the grid pulser signals obtained after the improvement. The time scale was 10 ns/div for the left and 500 ns/div for the right. The voltage scale was 20V/div for both sides.

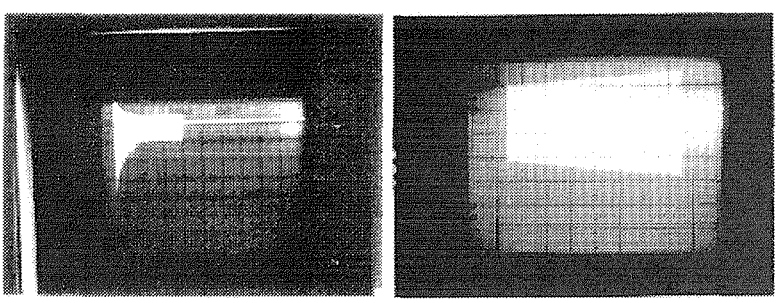

Fig. 11.7.4 The figures show electron beam signals observed by the same core monitor. The left is obtained before the improvement and the right after it. The time scale was 200μs/div for the left and 100μs/div for the right. The voltage scale was 200mV/div for both sides.

11.8 Measurement and Calculation of Electron Beam Bunching

M. Sawamura

(*E-mail:* sawamura@felwu0.tokai.jaeri.go.jp)

Beam Bunching Calculation

Method of Parameter Search

To substantiate the adequacy of the compressing section of the JAERI superconducting accelerator for FEL, the phase and energy spread were calculated with the beam dynamics code, PARMELA. All parameters, such as the amplitude and the phase of the accelerating field of each accelerator element, were optimized to minimize the phase spread as follows:

1) Each parameter was set and the longitudinal phase distribution was calculated with the PARMELA code. The average phase of all particles in the beam bunch at the final element was calculated.

2) Eighty percent of the particles with the phase nearest the average phase were selected. The phase spread for the set of the amplitudes and phases was defined in the above selected particles.

3) A Simplex method was used to search the minimum value of the phase spread by changing the amplitudes and the phases. This is an iterative method for nonlinear optimization of problems.

Compression with the SHB

PARMELA calculations for beam compression with only the use of the SHB were performed. The initial beam bunch is assumed to have a 200 keV energy, a 3 ns pulse length with a parabolic distribution, and a 1 mm beam radius with a uniform distribution. The phase spread $\Delta\phi$ is defined as the phase difference from a reference particle. As the phase is determined when the particle just reaches an element of the accelerator, the minus phase indicates that the particle is located ahead of the reference particle. Similarly the energy spread ΔW is defined as the energy difference from the reference particle. Figure 11.8.1 shows the longitudinal phase space distributions and the phase spectrums. As the phase space

distributions indicate, below 100 mA the electron beam is effectively compressed. However, 200 mA the beam compression is not good, mainly at the end of the beam bunch. As the space charge force increases with an increase in the beam current, the energy spread decreases, in spite of the high SHB. As a result of the decrease in velocity modulation, beam compression is not effective, particularly for the high current beams.

Compression with the SHB and Two Single-Cell modules

As mentioned above, beam compression is not satisfactory with only the use of the SHB due to the space charge effects. Thus, additional elements, two single-cell modules, are installed for compressing and accelerating the beam up to 2 MeV. Figure 11.8.2 shows the results or the beam compression with the SHB and the two modules of single-cell superconducting accelerators. Though the phase spread with the two single-cell modules is much improved over that with only the SHB, the phase and energy spread depends on the phase distribution at the end of the drift space after the SHB. The phase and energy spread is not good for the high-current beam due to insufficient compression at the entrance of the first single-cell module.

Measurement of the Beam Bunch Length

The bunch length has been measured at the exit of the second 5-cell superconducting module with the macro-pulse length of 10 μs. At this point, the bunch length is estimated to be several tens picoseconds. An aluminum plate profile monitor was installed. When the electron beam collided with an aluminum plate, optical transition radiation (OTR) was emitted. The bunch length was measured with the peak current of 4 A by detecting the OTR with the streak camera. Figure 11.8.3 shows the result of the bunch length measurement. It indicates a bunch length of 48 ps, which corresponds to 8.6 degrees.

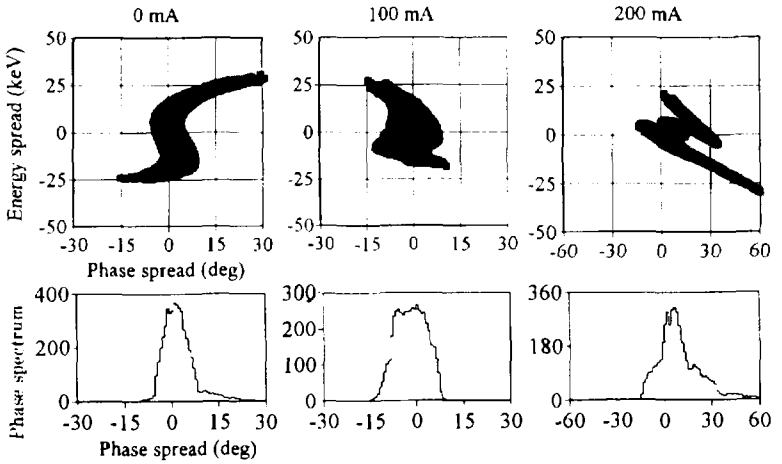

Fig.11.8.1 Longitudinal phase space distributions and the phase spectrum are calculated with only the SHB. The unit of the phase spread is degrees corresponding to 499.8 MHz.

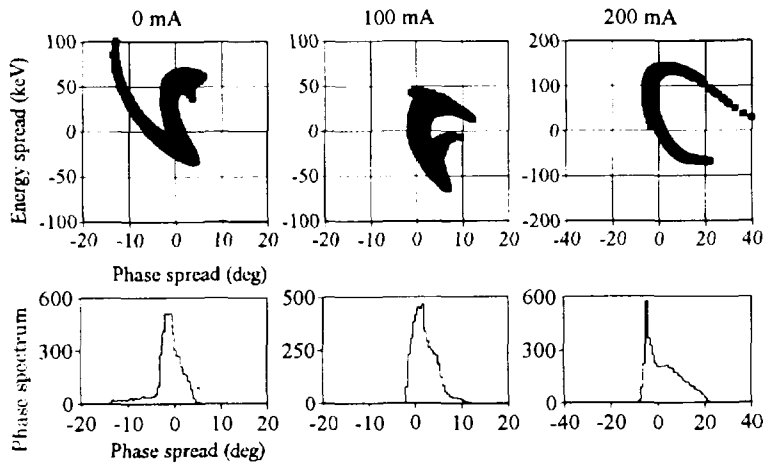

Fig.11.8.2 Longitudinal phase space distributions and the phase are calculated with the SHB and two single-cell modules.

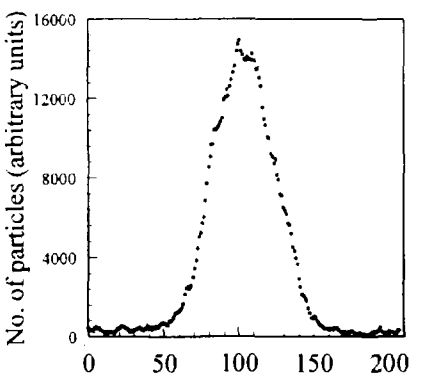

Fig.11.8.3 Bunch length at the exit of the second 5-cell superconducting module.

11.9 Optical Measurements of Spontaneous Emission

N. Kikuzawa, R. Nagai, M. Sawamura, N. Nishimori and E. Minehara
(*E-mail:* kikuzawa@felwu0.tokai.jaeri.go.jp)

The JAERI FEL driven by superconducting linear accelerator has been carried out to develop a compact far-infrared FEL. Detection of spontaneous emission is extremely important before an FEL starts lasing, because the spontaneous emission provides much information on such things as the correct steering of the electron beam and the alignment of the optical resonator. It is, however, difficult to detect the spontaneous emission because of the complex pulse structure. The JAERI FEL has a macropulse length of 50-1000 μs, but this is made up of 500-10000 micropulses, each a 40 ps long, separated by 100 ns.

For beam current of I [A] at wave length of spontaneous emission λ [μm], intensity of spontaneous emission P [W] can be calculated by

$$P = 2\times10^{-2}\times K^2 N_W I/\lambda ,$$

where N_W is number of period of an undulator and K deflection parameter of the undulator [1]. In case of 25 μm wavelength, 4 mA beam current, 0.7 K-value and 52 period of the undulator, the radiation power is estimated as 82 μW. However, the detectable power was estimated as 10^3 times smaller than the calculated value. It is considered that the difference comes from finite aperture and transmission of the KRS-5 window and diffraction loss during a external transport duct.

The detector requirements for the JAERI FEL are therefore severe. The most frequently used detectors for infrared FELs are photoconductive detectors. A Copper-doped Germanium (Ge:Cu) detector operated at liquid helium temperature has detectivity of infrared in 2 – 30 μm region and response time of 10^{-8} s [2]. Therefore the Ge:Cu detector is used to detect the spontaneous emission of the JAERI FEL.

In optical measurements, a scraper mirror was set in front of a downstream mirror of the optical resonator. The scraper mirror was 20 mm diameter gold-coated on a glass plate.

Spontaneous emission reflected by the scraper mirror was extracted through a KRS-5 window. The extracted radiation was guided through the external transport duct to the Ge:Cu detector operated at liquid helium temperature, which was installed in a measurement room to avoid radiation noise from the accelerator [3].

A tolerance of an angular alignment was calculated for the optical resonator [4]. The radiation loss was calculated as rotating the one-side resonator mirror horizontally or vertically. According to the calculated results, the rotation error must less than 10 μrad. Figure 11.9.1 shows the experimental results of rotating the downstream resonator mirror horizontally and vertically and detecting the output power on May 30, 1996. According to the result, the optical mirror can be adjusted to right direction less than 1 μrad.

Spectral distribution measurements have been carried out. The infrared spontaneous radiation was focused on an entrance slit of a monochrometer by concave mirrors. Figure 11.9.2 shows the experimental results of the spectral distribution measurements on March 25, 1997. The wavelength is defined by electron beam energy and a full width at half maximum of the spectral distribution depends on energy distribution and emittance of the electron beam. By measuring the spectral distribution, we can determine the electron beam parameters.

References

1) Hajima R. et al.: "Development of an Infrared Free-Electron Laser at University of Tokyo," Proceedings of the Symposium on Ion & Laser Processing for Advanced Materials –SILPAM '94, pp. 159-162 (1994).

2) M. F. Kimmitt: "Detectors for Infrared Free Electron Lasers," Infrared Phys. Vol. 32, pp213-224 (1991).

3) Kikuzawa N., Sawamura M. and Nagai R.: "FIR Detector for JAERI FEL," JAERI-Review 96-012, pp. 242-244 (1996).

4) Sawamura M., Nagai R., Kikuzawa N., Nishimori N. and Minehara E.: "Estimation of Optical Resonator for FEL," Free Electron Laser and Its Application in Asia, pp.195-199 (1997).

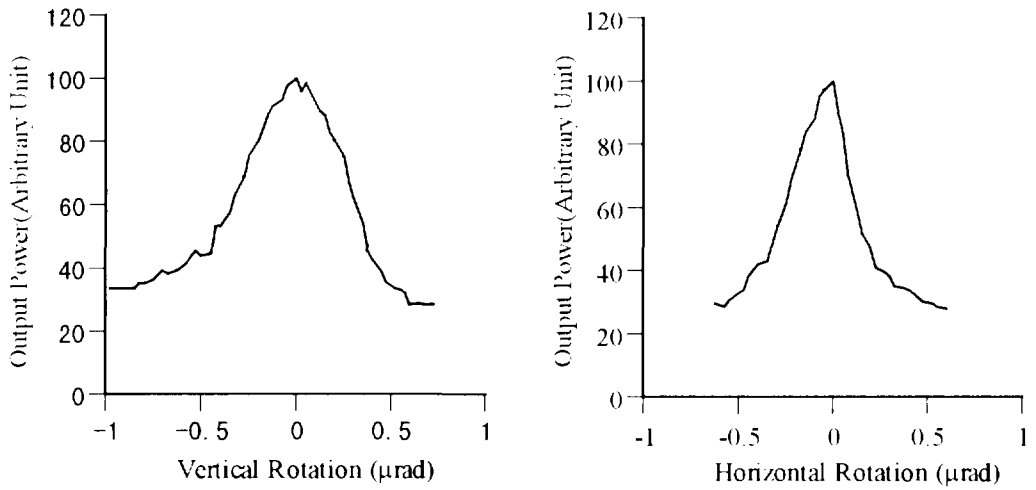

Fig.11.9.1 Experimental output power as function of vertical and horizontal rotation of the optical resonator mirror.

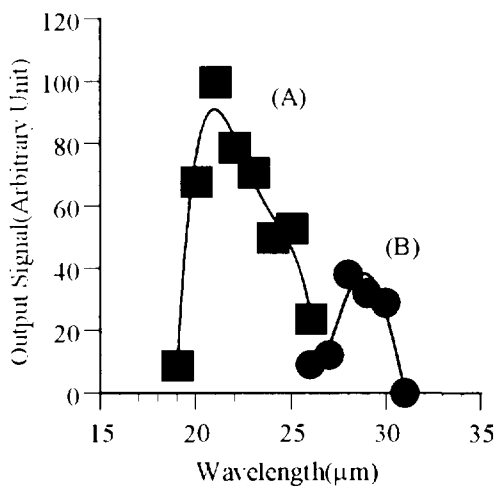

Fig.11.9.2 The spectral distribution of the undulator radiation at (A) electron beam energy E=17 MeV and (B) E=14.5 MeV.

11.10 Effects of the Undulator Field Roll-off

R. Nagai, M. Sawamura, N. Kikuzawa, N. Nishimori, M. Sugimoto and E. Minehara
(*E-mail*: nagai@felwu0.tokai.jaeri.go.jp)

The planar undulator for the free electron laser (FEL) experiment at JAERI has been made of Ne-F-B parmanent magnets and parmender poles. The undulator can provide a maximum field of 5 kGauss with less than 1% transverse roll-off at 2cm offset form the undulator axis. The transverse roll-off makes to degrade electron beam quality. The electron beam degradation makes to drop the performance of FEL.

Electron beam depression due to the roll-off was numerically evaluated by variation of the emittance and beam radius. As a result of the evaluation, in case of the roll-off is less than 1% at 20mm off from the undulator axis, the roll-off not makes to drop the performance of the FEL.

At offset from the undulator axis, the magnetic field became weak due to the magnet finite width of the undulator. An electron trajectory is distorted by the magnetic field strength distribution. The electron beam quality is degraded by the transverse field roll-off. The degradation was evaluated by calculating of the electron beam trajectory in the udulator field with the transverse roll-off. In the calculation, the field of the median plane (z-x plane) of the undulator is defined as follows,

$$B_{y0} = B_0 \sin(k_u z) \cdot (1 - ax^2) \qquad (11.10.1)$$

where B_{y0} is y-direction field component in the median plane, B_0 amplitude of the undulator field, k_u wave number of the field, a roll-off parameter. The roll-off is simulated by the value of the roll-off parameter. A set of the incident electron beam condition is summarized in Tabel 11.10.1. The emittance and beam radius variation of the electron beam passed through the undulator field are shown in Fig.11.10.1 and 11.10.2. In case of the roll-off is 1%, the emittance and beam radius enlargement are not so larger the 0% roll-off case. As shown in Fig.11.10.1 and 11.10.2, the effects of the transverse roll-off is negligible as long as the roll-off is less than 1%.

Table 11.10.1 Incident electron beam condition.

Energy (MeV)	15.0
Energy spread (%)	1.0
Emittance (π mm mrad)	1.0
Twiss parameter, a	0.8580
Twiss parameter, b	1.7362

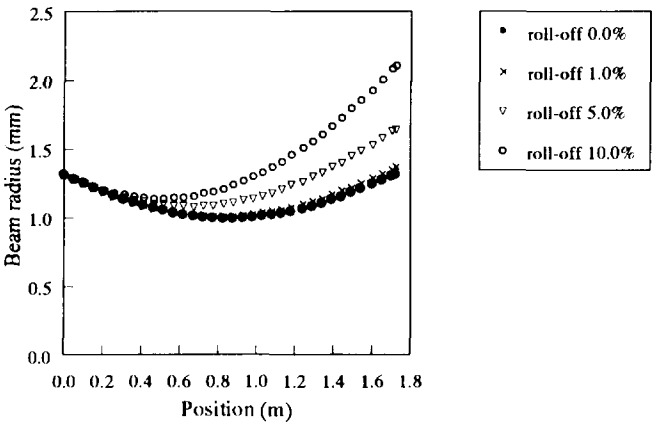

Fig. 11.10.1 The emittance variation of the electron beam passed through the undulator field.

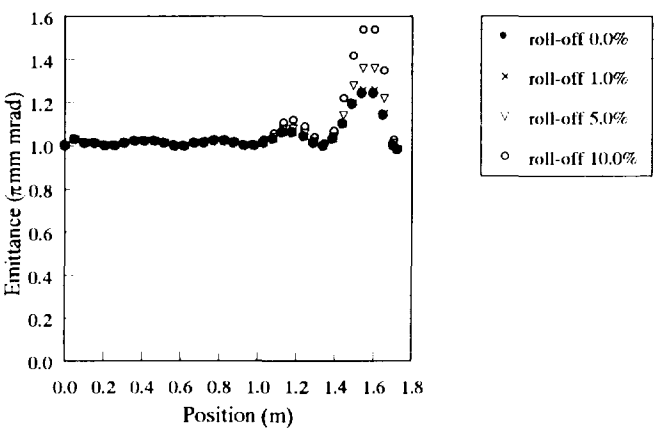

Fig.11.10.2 The beam radius variation of the electron beam passed through the undulator field.

References

1) R. Nagai, et al.: Nucl. Instr. and Meth. **A358** (1995) 403

11.11 A Progress in the High Intensity Proton Accelerator Development

M. Mizumoto, J. Kusano, K. Hasegawa, N. Ouchi, H. Oguri, M. Kinsho, Y. Touchi* K. Mukugi**, H. Ino***, Y. Honda***, F. Noda****, H. Kaneko*****, N. Akaoka****** and B. Fechner*******

(*E-mail* : mizumoto@linac.tokai.jaeri.go.jp)

The high- intensity proton linac with a beam power of 8MW has been proposed for the Neutron Science Project (NSP) in JAERI. The proposed NSP is aiming at exploring new basic researches and nuclear technologies such as condensed matter physics and nuclear waste transmutation based on a proton linac with an energy of 1.5GeV and an average current of 5.33 mA. The basic research facility will require the short pulse structure and high peak current of about 1 μs intermediate length. The R&D work and conceptual design studies have been carried out for the components of a low energy part and superconducting cavities of a high β linac. Preliminary design consideration has also started for the storage ring[1]. The schematic diagram of the proposed accelerator facility is shown in Fig. 11.11.1.

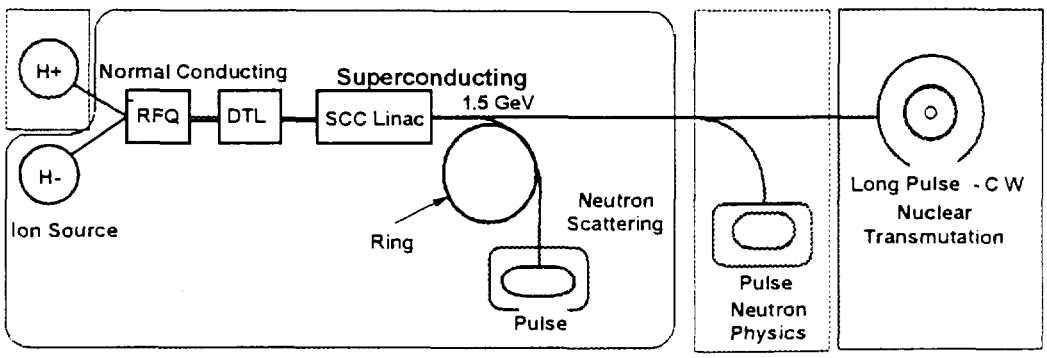

Fig. 11.11.1 A Schematic Diagram of the High Intensity Proton Accelerator Facility

JAERI had originally planned to study the pulsed linac with an energy of 1.5GeV and a peak current of 100mA with 10% duty factor. The design study has been continued to confirm technical validity to accelerate high peak current with high duty operation from the beam dynamics point of view. In this accelerator development, the R&D work has been

* Sumitomo Heavy Industries Ltd., ** Mitsubishi Electric Corporation
*** Mitsubishi Heavy Industries Ltd., **** Hitachi Ltd.
***** Toshiba Corporation, ****** Nippon Advanced Technologies Corporation
******* An STA Fellow during September, 1996 November, 1997

carried out on high brightness H^+ ion source, radio frequency quadrupole linac (RFQ), drift tube linac (DTL) and RF source. In the beam test, the current of 80mA with a duty factor of 8% has been accelerated from the RFQ at the energy of 2MeV[2].

Since 1995, the basic specifications for the accelerator has been changed due to the new requirements emphasizing the superconducting high β linac and the proton storage ring for short pulse operation. The superconducting linac is expected to have several favorable characteristics for high intensity accelerator such as short accelerator length, large bore radius resulting in low beam losses and cost effectiveness for construction and operation. This superconducting linac will be operated in pulse as a first stage and gradually upgraded toward CW by increasing duty factor. The new design modification and various development work have been started to meet the requirements such as for negative ion source, CW- RFQ, CW- DTL, superconducting cavity and storage ring.

A flow diagram for the work of the high intensity accelerator development is shown in Fig. 11.11.2. Four major R&D items are presently carried out. 1) the accelerator system design including beam dynamics calculation for the high β linac. 2) the low energy accelerator development of the negative ion source and the fabrication of high power test models for CW- RFQ and CW- DTL. 3) the high energy accelerator for superconducting cavity and 4) the high power RF source.

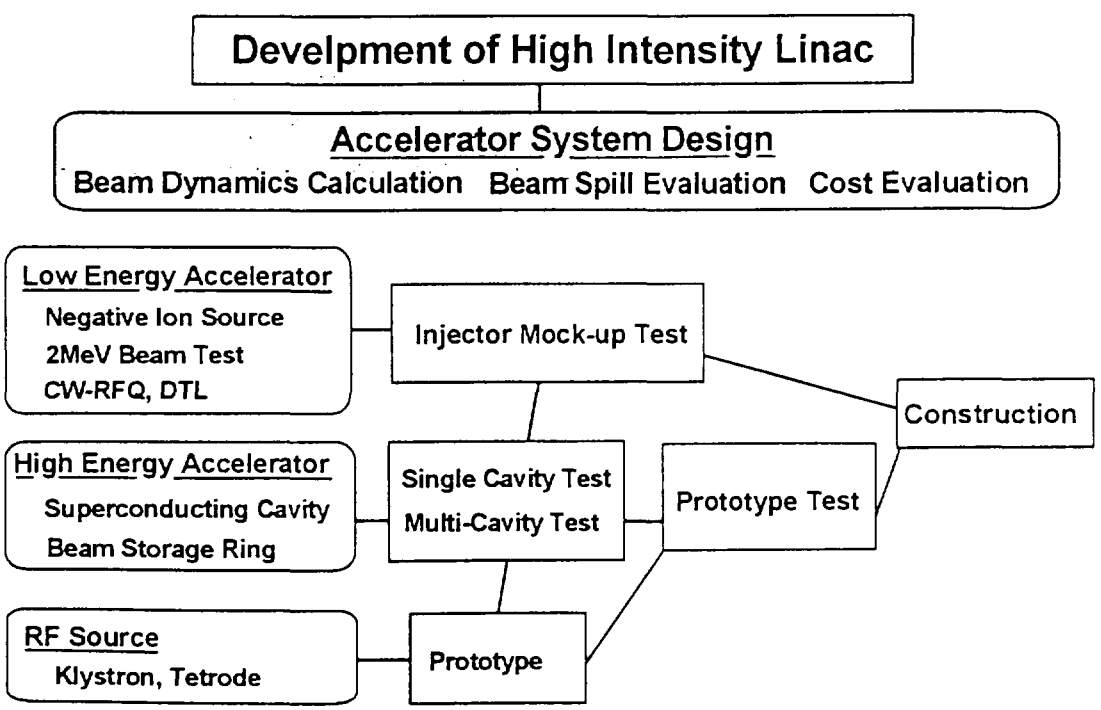

Fig.11.11.2 A Flow Diagram for the Work of the High Intensity Accelerator Development

The design and operating experiences for superconducting electron accelerator are accumulated which is operated in light velocity, β=1 (particle velocities divided by light velocity) at various laboratories. For proton accelerators, however, β values are gradually increased from about 0.5 to 0.9 and structures has to be adjusted according to these proton energies. The mechanical strength at lower β region is of major difficulty for proton accelerator. The superconducting accelerator development has been performed in collaboration with the KEK (National Laboratory for High Energy Physics). A preliminary specification for the NSP accelerator is given in Table 11.11.1.

Table 11.11.1 A preliminary specification of the NSP-Accelerator

Energy	1.5GeV
Accelerated particle	Negative and positive hydrogen ion
Average current:	5.33mA
Pulse structure	First stage ; Pulse mode operation Second stage; CW/pulse mode operation
Macropulse width	3.7ms -> maximum CW
Intermediate pulse width	400ns (interval 270ns)
Chopping factor: Peak current	60%; nominal 30mA

A superconducting cavity test stand was built at the JAERI Tokai Site with the equipment of cryogenics system, vacuum system, RF system and cavity processing and cleaning to test the physics issues and fabrication process. A single test cavity was fabricated for β=0.5 which corresponds to the proton energy 145MeV[3]. A first vertical test was conducted to examine the RF and mechanical properties. The maximum field strength of 16MV/m for 4K and 18.6 MV/m for 2K was successfully obtained as first time for proton accelerator. The design efforts for other various accelerator components have been simultaneous made which are described in the separate papers in this annual report.

References

1) M.Mizumoto et al, Development of High Intensity Proton Accelerator , 2nd Int. ADTT Conf., June 2-7, 1996, Kalmar, Sweden, p1004

2) K.Hasegawa et al., The R&D Status on the Front End of the High Intensity Proton Accelerator in JAERI , Proc. of the LINAC 96, Geneva, August 26-30, 1996, p665

3) N.Ito et al., Development of a Superconducting Cavity for the High Intensity Proton Linac in JAERI , ibid., p671

11. 12 Present Status of 2 MeV Beam Test with a Positive Ion Source and an RFQ Linac

H. Oguri, M. Kinsho, N. Ouchi and Y. Touchi*

(*E-mail:* oguri@linac.tokai.jaeri.go.jp)

The 2 MeV beam test has been performed to study the characteristics of the injector section of the high intensity proton linac for the Neutron Science Project at JAERI[1]. The layout of the beam test is shown in Figure. 11.12.1. The beam line consists of an high brightness ion source (IS), a Low Energy Beam Transport (LEBT), an RFQ and a Medium Energy Beam Transport (MEBT). We have obtained the RFQ peak current of 80 mA but remained 20 % less than the design value[1]. To investigate the reason for not to reach the peak current to the design value, we measured the RFQ input beam current by using a current transformer and evaluated the beam transmission rate in the LEBT and RFQ.

Figure 11.12.2 and Figure 11.12.3 show the peak beam current (Ip) and transmission rate (Tr) in the LEBT and the RFQ as a function of the IS beam current. An applied voltage ratio Γ in these figures is defined by the ratio of the electric potential at the first electrode and the second electrode of the IS. When Γ was large, the IS current decreased but the emittance became small[2].

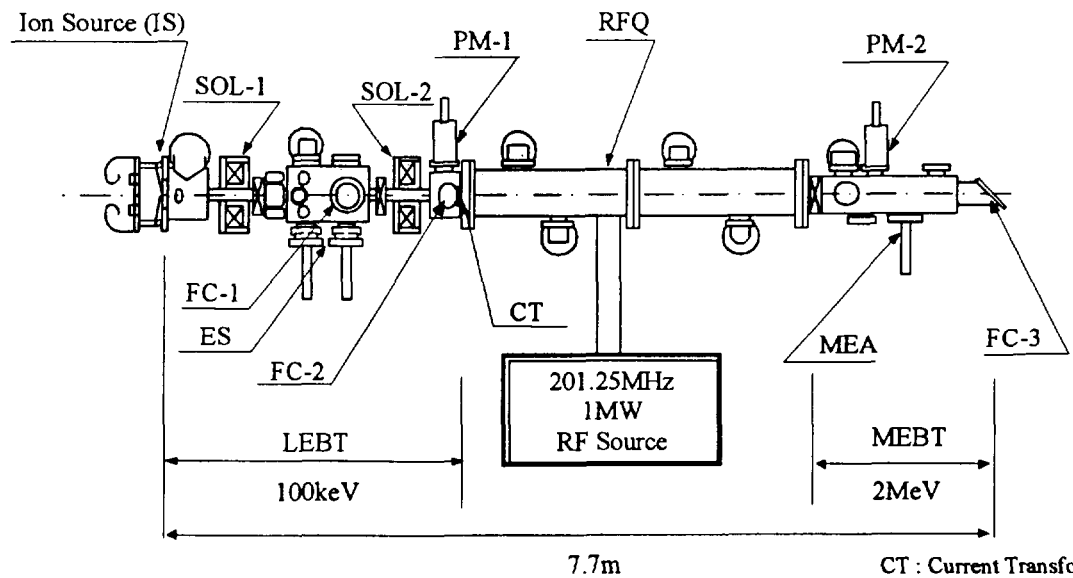

Fig. 11.12.1 Layout of R&D 2MeV Beam Test

* Sumitomo Heavy Industries, Ltd.

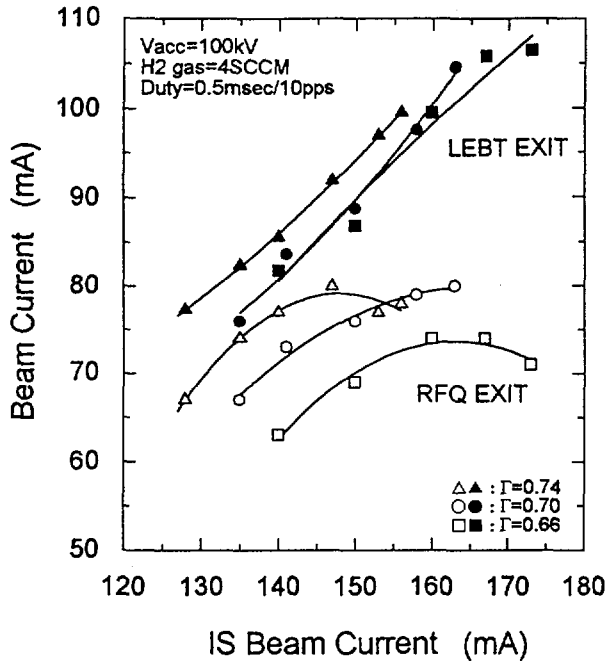

Fig. 11.12.2 Peak current in LEBT and RFQ as a function of the IS current

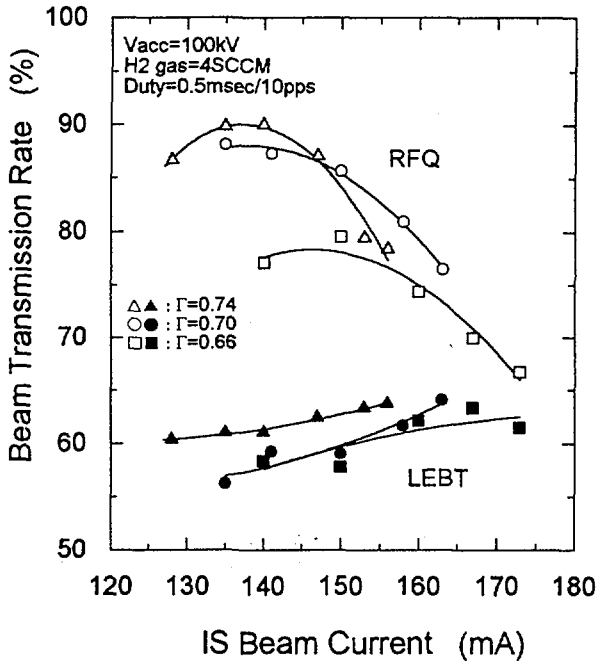

Fig. 11.12.3 Beam Transmission rate in LEBT and RFQ as a function of the IS current

The Ip and Tr in the LEBT increased linearly with the IS current. The maximum Tr was 65 %. By considering the proton fraction in the IS beam to be 80 % and mass separation effect of the solenoid lens, the maximum Tr of the proton beam is estimated to be 80 %. The Ip and Tr in the RFQ, on the other hand, had the peak value as a function of the IS beam current for each of Γ. When the Γ was large, the Ip and Tr became high. We consider that improvement of the beam emittance from the IS is expected to enhance the Ip and Tr in the RFQ. Figure 11.12.4 shows the rms emittance measured about 1 m downstream from the IS and the Tr in the LEBT and the RFQ as a function of the IS current at the Γ of 0.70. The solenoid lens was not used during this emittance measurement to keep the ion source emittance. The emittance became minimum at the beam current of 170 mA. We obtained an unexpected result that the Tr in the RFQ increased even if the emittance became large where the IS current is less than 170 mA. We consider that when the beam emittance from the IS is large, the beam of the peripheral region is lost in the LEBT, and the beam of the core region, which seems to have sufficient small emittance to be acceptable to the RFQ, can reach at the RFQ entrance. We have to perform more precise measurement of the emittance at the RFQ entrance and compare with the RFQ acceptance.

In the positive ion source, the source plasma is produced by an arc discharge by using the tungsten filament. The lifetime of the tungsten filament is a few hundred hours. A LaB_6 filament which has been manufactured at High Energy Accelerator Research Organization (KEK), on the other hand, has a long lifetime. It is reported to be 10 times as long as the life of the tungsten[3]. We performed the beam test by using a LaB_6 filament whose dimensions are 20 mm in diameter and 77 mm in length. The filament was obtained from KEK. The filament was successfully operated in pulse mode operation. In CW mode operation, however, the arc current suddenly increased and the electric power supply for the arc discharge stopped by the over current. We consider that the filament was heated up continuously due to the condense plasma in the central region of the plasma chamber. The geometry of the filament and the position to install the filament must be optimized for the CW mode.

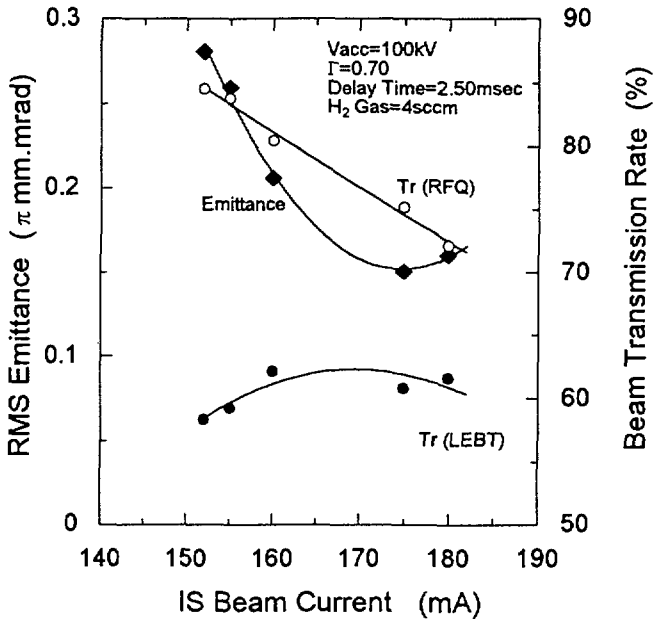

Fig. 11.12.4 Emittance of the IS beam and transmission rate in LEBT and RFQ

References

1) Hasegawa K., et al., Proceedings of the 1996 Linac Conference, Geneva, Switzerland, (1996) 665

2) Oguri H., et al., Proceedings of the 1994 Linac Conference, Tsukuba, Japan, (1994) 381

3) Takagi A., Private communication

11. 13 Development of a Negative Hydrogen Ion Source

H. Oguri, M. Kinsho, Y. Okumura and M. Mizumoto
(*E-mail:* oguri@linac.tokai.jaeri.go.jp)

At JAERI, a construction of a 1.5 GeV/10 mA proton linear accelerator has been proposed for engineering tests of accelerator-based nuclear waste transmutation and for various basic science researches[1]. A negative hydrogen ion source for the accelerator has been developed since 1995. The basic performance of a single aperture beam extraction system was investigated with the volume production type negative ion source which has been originally developed for a neutral beam injector for fusion application[2]. The extracted ion beam current of 36 mA was obtained at the arc discharge power of 45 kW[3]. To obtain higher beam current, the negative ion beam is extracted from multiple apertures and the beamlets are focused by aperture displacement technique. The positive ion source which was used for previous beam performance experiments[4] is modified to produce the negative ion beams in the present experiment.

Figure 11.13.1 shows a cross sectional view of the multi-aperture volume production type ion source. Negative ions are generated in a magnetically filtered multi-cusp plasma generator, whose dimensions are 200 mm in inner diameter and 170 mm in length. The dimension of the ion source is the same as the positive hydrogen ion source[4] except for the existence of the transverse magnetic field, which is created by changing the polarity of the cusp magnets near the plasma grid. The source plasma is produced by an arc discharge using four tungsten filaments, and confined by strong multicusp magnetic field. A magnetic filter, which is formed by Sm-Co permanent magnets, divides the generator into two regions and modifies electron energy distribution so as to produce negative ions. Negative ion production rate is enhanced by seeding a small amount of cesium[5] in the plasma generator.

The beam extractor consists of four grids such as a plasma (PG), an extraction (EXG), an electron-suppression (ESG) and a grounded grid (GG). The PG is made of molybdenum plate. The EXG is made of a 10 mm thick copper plate with a water cooling channel and magnet grooves. In the EXG, Sm-Co permanent magnets are inserted so as to produce a dipole magnetic field. This field deflects the extracted electron and prevents the leakage of the electron to the acceleration gap. The ESG is installed for trapping the leakage electron escaping from the EXG.

In the present experiment, produced negative ions are extracted from seven apertures of 9 mm in diameter. Figure 11.13.2 shows the cross sectional view of the extractor. The distance between the position of the central aperture and that of the peripheral one is 13 mm in the PG and the EXG. In the ESG and the GG, on the other hand, the peripheral aperture is displaced by 1 mm to the direction of center axis. A strong electrostatic lens is formed by the electric field applied in the gap between the ESG and GG. The beamlets extracted from the peripheral apertures are steered by the electrostatic lens to merge into a single beam.

Figure 11.13.3 shows the negative ion current as a function of the arc discharge power for the operations with and without cesium. The filling hydrogen gas pressure in the plasma generator (Ps) was 0.8 Pa. In the pure volume operation, the ion current tended to saturate at high arc discharge power and was limited to be 20 mA. In the cesium-seeded operation, on the other hand, the beam current was enhanced by about three times and increased lineally with the arc discharge power. The negative ion current (density) of more than 70 mA (16 mA/cm^2) was obtained at 25 kW. The current density is defined by the beam current divided by the total beam extraction area of 4.45 cm^2.

In the multi-aperture extraction experiment, the emittance in vertical plane was measured using a double slit with a Faraday-cup system at an acceleration voltage of 30 kV. The distance between the slits is 390 mm. The size of the first and second slit are 0.5 mm x 50 mm and 0.1 mm x 50 mm, respectively. Figure 11.13.4 shows the emittance diagrams at the ion source position. These three diagrams correspond to those which were extracted from central aperture (closed triangles) and lower aperture (closed circles), upper aperture (closed squares), respectively. The normalized 90 % emittance of each beam was calculated to be about 0.8 πmm.mrad. The beam steering angle is determined by comparing the angle of the peripheral beam axis with that of the central one. Because the beam from the lower (upper) aperture has the steering angle of + (-) 15 mrad, the beam trajectory was found to be deflected toward the center of the ion source. The focal point of the merged beamlets is estimated to be 800 mm downstream from the ion source.

The R&D work is to be continued so as to investigate the dependence of the steering angle on the various type of the displacement. The steering angle is 1.5-2 times larger than the value predicted by the linear theory using thin lens approximation[6]. The experimental result is to be compared with the value calculated by the 3-D beam trajectory code, which is under preparation.

References

1) M. Mizumoto, et al., Proceedings of the 1992 Linac Conference, Ottawa, Canada, (1992) 749

2) T. Inoue, et al., Rev. Sci. Instrum., 66 (7), 3859 (1995)

3) H. Oguri, et al., Rev. Sci. Instrum., 67 (3), 1051 (1996)

4) H. Oguri, et al., Proceedings of the 1994 Linac Conference, Tsukuba, Japan (1994) 381

5) Y. Okumura, et al., Rev. Sci. Instrum., 63(4), 2708 (1992)

6) Y. Okumura, et al., Rev. Sci. Instrum., 51(4), 471 (1980)

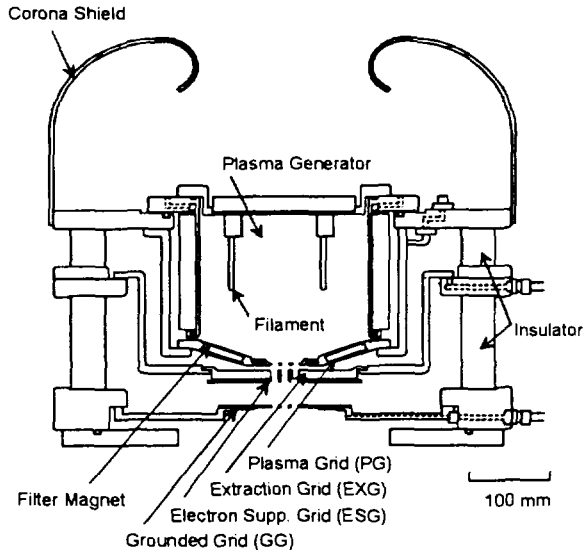

Fig. 11.13.1 Cross sectional view of the multi-aperture volume type negative ion source

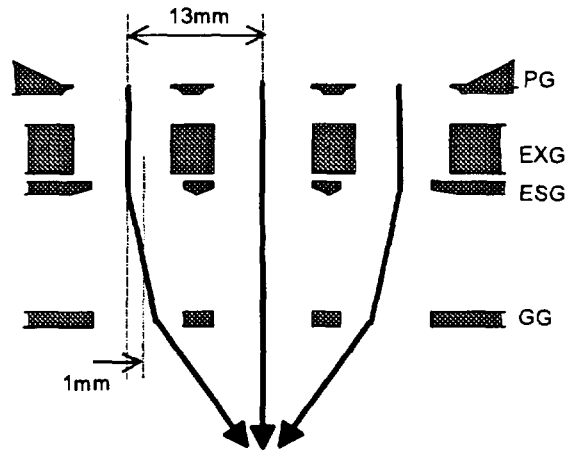

Fig. 11.13.2 Cross sectional view of the beam extractor with the aperture displacement technique

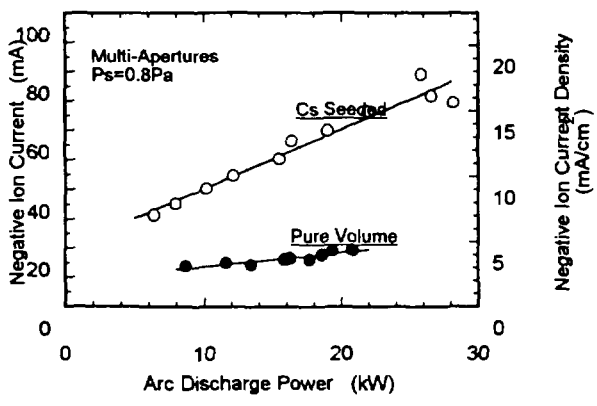

Fig. 11.13.3 Negative ion current (density) as a function of the arc discharge power for the operations with and without cesium

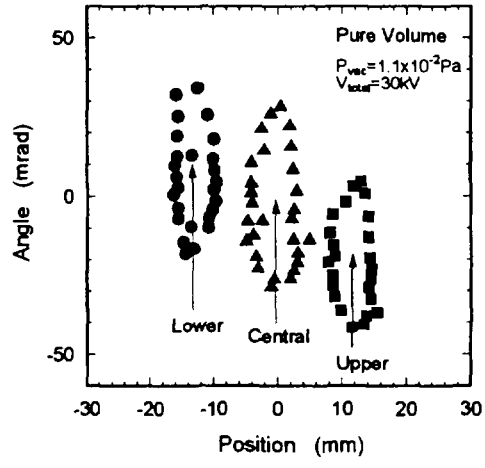

Fig.11.13.4 Emittance diagrams from the multi-apertures at the ion source position

11.14 A Conceptual Design of the CW-DTL for the JAERI High Intensity Proton Accelerator

H. Ino*, N. Ouchi, and M. Mizumoto
(*E-mail*: inoh@linac.tokai.jaeri.go.jp)

An accelerating structure called DTL (Drift Tube Linac) will be applied as a component of the low energy part of the JAERI High Intensity Proton Accelerator. Table 11.14.1 shows the basic requirements of the DTL design. The design has been carried out under the conditions listed in this table. Table 11.14.2 shows the present design parameters based on the Table 11.14.1. We discuss the parameters and beam dynamics issue below.

The DTL is divided into three tanks to keep the frequency spacing between the operating mode and other modes as large as possible. Each tank has about 50 kHz frequency spacing between the TM010 and TM011 mode without post couplers.

Since the DTL will be operated under CW condition, it is necessary to keep average electric field gradient E0 rather low and to cool the structure efficiently, in order to reduce beam loss due to the thermal distortion. We have done some heat transfer analyses of a drift-tube and find that E0=1.5 MV/m is sufficient. This causes a maximum temperature rise up to 54 ℃ approximately, and a shift of bore center to about 60 μm.

The synchronous phase angle starts at - 55 deg. ensuring a large enough rf bucket to capture 100% of the beam. It ramps up to - 30 deg. at about 33 MeV and remains constant for the rest of the tank.

The quadrupole gradient which ramps from 77.3 T/m to 9.2 T/m is determined on the basis of equipartitioning theory combined with coupled envelope equations for the bunched beam. The FODO quadrupole focusing lattice is selected because it produces small beam size compared with other lattice. As we have already developed the quadrupole magnet that produces field gradient of 80 T/m[1], the further consideration to achieve the field gradient of 77.3 T/m is unnecessary.

Fig.11.14.1 shows the effective shunt impedance (ZTT) of the DTL along the particle energy. We could keep ZTT above 28 MΩ/m throughout the DTL by setting the face angle α to drift-tubes in tank-2 (α=50 deg.) and tank-3 (α=60 deg). The wall loss (assumed 100%Q) of the DTL decreases from 4.56 MW (which is the value of no face angle one) to 3.58 MW as a consequence.

---

* Mitsubishi Heavy Industries, LTD.

We have been evaluating the beam-dynamics performance of the designed DTL using PARMILA code. This simulation uses 10,000 macro-particles. The input beam has a Gaussian distribution, and the emittance value of the RFQ output beam calculated by PARMTEQ code. No separate matching section between tanks are applied in the simulation. Fig.11.14.2 shows the transverse (x and y) and longitudinal normalized rms emittance along the particle energy. There are only a few present of growth in either transverse or longitudinal emittance.

Reference

1) Hasegawa K., et al. : R&D WORKS OF THE DTL FOR THE BTA IN JAERI , The 18 th Linear Accelerator Meeting in Japan, KEK, July 1993.

Table 11.14.1 Basic requirements for the CW-DTL

Injection/Final energy	[MeV]	2/100
Frequency	[MHz]	200
Particles		H-
Duty factor		~CW
Beam current	[mA]	30

Table 11.14.2 Design parameters of CW-DTL

Tank No.		1	2	3
Injection/Final energy	[MeV]	2/33	33/67	67/100
Average cavity gradient	[MV/m]	1.5	1.5	1.5
synchronous phase angle	[deg.]	-55 → -30	-30	-30
Quadrupole focusing Lattice		FODO	FODO	FODO
Quadrupole gradient	[T/m]	77.3 - 14.5	14.5 - 11.0	11.0 - 9.2
Effective shunt impedance	[MΩ/m]	28.3 - 31.4	52.9 - 37.1	40.9 - 30.9
Peak surface electric field		1.0 kilpatrick	1.0 kilpatrick	1.0 kilpatrick
Wall loss (100%Q)	[MW]	1.3	1.1	1.2
Cell Number		135	69	59
Tank length	[m]	32.2	32.2	34.9
Tank Diameter	[cm]	91.8	97.1	96.6
Drift-tube diameter	[cm]	20	20	20
Bore radius	[cm]	1	1.1	1.2
Corner radius	[cm]	1.9	1.9	7
Outer nose radius	[cm]	-	0.5	0.5
Inner nose radius	[cm]	0.5	0.5	0.5
Flat length	[cm]	-	0.5	1
Face angle	[deg.]	0	50	60

Total wall loss (100%Q) = 3.6 MW
Total cell number = 263
Total tank length = 99.3 m

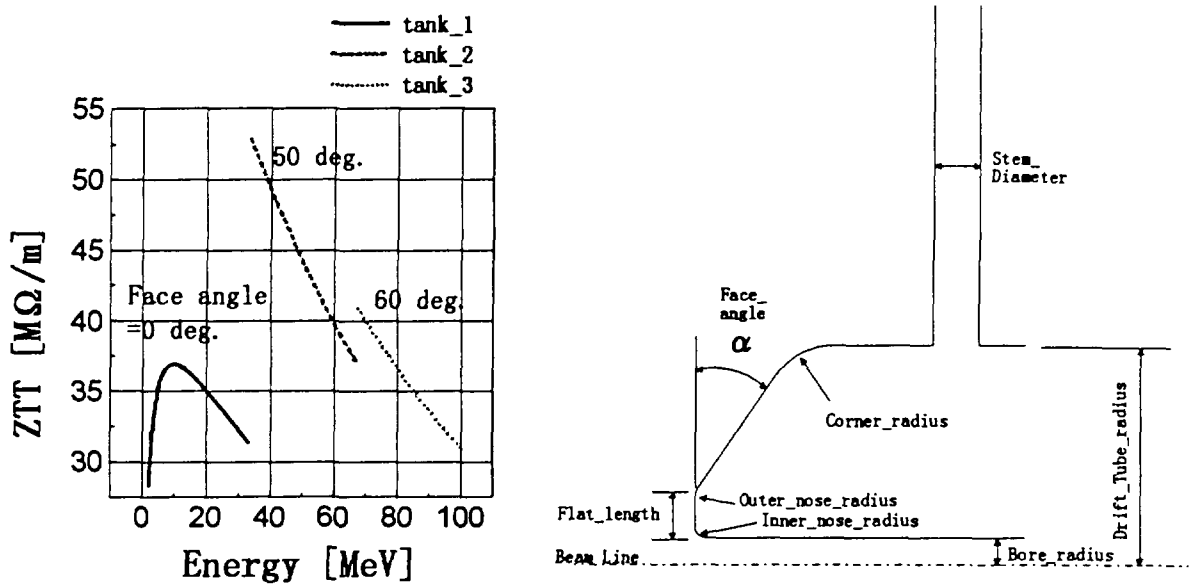

Fig. 11.14.1 Effective shunt impedance along the particle energy and the definition of the face angle

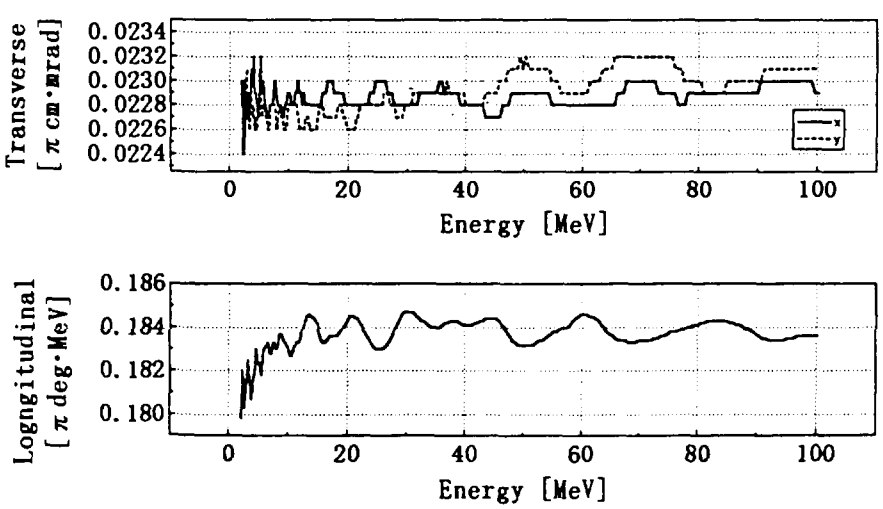

Fig. 11.14. 2 Transverse and longitudinal normalized rms emittance along particle energy

11.15 A Conceptual Design Study of RF System for the 1.5GeV Linac

Y. Touchi*, K. Mukugi**, N. Ouchi and H. Kaneko***
(*E-mail:* touchi@linac.tokai.jaeri.go.jp)

A high-intensity proton linear accelerator has been proposed for the Neutron Science Project (NSP). A design study for the high energy portion of the NSP-linac, above 100MeV, has been carried out using superconducting(SC) cavities. Compared with a normal conducting cavity the superconducting cavity has excellent characteristics: high Q-value and large bore radius. But tuning of it within its very narrow bandwidth is difficult to realize. It has been reported from TESLA project that the superconducting cavity which is made by niobium sheet may not have a sufficient strength for the Lorentz-force. This will be a serious problem when the linac is operated in pulsed condition. The calculation of the frequency shift due to the Lorentz-force[1] and the detuning caused by the beam loading has been done in our case. Finally we propose an RF system taking these effects into account by referring to the TESLA system.

Lorentz-force

The wall thickness of the present SC cavity design is 3mm. The calculation of the β=0.5 cavity wall displacement at an accelerating voltage of 4.2 MV/m was done. In this case, the maximum displacement of the cavity wall is 0.088 μ m, and the frequency shift is 208 Hz. This value is not small compared with the band-width of 327 Hz (Q_L=1.8E+06). So we should try to minimize this frequency shift, for example, by increasing the wall thickness and/or put the stiffening ring. The displacement of the cavity wall is shown in Fig. 11.15.1. Table 11.15.1 shows the frequency shift, phase error and decrease of cavity voltage caused by Lorentz-force for a number of cases of wall thickness. Fig. 11.15.2 shows the phase error and cavity voltage as a function of frequency shift.

Detuning

An RF power is supplied into the cavity to generate an accelerating field(**Eg**). The beam induces a wake field(**Eb**) while passing through the accelerating gap. Hence the beam is accelerated by vector sum of these field(**Eg**+**Eb**). To compensate this effect, in other word to get maximum accelerating efficiency, we detune the cavity resonant-frequency. The frequency shift: $\triangle$f is given as follows[2].

$$\frac{\Delta f}{f_0} = \frac{I_0}{2V_c}(R/Q)\sin\Phi_S$$

where I_0 is a beam current, V_C is an accelerating voltage including the transit time factor and cos(Φ_S), Φ_S is the synchronous phase. The calculated result is shown in Table 11.15.2.

---

* Sumitomo Heavy Industries Ltd.
** Mitsubishi Electric Corporation
*** Toshiba Corporation

RF control

The TESLA RF system[3] is similar to our system, and it is estimated that the frequency shift due to the Lorentz-force will be above 400 or 600 Hz with stiffening system. This is bigger than its bandwidth of 465 Hz. The tuning error of 400 Hz corresponds to the detuning angle 60°. Therefore, a fast tuning mechanism to compensate the effect of the Lorentz-force is needed for the TESLA RF system.

In our case, the calculation result indicates that the detuning due to the beam-loading is not so large, but the frequency shift due to the Lorentz-force in the present SC cavity design is not small compared with its band width. So we should try to suppress the frequency shift to less than 30 Hz which corresponds to the detuning angle 10°. It seems that the frequency shift will be suppressed to less than 30 Hz, by increasing of cavity wall thickness and/or using of a stiffening ring. The preliminary design study of the RF system will be continue without the particular control circuit like TESLA system. The feed forward control circuit[4] combined with the feed back circuit will be needed to realize voltage and phase stability, 0.1% and $\pm 1°$ respectively, under large beam loading operation. The proposed RF control system is shown in Fig. 11.15.3.

References

1) Haebel E. and Tuckmantel J.: "Electromagnetic Surface Forces in RF Cavities", CERN - AT - RF(Int) - 99

2) Furuya T.: "Choudenndou kuudou", KEK- OHO'94

3) Edwards D.A.: "TESLA TEST FACILITY LINAC - Design Report", DESY-TESLA 95 - 01

4)Touchi Y., et al.: "An RF system for the BTA", EPAC94 (1994)

Table 11.15.1 Displacement of the β=0.5 cavity wall due to the Lorentz-force and frequency shift, reduced cavity voltage and phase error

Thickness	Displacement	Frequency shift	Voltage	Phase error
mm	μm	Hz	%	deg
3	0.088	-208.2	56.5	55.2
4	0.045	-131.2	73.6	42.3
5	0.025	-62.9	91.5	23.6
6	0.016	-40.5	96.3	15.5

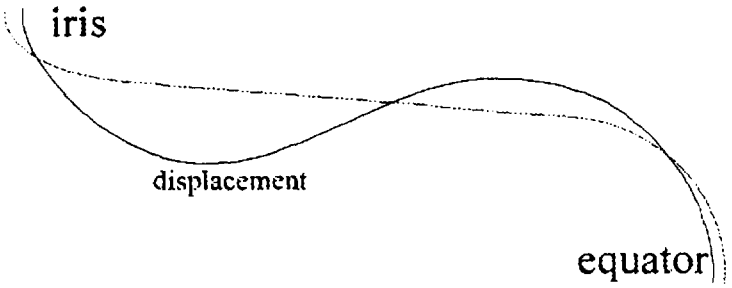

Peak RF field : 16 MV/m
Wall thickness : 3mm

Fig.11.15.1 Displacement of a cavity wall, β=0.5

Table 11.15.2 Detune by beam loading

Beam current	Detune	Voltage	Phase
mA	Hz	%	deg
1	-6.3	99.9	2.28
3	-18.8	99.3	6.8
5	-31.3	97.9	11.8
10	-62.6	92.5	22.2
15	-93.9	85	31.6
20	-125.2	77.3	39.1
30	-187.8	63	50.6

*Coupler is adjusted at 10mA beam load

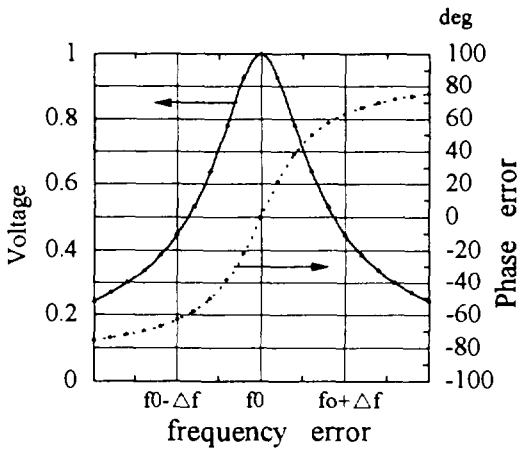

Fig. 11.15.2 Voltage and phase error as a function of frequency

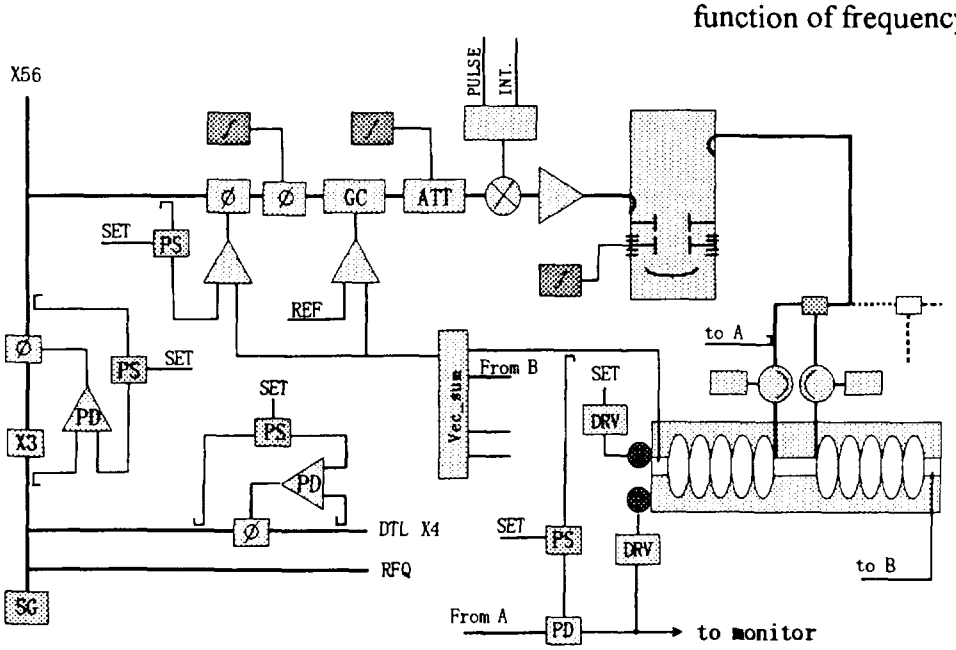

Fig. 11.15.3 Block diagram of auto-tuning, voltage and phase control system

11.16 Conceptual Design for the 100-1,500MeV Superconducting Proton Linac

Y. Honda*, K. Hasegawa, N. Ouchi, J. Kusano, and M. Mizumoto
(*E-mail* :honda@linac.tokai.jaeri.go.jp)

The Neutron Science Project has been proposed with the superconducting proton linac for the energy range from 100MeV to 1.5GeV. The studies of the linac structure and the beam dynamics simulation are performed to specify the scale of the accelerator. The basic linac parameters at present are in Table 11.16.1. Accelerating frequency, peak beam current and surface electrical peak field (Ep) are 600MHz, 30mA, and 16MV/m, respectively. The accelerated particles are H^+ and H^-.

In the proton accelerator, the velocity ratio to the light velocity β gradually changes from 0.43 to 0.92 corresponding to the energy from 100MeV to 1.5GeV. Accordingly, the length of the cell has to be changed. When the energy range covered with one kind of cavity, called a β section, is smaller, the length of accelerator and the number of module become shorter and smaller, respectively because the accelerating gain becomes larger. But in that case, the mass production effect and the number of transition become smaller and larger, respectively. In order to determine the layout of the accelerator structure, a typical case of the linac, which is composed of 8 sections with different cell length, has been studied. The current design parameters of the structure is described in Table 11. 16. 2. At first, the energy ranges of each section have been decided so that the maximum phase slips in the cell of each section were almost the same. Then the ranges have been adjusted for the demand from the RF division that the number of cavities in each section had to be multiples of four. The cell length($\beta_c \cdot \lambda/2$, λ:wave length, β_c:geometrical β of cell) have been decided to be the linac shorter under the condition of surface electrical peak field (Ep) up to 16MV/m.

The number of cavities in each section has been decided by the energy range of the section and the energy gain of each cavity. The constant energy gain of each cavity has been derived from the transit time factor(T) and the accelerating electrical field(Eo) .

Table 11.16.1 Basic linac parameters at present.

Frequency	600MHz	Focusing type	Doublet
Energy range	100-1,500MeV	Average phase	-30°
Beam current	30mA	Cavity per focusing period	2
Surface Ep	16MV/m	Accelerated particle	$H^+$and H^-
Number of cell per cavity	5		

*Mitsubishi Heavy Industries, LTD.

The Eo_{max} was derived from the facts that the maximum Ep was 16MV/m and that the Ep/Eo was decided from the figure of cavity. To make the accelerator shorter, Eo_{max} was multiplied by T_{min}. The Eo of the each cavity was derived from the following equation: $Eo \cdot T = Eo_{max} \cdot T_{min}$=constant.

T has been derived from the electrical field of 5cell-cavity calculated with SUPERFISH code. The Eo_{max} has been derived from Ep/Eo ratio of the cavity and Ep≦16MV/m. The total number of the cavities has been estimated to be 308.

The doublet focusing has been applied to the linac. One focusing period had 2 cavities as shown in Figure 11.16.1. The quadrupole magnetic field gradient was from 4.2 to 7.1 T/m on the condition of the equipartitioning derived from the relation between four parameters: transverse and longitudinal emittance, and transverse and the longitudinal beam size[1]. The gradient had to be also considered the limitation of H^- magnetic stripping[2]. Matching transports with four quadrupole magnets between the sections have been considered with TRACE3D code.

The total length of the linac has been estimated to be 733m. The RF wall loss has been estimated to be 26kW and 2.3kW at the operating temperatures of 4K(Rs=150nΩ) and 2K(Rs=13.6nΩ) are assumed, respectively, from the SUPERFISH calculation. But the RF wall loss has to be estimated again because the experimental results show that the real Rs must be bigger than above values[3].

Table 11.16.2 Design parameters of structure

β section no.	1	2	3	4	5	6	7	8
β_c	0.453	0.499	0.549	0.604	0.665	0.732	0.805	0.886
No. of cavities	20	24	24	24	24	32	52	108
Energy range [MeV]	100-123.5	123.5-159.9	159.9-209.8	209.8-276.2	276.2-361.9	361.9-502.3	502.3-782.2	782.2-1504.7
Length [m]	40.4	49.8	51.4	53.3	55.4	76.3	129.0	277.7
Eacc [MV/m]	2.45	2.86	3.56	4.30	5.01	5.59	6.23	7.03
Power per cavity [kW]*	21	27	38	50	64	79	97	121
Focusing gradient [T/m]	4.7-5.1	5.0-5.6	5.4-6.0	5.8-6.4	6.1-6.7	6.2-6.7	5.9-7.1	4.2-5.9

*In case of I =18mA(30mA × chopping(0.6))

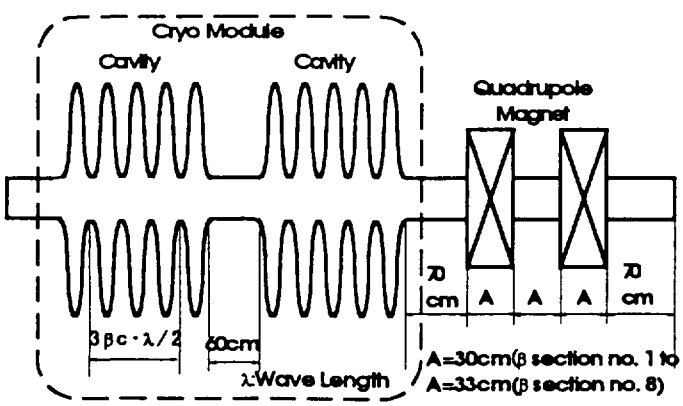

Figure 11.16.1 Focusing period

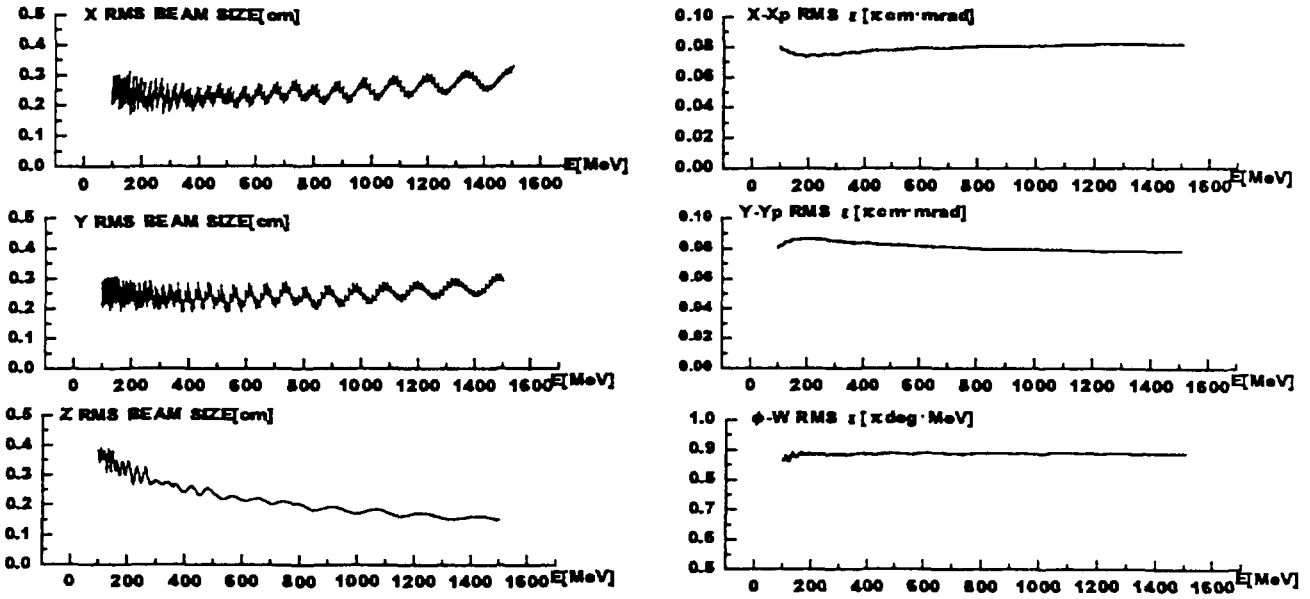

Figure 11.16.2 Example of simulated result.

The beam dynamics has been simulated with the modified PARMILA code. The simulation has considered the leak of electrical field from cavity to beampipe.

One typical result is shown in Figure 11.16.2. The current of the input beam has been adopted 90mA because the frequency is jumped from 200MHz to 600MHz at the transition between the DTL and this linac. The input transverse and longitudinal rms emittance have been respectively adopted 0.080 π cm·mrad and 0.86 π MeV·deg on trial. The output transverse and longitudinal rms emittance has been simulated 0.083 π cm·mrad and 0.89 π MeV·deg, respectively.

The current conceptual design study for the linac structure and the beam dynamics have been described. The following items have to be further studied:

(1) The number of section and the β_c of cell to optimize the efficiency of acceleration.

(2) The number of cavities in one focusing period to make the linac shorter.

(3) The design feedback with experimental data to make the design realistic.

(4) The reliable design concept to make the linac robust.

References

1) Reiser M. : "THEORY AND DESIGN OF CHARGED PARTICLE BEAMS",JOHN WILEY & SONS, INC., 573(1994)

2) Jason J.A, et al. :"NEUTRALIZATION OF H^- BEAMS BY MAGNETIC STRIPPING", IEEE TRANS. ON Nucl. Sci., NS-28, 2704(1981)

3) Ouchi.N., et al. "Fabrication and Test of a Superconductiong Single Cell Cavity of β=0.5 for the High Intensity Proton Linac in JAERI", this report.

11.17 Structural Analysis of Superconducting Cavities for High Intensity Proton Linac in JAERI

K. Mukugi*, N. Ouchi, J. Kusano and M. Mizumoto

(*E-mail*: mukugi@linac.tokai.jaeri.go.jp)

The Neutron Science Project (NSP) in JAERI proposes a superconducting (SC) linac as a main option for a high β part (β= velocity of particle / velocity of light). The SC linac undertakes the acceleration of the proton from the energy of 100 MeV to 1.5 GeV (β=0.43～0.92) at 600 MHz. The shape of an accelerating cavity is elliptical. Static and dynamic structural analyses of SC cavities were carried out using commercially available ABAQUS and NASTRAN computer codes. Characteristics of the cavity strength against the vacuum load were studied. And, the three-dimensional structural analysis was carried out on multi-cell cavities concerning mechanical natural frequency and gravity deformation. The main structural analysis was carried out on the β=0.5 cavity with the stiffening ring of Los Alamos type. [1)]

Fundamental Characteristics of Cavity Strength

On the structural strength of the cavity against the vacuum load, the structural analysis was carried out using the ABAQUS code. The cavity parameter variously changed (Iris radius, wall slope angle, ellipse shape, β=0.5, 0.7, 1.0, Iris fixed or Iris free), and the characteristics of the cavity strength against the vacuum load were studied. Figure 11.17.1 shows the cross section of the β=0.5 half-cell cavity shape.

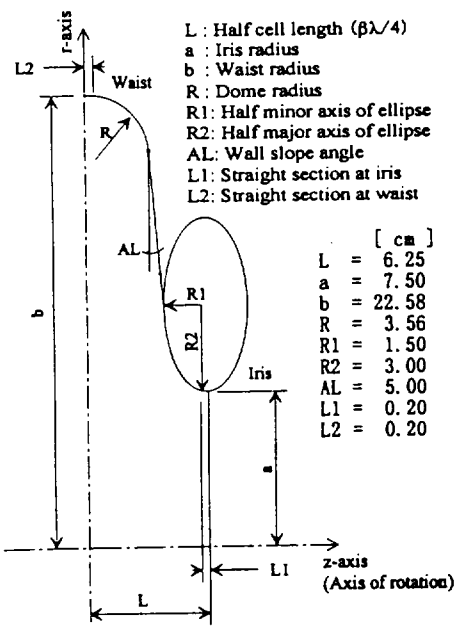

Fig. 11.17.1 β=0.5 half cell shape

* Mitsubishi Electric Corporation

Figure 11.17.2 shows the maximum von MISES stresses of the β=0.5, iris free cavity with the material thickness of 3 mm as a typical example. The axis of abscissa is the effective shunt impedance (ZT^2/L) which corresponds to the resistivity for copper at room temperature. The wall slope angle affects the cavity strength considerably.

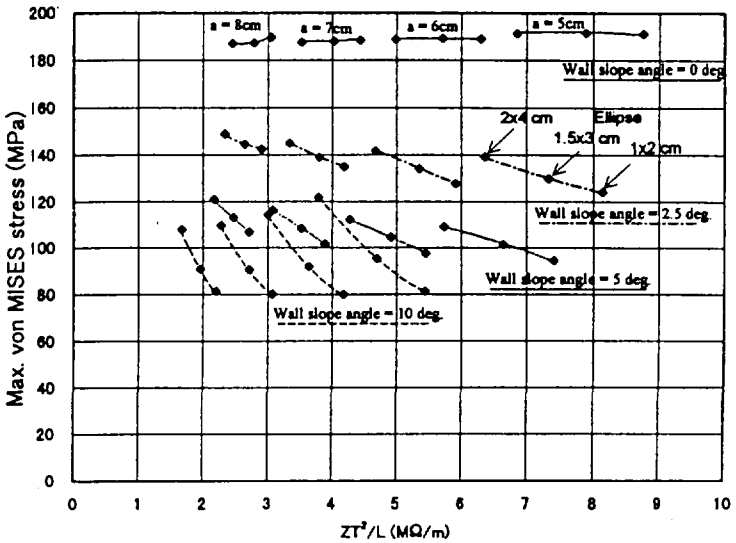

Fig. 11.17.2 Max. stresses of β=0.5, iris free cavity

These iris-free flatter cavities have the great possibility of the collapse owing to the very large stress over 80 MPa which is much greater than the annealed niobium's yield stress of ~40 MPa. The iris should be fixed. Figure 11.17.3 shows the maximum displacements, vacuum-side and atmospheric-side maximum von MISES stresses for seven kinds of iris fixed cavities. But, in the region where β is smaller than 0.6~0.7, an additional stiffening of the cavity is still necessary.

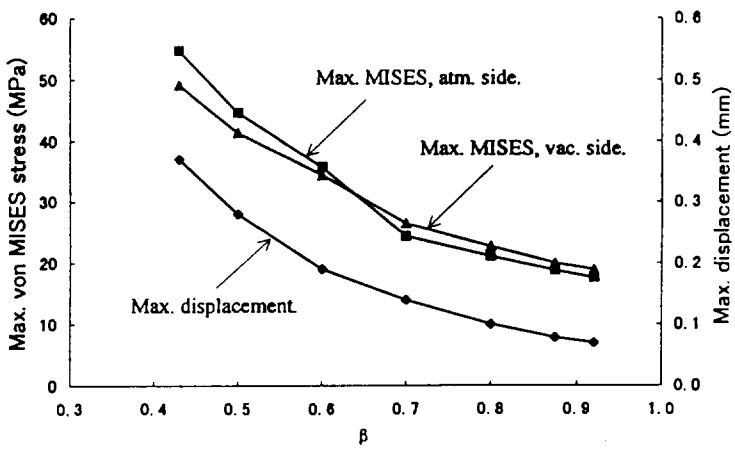

Fig. 11.17.3 Max. displacements and stresses

Stiffening of β=0.5 cavity against vacuum load

The two dimensional axi-symmetric structure analysis of the β=0.5 cavity with the stiffening ring was carried out using the ABAQUS code. It was found that by adding the stiffening ring, the maximum displacement could be reduced from 0.28 mm to 0.04 mm, and the maximum von MISES stress could be reduced from 44.7 MPa to 20.7 MPa. This stiffening structure seems to be a very effective way from the viewpoint of easing large deformation and stress due to the vacuum load.

Three-dimensional Natural Mode and Gravity Deformation Analysis

Table 11.17.1 shows the summary of the results calculated using the NASTRAN code. On the gravity deformation and stress, it seems to be out of the problem. However, on the mechanical natural frequencies of the present 4- and 5-cell cavity structures, several modes are close to 50 Hz of the commercial frequency and the beam repetition rate which can drive the cavity mechanically. The main structural analysis was carried out on the β=0.5 cavity with the stiffening ring of Los Alamos type. Figure 11.17.4 shows the model of the 5-cell cavity with the stiffener. An addition of the stiffening ring drastically raises the natural frequency. Figure 11.17.5 shows the mode of the lowest axial vibration (80 Hz). The lowest natural frequency nearly doubles from 38 Hz to 80 Hz by the stiffening. The sufficient study of the stiffened cavity structure including the control characteristics of the tuner is necessary in future.

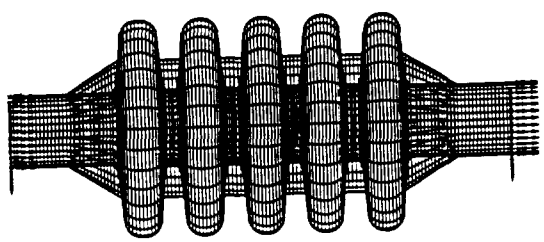

Fig. 11.17.4 Model of 5-cell cavity with stiffener

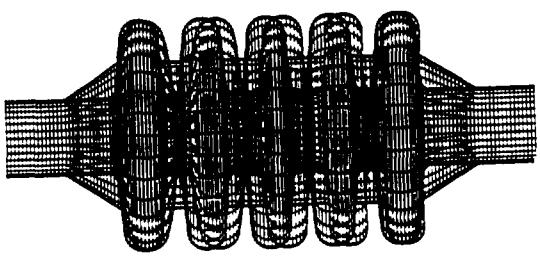

Fig. 11.17.5 Lowest axial vibration mode

Table 11.17.1 Natural frequency and displacement from gravitational load

β	Cell	Stiffener	Frequency (Hz) Mode 1	Mode 2	Mode 3	Mode 4	Mode 5	max. Disp. by g. (mm)	max. MISES by g. (MPa)
0.5	4	none	55.05	55.05	*63.01*	90.26	90.25	0.078	3.05
0.5	5	none	38.45	38.45	*49.64*	71.92	71.92	0.181	6.01
0.5	4	Cylindrical	*100.22*	112.56	112.56	195.19	195.19	0.020	1.23
0.5	5	Cylindrical	*79.82*	81.06	81.06	155.76	155.76	0.042	2.40
0.7	4	none	76.44	76.44	141.47	141.47	*143.72*	0.047	3.21
0.7	5	none	54.18	54.18	110.93	110.93	*114.71*	0.093	4.62
0.92	4	none	61.21	61.21	*120.42*	124.40	124.40	0.075	2.87
0.92	5	none	42.19	42.19	94.24	94.24	*96.79*	0.159	4.71

: Axial mode : Transverse mode

References

1) D. Schrage, et al., Proc. of the 7th Workshop on RF superconductivity, (1995) 629.

11.18 Fabrication and Test of a Superconducting Single Cell Cavity of β =0.5 for the High Intensity Proton Linac in JAERI

N. Ouchi, J. Kusano, N. Akaoka*, M. Mizumoto, K. Saito**, S. Noguchi**
(*E-mail:* iton@linac.tokai.jaeri.go.jp)

Design and development work of superconducting (SC) cavities of 0.43< β (ratio of proton velocity to light velocity) <0.92 have been continued for the high intensity proton linac since FY-1995 in collaboration with KEK. Preliminary cavity design has been made according to an RF eigenmode calculation and a structural analysis in half-cell geometry as well as considerations of fabrication and surface treatment[1]. A test stand for vertical tests has been installed to demonstrate cavity performance[2]. In FY-1996, a SC single cell cavity of β =0.5 has been fabricated and the RF performance has been examined at the test stand.

Figure 11.18.1 illustrates the cross cut view of the SC cavity of β =0.5; the shape has been determined from the preliminary cavity design[1]. The ratios of electric and magnetic peak field on the surface to the accelerating gradient are estimated to be 4.80 and 86.5 Oe/(MV/m), respectively. The resonant frequency has been calculated to be 586.5 MHz in the geometry with beam tube, while 600 MHz by the π-mode calculation without beam tube.

The fabrication has been made at the workshop in KEK. The thickness and RRR of niobium sheets were 3mm and ~250, respectively. The fabrication consists of three steps; deep drawing of half-cell parts, triming of half-cell parts and beam tubes and electron beam welding at equator and iris. Niobium

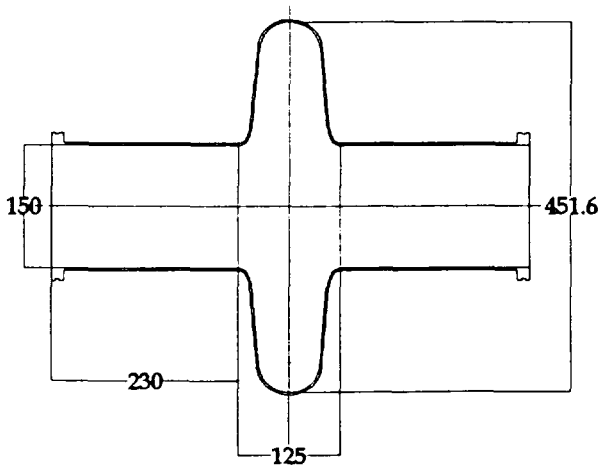

Fig. 11.18.1 Cross cut view of a SC single-cell cavity of β =0.5

* Nippon Advanced Technology, Co. Ltd.
** KEK: High Energy Accelerator Organization

flanges were also welded at the both ends of the beam tube.

Surface treatments of barrel polishing (BP)[3] and electropolishing (EP)[4] have been applied to the cavity, where the devices developed in KEK have been utilized. Figure 11.18.2 shows the distribution of removal thickness by both BP and EP. Average removal thicknesses by BP and EP have been 51 and 23 μ m, respectively, while the distribution depends on the position strongly as shown in Fig.11.18.2. After the surface treatment, heat treatment of 750° C has been applied for 3 hours to remove hydrogen absorbed during EP. High pressure rinsing has been carried out at JAERI[2] as a final rinsing for 1.5 hours with ultra pure water of 8~9 MPa.

Figure 11.18.3 shows a photograph of the cavity. The vertical test has been carried out at both 4.2 K and 2.1 K. Figure 11.18.4 shows the measured Q-values as a function of electric peak field on the surface (Ep). However, these measurements have been made in the condition that the liquid helium vessel was filled insufficiently because of the problem during the cooling down process. Although the cooling condition of the cavity was not good, the peak field up to 16 and 18.6 MV/m has been achieved at 4.2 K and 2.1 K, respectively, that exceed the specification of the cavities[5]. The Q-values, $\sim 7 \times 10^8$ at 4.2 K and $\sim 10^{10}$ at 2.1 K, agreed well to the expectations based on the BCS theory. Residual resistance has been also estimated to be about 10n Ω. We are planning to make re-measurement under a better cooling condition.

The second cavity of β =0.5 is in fabrication and will be tested soon. And we are planning to fabricate a single-cell cavity of β =0.7~0.8 that will be tested in FY-1997. In addition, fabrication of a multi-cell cavity of β =0.5 is scheduled.

References

1) Ito N., et al.: "Development of a Superconducting Cavity for the High Intensity Proton Linac in JAERI", Proc. of the XVIII International Linear Accelerator Conference, August 26-30, 1996, Geneva, Switzerland, p670-673.
2) Kusano J., et al.: "Design and Installation of a Test-stand for Superconducting RF Cavity", Reactor Eng. Dep. Annual Report, 222, JAERI-Review 96-012 (1996).
3) Higuchi T., et al.: "Investigation on Barrel Polishing for Superconducting Niobium Cavities", Proc. of the 7th Workshop on RF Superconductivity, October 17-20, 1995, Gif-sur-Yvette, France, p723-727.

4) Saito K., et al.: "R&D of Superconducting Cavities at KEK", Proc. of the 4th Workshop on RF Superconductivity, August 14-18, 1989, Tsukuba, Japan, p635-694.

5) Honda Y., et al.: "Conceptual Design for the 100-1500MeV Superconducting Proton Linac", this report

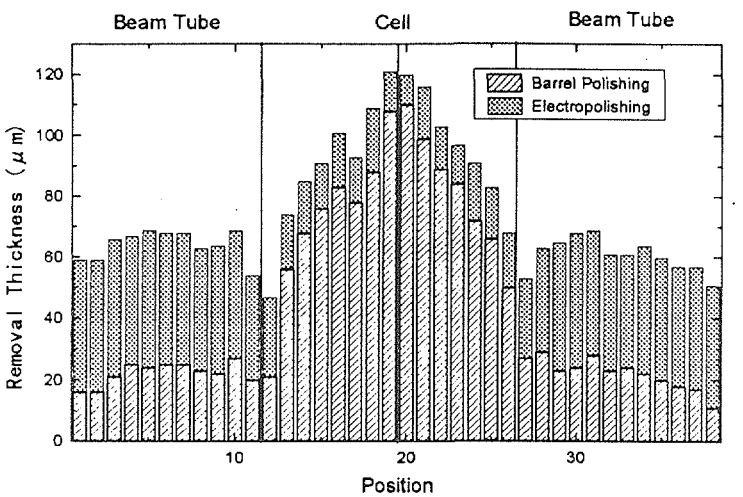

Fig. 11.18.2 Distribution of Removal thickness on both barrel polishing and electropolishing

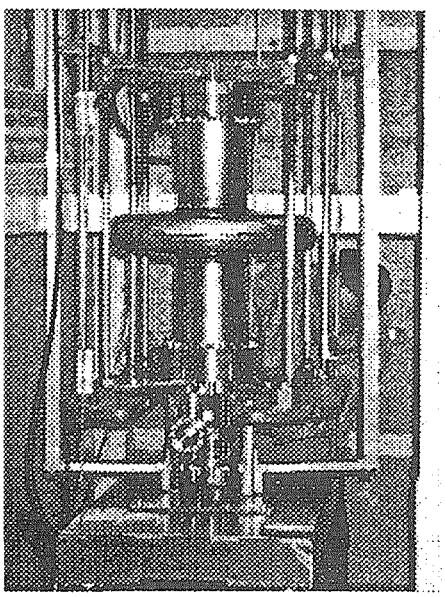

Fig. 11.18.3
Photograph of a SC single-cell cavity of β =0.5

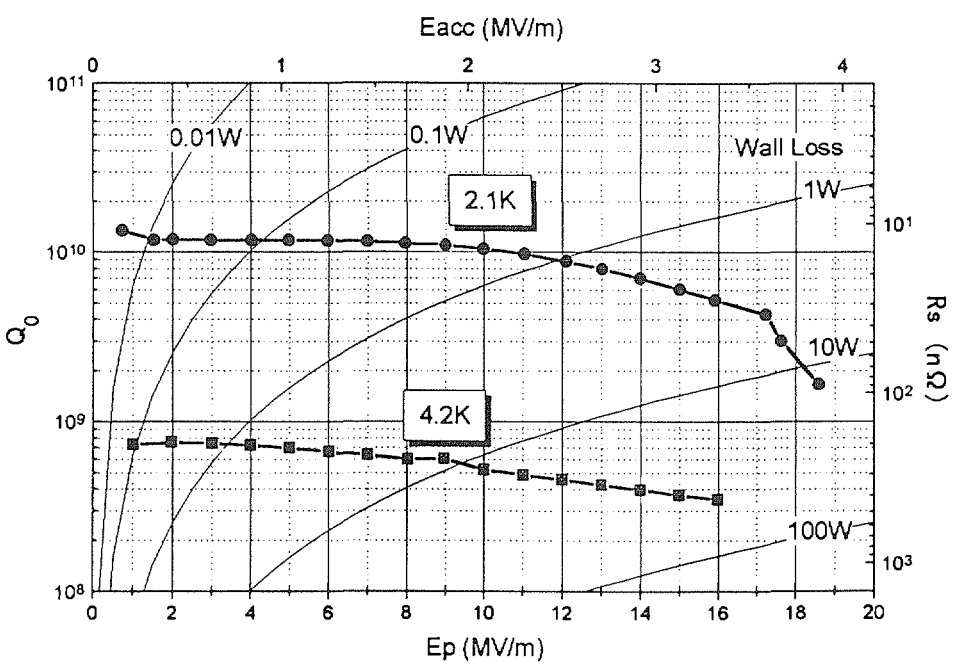

Fig. 11.18.4 Measured Q-value as a function of electric peak field on the surface

11.19 A Preliminary Study of 5MW Storage Ring for the Neutron Science Project in JAERI

M. Kinsho, F. Noda*, J. Kusano and M. Mizumoto
(*E-mail :* kinsho@linac.tokai.jaeri.go.jp)

In the beam storage ring, the pulsed beam from the linac is accumulated, and high intensity pulsed beam is produced for the neutron scattering experiment. The preliminary study of the ring which satisfies specification of the neutron science project is described in this report.

The pulse structure of the beam from the linac and preliminary parameters of the storage ring are shown in Fig. 11.19.1 and Table 11.19.1, respectively. The linac beam is chopped to 670ns bunch width with 60% duty cycle at 50Hz. The 1.5GeV H^- linac beam is compressed by means of a multi-turn charge exchange injection. When a harmonic number of the ring is 1, a circumference and a revolution frequency are 185m and 1.49MHz, respectively. The single bunch in the ring is contained by rf resonant cavity. To achieve a beam power of 5MW with this beam structure, it is necessary to accumulate 5553 bunches. This corresponds to 4.17×10^{14} protons. When the beam injection is completed, accumulated protons are extracted from the ring during 1 turn. The average current circulating in the ring with 1.49MHz revolution frequency becomes 99.5A. At such a high average current, a beam loss of a very small fraction makes a very high radioactivity around the ring. It is necessary to examine reduction and localization of the beam loss with sufficient consideration of the divergence of the beam by the space charge force, the resonance phenomena by the tune shift, longitudinal instability and so on.

Magnet Lattice

A large transverse beam emittance is required in the ring to restrict both the transverse space charge tune shift and to reduce the H^- or H^+ beam intersection with a stripping foil. The chosen values for an un-normalized 90% transverse emittance, a ring acceptance and a collimator acceptance are 2π mm.mrad, 450π mm.mrad and 200π mm.mrad, respectively. This transverse

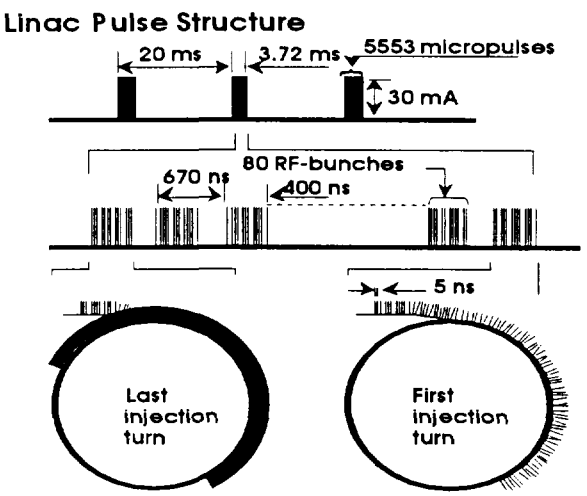

Fig. 11.19.1 A pulse structure of the linac beam

* Hitachi, Ltd.

emittance restricts the space charge tune shift to less than 0.1. The magnet lattice is temporarily selected to be normal 12 cell FBDO lattice. This lattice ensures the distance between defocusing quadruple magnet and focusing quadruple magnet at 7.5m. The operation tune is in the range where a phase advance per 1 cell becomes 80~110 degrees and provisionally selected to be (ν_x,ν_y) = (3.85,3.75). The beta function and energy dispersion function have been evaluated by using the lattice analysis program "MAD" developed at CERN.

Table 11.19.1 Preliminary parameters of the storage ring

Kinetic energy	1.5 GeV
Repetition frequency	50 Hz
Harmonic number	1
Revolution frequency	1.49 MHz
Circumference	185 m
Magnetic rigidity	7.51 Tm
Circulating current	99.5 A
Number of circulating protons	4.17×10^{14} protons
Lattice	12 Cell FBDO
Ring acceptance	450π mm.mrad
Collimator acceptance	200π mm.mrad
Betatron tune (ν_x,ν_y)	(3.85,3.75)
Betatron tune shift	< -0.1
rf cavity	
frequency	1.49 MHz
voltage	42 kV
Kicker magnet	
reflection angle	10 mrad
magnetic field strength	0.02 T
length	3.8 m

Beam injection

Injection is the main source of beam loss and hence the most critical item for the ring because the main loss is due to H^- or H^+ beam intersection with a stripping foil during and after injection. There are two types of injection method for charge exchange. One is the direct H^- injection method in which H^- beam is converted to H^+ beam with the stripping foil located in the injection magnet. The other method is the H^0 injection method in which H^- beam is firstly converted to H^0 beam in a stripping magnet outside of the ring and then H^0 beam is injected to the stripping foil inside the ring. In both method, it is very important to minimize delayed stripping of H^0 atoms in the ring. The lifetime of H^0 atoms depends on the Stark state in the magnet. The

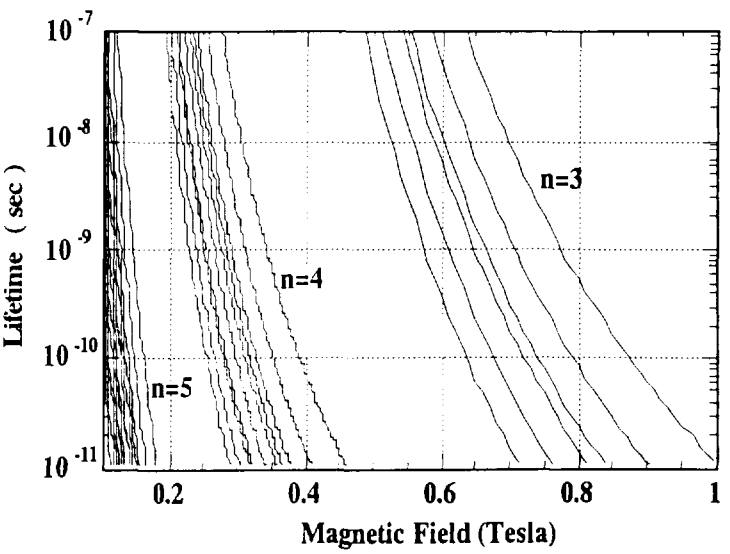

Fig. 11.19.2 Stark state lifetime in laboratory frame

life time of 1.5GeV H^0 atoms in laboratory frame shows in Fig. 11.19.2. When the magnetic field strength is 0.15T, atoms with $n \leqq 4$ remain as H^0 and may be removed from the ring, and atoms with n>5 rapidly become H^+ and are accepted in the ring. At present it is under consideration which method should be adopted to reduce the beam loss in the ring. The phase-space painting is also considered to obtain large transverse emittance.

Radio frequency cavity

Though the acceleration of the beam is not carried out in the rf cavity, the rf cavity is required for maintaining the bunch structure in the storage ring. The injection beam is chopped at the bunch revolution frequency of 1.49MHz. The necessary cavity voltage is the sum of voltage Vp which is proportional to the momentum spread of the injection beam and voltage Vsc which supplements the decreasing voltage by the space charge effect. The Vp voltage is about 27kV by assuming that the momentum spread is to be $\pm 0.58\%$. The necessary Vsc voltage changes according to the accumulated number of beam bunches. When all beam bunches are accumulated, the Vsc voltage becomes about 15kV under the condition that the longitudinal distribution is parabolic. The rf voltage is raised from 27kV to 42kV to maintain the beam bunches during injection with one rf cavity of 5m long.

The rf cavity consists of capacities, resistors, and ferrite. Because the circulating current is about 99.5A, it is likely that the cavity characteristics should be changed due to the high frequency magnetic field induced by circulating current. Therefore, the rf cavity is important issue to be developed.

Beam extraction

The fast extraction method is used from the request of the neutron scattering experiment. In this extraction method, when injection of all bunches is completed, accumulated beam is extracted from the ring during 1 turn. An interval between bunches is 270ns from the injection beam pulse structure which is chopped 670ns bunch width with 60% duty cycle. It is necessary that the magnetic field of a kicker magnet is enough to extract the beam from the ring to less than 270ns and is kept the strength to more than 400ns. In fact, the required field rise time of kicker magnet is less than 150ns considering the increase of the beam bunch due to synchrotron oscillation and divergence by the space charge effect during multi-turn ring injection. When the un-normalized 100% extraction emittance, beta function, dispersion function, and momentum spread are 200π mm.mrad, 15m, 3m, and 0.58%, respectively, the reflection angle becomes about 10 mrad. A kicker magnet of 0.02T and 3.8m is required in order to realize this extraction process.

12. Energy System Analysis and Assessment

The objective of this research is to identify the role of nuclear energy and its relevant technologies in future energy systems of Japan, and thereby to contribute to the establishment of long-term strategy of nuclear energy utilization by the government and to the promotion of research and development in JAERI. The analytical models and their databases have been developed for this purpose, and applied for the a variety of studies. Among those carried out in the year 1996, three major topics are presented here.

First, the role of high temperature nuclear heat was analyzed from the view point of reducing future CO_2 emissions in Japan. The MARKAL model was used for the analysis in order to find optimum sets of energy and technology options that will contribute to the emission reduction. Three analytical cases were compared ; the case without no nuclear investment after the year 2000, the case with expanding nuclear power generation, and the case with high temperature nuclear heat in addition to nuclear power. According to the results, although the emissions increased with time in the case without nuclear energy, they were reduced much by expanding nuclear power generation. When high temperature nuclear heat was used in addition, they were reduced well below the 1990 emission level.

Second, long-term plutonium balances were analyzed considering the recent change in the development plan of MOX fueled reactors from advanced thermal reactors to fully MOX fueled advanced boiling water reactors (ABWRs). The analytical cases were established with different assumptions on the total nuclear capacity and the combination of reactor types. It was found from the results that, under the assumed capacity of spent fuel reprocessing, fully MOX fueled ABWRs could hardly be introduced from the view point of plutonium balances, and the current plan of using plutonium in LWRs would not contribute much to the reduction of natural uranium consumption in the long-term.

Finally, a preliminary study was made on the life cycle characteristics of nuclear power generation. For this purpose amounts of material utilized in the facilities of power generation and fuel cycle processes were investigated. By using these data, the energy consumption and the CO_2 emission per kilo watt of electricity generated were estimated. In comparison with renewable energy technologies, it was found that nuclear energy is the best in the emission, and the second in the energy consumption after hydropower.

12.1 High Temperature Nuclear Heat Application – Potential Contribution to CO_2 Emission Reduction

O. Sato, K. Tatematsu and M. Shimoda
(*E-mail:* sato@kako32.tokai.jaeri.go.jp)

Nuclear energy is one of the most effective options to realize the substantial reduction of future CO_2 emissions. It has been utilized so far mainly for electric power generation, however it can also be applied for producing synthetic fuels by using nuclear heat from high temperature gas-cooled reactors (HTGRs). In this study, the role of high temperature nuclear heat was analyzed from the view point of potential contribution to the CO_2 emission reduction in Japan.

The MARKAL model was used in order to optimize energy systems over the time period from 1990 to 2050. The analytical procedure is as follows. First, future demand for energy services was estimated by assuming economic growths as shown in Table 12.1.1. Second, the reference energy system was designed by incorporating all energy carriers and technologies that might be used during the time period. The technologies were characterized with the data on its performances, costs, and so on. In addition, external constraints on their capacity were given as listed in Table 12.1.2.

Analytical cases are as follows. Case A : Without nuclear investment after 2000. Case B : With nuclear power generation. Case C : With nuclear power generation and heat application. In all cases, energy systems were optimized by minimizing the sum of the total system cost and the high penalty to the emissions of CO_2.

The structure of primary energy supply optimized as above is shown in Fig. 12.1.1. In the case A, the utilization of natural gas substantially increased with time. However, due to the constraints on its availability, large amount of coal was also utilized. When nuclear energy was used as in the case C, however, most of coal was replaced by it.

The CO_2 emissions increased much with time in the case A. But they were drastically reduced by expanding nuclear power generation as shown in Fig. 12.1.2. If, in addition, high temperature nuclear heat was used for producing synthetic fuels, the emissions were reduced well below the 1990 level. The amount of reduction in 2050 was about 200 million ton (CO_2) by using HTGRs of the total capacity 100 MWt.

Table 12.1.1 Social and economic indicators assumed for the analysis

	1990	2000	2010	2020	2030	2050
Population (Million)	123.6	127.4	130.4	128.3	123.0	111.5
Households (Million)	40.7	44.7	48.3	49.4	49.2	48.5
GDP (1985 Trillion Yen)	402	500	640	781	906	1150
Growth Rates (%/Year)		2.21	2.50	2.0	1.5	1.2

Table 12.1.2 External constraints on the capacity of nuclear reactors

	2000	2010	2020	2030	2040	2050
LWRs (GWe)	46.	70.	84.	95.	98.	100.
FBRs (GWe)			1.	5.	15.	25.
HTGRs (GWt)			3.	25.	60.	100.

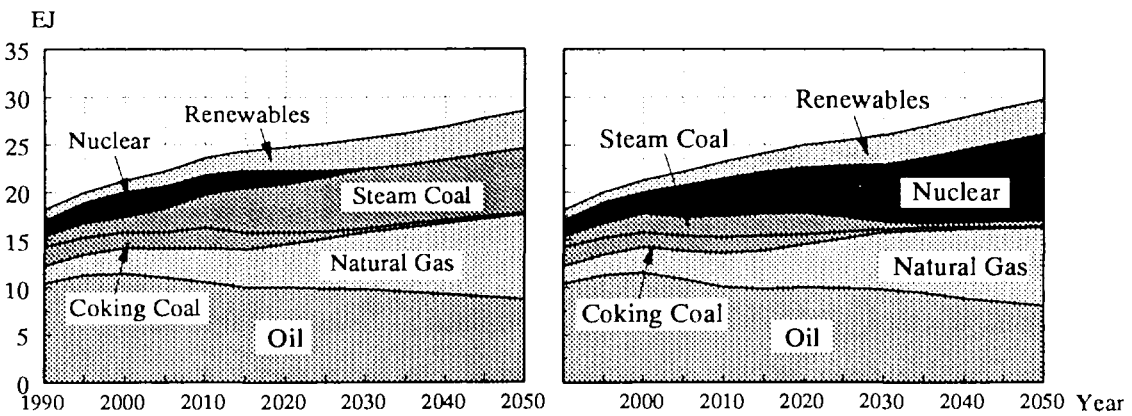

(a) Case A (Without Nuclear Energy) (b) Case C (With Nuclear Energy)

Fig. 12.1.1 Primary energy supply in the case A and C

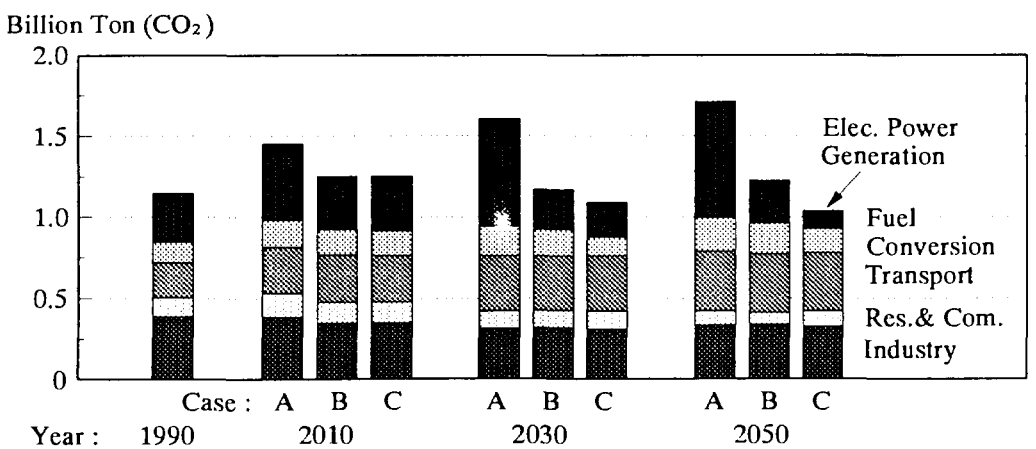

Fig. 12.1.2 Sectoral emissions of CO_2 in the case A, B and C

12.2 A Study on Plutonium Balances in Japan's Long-term Nuclear Power Development

O. Sato and T. Hasegawa
(*E-mail:* sato@kako32.tokai.jaeri.go.jp)

It has been planned to use uranium-plutonium mixed oxide (MOX) fuel in some of existing or new LWRs (in one third or half of their reactor core), and also in advanced thermal reactors (ATRs). However, since the development of ATRs was stopped because of little prospect to improve their poor economy, it is now planned to introduce advanced boiling water reactors (ABWRs) which install MOX fuel in their entire reactor core.

Accordingly, long-term balances of plutonium production and consumption in the new reactor development plan were analyzed with the nuclear fuel cycle systems model JALTES. Main assumptions for the analysis are summarized in Table 12.2.1. Two cases, low and high cases, were assumed for future nuclear power capacity. It was also assumed that FBRs would be introduced from the year 2030 either with a low or high capacity buildup rate. Cooling time of FBR spent fuel was assumed as 2 years or 4 years. By combining these cases, analytical cases were determined as listed in Table 12.2.1.

The combinations of nuclear reactor types are as follows. Case A : Enriched uranium LWRs (EU-LWRs) and FBRs. Case B : Case A + Partially MOX fueled LWRs of a total capacity 12.1GWe. Case C : Case B + Fully MOX fueled LWRs. Spent fuel of EU-LWRs would be reprocessed, as shown in Fig. 12.2.1, by the Rokkasho plant, and by the second plant in the private sector starting its operation either in 2020 with a maximum scale of 2100 ton/year or in 2025 with that of 1800 ton/year.

The analytical results are as follows. When only EU-LWRs were used to meet the assumed demand for the nuclear power capacity, the amount of excess plutonium would be as large as more than 100 ton Pu (fissile) in 2020, and 150 ton Pu (fissile) in 2030 as shown in Fig. 12.2.2 (a). When the conventional plan of using a certain capacity (12.1GWe) of partially MOX fueled LWRs was carried out, the excess amount of plutonium was lowered to less than 20 ton Pu (fissile) until 2020. See Fig. 12.2.2 (b).

Under the assumed capacity of spent fuel reprocessing, fully MOX fueled LWRs could hardly be introduced from the view point of plutonium balances as shown in Fig.

12.2.2 (c). If all spent fuel of EU-LWRs could be reprocessed by continuing reprocessing abroad, it would be possible to introduce two units of them with 1350 MWe each. However, in order to introduce further units, it would be necessary also to reprocess spent fuel of MOX fueled LWRs.

The current plan of using plutonium in LWRs will not contribute much to the reduction of natural uranium consumption in the long-term. See Table 12.2.2. Therefore, it is necessary to discuss how to combine the plan of using plutonium in LWRs with the long-term strategy of developing FBRs in order to save natural uranium.

Table 12.2.1 Main assumptions for the analysis

1. Total Nuclear Power Capacity (GWe)

Case	- 1999	2000	2010	2030	2050	2100
L	Actual	45.36	60.	80.	96.	116.
H	and Planned	45.36	72.	102.	126.	166.

2. Constraints on Installed Capcity of FBRs

Case	2030				2035						2040					2044
1	1	0	1	0	1	0	1	0	1	0	1	1	1	1	1	
2	1	1	1	1	1	1	1	1	1	1	2	2	2	2	2	

Note : Before 2030 ; 0.28 GWe (1995), 0.6 GWe (2005), 1 GWe (2020), 1 GWe (2027).
After 2044 ; No constraints were given externally.

3. Analytical Cases

Symbol	Nuclear Power Capacity	Constraints on FBR Capacity	Cooling Time of FBR Fuel
L1	Case L	Case 1	Case 1 (2 Years)
L2	Case L	Case 2	Case 2 (4 Years)
H1	Case H	Case 1	Case 1 (2 Years)
H2	Case H	Case 2	Case 2 (4 Years)

Table 12.2.2 Consumption of natural uranium (cumulative up to the year 2100)

(1000 ton U)

Case	A No Plutonium Use in LWRs	B Use of Partially MOX Fueled LWRs	C Use of Partially + Fully MOX Fueled LWRs		
			Fully MOX Fueled LWRs		
			2 Units	4 Units	6 Units
L1	757	743 (▲ 14)	728 (▲ 29)	762 (5)	800 (43)
L2	758	785 (27)	812 (54)	838 (80)	866 (108)
H1	940	926 (▲ 14)	948 (8)	935 (45)	1024 (84)
H2	1002	1030 (28)	1057 (56)	1084 (82)	1111 (110)

Note : ( ) indicates the change from the case without MOX fuel use in LWRs
▲ indicates the value is negative

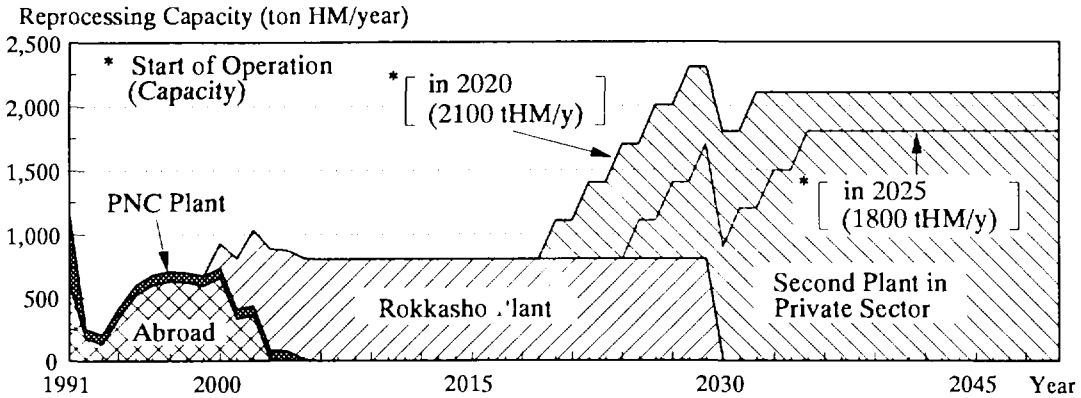

Fig. 12.2.1 Annual reprocessing capacity of enriched uranium spent fuel

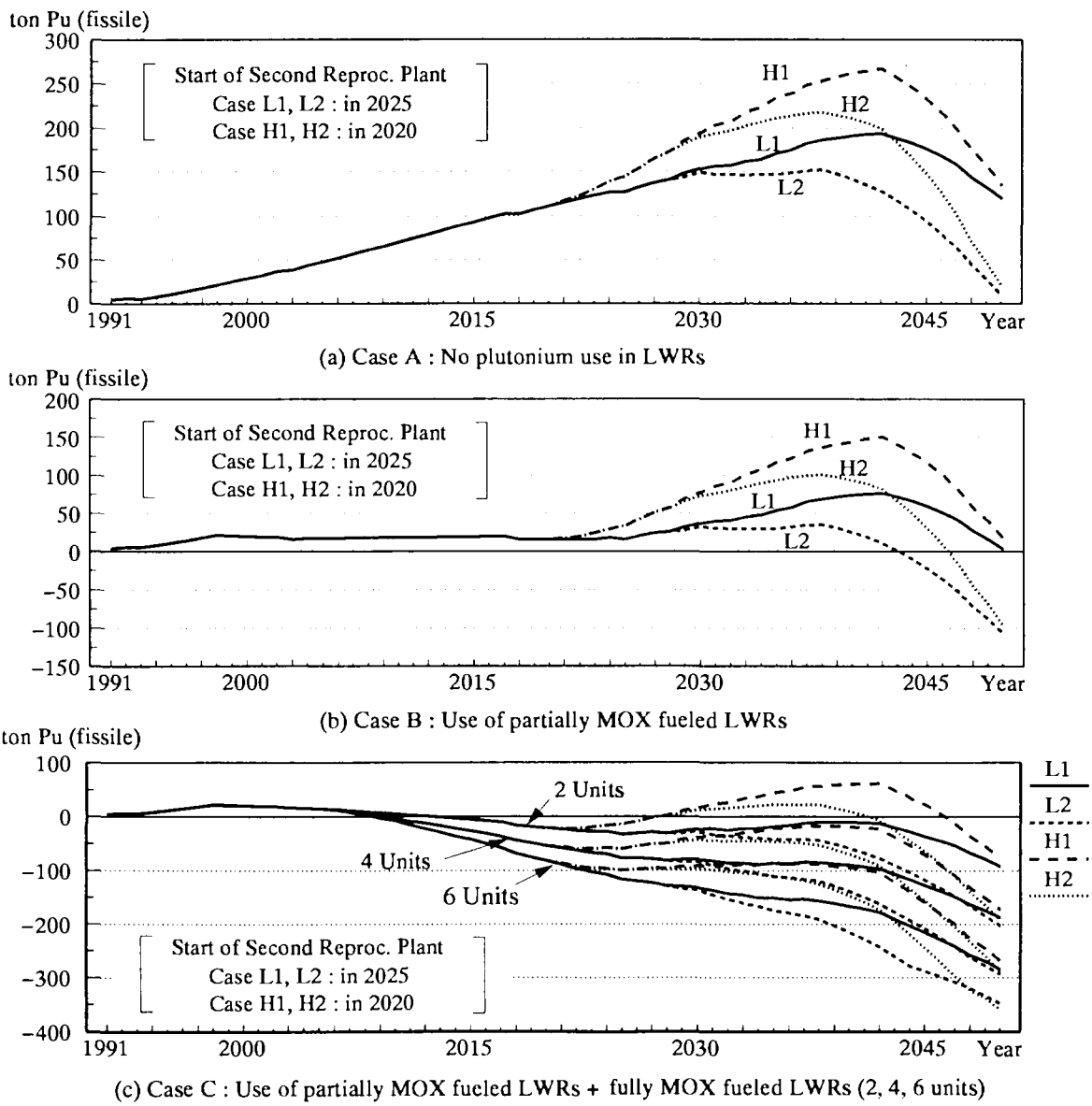

Fig. 12.2.2 Stock of fissile plutonium after balancing recovery and consumption

12.3 Preliminary Analysis on CO_2 Emissions from Nuclear Power Generation

Y. Tadokoro and O. Sato

(*E-mail:* tadokoro@kako32.tokai.jaeri.go.jp)

Direct emissions of CO_2 from nuclear power generation is really low, however, nuclear power has also a chance of releasing CO_2 if indirect process is taken into account. Indirect CO_2 emissions by nuclear power generation have been calculated based on the amount of materials used and the costs of nuclear power plants and fuel cycle facilities.

The amount of materials used in a typical large scale PWR power plant is listed in Table 12.3.1. The percentage share of each cost component in the total construction cost of this plant is listed in Table 12.3.2. The corresponding database have been also developed for fuel cycle facilities. In addition, industrial production induced by investments on nuclear plants and fuel cycle facilities have been derived from the I/O table.

Based on the above database, direct and indirect CO_2 emission by nuclear power generation has been calculated. Figure 12.3.1 gives the emission divided into the nuclear power plants, the front-end process and back-end process of nuclear fuel cycle. The life cycle CO_2 emission coefficient, a sum of a direct and an indirect component of the emission, is about 25.7 gCO_2 /kWh when gas diffusion process is utilized for uranium enrichment, and the indirect component shares about 89% of the total. The emission coefficient is also decomposed into the part of material production and the rest part. The former takes 8% of the emissions. Large part of CO_2 emissions comes from nuclear fuel cycle processes, in particular, from an enrichment process. This process takes 72% of the total emission.

When centrifuge process is utilized instead of gas diffusion process, the life cycle CO_2 emission coefficient reduces to 7.9 g CO_2 /kWh and the share of enrichment process becomes only 6.7%. In comparison with renewable energy technologies, the CO_2 emission coefficient of nuclear power is 40%, 10% and 4% of that of hydropower, windpower and photovoltaic power, respectively. In addition, the energy consumption per kilo watt of nuclear electricity generated becomes about twice as much as hydropower, however, it is about 1/2 of windpower and 1/4 of photovoltaic power. It is found that

nuclear power is one of the most promising energy for reducing CO_2 emissions.

Table 12.3.1 Materials used for a 1100MWe PWR power plant

Material	kg/kWe
Stainless Steel	2.34
Ordinary Steel	52.59
Special Steel	0.62
Aluminium	0.08
Composite Material	0.64
Copper	0.71
Titan	0.29
Cement	70.27
Insulation Materials	0.43
Total	127.97

Table 12.3.2 Construction cost of a 1100MWe PWR power plant

Component	Share in Total Construction Cost
1. Land and Land Rights	10 %
2. Structures & Site Facilities	15
2.1 Site Facilities	(3)
2.2 Reactor Containment Structures	(2)
2.3 Other Buildings	(10)
3. Reactor Plant Equipment	28
3.1 Reactor Equipment	(2)
3.2 Accessory Equipment	(10)
3.3 Waste Treatment & Disposal	(1)
3.4 Fuel Handling & Storage	(1)
3.5 Other Plant Equipment	(9)
3.6 Contorl & Safety Systems	(5)
4. Turbine Plant Equipment	15
5. Electric Plant Equipment	3
6. Engineering and Services	14
7. Interest during Construction	15
Total	100

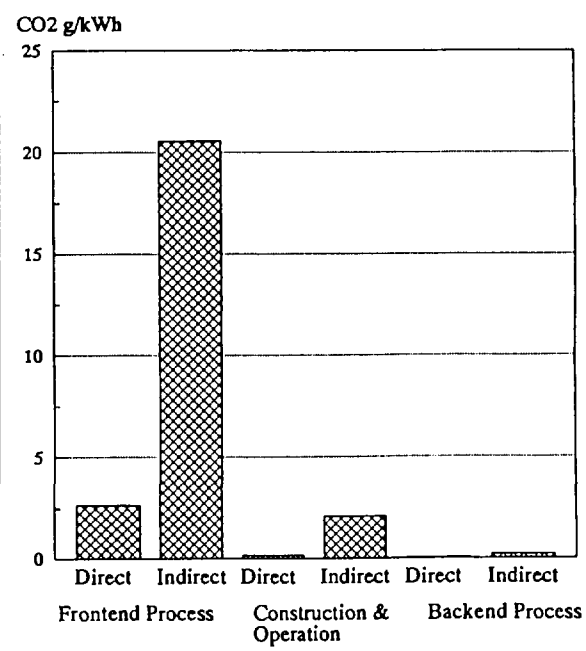

Fig. 12.3.1 CO_2 emission from nuclear power generation

13. Facility Operation and Techniques Development

There are three reactor engineering facilities and three accelerator engineering facilities such as Heat Transfer Fluid Flow Test Facility, Fast Critical Assembly (FCA), Very High Temperature Reactor Critical Assembly (VHTRC), Fusion Neutronics Source (FNS), Tandem Accelerator and Super conducting Booster. Operations of them were carried out as scheduled. Major activities of each facility of this fiscal year are summarized briefly below.

(1) The Heat Transfer Fluid Flow Test Facility was operated for various experiments such as core thermal-hydraulic transient test for PWR, etc. The designs and constructions of three test facilities were carried out.

(2) The FCA was operated according to various purposes of experiments and recorded the operation time of 657.48 hours. As for maintenance activities, the air compressor was renewed. The PIV of nuclear fuel materials were carried out.

(3) The VHTRC was operated as scheduled and recorded the operation time of 364 hours. The VHTRC cores were assembled and operated to obtain experimental data for establishment of the measurement methods of reactor physic characteristics at initial criticality of HTTR. The experimental operation of VHTRC was closed by the achievement of final purpose of verification the calculation accuracy related to the nuclear design of HTTR at September of 1996.

(4) The FNS was operated as scheduled according to various requirements of experiments and recorded the operation time of 683 hours. The rotating target cooling system was installed for a new type rotating target disk with microchannels.

(5) FNS has developed a high current ion source for increase of the neutron yield performance of FNS. A multicusp ion source was designed and developed for FNS incorporating with NBI Heating Laboratory. The ion source performance test carried out by using hydrogen. Deuteron ion beam of 30mA is obtained at present.

(6) The tandem accelerator was operated for 5260.4 hours and used for research experiments for 231 days. There was an unexpected tank opening due to a trouble of a power generator in the tank, which caused to cancel 9 days of scheduled beam time. Its associated booster was operated as scheduled and ran stably during the beam time of 35 days for research experiments. A satellite control console was built for the operation of the booster in the rf control room. In the booster target room, a heavy ion irradiation chamber was installed on the beam line for an investigation of metal-oxide superconducting materials. As development works on the tandem and its booster, carried out are several improvements for the booster, a development of an in-terminal highly charged heavy ion injector using a compact ECR ion source and an improvement of the concurrent processing control system of the tandem accelerator.

13.1 Operation Report of Heat Transfer Fluid Flow Test Facility

H. Watanabe, K. Nakajima, T. Satoh, M. Shibata, Y. Watanabe,
M. Kimura and H. Watanabe

In FY-1996, operation and maintenance of Heat Transfer and Fluid Flow Test Facilities were carried out as scheduled.

As for the maintenance of test facilities, annual official inspections of the pressure vessels and the steam generator located at both of Large Scale Reflood Test Building and Chemical/Mechanical Engineering Building were carried out and passed.

Core Thermal-Hydraulic Transient Tests for demonstration of core safety during abnormal transient in PWR have started in 1996 after construction for three years.

As for the operation of test facilities, the following eight tests were performed.

1) Core Thermal-Hydraulic Transient Test for PWR
2) Test with Multi-Dimensional Fluid Flow Mock-up Loop (IV)
3) Test with Two-Phase Flow Test Loop
4) Natural Circulation Flow Test
5) Flow Visualization Test in Lower Plenum
6) Ultra High Heat Flux Test
7) Two-Phase Flow Visualization Test by the NRG
8) Thermo Fluid Safety Test for Fusion Reactor

As for the design and construction of test facilities, the following test facilities were newly constructed.

1) Multi-Dimensional Fluid Flow Mock-up Loop (V)
2) Two-Phase Flow Test Section installed at Core Thermal-Hydraulic Transient Test Facility.
3) Residual Heat Removal Test Facility for LWRS

As for the representative R&D, Electric Power for Rod Bundle of Core Thermal-Hydraulic Transient Test Facility was calibrated with carorie metric method to be clarified it's characteristics as well as Flow Rate of recirculation water.

Continuously quick response of Electric Power control system and Frow Rate control system were achieved for LWR's transient tests through many adjustment.

13.2 Operation Report of FCA

K. Hayasaka, K. Satoh, H. Sodeyama, K. Kurosawa, and H. Watanabe

Operation of Fast Critical Assembly (FCA) was carried out in accordance with the experimental schedule on the FCA XIX-1 and XIX-2 assemblies. Operation of 124 times was carried out in 101 days. No scram was recorded during the operation. The total operation time was 657.48 hours and the integrated power was 1.34 kWh. A total number of 5161 criticality operation has been recorded at the end of this fiscal year since the first achievement of criticality on the 29th of April 1967. For the safety regulation of operation, two days were devoted to the monthly inspection and about 10 weeks from October 1996 to the annual inspection. Routine maintenance activities were done during the inspections to provide maximum operation days for the experiments.

As for maintenance activities , the air compressor , which supplies the driving force to safety / control rods , was renewed because of a pin hole found on a tank. A ladder of the stack was also renewed to cope with the deterioration by corrosion.

As for fuel management , the defects of coating on natural uranium metallic fuel were repaired for about 2000 plates by spraying the surface with colloidal solution of fluorocarbon in oder to prevent the fuel from oxidation. Weights of the coating on the fuel plates were obtained from the difference of the weight between before and after coating.

As for the physical protection (P/P), the management of the entrance and exit was done restrictively and the system was maintained properly.

In connection with safeguard, IAEA and NSB* carried out monthly inspection under the international treaty. The Physical Inventory Taking (PIT) of the fuels was performed from the 20th to the 24th of May by means of item counting, weighing and non-destructive assay. IAEA and NSB made the Physical Inventory Verification (PIV) from the 27th to the 29th of May.

---

* NSB: Nuclear Safety Bureau

13.3 Operation Report of VHTRC

S. Fujisaki, M. Takeuchi, T. Ono, K. Nakajima and H. Watanabe

(*E-mail* : fujisaki @ fca 001. tokai. jaeri. go. jp)

The VHTRC-7(2), VHTRC-9 and VHTRC-9(2) cores were assembled to obtain experimental data for neutron flux distribution and for establishment of the measurement methods of reactor physic characteristics at initial criticality of HTTR.

The VHTRC-7(2) core has an HTTR mockup control rod that is partially inserted in the central column of the movable half assembly of VHTRC.

The VHTRC-9 and VHTRC-9(2) cores were assembled to measure the reactor physic characteristics at annular core which was simulated to the fuel loading columns of initical critical core of HTTR with about 18 fuel columns.

The operations for this purpose were completed as scheduled without any problem disturbing execution of the experiment.

The results of the operation were as follows ;

1) Operations of 224 times in 67 days,
2) Critical operations of 91 times,
3) Total operation time of 364 hours,
4) Integrated power of 149 WH.

No scram was recorded during the operations. The integral operation time is 4768 hours at the end of this fiscal year since the first achievement of criticality on May 13, 1985.

According to the safety regulation for operation, one day was devoted to the monthly inspection and about 8 weeks to the annual inspection from October to November.

As for fuel management, Physical Inventory Taking (PIT) was carried out from May 8 to May 9 by means of item counting. IAEA and NSB made the Physical Inventory Verification (PIV) under the international treaty on May 10. No anomaly was confirmed. The maintenance activity was also taken on the physical protection (p/p) system. The sensitivity and function of the system were examined and calibrated.

Since 1985, in order to verify the calculation accuracy related to the nuclear design of HTTR, the critical experiments have been continued using the VHTRC. But, the experimental operations of VHTRC for HTTR finished by the obtained the experimental data of the nuclear design of HTTR at September 30, 1996. Then, the present status of VHTRC is doing the preservation for safety under the reactor regulation.

13.4 Operation Report of FNS

Y. Abe, C. Kutsukake, S. Tanaka, M. Seki, T. Ono and H. Watanabe
(*E-mail*: Abe@fnshp.tokai.jaeri.go.jp)

Accelerator

The operation of Fusion Neutronics Source (FNS) was carried out on schedule for the shielding experiments for ITER, the benchmark experiments and so on, while the heavy irradiation experiment was stopped at 40 % of the target neutron yield by trouble of the 400 kV DC power supply for beam acceleration. The total operation time was 683 hours in this fiscal year.

As for maintenance activities, the control circuit of the accelerator was inspected every six months. A sliding seal of the rotating target was replaced twice with a new one to keep good vacuum condition. Overhaul of the oil free vacuum pumps (dry pump) was carried out. The 400 kV DC power supply which had voltage failure at the heavy irradiation experiment was repaired after inspection of its inner parts.

As for renewal activities, a high current ion source was replaced from the duoplasmatron type to a multicusp type. The details of the new ion source are described in Sec. 13.5. A rotating target cooling system was installed for a new type rotating target disk with micro-channels. The oil rotary vacuum pump on the high voltage terminal was replaced with an oil free vacuum pump to reduce tritium waste and to get the simple maintenance. The replacement of all oil rotary vacuum pumps to oil free vacuum pumps was completed.

Tritium Handling

Five small tritium targets with 370 GBq and two tritium targets with 33 TBq were used for experiments at the 80° beam line and for heavy irradiation experiment at the 0° beam line, respectively. The Tritium Adsorption Processor (TAP) system processed a total amount of 4.7 TBq tritium in exhaust gas from the vacuum system of the accelerator.

Development

A new type of high speed rotating vacuum seal assembly with mechanical ball bearings and differential pumping was manufactured, and the rotating test has been begun to confirm the vacuum performance under 1800 rpm.

13.5 Development of a New High Current Ion Source for FNS

M. Seki, Y. Okumura, H. Oguri, N. Miyamoto*, C. Kutsukake, S. Tanaka,
Y. Abe, T. Ono and H. Watanabe
(*E-mail:* seki@fnshp.tokai.jaeri.go.jp)

FNS has been used for fusion neutron engineering experiments such as shielding experiments of ITER/EDA and IEA international experiments. The experiment require higher beam current and neutron production rate. To increase the neutron yield performance of FNS, we have developed a high speed rotating target assembly, a micro channel target disk and a high current ion source. The high current ion source was renewed to improve the ion beam performance in this fiscal year.

A multicusp ion source was designed and developed for FNS incorporating with NBI Heating Laboratory. The basic specifications of the ion source are listed in Table 13.5.1 and a cross-sectional view of the ion source is shown in Fig. 13.5.1. The multicusp ion source consist of a magnetically confined plasma chamber and three- electrodes. The plasma chamber has a strong magnetic cusp field. Dimensions of the plasma chamber are 120 mm in inner diameter and 100 mm in length. In the chamber, source plasma is produced by arc discharge using two tungsten filaments . A magnetic filter is formed by samarium cobalt permanent magnets on the plasma electrode. The ions are extracted and accelerated up to 50 keV by the first electrode. A negative potential of 6 kV is applied to the second electrode to repel backstream electrons from the beam plasma downstream.

The proton beam test was performed at the ion source test facility (ITS-2M) to investigate the beam properties of the ion source. Proton ion beam of 100 mA was extracted with a low normalized emittance of 13 mrad and high proton ratio of 80 % at an acceleration voltage of 50kV. Fig. 13.5.2 shows the perveance characteristics of the ion source.

The ion source was installed in the FNS acceleration system after the ITS-2M test. The ion source performance test carried out by using hydrogen. The beam was not stable by electric discharge of the 50 kV high voltage. To stabilize the extraction beam of the ion source, the gap length between the plasma electrode and suppressor electrode increased from 8.9mm to 11.0mm, the extraction electrode was polished and a small leak valve was installed to control the pressure in the electrode vacuum chamber. As a result, the high voltage breakdown rate decreased. Deuteron ion beam of 30 mA is obtained at present. With modification of cooling water system in Faraday Cups, the adjustment of the ion source will be continued to achieve stable 40mA deuteron beam.

* Nissin Electric Co. Ltd.

Table 13.5.1 Specification of the ion source for FNS

	Design	Achieved (ITS-2M)	Achieved (FNS)
Beam Energy	50keV	50keV	50keV
Beam Current(Total)	>95mA	130mA	>60mA(H+)
Beam Current(Proton)	>65mA	100mA	>30mA(D+)
Ion Species	H+	H+	D+
Beam Divergence	<17mrad	13mrad	
Proton Ratio	>65%	80%	
Pulse Length	DC	DC	DC
Arc Power	5kW	3kW	3kW
Source Pressure	5mTorr	6.5mTorr	
Gas Flow Rate	4SCCM	13SCCM	7SCCM

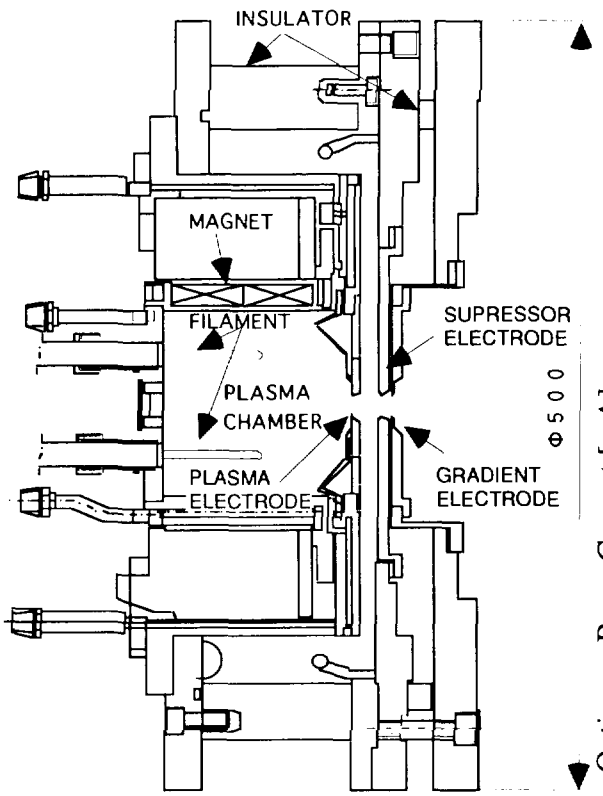

Fig.13.5.1 Cross-sectional view of the ion source for FNS

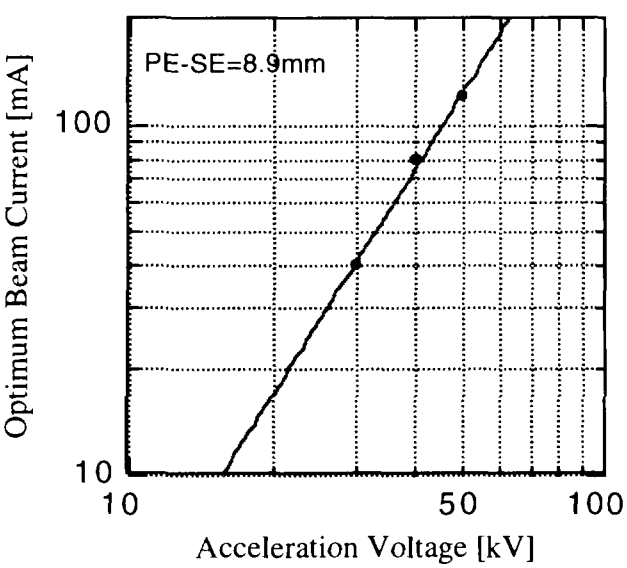

Fig.13.5.2 Perveance characteristics of the ion source for FNS

13.6 Tandem Accelerator and Superconducting Booster Operation

T. Yoshida

(E-mail: yoshida@tdmalph1.tokai.jaeri.go.jp)

Tandem Accelerator and Booster

The scheduled operations of the tandem accelerator for experiments were performed through the past one year. There were two short periods of scheduled maintenance. The running time was 5260.4 hours. The summary of the operation from April 1, 1996 to March 31, 1997 is as follows.

1) Time distribution by terminal voltage (Tandem accelerator)

>16 MV	26 days	11.3 %	11-12	19	8.2 %
15-16	100	43.3	10-11	22	9.5
14-15	20	8.7	9-10	1	0.4
13-14	21	9.1	8-9	0	
11-12	19	8.2	<8	6	2.6

Booster operation

^{33}S	600 MeV	2 days
^{58}Ni	281	7
^{74,76}Ge	550-651	14
^{90}Zr	340-430	10
^{127}I	510-650	2

2) Time distribution by projectile

^{1}H (2H,3H)	52 days	^{27}Al	5 days
^{6,7}Li	28	^{28}Si	23
^{11}B	4	^{31}P	9
^{12,13}C	2	^{32,33}S	11
^{16,18}O	5	^{35,37}Cl	11
^{19}F	4	^{54,56}Fe	2

^{58,60}Ni	32	^{90}Zr	10
^{63}Cu	1	^{107}Ag	2
^{74}Ge	15	^{127}I	8
^{79,81}Br	1	^{197}Au	5

3) Time distribution by activity

Operation for research		231 days
Atomic and solid state physics	(39.7)	
Radiation effects in materials	(13.8)	
Nuclear chemistry	(35)	
Nuclear physics	(116)	
Fast neutron physics	(22)	
Radiation chemistry	(0)	
Detector development	(2)	
Nuclear fusion	(0)	
Accelerator test operation	(2.5)	
Voltage conditioning		2
Scheduled maintenance(2 tank openings)		77
Unexpected repair with tank opening		9
Holidays		46
Training of the operation		2

The tandem accelerator had the unexpected tank opening at the end of August due to a trouble of the power generator in the shorted section. After 9 days cancellation of the scheduled experiments, the accelerator was operated until 24th in October. The tandem booster and the helium refrigeration system were operated 3 times during 3 scheduled machine times. There are some small troubles on the control computer systems, SattCon 31 type computer manufactured in Sweden, which is a module type small computer. The control system recovered immediately by exchanging the control circuit board. Some control valves for liquid helium distribution to the cryostats sometimes ran in the wrong. The trouble of the distribution valves was a little bit serious, because it was due to lack of reliability of electronic circuits and piezo electric valves. Before resuming refrigerator operation, we always checked up all the valves of the cold boxes

and the liquid helium distribution lines.

The helium refrigeration systems were in operation for 22 days from May 23 in 1996, 31 days from August 13 and for 76 days from January 14 in 1997. During these times, the super-conducting booster was utilized for 35 days for 12 experimental subjects. The booster ran steadily in every operation. The accelerating field gradients of the super-conducting resonators were between 2.9MV/m and 4.2MV/m.

An irradiation chamber for solid-state physics was installed on the middle of this fiscal year, and irradiation experiments for the super-conducting materials were carried out with high energy heavy ion from the tandem booster.

2MV Van de Graaff accelerator; The 2MV Van de Graaff accelerator was operated for 285.3 hours from April 1,1996 to March 31,1997. The main research subjects are solid state physics, atomic and molecular physics, and material physics.

13.7 Improvements for the JAERI Tandem Superconducting Booster

S. Takeuchi and M. Matsuda
(*E-mail* : takeuchi@tdmalph0.tokai.jaeri.go.jp)

The superconducting booster for the JAERI tandem accelerator has been running well without serious troubles since its completion in 1994. There are, however, some points which we want to improve.

(1) Some resonators are suffering from *Q-disease*(resonator Q degradation due to an increase of rf surface resistance with niobium hydride precipitation)

(2) Beam transmission was frequently much lower than the expected value of 60%(the bunching efficiency).

(3) A low-β resonator section is necessary to accept and boost efficiently very heavy ions from the tandem accelerator.

The point 3) is a big improvement project we want to do for the booster, which is to instal low-β(v/c=0.06) superconducting resonators into the entrance part of the booster linac. The low-beta section allows to accelerate very heavy ions like Pb without multiple steps of electron stripping in the tandem accelerator. There are strong demands for such very heavy ions, such as from a group of gamma-ray spectroscopy. We, however, postponed a fabrication plan of a prototype resonator in FY 1996 for some reasons. We rather decided to concentrate ourselves to the intallation project of a compact ECR(electron cycrotron resonance) ion source into the high voltage terminal of the tandem accelerator. This project is reported elsewhere in this annual report. several kinds of very heavy ions can be boosted without the low-beta section. several kinds of very heavy ions can be boosted without the low-beta section. Several kinds of very heavy ions can be boosted without the low-β section, if their charge states are higher than those after an electron stripper at the high voltage terminal in the usual tandem acceleration mode.

Following are the improvements we did in the fiscal year of 1996:

Q-disease problem : The Q degradation is due to hydrogen absorption in their chemical surface treatment and niobium-hydride precipitation which occurs approximately between 130 K and 90 K in the precooling process. Two of the 40 resonators in the booster linac were severely damaged in their on-line performance with this problem. We were forced to operate them at a field gradient of 2.0-2.5 MV/m. About 14 resonators could be operated at 3.5-5.0 MV/m. Those are installed in the first four cryo-modules. The rest 24 resonators are not affected by the Q-degradation, fortunately. There are two methods of recovering high Q; (a) One is to precool the resonators as fast as possible over the temperature range

of 130K to 90K. The fast cooling is effective in preventing absorbed hydrogen from precipitating as a form of niobium-hydride on the niobium resonator surface; that is, in preventing a large increase of rf surface resistance. (b) The other one is to extract hydrogen out of the niobium.

(a) The cryogenic system of the booster is composed of two identical refrigerators. Cooled helium gas parallely flows into six or seven cryo-modules, in each of which four resonators are housed and cooled in series. Cooling rate can be improved if all the cooled helium gas flow is limited to a group of fewer number of cryo-modules. All the resonators can be cooled fast over the temperature region of 130 K to 90 K by switching the flow group after group. Such a sequential cooling method was carried out for the first five cryo-modules of the booster linac. The cooling rate (in average) was, as a result, improved to -20 K/h for 3 cryo-modules and to -28.5 K/h for 2 cryo-modules, from -12K/h for the normal cooling. Averaged resonator Q values except the severely damaged two resonators were, respectively, recovered to 64% and 74% of those obtained at a rapid cooling rate as fast as or faster than - 40 K/h in off-line testing. With respect to the field gradients, a clear result was not obtained because electron field emission at high field gradients has been increasing with increasing particles on the resonator surfaces as time elapsed.

(b) Various trials except heat treatments were made to extract hydrogen from hydrogen polluted niobium using a spare resonator and niobium samples, but resulted in no effect. A heat treatment above 600 C is not applicable for our resonators because their outer cans are made of niobium and copper composite materials. The next or the last trial would be to partially heat the center conductor part in vacuum without heating the outer can.

Beam transmission : Misalignment was most likely to worsen the beam transmission from our experimental result that beams were steered away from the axis by quadrupole lenses and resonators. After improving the alignment set of laser beams and position detectors, the positions of the quadrupole lenses and cryo-modules(resonators) were carefully measured and many of them were found to be misplaced as much as 2 mm. After correcting them, the beam transmission was improved to more than 80% of the theoretically expected value.

RF power increase : A hundred watts rf power amplifires which have been placed by the resonator control stations in the rf control room are not powerfull enough to control the resonators stable in case of loosing helium pressure stability. Their output power were increased to more than150W by tuning them up. The amplifires were also made remote controllable in order to change their position to the sides of the cryo-modules. These changes can increase allowable forwarding rf power at input couplers from 80W to 135 to widen a phase control band width. There is an additional advantage that a loud noise from the amplifire's cooling fans vanishes from the rf control room.

Beam/Resonator phase prediction : Beam and resonator phases for different heavy ions can be predicted from calculation, if field gradients, resonator positions, rf signal propagation times and respective linearity of amplitudes and phases to their setting values of the controllers have been accurately measured. It is not so easy to keep accurate values for all the parameters. We, however, dared start trying such a prediction, because from the work we could extract some useful knowledge about the beam dynamics and the rf system of the booster. For example, we learned that velocity changes in the resonators and beam spread in the longitudinal phase space have to be taken into account in the beam phase calculation at an incident velocity much smaller than the optimum beam velocity of 0.1c for the booster resonators. The work is developping as a theoretical and experimental program.

Others : Problems in the cryogenic system and rf control stations were routinely cared for by S. Kanazawa et al, and I. Ohuchi et al, respectively. The systems were improving and running well. There were no serious troubles to report. A satellite control station of the tandem accelerator was developed by S. Hanashima, which was to be placed next to the resonator control stations. Resonator operation including conditioning was done mainly by N. Ishizaki and H. Tayama.

13.8 ECR Ion Source for the JAERI TANDEM Accelerator

M. Matsuda, S. Takeuchi and C. Kobayashi*

We have pushed forward a plan of an electron cyclotron resonance(ECR) ion source in the terminal of the JAERI tandem accelerator in order to increase beam intensity, beam energy and beam species. A compact ECR ion source, so called "NANOGAN" source [1], with a permanent magnet structure has been developed at GANIL, France, for accelerating the radio active ions. Its size and reliability are quite fitted to our plan. A way for stable acceleration of high intensity beams is expected to be opened by the use of the ECR ion source, since the beams from the source are in high charge states and with high intensity, and the operation without foil-strippers bring us no influence of a change of the terminal voltage on the charge state of the beams. In addition, it is possible to accelerate noble gas ions, which are impossible for conventional negative ion sources.

However, many difficulties have to be solved to install the source in the tandem terminal, such as the problems of the limited space, power supply, cooling system, RF source, vacuum system, control system, beam optics and so on. Some measures should be taken into consideration against electronic discharges and high pressure, because the source environment is on a high voltage of 16 MV and at the high pressure gas of 4.5 $kg/cm^2 \cdot G$. In spite of these difficulties, we could find some steps for solving above problems. The problems with the space, power supply and control system will be solved by the replacement of the Duo-plasmatron type ion source, which has been used, so far to the ECR ion source with some modifications. A TWT-type amplifier made for airplane is applied for the 10GHz RF source, and is set in the airtight vessel at the atmospheric pressure, for the vacuum system an ion pump encloses a gas flow. With an ion pump, ion extractions from the source were successfully examined for noble gases in accord with a small gas flow.

Several experiments with the ion source until now have proved the performance as expected. The optimum condition and the simplification of the operational parameters were searched on the assumption of installing the ion source in the tandem accelerator. The results of this experiment enabled us to reduce the six operational parameters to the three, which were the gas flow, bias voltage and the RF power. In this experiment, the gases used was previously mixed in the optimum and the RF tuner was fixed. This experimental procedure was brought from the experimental purpose, which was not to obtain maximum performance of the ion source, but to obtain stable intensity of ion beams against a change in the operational parameters. The gas flow, or, the vacuum of the system was the critical parameter for the stable operation. The results of the experiment for three gases, Ar, Kr and Xe, mixed with N_2 or O_2, are shown in Fig.1. The emittance for Ar ions from the above experiment was about $10mm \cdot mrad \cdot MeV^{1/2}$ (80%) and its form profile was very complicate.

The arrangement of the ion source is planned as is shown in Fig.2. The ion beams

---

* Nihon Advanced Technology. Co.

extracted by 30kV from the ion source are focused by an einzel lens, and then the mass and charge of them are roughly selected by the 45° pre-analyzing magnet. The pre-analyzing magnet is used to reduce the load of the pre-acceleration, since the beams from the ion source amount to 2mA. The beams are accelerated again by a 80 kV pre-acceleration tube, and are finally led to the tandem accelerator tube after the desired beams are selected by the 45° analyzing magnet. Only a small part of beams are injected into the tandem after reducing the large emittance by several apertures.

Comprehensive examinations including the beam optics and the control system will be made in the near future prior to the installation in the high voltage terminal. The installation and the experiments with the ECR ion source will be carried out at the end of the next fiscal year. Acceleration of heavy metal ions is also considered as our future plan.

Reference

1) P. Sortais et al., Proc. 12th Int. Work. on ECR ion sources, RIKEN, 1995, p.44.
2) D. K. Olsen et al., Proc. 10th Int. Work. on ECR ion sources, Oak Ridge, 1990, p.1.

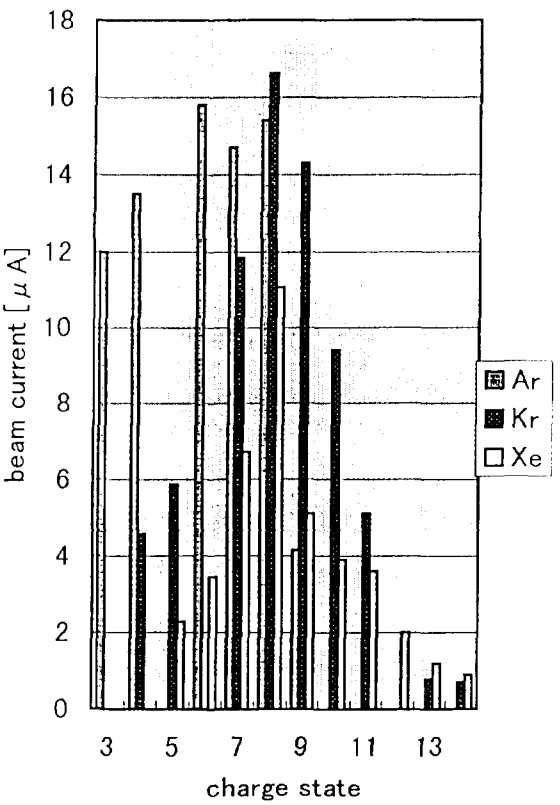

Fig. 1 Charge state distribution for three gases, Ar, Kr and Xe, mixed with N_2 or O_2

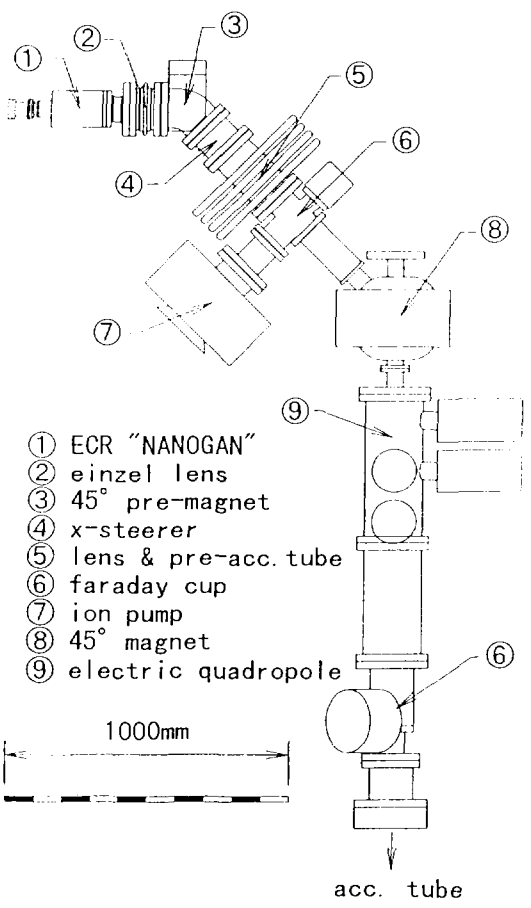

Fig. 2 Installation arrangement of the ion source

13.9 Control System for the JAERI Tandem Accelerator

S.Hanashima

A control system of JAERI tandem accelerator is a concurrent processing system using several transputers[1,2]. In this fiscal year, we have made several improvements on the system. They are installation of the second control console, replacement of CAMAC serial highway drivers, improvement of valuators on the control console, replacement of processor modules of central multi processor etc. Figure 13.9.1 shows the configuration of the system.

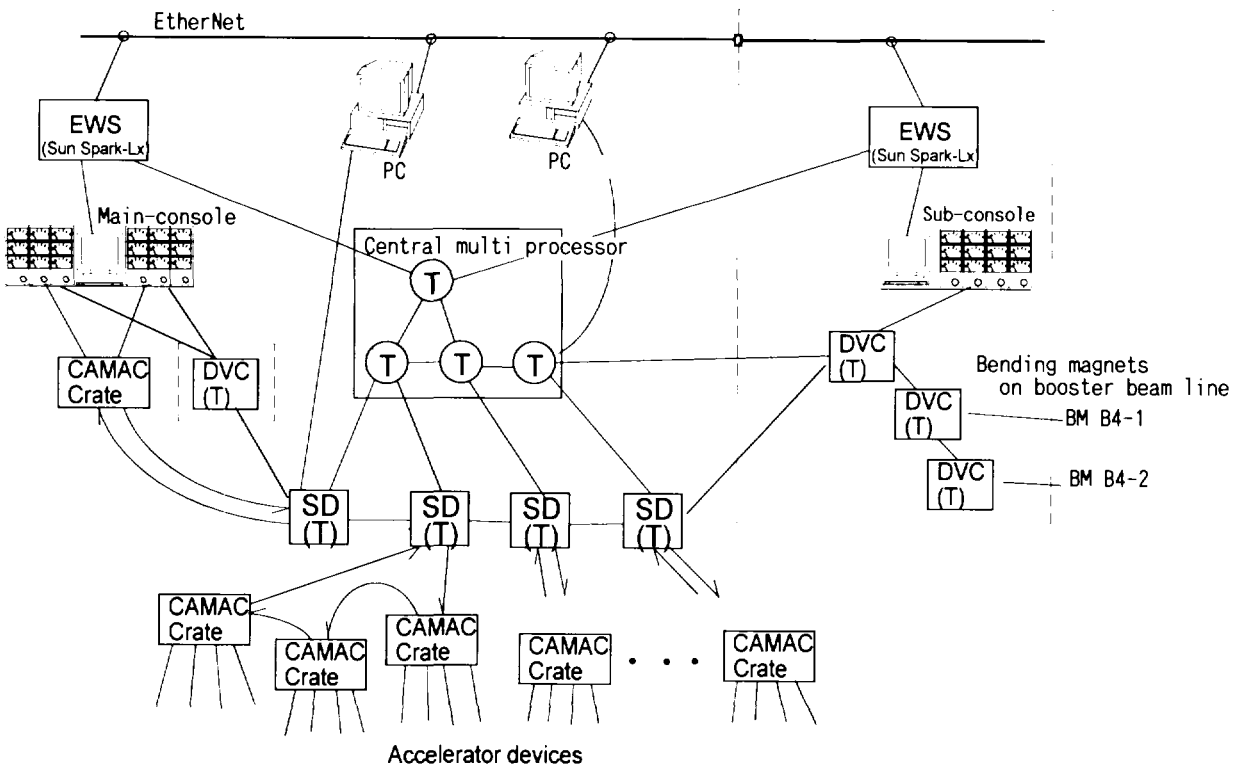

Fig.13.9.1 Configuration of control system for JAERI tandem accelerator :
T: transputer, SD:Serial highway driver,
DVC : Device controller. Dashed lines denote present expansion.

JAERI tandem accelerator has a post superconducting booster. The RF systems of the booster are controlled by dedicated control equipments which are independent of the control system of the tandem. It is the best choice to build a unified control system for both accelerators, for smooth operation of the two accelerators in the connected mode. But in our case, it was difficult because the control systems of the booster have been made

independently from the control system of the tandem. As the second choice, we made a sub console of the tandem control in the RF control room of the booster. The console has a window display, eight assignable meter units and four assignable shaft encoders(valuators). We can control the tandem from the console in the same way as from the main console. The window display is controlled by an engineering workstation. The other part of the console is controlled by a transputer. Both processors are linked to the central processor of the control system through optical fibers. Adding to the fiber link, the workstation has connection to an Ethernet of the control system.

The serial highway drivers[3] are located at the front ends of the control processors to CAMAC serial highway system. We have developed a new type of driver to improve reliability and performance. The new drivers are separated into two parts, a control processor and one or more serial highway interfaces. The interfaces perform much of the functions which have been done by the software in the old driver. These functions are generation and analysis of message packets and displaying highway error status on the front panels. The control processor controls the interfaces through a simple field bus. We can install several interfaces on the bus. The driver can control byte serial transfer, which our old drivers could not control. The major parts of the logic circuits are implemented in an FPGA(field programmable gate array).

The valuators on the control console are modified to accept a change in values crossing zero. A setting value of the valuator follows linearly to the rotation of the dial in the new specification. This modification enables natural control of beam steerers on a beam line of the accelerator. The old ones had an exponential control and could not allow crossing zero.

The central multi processor is the main engine of real time processing of the control system. Four transputer modules are connected together to construct the multi processor. New modules were made using almost same transputers(T805) as the previous modules, but their reliability on signal connections was greatly improved.

Controls of two bending magnets on the booster beam line have been included in the control system. They are controlled through device controllers using transputers. We intend to introduce local feed back control of magnetic fields using the controllers.

According to the change of the hardware configuration of the system, software of the system was modified at several points. They are an address scheme of data points of devices around the accelerator, protocols between the central system and the front end

processors, programs of serial highway drivers etc. The programs were expanded to accept two control consoles and data points directly controlled by transputers.

References

1)Hanashima S.: JAERI TANDEM & V.D.G. Annual Report 1993 pp7- 8.

2)Hanashima S. et al.: Transputer/Occam Japan 5 IOS Press, 1993 pp69-81.

3)Hanashima S.: JAERI TANDEM & V.D.G. Annual Report 1995 pp7.

14. Activities of the Research Committee

The Department of Reactor Engineering works as a secretariat of several research committees organized by JAERI. Members of committees are invited senior experts from domestic institutions in the related field. Name and task of each committee are as follows;

Japanese Nuclear Data Committee

The committee is organized to promote evaluation of nuclear data and production of group constants. The committee takes a task of compiling the activities of the International Nuclear Data Committee and the Working Party on International Evaluation Cooperation under OECD/NEA/NSC. A symposium is held annually to discuss research activities on nuclear data.

Research Committee on Reactor Physics

The Committee is organized to discuss research activities on reactor core analysis method and neutronics of new reactor concepts, and supports activities of OECD/NEA/NSC. Two subcommittees on the reactor system and the high energy nucleonics are organized under the committee.

Atomic and Molecular Data Research Committee

The committee is organized to promote compilation and evaluation of atomic and molecular data for controlled fusion research. Three working groups are organized under the committee. Workshops on atomic and molecular data are held to discuss current problems relevant to fusion research.

Research Committee on Advanced Reactors

The committee is organized to broadly review and discuss advanced reactor concepts and related fuel cycle. At present, new reactor concepts have been studied in JAERI with emphasis on the Pu utilization or the passive safety.

Committee on the International Conference on Physics of Reactors

The international conference on physics of reactors was held on September 16～20, 1996 in Mito city under the organization of JAERI. There are the organizing committee, the technical program subcommittee and the planning and management subcommittee.

14.1 Activities of Japanese Nuclear Data Committee

A. Hasegawa

The Japanese Nuclear Data Committee (JNDC) consists of three subcommittees, six standing groups, a steering and one adhoc committees. Each subcommittee also consists of several working groups (WG).

The Committee Meeting was held in July 1996 to discuss the nuclear data activity in the previous fiscal year and plans for the fiscal year 1996. Furthermore, discussion was made on several topics including the planning of the 1996 Symposium on Nuclear Data, JAERI's new project for neutron science and the international activity on nuclear data.

The activities of subcommittees and standing groups are briefly summarized below.

Subcommittee on Nuclear Data

1) High Energy Nuclear Data Evaluation WG : JENDL High Energy Files are being made by this WG. The evaluation is made in two phases. In the phase-I, the data up to 50 MeV will be evaluated for neutron and proton induced reactions. Evaluation of the phase-I for the neutron-induced reaction data has been finished and the results are being reviewed. That for proton-induced reaction data of structural materials was made. The energy range will be extended up to a few GeV in the phase-II. For Phase-II evaluation, the data of Al, Si, Cr, Ni, Cu, Pb and Bi have been evaluated up to 1GeV. The review of the evaluated results is in progress.

2) Covariance Data Evaluation WG : Methods of covariance matrix evaluation have been investigated. Covariance matrices for O-16, Na-23, Fe, U-235, U-238 and Pu-239 have been evaluated in ENDF/B-6 format. Evaluations were made by using a least-squares program GMA for the case of rich experimental data available. For the data evaluated by model calculations, covariances were obtained by using the KALMAN code system developed at Kyushu University. Discussion was also made about how to get the covariances for resonance parameters.

3) Evaluation and Calculation System WG : Investigation on evaluation method for light and medium-mass nuclides was made. Importance of the dispersion term in the OMP for the estimation of total cross section in low energies was discussed.

4) Fission Product Nuclear Data WG : Preparation of the evaluation report for JENDL-3.2 has been progressed. To check the methodology taken for the evaluations of JENDL-3.2, DWBA calculations were made for Mo-100 inelastic scattering cross sections. The value was compared with the new experimental data measured in Geel. It was found that adjusting a

deformation parameter (reducing about 30%) gives best fitting to the experimental data.

5) Activation-Cross-Section Data WG : The first version of Activation Cross Section File was completed and released in March 1996. Preparation for the evaluation report has been progressed. Some activation cross sections for unstable nuclides(Ca-45, Ni-59) were calculated and compared with other available evaluations.

6) PKA Spectrum WG : Development of a code system of ESPERANT for making PKA/KERMA files was finished last year. A PKA file for 72 nuclei from F-19 to Bi-209 on the basis of JENDL Fusion File was produced by this code. Evaluation method for light mass nuclei at the energy range below 50 MeV was determined. By this method H and C-12 evaluation was made.

7) Charged Particle Nuclear Data WG : This WG is responsible for the JENDL (α,n) Reaction File. The reevaluation has been progressed . Calculation scheme for the angular distributions of secondary neutrons was discussed.

8) Photonuclear Data WG : Total number of 26 nuclei evaluation was finished in FY1995. No meeting and no progress were made due to the group leader's problem in this year. This group will be merged to High Energy Nuclear Data Evaluation WG in the next year.

Subcommittee of Reactor Constants

1) Reactor Integral Test WG : Benchmark test of JENDL-3.2 for fast and thermal reactors has been made. Results are compared with those of ENDF/B-VI. Pointing out the problems in cross-section of JENDL-3.2 was made based on these data. They are inelastic cross sections and averaged cosine of elastic-scattering angles for U-238, capture and fission cross-section of U-235, etc. Especially large differences in Keff are observed when using inelastic cross-sections of U-238 of ENDF/B-VI and JENDL-3.2. In the benchmarks for U-235 cores, a large difference in capture resonance integral values between JENDL-3.1 and 3.2 gives a significant effect on Keff for FCA-IX series rather than thermal system.

A project for refining benchmark models was progressed.

2) Shielding Integral Test WG : Benchmark tests of total cross sections for Na, N-14, O and Stainless Steels were made using benchmark data of ORNL Broomstick experiments. Significant improvements were obtained for N-14 compared with the result of JENDL-3.1. For Na, some improvements were made compared with JENDL-3.1 but still overestimated relative to the experiment. As to the intermediate nuclear data investigation, a code TTNY which generates Thick target yields from the Evaluated Nuclear Data File is examined.

3) Dosimetry Integral Test WG : Reevaluation work has been progressed. Revision work for covariance data is a key item in this WG. Revised library of JENDL Dosimetry file was presented at nineth International Conference of Reactor Dosimetry held in Plague, Sept,1996.

4) Fusion Neutronics Integral Test WG : This is a joint working group established between JNDC and the Committee of Reactor Physics of JAERI. Integral tests of JENDL-3.2 for fusion applications have been made thoroughly using Monte-Carlo and stochastic calculations. Comparisons have been made especially with the results from the FENDL-1 library and EFF(European Fusion File). A multi-group cross section library was generated for conventional Sn codes.

5) Standard Group Constants WG : Revision work for JSSTDL library has been progressed.

Subcommittee on Nuclear Fuel Cycle

The subcommittee on nuclear fuel cycle consists of two WGs, Decay Heat Evaluation WG and WG on Evaluation of Nuclide Generation and Depletion. Generation of an ORIGEN-2/JNDC library based on JENDL-3.2 has been completed as a joint effort of the two WGs. One-group cross-section libraries for ORIGEN code were also generated for PWR, BWR and FBRs. The decay and fission yield data for the ORIGEN code have been progressed.

Standing Groups

1) CINDA Group : Papers on neutron induced reaction data published in Japanese journals and reports are surveyed. The 201 entries were sent to the NEA Data Bank in the last one year.

2) ENSDF Group : The evaluation of nuclear structure data is the duty of this group for nuclei with mass numbers from 118 to 129. Re-evaluated data for A= 129 has been published. Revised data for A=120 and 124 were sent to BNL host center. Re-evaluation of data for A=119 and 123 is in progress. The latest Chart of Nuclides 1996, which is scheduled to be published every four years, has been published.

3) Group on Atomic, Molecular and Nuclear Data for Medical Use : Survey work has been made for the radiopharmaceutical data needed in the field of nuclear medicine. Especially photo reaction data were discussed in details.

4) JENDL Compilation Group : Discussions were made about the strategy for the revision of JENDL-3.2 in the reorganized framework of JNDC.

5) Editorial Group of "Nuclear Data News" : Three issues of "Nuclear Data News" (No.54-56) which is a periodic informal journal in Japanese were published in a year.

6) WRENDA Group No formal activities were made.

14.2 Activities of the Research Committee on Reactor Physics

S. Matsuura, M. Nakagawa and Y. Ikeda

The committee reviews research activities related to reactor physics in Japan and supports the activities of Nuclear Science Committee (NSC) of OECD/NEA. In the fiscal year 1996, the committee reorganized three sub-committees into two. The reactor system sub-committee discusses topics of theory and experiments of fission reactors. The sub-committee on high energy nucleonics involves neutronics and diagnostics of fusion reactors, and various issues related to high energy neutrons, protons, etc., associated with high energy particle accelerators.

The 66th meeting of the Research Committee on Reactor Physics (RCRP) was held in June 1996. The following subjects relating to Excess Plutonium Disposition were discussed: 1) quantity of fissile plutonium, 2) status of world research activities for plutonium disposition and 3) conceptual design study of plutonium disposition reactor with ROX fuel. Documents discussed at the 7th meeting of NEA NSC held at OECD Head quarters, Paris, May 29 - 30, 1996 were distributed. The committee summarized the activities: the working parties and the task forces on the physics of plutonium recycling, international evaluation cooperation of nuclear data and the physics aspects of different transmutation concepts, and the status of the criticality benchmark working group.

At the 44th meeting of the reactor system sub-committee in August of 1996 and at the 45th meeting in March of 1997, recent activities and future plans were introduced concerning core analysis methods and reactor physics experiments. The following focal topics were discussed at the 44th meeting:

- Improvements on Monte Carlo codes MVP/GMVP (by JAERI),
  Processing nuclear data in ENDF/B-VI file format, Solving time dependent problems, Calculating reaction rates with the pointwise response library, General description method of external source geometry, Burnup calculation
- Recent development of in-core monitoring system in PWR (by Mitsubishi Heavy Industries, Ltd.),
  Measurement and data processing of power distribution
- Development of neutron detectors and their applications to the reactor physics experiments in Kyoto University Critical Assembly KUCA (by Nagoya Univ.),
  Position sensitive proportional counter, Scintillation detector using plastic fiber
- Design study of ABWR fully loaded with MOX fuel (by Hitachi, Ltd.).

At the 45th meeting, the following topics were highlighted:

- Experiment of core characteristics in Transient Experiment Critical Facility TRACY

(by JAERI),

- Recent development of in-core monitoring system in BWR (by Toshiba Corp.), Measurement and data processing of power distribution
- Present design of the Demonstration FBR plant (by Japan Atomic Power Company),
- Proposal for 3D radiation transport code benchmarks in simple geometries with void region (by Kyoto Univ.).

The first sub-committee meeting of High Energy Nucleonics was held in August, 1996. The sub-committee was newly formed, as mentioned above, by merging the two former sub-committees of "Fusion Reactor" and "Shielding" into "High Energy Nucleonics" which covers broader research areas associated with high energy particles, in particular, neutrons and protons. Almost all members serving in the former sub-committees are participating in this new committee. In the first meeting, the sub-committee summarized activities of the former Fusion and Shielding sub-committees to deepen mutual understanding. Three working groups, i.e. Fusion Neutronics, Accelerator Shielding and High Energy Data Library, were proposed to be organized under the sub-committee for continuing the activity in each area, and promoting the future synthesis of research coordination. Committee members were encouraged to participate in any working groups. Besides the discussion on the new organization, a report on the ANS Topical Meeting on Radiation Shielding and Protection was presented. The meeting of the Fusion Neutronics working group was held in December, 1996 to discuss several urgent topics and strategies. The status of the ITER nuclear design was also reported. The second sub-committee meeting was held in March, 1997. Research activities relevant to particle accelerators in China, and the activities of high energy neutron experiments in Europe were presented. The secretariat of SARE 3 and SATIF-3, to be held in May, 1997, reported the status of submitted papers, participants and so on. A discussion went on concerning the preparation for the 9th International Conference on Radiation Shielding planned for 1999 in Japan.

14.3 Activities of Atomic and Molecular Data Research Committee

T. Shirai

The Atomic and Molecular (A&M) Data Research Committee is organized to promote activities on A&M data for the research and development of controlled thermonuclear fusion. The committee consists of members from JAERI, universities and other research institutions. Three working groups concerning particle-material interaction, atomic collision and atomic structure are organized under the Research Committee.

In collaboration with the A&M Data Research Committee, compilation and evaluation work is continued for making the 4th edition of Japanese Evaluated Atomic and Molecular Data Library (JEAMDL-4) as a five-year project since 1992. The activities of these three working groups are briefly summarized below.

Particle-material interactions relevant to the hydrogen-recycling in edge plasma was surveyed and reviewed for retention and re-emission of hydrogen in beryllium and for retention of hydrogen isotopes in beryllium by simultaneous H^+ and D^+ irradiation. Data surveys were carried out for radiation damage on silica glass induced by D^+ and He^+ irradiation and for the differential cross sections for H(He, He)H, ^{16}O(He, He)^{16}O and D(He, He)D elastic scattering as basic data for elastic recoil detection analysis.

Analytical least-squares fits was made to the recommended cross sections for collision processes between electrons and hydrocarbon molecules, such as CH_4 and so forth, that occur as impurities in divertor plasma, as is presented in 1.13 of this report. A similar work is now in progress for collision processes between electron and H_2O, CO and CO_2 relevant to edge plasma impurities. In parallel, data compilations have been continued of recent experimental data for collisions of H, H_2, He and Li atoms and ions with atoms and molecules, and for collisions of metallic ions in low ionization stages with rare gases and carbon-containing molecules. Cross sections for various collision processes between electron and H_2^+ (and isotopic variants) was calculated theoretically.

Data compilation has been made of wavelengths, energy levels, ionization energies, line classifications, intensities and transition probabilities for argon in all stages of ionization.

14.4 Activities of the Research Committee on Advanced Reactors

H.Takano and M.Ochiai

The Research Committee on Advanced Reactors (RCAR) reviews and discusses broadly reactor concepts and fuel cycle with emphasis on Pu utilization and passive reactor safety. The RCAR and its two subcommittees comprise members from Japan Atomic Energy Research Institute (JAERI), universities, Power Reactor and Nuclear Fuel Development Corporation (PNC) and industries including utilities and reactor manufacturers.

The RCAR meeting is scheduled to be held once a year. At the meeting in February 1997, the RCAR reviewed activities of the subcommittees during the FY1996.

Subcommittee on Pu Utilization Reactors

Two meetings were held in June and December 1996 for the discussions on emerging (1) Pu utilization and excess Pu dispositions in LWRs and (2) Advanced reactors and fuel recycling. In the discussion on the Pu-utilization in LWRs, the study of reprocessing for spent MOX fuels with mixing UO_2 fuels in Rokkasho Reprocessing Facility was reported by JAERI. In order to reduce the spent fuel accumulation and fuel cycle cost , a concept of very high-burnup (100GWd/t) MOX fuel PWR was introduced by JAERI, and the development issues for fuel and cladding materials were reported. As a current activity for the excess Pu disposition in JAERI, two concepts for Pu-burning system of the ROX(rock-like oxide) fuel PWR and HTGR with Pu and Th sphere fuels were reported, and core reactivity coefficients and Pu-annihilation rate were discussed. In the discussion on Advanced reactors and fuel recycling, Prof. Kanagawa (Chairman) reviewed that some technical problems for the advanced fuel recycling technologies as compared new nitride / metallic fuels-pyrochemical and metallic reprocessing methods with the present MOX fuel purex-reprocessing. A feature of a simplified purex-reprocessing with low decontamination process to enhance economics and proliferation resistance was reported by PNC. TEPCO introduced the dry-reprocessing and vibration compaction fuel fabrication system developed for the oxide fuels in Russia. For the development of the nitride fuel and its pyrochemical reprocessing , the irradiation behavior for FP-gas release and fuel-cladding-interaction were reported, and current status of electrolytic cell equipment installed in Oharai site was introduced by JAERI.

Subcommittee on Research and Development of Passive Safety Reactors

The subcommittee meeting, which was the fifth one, was held one time in October 1996 this fiscal year. The main topic for the meeting was the change or expansion of the passive safety reactor research activities in JAERI this year to the research activities on the future reactor aiming at more attractive reactor concept for users and local societies. That is, in the new research objectives, more emphasis would be placed on contribution to the local society and increase in economics.

Corresponding to the above activities, light water reactor engineering related research activities in JAERI were presented for discussion especially to get comments from the committee members. Presented areas were the nuclear data, the reactor physics analyses and experiments, the thermal hydraulics, the reactor instrumentation, the reactor control and diagnosis, the fuel research, the material research and the conceptual designing of the future reactor. They are all what is called the basics research on the reactor engineering, and the present status and the future plan of each research area were presented and discussed. On the future light water reactor development, proposed necessary R&D items were pointed out and summarized in a table form. It was noted there were many items which could not be covered only by JAERI, and hence, future cooperation with members outside of JAERI was indispensable and expected to complete them.

Furthermore, it was also announced that questionnaires on the JAERI's future light water reactor research activities would be sent later to the members, and was asked to answer them to reflect them fruitfully to the JAERI's future activity plan.

14.5 Activities of Committee on the International Conference on Physics of Reactors PHYSOR 96

T. Okabe
(*E-mail:* okabe @ clsu3a0.tokai.jaeri.go.jp)

Preparation for holding the International Conference on Physics of Reactors (PHYSOR96), the subtitle of which had been set "Breakthrough of Nuclear Energy by Reactor Physics", was actively continued from the previous fiscal year. PHYSOR 96, sponsored by Atomic Energy Society of Japan (AESJ), Reactor Physics Division of AESJ and Reactor Physics Division of American Nuclear Society, was considered most suitable to be organized by JAERI and Power Reactor and Nuclear Fuel Development Corporation.

On May 20, 3rd Local Technical Program Committee (LTPC) was convened and key issues such as the structure of session and selection of chair persons were discussed.

By the end of July, the final announcement was put in circulation.

On August 9, 4th LTPC was held and drafted the final program.

On August 19, 3rd organizing committee was convened and discussed the final schedule, program and others.

With all the necessary preparations made, the conference was held from September 16 through 20 at Mito Plaza Hotel. The schedule is given in Table 14.5.1.

At the conference, 311 people from 24 countries gathered and 132 oral and 93 poster presentations were made as shown in Table 14.5.2. The number of 155 presentations from foreign countries marked the largest ever presented in the series of this meetings.

Due to recent situations against nuclear energy on a worldwide level, a small number of participants had been expected at first. However, more than double the expected number of papers was received and 225 papers were selected by strict paper review screening.

Research on core management of LWRs and others showed steady progress. Similarly, studies on calculation method for prediction of core behavior and the development of widely applicable software/data indicated sustained headway. Among others, uranium core study seemed to have reached maturity.

On the other hand, except certain countries, experiments relating to MOX utilization and improvement of data and calculation method showed progress and its inclination, gradually translating them into reality, seemed to continue in the next century as well.

The number of papers relating to transmutation in downstream and criticality safety increased, those studies gradually playing an important role in the application field of reactor physics. Especially, the former seemed to be forming a large stream. Also, studies on 3-D

neutronics-thermal hydraulics coupled kinetics codes indicated progress in each country and these results were expected to contribute largely to reactor operation and safety.

Presentation on fast reactors were made only by France, Russia and Japan, which indicated the present situation of the world.

Among the advanced reactor research, studies on evolutional reactors were the main topics and innovative ones were limited.

Above-mentioned move of research showed that many scientists in each country were actively conducting reactor physics research as the major pillar sustaining nuclear energy technology of the nation and international cooperation was being implemented effectively.

Table 14.5.1 Conference schedule

	Monday Sept.16	Tuesday Sept.17	Wednesday Sep.18	Thursday Sept.19	Friday Sept.20
08:00		Registration			
			3 Parallel Oral		
09:00		Opening Session	E2,J1,A3/A4	E5/H1,L1/L2, C2/D1	Technical Tour (PNC&JAERI)
10:00					
			3 Parallel Oral		
11:00					
		3 Parallel Oral E1,I1,A1	E3,J2,A4/A5	H1/H2,L2/M1, B1	
12:00					
13:00		Lunch	Lunch		
14:00					
			3 Parallel Oral	3 Parallel Oral	
15:00		3 Parallel Oral	E4,J3,A5/C1	K1/K2,M1/M2, A6/A7	
16:00		E1/F1,I2,A2			
		Poster Sessions			
17:00					
	Registration & Welcome Cocktail	Display I	Display II	Closing	
18:00					
19:00		Reception			

Subject Categories of papers

A New or Improved Computational Methods (Nodal, Transport, Monte Carlo)
B Advanced Software for Reactor Design and Management
C Benchmark and Validation of Codes
D Advanced Reactor Design (Fast and Thermal Reactor, Research Reactors, any Reactor closely related with Fuel Cycle)
E Experiment, Management and Analysis
F Nuclear Data Utilization
H Pu Burning and Recycling
I Fuel Management
J Kinetics Codes, Experiments and Transient Analysis
K Reactor Operation and Control
L Criticality Safety
M Transmutation

Table 14.5.2 Participants and papers

COUNTRY	PARTICIPANTS	PAPERS (ORAL,POSTER)	COUNTRY	PARTICIPANTS	PAPERS (ORAL,POSTER)
ARGENTINA	2	2 (0, 2)	MEXICO	1	2 (0, 2)
BELARUS	1	1 (1, 0)	NETHERLANDS	5	7 (4, 3)
BELGIUM	7	7 (6, 1)	NORWAY	2	2 (0, 2)
BRAZIL	2	3 (1, 2)	P.R.CHINA	2	2 (1, 1)
CANADA	1	0	POLAND	1	1 (1, 0)
FINLAND	1	2 (1, 1)	RUSSIA	13	21 (9,12)
FRANCE	29	36 (29, 7)	SPAIN	2	2 (1, 1)
GERMANY	4	5 (5, 0)	SWEDEN	8	6 (5, 1)
HUNGARY	1	1 (1, 0)	SWITZERLAND	4	4 (4, 0)
ITALY	3	3 (3, 0)	TAIWAN	2	1 (1, 0)
JAPAN	175	71 (36,35)	UK	9	8 (6, 2)
KOREA	16	18 (6,12)	USA	20	20 (11,9)
			TOTAL	311	225 (132,93)

Publication List

1. Nuclear Data, and Atomic and Molecular Data

1) Shibata, K., *et al.*: "Estimation of Uncertainties in ^{1}H, Zr and ^{238}U Nuclear Data Contained in JENDL-3.2", JAERI-Research 96-041 (1996) [in Japanese].
2) Shibata, K., *et al.*: "Curves and Tables of Neutron Cross Sections in JENDL-3.2", JAERI-Data/Code 97-003 (1997).
3) Shibata, K., *et al.*: "Estimation of Covariance Data for JENDL-3.2", Proc. Int. Conf. on Physics of Reactors (PHYSOR96), Mito, 1996, F31 (1996).
4) Shibata, K.: "Activities on Covariance Estimation in Japanese Nuclear Data Committee", Proc. 1996 Symp. on Nucl. Data, JAERI-Conf 97-005, 102 (1997).
5) Ito, R., Tabata, T., Shirai, T. and Phaneuf R.: "Analytic cross sections for collisions of H, H_2, He and Li Atoms and Ions with Atoms and Molecules, IV", JAERI Data/Code 96-024 (1966).
6) Igarashi, A. and Shirai, T.: "Excitation and Ionization of Excited Helium Atoms in Collisions with Bare Ions", Phys. Scr., T62, 95 (1996).
7) Ichihara, A., Shirai, T. and Yokoyama, K.: "A Study on Ion-Molecule Reactions in the H_3^+ System with Trajectory-Surface-Hopping Model", J. Chem. Phys., 105, 1857 (1996).
8) Ichihara, A., Shirai, T. and Eichler, J.: "Radiative Electron Capture and the Photoelectric Effect at High Energies", Phys. Rev., A54, 4954 (1996).
9) Igarashi, A. Toshima, N. and Shirai, T.: "Hyperspherical Coupled-channel Calculations of Positronium Formation in Low-Energy Positron-Helium Collisions", Phys. Rev., A54, 5004 (1996).
10) Katakura, J.: "Decay and Fission Yield Data Library for ORIGEN2 Code to Reproduce the Decay Heat Values Recommended by the Atomic Energy Society of Japan", J. At. Energy Soc. Jpn., 38[7], 609 (1996) [in Japanese].
11) Tendow, Y.: "Nuclear Data Sheets for A=129", Nucl. Data Sheets, 77, 631 (1996).
12) Katakura, J.: "Evaluation of the 2039 keV Level Property in ^{124}Te", JAERI-Conf 97-004, 37 (1997).
13) Katakura, J.: Decay Data File Based on the ENSDF File", JAERI-Conf 97-005, 312 (1997).

14) Chiba S., *et al.*: "Analysis of Proton-induced Fragment Production Cross Sections by the Quantum Molecular Dynamics Plus Statistical Decay Model", Phys. Rev., C54, 285 (1996).

15) Chiba, S., Morioka, S. and Fukahori, T.; "Evaluation of Neutron Cross Sections of Hydrogen from 20 MeV to 1 GeV", J. Nucl. Sci. Technol., 33[8], 654 (1996).

16) Harada, M., Watanabe, Y., Chiba, S. and Fukahori, T.; "Evaluation of Neutron Cross Sections of ^{12}C for Energies up to 80 MeV", J. Nucl. Sci Technol., 34[2], 116 (1997).

17) Hirayama, H., *et al.*: "Review of Actions in Japan after SATIF-I", Proc. Specialists' Meeting on Shielding Aspects of Accelerators, Targets and Irradiation Facilities (SATIF-II), Oct. 12-13, 1995, Geneva, Switzerland, OECD Documents, 35 (1996).

18) Hayashi, K., *et al.*: "Survey of Thick Target Neutron Yield Data and Accelerator Shielding Experiments", Proc. Specialists' Meeting on Shielding Aspects of Accelerators, Targets and Irradiation Facilities (SATIF-II), Oct. 12-13, 1995, Geneva, Switzerland, OECD Documents, 41 (1996).

19) Chiba, S., *et al.*: "Analysis of Proton-induced Fragment Production Cross Sections by the Quantum Molecular Dynamics Plus Statistical Decay Mode", JAERI-Conf 97-004, 9 (1997).

20) Fukahori, T. and Chiba, S.; "Systematics of Proton-induced Fission Cross Section at the Intermediate Energy Region", JAERI-Conf 97-004, 95 (1997).

21) Yoshioka, S., *et al.*: "A Consistent Analysis of (p,p') and (n,n') Reactions Using the Feshbach-Kerman-Koonin Model", JAERI-Conf 97-005, 301 (1997).

22) Fukahori, T., Iwamoto, O. and Nakagawa, T. (Eds.) : "Proc. of the First Internet Symposium on Nuclear Data, Apr. 8 - Jun. 15, JAERI, Tokai, Japan", JAERI-Conf 97-004 (1997).

23) Iguchi, T. and Fukahori, T. (Eds.) : "Proc. of the 1996 Symposium on Nuclear Data, Nov. 21-22, 1996, JAERI, Tokai, Japan", JAERI-Conf 97-005 (1997).

24) Akie, H., Kaneko, K. and Takano, H.: "Fast and Thermal Benchmark Test for JENDL-3.2 and ENDF/VI", Proc. Int. Conf. on Physics of Reactors (PHYSOR96), Mito, F-72 (1996).

25) Rahman, M. and Takano, H.: "Generation of WIMS-D/4 Multigroup Constants Library Based on the JENDL-3.2 Nuclear Data and Its Validation Through Some Benchmark Experiments Analysis" , JAERI-Research 96-056 (1996).

26) Charlton, S. W., *et al.*: "Delayed Neutron Emission Measurements from Fast Fission of

U-235 and NP-237", Proc. Int. Conf. on Physics of Reactors (PHYSOR96), Mito, Japan, September 16-20, 1996, Vol.3, F-11 (1996).

2. Theoretical Method and Code Development

1) Murata, I., Mori, T. and Nakagawa, M.: "Continuous Energy Monte Carlo Calculations of Randomly Distributed Spherical Fuels in High-Temperature Gas-Cooled Reactors Based on a Statistical Geometry Model", Nucl. Sci. Eng., 123, 96 (1996).
2) Kugo, T. and Nakagawa, M.: "Application of Neural Network to Multi-dimensional Design Window Search", Proc. Int. Conf. on Physics of Reactors (PHYSOR96), Mito, Japan, B-73 (1996).
3) Yoshikawa, H., Kugo, T. and Tsuchihashi, K.: "Virtual Environment for Integrated Design Support (VINDS) for Conceptual Design of a Space Power Reactor Core", Proc. Int. Conf. on Physics of Reactors (PHYSOR96), Mito, Japan, B-92 (1996).
4) Sasaki, M., Nakagawa, M. and Mori, T. : "Pararell Processing of Monte Carlo Simulation for Neutron and Photon Transport Problems", Proc. Int. Conf. on Physics of Reactors (PHYSOR96), Mito, Japan, A-339 (1996).
5) Mori, T., Nakagawa M. and Kaneko, K.: "Neutron Cross Section Library Production Code System for Continuous Energy Monte Carlo Code MVP LICEM", JAERI-Data/Code 96-018 (1996).
6) Ueki, T., Mori, T. and Nakagawa, M.: "Error Estimates and Their Biases in Monte Carlo Eigenvalue Calculations", Nucl. Sci. Eng., 125, 1 (1997).
7) Nakagawa, M. : "New or Improved Computational Methods and Advanced Reactor Design", J. At. Energy Soc. Jpn., 39, 3 (1997).
8) Nakagawa, M.: "Development of Efficient General Purpose Monte Carlo Code Used in Nuclear Engineering", IFIP Working Conf. on Quality of Numerical Software, London, 349 (1997).

3. Reactor Physics Experiment and Analysis

1) Rimpault, G., Oigawa, H. and Smith, P.: "Assessment of Latest Developments in Sodium Void Reactivity Worth Calculations", Proc. Int. Conf. on Physics of Reactors (PHYSOR96), Mito, Japan, September 16-20,1996, Vol.2, E-11 (1996).

2) Osugi, T., *et al.*: "Mock-up Experiment for Moderator Added Fast Reactor", Proc. Int. Conf. on Physics of Reactors (PHYSOR96), Mito, Japan, September 16-20, 1996, Vol.2, E-21 (1996).

3) Iijima, S., *et al.*: "Benchmark Experiment for Physics Parameters of Metallic-Fueled LMFBR at FCA", Proc. Int. Conf. on Physics of Reactors (PHYSOR96), Mito, Japan, September 16-20, 1996, Vol.2, E-46 (1996).

4) Okajima, S.: "Analysis of Doppler Effect Measurement in FCA Cores Using JENDL-3.2 Library", Proc. Int. Conf. on Physics of Reactors (PHYSOR96), Mito, Japan, September 16-20, 1996, Vol.2, E-247 (1996).

5) Akino, F., Takeuchi, M., Ono, T. and Fujisaki, S.: "Measurement of Control Rod Reactivity Worth in Axially Heterogeneous Fuel Core(VHTRC-4) by PNS Method", Proc. Int. Conf. on Physics of Reactors (PHYSOR96), Mito, Japan, September 16-20, 1996, Vol.2, E-281 (1996).

6) Yamane, T., Akino, F. and Yasuda, H.: "Temperature Effect on Critical Mass and Kinetic Parameter β eff/Λ of VHTRC-4 Core", Proc. Int. Conf. on Physics of Reactors (PHYSOR96), Mito, Japan, September 16-20, 1996, Vol.2, E-290 (1996).

7) Kaneko, Y., Yamane, T., Shimakawa, S. and Yamashita, K.: "Delayed Integral Counting Method for Rod Drop Experiments", J. At. Energy Soc. Jpn., 38 [11], 907 (1996) [in Japanese].

8) Kaneko, Y., *et al.*: "A Proposal of Revised Method for Determination of Large Positive Reactivity", JAERI-Research 97-003 (1997) [in Japanese].

9) Andoh, M. and Okajima, S.:"Measurement of Doppler Effect up to 2000℃ at FCA (4) - Investigation on Calculation Model for the Doppler Effect Measurement with a Heated Foil Using MVP Code - ," JAERI-Research 97-014 (1997).

10) Akino, F., Takeuchi, M., Ono, T. and Kaneko, Y.: "Experimental Verification and Analysis of Neutron Streaming Effect through Void Holes for Control Rod Insertion in HTTR", J. Nucl. Sci. Technol., 34[2], 185 (1997).

11) Okajima, S., Oigawa, H., Andoh, M. and Mukaiyama, T. : "High Temperature Doppler Effect Experiment for ^{238}U at FCA --- (II) Reaction rate measurement up to 2,000℃ with a foil heated by laser exposure", J. Nucl. Sci. Technol., 34[1], 13 (1997).

12) Okajima, S., Sakurai, T. and Mukaiyama, T. : "Status of International Benchmark Experiment for Effective Delayed Neutron Fraction (β eff)", JAERI-Conf 97-005, 71 (1997).

13) Sakurai, T. and Nemoto, T. :"Measurements and Analyses of ^{238}U Capture to ^{239}Pu Fission Rate Ratio and ^{238}U Capture to ^{235}U Fission Rate Ratio at Fast Critical Facility FCA", Proc. of Ninth Int. Symp. on Reactor Dosimetry, Prague, Chzec Republic, September 2-6 (1996).

14) Okajima, S., Oigawa, H., Andoh, M. and Mukaiyama, T. : "Doppler Effect Measurements up to 2000℃ in the Fast Critical Facility FCA", Proc. of Ninth Int. Symp. on Reactor Dosimetry, Prague, Chzec Republic, September 2-6 (1996).

4. Advanced Reactor System Design Studies

1) Iwamura, T., Araya, F. and Murao, Y.: "Application of PSA Methodlogy to Design Improvement of JAERI Passive Safety Reactor (JPSR)", J. Nucl. Sci. Technol., 33[4], 316 (1996).

2) Araya, F., Iwamura, T., Yoshida, H. and Murao, Y.: "Computational Study on Long Term Cooling of JAERI Passive Safety Reactor JPSR under Accident Condition", Proc. 73rd JSME Spring Annual Mtg., 491(1996).

3) Araya, F., *et al.*: "Safety Analysis of a Passive Safety Light Water Reactor JPSR", Proc. 10th Pacific Basin Nucl. Conf., 299(1996).

4) Ochiai, M. and Murao, Y.: "Design Study on A Passive Safety Reactor", Proc. JSME 5th National Symposium on Power and Energy System, 209 (1996) [in Japanese].

5) Kunii, K., Iwamura, T. and Murao, Y.: "Evaluation on Driving Force of Natural Circulation in Downcomer for Passive Residual Heat Removal System in JAERI Passive Safety Reactor JPSR", J. Nucl. Sci. Technol, 34[1], 21 (1997).

6) Kunii, K.: "Experimental Analysis for 3-D Flow in Lower Plenum by Flow Visualization", Proc. 1st Pacific Symp. on Flow Visualization and Image Processing, 592(1997).

7) Tsujimoto, K., *et al.*: "Improvement of Reactivity Coefficients of Metallic Fuel Fast Breeder Reactor by Addition of Zirconium-Hydride Moderator", Proc. Int. Conf. on Physics of Reactors (PHYSOR96), Mito, Japan, September 16-20, 1996, Vol.2, D-21 (1996).

5. Fusion Neutronics

1) Smith, D.L. , Ikeda, Y. and Uno, Y. : "An Investigation into the Possibility of Performing

Radiography with Gamma rays Emitted from Water Made Radioactive by Irradiation with 14 MeV D-T Fusion Neutrons", Fusion Eng. Des., 31, 41 (1996).

2) Maekawa, F. and Oyama, Y. : "Measurement of Low Energy Neutron Spectrum below 10 keV with the Slowing down Time Method", Nucl. Instrum. Method, A372, 262 (1996).

3) Verzilov, Y., Maekawa, F. and Oyama, Y. :"A Novel Method for Solving Lithium Carbonate Pellet by Binary-Acid for Tritium Production Rate Measurement by Liquid Scintillation Counting Technique", J. Nucl. Sci. Technol., 33, 390 (1996).

4) Meadows, J.W., *et al.*: "Measurement of Fast-Neutron Activation Cross Sections for Copper, Europium, Hafnium, Iron, Nickel, Silver, Terbium and Titanium at 10.0 and 14.7 MeV and for the Be(d,n) Thick-Target Spectrum", Ann. Nucl. Energy, 23, 877 (1996).

5) Smith, D.L, *et al.*: "Water Activation in a Fusion Environment", Fusion Technol., 30, 1049 (1996).

6) Maekawa, F., *et al.*: "Validate Assessment of Shielding Design Tools for ITER Through Analysis of Benchmark Experiment SS316/Water Shield Constructed at FNS/JAERI", Fusion Technol., 30, 1081 (1996).

7) Youssef, M.Z., *et al.*: "Benchmarking FENDL Libraries Through Analysis of Bulk Shielding Experiments on Large SS316 Assemblies for Verification of ITER Shielding Characteristics", Fusion Technol., 30, 1101 (1996).

8) Kumar, A., *et al.*: "Experimental Demonstration of Differing Impacts of Pulsed and Continuous Operation of a Deuterium-Tritium Neutron Source on Induced Radioactivity in the Context of ITER", Fusion Technol., 30, 1118(1996).

9) Mori, C., *et al.*: "Development of Fast Neutron Spectrometer of Proportional Counter and Si-Detector Telescope Type", Fusion Technol., 30, 1134 (1996).

10) Ikeda, Y. and Smith, D.L. : "Measurements of Activation Cross Sections for Waste Management", Fusion Technol., 30, 1190 (1996).

11) Kasugai, Y., Ikeda, Y., Yamamoto, H. and Kawade, K. : "Systematics for (n,p) Excitation Functions in the Neutron Energy between 13.3 and 15.0 MeV", Ann. Nucl. Energy, 18, 1429 (1996).

12) Nishitani, T., *et al.*: "Irradiation Tests on Diagnostics Components for ITER in 1995", JAERI-Tech 96-040 (1996).

13) Kosako, K., Yamano, N., Maekawa, F. and Oyama, Y., : "Production and Verification of

the MCNP Cross Section Library FSXLIB-J3R2 Based on JENDL-3.2", Proc. 1996 Topical Meeting on Radiation Protection and Shielding, Cape Cod, Massachusetts, April 21-25, 1996, 1088 (1996).

14) Maekawa, F. and Oyama, Y. : "Benchmark Test of 14-MeV Neutron Induced Gamma-Ray Production Data in JENDL-3.2 and FENDL/E-1.0 Through Analysis of the OKTAVIAN Experiments", Nucl. Sci. Eng., 123, 272 (1996).

15) Maekawa, F. and Oyama, Y. : "Measurement of Neutron Spectrum below 10 keV in an Iron Shield Bombarded by Deuterium-Tritium Neutrons and Benchmark Test of Evaluated Nuclear Data from 14 MeV to 1 eV", Nucl. Sci. Eng., 125, 205 (1997).

16) Maekawa, F. : "Integral Test of JENDL Fusion File", JAERI-Conf 97-005, 21 (1997).

17) Maekawa, F. and Ikeda, Y. : "Development of Whole Energy Absorption Spectrometer for Decay Heat Measurement on Fusion Reactor Materials", JAERI-Conf 97-005, 182 (1997).

18) Maekawa, F. : "Compilation of Point-wise Cross Sections for MCNP", JAERI-Review 97-003, 5 (1997) [in Japanese].

19) Maekawa, F. : "Neutron and Gamma-ray Transport Calculation of Fusion Reactor", JAERI-Review 97-003, 18 (1997) [in Japanese].

6. Radiation Shielding

1) Kotegawa, H.: "A Point Kernel Shielding Code, PKN-HP, for High Energy Proton Incident", JAERI-Data/Code 96-020 (1996).

2) Nakashima, H., Hasegawa, A. and Suzuki, T.: "A New Library of Gamma Rays Group Constants for BERMUDA Based on JENDL-3.2 Nuclear Data File", JAERI-Data/Code 96-021 (1996) [in Japanese].

3) Hayashi K. and Sakamoto Y.: "Survey of Thick Target Neutron Yield Data and Accelerator Shielding Experiments", Proc. 2nd Specialists' Meeting on Shielding Aspects of Accelerators, Targets and Irradiation Facilities, OECD Document, 41 (1996).

4) Nakashima, H., *et al.*: "Accelerator Shielding Benchmark Experiment Analyses", Proc. 2nd Specialists' Meeting on Shielding Aspects of Accelerators, Targets and Irradiation Facilities, OECD Document, 115 (1996).

5) Sakamoto, Y., *et al.*: "Approximate Description of Dose Attenuation Profiles of Intermediate Energy Neutrons -I", Proc. 2nd Specialists' Meeting on Shielding Aspects

of Accelerators, Targets and Irradiation Facilities, OECD Document, 147 (1996).

6) Ban, S., *et al.*: "Calibration of a Modified Andersson-Braun Rem Counter", Proc. 2nd Specialists' Meeting on Shielding Aspects of Accelerators, Targets and Irradiation Facilities, OECD Document, 209 (1996).

7) Nakamura, T., *et al.*: "Activation Cross-Section Measurements Using Quasi-Monoenergetic Neutron Field from 20 to 150 MeV", Proc. 2nd Specialists' Meeting on Shielding Aspects of Accelerators, Targets and Irradiation Facilities, OECD Document, 215 (1996).

8) Iwai, S., *et al.*: "Evaluation of Fluence to Dose Equivalent Conversion Coefficients for High Energy Neutrons -Calculation of Effective Dose Equivalent and Effective Dose", Proc. 2nd Specialists' Meeting on Shielding Aspects of Accelerators, Targets and Irradiation Facilities, OECD Document, 233 (1996).

9) Nakane, Y., *et al.*: "Neutron Transmission Benchmark Problems for Iron and Concrete Shields in Low, Intermediate and High Energy Proton Accelerator Facilities", JAERI-Data/Code 96-029 (1996).

10) Nakane, Y., Nakashima, H., Sakamoto, Y. and Tanaka, Sh. : "Measurement of Reaction Rate Distributions in a Plastic Phantom Irradiated by 40 and 65MeV Quasi-Monoenergetic Neutrons", Trans. 18th Int. Conf. on Nucl. Tracks in Solids, Sept. 1-5, 1996, Cairo, Egypt (1996).

11) Nakao, N., *et al.*: "Transmission Through Shields of Quasi-Monoenergetic Neutrons Generated by 43- and 68-MeV Protons -I: Concrete Shielding Experiment and Calculation for Practical Application", Nucl. Sci. Eng., 124, 228 (1996).

12) Nakashima, H., *et al.*: "Transmission Through Shields of Quasi-Monoenergetic Neutrons Generated by 43- and 68-MeV Protons -II: Iron Shielding Experiment and Analysis for Investigating Calulational Method and Cross Section Data", Nucl. Sci. Eng., 124, 243 (1996).

13) Hoefert, M., *et al.*: "Radiation Protection Considerations in the Design of the LHC, CERN's Large Hadron Collider", Proc. 30th Midyear Topical Meeting, San Jose, 343 (1997).

7. Reactor and Nuclear Instrumentation

1) Kishimoto, M., *et al.*: "Reconstruction of Plasma Current Profile of Tokamaks Using

Combinatorial Optimization Techniques", IEEE Trans. Plasma Sci., 24[2], 528 (1996).

2) Ebine, N., Takeuti, S. and Ara, K.: "Experimental Studies on a Structure of Eddy Current Probe for Detection of Magnetic Flux Distorted by a Flaw", Proc. 1st US-Japan Symp. on Advances in NDT, 98 (1996).
3) Ara, K., Ebine, N. and Nakajima, N.: "A Magnetic Interrogation Method for Nondestructive Measurement of Radiation Hardening of Nuclear Reactor Pressure Vessels", Proc. 8th Int. Conf. on Pressure Vessel Tech., Vol. 1, 183 (1996).
4) Ara, K., Nakajima, N. and Ebine, N.: "A New Method of Nondestructive Measurement for Assessment of Material Degradation of Aged Reactor Pressure Vessels", J. Pressure Vessel Tech., Trans. ASME,Vol. 118, Nov., 447 (1996).
5) Kaneko, J. and Katagiri, M.: "Diamond Radiation Detector Using a Synthetic IIa Type Mono-crystal", Nucl. Instrum. Methods in Phys. Reserch, A 383, 547 (1996).
6) Kaneko, J., *et al.*: "A directional neutron detector based on a recoil proton telescope for neutron emission profile monitor", Nucl. Instrum. Methods in Phys. Reserch, A 385, 157 (1997).

8. Reactor Control, Diagnosis and Robotics

1) Suzudo, T., Turkcan, E. and Verhoef, J.P.: "Analysis of Direct Current Signals Measured at the Borssele Reactor", ECN-R--96-010(1996).
2) *idem*: "On the Space-Dependent Dynamics of PWR", Proc. of INCORE 96, 3.2(1996).
3) *idem*: "Monitoring and Analysis of Nuclear Power Plant Signals Based on Nonlinear Dynamical Methodology", J. Nucl. Sci. Technol., 34[3], 240(1997).
4) Suzudo, T., Verhoef, J.P and Turkcan, E.: "Power-Law Spectra Found in Plant Signal of the Borssele NPP - An Analysis Using Wavelet", ECN-R--96-010(1996).
5) Nabeshima, K., Suzuki, K., Nose, S. and Kudo, K.: "Development of Nuclear Power Plant Monitoring System with Neural Network using On-line PWR Plant Simulator", Specialists' Meeting on Monitoring and Diagnosis Systems to Improve Nuclear Power Plant Reliability and Safety, Barnwood, UK, May 14-17 (1996).
6) Nabeshima, K., Nose, S., Kudo, K. and Suzuki, K.: "A Study of Reactor Diagnosis Method with Neural Network using PWR Plant Simulator", JAERI-Research 95-076 (1995) [in Japanese].
7) Hayashi, K. , Shinohara, Y., Watanabe, K. and Nabeshima K.: "Twice Squaring

Method : Non-linear Acoustic Signal Processing Technique for Real-Time Detection of Sodium Boiling," Ann. Nucl. Energy, Vol.23, No.10, 863 (1996).

8) Hayashi, K. , Shinohara, Y. and Watanabe, K.: "Acoustic Detection of In-Sodium Water Leaks Using Twice Squaring Method," Ann. Nucl. Energy, 23 [15], 1249 (1996).

9) Hayashi, K.: "Modeling of nuclear power plant using auto associative neural network," Coordination research reports No.94 - Inverse problem and its around (3), Institute of Statistical Mathematics, 61 (1997) [In Japanese].

10) Ishikawa, N. and Suzuki, K.: "Application of 2DOF Controller for Reactor Power Control", JAERI-Research 96-048 (1996) [in Japanese].

11) Maeyama, S., Ishikawa, N. and Yuta, S.: "Rule Based Filtering and Fusion of Odometry and Gyroscope for Fail Safe Dead Reckoning System of a Mobile Robot", Proc. 1996 Int. Conf. on Multisensor Fusion and Integration for Intelligent Systems, 541 (1996).

9. Heat Transfer and Fluid Flow

1) Ohnuki, A., Kamo, H. and Akimoto, H.: "Prediction of Developing Bubbly Flow along a Large Vertical Pipe by Multidimensional Two-Fluid Model (Development of Multidimensional Two-Fluid Model Code and Analysis under a Low Velocity)", Proc. Japan-US Seminar on Two-Phase Flow Dynamics, Fukuoka, Japan, 75 (1996).

2) Ohnuki, A. and Akimoto, H.: "An Experimental Study on Developing Air-Water Two-Phase Flow along a Large Vertical Pipe: Effect of Air Injection Method", Int. J. Multiphase Flow, 22[6], 1143 (1996).

3) Ohnuki, A., Kamo, H. and Akimoto, H.: "Development of Multidimensional Two-Fluid Model Code ACE-3D for Evaluation of Constitutive Equations", JAERI-Data/Code 96-033 (1996) [in Japanese].

4) Akimoto, H., Kukita, Y. and Ohnuki, A.: "Current and Anticipated Uses of Thermal Hydraulic Codes at the Japan Atomic Energy Research Institute", OECD/CSNI Workshop on Transient Thermal-Hydraulic and Neutronic Codes Requirements, Nov. 5-8 (1996).

5) Takase, K., *et al.*: "A Fundamental Study of a Water Jet Injected into a Vacuum Vessel of Fusion Reactor under the Ingress of Coolant Event", Fusion Technol., 30 [3], 1453 (1996).

6) Takase, K., Kunugi, T. and Seki, Y. : "Effect of Breach Area and Length to Exchange

Flow Rates under the LOVA Condition in a Fusion Reactor", Fusion Technol., 30 [3], 1459 (1996).

7) Takase, K. and Hasan, M. Z. : "Heat Transfer Characteristics of Rectangular Coolant Channels with Various Aspect Ratios in the Plasma-Facing Components under Fully Developed MHD Laminar Flow", 16th IEEE Symp. on Fusion Eng., 16, 1538 (1996).

8) Takase, K., Kunugi, T., Ogawa, M. and Seki, Y. : "Experimental Study of Buoyancy-Driven Exchange Flow from Breaches under the LOVA Condition", 16th IEEE Symp. on Fusion Eng., 16, 317 (1996).

9) Takase, K. : "Numerical Simulation of Heat Transfer in an Annular Fuel Channel with Three-Dimensional Spacer Ribs Setup Periodically under a Fully Developed Turbulent Flow", JAERI-Research 96-031 (1996).

10) Takase, K. : "Numerical Prediction of Augmented Turbulent Heat Transfer in an Annular Fuel Channel with Repeated Two-Dimensional Square Ribs", Nucl. Eng. Des., 165, 225 (1996).

11) Takase, K., Kunugi, T., Ogawa, M. and Seki, Y. : "Experimental Study of Buoyancy-Driven Exchange Flows of a Tokamak Vacuum Vessel in a Fusion Rector under the Loss-of-Vacuum-Event Condition", Nucl. Sci. Eng., 125, 223 (1997).

12) Takase, K., Kunugi, T., Shibata, M. and Seki, Y. : "A Preliminary Experiment for a Loss of Vacuum Events of Fusion Reactors", J. At. Energy Soc. Jpn., 38 [11], 904 (1996) [in Japanese].

13) Ezato, K, Kunugi, T and Shimizu, A.: "Monte Carlo/Molecular Dynamics Simulation on Melting and Evaporating Processes of Material due to Laser Irradiation", ASME HTD-323, Vol. 1, 171 (1996).

14) Kunugi, T., Ezato, K. and Shimizu, A. : "Monte Carlo/Molecular Dynamics Simulation on Laser Melting and Evaporating", Proc. 2nd Japan-Central Europe Joint Workshop on Modeling of Materials and Combustion, Budapest, Hungary, 205 (1996).

15) Kunugi, T. : "Simulation for Merging Bubbles Behavior in Water Column", Proc. 33rd National Heat Transfer Symp. of Japan, 447 (1996) [in Japanese].

16) Sakamoto, Y., Kunugi, T. and Ichimiya, K. : "Numerical Analyses of Buoyancy-Driven Flow with Properties that Depend on the Local Temperature", Thermal Sci. and Eng., 4 [3], 17 (1996) [in Japanese].

17) Ezato, K. and Kunugi. T. : "Molecular Dynamics Simulation of Atomic Beam Bombardment on Solid Surface", Proc. US-Japan Joint Seminar on Molecular and

Microscale Transport Phenomena, Santa Barbra (1996).

18) Kunugi, T. : "Direct Numerical Simulation on Bubble Formation and Agglomeration in Bubble Column", Proc. 10th Computational Fluid Dynamics Symp., 388 (1996) [in Japanese].

19) Sakamoto, Y. Kunugi, T. and Ichimiya, K. : "Experimental and Numerical Flow Visualizations of Mixed Convection with Flow Reversal in a Horizontal Channel with Constant Wall Temperature", J. Visualization of Japan, Vol. 16, No. 63 (1996).

20) Ezato, K., Shehata, M. A., Kunugi. T. and McEligot, D. M.: "Numerical Prediction of Local Transitional Features of Turbulent Forced Gas Flows in Circular Tubes with Strong Heating", JAERI-Research 97-029 (1997).

21) Takase, K., Kunugi, T., Fujii S. and Shibazaki, H.: "Visualization of Exchange Flows Through Breaches of a Vacuum Vessel in a Fusion Reactor under the LOVA Condition", Proc. Flow Visualization and Image Processing, Honolulu, Hawaii, 185 (1997).

22) Kunugi, T., Takase, K., Ogawa, M. and Shibata, M. : "Development of Flow Visualization Technique for Measurment of Exchaneg Flow Rates under the LOVA Condition and Results of the Preliminary Flow Visualization Experiment", JAERI-Tech 96-012 (1996) [in Japanese].

23) Kunugi, T., Takase, K., Ogawa, M. and Seki, Y. : "Fusion Safety Experiments in JAERI", 16th Symp. of Fusion Eng., Vol.2, 1369 (1996).

24) Takase, K., *et al.*: "Results of a Preliminary Experiment Under the Ingress of Coolant Events into Vacuum Vessels of Fusion Reactors", Proc. JSME 5th National Symp. on Power and Energy System, 120 (1996).

25) Takase, K., Kunugi, T., Shibata, M. and Seki, Y. : "Study on Buoyancy-Driven Exchange Flows Under the Loss of Vacuum Events in Fusion Reactors", Proc. JSME 5th National Symp. on Power and Energy System, 122 (1996).

10. Transmutation System

1) Takizuka, T., Nishida, T. and Sasa, T.: "Conceptual Design Study of Accelerator-Driven Systems for Nuclear Waste Transmutation", Proc. 2nd Int. Conf. of Accelerator-Driven Transmutation Techno. and Applications, Kalmar, June 3-7, 1996 , 179 (1997).

2) Nishida, T., *et al.*: "Conceptual Study of Accelerator-Based Transmutation Plant", Proc. 2nd Int. Conf. of Accelerator-Driven Transmutation Technol. and Applications, Kalmar,

June 3-7, 1996, 210 (1997).

3) Nishida, T. , Sasa, T., Takada, H. and Takizuka, T.: "Development of the Code System ACCEL for Accelerator-Based Transmutation Research", Proc. 2nd Int. Conf. of Accelerator-Driven Transmutation Technol. and Applications, Kalmar, June 3-7, 1996, 668 (1997).

4) Takada, H.: "Intranuclear Cascade Calculation Including Nuclear Medium Effects", JAERI-Conf 96-009, 50 (1996) [In Japanese].

5) Takada, H. and Sakamoto, Y.: "A Study of Nuclear Heating and Bulk Shielding of Targets", JAERI-Conf 96-014, 49 (1996) [in Japanese].

6) Takizuka, T.: "Technical Issues of Accelerator-driven Transmutation and a Research Facility", JAERI-Conf 96-014, 170 (1996) [in Japanese].

7) Nishida, T., *et al.*: "Conceptual Study of Target Irradiation Test Facility for Transmutation", JAERI-Conf 96-014, 191 (1996) [in Japanese].

8) Takada, H.: "Nuclear Medium Effects in the Intranuclear Cascade Calculation", J. Nucl. Sci. Technol., 33, 265 (1996).

9) Takada, H.: "Analysis of Experiments with Protons Using An Intranuclear Cascade Model", Genshikaku Kenkyu, 41, 39 (1996) [in Japanese].

10) Meigo S., *et al.*: "Measurements and Analyses of Neutron Spectra Produced in Thick Targets.", *ibid.*, 49 (1996) [in Japanese].

11) Takada, H., Yoshizawa, N. and Ishibashi, K.: "HETC-3STEP Calculations of Proton Induced Nuclide Production Cross Sections at Incident Energies between 20 MeV and 5 GeV ", JAERI-Research, 96-040, (1996).

12) Takada, H., *et al.*: "Spallation Integral Experiment Analysis by High Energy Nucleon-Meson Transport Code", JAERI-Conf 97-005, 114 (1997).

13) Meigo S., *et al.*: "Measurements of Neutron Spectrum from Stopping-Length Targets Irradiated by Several Tens-MeV/u Particles ", *ibid.*, 252 (1997).

11. Accelerator Development

1) Minehara, E.J., *et al.*: "JAERI Free Electron Laser Driven by a Superconducting RF Linac", Gennshiryoku Kogyou (Nucl. Eng.), 42[9], 61 (1996) [in Japanese].

2) Sawamura, M., *et al.*: "Comparison of Measurement and Calculation of Electron Beam Bunching", Proc. 21st Linear Accelerator Meeting in Japan, 317, Tokyo, Sep.30-Oct.2

(1996).

3) Nishimori, N., *et al.*: "Measurement of Spontaneous Emission at the JAERI FEL", Proc. 21st Linear Accelerator Meeting in Japan, 314, Tokyo, Sep.30-Oct.2 (1996).

4) Minehara, E.J., *et al.*: "Recent Status of the Superconducting RF Linac Driver for the JAERI FEL", Proc. 21st Linear Accelerator Meeting in Japan, 18, Tokyo, Sept.30-Oct.2 (1996).

5) Nagai, R., *et al.*: "Electron Beam Derpression due to Undulator Field Roll-off", Proc. 21st Linear Accelerator Meeting in Japan, 320, Tokyo, Sep.30-Oct.2 (1996).

6) Sugimoto, M. and Sawamura, M. : "Digital Feed-Back of SHB Cavity Phase for JAERI FEL", Proc. 21st Linear Accelerator Meeting in Japan, 322, Tokyo, Sept.30-Oct.2 (1996).

7) Minehara, E.J., *et al.*: "Recent Development of the JAERI FEL Driven by a Superconducting RF Linear Accelerator", Proc. 5th Topical Meeting on Free Electron Laser and High Power Radiation, 297, Sendai, Oct.4-5, 1995 (1996).

8) Nishimori, N., *et al.*: "Diagonostic System for resonator length at the JAERI FEL", Proc. 3rd Asian Symp. on FEL, 201, Osaka, Jan. 22 (1997).

9) Minehara, E.J., *et al.*: "Recent Progress of the JAERI Free Electron Laser driven by a Compact Superconducting RF Linac", Proc. 3rd Asian Symp. on FEL, 39, Osaka, Jan. 22 (1997).

10) Sawamura, M., : "Estimation of optical resonator for FEL", Proc. 3rd Asian Symp. on FEL, 195, Osaka, Jan. 22 (1997).

11) Mizumoto, M., *et al.*: "Development of High Intensity Proton Accelerator", Proc. 2nd Int. Conf. on Accelerator-Driven Transmutation Technol. and Applications , June 3-7, 1996, Kalmar, Sweden (1996).

12) Oguri, H., *et al.*: "Development of a Negative Hydrogen Ion Source for a High Intensity Linac", Proc. 18th Int. Linac Conf., Aug. 21-26, 1996, Geneva, Switzerland (1996).

13) Mizumoto, M., *et al.*: "A High Intensity Proton Linac Development for Neutron Science Research Program", *ibid.* (1996).

14) Hasegawa, K., *et al.*: "R&D Status on the High Intensity Proton Accelerator Hin JAERI", *ibid.* (1996).

15) Ito, N., *et al.*: "Development of a Superconducting Cavity for the High Intensity Proton Linac in JAERI", *ibid.* (1996).

16) Kusano, J., *et al.*: "Status of the High Intensity Proton Linear Accelerator Development

In JAERI", Proc. 4th NEA P&T Int. Information Exchange Meeting, Sept. 1996, Mito, Japan (1996).

17) Mizumoto, M.: "Development of High Intensity Proton Accelerator", Proc. 6th China-Japan Joint Symp. on Accelerators for Nucl. Sci. and Their Applications, Oct. 1996, China (1996).

18) Oguri, H., *et al.*: "Development of a High Brightness Negative Hydrogen Ion Source", Rev. Sci. Instrum, 67[3], 1051 (1996).

19) IFMIF-CDA Team (Ed.) Martone, M.: "IFMIF,International Fusion Materials Irradiation Facility Conceptual Design Activity, Final Report", ENEA Frascati Report, RT/ERG/FUS/96/11 (1996).

20) IFMIF-CDA Team (Ed.) Martone, M.: "IFMIF, International Fusion Materials Irradiation Facility Conceptual Design Activity, Executive Summary", ENEA Frascati Report, RT/ERG/FUS/96/17 (1996).

21) IFMIF-CDA Team(Compiled) Rennich, M.J.: "IFMIF, International Fusion Materials Irradiation Facility Conceptual Design Activity, Cost Report", ORNL/M-5502 (1996).

22) Ida, M., Kato, Y., Nakamura, H. and Maekawa, H.: "Preliminary Analyses of Li Jet Flows for the IFMIF Target", JAERI-Research 97-030 (1996).

12. Energy System Analysis and Assessment

1) Sato, O., *et al.*: "Energy and Technology Options for Reducing CO_2 Emissions in Japan", Proc. IEA-ETSAP/Annex VI 1st Workshop, Leuven, Belgium, May 3-10 (1996).

2) Tadokoro, Y.: "High Temperature Gas-Cooled Reactor", Nucl. Almanac, Japan Atomic Industrial Forum, 124(1996) [in Japanese].

3) Sato, O., Tatematsu, K. and Shimoda, M.: "Potential of CO_2 Emission Reduction and Its Cost in Japan", Proc. IEA-ETSAP/Annex VI 2nd Workshop, IIASA, Laxenburg, Austria, Oct.30-Nov.8 (1996).

4) Sakurai, M., *et al.*: "Nuclear Hydrogen Production by Adiabatic UT-3 Thermochemical Process", Hydrogen Energy Progress, XI, 837(1996).

13. Facility Operation and Technique Development

1) Yoshida, T., *et al.*: "The Status of the JAERI Tandem Accelerator", Proc. 9th Workshop of Tandem Accelerator and their Associated Technol., Tokai, July 4-5 (1996).
2) Takeuchi, S., *et al.*: "Acceleration of heavy ions by the JAERI tandem superconducting booster", Nucl. Instr. Methods, A382, 153 (1996).
3) Takeuchi, S., *et al.*: "Status of the JAERI tandem superconducting booster", Proc. 9th Workshop on Tandem Accelerators and Associated Technol., 42, Tokai, July 4-5(1996).

Appendix I

Department of Reactor Engineering Organization Chart

March 1997

Department of Reactor Engineering

Director :	Y. Murao
Deputy Director :	H .Mackawa
Deputy Director :	M. Nakagawa

M. Okazaki M. Yamada
S. Momiyama H. Katsuta(2)

Administrative Service

T. Okabe (Administrative Manager)

I. Nakaigawa	A. Motoishi	M. Sato	H. Tomita
Y. Tamura	J. Kurosawa	S. Maruyama	

Reactor Engineering Facility Operation Division

H. Watanabe (Head)

K. Nakajima	S. Fujisaki	H. Watanabe	K. Kurosawa	M. Takeuchi
K.Satoh	T. Kutsukake	S.Tanaka	T. Sato h	T. Ono
M. Kimura	Y. Watanabe	M. Shibata	Y. Abe	K.Hayasaka
M. Seki	H. Sodeyama			

Accelerators Division

T. Yoshida (Head)

S. Kanda	S. Takeuchi	T. Syouji	I. Ouchi	K. Horie
Y. Tsukihashi	S. Abe	S. Hanashima	S. Kanazawa	N. Ishizaki
H. Tayama	M. Matsuda	Y. Maeda(2)	Y. Sugiyama(1)	H. Ikezoe(1)
M. Oshima(1)	Y. Tomita(1)	M. Sataka(2)	Y. Nagame(5)	
Y. Yamanouchi(1)	S. Ichikawa(5)	T. Ishii(1)	S. Hamada(1)	

Nuclear Data Center

A.Hasegawa (Head)

T. Shirai	J. Katakura	K.Shibata	S. Chiba	T. Fukahori
T. Narita	A. Ichihara	O. Iwamoto	Y. Hayashi	H. Naramoto(11)
H. Takano(7)	M. Sataka(2)	H. Iimura(5)		

Reactor Analysis Laboratory

M. Nakagawa (Head)

T. Fujimura	K.Okumura	T. Kugo	Y. Nagaya	H. Takano(7)

Rector Physics Laboratory

T. Osugi (Head)

S. Iijima	F. Akino	S. Okajima	T. Yamane	T. Nemoto
T. Sakurai	H. Oigawa	M. Andoh	T. Ogawa(3)	

Sensing Technology Laboratory

K. Ara (Head)

H. Yagi	M. Haruyama	H. Yamagishi	H. Itoh	J. Kaneko
K.Seki	Y. Sugimoto	M.Katagiri(1)	T. Kakuta(1)	K. Sakasai(1)
M. Kishimoto(1)	N. Ebine(6)			

Control & AI Laboratory

K. Suzuki (Head)

S. Sasaki	H. Usui	K. Watanabe	Y. Fujii	K. Hayashi
T. Suzudo	K. Nabeshima	N. Ishikawa		

Applied Radiation Laboratory

H. Yasuda (Head)

Y. Sakamoto	H. Nakashima	H. Takada	Y. Nakane	S. Meigo
T. Nagao	T Sasa(8)			

Heat Transfer & Fluid Flow Laboratory

H. Akimoto (Head)

T. Iguchi	T. Kunugi	A. Ohnuki	K. Takase	C. Iwaki
M. Kureta				

Fusion Neutronics Laboratory

Y. Ikeda (Head)

C. Konno	F. Maekawa	Y. Kasugai	Y. Uno	M. Wada
Y. Seki(9)				

Passive Safety Reactor Systems Laboratory

M. Ochiai (Head)

T. Okubo	F. Araya	K. Kunii	H. Yoshida	T. Ishida(4)

Transmutation System Laboratory

T. Takizuka (Head)

T. Nishida	Y. Asahi	S. Ishikura	T. Akie	K. Tsujimoto
T. Mukaiyama(8)	T. Sasa(8)	K. Hayashi(3)	M. Akahori(8)	Y. Kondo(8)
R. Hino(12)				

Proton Accelerator Laboratory

M. Mizumoto (Head)

J. Kusano	K. Hasegawa	Y. Touchi	N. Ouchi	H. Oguri
M. Kinsho	Y. Honda	Y. Okumura(9)	S. Moriyama(10)	

Free Electron Laser Laboratory

E. Minehara (Head)

M. Sawamura	R. Nagai	N. Kikusawa	N. Nishimori	

Intense Neutron Source Laboratory

H. Mackawa (Head)

Y. Kato	M. Sugimoto	Y. Houjyou	I. Ida	M. Chernogubovsky
T. Saito(2)	T. Aruga(2)	H. Nakamura(6)		

Energy System Assessment Laboratory

O. Sato (Head)

M. Shimoda	Y. Tadokoro	K. Tatematsu	S. Hasegawa	

Research Committee

Japanese Nuclear Data Committee
Research Committee on Reactor Physics
Atomic and Molecular Data Committee
Research Committee on Advanced Reactor
Committee on the International Conference on Physics of Reactor

(No.) Original organization of the Shared-Time Members

(1) Advanced Science Research Center
(2) Dept. of Materials Science and Engineering
(3) Dept. of Chemistry and Fuel Research
(4) Office of Nuclear Ship Research and Development
(5) Dept. of Radioisotope
(6) Dept. of Reactor Safety Research
(7) Plutonium Rock-Like Integrated R&D Team
(8) Special Task Force for Neutron Science Initiative
(9) Dept. of Fusion Engineering Research
(10) Dept. of Fusion Facilities
(11) Dept. of Material Development
(12) Dept. of Advanced Nuclear Heat Technology

Appendix II Engineering Facilities Related to the Department

FCA : Fast Critical Assembly

The FCA is a split-table type facility of horizontal matrix structure designed for studying nuclear characteristics of fast reactor. The construction of the FCA was started in 1965 and the first core went critical on 29th April,1967. The main features of facility are summarized as follows:

Type:	Split-table type of horizontal matrix structure
Size:	2.8m×2.8m×1.3m (each half assembly)
Fuel:	Enriched uranium and plutonium (Plate type)
Other material:	Sodium, stainless steel, aluminum oxide, polystyrene etc. (Plate type)
Maximum power:	2kW
Assembly name:	FCA-I～FCA-XIX

Critical experiment using enriched uranium cores were made in 1960s investing basic characteristics of fast reactor cores. Mock-up experiments were extensively made in 1970s for the Fast Experimental Reactor JOYO and the Prototype Fast Breeder Reactor MONJU. In 1980s, the main subjects of experiments were the investigation of the core characteristics of an axially heterogeneous large fast breeder reactor and the core physics study on a high conversion light water reactor. In early 1990s, the reactor physics experiment of metallic-fueled LMFBR was carried out. Since 1995, international benchmark experiments for β_{eff} have been carried out by using FCA XIX core.

FNS : Fusion Neutronics Source

The FNS is an accelerator based D-T neutron source installed for the purpose of investigating the neutronics on the D-T fusion reactor blanket and shielding. It provides following three functions to meet experimental requirement:

1) high intensity DC point source
2) DC point source with wide variation of neutron yield rate
3) Pulsed neutron source

The D-T neutrons are generated via $^{3}T(d,n)^{4}He$ reaction. There are tow beam lines; one is so called 0° line for high current operation, and the other is so called 80° line for rather low current operation. The major specifications of the FNS accelerator are shown in the following;

Items	0°	80°
• Beam current	>20mA	3mA
• Beam size	<15mm	<15mm
• Pulse width	--	2ns
• Frequency	--	2MHz
• Peak current	--	40mA
• Target assembly	Rotating (Water cooled)	Stationary (Water cooled, Air cooled)
• Amount of ^{3}T	<37T Bq	370G Bq
• Neutron yield	4×10^{12}/s	5×10^{11}/s

The major experimental subjects are as follows:

1) Tritium production rate in the various blanket configurations
2) Nuclear heating rate in materials
3) Shielding performance for D-T neutrons in the various configurations
4) Induced effects on materials by D-T neutrons

HTTR : High Temperature Engineering Test Reactor

JAERI is constructing the HTTR to carry out the necessary R&D for establishment and upgrading the HTGR (High Temperature Gas-cooled Reactor) technology basis, and to conduct various innovative basic researches on high-temperature technologies. The HTTR consists of a reactor core, a main cooling circuit, an auxiliary cooling circuit and related components. The size of active core is 2.3m in diameter and 2.9m high. The reactor pressure vessel of 13.2m in height and 5.5m in diameter contains the core, graphite reflectors, core support structures and core restraint mechanism.

Specification of HTTR

Thermal power :	30MV
Outlet coolant temperature :	850℃/950℃
Inlet coolant temperature :	395℃
Fuel:	3~10wt% enriched UO_2
	(coated particle fuel compact)
Fuel element type:	Prismatic block (pin-in block)
Primary coolant:	Helium gas, 4MPa, Downward-flow in core
Pressure vessel:	Steel
Number of main cooling loop:	1
Heat removal:	IHX(10MW) and PWC(30MW)
Containment type:	Steel containment

VHTRC : Very High Temperature Reactor Critical Assembly

The VHTRC is a low-enriched uranium fueled and graphite moderated / reflected critical assembly. At VHTRC, reactor physics experiments have been carried out mainly for the verification of the neutronics design of the HTTR.

Main features of VHTRC

Type:	Split table of hexagonal prism (prismatic block structure)
Size:	2.4m across the flats and 2.4m long
Fuel:	2,4 and 6wt% enriched UO_2
	Coated particle fuel compact, Pin-in-block type
Moderator/reflector:	Graphite
Core temperature:	Room temperature to 210℃ by electric heaters
Maximum power:	10W
Auxiliary equipments:	① Sample heating device (Up to 800℃)
	② Pulsed neutron source

Tandem Accelerator Facility

The tandem accelerator has been used since 1982 for the purpose of studying nuclear physics, nuclear chemistry and solid state physics by means of heavy ions. The specification of the tandem accelerator is as follows:

Accelerator model:	NEC folded type Pelletron 20UR
Terminal voltage:	2.5-18.5MV
Ion beam species:	Ions of stable isotope from proton to bismuth, which can be negatively charged at ion sources
Ion beam energy:	$E_0 + (1 + q) V$ where, E_0 is the injection energy of negative ions into the tandem (normally 0.2 MeV), q the charge state of the ions after electron stripping at the high voltage terminal (typically, q=12 for ions heavier than medium mass ions), and V the terminal voltage.

The facility has 5 target rooms and 13 beam lines. The experimental apparatuses are a heavy ion spectrometer(QDMDQ type), an isotope on-line separator, a neutron scattering goniometer, a 1-meter-diameter scattering chamber, gamma-ray goniometers, irradiation chambers (at room, high and low temperatures) and so on.

A superconducting booster has been built at the end of a beam line in order to increase the energy performance 2 to 4 times. It consists of 46 superconducting quarter wave resonators made of niobium and copper. The total accelerating voltage is 30 MV. The maximum beam energy is as high as 1 GeV or exceeds Coulomb barrier energy necessary for nuclear reactions up to ion (and target nucleus) mass number of about 200. Operations for experiments started in 1995. It has 3 beam lines, which are equipped with a recoil mass separator for studying exotic nuclei, a multi- gamma-ray detector array for nuclear structure study and an irradiation chamber for solid state physics.

国際単位系 (SI) と換算表

表1　SI基本単位および補助単位

量	名称	記号
長さ	メートル	m
質量	キログラム	kg
時間	秒	s
電流	アンペア	A
熱力学温度	ケルビン	K
物質量	モル	mol
光度	カンデラ	cd
平面角	ラジアン	rad
立体角	ステラジアン	sr

表2　SIと併用される単位

名称	記号
分，時，日	min，h，d
度，分，秒	°，′，″
リットル	l，L
トン	t
電子ボルト	eV
原子質量単位	u

1 eV = 1.60218 × 10^{-19} J

1 u = 1.66054 × 10^{-27} kg

表3　固有の名称をもつSI組立単位

量	名称	記号	他のSI単位による表現
周波数	ヘルツ	Hz	s^{-1}
力	ニュートン	N	m·kg/s^2
圧力，応力	パスカル	Pa	N/m^2
エネルギー，仕事，熱量	ジュール	J	N·m
工率，放射束	ワット	W	J/s
電気量，電荷	クーロン	C	A·s
電位，電圧，起電力	ボルト	V	W/A
静電容量	ファラド	F	C/V
電気抵抗	オーム	Ω	V/A
コンダクタンス	ジーメンス	S	A/V
磁束	ウェーバ	Wb	V·s
磁束密度	テスラ	T	Wb/m^2
インダクタンス	ヘンリー	H	Wb/A
セルシウス温度	セルシウス度	℃	
光束	ルーメン	lm	cd·sr
照度	ルクス	lx	lm/m^2
放射能	ベクレル	Bq	s^{-1}
吸収線量	グレイ	Gy	J/kg
線量当量	シーベルト	Sv	J/kg

表4　SIと共に暫定的に維持される単位

名称	記号
オングストローム	Å
バーン	b
バール	bar
ガル	Gal
キュリー	Ci
レントゲン	R
ラド	rad
レム	rem

1 Å = 0.1 nm = 10^{-10} m

1 b = 100 fm^2 = 10^{-28} m^2

1 bar = 0.1 MPa = 10^5 Pa

1 Gal = 1 cm/s^2 = 10^{-2} m/s^2

1 Ci = 3.7 × 10^{10} Bq

1 R = 2.58 × 10^{-4} C/kg

1 rad = 1 cGy = 10^{-2} Gy

1 rem = 1 cSv = 10^{-2} Sv

表5　SI接頭語

倍数	接頭語	記号
10^{18}	エクサ	E
10^{15}	ペタ	P
10^{12}	テラ	T
10^{9}	ギガ	G
10^{6}	メガ	M
10^{3}	キロ	k
10^{2}	ヘクト	h
10^{1}	デカ	da
10^{-1}	デシ	d
10^{-2}	センチ	c
10^{-3}	ミリ	m
10^{-6}	マイクロ	μ
10^{-9}	ナノ	n
10^{-12}	ピコ	p
10^{-15}	フェムト	f
10^{-18}	アト	a

（注）

1. 表1－5は「国際単位系」第5版，国際度量衡局 1985年刊行による。ただし，1 eVおよび1 uの値はCODATAの1986年推奨値によった。
2. 表4には海里，ノット，アール，ヘクタールも含まれているが日常の単位なのでここでは省略した。
3. barは，JISでは流体の圧力を表わす場合に限り表2のカテゴリーに分類されている。
4. EC閣僚理事会指令ではbar，barnおよび「血圧の単位」mmHgを表2のカテゴリーに入れている。

換算表

力	N(=10^5 dyn)	kgf	lbf
	1	0.101972	0.224809
	9.80665	1	2.20462
	4.44822	0.453592	1

粘度　1 Pa·s(N·s/m^2) = 10 P(ポアズ)(g/(cm·s))

動粘度　1 m^2/s = 10^4 St(ストークス)(cm^2/s)

圧力	MPa(=10 bar)	kgf/cm^2	atm	mmHg(Torr)	lbf/in^2(psi)
	1	10.1972	9.86923	7.50062 × 10^3	145.038
	0.0980665	1	0.967841	735.559	14.2233
	0.101325	1.03323	1	760	14.6959
	1.33322 × 10^{-4}	1.35951 × 10^{-3}	1.31579 × 10^{-3}	1	1.93368 × 10^{-2}
	6.89476 × 10^{-3}	7.03070 × 10^{-2}	6.80460 × 10^{-2}	51.7149	1

エネルギー・仕事・熱量	J(=10^7 erg)	kgf·m	kW·h	cal(計量法)	Btu	ft·lbf	eV
	1	0.101972	2.77778 × 10^{-7}	0.238889	9.47813 × 10^{-4}	0.737562	6.24150 × 10^{18}
	9.80665	1	2.72407 × 10^{-6}	2.34270	9.29487 × 10^{-3}	7.23301	6.12082 × 10^{19}
	3.6 × 10^6	3.67098 × 10^5	1	8.59999 × 10^5	3412.13	2.65522 × 10^6	2.24694 × 10^{25}
	4.18605	0.426858	1.16279 × 10^{-6}	1	3.96759 × 10^{-3}	3.08747	2.61272 × 10^{19}
	1055.06	107.586	2.93072 × 10^{-4}	252.042	1	778.172	6.58515 × 10^{21}
	1.35582	0.138255	3.76616 × 10^{-7}	0.323890	1.28506 × 10^{-3}	1	8.46233 × 10^{18}
	1.60218 × 10^{-19}	1.63377 × 10^{-20}	4.45050 × 10^{-26}	3.82743 × 10^{-20}	1.51857 × 10^{-22}	1.18171 × 10^{-19}	1

1 cal = 4.18605 J（計量法）
= 4.184 J （熱化学）
= 4.1855 J （15 °C）
= 4.1868 J（国際蒸気表）

仕事率　1 PS（仏馬力）
= 75 kgf·m/s
= 735.499 W

放射能	Bq	Ci
	1	2.70270 × 10^{-11}
	3.7 × 10^{10}	1

吸収線量	Gy	rad
	1	100
	0.01	1

照射線量	C/kg	R
	1	3876
	2.58 × 10^{-4}	1

線量当量	Sv	rem
	1	100
	0.01	1

（86年12月26日現在）

REACTOR ENGINEERING DEPARTMENT ANNUAL REPORT (April 1, 1996 – March 31, 1997)